UNCLASSIFIED

SECURITY CLASSIFICATION OF THIS PAGE

(2)

DOCUMENTATION PAGE

Form Approved
OMB No. 0704-0188

AD-A243 388

DTIC
ELECTE
DEC 1991
S C D

1b. RESTRICTIVE MARKINGS	
2b. DECLASSIFICATION / DOWNGRADING SCHEDULE	3. DISTRIBUTION / AVAILABILITY OF REPORT Approved for public release, distribution unlimited
4. PERFORMING ORGANIZATION REPORT NUMBER(S) VPI - AOE- 179	5. MONITORING ORGANIZATION REPORT NUMBER(S)
6a. NAME OF PERFORMING ORGANIZATION Aerospace and Ocean Engineering Department	6b. OFFICE SYMBOL (If applicable)
7a. NAME OF MONITORING ORGANIZATION Office of Naval Research Fluid Dynamics Program	
6c. ADDRESS (City, State, and ZIP Code) Virginia Polytechnic Institute and State University Blacksburg, VA 24061	7b. ADDRESS (City, State, and ZIP Code) 800 N. Quincy St. Arlington, VA 22217
8a. NAME OF FUNDING / SPONSORING ORGANIZATION Defense Advanced Research Projects Agency	8b. OFFICE SYMBOL (If applicable)
9. PROCUREMENT INSTRUMENT IDENTIFICATION NUMBER N00014-89-J-1275, N00014-90-J-1909	
8c. ADDRESS (City, State, and ZIP Code) Submarine Technology Program 1400 Wilson Blv. Arlington, VA 22209	10. SOURCE OF FUNDING NUMBERS PROGRAM ELEMENT NO. / PROJECT NO. / TASK NO. / WORK UNIT ACCESSION NO.

11. TITLE (Include Security Classification)

An Experimental Study of a Turbulent Wing-Body Junction and Wake Flow

12. PERSONAL AUTHOR(S)

J. L. Fleming, R. L. Simpson, and W. J. Devenport

13a. TYPE OF REPORT	13b. TIME COVERED	14. DATE OF REPORT (Year, Month, Day)	15. PAGE COUNT
Technical	FROM 6/1/89 TO 8/31/91	1991 September 1	392

16. SUPPLEMENTARY NOTATION

17. COSATI CODES			18. SUBJECT TERMS (Continue on reverse if necessary and identify by block number)
FIELD	GROUP	SUB-GROUP	Boundary Layer Three Dimensional Separation Turbulence
13	10	01	
14	02		

19. ABSTRACT (Continue on reverse if necessary and identify by block number)

Extensive hot-wire measurements were conducted in an incompressible turbulent flow around a wing-body junction. The measurements were performed adjacent to the body and up to 11.56 chord lengths downstream of the body. The junction wake flow entered an adverse pressure gradient region approximately 6 chord lengths downstream. This region's geometry approximated the aft portion of an aircraft fuselage or a submersible's hull. The body geometry was formed by joining a 3:2 elliptic nose to a NACA 0020 tail section at their respective maximum thickness locations. The author's measurements were taken with approach flow conditions of Re_θ = 6,300, and δ/T = .515, where T is the maximum body thickness.

The results clearly show the characteristic horseshoe vortex flow structure. The vortex flow structure is elliptically shaped, with $\omega(W)/\partial Y$ forming the primary component of streamwise vorticity. Near wall measurements show a thin layer of highly concentrated vorticity, underneath and opposite in sign to the primary vortex, which is created by the wall no-slip

20. DISTRIBUTION / AVAILABILITY OF ABSTRACT	21. ABSTRACT SECURITY CLASSIFICATION
☒ UNCLASSIFIED/UNLIMITED ☐ SAME AS RPT ☐ DTIC USERS	NONE
22a. NAME OF RESPONSIBLE INDIVIDUAL	22b. TELEPHONE (Include Area Code) / 22c. OFFICE SYMBOL

DD Form 1473, JUN 86 *Previous editions are obsolete.* SECURITY CLASSIFICATION OF THIS PAGE

UNCLASSIFIED

condition. The development of the flow distortions and associated vorticity distributions are highly dependent on the geometry-induced pressure gradients and resulting flow skewing directions. A quantity known as the "distortion function" was used to separate the distortive effects of the secondary flow from those of the body and the local "2-D" boundary layer. The distortion function revealed that the adverse pressure gradient flow distortions grew primarily because of the increasing boundary layer thickness.

The author's results were compared to several other data sets obtained using the same body shape, enabling the determination of the approach boundary layer effects. The primary secondary flow structure was found to scale on T in the vertical and cross-stream directions, revealing that the juncture flow is driven by the appendage geometry and associated pressure gradients. A parameter know as the *momentum deficit factor* ($MDF = (Re_\theta)(\theta/T)$) was found to correlate the observed trends in mean flow distortion magnitudes and vorticity distribution. Variations in flow skewing were observed to be comparable to changes in MDF, suggesting that this flow parameter changes the effective skewing magnitudes around a wing-body junction. Mean flow distortions were found to increase with decreasing values of MDF.

A numerical study was also performed to gain additional insights into the effects of appendage nose geometry. The velocity distributions around approximately 30 different appendage cross-sections were estimated using 2-D potential flow calculations. A correlation was found between the appendage nose bluntness and the average vortex stretching rate, and also between the inviscid velocity distribution and an experimentally determined non-dimensional circulation estimate.

Table of Contents

List of Tables

List of Figures

List of Symbols

A,B,C,F . . . . . coefficients used in hot-wire data reduction

A^*,B^* . . . . . King's Law Coefficients

b . . . . . general constant used for various curve fits (y-intercept)

C . . . . . chord length of appendage

C_f . . . . . skin friction coefficient based on U_{ref} ($C_f = \tau_w/.5(\rho)(U_{ref})^2$)

C_p . . . . . pressure coefficient, $C_p = 1 - (U/U_{ref})^2$

D . . . . . cylinder diameter

e',e . . . . . rms and instantaneous anemometer voltage fluctuations, respectively

E,E′ . . . . . time mean and instantaneous anemometer voltage

Fo_V . . . . . Vortex Fourier number, $Fo_V = \nu\Omega/(U_{ref})^2$

G . . . . . constant used in equation (3.2)

h . . . . . hot-wire probe pitch sensitivity (eqn. 2.6), or helicity density (eqn. 4.3)

H ..... boundary layer profile shape factor, $H = \delta^*/\theta$, or helicity

k ..... hot-wire probe axial sensitivity (eqn. 2.6), or constant used in eqn. (3.2)

m ..... constant used to curve fit data (slope)

MDF ..... Momenum Deficit Factor, MDF = $(Re_T)^2(\theta/T)$

n ..... King's Law exponent

p_{atm} ..... atmospheric pressure

$Re_{( )}$ ..... Reynolds number based on ( )

S ..... arc length along appendage surface (usually from stagnation point)

Sh ..... Strouhal number, Sh = fL/U_{ref}

Sh_V ..... Vortex Strouhal number, defined by Belik (1973) as $Sh_V = U_{ref}/D\Omega$

T ..... thickness of appendage, or fluid temperature

u',v',w' ..... root mean square of X,Y,Z velocity fluctuations

u,v,w ..... instantaneous X,Y,Z velocity fluctuations

$-\overline{uv},-\overline{uw},-\overline{vw}$ ..... time-mean Reynolds stresses

$-uv,-uw,-vw$ ..... instantaneous Reynolds stresses

u_τ ..... friction velocity, $u_\tau = (\tau_w/\rho)^{.5}$

U,V,W ..... time-mean velocity components in X,Y,Z directions

U′,V′,W′ ..... instantaneous velocity components in X,Y,Z directions

U_E ..... local mean edge velocity

U_{eff} ..... effective mean cooling velocity of hot-wire probe

U_{local} ..... local mean velocity

U_{ref} . . . . . reference velocity (or U_∞)

U^+ . . . . . wall variable, $U^+ = U/u_\tau$

V_S . . . . . velocity tangential to appendage surface

X . . . . . streamwise direction

X_o . . . . . virtual origin of equilibrium boundary layer

X_S . . . . . location of primary separation (saddle point)

X_V . . . . . location of secondary separation (vortex position)

Y . . . . . direction normal to X and Z, positive going away from wall

Y^+ . . . . . wall variable, $Y^+ = Yu_\tau/\nu$

Z . . . . . transverse, or spanwise direction

Greek Symbols

α . . . . . flow angle with respect to a given coordinate system

δ . . . . . boundary layer thickness, where $U/U_{FS} = .995$

δ^* . . . . . boundary layer displacement thickness

$\Delta( )$ . . . . . signifies maximum change in ( )

Γ_X . . . . . Mehta's circulation estimate, defined by equation 5.1

Γ'_X . . . . . a modified form of Γ_X, defined in section 6.3.3

θ . . . . . boundary layer momentum thickness, local vortex panel angle

μ . . . . . fluid viscosity

ν . . . . . fluid kinematic viscosity

ρ . . . . . fluid density

ρ_{LE} . . . . . appendage leading edge radius

ρ_{XY} . . . . . correlation coefficient

σ . . . . . standard deviation of curve fit

τ_w . . . . . wall shear stress

$\Omega_x,\Omega_y,\Omega_z$ . . . . . vorticity in X,Y,Z directions (tunnel coordinates)

Ω . . . . . vorticity of a horseshoe vortex system

Subscripts

$( )_{APP}$ . . . . . approach boundary layer value

$( )_{FS}$ . . . . . local freestream coordinate system

$( )_o$ . . . . . quantity evaluated at stagnation point

$( )_S$ . . . . . local stream coordinate system

$( )_{TC}$ . . . . . tunnel coordinate system

$( )_{Tmax}$ . . . . . quantity evaluated at maximum thickness location

$( )_W$ . . . . . probe (wire) coordinate system

1.0 Introduction

The turbulent flow around a wing-body junction is a very complex, highly three dimensional flow, yet it is commonly encountered. Figure 1.1 shows a simpified wing-body junction flow. Note that the tunnel coordinate system is shown, which will be used to present the majority of the data. The dominating flow characteristic is the mean secondary flow structure known as the horseshoe (or necklace) vortex. Near the appendage nose, the flow is highly unsteady, and velocity histograms show bimodal behavior, termed the zero-flow and backflow modes (Devenport and Simpson, 1990b). Flow visualizations performed in this region using hydrogen bubbles in water (Kim, 1991) show a very complex, highly turbulent flow, where the instantaneous velocity distribution is often very unlike the mean flow patterns associated with either flow mode. The flow field resulting as this unsteady vortical structure is stretched and skewed around the body is complex and not well understood. The author's study attempts to gain insight into the physical nature of the junction vortex flow by examining and comparing his

measurements to those of other researchers with the same body shape, but varying approach boundary layer flow conditions.

The horseshoe vortex is created by a combination of two effects, the skewing and stretching of the transverse vorticity present in the incoming turbulent boundary layer as it passes the wing, and the rolling up of the incoming fluid along the centerline due to the large adverse pressure gradient created by the wing geometry. The term horseshoe vortex is a misleading description, since it is not a typical "tornado" type vortex. The mean vorticity distribution tends to be flattened into a more elliptical shape, and the majority of the streamwise vorticity (Ω_x), except near the appendage surface, is contributed by the transverse skewing term, $\partial W/\partial Y$. Dickinson's (1986a,b) work in particular shows these results to be true.

McMahon *et al.* (1987) discusses the two general types of secondary flow , first described by Prandtl, flows of the "first kind" and "second kind". Secondary flows of the first kind are caused by a shear layer which becomes skewed about a streamwise axis. The subsequent transport of vorticity into the streamwise direction results in the generation of secondary flow. A wing-body junction flow falls into this category. The curvature of the streamlines and resulting pressure gradients skew the shear layer and stretch the resulting streamwise vorticity. Secondary flows of the second kind are caused by Reynolds stress gradients in planes normal to the streamwise direction. This type of flow occurs in corners created by intersecting semi-infinite planes, and is described by Gessner (1973).

There are many initiatives for researching junction flows. Junction flows are commonly present at aircraft wing roots, at ship and submarine appendage-hull junctions, at bases of bridge supports, in turbo-machinery flows, and also in flows with injection, or a component of the injection, normal to the main flow. The vortical flow structure can cause problems such as scouring and deterioration of support foundations, excessive heat transfer, and excessive noise and vibration due to the creation of additional turbulence in the junction. Further research leads to a greater understanding of the physical nature of juncture flows, and also, vortical and 3-D turbulent shear flows in general, enabling control of their adverse effects. Also, additional experimental work gives CFD researchers a larger data base for comparison of numerical results.

The author's investigation of a wing-body junction flow was performed by taking U, W, u', w', and $-\overline{uw}$ hot-wire measurements in 6 YZ planes adjacent to and downstream of an appendage-flat plate junction (Figure 1.1). These planes are designated 5 through 11. The locations of planes 12-15 are given in Table 1.1. The appendage geometry was a 3:2 elliptical nose joined at its maximum thickness to a NACA 0020 section which formed the tail. A total of 64 profiles of approximately 30 points each were taken using a boundary layer type single hot-wire probe. Much farther downstream, U and u' data were obtained in 3 YZ planes (planes 13-15) located in the far-wake region, again using a single hot-wire probe. A total of 45 profiles were taken in these planes. Two of these far wake planes were located in a diverging section of the wind tunnel, in order to study the effects of an adverse pressure gradient on the trailing legs of the horseshoe vortex. This configuration, described fully in section 2.2, simulates the conditions over the aft

portion of a body with a tapering surface, such as an aircraft fuselage or the hull of a submersible.

The main emphasis of this study, however, is the comparison of data from junction flow experiments involving the same body shape, the aforementioned 3:2 elliptic nose with a NACA 0020 tail. The purpose of the comparisons is to determine the approach boundary layer effects on the junction flow. Section 1.1.2 describes these experiments, and section 1.2 outlines the author's research goals. The literature review focuses on junction flow experiments which examined the effects of varying the approach boundary layer, since these studies are most relevant to the author's work.

1.1 Review of Previous Work

A great amount of previous work has been done researching the flow in a turbulent wing-body junction. Past research has involved various measurement methods and also various appendage geometries. Juncture flow studies can be divided into two broad categories based on geometry, 1) flows around a cylinder mounted normal to a flat plate, and 2) flows around a more streamlined or airfoil shape mounted normal to a flat plate.

1.1.1 Cylindrical Appendage-Flat Plate Juncture Flow Studies

Measurements for these flows are usually taken only upstream of the maximum thickness due to the large scale separation and unsteadiness present in the large wake region. These experiments are useful in studying the formation of the horseshoe vortex, and the flow structure in the steady flow region is similiar to that in the nose regions of more streamlined shapes.

Baker (1980) studied the changes in the horseshoe vortex structure at the base of a cylinder due to variations in the incoming boundary layer. Using oil-flow visualization, he examined the change in distances X_S and X_V as Re_{δ^*} and δ^*/D changed. X_S is the location of the saddle point, or primary separation, and X_V is the location of the secondary separation, which indicates the main vortex position. Re_{δ^*} is the Reynolds number based on the approach boundary layer displacement thickness (δ^*), and D is the cylinder diameter. Figure 1.2 shows sketches of the oil-flow pattern observed, and the significance of X_S and X_V. Baker conjectured that a 4-vortex mean flow model was applicable for this pattern, also shown in Figure 1.2. By measuring mean pressure along the flow centerline, he found a local minimum in pressure which corresponded to the primary vortex location, X_V (see Figure 5.3). From these mean pressure measurements, Baker postulated that changes in Re_{δ^*} or δ^*/D do not change the vertical dimension of the vortex system in the plane of symmetry. From the oil-flow results, he concluded that the 4-vortex mean flow model existed along the centerline for $4{,}000 < Re_{\delta^*} < 90{,}000$ and $.0333 < \delta^*/D < .25$.

Later studies by Baker (1985) attempt to further quantify the effects of Re_{δ^*} and δ^*/D on the locations of minimum and maximum τ_w, corresponding to X_S and X_V respectively. Using his data as well as data from Ram (1963), Langston and Boyle (1982), and Peake and Galway (1965), he attempted to correlate X_V/D, $X_S/D = f(Re_{\delta^*}, \delta^*/D)$ for laminar and turbulent boundary layers. For turbulent boundary layers, his results were

$$X_V/D = 0.100(Re_{\delta^*})^{.1} \qquad \text{For } 1{,}000 < Re_{\delta^*} < 11{,}000$$

$$X_S/D = 0.373(Re_{\delta^*})^{.033} \qquad \text{For } 1{,}500 < Re_{\delta^*} < 10{,}000$$

$$X_S/D = 15.6(Re_{\delta^*})^{-.35} \qquad \text{For } 10{,}000 < Re_{\delta^*} < 18{,}000$$

where X_V and X_S are measured from the cylinder leading edge. Note the lack of dependence on δ^*/D. Baker (1985) also presents a theoretical investigation supporting the lack of dependence on δ^*/D. Note that the author has included the references for Ram and Peake and Galway for informational purposes only, as he was unable to obtain copies of these references.

Belik (1973) performed research similiar to Baker's. The goal of his experimental work was to correlate X_S/D, found using oil-flow visualization, for a cylinder-end wall junction flow, as functions in the form $f(Re_D, Sh_V)$ or $f(Sh_V, Fo_V)$. Sh_V is the vortex Strouhal number, defined by Belik as $U_{ref}/(D\Omega)$, where Ω in this case is the vorticity of the horseshoe vortex system. He assumed Ω to be constant in a plane perpindicular to the cylinder's surface. Fo_V is the vortex Fourier number, defined as $\nu\Omega/(U_{ref})^2$. Belik assumes that $\Omega \sim \omega_X \sim (\partial(U)/\partial Y)_{ave}$. For a typical turbulent boundary layer, he assumes

$(\partial(U)/\partial Y)_{ave} = .5(U_{ref}/\delta)$. After substitution, $Sh_V = 2\delta/D$, and $Fo_V = .5(\nu/U_{ref}\,\delta)$. It can then be seen that $Fo_V \sim Re_\delta^{-1}$.

Belik also found X_S/D for a variety of artificially produced turbulent boundary layers with differing $(\partial(U_{ref})/\partial Y)_{ave}$ values, and therefore different values of Fo_V. He reached the final functional relationship of $X_S/D = f(Fo_V, Re_D)$ for the range $36{,}000 < Re_D < 220{,}000$ and $.4 \times 10^{-5} < Fo_V < 3.5 \times 10^{-5}$. The function correlating the data is

$$X_S/D = (10^{-5}/Fo_V)^{.19}(.516 + .111(10^{-5}Re_D)) \qquad (\sigma = .016)$$

This is a very weak function of Re_D. The approximation to $X_S/D = f(Fo_V)$ is

$$X_S/D = .57(10^{-5}/Fo_V)^{.19} \qquad (\sigma = .0202)$$

One can see that $X_S/D \propto (Re_\delta)^{.19}$. This is the same type of functional relationship which Baker later observed.

Belik also measured mean static pressures at the wall along the centerline. For the cases presented, the local minimum in C_p corresponding to the vortex core location was relatively constant, remaining at $X_V/D = .21$ (again comparable to Baker's results). The oil-flow visualizations shown seem to indicate a vortex system similiar to Baker's. Unfortunately, Belik does not give details of the incoming boundary layer parameters such as ϑ or δ^* for a more direct comparison to Baker's work. The estimated range of δ/D is .097 to 1.48, and from this, an estimate of the δ^*/D range would be approximately $.015 < \delta^*/D < .22$. This corresponds to a Re_{δ^*} range of 540 to 48,400.

Eckerle and Langston (1987) also performed studies on a junction flow around a circular cylinder. They performed surface static pressure measurements, surface flow visualizations, and mean velocity measurements with a five-hole probe. Their test

conditions were U_{ref} = 30.5 m/s, Re_D = 550,000, Re_{δ^*} = 8,470, Re_θ = 6,270, δ/D = .099, and δ^*/D = .0154, where D = 29.8 cm. The saddle point location, X_S/D, for these flow conditions was approximately .4, while X_V/D was approximately .22. Baker's correlation gives values of .503 and .25 respectively. Eckerle and Langston concluded that for their case, the single primary vortex model applied, and that the horseshoe vortex structure became fully formed between the 5° and 25° planes (centerline plane at 0°). Note that their vortex model conclusion does not violate Baker's earlier findings, as δ^*/D = .0154, which is outside the range given by Baker.

LaFleur and Langston (1990) present an intriguing study of an iceformation design of a hull near a cylinder/hull juncture. The geometrical features of the resulting iceformation are directly related to flow and thermal boundary conditions. The test parameters varied were $\theta_T = (T_F - T_o)/(T_o - T_R)$ and Re_D, where T_F = temperature of fluid, T_o = freezing temperature, and T_R = temperature of boundary surface. The Re_D range was 737 to 1,843.

LaFleur and Langston present sketches of their results, showing separations as ridges in the ice, and valleys being formed by reattaching flow. For θ_T fixed at .37, the Re_D = 737 case resulted in only 1 visible vortex in the plane of symmetry, while the other cases produced 2 predominate vorticies (Baker's 4 vortex model). Finally, they found when using an iceform contour in the junction, a 5 to 6% drag reduction over the flat-plate case could be achieved.

Agui and Andreopoulos' (1990) study of the flow around a cylinder was concerned with the mean and fluctuating wall static pressures. Their main goal was an increased

physical understanding of junction flows. They were hoping to gain information about the vorticity flux out of the wall by measuring the wall static pressures. They describe the relationship between the wall vorticity flux and wall pressure in a later paper (1991). From the momentum equation evaluated at the wall, the equations are

$$\frac{\partial(p)}{\partial X} = -\mu\frac{\partial(\Omega_Z)}{\partial Y}$$
$$\frac{\partial(p)}{\partial Z} = \mu\frac{\partial(\Omega_X)}{\partial Y} \qquad (1.1)$$

These relationships show the importance of the wall pressure gradient caused by the body.

Two cylinder junction flow cases are presented, $Re_D = 1.0 \times 10^5$ and 2.2×10^5 (Agui and Andreopoulos, 1990). The given X_S/D values for these cases are .26 and .32, respectively. The time averaged flow structure was taken to be represented by the 2 vortex model (1 main vortex). An estimate of the boundary layer thickness is given as $\delta/D = .1$. It is not clear if this is constant for both Reynolds numbers, and one would think that δ would decrease as Re_D increased. However $\delta/D = .1$ gives Re_{δ^*} estimates of 1,500 and 3,300 for δ^*/δ ratios of .15, and $\delta^*/D = .015$, which shows X_S increasing as Re_{δ^*} increases, agreeing with Baker's and Belik's results.

1.1.2 Streamlined Appendage-Flat Plate Juncture Flow Studies

The past decade has seen much research concerning the juncture flow around a streamlined appendage. The pressure gradients around the aft portion of most streamlined shapes, unlike a cylinder, are usually mild enough to delay separation until the trailing edge region. As oil-flow patterns show (Figure 3.10a), most streamlined appendage

juncture flows have a distinctive fish-tail wall-limiting streamline pattern, resulting from separation at the trailing edge. Because of the lack of large scale separation, and corresponding unsteadiness, measurements can be made adjacent to and in the wake of the appendage.

Dickinson (1986a,b) presents a juncture flow study on a body with a 3:2 elliptic nose joined to a 0020 tail section at their respective maximum thicknesses. He first tested a 0020 appendage shape, but he reports that this more streamlined shape did not produce crossflow velocities as great as the modified 0020 appendage. The larger crossflow velocities caused by the more rounded, blunter nose enables the trailing horseshoe vortex structure to be more easily identified.

Devenport *et al.* (1990) examined the horseshoe vortex legs produced by the modified NACA 0020 geometry in a YZ plane at X/C = 3.00. Two junction geometries were used: the unmodified junction (appendage surface normal to floor at wing-body intersection), and a junction wrapped by a fillet of radius 3.81 cm (.53 T). Two different approach boundary layers were produced. The *thick* boundary layer case is identical to the author's approach flow. The *thin* boundary layer case, created using a false floor, was approximately 50% as thick as the former case (see Table 3.3). Devenport *et al.* mainly studied the effects of adding the fillet to the appendage base. They found that the vortex legs were further apart and that the region of boundary layer distortion was larger when using the fillet. They concluded that the fillet's primary consequence was to increase the effective appendage nose radius. It was also seen that the horseshoe vortex was only slightly effected by the changing approach boundary layer thicknesses.

In addition to the above studies, many other experiments have been performed using the modified NACA 0020 appendage shape, which has become somewhat of a standard test case within the past decade. Aside from the studies done using it within the Aerospace and Ocean Engineering Department at Virginia Tech, measurements were done on this shape in the Mechanical Engineering Department at Virginia Tech (Shin, 1989). McMahon *et al.* (1987) also performed junction flow studies using the modified NACA 0020 geometry. Table 1.1 lists the locations and types of measurements taken in juncture flows with this same geometry. Note that Table 1.1 includes measurements made in YZ planes only, which are comparable to the author's measurements. Complete data sets from Dickinson (1986b), McMahon *et al.* (1987), Devenport and Simpson (1990a), and Devenport *et al.* (1990) were made available to the author on disk, while tabular data and figures from Shin (1989) were available. Selected profiles of Shin's data, with Z/T locations matching the author's locations almost exactly, were entered into computer data files for plotting and numerical calculations. The availablity of data from the other researchers made comparison of their experimental results possible.

Other research done on the junction flow produced by the modified NACA 0020 appendage shape includes upstream boundary layer profiles along a streamline, showing the pressure induced skewing of the incoming flow (Olcmen, 1990), and skin-friction measurements made with an oil-flow laser interferometer (Ailinger, 1990). Shin (1989) reports on the effects of various short, strake-like leading edge fairing geometries added to the modified NACA 0020 appendage. Devenport and Simpson (1990b) made LDV measurements in the plane of symmetry at the appendage nose. These results, as

mentioned at the beginning of the chapter, clearly show the bimodal characteristics of the flow in the nose region. The wind tunnel and inflow boundary layer parameters for Devenport and Simpson's LDV measurements were the same as for the author's work. Rife (1991) studied the relationship between velocity and surface pressure fluctuations in the bimodal flow region using an LDV and microphones. Kim (1991) also made measurements on the same appendage shape, but in a water tunnel. Using an LDV, he made measurements in the plane of symmetry at two different Reynolds numbers. His data also show the bimodal characteristics of the flow quite clearly.

Many other experimenters have researched wing-body flows around various streamlined appendages. Mehta (1984) studied the effects that the appendage nose shape had on the transport of vorticity in the streamwise direction. Shin (1989) also examined the effects of nose geometry on the horseshoe vortex mean flow structure. The results of these researchers are used in chapter 6.

Kubendran *et al.* (1986) examined the turbulent juncture flow around a constant thickness body with a 3:2 elliptic nose. They documented the mean vortex path, and noted similarities between the turbulent shear stresses and the mean flow strain rates. Similarities between profiles of u' and w' were also found. Shabaka and Bradshaw's (1981) measurements in a wing-body junction revealed that the eddy viscosities for the $-\bar{u}\bar{v}$ and $-\bar{u}\bar{w}$ Reynolds stresses are anisotropic and are negative over large regions. They concluded that calculation methods based on eddy viscosities are likely to be unsuitable for juncture flows.

Wood and Westphal (1991) present measurements taken in a lifting wing-body junction. They report that the trailing suction-surface leg is the stronger of the two trailing vorticies. Since streamlines passing over the suction side of the appendage are more distorted, this is an intuitive result. Moore and Forlini examined the junction flow around a Rankine half-body, a geometry with a well known potential flow solution. Their measurements, which include mean velocity results in 4 cross-stream planes, were primarily intended for validation of numerical calculations.

Rood (1984) investigated the temporal flow features inherent in a wing-body junction flow. He found distinct flow structures in the approach boundary layer, in the wing-body horseshoe vortex, and in the junction vortex-wake flow. These flow structures were all due to the presence of the wing, one resulting from the distortion of pre-existing structures in the approach boundary layer, and the others newly created by the wing. Rood reports that the structures' characteristic frequencies were at least an order of magnitude lower than the Strouhal-type shedding from the wing trailing edge.

Several researchers have performed experiments involving vortices embedded in turbulent boundary layers. Cutler and Bradshaw (1986) studied the pair of trailing vortices generated by a delta wing along a flat plate, simulating a close-coupled canard and aircraft wing. Westphal *et al.* (1985) examined the behavior of a vortex embedded in a turbulent boundary layer subjected to an adverse pressure gradient, using zero pressure gradient results for comparison. Shizawa and Eaton (1990) investigated the interaction of a vortex embedded in a skewed turbulent boundary layer, a configuration similiar to the trailing edge region of a streamlined appendage-flat plate junction.

Westphal *et al.* and Shizawa and Eaton both used half-delta wings protruding from the flat plate to generate the embedded vortices. Even though the vorticity magnitudes encountered and distribution patterns produced by these flows are somewhat different than encountered in a junction vortex, the results of these studies are relevant to the author's work and are discussed in chapter 4.

1.1.3 Numerical Work in Appendage-Junction Flows

Some numerical work has been performed on the juncture flow problem for both laminar and turbulent flows. While accurate solutions for the laminar cases are relatively common, the turbulent flow solutions suffer from the lack of an adequate 3-D turbulence model.

Visbail (1991) studied the laminar juncture flow around a circular cylinder. He obtained solutions for $\delta/D = .1$ and Re_D values in the range of 500 to 5,400. He observed a non-unique relationship between wall limiting streamline patterns and the flow above the plate. He also observed that the flow became unsteady above $Re_D = 4{,}000$, with the resulting Strouhal number (defined as fD/U_{ref}) equal to .21. This result agrees quite well with Sh = .20, found by experiment (referenced in Visbail, 1991). Visbail reports that this unsteady behavior is not due to Karman vortex shedding in the cylinder's wake.

Deng *et al.* (1990), performed calculations on the turbulent flow in the junction around an appendage with the same geometry studied by the author and several others. The inflow boundary layer conditions matched Dickinson's thick boundary layer test case (1986a,b, see Table 3.3). The streamwise velocity contours compare well qualitatively

with experimental results, but quantitatively, the calculated isovels are consistently less than the experimental results. This may be due to appendage blockage effects present in Dickinson's test. These effects are discussed in section 4.4. No turbulent fluctuation results are presented.

Sung and Lin (1988) obtained solutions to the Navier-Stokes equations using the Baldwin-Lomax turbulence model for the flow through a wing-body junction. Their primary interest was to investigate the effects of adding triangular shaped fairings to the leading and trailing edges of the appendage, similiar to fairings used by Shin (1989). From the three different leading edge fairing configurations, they found that a longer fairing, which extended further upstream, was optimum in terms of reducing the mean velocity distortion in the wake. They also determined that trailing edge fairings are marginally beneficial when combined with a leading edge fairing. Maximum total drag reduction was 5% less than the no fairing case.

1.2 Author's Research Program and Objectives

1.2.1 Experimental Research Goals

The experimental research program of the author was designed to meet several goals. 1) To further expand the 3:2 elliptic nose, 0020 tail junction flow database with high quality (low uncertainty) measurements. 2) To examine the data closely to gain a more complete understanding of the physical nature of the flow. 3) Most importantly, to

compare these data to other measurements taken in juncture flows with the same geometry. The other data sets to be used for comparisons are shown in Table 1.1. Table 3.3 shows the inflow conditions for each data set, and section 3.2 discusses the varying approach boundary layer parameters. Through comparisons, the effects of Re_{δ^*}, Re_θ, δ^*/T, U_{ref}/T, U_{ref}/δ, and other parameters on the junction flow will be more fully understood.

A final goal is to compare the author's hot-wire data to that obtained by LDV where possible. Olcmen (1990) noticed discrepancies in comparing the results of hot-wire and LDV measurements. He found that near wall turbulence measurements and mean velocity measurements very near the wall ($Y^+ < 50$) did not agree between the two experimental techniques. Additional information is sought concerning this problem. C_f estimates were also made and compared to Ailinger's (1990) results.

1.2.2 Description of Numerical Work

In addition to wind tunnel measurements, numerical computations using vortex panels were used to gain insight into the effects of geometry on the horseshoe vortex structure. This was accomplished by using a 2-D inviscid vortex panel calculation given by Kuethe and Chow (1986) to predict the velocity distributions around various appendage shapes.

The geometry of an appendage effects the distribution and total amount of vorticity (circulation) present in a horseshoe vortex in two ways. High velocity gradients around the appendage nose lead to high rates of vortex stretching, increasing the peak

vorticity and affecting the shape of the vortex structure. In addition, the geometrical bluntness of the appendage causes a stronger adverse pressure gradient, increasing the initial vortex roll-up, which increases the circulation in the horseshoe vortex.

Mehta (1984) experimentally studied the horseshoe vorticies produced by different appendage nose shapes. He verified that increased appendage bluntness causes a stronger, more structured vortex. Also, by comparing their work to other researchers, Kubendran *et al.* (1986) found that the horseshoe vortex path and its strength are related to the nose slenderness ratio. They report that the secondary flow in a junction created by an appendage with a large nose slenderness ratio (12:1) is mainly due to the cross-stream gradients of the Reynolds stresses (Prandtl's "second kind" secondary flow).

The numerical work was carried out by computing the velocity distributions around a wide variety of appendage shapes. The final results include correlations between appendage geometries and average vortex stretching rates, and between a vorticity transport parameter (determined numerically) and a non-dimensional circulation estimate from Mehta's experimental work (1984). The numerical research goals and results are fully discussed in chapter 6.

2.0 Experimental Apparatus and Techniques

Unless otherwise noted, all data presented were taken in the Virginia Tech Low Speed Boundary Layer Tunnel. This tunnel has been used in much previous work at VPI and SU as well as Southern Methodist University (Ahn, 1986, Devenport and Simpson, 1990a, 1990b, Devenport *et al.*, 1989, Simpson *et al.*, 1980).

This chapter describes the appendage, wind tunnel, instrumentation and experimental techniques, data collection and reduction, and uncertainty estimates.

2.1 Appendage Description

The appendage (or wing) used in this study was made up of a 3:2 elliptic nose joined to a NACA 0020 tail section at its maximum thickness. The section coordinates are given in Table 2.1, and Figure 2.1 shows its cross section. As mentioned in chapter

1, this body shape has been studied in many other experiments. It has a maximum thickness (T) of 7.17 cm, a chord (C) of 30.5 cm, and is 22.9 cm high.

To prevent unsteadiness due to natural flow transition, boundary layer trips made from 6.35 mm wide strips of 120 grade sandpaper were attached to the appendage with the sandpaper leading edge positioned 28.2 mm downstream of the wing leading edge. Appendage boundary layer data were presented by Devenport and Simpson (1990a) using these trips. The appendage boundary layer thickness at its trailing edge is $\approx .25$ T in the two dimensional flow region. The symmetry of the appendage boundary layer was taken to be a good indication of overall flow symmetry (Figure 3.7). Devenport and Simpson also report no separation is visible in the two dimensional flow region of the appendage ($1.06 < Y/T < 2.12$) using oil-flow visualization. Section 3.1.2 presents the data describing the appendage boundary layer.

2.2 Wind Tunnel

The Virginia Tech AOE Low Speed Boundary Layer Tunnel test section is shown in Figure 2.2. The test section, which measures 8 m long by .91 m wide, can be divided into 3 regions as shown. These different regions will be described in following sections. The test flow for this open circuit tunnel is driven by a 25 horsepower centrifugal blower. The flow passes through an air filter, blower, fixed-setting flow damper (to control flow speed), a section of honeycomb to straighten and remove flow swirl, 7 turbulence screens,

and a two dimensional 4:1 contraction nozzle before entering the test section. The test section floor is constructed of fin-form plywood 19 mm thick, except for two access panels around the wing, which are 6.4 mm plexiglas. The side walls are float plate glass, and the ceiling is made of 6.4 mm plexiglas reinforced with aluminum channel.

2.2.1 Test Section Description, Regions 1 and 2

Within the first 1.63 m of region 1, the flow undergoes a further 1.5:1 contraction, ending at a throat 25.4 cm in height. From the throat to the end of region 2, the upper wall diverges slowly to a height of 26.67 cm over a length of 3.54 m. This divergence reduces the variation in C_p of the test flow due to boundary layer growth along the floor and ceiling. A 6.3 mm forward facing step trips the boundary layer at the beginning of region 1.

Plexiglas wall liners 6.4 mm thick support the ceiling in regions 1 and 2. Positioning the wall liners 330 mm (X/C = 1.08) upstream of the appendage leading edge, and 203 mm (X/C = .605) downstream of the trailing edge allowed the appendage blockage effects to be reduced by crudely approximating its two dimensional potential flow streamlines (Figure 2.3). Note that the discontinuities caused by the wall liners were faired over with tape. By comparing potential flow results to measurements of the static pressure at the wall, Devenport and Simpson (1990a) show the absence of any substantial blockage effects in the flow.

2.2.2 Test Section Description, Region 3

Region 3 of the test section was modified by the author for gathering appendage far-wake data. It was designed to study the decay of the trailing vortex/wake structure in the presence of an adverse pressure gradient. This region utilizes the tunnel's active boundary layer control to bleed off a portion of the incoming side wall boundary layers. Figure 2.4 shows oil flow results of the areas around the boundary layer control suction slots. The oil flows and tufts were used to adjust the mass flow through the slots so that the inner side wall boundary layer would be bled off while maintaining a two dimensional flow in the freestream. The active boundary layer control system is further described by Simpson *et al.* (1980). A boundary layer "scoop" was built into the ceiling of region 3 (Figure 2.5). Its purpose was to skim off the inner 2 cm of the ceiling boundary layer, and thus prevent separation in the diverging section.

Figure 2.5 also presents the dimensions of the diverging section. Research by Reneau, Johnston, and Kline (1967), shows that for a diffuser with these dimensions, no separation should occur downstream of the throat. The inner side wall liners were made of 9.5 mm thick plexiglas, while the ceiling sections were made of 6.4 mm thick plexiglas reinforced with aluminum channel. The scoop section was constructed of plexiglas 3.2 mm thick to facilitate the needed ceiling curvature. The leading edge was tapered to 1.6 mm, rounded, and angled upwards approximately 2° to prevent separation off the lower side of the scoop. Figure 2.6 shows a portion of the results from an oil-flow visualization performed at the scoop leading edge. No separation was in evidence at the scoop leading edge.

A back-pressure screen was constructed to match the static pressure in region 2 to the atmospheric pressure and minimize air leakage into the test section. After adjusting the open area ratio of the screen with tape, the final pressure difference was approximately -.1 inches of water (atmospheric pressure slightly greater than region 2 pressure). This allowed for a small factor of safety, as a positive pressure difference would tend to raise the test section ceiling in regions 1 and 2. The ceiling section in region 3 had to be held in place due to the increasing internal pressure as the flow diverged. Oil flow visualization was used extensively in region 3 to assure that the flow was not separating, particularly in the side wall/floor junction areas. The oil flows showed no substantial separation present for $X/C < 12$, where C is the appendage chord length.

2.2.3 Appendage Mounting

The leading edge of the appendage was located 1.39 m downstream of the throat in region 2. The ceiling curvature defining the start of region 3, begins 2.24 m downstream of the appendage leading edge. The body was mounted at zero incidence and sweep along the tunnel centerline. A 37 mm gap was left between the end of the appendage and the tunnel ceiling to prevent the formation of a second junction vortex along the ceiling.

2.2.4 Wind Tunnel Performance

The flow characteristics of regions 1 and 2 have been documented in previous work. Devenport and Simpson (1990a) report that the freestream flow of region 2 is uniform to within .5% in the spanwise (Z) direction and 1% in the vertical (Y) direction, with a rms turbulence intensity of .2% at U_{ref} = 27 m/s. Detailed documentation of regions 1 and 2 was performed by Ahn (1986). He reports that the boundary layer in regions 1 and 2 is an equilibrium boundary layer and that it closely satisfies the two dimensional momentum integral equation. Also, the velocity and pressure spectra show no preferred frequencies. Figure 2.7 shows mean velocity measurements in the potential core of regions 1 and 2, and displays the lack of any substantial pressure gradients past X = 70 inches (1.78 m).

The flow characteristics in the diverging section (region 3) were documented by the author and will be discussed in section 3.1.

2.3 Experimental Techniques and Instrumentation

2.3.1 Coordinate Systems

Four different coordinate systems were used to reduce and present the data; wire, local stream, local freestream, and tunnel coordinate systems. The Y-axis for all of these systems is always perpendicular to the floor. Figure 2.8 shows the relationship between tunnel and local freestream coordinates. The local freestream coordinates are defined by

setting W = 0 in the freestream. This coordinate system is fixed with respect to Y, but its orientation changes as X and Z change. The tunnel coordinate system is fixed for all X, Y, and Z, and its orientation is shown in Figure 1.1. The angle α is defined positive by right-hand rule convention, and when subscripted, the subscript refers to the coordinate system from which the angle is measured (the angle in Figure 2.8 would be α_{TC}). The majority of the data is presented in tunnel coordinates.

Figure 2.9 shows two coordinate systems fundamental to the initial data reduction, the wire and local stream coordinate systems. The wire system is fixed with respect to the hot-wire probe. The local stream coordinate system is defined by W = 0 at every X, Y, and Z location. Outside the boundary layer, the local freestream and local stream coordinates should be identical. Figure 2.9 also shows the local flow angle being measured from some arbitrary coordinate system. The importance of the wire and local stream coordinate systems can be seen in section 2.5.2.

2.3.2 Instrumentation and Data Collection

All data collection, with the exception of the streamwise traverses made in the potential core of region 3, was performed with a TSI model 1218-T1.5 boundary layer hot-wire probe. The streamwise traverse data was collected with a TSI model 1210-T1.5 straight hot-wire probe. Each probe sensor is approximately .004 mm in diameter and 1.3 mm in length.

For both probes, a Miller-type integrated circuit constant temperature hot-wire anemometer was used. Details of this anemometer are given by Miller (1976). A method

of frequency response testing using a sine wave generator is given by Simpson *et al.* (1979). Employing this method, the author found the frequency response of the anemometer to be in excess of 20 kHz for an overheat ratio of 1.7 and U_{eff} = 27 m/s.

Calibrations were made with a TSI model 1125 calibrator from flow speeds of approximately 9.5 m/s to 29.5 m/s. Using King's Law for a constant temperature anemometer in incompressible flow,

$$E^2 = A^* + B^* U_{eff}^n \tag{2.1}$$

the velocity versus output voltage relationship could be linearized within the data reduction computer program. The probe was calibrated by fixing the exponent n at .45 and then finding the coefficients A^* and B^* using a linear least-squares curve fit. The computer then varied n to obtain the maximum correlation coefficient. The final value of n was usually in the range $.39 < n < .41$. Correlation coefficients in excess of .99999 were attainable using this method.

Figure 2.10 shows a block diagram of the equipment used for calibration and data acquisition. An IBM AT computer with a 12 bit Data Translation DT2801 A/D converter was used to sample, reduce, and record the anemometer signals. The offset amplifier, with a cutoff frequency of approximately 40 kHz, served as a signal conditioner for the A/D board and also as a signal buffer. The voltmeters were used to calibrate the amplifier (which was done every 60 to 90 minutes) and also, along with the oscilloscope, to monitor the anemometer signal.

U_S, u'_S, w'_S, $-\overline{uw}_S$, and α_{TC} measurements were taken at a single location by yawing the hot-wire (held in the XZ plane) about the Y-axis (perpendicular to the floor)

to three different angles. These angles were approximately ±30° and 0° relative to the local streamwise direction. This procedure is explained in greater detail in section 2.5. At each orientation, 7000 samples were taken at 5 kHz, for a record length of 1.4 seconds. The effective record length was longer than this, since the computer processed blocks of 1000 samples, each block taking approximately 5 to 8 seconds to process. Therefore, the 7000 samples were distributed over 35 to 50 seconds. No time series data were recorded, as all the initial data processing was done by the data acquisition program.

To take measurements, the probe was positioned in the flow on a rotating support (Figure 2.11). Because the probe sensor is offset from its support axis, a "dog-leg" probe holder was used to position the sensor at the center of rotation. The probe support was held by a lead screw traverse system positioned above the test section ceiling, enabling movement in the YZ plane. The initial probe position from the wall was determined using a cathetometer to measure the distance from the probe to its reflected image from the floor. Table 2.2 presents the estimated X, Y, and Z location uncertainties. Note that the uncertainties in X and Z increase with height above the floor due to slight probe holder tilt (at most 1 or 2 degrees from vertical).

2.4 Uncertainty Estimates

One of the goals for these measurements to obtain low uncertainty data. The "jitter" program method, presented by Moffat (1982), was used to estimate the 95%

confidence levels for the reduced data using the data reduction technique discussed in the next section. The experimental uncertainties are shown in Table 2.3. Nominal uncertainty estimates for the reduced data (tunnel or freestream coordinates) are shown in Table 2.4. Although the jitter program estimates a 5% uncertainty for the w' and $-\overline{uw}$ data, the scatter in the results seem to indicate that 7% to 10% may be a better, or even optimistic, uncertainty estimate.

To aid in future measurements, the contributions of each of the experimental uncertainties to the total uncertainty of the reduced results were broken down by percentage. The major contributors for each quantity can be seen in Table 2.5. Of note is the major contribution (greater than 95%) of probe yaw angle uncertainty to the total uncertainty in α_{TC} and W_{TC}.

It should be noted that these uncertainty estimates do not account for systematic or bias errors in the experiment. These figures merely represent the likely scatter due to random effects. Systematic errors were hard to avoid when aligning the probe with the tunnel coordinate system. Using a 2-D inviscid flow calculation, attempts were made to identify and correct for these errors. Section 4.3.3 discusses the corrections made for these alignment errors. Another known source of systematic errors can be seen in some of the profile plots of u'_{TC}/U_{ref} and w'_{TC}/U_{ref} (plane 10 data in Figures 4.99 and 4.101, for example). A small amount of noise ($\approx$ 3 mV rms) could be seen using an oscilloscope when the hot-wire probe was in the freestream. The origin of the noise was finally traced to a computer monitor, and moving the monitor solved the problem. The other fluctuating quantity ($-\overline{uw}$) was not affected due to the nature of the data reduction

equations and only the freestream data seemed to be affected for u' and w'. To check repeatibility, a test was performed by taking multiple U_S and α_{TC} measurements at X/C = 1.05, Z/T = -.2. The test showed the mean streamwise velocity results to be repeatible within 1% of U_{ref}, with nominal differences in α_{TC} of 1.5°.

Finally, the errors of the other data sets examined in this study need to be estimated to compare with the author's data. Table 2.6 lists the errors given in the references for each of the data sets. McMahon *et al.* and Dickinson both give uncertainties in the same form as the author, as a percentage of measured value. Devenport and Simpson report uncertainties as absolute quantities, regardless of the value being measured. The errors listed for McMahon's case are the maximum possible errors, and 90% of the uncertainties are only half of the given maximum values. Dickinson reports uncertainties only for mean quantities. Not listed in Table 2.6 are Ailinger's skin friction uncertainties. For the locations in planes 5, 8, and 10, the uncertainties of his data ranged from 2% to 10%. A good nominal uncertainty estimate would be 5% or 6% of the measured C_f value.

The experimental techniques varied for each data set, and this in itself may have brought about bias errors, or "bias differences" between each data set. A discussion on this subject is beyond the scope of this thesis, but the reader should be aware of this fact. It is the author's opinion that none of the data sets, as a whole, suffer from uncertainties or bias errors that would invalidate general comparisons.

2.5 Data Reduction

A method previously used by Devenport and Simpson (1990a) was used to obtain the desired quantities. This method avoids the problem of having to linearize every voltage sample and thus speeds up the data reduction.

2.5.1 Calculation of U_{eff} and u'_{eff}

By letting

$$U'_{eff} = f(E') = \left(\frac{E'^2 - A^*}{B^*}\right)^{\frac{1}{n}} \tag{2.2}$$

and

$$E' = E + e \tag{2.3}$$

$$U'_{eff} = U_{eff} + u_{eff} \tag{2.4}$$

f(E') can be expanded in a Taylor series about E. In doing so, U_{eff} and u'_{eff} can be found in terms of E, E^2, E^3, and E^4 (note that these are mean quantities, e.g. the average of the square of the voltages). These quantities can be obtained by looping through the voltage arrays only one time. A more complete listing and derivation of the equations involved is given in appendix A.

To test the accuracy of this method, a simulation was done using a computer routine that generated a set of random samples with a Gaussian distribution. Since the

mean and variance of this simulated velocity distribution were known *a priori*, the errors using this method could be calculated, given nominal values of the calibration coefficients A^*, B^*, and n. A record length of 5,000 data samples were used, and the coefficients were $A^* = .1225$, $B^* = .09$, and $n = .41$. No attempt was made to simulate the skewness present in a real boundary layer velocity histogram.

Figures 2.12a and 2.12b show the results of the simulations using various U_{local}/U_{ref} values. The calculated errors diverged rapidly when u'/U_{local} became greater than approximately .25. The absolute values of the errors are plotted, so it should be noted that u'/U_{ref} was always underestimated by the method in Appendix A. As seen from Figure 2.12b, both of the error functions seem to have a correlation in the form log(error) = $\log(u'/U_{local})$ + constant. Below the divergence limits, the absolute value for U_{error}/U_{local} was less than .0005 and u'_{error}/U_{local} was less than .003. The maximum local turbulence value ever encountered is usually around .30 for an equilibrium boundary layer, so this method is quite accurate at common u'/U_{local} values. The maximum local turbulence levels encountered by the author in the vicinity of the wing/body junction was .27, in plane 10 at the wing trailing edge. The maximum values were always near the wall, usually at $Y/T < .01$. Nominal near wall values of u'/U_{local} in plane 10 were .14 to .25. In other planes near the appendage, the nominal near wall values were rarely greater than .20. In region 3, the near wall values of u'/U_{local} were much higher, with nominal values of .2 to .31, and a maximum value of .39 in plane 15. For this reason, attempts were made to correct the data in region 3.

The corrections were made by curve fitting the error functions (Figure 2.12b). The final equations were

$$U_{err}/U_{local} = (e^{-.276311})(u'/U_{local})^{4.96319} \qquad \rho_{XY} = .9973 \qquad (2.5a)$$

$$u'_{err}/U_{local} = (e^{-.854253})(u'/U_{local})^{3.32358} \qquad \rho_{XY} = .9984 \qquad (2.5b)$$

The correction criteria used was a correction greater than 1% of the value being corrected, and a local turbulence intensity of more than .05. Using these criteria, no U/U_{ref} data was corrected. In plane 13, 31 corrections were made, with an average correction of -.001. In plane 14, 96 corrections were made, with an average of -.0012, and in plane 15, 180 corrections were made, with an average of -.0011. The maximum correction ever made was only 2.5% of the original value, with the nominal corrections in the range 1% to 1.5%. The effects of these corrections can be seen in the profile plots of the u' data in planes 13-15 (see section 4.3.2).

2.5.2 Calculation of U_S, u'_S, w'_S, $-\overline{uw}_S$, and α_S

As mentioned earlier, the procedure for obtaining U_S, u'_S, w'_S, $-\overline{uw}_S$, and α_S in planes 5 through 11 is the same as described by Devenport and Simpson (1990a). This procedure is similiar to the "conventional" method described by Rodi (1975). He reports that this method is accurate for turbulence intensities below 25% of U_{ref}. The two coordinate systems used for the calculations are shown in Figure 2.8. The angle α is positive as shown following right hand rule convention. Using the equation

$$U_{eff}^2 = U_W^2 + h^2V_W^2 + k^2W_W^2 \tag{2.6}$$

as shown in Jorgensen (1971), the expression for the effective cooling velocity can be written as

$$\begin{aligned} U_{eff}^2 = {} & (U_S\cos\alpha + W_S\sin\alpha)^2 + h^2V_S^2 \\ & + k^2\,(-U_S\sin\alpha + W_S\cos\alpha)^2 \end{aligned} \tag{2.7}$$

where α has been measured with respect to the wire coordinate system. One can expand equation (2.7) into a more convenient form:

$$U_{eff}^2 = AU_S^2 + BV_S^2 + CW_S^2 + FU_SW_S \tag{2.8}$$

where

$$\begin{aligned} A &= \cos^2\alpha + k^2\sin^2\alpha \\ B &= h^2 \\ C &= \sin^2\alpha + k^2\cos^2\alpha \\ F &= 2(1-k^2)\cos\alpha\,\sin\alpha \end{aligned}$$

Since U_S, V_S, and W_S are components in the time-mean flow coordinate system, $W_S = 0$ by definition, and

$$\begin{aligned} U'_S &= U_S + u_S \\ V'_S &= V_S + v_S \\ W'_S &= w_S \end{aligned} \tag{2.9}$$

If it is further assumed that

$$u_S\ ,\ v_S\ ,\ w_S\ ,\ V_S\ <\ .25U_S$$

then

$$u_S^2 \ , \ v_S^2 \ , \ w_S^2 \ , \ uw_S \ , \ V_S v_S \ , \ V_S^2 << U_S^2 \ , \ U_S u_s \ , \ U_S w_S$$

After dropping these second order terms, the relevant equations become

$$U_{eff} = U_S\sqrt{A} \tag{2.10}$$

$$(u'_{eff})^2 = A(u'_S)^2 + \frac{1}{4}\frac{F^2}{A}(w'_S)^2 + F\,\overline{uw}_S \tag{2.11}$$

where A and F are functions of the local stream mean flow angle measured with respect to the probe, which changes as the probe is yawed. Using equation 2.10 and two measurements taken at yaw angles of approximately ±30°, the flow yaw angle with respect to an arbitrary datum and the magnitude of the mean velocity vector can be found. The angle datum was selected such that $\alpha = 0°$ when the velocity vector was aligned with X_{TC}. After taking another measurement at a third yaw angle, preferably aligned with α_{TC}, a simultaneous system of equations can be solved to yield values for u'_S, w'_S, and $-\overline{uw}_S$, with redundant values of U_S and α_S. The coefficient of axial sensivity, k, was taken to be .13 for these measurements. There is a great amount of uncertainty in this figure, but as Table 2.5 shows, this uncertainty does not greatly effect the reduced quantities.

The output from the data acquistion program (mean velocity vector magnitude and direction, and 3 components of the Reynolds stress tensor in the XZ plane) was given in the local stream coordinate system. This output was then transformed into the tunnel coordinate system. Since the initial probe alignment was done by eye, a relatively large error could propagate through the results of data presented in tunnel coordinates. Profile data presented in the local freestream coordinate system would eliminate the alignment

error, since the relative angular measurements for different Y locations in each profile are more accurate. The tunnel coordinate system was used, however, since it was considered better for comparing data sets. Note that for planes 13, 14, and 15, the probe was not rotated and only U_{TC} and u'_{TC} were measured. This was done mainly in the interest of time, as this meant only a third as much time was spent taking data. Also, it is reasonable to assume that much of the secondary flow structure present from the horseshoe vortex becomes diffused and washed out, particularly as the flow diverges in the adverse pressure gradient.

3.0 Description of Test Conditions

An effort was made to keep the daily test conditions as uniform as possible. The wind tunnel lab area was air-conditioned, and temperature equilibrium was established at approximately 25° C after running the wind tunnel and laboratory air-conditioner for 30 minutes. Constant temperature was important for accurate hot-wire measurements and also to keep flow characteristics (flow properties, separation locations, etc.) from varying. The daily variation in temperature was estimated at ± .5° C. Note that a temperature uncertainty of ± 1° C was used in table 2.3. This figure was used as a worst case estimate.

The daily atmospheric pressure was approximately 945 ± 10 mb, and the daily reference velocity was approximately 26.75 ± .75 m/s. Small changes in U_{ref} were constantly updated as measurements were made.

3.1 Flow Characteristics

3.1.1 Empty Tunnel Flow Characteristics

To document the flow characteristics in the adverse pressure gradient region, potential core and boundary layer measurements were taken in regions 2 and 3 without the wing. When taking these measurements, side wall inserts were used in region 2 to fill the gaps used to approximate the potential flow streamlines when the wing was installed.

Data from the potential core streamwise traverses are shown in Figure 3.1. A 1-dimensional inviscid continuity calculation was done for comparison to the U/U_{ref} and C_p results, and is shown in Figure 3.1 by the solid line. The variation is mainly due to the additional blockage caused by the growing boundary layer. An increase in the freestream value of u' from .2% to .7% occurs as the flow passes through region 3. Note the slight "hump" in the U/U_{ref} and C_p data where region 3 begins. This is due to the blockage effects of the suction slots and the boundary layer bleed scoop at the ceiling. The change in C_p with respect to X/C was estimated using central differencing. The results for $d(C_p)/d(X/C)$ are also shown in Figure 3.1.

Figure 3.2 shows U/U_{ref} and u'/U_{ref} profile data for 3 locations in region 3. The mean velocity seems to decrease almost uniformly as X/C increases. The turbulence intensity in the inner boundary layer region decreases as U_{FS} decreases, contrary to the turbulence behavior in the freestream. As seen from Figure 3.2, the boundary layer

profiles seem to have similiar shapes. Calculations were done to determine if these profiles resulted from an equilibrium boundary layer which could be described by

$$U_{FS} \propto (X-X_o)^m \tag{3.1}$$

as given by Rotta (1962). These profiles, however, failed to meet the criteria required for an equilibrium turbulent boundary layer.

Using Spalding's wall law (Spalding, 1961) for the inner region, C_f estimates were calculated for the three boundary layer profiles measured in region 3. Spalding's equation is given as

$$Y^+ = U^+ + \frac{1}{G}(e^{kU^+} - 1 - kU^+ - \frac{1}{2!}(kU^+)^2 - \frac{1}{3!}(kU^+)^3 - \frac{1}{4!}(kU^+)^4) \tag{3.2}$$

where k = 0.407 and G = 10. Figure 3.3 gives an example of how well equation (3.2) fit these profiles. Table 3.1 lists the profile parameters. The displacement thickness (δ^*) results were used to perform a more accurate 1-D "inviscid" calculation for the velocity distribution in region 3. The dashed line in Figure 3.1 shows the results of the calculation. The calculated U/U_{ref} values with the δ^* correction are closer to the measured values, but as X/C increases, the results diverge. To perform the calculation correctly, the boundary layer growth along the tunnel roof and sidewalls must also be accounted for. A simple calculation shows that although the physical angle of divergence of region 3 is 4.996°, the U/U_{ref} vs. X/C potential core data show a mean "inviscid" divergence angle of 3.276° with a standard deviation of 1.16% for X/C > 8.

3.1.2 Appendage Flow Characteristics

As previously mentioned, a large amount of data are presented regarding this flow in Devenport and Simpson (1990a). Some of the data are presented here to give additional information about the wing-body junction flow characteristics.

Figure 3.4 shows a surface plot of the C_p distribution on the test wall surrounding the appendage, and is good for showing the qualitative features of the pressure field. Note the large adverse pressure gradient imposed on the incoming boundary layer at the nose of the appendage. As the flow is accelerated around the appendage sides, the pressure reaches a minimum value just forward of the maximum thickness. At the minimum pressure locations, an extremely large adverse pressure gradient exists in the direction of increasing $|Z/T|$. As the flow decelerates, in the presence of a more mild adverse pressure gradient in the streamwise direction, positive values of C_p occur at the trailing edge. As oil-flow visualizations show, separation occurs in this region due to the effects of the pressure gradient and the horseshoe vortex. Separation does not occur in the 2-dimensional flow region toward the mid-span of the appendage. A comparison of the wall pressure distribution and that produced by an unbounded potential flow is shown in Figure 3.5. While the qualitative distribution is the same, the magnitudes of the measured C_p distribution are less than the calculated values by approximately 25% to 30%. Figure 3.6 shows a comparison of the actual C_p distribution at $Z/T = \pm 3.17$ with that predicted from potential flow. This data demonstrates the lack of significant blockage effects in the test flow.

As mentioned in section 2.1, symmetry of the appendage boundary layer was taken as a good indication of the flow symmetry (Figure 3.7). Figures 3.8 and 3.9 show the results of mean velocity and turbulent fluctuation measurements 1 mm downstream of the trailing edge at various Y/T locations. The 2-dimensionality of the boundary layer indicates that the junction flow is independent of the height of the wing (Devenport and Simpson, 1990a). These measurements can be used to determine what features of the junction flow can be attributed to the wing boundary layer and also for determining the dissipation characteristics of the wake.

3.1.3 Oil-Flow Visualization Results

Oil-flow visualizations were performed by previous researchers (Devenport *et al.*, 1990, Devenport and Simpson, 1990b, and Olcmen, 1990), and Figures 3.10a,b display the results. Note that the individual measurement locations are indicated by the white dots, and the individual XY planes are also indicated in Figure 3.10a. To produce the oil-flow visualizations, a mixture of kerosine, titanium dioxide powder, and oleic acid was spread on sheets of adhesive glossy black plastic sheeting (Olcmen, 1990). Using this technique, the original oil flows could be preserved, since the sheet could be removed from the wind tunnel when the oil had dried.

Examing Figure 3.10b, one can identify the primary separation point (saddle point) and, closer to the appendage, the collection of pigment along what can be called a line of low shear (LOLS) (Devenport and Simpson, 1990b). This line is not a separation line since oil streaks pass through it near the plane of symmetry. This is in contrast to

previous researchers' conclusions. The 4-vortex structure deduced by Baker (1980) and others may exist instantaneously, but time mean velocity measurements along the centerline upstream of the wing show only one vortex in the plane of symmetry (Devenport and Simpson, 1990b). It can be postulated, however, that the LOLS location and Baker's X_V location are directly related, since away from the plane of symmetry, the LOLS more closely resembles an ordinary separation line. This theory is supported by the fact that for the thin and thick boundary layer cases documented by Devenport *et al.* (1990), the variation in X_S and X_{LOLS} follow the same trends as Belik (1973) and Baker found for X_S and X_V. Note that the oil-flow visualization does show evidence of a small, counter-rotating vortex very close to the base of the wing, suggesting a mean two vortex flow structure.

At the appendage nose, an ordinary separation line emanates from the singular separation point. Figure 3.11 presents a sketch showing how the initial vortex roll-up causes this line. Also note the skewing of the outer streamlines shown in this figure. As this initial vortical structure wraps itself around the appendage, the separation line and initial LOLS merge to form what appears to be an ordinary separation line, at least in the region adjacent to the appendage. This blending suggests that the initial vortex structure present at the nose is of no consequence downstream of the wing maximum thickness, since any individual vortices (aside from the small corner vortex) combine to form one primary vortex. At the appendage trailing edge, a "fish tail" wake pattern occurs. This separation pattern is caused by the pressure recovery at the trailing edge, and the secondary flow structure helps to shape it. Figure 3.12 gives the dimensions of the

characteristic oil-flow pattern, and Table 3.2 lists the locations of the LOLS for planes 5-10.

3.2 Comparison of Incoming Boundary Layer Test Parameters

One of the main objectives of this research is the determination of the effects of varying inflow conditions on the properties of a turbulent wing-body junction. The proper comparison of inflow conditions for the various data sets becomes a key issue because of this objective.

Approach boundary layer data from Dickinson (1986a,b), McMahon *et al.* (1987), and Devenport and Simpson (1990a) was used to evaluate the incoming boundary layer test parameters. Note that the boundary layer parameters for the author's data is exactly the same as for Devenport and Simpson's data. Incoming boundary layer data for Shin's (1989) research was unavailable to the author, and the given values will be used for his data.

Figure 3.13 shows the approach boundary layer profiles for the three main test conditions. This data was taken with the wing in place. Devenport's and McMahon's data is nearest the wing, and therefore is affected by the adverse pressure gradient caused by the wing geometry more than Dickinson's data. Since Dickinson's and McMahon's profiles do not include data below $U/U_{ref} = .5$, Spalding's wall law (equation (3.2)) was used to estimate additional data points closer to the wall to obtain more accurate

momentum and displacement thicknesses (as discussed in section 4.1.3). By fitting this equation to the data, an estimate of C_f is also found. Figures 3.14 (a-c) show the results of using this equation to extrapolate additional data points down into the laminar sublayer. For each profile, 4 additional points were calculated, and are indicated on the figures by the solid squares. Devenport's data, taken with a hot-wire held horizontal to the floor, shows quite good agreement with equation (3.2). Dickinson's data seems to agree well also, but suffers slightly from having few points in the inner region. A good fit to McMahon's data using equation (3.2) could not be found, so the C_f value which matched the slope of the linear portion of the inner region was used to extrapolate data closer to the wall. Several possible explanations exist as to why McMahon's data and Spalding's equation do not agree well. The data was obtained using a digitizer, which could lead to some inaccuracies. The size and design of the probes may have been a problem near the wall, since one of the probes was a slant wire with its supports protruding from the floor, a design which could have possibly biased the measurements. The combination of a thick boundary layer and the close proximity of the wing creating an adverse pressure gradient could invalidate equation (3.2) near the wall. The latter reason seems the most likely. Ludwieg-Tillmann's skin-friction correlation, given by White (1974), was used to check for internal consistency of the C_f results. The Ludwieg-Tillmann C_f results were very near those calculated from Spalding's equation, with errors of 4% for Devenport's and Simpson's data, and 2% for both Dickinson's and McMahon's data.

After fitting equation (3.2) to the three profiles, δ^* and θ were calculated. The extra points increased these thicknesses appoximately 5% for McMahon's and Dickinson's

data, but the changes in Devenport's results were negligible. McMahon's and Dickinson's profile results were corrected to X/T = -2.146 to match Devenport's location. Power-laws were used to correct the data. The relationships (from White, 1974) used were

$$C_f \approx .0592\ Re_X^{-.2}$$

$$\delta/X \approx .37\ Re_X^{-.2} \qquad (3.3)$$

$$\theta/X \approx .036\ Re_X^{-.2}$$

where X is measured from a virtual origin. The shape factor, H, was assumed constant and used to evaluate δ^*. Table 3.3 lists the approach boundary layer parameters for all data sets considered in this study. Two important facts to note are (1) that in Shin's investigation, the approach boundary layer parameters were measured at X = 0, with no wing in place, and (2) that Devenport's data at X/C = 3.00 (plane 12) is from what was called the *thin* boundary layer case (Devenport *et al.*, 1990), those parameters being listed in the last column. The first column lists approach boundary layer comparisons for the author's (JLF) hot-wire data, Devenport and Simpson's (WJD) LDV data, and Devenport *et al.*'s (1990) hot-wire data for the *thick* boundary layer case.

4.0 Experimental Results

This chapter presents the experimental results of the author's research. The like quantities are grouped together, with the contour plots and secondary velocity vector plots shown first, followed by selected individual profile plots which enable a more detailed examination of the results. Because of the large volume of results, no tabular listings are given. The data files are available on magnetic disk, and Appendix B describes their organization.

As mentioned previously, the author's experimental results include U_{TC}, W_{TC}, u'_{TC}, w'_{TC}, $-\overline{uw}_{TC}$, and ω_{TC} information. In addition to these fundamental quantities, $(\partial(W)/\partial Y)\delta/U_{ref}$, helicity density (h), the distortion function (f_D), δ^*, θ, and C_f, the skin-friction coefficient based on U_{ref} are also presented. The calculation of these quantities is described in the next section. Hodograph plots are also presented, displaying the relationship between W_{FS} and U_{FS}.

Note that *all* data were taken on the starboard side of the appendage. The contour plots of data in a YZ plane are oriented as if the observer were looking upstream, with

the appendage on the left side, and -Z/T increasing to the right. All contour and secondary velocity plots are scaled to 1 inch = 1.0 T.

4.1 Description of Calculated Quantities

The following quantities discussed were all estimated from experimental data.

4.1.1 Streamwise Vorticity (∂(W)/∂Y) and Helicity Density (h)

The streamwise vorticity was calculated since it is a direct indication of the strength of the secondary flow. The streamwise vorticity is given by

$$\Omega_X = \frac{\partial(W)}{\partial Y} - \frac{\partial(V)}{\partial Z} \qquad (4.1)$$

where all quantities are in tunnel coordinates. The differentials were estimated by fitting a parabola through 5 consecutive data points using a least squares method, and then evaluating the derivative of this curve fit at the central (third) point. For the author's data, only the contribution due to W could be calculated, as no V information was available. This problem was not serious, however, because the mean secondary flow structure in the junction tends to be flattened into an elliptical shape near the wall (Dickinson, 1986a,b). Within the secondary flow region, the contribution of the W term to Ω_X is usually at least an order of magnitude larger than the V contribution. Figure 4.1 illustrates this imbalance by comparing ∂(W)/∂Y and -∂(V)/∂Z in planes 5 and 8 for data

sets where V data is available (Devenport and Simpson, 1990a, and Dickinson, 1986a,b). The W term has the larger contribution by far in both planes, to the extent that it characterizes the vorticity inherent in the secondary flow structure by itself. For this reason, $\partial(W)/\partial Y$ was the quantity plotted in contour and profile plots, enabling direct comparisons between all the data sets. Since the term U_{ref}/δ is proportional to the voritici y present in the approach boundary layer data, all vorticity data was non-dimensionalized by dividing through by this term, unless otherwise specified. Figure 4.1 was non-dimensionalized in this way.

Helicity is directly related to the vorticity, and is defined by

$$H = \int \overline{V} \cdot \overline{\Omega} \; d(Volume) \tag{4.2}$$

The integrand of equation (4.2) is known as the helicity density, and is designated h. Hussain (1986) discusses the importance of helicity in the study of coherent structures. He explains that when structures with large values of helicity are present, they will have low dissipation rates and the breakup of large scale into smaller scale motions is slowed. This occurs as a consequence seen in a form of the Navier-Stokes equation, and the reader is referred to Hussain (1986) for further reading.

With regards to the author's work, the non-dimensional helicity density was estimated for all data sets by letting

$$h \approx \left(\frac{\partial (W_{TC})}{\partial Y} U_{TC} - \frac{\partial (U_{TC})}{\partial Y} W_{TC} \right) \frac{\delta}{U_{ref}^2} \tag{4.3}$$

This approximation results from ignoring the mean velocity partial derivatives in the X and Y directions. In a fashion similar to Ω_X, h is non-dimensionalized by $\delta/(U_{ref})^2$. Larger values of helicity density, from the preceeding discussion, will indicate longer lasting vortical structures, with less dissipation due to turbulent momentum transport. Helicity density contours are presented in chapter 5.

4.1.2 Distortion Function (f_D)

The distortion function was used to separate the effects of the secondary flow structure from the effects of the incoming boundary layer and of the appendage geometry. The distortion function is defined by the equation

$$\frac{U_{TC}}{U_E} = f_D\left(\frac{Y}{T}, \frac{Z}{T}\right) g\left(\frac{Y}{\delta}\right) \tag{4.4}$$

for a constant X/C value. U_E, the local boundary layer edge velocity, was predicted by a potential flow calculation. These potential flow calculations compare favorably to the experimental results, as can be seen in Figure 4.4. The function g is defined by the outer "2-D" mean flow distribution in the boundary layer in the given YZ plane location. One can see that f_D describes the effects of the horseshoe vortex on the mean streamwise flow distribution, and its value should go to 1 at large Z/T or Y/T.

4.1.3 δ^*, θ, and C_f Estimates

Results from estimating C_f, δ^*, and θ were used to compare and contrast the effects of the horseshoe vortex structure in the different data sets. These results are discussed in section 5.3.4. All results were calculated in the local freestream coordinate system ($(W_E)_{FS} = 0$).

The local boundary layer displacement and momentum thicknesses in the local freestream direction are given by

$$\frac{\delta^*}{T} = \int_0^{\delta} \left(1 - \frac{U_{FS}}{U_E}\right) d\left(\frac{Y}{T}\right) \tag{4.5}$$

$$\frac{\theta}{T} = \int_0^{\delta} \frac{U_{FS}}{U_E}\left(1 - \frac{U_{FS}}{U_E}\right) d\left(\frac{Y}{T}\right) \tag{4.6}$$

These expressions were integrated using the trapezoidal rule. The integrand of equation (4.5) is a maximum at $U_{FS}/U_E \simeq 0$, so using the trapezoidal rule to evaluate δ^* for profiles lacking near wall data was considered a reasonable approximation. The integrand of equation (4.6) reaches a maximum at $U/U_E = .5$, and goes to zero as U_{FS}/U_E approaches zero. Therefore, using the trapezoidal rule to evaluate θ for profiles where $(U_{FS}/U_E)_{MIN} > .5$ can result in significant errors. When profile data did not meet the $(U_{FS}/U_E)_{MIN} < .5$ criteria, the $U_{FS}/U_E = .5$ location was roughly estimated using linear interpolation, and then equation (4.6) was used to estimate θ for all data sets.

Several method's were used to estimate C_f in the local freestream direction ($(C_f)_{FS}$) for each profile. Johnston (1960) discusses a technique involving what he refers to as

hodograph or polar plots of W_{FS}/U_{ref} vs. U_{FS}/U_{ref} to obtain a wall law relationship for 3-dimensional turbulent boundary layers. He suggested the form

$$\frac{U^+}{\cos(\alpha_{WALL})} = \frac{1}{.41}\ln(Y^+) + 5.0 \qquad (4.7)$$

where α_{WALL} is measured with respect to the local freestream coordinate system, and U^+ is defined using the magnitude of the wall shear stress vector. This angle can be found by evaluating

$$\alpha_{WALL} = \tan^{-1}\left(\frac{W_{FS}}{U_{FS}}\right) \qquad (4.8)$$

as U_{FS} approaches zero, and is presumably also the direction of the local wall shear stress vector. Figure 4.2, from White (1974), illustrates the above relationship. Johnston reports some success using equation (4.7) for boundary layers with small secondary flows.

Unfortunately, the hodograph plot idea and Johnston's wall law breaks down when bidirectional or "cross-over" profiles are encountered, as shown in Figure 4.2, or for extreme flow angles. The horseshoe vortex creates such bidirectional polar plots. The skewing created by the strong secondary flow made estimates of C_f obtained using equations (4.7) and (4.8) highly erratic. The results at some locations, usually well away from the wing, were encouraging, but overall results were unacceptable.

The other methods used to estimate C_f in the local freestream direction were two skin-friction correlation formulas, given by

$$C_f = 0.246\ Re_\theta^{-0.268} 10^{-.678H} \tag{4.9}$$

$$C_f = \frac{0.3e^{-1.33H}}{(\log_{10} Re_\theta)^{(1.74+0.31H)}} \tag{4.10}$$

where H is the shape factor. The former equation is the classical Ludwieg-Tillmann relation, while the latter is a skin-friction correlation given by White (1974) using Coles' wall law coefficients. These two correlations are considered accurate only for mean 2-dimensional flows, but were used to provide "last resort" estimates to facilitate at least a qualitative comparison of skin-friction results between data sets. Note that $(C_f)_{FS}$ can be used to find the total skin-friction coefficient if α_{wall} is known.

Figure 4.3 shows an example of the typical C_f estimates using the different equations. Note that the results from equation (4.9) and (4.10) are almost identical. Equation (4.10) and the local velocity profile properties were used to generate C_f data for the local streamwise component of the wall shear stress. These results are compared to Ailinger's (1990) C_f results obtained using laser interferometry, and are discussed in section 5.3.6. Since the C_f estimates from equation (4.10) are based on the local freestream dynamic pressure, the skin-friction coefficients were multiplied by $(U_E/U_{ref})^2$ to non-dimensionalize C_f on the reference dynamic pressure.

4.2 Near Wing Data Corrections

A 2-D potential flow solution was obtained for the appendage shape studied using the vortex panel solution described in chapter 6. The comparison of the author's experimental results to the 2-D numerical solution (Figure 4.4) led to corrections of the flow angle datum in planes 9, 10, and 11.

Plane 5 comparisons (Figure 4.4a) show good agreement for freestream values of U_{FS}/U_{ref}. The author's freestream values of α_{TC} do not compare very well, and are approximately 1.5° to 2.0° off at most locations. Initially, a correction was thought to be in order, but after examination of the profile plots of W_{TC}/U_{ref} in plane 5 (Figure 4.32), one can see that α_{TC} never reaches a constant or what could be considered a freestream value. Considering this fact, no corrections could be justified.

In planes 6 and 7 (Figures 4.4b,c), good overall agreement of both the freestream velocity and flow angle was observed, and no corrections were needed. In plane 9 (Figure 4.4e), the flow angles were corrected by -2° for the outer 7 profiles. these profiles were measured almost 2 weeks after the inner 3 profiles (which were not corrected), and show a systematic bias error in the probe alignment of -2°. Figure 4.4e shows the corrected results.

Comparisons in planes 10 and 11 (Figures 4.4f,g) show good agreement for the freestream velocities, but the author's experimental freestream α_{TC} results show some scatter. These results also showed a possible bias error for all profiles in these two planes. Tests for symmetry in plane 11 showed that a correction of -1.5° would lead to

symmetric flow angles, and repeatibility tests showed the α_{TC} measurements to be precise. Therefore, a -1.5° correction in α_{TC} was made for planes 10 and 11.

The effects of the corrections in flow angle for planes 9, 10, and 11 are visible only in W_{TC} and α_{TC}. The other quantities measured were effected very slightly, which is expected, since the cosine of 1.5° is .99966.

4.3 Examination of the Present Flow Characteristics

The results of the author's measurements are discussed in this section. Devenport and Simpson's (1990a) LDV data and Devenport *et al.*'s (1990) data from the thick boundary layer case is used for continuity from planes 5-15. The LDV data also reveals additional detail since it contains V velocity component information. Appendix B describes the organization of the data on magnetic disk. The plots are organized according to the quantity being presented, with the contour and velocity vector plots shown first, followed by boundary layer profile plots from selected X/C, Z/T locations.

The inclusion of individual boundary layer profile plots presents the data in such detail that to fully discuss the results is beyond the primary objectives of the author's research. These plots are included primarily for the interested reader, and therefore will not always be mentioned. At times, however, the profile plots show needed detail unavailable from the contour plots, particularly near the wall, and they also display results

not presented in the contour plots. In chapter 5, the profile plots aid in the comparison of data sets, as well as the determination of the flow scaling parameters.

4.3.1 Near Appendage Data, Planes 5-11

Figures 4.5a and 4.6a display the contours of mean velocity and distortion function, while Figure 4.7 shows the secondary velocity vectors where available. The term "secondary velocity vector" is used loosely here in describing the vectors formed by the W_{TC} and V_{TC} data. Ideally, the velocity vectors should be presented in a way that distinguishes the actual secondary flow due to the horseshoe vortex from the spanwise flow due the appendage. Presentation of the vectors in a plane orthogonal to the vortex axis (or line of low shear) or in freestream coordinates may be more appropriate than tunnel coordinates, which is the coordinate system used. This system was chosen primarily to enable clear comparisons with other data sets (chapter 5).

Contours of U_{TC}/U_{ref} for planes 5-11 show the significance of the line formed by the merging of the line of low shear location (LOLS) and the separation line. It is designated by the dashed line in Figure 4.5a, while the solid line indicates the appendage surface location. A "tongue" or plume of low momentum fluid grows as the flow moves past the junction. This upward distortion of the boundary layer is always near the LOLS. The secondary velocity vector plots which contain V information show the maximum vertical velocities near the LOLS, which also correspond to the distortion function contour patterns. From examining the relationship between U_{TC} and the secondary velocities, one can easily see the characteristic pumping action of the horseshoe vortex at work, a

mechanism which brings higher momentum fluid into the junction, and ejects lower momentum fluid from the near wall region. Cutler and Bradshaw's (1986) experimental results display the same general features, with an initially large crossflow leading to the transport of fluid away from the wall.

The tongue of low momentum fluid extending from the near-wall boundary layer changes in shape as X/C increases, growing narrower as the appendage trailing edge is approached, and then broadening aft of the trailing edge separation location. The contours of f_D change from a more vertical orientation and begin to tilt inwards toward the centerline as the distortion pattern broadens.

The flow created around an appendage is subjected to skewing and hence should be similiar to Shizawa and Eaton's (1990) experimental flow. They studied a vortex embedded in a skewed boundary layer created by deflecting the freestream flow 30° in the transverse di ection, and examined the cases resulting from the two possible vortex rotational directions. It was found that the vortex decayed much quicker in a skewed rather than 2-D boundary layer case, and that the vortex persisted longer and produced larger flow distortions in the case where the skewed fluid velocity near the wall was of opposite sense to the flow induced by the embedded vortex. This flow was designated case 2 by Shizawa and Eaton. The distortions produced by the opposite case, designated as case 1, decayed the quickest because the near-wall secondary flow, moving in the same direction as the vortex induced flow, suppressed separation and inhibited the creation of the characteristic plume of low momentum fluid. Shizawa and Eaton observed that fluid

containing vorticity of opposite sign was able to pass underneath the remains of the case 1 vortex core as the flow developed downstream.

The region upstream of the trailing edge, in planes 6-8, and also in planes 9 and 10 to a lesser extent, exhibits characteristics of Shizawa and Eaton's case 2 flow. The secondary velocity vectors clearly show the vortex-induced skewing opposing the boundary layer skewing caused by the appendage geometry. These conflicting flow patterns merge to form an energetic separation, as seen by the V velocities in plane 8 (X/C = .75). This accounts for the more upright distortion function contours adjacent to the wing.

Case 1 simulates the wake region of a junction flow, and produces distortion patterns in mean velocity similiar to the present experiment. Plane 11, at X/C = 1.50 shows very similiar secondary velocity and mean velocity distortion patterns. These observations suggest that the same vortex decay mechanisms are at work in the two flows, both adjacent and downstream of the body, even though the skewing for Shizawa and Eaton's flow is much stronger. Profile plots of vorticity from plane 11 (Figure 4.90), showing near-wall regions of negative vorticity, provide further evidence of similiar vortex decay mechanisms at work. The adverse pressure gradient encountered at the appendage trailing edge also encourages the broadening of the flow distortions and diffusion vortical flow structures.

Looking again at the planes adjacent to the appendage, a region of negative vorticity can be seen near the wall outboard of the primary vortex structure in Figure 4.8 and in the profile plots of vorticity. This region is larger than that observed by Cutler and

Bradshaw (1986) for a 2-D, unskewed boundary layer, but not as large as seen for Shizawa and Eaton's case 2. These two studies show that the magnitude of "background" boundary layer skewing plays a major role in determining the behavior of any embedded vortices.

One must be careful about viewing a wing-body junction flow as a vortical flow structure superimposed over a "background" turbulent boundary layer flowing around an appendage. These two features of a junction flow are inseparable, and both influence each other. To illustrate this fact, consider the following relationships. Without an approach boundary layer, the appendage-generated pressure gradients could not create a root junction vortex. The resulting vortical flow structure affects the boundary layer mean flow distribution, which in turn changes the wall pressure gradients, which can then affect the vorticity flux out of the wall (Agui and Andreopoulos, 1991).

Examining the vorticity distribution, shown by contours of $(\partial(W)/\partial Y)\delta/U_{ref}$ in Figure 4.8, one observes that the vortex is elliptically shaped and near the wall. This is similiar to Dickinson's (1886a) earlier findings. The initial time-averaged elliptical shape of the maximum vorticity contours in planes 5-8 suggests that the vortex may be meandering. Beginning in plane 9, near the trailing edge, the core vorticity contours begin to appear more circular in nature. This apparent stabilizing effect may be due to the increase in distance from the bimodal flow in the nose region. Note that the LOLS is always located outboard of the vortex core, as expected from the previous examination of the flow separation mechanism.

Comparing Figures 4.5a and 4.8, one can see that the vortex core locations coincide with regions where the streamwise mean flow gradients in the spanwise (Z) direction are large (the isovels of U_{TC} are almost vertical). This observation clearly demonstrates the relationship between the redistribution of the mean velocity in the boundary layer and the vortex position. The vortex depresses the contours of U_{TC} by drawing in high momentum fluid from the outer boundary layer, displacing low momentum, near wall fluid upward, and therefore creating large spanwise mean flow gradients. Table 4.1 lists the maximum levels of $(\partial(W)/\partial Y)\delta/U_{ref}$ found in the vortex core at each measurement plane. The decrease in vorticity from the maximum thickness location to the trailing edge displays evidence of the diffusion and decay occurring in the vortex core.

Due to the no slip condition at the wall, a very thin region of negative vorticity is concentrated underneath the outer edge of the positive vorticity region near the wall. In plane 5, this vorticity is confined to a region below Y/T = .04 (Figure 4.84), and extends outward from approximately the LOLS location. As the flow develops, the area of negative vorticity gradually increases and the resulting induced flow lifts the primary vortex away from the wall. Similiar behavior is observed by Cutler and Bradshaw (1986). Profile plots (Figures 4.84-90) and enlarged contours plots of $(\partial(W)/\partial Y)\delta/U_{ref}$ (Figures 5.27-5.39) may be referred to for details of the negative vorticity region.

The characteristic patterns formed by contours of the square root of the Reynolds normal stress u'_{TC}/U_{ref} are shown in Figure 4.9a. Note how the local peaks in turbulence intensity are centered slightly outboard of the LOLS location, except at X/C = .93, which

is near the trailing edge separation. The $|Z/T|$ location of the LOLS at X/C = .93 is a minimum, therefore the relationship between the primary vortex position and the LOLS may change near this location. Devenport *et al.* (1990) suggests several causes for the local turbulence peaks. These are a) increased mixing of the boundary layer fluid by the horseshoe vortex, b) spanwise meandering of the trailing vortex legs, and c) a destabilizing of the boundary layer caused by the lifting action of the secondary flow near the LOLS, similiar to the effects of an adverse pressure gradient. The first and third causes seem to be the most likely. The coincident locations of the steep spanwise gradients in U_{TC} and the vortex cores, both positioned *inboard* of the LOLS, would seem to discount the second possible cause of the turbulence peaks.

The individual profile plots show the effects of the secondary flow structure in greater detail. The kinking of the U_{TC}/U_{ref} profiles (Figures 4.10-4.22) shows the effects of adding higher momentum fluid near the wall, and displacing the lower momentum fluid further out of the boundary layer. As the flow moves downstream, the distortion of these profiles becomes much greater. Plots of V_{TC}/U_{ref}, available from Devenport and Simpson's (1990a) LDV data, show local minima for locations inboard of the time-averaged vortex center, and local maxima outboard of the vortex center (Figures 4.29-4.31). Also note that the V velocities always approach zero near the wall, even near the LOLS location.

Profile plots of W_{TC}/U_{ref} (Figures 4.32-4.38) and α_{TC} (Figures 4.39-4.45) show the large changes the spanwise flow. In plane 5, the spanwise skewing exceeds 40% of U_{ref}. In the downstream planes, bi-directional skewing is often present, particularly inboard of

the LOLS location. The complexity of the 3-D boundary layer at these locations invalidates triangular flow models based on hodograph plots (Johnston, 1960). The hodograph, or polar plots, are displayed in Figures 4.77-4.83, and show the complex relationships existing between W_{FS} and U_{FS} in the junction vortex flow region. At larger values of |Z/T|, however, the boundary layer skewing often resembles Johnston's (1960) experimental flow, in which a duct end wall created the skewed boundary layer.

Profiles of the fluctuating quantities u'_{TC}, v'_{TC}, w'_{TC}, $\overline{uv}_{TC}$, and $\overline{uw}_{TC}$ are given in Figures 4.46-4.76. The profiles of v'_{TC} and $\overline{uv}_{TC}$ were obtained from Devenport and Simpson's (1990a) LDV data. The details of the mean flow influence on the distribution of these quantities within the boundary layer are displayed in these figures. Near the LOLS, the profile plots usually show local absolute maxima. This is particularly evident in plane 5, where v'_{TC} and w'_{TC} show large levels near Z/T = -.88, the approximate LOLS location. The large values in w'_{TC} occur near the wall (Y/T < .01), while smaller increases in w' and large peaks in v'_{TC} occur at Y/T of approximately .09. This location coincides precisely with the peaks in u'_{TC} in plane 5. As the flow moves downstream, the distributions of the normal stresses are more uniform, but small peaks are still present, and seem to be related to one another. This apparent relationship suggests that the flow mechanism responsible for altering the distribution of u'_{TC} affects v'_{TC} and w'_{TC} in a similiar fashion.

It is interesting to compare the normal stresses in plane 5 to the nominal values occuring for a 2-D flow over a flat plate. Klebanoff's classical turbulent boundary layer over a flat plate (from Schetz, 1984) shows maximum values of u'/U_E, v'/U_E and w'/U_E

to be around .11, .04, and .06, respectively. Allowing for the fact that the present experimental data are non-dimensionalized by U_{ref}, not U_E, the values for u'_{TC}/U_E near the wall are approximately the same as Klebanoff's results, but the other two turbulent quantities are much higher. The maximum values of v'_{TC}/U_E and w'_{TC}/U_E present in plane 5 are well over twice those given by Klebanoff's data. Presenting the data in freestream coordinates does not affect this comparison with 2-dimensional data. As X/C increases, the local maxima in v'_{TC} and w'_{TC} decrease to more comparable levels, and by plane 8, these maximum values are approximately .05 and .07, respectively.

The mean Reynolds shearing stresses $\overline{uv}_{TC}/(U_{ref})^2$ and $\overline{uw}_{TC}/(U_{ref})^2$ profile plots are shown in Figures 4.67-4.76. The effects of the altered mean flow gradients are revealed in these figures. Large negative values of $\overline{uw}_{TC}$ exist underneath the mean vortex structure because of the spanwise gradient in U_{TC} at this location, and also because of the large transverse velocities near the wall. The large values in $\overline{uw}_{TC}$ may also be indicative of vortex meandering. Positive or negative regions of $\overline{uw}_{TC}$ can usually be explained by examining the spanwise gradient in U_{TC}. Local maxima or minima seem to occur in regions marked by high normal stresses as well.

Interestingly, no significant regions of positive $\overline{uv}_{TC}$ were found in planes 5, 8, or 10. Local maxima of $\overline{uv}_{TC}$ which tended toward zero can be easily identified at Z/T locations strongly effected by the horseshoe vortex.

Figures 4.91 and 4.92 show the similiar variations of δ^*/δ^*_{APP} and θ/θ_{APP} in the spanwise direction for each of the YZ measurement planes. These are freestream coordinate system results. Planes 5 and 6 display a sharp drop in δ^* and θ as the body

is approached, which is a combination of the thinning effects of the near wing pressure gradients and the developing horseshoe vortex. As |Z/T| increases, the boundary layer thicknesses are relatively constant in these planes. Beginning with plane 7, the variation of δ^* and θ show local maxima near the LOLS locations. This result is expected from earlier observations of the streamwise mean velocity contours. The local spanwise variations in δ^* and θ increase monotonically with downstream distance. Figure 4.94 shows the variation in $\Delta(\delta^*/T)$ and $\Delta(\theta/T)$ vs. X/C. These parameters, which are a measure of the extent of the distortive effects due to the horseshoe vortex, increase as the flow moves downstream. The initial distortion rate grows very quickly, but levels off to an almost constant growth rate. The rapid distortion growth is an indication of the skewing direction of the primary flow over the aft portion of the body, which tends to increase the distortions (case 2, Shizawa and Eaton, 1990). The reversal in the primary flow skewing direction decreases the rate of growth of $\Delta(\delta^*/T)$ and $\Delta(\theta/T)$ past X/C = 1. The maximum changes in δ^*/T and θ/T for planes 5-12 are listed in Table 4.1.

Local C_f estimates were calculated using equation (4.10), and the results are shown in Figure 4.93. These results are presented using the freestream coordinate system. From the form of equation (4.10), the variation in C_f is expected to decrease when θ increases. This is in fact what happens, with a local minima occuring near the oil-flow visualization LOLS location. Of course, it is the local shear minima that causes this line, and ideally, the $(C_f)_{MIN}$ and LOLS locations should coincide precisely. The expected general decrease in skin friction magnitudes is observed as the boundary layer continues to develop in the streamwise direction.

4.3.2 Far Wake Data, Planes 12-15

This section discusses the author's data taken at X/C locations of 5.89, 9.14, and 11.56, and the data from Devenport *et al.*'s (1990) thick boundary layer at X/C = 3.00. The two most downstream positions are in the adverse pressure gradient section (region 3, discussed in section 3.1.1). Only U_{TC}/U_{ref} and u'_{TC}/U_{ref} measurements were taken in these planes. The data planes spanned $0 < -Z/T < 4.5$, which is a large region considering that the half width of the wind tunnel is approximately 6 wing thicknesses.

Contours of U_{TC}/U_{ref} and u'/U_{ref} in planes 12-15 are given in Figures 4.5b and 4.9b. The continuing distortion patterns are well defined in these far wake planes. It is interesting to note that for the *Los Angeles* (688) class and *Ohio* class submarines, the propulsor planes are located at approximately X/C = 9 and 11, respectively.

From X/C = 1.05 to 9.14, the vortex induced m an flow distortions move away from the centerline due to the induced flow of the wall image vortex. From X/C = 9.14 to X/C = 11.56, the spanwise position of the distortion patterns changes only slightly, if at all. The vortical flow structure appears to be quite diffused in the far wake, as the contours of u'_{TC}/U_{ref} do not show the local maxima "islands" as in plane 11. Further evidence of the vortex decay and diffusion is shown by the changing shape of the contours of u'_{TC}/U_{ref}. The almost horizontal "tongue" of high turbulent fluid at X/C = 3.00 recedes to the point where the contours of u'_{TC} are almost identical in shape to those of U_{TC}. The adverse pressure gradient seems to accelerate this change. Note that the contour plots also show the effects of the sidewall and ceiling boundary layers.

Westphal *et al.* (1985) compared vortices embedded in turbulent boundary layers in the presence of constant pressure and increasing pressure. Their resulting contours of mean streamwise velocity show a more defined distortion pattern for the constant pressure case. They observed that the adverse pressure gradient increased the rate of vortex core growth, but lowered the peak vorticity. The decrease in peak vorticity, which is expected from Helmholz's inviscid vorticity theorems, explains the decrease in distortion for the adverse pressure gradient case. Comparing the contours of U_{TC}/U_{ref} and f_D at X/C = 3.00, 5.89, and 9.14 in Figures 4.5b and 4.6b, one can observe the slight diffusion of the horseshoe vortex distortion pattern. The contours of f_D which mark the plume of low momentum fluid become more vertical, indicating a weakening of the vortex's recirculatory action. Comparing the similiarities of the contours of f_D from planes 14 and 15, one can see that the increase in the apparent distortion is due primarily to the growing boundary layer. The rapid growth of the boundary layer makes it difficult to determine if the distortion pattern is decaying more quickly due to the adverse pressure gradient. The lack of spanwise movement from plane 14 to 15, does indicate the relative weakness of the trailing horseshoe vortex in region 3. The dominant factor controlling the growth of the contours of U_{TC} and u'_{TC} seems to be the expanding boundary layer, and from X/C = 5.89 to 11.56, the spanwise dimension of the contour distortions appear to grow very little.

It is of interest to note that Westphal *et al.* also observed that an adverse pressure gradient seemed to increase vortex core aspect ratio, meaning that a more elliptic vortex was created. They report that this elliptic shape does not appear to be caused by core

meandering. This result could not be verified by the present experimental data, since no W_{TC} information was obtained.

The diffused effects of the horseshoe vortex can be seen in the slight deformation of the U_{TC}/U_{ref} far-wake profiles (Figures 4.26-4.28). The profiles of u'_{TC}/U_{ref}, show more kinking, with the local maxima being much further away from the wall (Figures 4.54-4.56). The profile kinking, which tends to produce closed contours of u'_{TC}, decays rapidly in the adverse pressure gradient. The peak magnitudes of the velocity fluctuations away from the wall remain approximately constant downstream of X/C = 3.00, with $(u'_{TC}/U_{ref})_{MAX}$ = .07 to .08. Note that Figures 4.54-4.56 shows the original vs. the corrected values of u'_{TC}, as discussed in section 2.5.1.

Figures 4.91b and 4.92b show the far-wake variation of δ^*/δ^*_{APP} and θ/θ_{APP} in the spanwise direction. Examining these figures, and also the far-wake contour plots, one can discern the effects of another region of secondary flow at a larger value of |Z/T|. One possible source of the smaller secondary flow structure is a flow disturbance occurring far upstream of the test section. An example of such a disturbance is a small corner separation in the adverse pressure gradient of the tunnel settling chamber. Another possible cause is a secondary flow in the corner formed by the wind tunnel side wall and floor. This is an example of Prandtl's secondary flow of the second kind, created by shearing stresses, as described by Gessner (1973). Figures 4.91b-4.93b reveal the disturbances due to this outer secondary flow, in terms of increased δ^* and θ, and decreased C_f. The position of the local increase in δ^* is approximately constant at Z/T = -3.5. The position of maximum δ^* and θ moves from Z/T = -1.5 at X/C = 3.00 to Z/T

= -1.8 at X/C = 5.89, where it remains nearly constant with increasing X/C. Figure 4.94 displays the rapid increase in $\Delta(\delta^*/T)$ and $\Delta(\theta/T)$ from X/C = 9.14 to 11.56, which is due to the adverse pressure gradient. Surprisingly, the data do not show a substantial increase in slope from X/C = 5.89 to 9.14. Table 4.2 lists the maximum changes in δ^*/T and θ/T for planes 13-15.

5.0 Data Set Comparisons

This chapter focuses on the primary motivation for this experimental study: the determination of the effects of the incoming boundary layer and flow parameters on a turbulent junction vortex. Tables 1.1 and 3.3 describe the data sets, and Table 2.6 gives their experimental uncertainties. For discussion purposes, SCD will identify Dickinson's (1986a,b) data, HMM will identify McMahon *et al.*'s (1987) data, JS will designate Shin's (1989) data, JLF will denote the author's present data, WJD will identify Devenport and Simpson's (1990a) LDV data, as well as Devenport *et al.*'s (1990) hot-wire data. The contour and velocity vector plots all use the scale 1.0" = .5(T), except plane 12 (X/C = 3.00), where 1.0" = 1.0(T).

The symbols used to designate the various data sets are consistent for all plots. The symbol denoting the author's data is a square, for Devenport and Simpson's LDV data, a triangle, for Dickinson's data, a solid circle, for McMahon *et al.*'s data, a diamond, and for Shin's data, an open circle.

5.1 Examination of Data Set Blockage Effects

As discussed in section 4.2, Figure 4.4 shows comparisons between 2-D potential flow results and the freestream experimental results from the different data sets. This was done to obtain a greater understanding of the possible blockage effects for each data set to avoid any possible misinterpretions of the differences between the flows. Shin's data was corrected to account for the variation in the freestream test section velocity from the reference velocity ($U_{TEST}/U_{ref} = 1.077$).

Dickinson's measurments were performed using a 24 inch wide tunnel, with a model that was 2.4 inches thick, creating a physical blockage of 10%. No allowances for streamline curvature were made in his case. Shin's data was obtained in a 36 inch wide tunnel, with a 2.8 inch thick model, creating a physical blockage of 7.8%. Again, no allowances for streamline curvature were made. Devenport's and the author's data was taken in a 36 inch wide tunnel with a 2.4 inch thick model, producing a physical blockage of 6.7%. However, as described in section 2.2.1, side wall inserts were used to allow for the outer streamline curvature, in an effort to create negligible blockage effects. Figure 3.6 shows that the blockage effects, if any, are very small.

McMahon *et al.*'s experimental data was obtained with the appendage located in a free jet 12 inches downstream of the tunnel exit plane. This configuration is not actually free of interference effects. The free jet/ambient air interface is constrained to follow a flow streamline, and the static pressure along this line must be equal to the ambient pressure. However, the pressure along a streamline is not constant, so these two interface conditions conflict, leading to some form of flow interference. No oil-flow

visualizations of McMahon *et al.*'s data were available, but the mean flow contours at X/C = 1.00 show evidence of a large separated flow region in the junction corner, which may be a consequence of the free jet test flow conditions.

Figure 4.4 shows good general agreement for the velocity magnitudes for all data sets, especially when one considers that the potential flow calculation did not account for the appendage boundary layer. The notable exceptions are in plane 8, where McMahon's freestream velocities are considerably lower (5-10%) than the calculated results. This result is surprising considering that in plane 10, McMahon's freestream velocities deviate only a few percent from the 2-D potential flow results. This apparent anomaly may be a consequence of the separated flow in the appendage trailing edge region.

The results from plane 9 show another unexpected result. Figure 4.4e reveals that the author's freestream velocities deviate more from the calculated results than those of Dickinson's case, which had a higher physical blockage and also did not allow for streamline curvature. The majority of the data shows both Dickinson's and the author's data to agree surprisingly well, with Dickinson's freestream velocities usually a few percent higher.

The effects of blockage are further revealed by examing the freestream skew angles. Plane 5 data shows a general overestimation of α_{TC} near the wing, and values of α_{TC} that are too low away from the wing. This latter effect is easy to see, as blockage will cause the flow angle to tend toward zero. Of all the data, Devenport's LDV data and Shin's data appear to agree the best, especially near the maximum values of α_{TC}. Plane 6 shows good α_{TC} agreement for both the author's and Shin's data sets, within 1° at

almost all locations. Plane 7 shows excellent agreement for the author's data. Dickinson's results here are not as good, showing some possible blockage effects. Plane 8 tells the same story, with Devenport's and McMahon's data agreeing very well with the numerical results, but Dickinson's data is constantly offset by 2°. This can be explained by tunnel blockage, but one cannot discount a bias error in the measurements. At plane 9, the author's data shows some scatter, but shows general agreement with the potential flow results. Dickinson's data again does not exhibit freestream flow angles as large as the potential flow solution predicts. Skipping to plane 11, the α_{TC} results for all concerned data sets agree well, with the author's data showing some scatter. The good agreement here is most likely a result of small flow angles and reduced blockage effects since the flow has passed by the wing at this location (X/C = 1.50).

Considering plane 10 (Figure 4.4f), one observes two things right away. First, the freestream flow angle near the centerline, as predicted by potential flow, changes radically from X/C = .93 to 1.05. Second, Dickinson's results are not even close to comparing with the potential flow results, or with the results of the other data sets. The other data sets, although displaying some scatter, follow the general trend set by the numerical results for freestream α_{TC} quite well. Dickinson's data shows angles that differ by 4° to 8°. This discrepancy is difficult to explain simply by blockage effects, and section 5.3 will further discuss this problem.

5.2 Expected Effects of the Approach Boundary Layer Properties

Before comparing data sets to examine the effects of varying the approach boundary properties, it is helpful to use intuition to gain any possible *a priori* knowledge, so that one knows what to look for and what differences to expect. This section discusses what effects different approach boundary layers may have on the wing-body flow structure.

From the previous discussion of Baker's (1980, 1985) and Belik's (1973) work, we see that the initial vortex structure in front of a cylinder (equivalent to the nose of an appendage) is primarily a function of two parameters, Re_θ and θ/T. The displacement thickness δ^* is interchangeable with θ. Re_{δ^*} (or Re_θ) effects the positions of X_V and X_S, and the basic vortex structure seems to be dependent on δ^*/D (or δ^*/T) for a given range of Re_{δ^*}.

5.2.1 Expected Re_θ Effects

Baker (1980, 1985) found that X_V increases as Re_{δ^*} increases, which means that the vortex's horizontal size is increasing. He conjectured that changing Re_{δ^*} does not change the vertical size of the primary vortex. For $Re_{\delta^*} < 10{,}000$, X_S increases also, but at a slower rate than X_V, which means that the distance between X_V and X_S is decreasing as Re_{δ^*} increases. This distance decreases even faster when $Re_{\delta^*} > 10{,}000$, as X_S starts to decrease at the larger Reynolds numbers. One can conclude then, that as Re_{δ^*}

increases, the main vortex will increase in size (X_V increases), and will have a more energetic initial roll-up (X_S - X_V decreases).

Ignoring the large scale unsteadiness present in the junction flow, a rather simple, intuitive argument would go as follows. Re_θ or Re_{δ^*}, for the flows considered in this study, is essentially a function of $U_{ref}\theta$ (or $U_{ref}\delta^*$), since ν is fairly constant for a given fluid medium (air or water). The freestream fluid momentum is directly proportional to U_{ref} and the lack of high momentum fluid near the wall is indicated by θ. Therefore, the product $U_{ref}\theta$ is indicative of the absolute relative difference in fluid momentum between the boundary layer and the freestream. If the momentum difference is large (large Re_θ), then the incoming high momentum fluid easily circulates down into the boundary layer and forms a strongly defined backflow region. If the momentum difference is small (small Re_θ), the backflow region is more diffuse. Realizing that $U_{ref}\theta$ indicates the typical magnitudes of the inertial forces in the boundary layer, yields the same hypothesis.

Studies done in a water tunnel within the Virginia Tech Aerospace Department by Kim (1991), support these speculations. As previously mentioned, Kim performed experiments at 2 different values of Re_θ, 330 and 1,100, on the same body shape as the author's. Mean velocity profiles along the centerline for the 2 test cases display a thinner and stronger backflow region the higher Reynolds number case (Figure 5.1). The higher Reynolds number case displays the enhanced secondary flow "jetting" effect due to the relative lack of momentum near the wall. Figure 5.2 presents contours of turbulence intensity, showing more distinct local maxima concentrated near the wall for Re_θ = 1,100. The lower Reynolds number case shows several turbulent "pockets", suggesting a more

complex mean flow pattern. The turbulence is spread over a much wider area for the Re_t = 330 case, displaying a more diffused secondary flow structure.

Realizing that $U_{ref}\theta$ is not actually the relative momentum difference between the outer and inner boundary layer regions, the author has come up with a new parameter, referred to as the momentum deficit factor (MDF). The momentum flux through a boundary layer is $(\rho)(U_{ref})^2(\delta-\theta)$ per unit width. The "momentum deficit" is equal to $\rho(U_{ref})^2(\theta)$ per unit width. If T is used as a characteristic width, then a form of MDF is $\rho(U_{ref})^2(\theta)(T)$. This is dimensional, however, so the final, non-dimensional form for MDF is $(Re_T)^2(\theta/T)$ which is also equal to $(Re_T)(Re_\theta)$. Flows with large values of MDF will tend toward smaller flow distortions and the vortical and turbulent flow structures will be more intense near the wall, since the low momentum fluid region acts as a type of "relief valve". Table 3.3 shows that for the flows examined in this study, Re_θ usually varies as MDF. The exception to this trend is at the lower Re_θ cases, where McMahon *et al.*'s data has the lowest MDF, despite having a higher Re_θ than either the author's or Devenport *et al.*'s thin boundary layer case.

The downstream effects on vortex position and resulting flow distortion due to the resistance of the inner boundary layer to the intrusion of freestream fluid can be predicted by considering Shizawa and Eaton's (1990) study. As previously discussed in section 4.3, two cases of a vortex embedded in a skewed boundary layer were studied. Case 1, where the near wall skewing-induced velocity was in the same direction as the vortex-induced velocity, corresponds to a case with very low resistance to the intrusion of outer fluid into the boundary layer (high MDF). Case 2, where the near wall skewing- and vortex-

induced velocities opposed one another, corresponds to a case with high resistance to the intrusion of outer fluid into the boundary layer (low MDF). Shizawa and Eaton found that the vortex associated distortion patterns for case 1 were not as strong and decayed more quickly than case 2. This was because the primary flow distortion mechanism (the upward transport of low momentum fluid due to separation) was enhanced in case 2. The vortex core position moved further away from the wall for case 2. More information concerning the vorticity distributions for the two cases is discussed in section 4.3.

5.2.2 Expected δ^*/T Effects

As mentioned previously, the ratio δ^*/T (or θ/T) may effect the initial vortex structure. Based on the research of previous workers (Baker (1980, 1985), LaFleur and Langston (1990), and Eckerle and Langston (1987)), it can be postulated that the number of vorticies along the centerline increases as δ^*/T increases. An argument supporting this hypothesis is that as δ^* increases, the corresponding decrease in near wall momentum effects the primary separation mechanism, causing a larger number of discrete vorticies to be formed in the plane of symmetry. Using flow topology, researchers have suggested several initial vortex configurations (2, 4, 6 vortex models), and for certain ranges of δ^*/T values, the number of vorticies seems to be constant. A sketch showing the various vortex configurations is given in Figure 5.3.

However, the relevance of the initial vortex structure on the downstream flow is moot issue, based on the conclusions drawn from the surface oil-flow visualizations (section 3.1.3). Any instantaneous, discrete vortex structure present in the nose region

appears to form a time-averaged primary vortex structure downstream of the body's maximum thickness location. The primary effect of δ^*/T may be its influence on the bimodal flow structure at the appendage nose, which would in turn affect the downstream turbulence characteristics.

The ratio δ^*/T is also an indication of the mass entrainment potential of the vortex. Since previous measurments (Devenport *et al.*, 1990) show that the primary vortex dimensions scale on T, this parameter relates the relative size of the boundary layer to the horseshoe vortex. Smaller values of δ^*/T will enable the vortical flow to have a greater effect on the entire boundary layer, and on the availability of high momentum fluid which energizes the secondary flow.

5.2.3 Significance of U_{ref}/T and U_{ref}/δ

U_{ref}/T and U_{ref}/δ form two additional parameters of interest. These ratios are dimensional (units of sec^{-1}), and as such, they are not true flow parameters by themselves. These parameters are useful, however, for non-dimensionalization of vorticity, and understanding their effects gives some insight into the basic flow physics.

The average vortex stretching rate for a particular appendage geometry is controlled by U_{ref}/T. According to potential flow theory, as the vortex stretching rate increases, the peak dimensional vorticity should increase, due to the shrinking of the vortex tube. The parameter U_{ref}/δ is related to the average spanwise vorticity in the incoming boundary layer. Therefore, increasing U_{ref}/δ should also increase the dimensionalized strength of the horseshoe vortex, but not the non-dimensionalized

strength. Determining the which of these two parameters are most appropriate for non-dimensionalizing the vorticity increases understanding of the junction vortex flow.

5.2.4 Parametric Space of Data Sets

Figure 5.4 clearly displays the varying parameters of each of the data sets examined in this study. Shin's parameters, when measured under conditions comparable to the other data sets, may fall within the region enclosed by the dashed line in the upper right corner. This is further discussed at the beginning of section 5.3.

The lines of constant MDF in Figure 5.4 show its variation with changing Re_θ and θ/T. The influences of Re_θ and θ/T on the juncture flow can be easily compared to the effects of MDF using this figure. Figure 5.4 also can be used as an aid in the design of future parametric studies of wing-body junction flows.

5.3 Data Set Comparison Results

The contour and secondary velocity plots will be the main tools for comparing the data. The profile plot comparisons provide much more detail, and in some instances this will help to see the effects of the approach boundary layer. One must be cautious, however, that the experimental uncertainties do not become a factor when comparing subtle details between the flows.

One fact is readily apparent when comparing the data sets. The secondary flow structure scales on T, the maximum appendage thickness, in both the Y and Z directions, as can be seen by the profile plots of W_{TC}/U_{ref} (Figures 4.32-4.38), the contour plots of turbulence intensity (Figures 5.40-5.46), and secondary velocity vector plots (Figures 5.20-5.26). The profile plots of f_D show that the distortion function also scales on T. The data sets do not compare precisely, but one can easily observe that T is more appropriate as a scaling factor than δ. The importance of T as a scaling factor reflects the dependance of the secondary flow on the pressure field created by the appendage geometry. All significant flowfield characteristics originate from the geometry of the wing-body junction.

A few things to note before continuing are listed as follows:

- The momentum deficit factor for Shin's data may be effectively larger than the listed value, even larger than Dickinson's value. This is because the actual test section velocity is higher than the given reference velocity (by a factor of 1.077), and also the given value of θ was determined with no appendage in the tunnel. Correcting MDF for just the velocity alone increases it by 16% to 13.0×10^8. Only a 2% increase in θ/T would create a value of MDF equal to Dickinson's.

- Shin's secondary velocities near the wall usually show an extremely large V component, which is not seen in flows with similiar boundary layer parameters (the SCD data set). The author believes this apparent anomaly was caused by the probe. This was the only data obtained using a 5 hole pressure probe, and the relatively large size of this probe could have interfered with the flow and/or caused bias errors to occur near the wall.

The probe was 3.18 mm in diameter, and measurements were taken to within 3.7 mm of the wall.

- Dickinson's secondary velocity and vorticity distribution data appear to be in error in plane 10 (Figures 5.25 and 5.35). The flow shown by his data is markedly different from the other data sets, and no reason can be found to explain it. The data in planes 9 and 11 compare well with other data sets, which leads the author to believe that the unusual secondary flow pattern in plane 10 is due to an error. The streamwise mean and fluctuating velocities in plane 10 do not appear to be significantly effected by this problem.

- A relatively large separated flow region is apparent in McMahon *et al.*'s flow at the trailing edge. This can be seen in contours of U_{TC}/U_{ref} in plane 10 (Figure 5.14).

5.3.1 Mean Velocity Distribution

Contour plots of U_{TC}/U_{ref} and the associated contours of distortion function (f_D) are shown in Figures 5.5-5.19. Secondary velocity plots are given in Figures 5.20-5.26. These figures reveal the distribution of the mean velocity components within the junction flow. When comparing "distortion levels", it is the plume of low momentum fluid near the line of low shear location that is being referred to. Greater flow distortion is indicated by lower values of f_D.

In general, the SCD and JS data sets show broader, more diffused distortion patterns for the contours of U_{TC}, while contours of f_D reveal that the HMM data has the highest distortion rates, with the JLF/WJD data falling in between. This is the trend predicted by the variation in MDF. Using Re_θ as a predictor, the JLF/WJD data would

have the highest distortion, followed by the HMM data, and then the SCD and JS data sets.

The validity of the concept behind the momentum deficit factor is perhaps best shown in plane 12, the farthest downstream location where comparisons were made. Figures 5.18 and 5.19 show the contours of U_{TC} and f_D. The WJD thin boundary layer case, has the lowest Re_θ (4,500 compared to 6,300 and 6,800 for the JLF/WJD and HMM data sets respectively). However, the distortion function results clearly show that the HMM data has the largest distortion levels (lowest values of f_D), while the distortion pattern in the "tongue" of low momentum fluid is approximately the same for the WJD thick and thin boundary layer cases. These latter two cases differ in MDF by 11%, while the WJD thin boundary layer case has an MDF which is 42% greater than the HMM case.

From the examination of the WJD thin and thick boundary layer data in plane 12, and also the HMM and WJD data in plane 8 (Figure 5.10), one can see that f_D does scale on T in the Y direction. One can conclude that if the HMM and WJD data had more similiar values of MDF, then the f_D contours would look more alike.

Plane by plane comparisons consistently yield the same results. The distorted contours of U_{TC} are more peaked for the cases with low values of MDF, and are broader for the cases with high MDF. The contours of f_D show this trend in even greater detail.

The effects of boundary layer thicknesses to body thickness ratios are seen primarily in the region between the body and the LOLS, where the local boundary layer is thinned by the sweeping of high momentum fluid into the junction by the horseshoe vortex. The increase in relative size of the horseshoe vortex compared to the boundary

layer for flows with low values of δ/T results in higher momentum fluid being available for entrainment into the junction. Figures 5.6-5.19 show slightly larger values of f_D (> 1.0) inboard of the horseshoe vortex for flows with low values of δ/T. This is a more subtle effect than the distortions due to the uplifting of low momentum fluid away from the wall, and in some instances, such as plane 11, the contours of f_D in the thinned region look almost identical for different values of δ/T.

As the flow moves downstream, another consequence of the momentum deficit factor is seen. The distortion patterns of the flows with higher MDF are centered further outboard, at larger values of |Z/T|. This is an expected trend, and can be explained as follows. For flows with higher values of MDF, the flows are similiar to Shizawa and Eaton's (1990) case 1 flows (see sections 5.2 and 4.3). The vortex-induced velocities between the wall and the vortex core are larger for case 1 than for case 2, which is more like a flow with high MDF. This condition leads to larger vorticity values for the high MDF cases (Shizawa and Eaton's case 1 data show this), and the increased vortex-induced velocities move the horseshoe vortex further from the centerline. The observed similarities to Shizawa and Eaton's flows suggests that changing MDF results in a change in the effective geometry-induced skewing magnitudes.

In planes 10 and 11, the secondary velocity vector plots show the horseshoe vortex structure centered farther from the centerline for flows with larger MDF values. In plane 11, it appears that the author's earlier hypothesis that MDF for the JS data may actually be slightly higher than for the SCD data is correct, since Shin's data shows the most outboard vortex location. Surprisingly, the spanwise positions for the primary distortion

do not vary much between the data sets in plane 12. The position for the HMM data seems farthest from the centerline, contrary to the previous discussion. This contradiction may be due to the trailing edge separation present in HMM's case.

The HMM secondary velocity results in plane 10 reveal a quite circular secondary flow pattern near the centerline, unlike that observed for the flows with higher MDF values. The proximity of this flow structure to the appendage trailing edge may be the cause of the significant flow separation for the HMM data set. The other flows all have a rather flat, elliptically shaped pattern, with no substantial V velocities except perhaps near the LOLS location or the body. These observations substantiate the predicted "relief valve" effect provided by the inner boundary layer for flows with high MDF. The near wall channelling of this fluid marked by positive vorticity is discussed in the next section.

The profile plots of mean velocities reveal additional information concerning the correct scaling of the mean flow distribution. The "kinking" of the U_{TC}/U_{ref} profiles (Figures 4.10-4.24) tends to scale on T, although the magnitudes are generally not the same. The distortion function filters out the effects of the "background" flow.

The appropriate scaling for the distribution of V_{TC}/U_{ref} is more difficult to determine. Some profiles display an apparent δ scaling (Figure 4.29), and others seem to scale on T (Figure 4.30). Flows with lower MDF show higher V_{TC} magnitudes, which is expected due to the observed higher distortion levels for these flows.

Most profiles of W_{TC}/U_{ref} show a very strong dependence on T (Figures 4.32-4.38). The variation in freestream flow angles makes it difficult to compare the relative skewing magnitudes for the data sets. The hodograph plots (Figures 4.77-4.83) reveal

very sharply defined crossover profiles for data sets with low δ/T ratios. The skewing magnitudes in general appear to be slightly greater for these flows also. This is indicative of the availability of higher momentum fluid closer to the horseshoe vortex secondary flow structure. When this fluid is swept into the boundary layer, it causes larger skewing angles and steeper gradients in W_{TC}.

5.3.2 Vorticity and Helicity Distribution

From observing the contours of $(\partial(W)/\partial Y)\delta/U_{ref}$ and helicity (defined by equation (4.3)), the concentration of vorticity near the wall is immediately evident for flows with higher values of MDF (Figures 5.27-5.38). JS vorticity levels are shown in the individual profile plots of $(\partial(\bar{W})/\partial Y)\delta/\bar{U}_{ref}$ (Figures 4.84-4.90), and are most similiar to the SCD distribution patterns, reaching higher values near the wall in some cases. This effect is a result of the relative lack of resistance to the instrusion of the secondary flow, creating a channelling effect near the wall. The profile plots of vorticity also indicate that the peaks in vorticity scale more appropriately on T than on δ. The no-slip condition at the wall was *not* used for calculating $(\partial(\bar{W})/\partial Y)$ near the wall, since this technique can lead to significant errors for estimating derivatives.

The trend in the distribution of positive and negative vorticity between the flows with high and low MDF are again similiar to the flows studied by Shizawa and Eaton (1990). The lower MDF flows (HMM, JLF/WID), previously showing characteristics of Shizawa and Eaton's case 2 flow, show a relatively stronger pocket of negative vorticity outboard of the primary vortex (Figure 5.31). A stronger negative vorticity region is also

observed for Shizawa and Eaton's case 2 flow, when compared to case 1. The strengths of the negative vorticity regions are reflected by the Y/T locations of the vortex cores. The variation in MDF between the data sets correctly predicts the relative Y/T positions of the vortex cores (as MDF increases, the core is closer to the wall).

By comparing the JS and SCD data to the JLF/WJD data sets, the correct vorticity scaling parameter appears to be T/U_{ref} (remember that $(T/\delta)_{JLF} \approx 2$, and $(T/\delta)_{SCD,JS} \approx 1$). This may be because the average vortex stretching rate, which is proportional to U_{ref}/T, is a dominant factor affecting vorticity magnitudes around the appendage nose. Comparisons between the HMM and WJD data in plane 8 (Figure 5.31), and also between the JS and SCD data sets (Figures 4.84-4.90), reveal that δ/U_{ref} is the appropriate scaling parameter for the magnitudes seen in the vortex core region. Plane 10 (Figure 5.35) shows similiar results, although the HMM contours show no well defined "core". The regions of high positive vorticity near the wing-body corner seen for the HMM data is likely due to the separation observed in that region.

The determination of which flows scale on the same parameters may be an indication of the flows' similiarity in MDF or Re_θ. The contour levels of $(\partial(W)/\partial Y)\delta/U_{ref}$ seen in the SCD and JS data are approximately twice as large as for the HMM or JLF/WJD data sets. The ratios of δ/T for the JS and SCD cases are twice as large as for JLF/WJD, but are approximately the same as for HMM's case, indicating that neither T/U_{ref} or δ/U_{ref} would scale the SCD/JS and HMM flows to the same levels. Note that Re_θ for the JS and SCD data is twice as large as JLF/WJD's and HMM's values. Observing that the vorticity levels for the SCD and JS data compare when scaled on

δ/U_{ref}, and that the vorticity levels for the HMM and JLF/WJD data are also approximately scaled by δ/U_{ref}, one may postulate that the vorticity levels, non-dimensionalized by δ/U_{ref} are dependent on Re_θ or MDF. The contours of helicity support these observations, indicating that flows with high values of MDF have more coherent large scale structures.

The decay of vorticity in the horseshoe vortex core vs. X/C is shown in Figure 5.39. Note that the maximum core values of $(\partial(W)/\partial Y)\delta/U_{ref}$ at X/C = 1.05 and 1.5 for the JLF/WJD and HMM data sets were estimated from the contour plots. The semi-log plots show that a power-law relationship may describe the decay of voriticity. The decay rate increases as MDF increases, but this trend may be the result of the scaling effects of δ/U_{ref}. The curves appear to be merging (except for the SCD data at X/C = .93 and 1.50) with increasing X/C, suggesting a growing dependence on δ/U_{ref} instead of T/U_{ref}.

5.3.3 Distribution of Turbulent Quantities

In general, the five turbulent quantities measured agree quite well between the data sets. The profile plots of these quantities (Figures 4.46-4.76) and the contours of u'_{TC}/U_{ref} show that the turbulence structure is largely governed by the appendage geometry, therefore scaling on T in the Y and Z directions.

Kim's (1991) contours of $(u'_{TC}/U_{ref})^2$, taken in the plane of symmetry at the appendage nose, show that increasing Re_θ confines and concentrates the turbulence structure in a near-wall region (Figure 5.2). This result seems to indicate that the higher Re_θ flow (SCD) would show a higher concentration of turbulent structures near the wall,

but this is not necessarily true. There is no obvious concentration of turbulent fluid near the wall, but in planes 8-11, the contour plots show slightly larger values of u'_{TC}/U_{ref} near the wall for the SCD data. The profile plots of u'_{TC} reveal how well T scales the flow.

The JLF/WJD contours of u'_{TC} shows more distinct "islands" of local turbulence peaks. This may be an effect of the ratio δ/T, since a thinner boundary layer has an initially thinner region marked by highly turbulent fluid, resulting in a less diffused turbulence structure in the wing-body junction. The HMM contours show neither local "islands" of peak turbulence intensity nor relatively high regions of turbulence near the wall. This is indicative of the low Re_θ, high δ/T approach flow parameters. Note the large separation region at the trailing edge for the HMM flow, revealed by the high turbulence levels as Z/T goes to zero (Figure 5.44).

By plane 12, at X/C = 3.00, the flow does not scale on T quite as well as it does near the appendage (Figure 5.46). The vertical growth of the turbulent structures as X/C increases appears to be limited by the boundary layer thickness, since they cannot grow as quickly into the freestream. When one considers that δ/T roughly doubles for each contour plot in Figure 5.46, the scaling effects of T are quite remarkable.

Data for v'_{TC}/U_{ref} was compared in planes 5, 8, and 10 (Figures 4.57-4.59). The data from plane 5 clearly shows the scaling effects of T. The cause of the larger peaks in v'_{TC} at this location for the WJD data is not obvious, as plane 8 shows similiar turbulence levels for the SCD and WJD data sets. The initial separation for the lower Re_θ (or MDF) flow may be "stronger" in a time-averaged sense, causing higher rms V velocity fluctuations. The HMM data in planes 8 and 10 show significantly higher levels

of v'_{TC}. This appears to be a combination of low Re_θ, high δ/T effects, since the SCD and WJD data sets are comparable. Judging from profiles of V_{TC}/U_{ref} in plane 10 (Figure 4.31), high V fluctuations may be a direct result of large mean V velocities, caused by the combination of low Re_θ, high δ/T.

The spanwise velocity fluctuations are different from the others, in that the distribution of w'_{TC}/U_{ref} seems to scale on δ instead of T. This may be because w'_{TC} does not show much variation through the boundary layer, and in most instances the only identifiable change occurs when the turbulence levels drop to their freestream values. The location of this drop, of course, scales on δ. In planes 8 and 10 (Figures 4.63 and 4.65), the w' levels from the HMM data set are slightly lower than the other 2 data sets (SCD and JLF/WJD). This again appears to be a low Re_θ, high δ/T effect, since the SCD and WJD data sets agree very well in the inner boundary layer. It is perhaps linked to the generally lower spanwise mean flow velocities observed in the HMM flow, particularly evident in plane 8 (Figure 4.63).

In a fashion similiar to w'_{TC}, the distribution of the mean Reynolds stress $\overline{uv}_{TC}/(U_{ref})^2$ appears to generally scale on δ, not T (Figures 4.67 and 4.69). This is seen by comparing the local maxima and minima, and noting that the SCD and HMM data compare better to each other than to the WJD data. The most negative values of $\overline{uv}_{TC}$ are usually seen for the HMM data set. It is difficult to draw any definite conclusions regarding $\overline{uv}_{TC}$, due to the scatter in the data and the lack of data for comparison.

The final turbulence quantity compared is $\overline{uw}_{TC}/(U_{ref})^2$. Unlike $\overline{uv}_{TC}$, the distribution of $\overline{uw}_{TC}$ clearly scales on T (Figures 4.70-4.76). Except for the separated

regions present in the HMM flow, the magnitudes of $\overline{u'w'}_{TC}$ ususally agree quite closely between the data sets. This similiarity shows that $\overline{u'w'}_{TC}$ is controlled by the horseshoe vortex flow structure, which is driven by the junction geometry. This is contrary to $\overline{u'v'}_{TC}$, which appears to depend more on the initial boundary layer thickness.

5.3.4 Boundary Layer Thickness and C_f Distributions

Figures 4.91 and 4.92 show results of δ^*/δ^*_{APP} and θ/θ_{APP} vs. Z/T for all the data planes (5-15). These results are in the freestream coordinate system. The substantial differences shown by JS's data in plane 5 (δ^*) is an indication of the approach boundary layer properties being determined with no appendage in the tunnel. The δ^* and θ data, in general, shows that the data sets with lower MDF values have a larger peaks near the JLF locations, while the data sets with higher MDF values tend not to have peaks in the boundary layer thicknesses. The ratio δ/T appears to play some importance here, since the JLF/WJD data, while similiar to the HMM data, has steeper gradients of δ^* in the spanwise direction. The larger values of δ^* and θ near the body for HMM's data is due to the flow separation for that case. The JS and SCD data sets show no local maxima in the majority of the measurement planes, but δ^* and θ do decrease as $|Z/T|$ decreases toward the wing.

Surprisingly, the distortive effects when scaled on T ($\Delta(\delta^*/T)$ and $\Delta(\theta/T)$) compare very closely. The values for the HMM data are highest, but are lowest for the JLF/WJD data, so nothing definite can be said relating MDF or Re_θ to the variation in $\Delta(\delta^*/T)$ or $\Delta(\theta/T)$ vs. X/C.

Results of $(C_f)_{FS}$ vs. Z/T are shown in Figure 4.93 for all data sets. The skin-friction coefficient in the freestream direction was estimated using equation (4.10). As expected, the data sets with the largest boundary layer thicknesses had the smallest C_f values. These data sets also had a much smaller spanwise variation in C_f. A local minima in C_f was usually located just outside the LOLS as determined by the oil-flows, and C_f increased for all data sets once inside the LOLS location. Plane 5 is an exception, as no local minima was found in C_f at this X/C location. C_f decreased monotomically as |Z/T| increased. The LOLS, however, is not well defined at the maximum thickness, so this result is not unexpected.

5.3.5 Comparison of Hot-Wire and LDV Results

Overall, these results agree well. The profile plots comparing the JLF data to the WJD LDV data in planes 5 and 10 show the closeness of the data sets. The mean streamwise velocities compare quite well, even at X/C = 1.05, Z/T = 0.0, which one would not expect. The data sets slightly disagree at some locations near the wall, which is due to a shallower slope in the log region for the JLF hot-wire data. This increases the values of U_{TC} near the wall for the hot-wire data by a few percent at the most.

The differences are greater for the spanwise velocities. There are 4 factors which influence these differences. These are 1) variation in initial probe alignment, affecting the freestream flow angle, 2) errors in aligning the hot-wire probe from point to point, 3) differences in vertical position, and 4) apparent hot-wire probe interference near the wall, which is seen as odd variations in W_{TC} as Y decreases. For the most part, the

effects of probe interference appear to be rather limited. From the hodograph plots (Figure 4.77), some differences in the relationship between U_{FS} and W_{FS} can be observed, which would tend to rule out vertical positioning as a source of the discrepancies.

The streamwise and spanwise rms normal stress values are always less for the JLF data near the wall if the hot-wire and LDV data do not agree. These differences are considerable for the u'_{TC}/U_{ref} data, especially in plane 5 (15% variations). The general agreement for the w'_{TC}/U_{ref} data is much better, usually within 5%. Section 2.5.1 discusses some inherent errors in the hot-wire data reduction equations. Judging by the results of the corrections in planes 13-15, where the local turbulence levels were much higher than near the wing, the data reduction errors can be ruled out as a cause of the observed differences. A likely cause is a damping effect of the hot-wire probe on the flow as it nears the wall, which would lower the measured turbulent fluctuations. This hypothesis is supported by the apparent linear growth in the variations with ln(Y/T), a functional form which is present in the solution describing a laminar flow near an oscillating wall, which is analogous to a turbulent flow near a stationary wall (Stokes (1851), and Van Driest (1965), both referenced in Schetz, 1984). Pursuing this discussion is beyond the scope of this research.

The similiarities in $\overline{uw}_{TC}/(U_{ref})^2$ are remarkable considering the uncertainties involved. However, a hot-wire probe damping effect is evident in Figures 4.70 and 4.75 as well. These plots show that the turbulent magnitudes obtained using a hot-wire were usually less than those obtained using a LDV.

5.3.6 Comparison to Ailinger's C_f Results

The C_f results obtained using oil-flow interferometry by Ailinger (1990) were converted to freestream coordinates and compared to results obtained using equation (4.10) (Figure 4.93). The wall skew angles reported by Ailinger were used to convert his data to freestream coordinates.

Knowing that this is a highly 3-dimensional flow, with separation regions and large spanwise velocities, one would not expect equation (4.10) to estimate C_f to within 10-15% of the actual value. Also knowing that Ailinger reported some difficulties in obtaining low uncertainty skin-friction data, especially near the line of low shear, it is surprising that the C_f results compare usually to within 10%. The largest difference in skin friction estimates occurs in the highly skewed flow inboard of the LOLS in Plane 5. A cautious optimist would view the good agreement between C_f estimates as an indication of the robustness of skin-friction correlations based on Re_θ and the shape factor, H. A C_f estimate accurate to within 10% for highly 3-D flows, based on a relatively simple formulation, would certainly aid rough engineering calculations.

6.0 Vortex Panel Calculations

In order to get a feel for the qualitative differences inherent in horseshoe vortices of various appendage shapes, a vortex panel calculation was used to examine the inviscid flow around several different appendage geometries. This chapter discusses the goals, methods, and results of the author's numerical research.

6.1 Numerical Research Program and Objectives

As mentioned in section 1.2.2, the distribution and circulation present in the horseshoe vortex is affected by the appendage in two ways. The geometrical bluntness increases the average vortex stretching rate, which increases the peak vorticity and affects the vortex structure. The appendage bluntness also affects the initial vortex roll-up, which increases the overall strength of the secondary flow. The author's findings support

Mehta's (1984) earlier research on the effects of nose shape on the horseshoe vortex. He found that a non-dimensionalized estimate of the streamwise circulation, Γ_X, defined as

$$\Gamma_X = \int_0^\delta \frac{\Omega_X}{U_e} \, dY \tag{6.1}$$

increases as the appendage nose becomes blunter. In evaluating equation (6.1), Mehta used the same Z location for all nose shapes, chosing one which passed near the vortex center. His results were used to obtain a correlation between appendage nose geometry and the horseshoe vortex strength.

One of the main quantities of interest is the partial derivative, $\partial(V_S)/\partial S$, which is the inviscid vortex stretching rate in the direction locally tangent to the body surface. V_S is the local tangential velocity, and S represents the distance, or arc length, along the body's surface. Integrating this derivative around the nose to the maximum thickness:

$$\frac{1}{S_{Tmax} - S_o} \int_o^{Tmax} \frac{\partial(V_S)}{\partial S} \, dS = \left(\frac{V_S}{S - S_o} \right)_{Tmax} \tag{6.2}$$

one can calculate the average vortex stretching rate. A major part of the numerical research work was spent examining the dependence of this quantity on the appendage nose geometry. Calculating equation (6.2) was performed numerically using a 2-D inviscid vortex panel method from Kuethe and Chow (1986). This method uses panels with linearly varying vortex strengths and solves for no flow through the surface (tangential flow only) at each panel's control point. The control points bisected their respective panels. The computer code from Kuethe and Chow output the tangential velocity (V_S) and coordinate information for each panel's control point.

The last numerical research objective involves the temporal flow characteristics of the wing-body junction flow. Rood (1984) concluded that the frequency of large scale structures in the junction-appendage wake flow are dependent on the appendage nose shape. Also, many researchers, notably Devenport and Simpson (1990b), have shown that a bimodal flow structure exists in the stagnation region of the appendage-body junction. The bluntness and resulting velocity gradients at the stagnation point may greatly affect this bimodal flow structure. The ratios

$$\frac{f}{\left(\frac{\partial(V_s)}{\partial S}\right)_o} \quad , \quad \frac{f}{\left(\frac{V_s}{S-S_o}\right)_{Tmax}} \tag{6.3}$$

form two possible Strouhal numbers characterizing the bimodal structure, where f is the bimodal switching frequency. The subscripts o and Tmax indicate where the expressions are evaluated. Tmax indicates the maximum thickness, o indicates the appendage 2-D stagnation point. These parameters may also be related to the surface pressure fluctuations along the stagnation line of the wing-body flow. While f must be determined by experimental data (surface pressure fluctuations or velocity measurements), the terms in the denominators of equation (6.3) can be estimated numerically, aiding in future research of the junction temporal flow characteristics.

6.2 Appendages Shapes Studied

A total of 30 appendage shapes were studied at 0° angle of attack, while 15 shapes were studied at 12° angle of attack. Only the geometries with rounded leading edges were studied at 12° angle of attack, since a sharp leading edge would cause separation in a viscous flow. The results from an inviscid calculation in such a case would be meaningless. The appendage shapes studied were

- NACA 00XX family (0006 through 0024)
- Mehta's body shapes (1984) with faired on tail sections
- 688 submarine sail cross section
- Circular nose with streamlined fairing
- 3:2 elliptic nose with 0020 tail
- Sand 1850 airfoil section
- Shin's body shapes (1989)

The modelling of the appendages was done one of two different ways. For Mehta's body shapes and the circular nose shape, analytical expressions were used (Z = f(X)) to achieve the final panel resolution of 132 panels. For all the other shapes, coordinate data was input, and then cubic splines were used to obtain the final panel resolution. In all cases, a modified circular arc point distribution was used to establish the final X/C values. This method automatically clusters control points at the leading and trailing edges, where higher densities are needed. Figures 6.1(a-e) show the results of the panelling schemes. Errors inherent in this numerical modelling process resulted in

geometrical deviations from the actual appendage shapes. Geometric characteristics such as maximum thickness location and leading edge radius (ρ_{LE}) are usually in error by at least few percent. These errors are not significant when examining the relationship between numerically calculated quantities (as in section 6.3.2). When applying the same relationships to experimental data, however, one should be careful to use the correct geometric parameters.

Mehta and Shin both used equations in the form

$$\left(\frac{X}{a}\right)^n + \left(\frac{Z}{b}\right)^n = 1 \tag{6.4}$$

to define the nose shapes of their "wedge elliptic" geometries. If $n < 2$, the nose comes to a point, while increasing n leads to a blunter nose. Figure 6.2 shows how n affects the nose shape for these appendages. In Mehta's experiment, the actual appendages had "chopped" tails (no trailing edges). A tail was numerically faired onto these appendage shapes for the computations, utilizing equation (6.4). The tail length was set at 200 mm ($a = 200$) and n was always 1.2. For the numerical work, values of n from 1.5 to 3.5, and T/C ratios of 5 and 10 percent were used to generate a "family" of Mehta-like appendage shapes. To calculate the nose geometry, the actual values that Mehta used, $a = 150$ mm and $b = 21$ mm, were used. Shin (1989) used values of 1.5 and 2.0 for his two wedge elliptic shapes, with $a = 142.24$ mm and $b = 35.56$ mm. The appendages used had NACA 0020 tails faired on to the nose sections at the maximum thickness, and the coordinates listed in Shin (1989) were used to define the appendage geometry.

6.3 Vortex Panel Calculation Results

To accomplish the goals set for this work, the inviscid velocity distribution around the nose of varying airfoil sections was examined by calculating $\partial(V_S)/\partial S$, which controls the horseshoe vortex stretching rate. This derivative, and the derivatives used to approximate ρ_{LE}, were estimated numerically using central differencing. After much trial and error, a correlation between the average vortex stretching rate and appendage geometric parameters was established. A relationship between a vortex transport parameter (VTP) and Mehta's experimental circulation estimates (Γ_X) was also found.

6.3.1 Preliminary Numerical Results

To verify the vortex panel code results, the output velocity distribution results from the NACA 00XX sections were compared to wind tunnel data from Abbott and Von Doenhoff (1959). As Figures 6.3(a-f) indicate, the inviscid approximation is quite accurate compared to wind tunnel data, especially for the thinner sections. The largest error encountered was about 1.5% of the maximum value of V_S/U_{ref}. This error, which increases with appendage thickness, is likely due to the presence of the boundary layer in the viscous flow. The effect of the boundary layer is to increase the apparent thickness of the wing, therefore causing the local velocity to increase. The spurious results at the trailing edge seem to be affected by the relative length of the trailing edge panels. The shorter these panels became, the greater the jump in the calculated V_S/U_{ref}. This anomaly

was judged to be inconsequential with regard to the final results, as the nose region, in the range $0 < X/C < (X/C)_{Tmax}$, was the region of interest.

Figures 6.4 and 6.5 present the velocity distributions for the other appendage shapes. Figures 6.6(a-j) show the results for the 12° angle of attack cases. The sharp peaks in the velocity distribution for the thin appendages are unlikely to occur in the presence of a viscous fluid. The astute observer will notice that the velocity distributions around the 688 sail and Sand 1850 sections are not as smooth as the other appendage results. This is because the coordinates for these appendages were obtained by graphical methods, and small inaccuracies were inevitable.

6.3.2 Average Vortex Stretching Rate vs. Body Geometry

The results of attempting to correlate the average vortex stretching rate (non-dimensionalized by ρ_{LE}/U_∞) and appendage nose geometry are shown in Figures 6.7(a-d). This correlation involves only numerically calculated parameters. The quantity BF is defined as

$$BF = \frac{1}{2}\frac{\rho_{LE}}{X_{Tmax}}\left(\frac{T_{max}}{S_{Tmax}} + \left(\frac{S}{X}\right)_{Tmax}\right) \qquad (6.5)$$

This "bluntness factor" was found through trial and error, and represents a great deal of calculations. More rudimentary parameters were tried, without much success. Examining its terms, it takes into account the nose leading edge sharpness (ρ_{LE}), the "stubbiness" of the appendage nose ($(S/X)_{Tmax}$), and an indicator of the average appendage surface slope (T_{max}/S_{Tmax}). For the appendages with pointed leading edges, ρ_{LE} was not set at zero,

but was estimated numerically using the control points generated by the inviscid code. The results of the estimate, however, are still quite small. The correlating parameters of the non-dimensional stretching to appendage geometry was determined for $\alpha = 0°$ independent of $\alpha = 12°$. When calculated for the $\alpha = 12°$ cases, the average vortex stretching rate was calculated from the stagnation point around the suction side, to the maximum thickness location. At $\alpha = 12°$, the correlation still held remarkably well, but not quite as well as for the 0° cases. It should be noted that BF is not a function of the angle of attack.

Three types of curve fits were applied to the $V_S\rho_{LE}/SU_\infty$ vs. BF data, linear ($y = mx + b$), and two types of log curve fits ($\log(y) = m \log(x) + b$). The log curve fits were minimized on linear least squares, ($error^2 = (y - 10^b x^m)^2$) and log least squares ($error^2 = (\log(y) - m \log(x) - b)^2$. The linear least square fit was done to minimize the error of the curve fit at high values of BF. Table 6.1 shows the values obtained from these three curve fits. The log curve fit based on linear least squares gives the best results in terms of the correlation coefficient (ρ_{XY}), and variance estimate (σ). Figures 6.7(a-d) also show the results of the curve fits.

Velocity profile data from Shin's (1989) three appendage nose geometries were used to evaluate the $(\partial(W)/\partial Y)\delta/U_{ref}$ distribution at the maximum thickness location for each geometry. The spanwise location of the profiles was Z/T = -.901, approximately the vortex center location as defined by the peak vorticity contour. Figure 6.8 shows the results of the vorticity calculations. The baseline geometry has by far the largest vorticity levels. Note that the vertical location of maximum vorticity for each case roughly

coincide with one another, revealing that this dimension may only be weakly effected by nose shape. Also note the steeper gradient in vorticity for the baseline case, indicating a greater relative concentration of vorticity. Figure 6.9 displays how the maximum vorticity increases with BF. This is an expected result since increasing BF increases the average vortex stretching rate. However, with the limited number of data points, a definitive correlation cannot be found.

6.3.3 Streamwise Circulation vs. Vorticity Transport Parameter

The correlation of average vortex stretching rate vs. BF involves only numerical data, but the second correlation found relates a numerically estimated quantity to experimental results. Mehta (1984) derives a simplified vorticity transport equation which models the transport of transverse vorticity into the streamwise direction. By ignoring viscous terms, the convection of vorticity by V and W, and the contributions due to ω_Y, Mehta presents the following equation:

$$\frac{\partial}{\partial X}\left(\frac{\Omega_X}{U}\right) = \frac{\Omega_Z}{U^2}\frac{\partial W}{\partial X} \tag{6.6}$$

This equation shows that geometries generating large values of $\partial(W)/\partial X$ and small values of U will create the strongest horseshoe vorticies. An appendage with a high bluntess factor meets both these criteria.

From equation (6.6), a vortex transport parameter (VTP) can be derived, relating the transported streamwise vorticity to inviscid quantities. Integrating both sides of

equation (6.6) along the X direction, and setting $W = V_S \sin(\theta)$, where θ is the local panel angle, the following equation is obtained:

$$\frac{\Omega_X}{U} = \int \frac{\Omega_Z}{U^2} \, d(V_S \sin(\theta)) \tag{6.7}$$

By assuming that $\omega_Z \propto U_E/\delta$, and realizing that $U = U_E = V_S \cos(\theta)$, the following relationship can be derived:

$$\delta\left(\frac{\Omega_X}{U}\right) \propto \int \frac{1}{V_S \cos(\theta)} \, d(V_S \sin(\theta)) \tag{6.8}$$

Evaluating the right hand side of equation (6.8) from the stagnation point to the maximum thickness location forms the vorticity transport parameter (VTP), which is related to Γ_X.

Figure 6.10 shows the correlation between Mehta's non-dimensional circulation estimate and the VTP. Note that the results for the 5% and 10% thick appendages are shown. To correlate the two cases with different thickness ratios, Γ_X was divided by $\partial(V_S/U_{ref})/\partial(S/C)$ evaluated at the stagnation point. This quantity is defined as Γ'_X. Doing this does not correlate the two set of data completely, as the two lines have slightly different slopes. Γ'_X was found to have some dependence on the bluntness factor as well. The results in Figure 6.10 are only preliminary, since not much data is available for different appendage shapes. The reader should note that Γ'_X depends strongly on the approach boundary layer properties, and Mehta's results correspond to one particular boundary layer. Mehta's experimental values for Γ_X were .076, .102, and .124 for n = 1.5, 2.0, and 3.0, respectively. The experimental parameters were U_{ref} = 25 m/s, δ/T =

.595, and Re_θ = 58,000 in the undisturbed boundary layer at the wing leading edge location.

Γ_X and Γ'_X were calculated for Shin's geometries, using the $(\partial(W)/\partial Y)$ component of Ω_X only, and the results tabulated in Table 6.2. Results for Γ'_X are plotted in Figure 6.10 as well. One can see a different relationship between Γ'_X and VTP for Shin's data. This variation is due to the different approach boundary layer, and may also be due to the different geometries involved.

Appendix C lists all results in tabular form for both the 0° and 12° angle of attack cases, including the ratios relevant to equation (6.3).

7.0 Conclusions

This chapter attempts to collect and list the most important and significant conclusions of this study. When discussing the results, the phrase *in general* was used quite often to describe certain trends or tendencies. This wording was used because a contradiction to any statement concerning the data comparisons could be found if the data is examined long enough. The conclusions were based on observations of all the available data, and reflect the prevalent trends discovered.

7.1 Basic Flow Physics

Conclusions concerning the basic flow physics resulted from examining the author's hot-wire data and Devenport and Simpson's (1990a) LDV data. These conclusions are:

- The primary horseshoe vortex flow structure is elliptically shaped and near the wall, similiar to what Dickinson (1986a,b) observed. This characteristic shape may be due to vortex meandering, caused by the unsteadiness in the nose bimodal flow region.
- The vorticity in the junction vortex is dominated by the change in spanwise velocity, and the term $(\partial(W)/\partial Y)$ defines the characteristic distribution of vorticity in the flow.
- The wall no-slip condition creates a very thin region of high negative vorticity near the wall underneath the primary vortex, which thickens outboard of the LOLS.
- The line of low shear (LOLS) position defines locations of peak turbulence intensity and boundary layer thicknesses. The time-averaged position of the horseshoe vortex core is inboard of the LOLS, and coincides with the location of large spanwise gradients in U_{TC}/U_{ref}.
- A quantity termed the "distortion function" (f_D) reveals the effects of the secondary flow distortions, which enables more conclusive flow comparison results in chapter 5.
- From examining and drawing conclusions from the results of Shizawa and Eaton's (1990) study, the importance of the geometry-induced skewing was seen. The conflicting directions of the skewing-induced and vortex-induced flows near the wall controls the flow separation. Therefore, the skewing affects the growth of the streamwise mean velocity distortions, and also the secondary flow structure and associated vorticity distribution.
- Flow distortion increases with X/C, and grows rapidly when enhanced by a favorable boundary layer skewing direction. Adverse pressure gradients also enhance the

growth of flow distortions. The flow over the aft portion of the appendage subjects the horseshoe vortex to skewing and a mild adverse pressure gradient, which work together to increase the boundary layer distortions.

- The characteristic peaks in streamwise normal stresses can be explained by the increased mixing of the boundary layer fluid, and a destabilizing of the boundary layer caused by the lifting action of the secondary flow.
- The far wake flow distortion patterns reveal a more diffused vortical flow structure. However, the growing boundary layer, particularly in the adverse pressure gradient, is the primary cause of flow distortions growth X/C increases.
- The spanwise location of maximum boundary layer thickness (and minimum skin friction) remains fairly constant at $|Z/T| \approx 1.8$ for X/C values greater than 6.

7.2 Effects of the Approach Boundary Layer

The conclusions of the main focus of this study are rather qualitative in nature, but this does not diminish their significance. These conclusions were obtained by comparing the data sets listed in Tables 1.1 and 3.3, and are as follows:

- The secondary flow structure and distortion function (f_D) scale on T in the Y and Z directions. This fact reveals that the horseshoe vortex flow structure is primarily driven by the appendage geometry and associated pressure gradients.

- The effects of Re_θ can be easily seen in the nose region using Kim's (1991) LDV measurement results. The larger Reynolds number increases the local mean flow distortions and gradients near the wall, and also concentrates and amplifies the near wall turburlence levels.

- From the observing the effects of Re_θ in the nose region, the author postulated that these effects may be more effectively described by a parameter termed the *momentum defect factor* (MDF). This factor, equal to $(Re_T)^2(\theta/T)$, is indicative of the relative decrease in momentum flux near the wall. Flows with large values of MDF would experience an enhanced near wall jetting of the secondary flow due to the "relief valve" effect of near wall, low momentum fluid.

- Comparison of the data sets reveals that the MDF correctly predicts the variation in mean flow distortion magnitudes and associated horseshoe vortex characteristics. Re_θ incorrectly predicts the relative distortion magnitudes.

- The two vortex configurations studied by Shizawa and Eaton (1990) were found to have characteristics which corresponded to flows with large MDF (case 1) and flows with small MDF values (case 2). One can conclude that the effects of the relative momentum near the wall are to modify the effective flow skewing around the appendage. Low MDF increased the effective flow skewing, and high MDF decreased the effective flow skewing.

- As MDF increases, the following effects are observed:
  - the mean streamwise velocity distortions are not as large
  - the secondary flow patterns are more elliptic

- the positive vorticity is increasingly concentrated in a near wall region
- the regions of negative vorticity outboard of the LOLS are less significant
- the movement of the vortex core away from the wall is decreased
- the downstream spanwise location of the vortex core is slightly further from the plane of symmetry

- The vorticity and helicity levels, non-dimensionalized by δ/U_{ref}, are greater for the high MDF flows. This may be due in part to increasing U_{ref}/T, which affects the average vortex stretching rate, and T/U_{ref} may be a more appropriate scaling factor for vorticity. Definite conclusions regarding the vorticity scaling could not be reached due to the variation of MDF, δ/U_{ref}, and T/U_{ref} between the data sets.

- The effects of decreasing δ^*/T are seen primarily by increased boundary layer thinning between the appendage surface and the line of low shear. The increase in relative size of the vortex to the boundary layer height increases the availability of high momentum fluid, leading to larger skin friction values. Also, the contours of u'_{TC}/U_{ref} show more distinct local maxima for lower values of δ^*/T, due to the initially thin layer of turbulent fluid.

- In general, the turbulence quantities show good agreement between the data sets. The higher Re_θ flows show only slight increases in streamwise turbulence intensity near the wall, which is surprising in light of Kim's (1991) observations at the appendage nose.

- The quanitities u'_{TC}, v'_{TC}, and $\overline{uw}_{TC}$ all appear to scale on T in the vertical direction, while w'_{TC} and $\overline{uv}_{TC}$ seem to scale more appropriately on δ.

- The maximum spanwise variations of δ^* and θ scale on T.

- The LDV results of Devenport and Simpson (1990a) generally compare well to the author's hotwire results (to within 2-3%). The near wall turbulence measurements disagree, which may be due to damping of the velocity fluctuations by the hot-wire probe.
- White and Ludwieg-Tillmann's correlations predict $(C_f)_{FS}$ to within approximately 5-10% of Ailinger's measured values. This is remarkable considering the highly 3-dimensional nature of this flowfield.

To gain further understanding of the effects of the approach boundary layer flow, a more rigidly controlled experiment, with less "interfering inputs", could be designed. This experiment would use the same appendage geometry, facilities and experimental apparatus. The only variations would be in the approach flow conditions.

7.3 Numerically Predicted Effects of Body Geometry

The vortex panel calculations produced numerical results which revealed a definite relationship between

- average vortex stretching rate and a parameter describing the geometric bluntness of the body shape (the bluntness factor, BF)
- streamwise horseshoe vortex circulation and a vortex transport parameter (VTP)

Calculations were also done to aid in the further study of the junction temporal flow characteristics.

All of the numerical results are preliminary, and more work needs to be done to fully understand the effects of nose shape on the junction flow. In light of the author's

experimental conclusions, the examination of the 2-D potential flow skewing away from the body may yield further insights into the effects of geometry. Any joint experimental/numerical study of various appendage shapes would certainly produce valuable information. An even more in depth program could further study and account for the effects of changing the approach boundary layer.

References

Abbott, I. H., and Von Doenhoff, A. E., *Theory of Wing Sections*, Dover Publications, Inc., New York, 1959.

Agui, J., and Andreopoulos, J., "Experimental Investigation of a Three-Dimensional Boundary Layer Flow in the Vicinity of an Upright Wall Mounted Cylinder", AIAA 21st Fluid Dynamics, Plasma Dynamics, and Lasers Conference, AIAA 90-1545, June 18-20, 1990.

Agui, J., and Andreopoulos, J., "Near Wall Vorticity Flux Dynamics in a Three Dimensional Boundary Layer with Separation", AIAA Paper 91-0733, January 1991.

Ahn, S., "Some Unsteady Features of Turbulent Boundary Layers", Master's Thesis, Virginia Polytechnic Institute and State University, Blacksburg, VA, 1986.

Ailinger, Kevin G., "Measurements of Surface Shear Stresses under a Three-Dimensional Turbulent Boundary Layer using Oil-Film Laser Interferometry", Master's Thesis, Virginia Polytechnic Institute and State University, Blacksburg, VA, 1990.

Baker, C. J., "The Turbulent Horseshoe Vortex", *Journal of Wind Engineering and Industrial Aerodynamics*, Vol. 6, Nos. 1-2, pp. 9-23, 1980.

Baker, C. J., "The Position of Points of Maximum and Minimum Shear Stress Upstream of Cylinders Mounted Normal to Flat Plates", *Journal of Wind Engineering and Industrial Aerodynamics*, Vol. 18, pp. 263-274, 1985.

Belik, L, "The Secondary Flow About Circular Cylinders Mounted Normal to a Flat Plate", *Aeronautical Quarterly*, Vol. 24, pp. 47-54, February 1973.

Cutler, A. D., and Bradshaw, P., "The Interaction Between a Strong Longitudinal Vortex and a Turbulent Boundary Layer", AIAA Paper 86-1071, 1986.

Deng, G. B., Piquet, J., and Queuty, P., "Navier-Stokes Computations of Vortical Flows", AIAA 21st Fluid Dynamics, Plasma Dynamics, and Lasers Conference, AIAA 90-1628, June 18-20, 1990.

Devenport, W. J., Agarwal, N. K., Dewitz, M. B., Simpson, R. L., and Poddar, K., "Effects of a Fillet on the Flow Past a Wing-Body Junction", *AIAA Journal*, Vol. 28, pp. 2017-2024, December 1990.

Devenport, W. J. and Simpson, R. L., *An Experimental Investigation of the Flow Past an Idealized Wing-Body Junction: Preliminary Data Report v. 5*, AOE Dept., VPI&SU, 1990a.

Devenport, W. J. and Simpson, R. L., "Time-Dependent and Time-Averaged Turbulence Structure near the Nose of a Wing-Body Junction", *Journal of Fluid Mechanics*, Vol. 210, pp. 23-55, 1990b.

Dickinson, S. C., *An Experimental Investigation of Appendage-Flat Plate Junction Flow Volume 1: Description*, DTNSRDC-86/051, December 1986a.

Dickinson, S. C., *An Experimental Investigation of Appendage-Flat Plate Junction Flow Volume 2: Elliptical Nose Appendage Data Base*, DTNSRDC-86/052, December 1986b.

Eckerle, W. A., and Langston, L. S., "Horseshoe Vortex Formation Around a Cylinder", *Journal of Turbomachinery*, Vol. 109, pp. 278-285, April 1987.

Gessner, F. B., "The Origin of Secondary Flow in Turbulent Flow Along a Corner", *Journal of Fluid Mechanics*, Vol. 58, pp. 1-25, 1973.

Hussain, A., "Coherent Structures and Turbulence", *Journal of Fluid Mechanics*, Vol. 173, pp. 303-356, 1986.

Johnston, J. P., "On the Three-Dimensional Turbulent Boundary Layer Generated By Secondary Flow", *Journal of Basic Engineering*, Vol. 82, pp. 233-248, 1960.

Jorgensen, F. F., "Directional Sensitivity of Wire and Fiber-Film Probes", *DISA Information*, No. 11, pp. 31-37, 1971.

Kim, Sangho, "Observation and Measurements of Flow Structures in the Stagnation Region of a Wing-Body Junction", Ph.D. Dissertation, Virginia Polytechnic Institute and State University, Blacksburg, VA, 1991.

Kubendran, L. R., McMahon, H. M., and Hubbartt, J. E., "Turbulent Flow Around a Wing/Fuselage-Type Juncture", *AIAA Journal*, Vol. 24, No. 9, pp. 1447-1452, September 1986.

Kuethe, A. M., and Chow, C., *Foundations of Aerodynamics*, Fourth Ed., John Wiley and Sons, Inc., United States, 1986.

LaFleur, R. S., and Langston, L. S., "Iceformation Design of a Cylinder/Hull Juncture with Horseshoe Vortices and Unsteady Wake", *Proceedings of the Second International Symposium on PERFORMANCE ENHANCEMENT for Marine Applications*, Newport, RI, pp. 87-97, 1990.

Langston, L., and Boyle, M., "A New Surface Streamline Flow Visualisation Technique", *Journal of Fluid Mechanics*, Vol. 125, pp. 53-59, 1982.

McMahon, H. M., Merati, P., and Yoo, K. M., *Mean Velocities and Reynolds Stresses in the Juncture Flow and in the Shear Layer Downstream of an Appendage*, Final Report Under Contract #N00014-85-K-0234, prepared for Office of Naval Research, Georgia Institute of Technology, GITAER 87-4, September 1987.

Mehta, R. D., "Effect of Wing Nose Shape on the Flow in a Wing/Body Junction", *The Aero. J. of the Royal Aero. Soc.*, pp. 456-460, December 1984.

Miller, J. A., "A Simple Linearized Hot-Wire Anemometer", *Journal of Fluids Engineering*, Vol. 98, pp. 550-557, 1976.

Moffat, R. J., "Contributions to the Theory of Single-Sample Uncertainty Analysis", *Journal of Fluids Engineering*, Vol. 104, pp. 250-260, 1982.

Moore, J. and Forlini, T. J., "A Horseshoe Vortex in a Duct", *Journal of Gas Turbines and Power*, Vol. 106, pp. 668-676, July 1984.

Olcmen, Semih M., "An Experimental Study of a Three-Dimensional Pressure-Driven Turbulent Boundary Layer", Ph.D. Dissertation, Virginia Polytechnic Institute and State University, Blacksburg, VA, 1990.

Peake, D., and Galway, R., "The Three Dimensional Separation of a Plane Incompressible Laminar Boundary Layer Produce by a Circular Cylinder Mounted Normal to a Flat Plate", N.R.C. (Canada), Rep. LR 428, 1965.

Ram, V. V., "Untersuchen uber die Eckengrenz schicht an einem Kreizylinder mit Seitenwand", Institute of Fluid Mechanics, Branschweig, Rep. 63/46, 1963.

Rife, M., "An Experimental Study of the Relationship Between Velocity and Pressure Fluctuations in a Wing-Body Junction", Master's Thesis, Virginia Polytechnic Institute and State University, Blacksburg, VA, 1991.

Reneau, L. R., Johnston, J. P., and Kline, S. J., "Performance and Design of Straight, Two-Dimensional Diffusers", *Journal of Basic Engineering*, Vol. 89, pp. 141-150, 1967.

Rodi, W., "A New Method of Analysing Hot-Wire Signals in Highly Turbulent Flow, and Its Evaluation in a Round Jet", *DISA Information*, No. 17, pp. 9-18, February 1975.

Rood, E. P., "Experimental Investigation of the Turbulent Large Scale Temporal Flow in the Wing-Body Junction", Ph.D. Dissertation, The Catholic University of America, Washington, D.C., 1984.

Rotta, J. C., "Turbulent Boundary Layers in Incompressible Flow", *Progress in Aeronautical Sciences*, Vol. 2, pp. 1-219, 1962.

Schetz, J. A., *Foundations of Boundary Layer Theory for Momentum, Heat, and Mass Transfer*, Prentice-Hall, Inc., Englewood Cliffs, NJ, 1984.

Shabaka, I. M. M. A., and Bradshaw, P., "Turbulent Flow Measurements in an Idealized Wing/Body Junction", *AIAA Journal*, Vol. 19, No. 2, pp. 131-132, February 1981.

Shin, J., "Effective Methods of Controlling a Junction Vortex System in an Incompressible, Three-Dimensional, Turbulent Flow", Ph.D. Dissertation, Virginia Polytechnic Institute and State University, Blacksburg, VA., 1989.

Shizawa, T., and Eaton, J. K., "*Interaction of an Embedded Longitudinal Vortex with an Attached, Three-Dimensional, Turbulent Boundary Layer*", Report No. MD-56, Thermosciences Division, Department of Mechanical Engineering, Stanford University, Stanford, CA, August 1990.

Simpson, R. L., Heizer, K. W., and Nasburg, R. E., "Performance of a Simple Linearized Hot-Wire Anemometer", *Journal of Fluids Engineering*, Vol. 101, pp. 381-382, 1979.

Simpson, R. L., Chew, Y. T., and Shivaprasad, B. G., *Measurements of a Separating Turbulent Boundary Layer*, Project SQUID Report SMU-4-PU, SMU, Dallas, Texas, 1980.

Spalding, D. B., *Conference Internal Developments in Heat Transfer*, ASME, Boulder, CO, Part II, pp. 439-446, 1961.

Sung, Chao-Ho, and Lin, Cheng-Wen, "Numerical Investigation on the Effect of Fairings on the Vortex Flows Around Airfoil/Flat-Plate Junctures", *Proceedings of the AIAA 26th Aerospace Sciences Meeting*, AIAA, Washington DC, January 1988.

Visbail, M. R., "Structure of Laminar Juncture Flows", *AIAA Journal*, Vol. 29, pp. 1273-1281, August 1991.

Westphal, R. V., Eaton, J. K., and Pauley, W. R., "Interaction Between a Vortex and a Turbulent Boundary-Layer in a Streamwise Pressure Gradient", *Proceedings of 5th Symposium on Turbulent Shear Flows*, Cornell University, Session 7, pp. 1-8, August 1985.

White, Frank M., *Viscous Fluid Flow*, McGraw-Hill, Inc., United States, 1974.

Tables

Table 1.1. Comparison of measurement locations and quantities measured, 3:2 elliptic nose, NACA tail junction flow studies

	Fleming (JLF)	Dickinson (SCD)	McMahon *et al.* (HMM)	Shin (JS)	Devenport *et al.* (WJD)
Measurement Planes (X/C)	.18 (5)	.18 (5)		.18 (5)	.18 (5)
	.42 (6)			.43 (6)	
	.64 (7)	.64 (7)			
		.75 (8)	.75 (8)		.75 (7)
	.93 (9)	.93 (9)			
	1.05 (10)	1.05 (10)	1.00 (10)	1.00 (10)	1.05 (10)
	1.50 (11)	1.50 (11)		1.50 (11)	
			3.00 (12)		3.00 (12)*
	5.89 (13)*				
	9.14 (14)*				
	11.56 (15)*				

Notes:

JLF measurements: U, u', W, w', $-\overline{uw}$ taken with single, yawable hot-wire, except locations designated ()* indicate measurements of U and u' only.

SCD measurements: U, u', W, w', V, v', $-\overline{uv}$, $-\overline{uw}$ taken with hot-film probe. Dickinson also found mean pressures on wall and made oil-flow visualizations.

HMM measurements: U, u', W, w', V, v', $-\overline{uv}$, $-\overline{uw}$, $-\overline{vw}$ taken with rotating, slant-wire probes.

JS measurements: U, V, W taken with 5-hole probe.

WJD measurements: U, u', W, w', V, v', $-\overline{uv}$, $-\overline{uw}$, $-\overline{vw}$, taken with LDV (Devenport and Simpson, 1990a). Location designated ()* indicates hot-wire measurements of U and u' only (Devenport *et al.*,(1990)). Also, measurements were made for both *thick* and *thin* approach boundary layers at X/C = 3.00.

Table 2.1. Offsets for 3:2 elliptic nose, 0020 tail appendage

X/C	Y/C
0.0	0.0
0.015	0.047
0.029	0.065
0.059	0.088
0.088	0.102
0.118	0.111
0.176	0.118
0.294	0.114
0.412	0.104
0.529	0.089
0.647	0.072
0.765	0.051
0.882	0.028
1.0	0.0

Table 2.2. X, Y, and Z location uncertainties (95% confidence levels)

Uncertainty in X:	$\pm(1 + (Y)\sin(2°))$ (mm)
Uncertainty in X/T:	$\pm(.014 + (Y/T)\sin(2°))$
Uncertainty in Y:	± .08 mm
Uncertainty in Y/T:	± .001
Uncertainty in ΔY:	± .03 mm
Uncertainty in Z:	(Same as X)
Uncertainty in Z/T:	(Same as X/T)

Table 2.3. Nominal experimental uncertainties (95% confidence levels)

Temperature drift and uncertainty:	± 1° C
Pressure drift and uncertainty:	± 5 mb
Manometer uncertainty:	± .012 in
Amplifier offset drift:	± .001 V (± .2%)
Amplifier gain drift:	± .1 (± .5%)
Axial coefficient uncertainty:	± .05
Probe angular positioning error:	± .5°
Mean voltage error:	± .5%

Note: Velocity gradient effects were not considered.

Table 2.4. Reduced data uncertainty (95% confidence levels)

Uncertainty in:	Uncertainty:
U/U_{ref}	± 1.5%
W/U_{ref}	± U/U_{ref} sin(.5°)
u'/U_{ref}	± 1.5%
w'/U_{ref}	± 5%
$-\overline{uw}/U^2_{ref}$	± 5%
α_{FS}	± .5°
α_{Γ}	± 2.5° (worst case)

Note: Data in tunnel coordinates

Table 2.5. Typical contributions of experimental uncertainties to reduced uncertainties (percentage of total uncertainty)

Experimental Uncertainty	U/U_{ref}	W/U_{ref}	u'/U_{ref}	w'/U_{ref}	$-\overline{uw}/U^2_{ref}$	α_{FS}
Temperature	1.4	0.1	1.3	1.1	0.7	0.0
Pressure	3.4	0.1	3.1	2.8	1.7	0.0
Manometer	8.7	0.3	8.4	7.5	4.6	0.0
Axial coeff. (k)	0.0	1.8	0.5	11.2	23.0	1.8
Probe angle	0.5	94.6	2.2	10.3	22.5	98.1
E (calibration)	0.0	0.0	0.0	0.0	0.0	0.0
E (amp. offset)	49.0	1.5	26.2	35.6	13.2	0.0
E (amp. gain)	36.8	1.6	58.4	31.5	34.4	0.0

Note: Data point location is X/C = .42, Y/T = .0064, Z/T = .692
Data in tunnel coordinates

Table 2.6. Quoted experimental uncertainties of data sets used for comparisons of wing-body junction flows

Quantity	SCD[1]	WJD[2]	HMM[3]	JS[4]
U/U_{ref}, V/U_{ref}, W/U_{ref}	±2.5%	±.035	±2%	±.007
u'/U_{ref}, v'/U_{ref}, w'/U_{ref}	N/A	±.003	±8%	-
$-\overline{uv}/(U_{ref})^2$, $-\overline{uw}/(U_{ref})^2$	N/A	±.0002	±6%	-
Flow angle	N/A	N/A	±1.0°	-

Notes:

These figures are all nominal uncertainties

[1]From Dickinson (1986a)

[2]LDV uncertainties estimated from Devenport and Simpson (1990a) (note also that these uncertainties are not given as percentages)

[3]Estimated from McMahon *et al.* (1987) (these figures are the upper uncertainty limits)

[4]Nominal upper limit on mean velocity uncertainties, from Shin (1989)

Table 3.1. Adverse pressure gradient boundary layer profile properties

X/C location	10.135	11.08	12.06
U_{FS}/U_{ref}	.853	.817	.782
$\delta_{.995}/T$	1.427	1.718	1.910
δ^*/T	.273	.325	.400
θ/T	.152	.166	.184
H (= δ^*/θ)	1.80	1.96	2.18
C_f	.00142	.00124	.00101

Notes:

C_f estimated using Spalding's wall law (equation 3.2)

Although T and C do not have any physical meaning for these profiles (wing not mounted in tunnel), the results are non-dimensionalized by T and C to be consistent

Table 3.2. Line of low shear locations

Plane #, X/C	$(Z/T)_{LOLS}$
5, .18	-.88*
6, .42	-.99
7, .64	-.94
8, .75	-.90
9, .93	-.87
10, 1.05	-.89

Notes:

*LOLS location in plane 5 is not well defined, location given is an estimate.

Table 3.3. Approach boundary layer parameters, 3:2 elliptic nose, NACA 0020 tail wing-body flow studies

Data Set ID	JLF,WJD[1]	SCD[2]	HMM[3]	JS[4]	WJD[5]
T (cm)	7.17	6.1	7.1	7.1	7.17
C (cm)	30.5	25.9	30.9	30.2	30.5
T/C	.235	.234	.230	.235	.235
U_{ref} (m/s)	26.75	30.5	15.24	20.9	32.0
δ/T	.513	1.197	.947	1.15	.263
δ^*/T	.0779	.1345	.1467	.148	.043
θ/T	.0548	.1014	.1003	.1227	.031
H (= δ^*/θ)	1.42	1.33	1.46	1.206	1.387
Re_θ	6,300	11,600	6,800	11,700	4,500
Re_{δ^*}	8,900	15,400	10,000	14,100	6,200
Re_T	115,000	114,400	67,800	95,400	145,200
C_f	.00247	.00247	.00232	.00256	.0028
U_{ref}/T (1/sec)	373.1	500.0	214.6	294.4	446.3
U_{ref}/δ (1/sec)	727.3	417.7	226.7	256.1	1,697
MDF ($x10^8$)	7.24	13.3	4.61	11.2	6.53

Notes:

[1]JLF hot-wire and WJD LDV and hot-wire data, *thick* boundary layer case, approach boundary layer profile measured at X/T = -2.146, Z/T = 0.0, with wing in place.

[2]SCD hot-film data, approach boundary layer profile data corrected from X/T = -3.167, Z/T = 0.0 to WDJ location, wing in place.

[3]HMM hot-wire data, approach boundary layer profile data corrected from X/T = -2.087, Z/T = 0.0 to WDJ location, wing in place.

[4]JS 5-hole probe data, approach boundary layer data at X/T = 0.0, no wing installed.

[5]WJD hot-wire data, *thin* boundary layer case, plane 12 (X/C = 3.00) only, approach boundary layer profile measured at X/T = -2.146, Z/T = 0.0.

Table 4.1. Wing-body junction flow horseshoe vortex effects, planes 5-12

P#	Data Set ID	Z/T limits	$(\partial(W)/\partial Y)_{MAX}$	h_{MAX}	$\Delta(\delta^*/T)$	$\Delta(\theta/T)$
5	JLF	.775,1.525	2.178	2.137	.0220	.013
	WJD	.55,1.525	2.243	2.049	.0203	.029
	SCD	.55,1.525	4.917	5.146	.0318	.022
6	JLF	.692,2.00	1.112	1.112	.0320	.021
7	JLF	.555,2.00	.6583	.483	.0499	.032
	SCD	.555,2.00	.8048	.7003	.0649	.045
8	WJD	.308,1.48	.4637	.391	.0772	.049
	SCD	.308,1.48	.5157	.388	.0617	.044
	HMM	.308,1.48	.350	.30	.0939	.065
9	JLF	.327,2.00	.3500	.273	.0818	.048
	SCD	.327,2.00	.9767	.670	.0835	.057
10	JLF	.200,2.00	.300	.200	.0921	.055
	WJD	.200,1.60	.300	.200	.0944	.055
	SCD	.200,2.00	-	-	.0894	.063
	HMM	.200,2.00	.300	.150	.0772	.063
11	JLF	.200,2.00	.250	.200	.0933	.061
	SCD	.200,2.00	.715	.696	.0991	.064
12	WJD (thin)	.354,4.603	-	-	.0969	.0626
	WJD (thick)	.354,4.603	-	-	.1086	.0689
	HMM	.354,2.833	-	-	.1559	.0919

Note: $(\partial(W)/\partial Y)_{MAX}$ and h are non-dimensionalized by δ/U_{ref} and $\delta/(U_{ref})^2$ respectively.

Table 4.2. Wing-body junction flow horseshoe vortex effects, planes 13-15

P#	Data Set ID	Z/T limits	$\Delta(\delta^*/T)$	$\Delta(\theta/T)$
13	JLF	0,4.80	.136	.092
14	JLF	0,4.80	.188	.111
15	JLF	0,4.00	.392	.187

Table 6.1. Curve fitting results for $(V_S/S)_{Tmax}\rho_{LE}/U_{ref}$ vs. BF data (α = 0° and 12°)

	$y = 10^b x^m$	$\log(y)=m \log(x)+b$	$y = mx + b$
m	.88157, .80749	.94010, .86617	1.1150, 1.0061
b	.048231, .014203	.10727, .057897	.016204, .03953
ρ_{XY}	.99969, .99806	.99871, .997165	.99747, .99356
σ	.005777, .01765	.031187, .038464	.016294, .03201

Notes:

Columns contain both 0° and 12° cases, separated by a comma
28 points were used for the α = 0° data (J. Shin appendages not used)
14 points were used for the α = 12° data (J. Shin appendage not used)

Table 6.2. Effects of nose shape at maximum thickness locations for Shin's geometries

Appendage Geometry	Γ_x	Γ'_x	$(\partial(W)/\partial Y)_{MAX}$
3:2 elliptic nose, NACA 0020 tail	.140	.0066	2.819
4:1 elliptic nose, NACA 0020 tail	.0722	.00134	.9568
4:1 wedge elliptic nose, NACA 0020 tail	.0605	.000068	.7724

Note: $(\partial(W)/\partial Y)_{MAX}$ is non-dimensionalized by δ/U_{ref}.

Figures

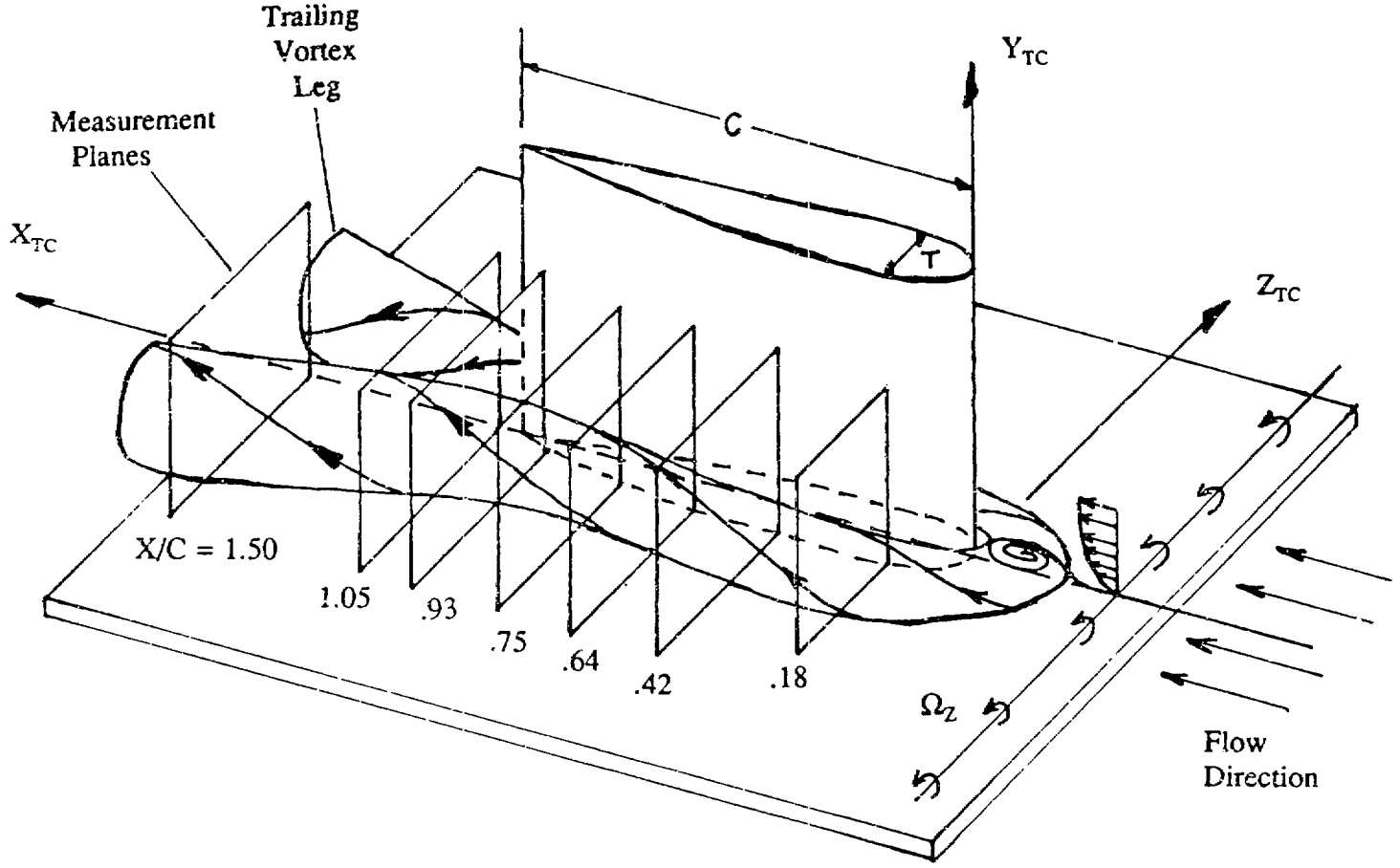

Figure 1.1. Sketch of Wing-Body Junction, Showing Measurement Planes and Tunnel Coordinate System

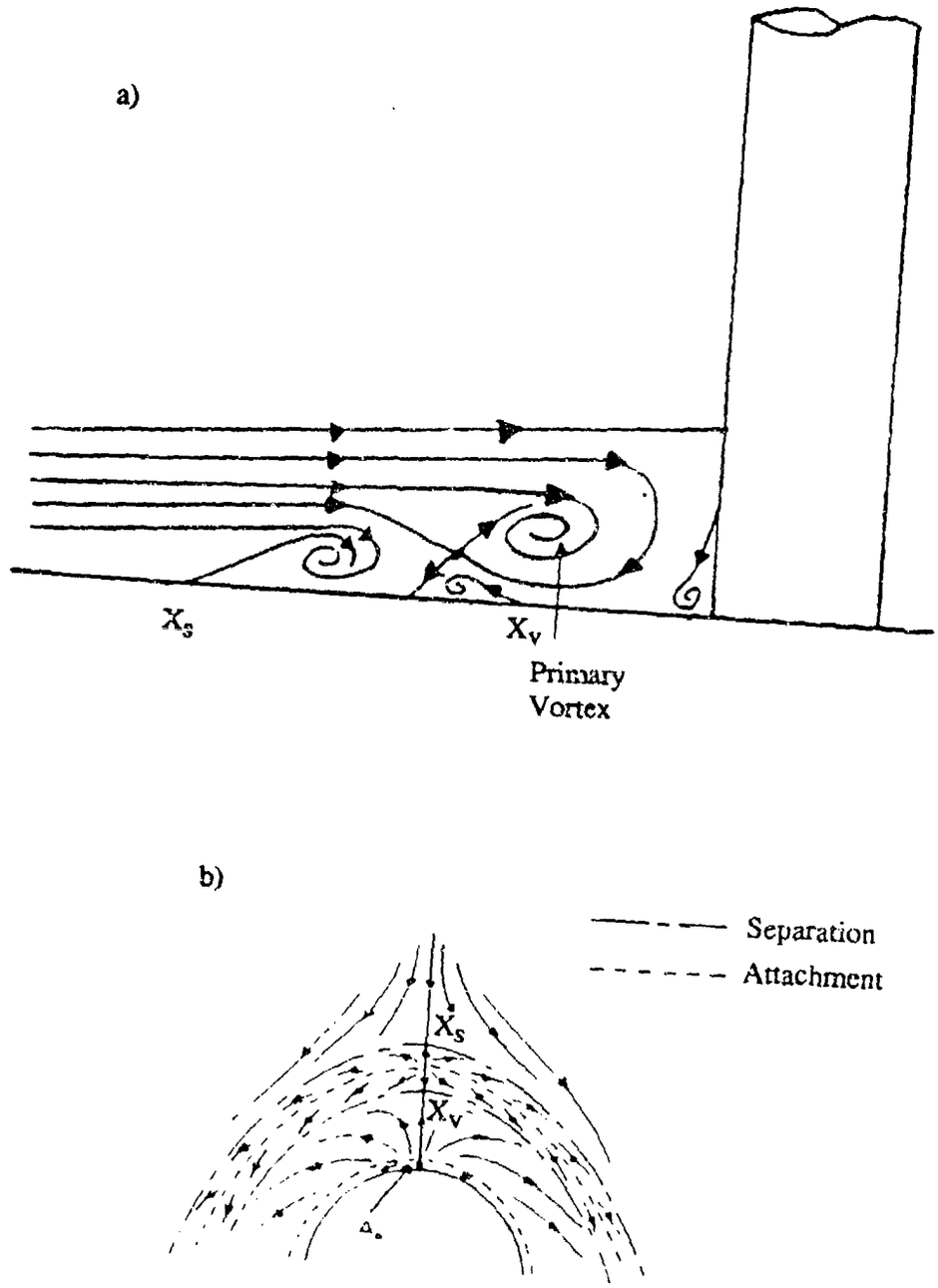

Figure 1.2. a) Postulated 4-Vortex Mean Flow Model and b) Resulting Oil-Flow Visualization of the Flow Around a Cylinder (From Baker, 1980)

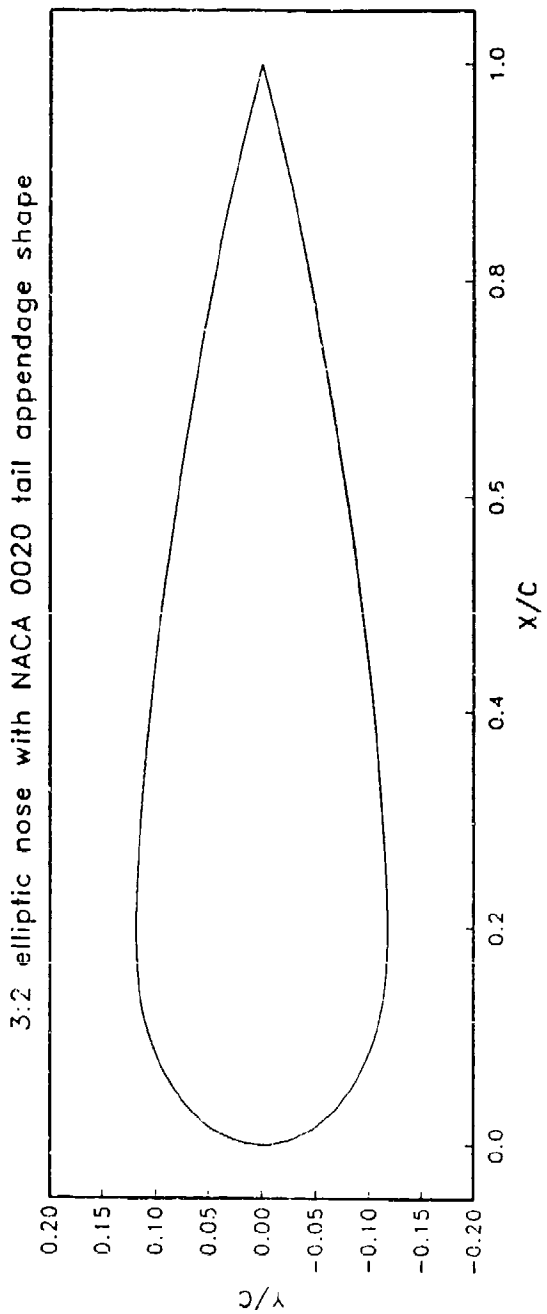

Figure 2.1. Baseline Appendage Geometry

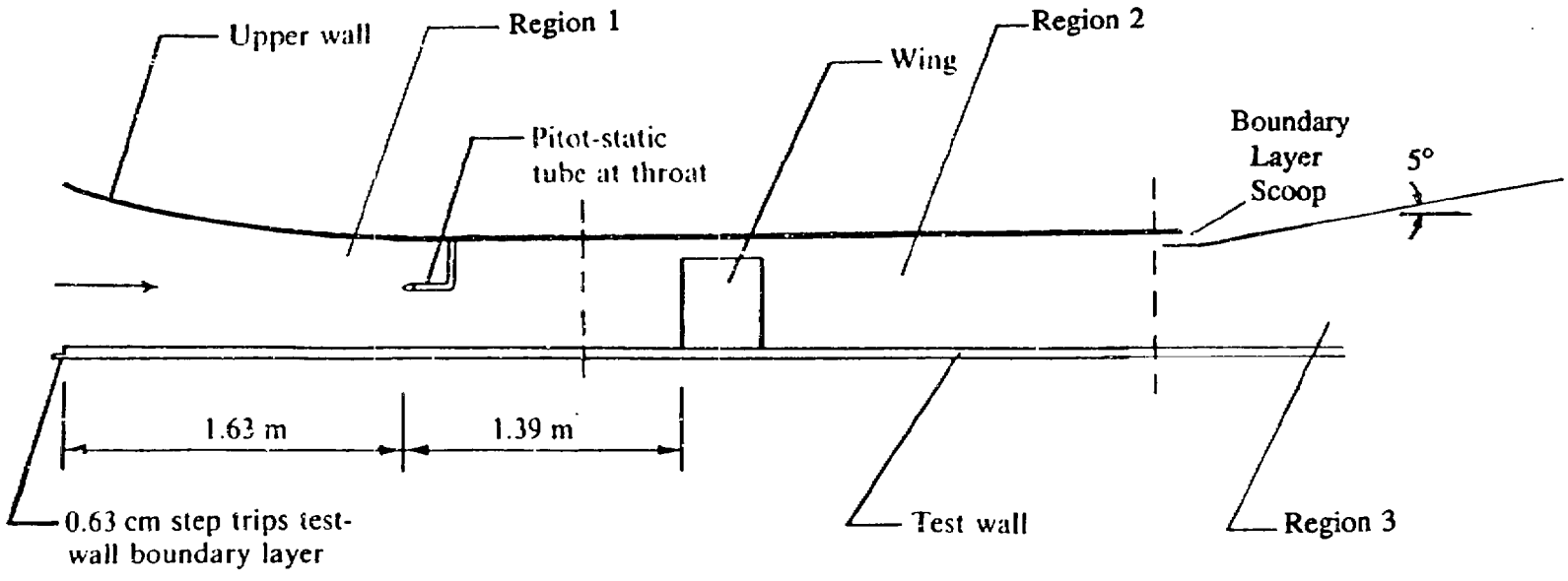

Figure 2.2. Diagram of Virginia Tech Boundary Layer Wind Tunnel, Displaying the Different Flow Regions (not to scale)

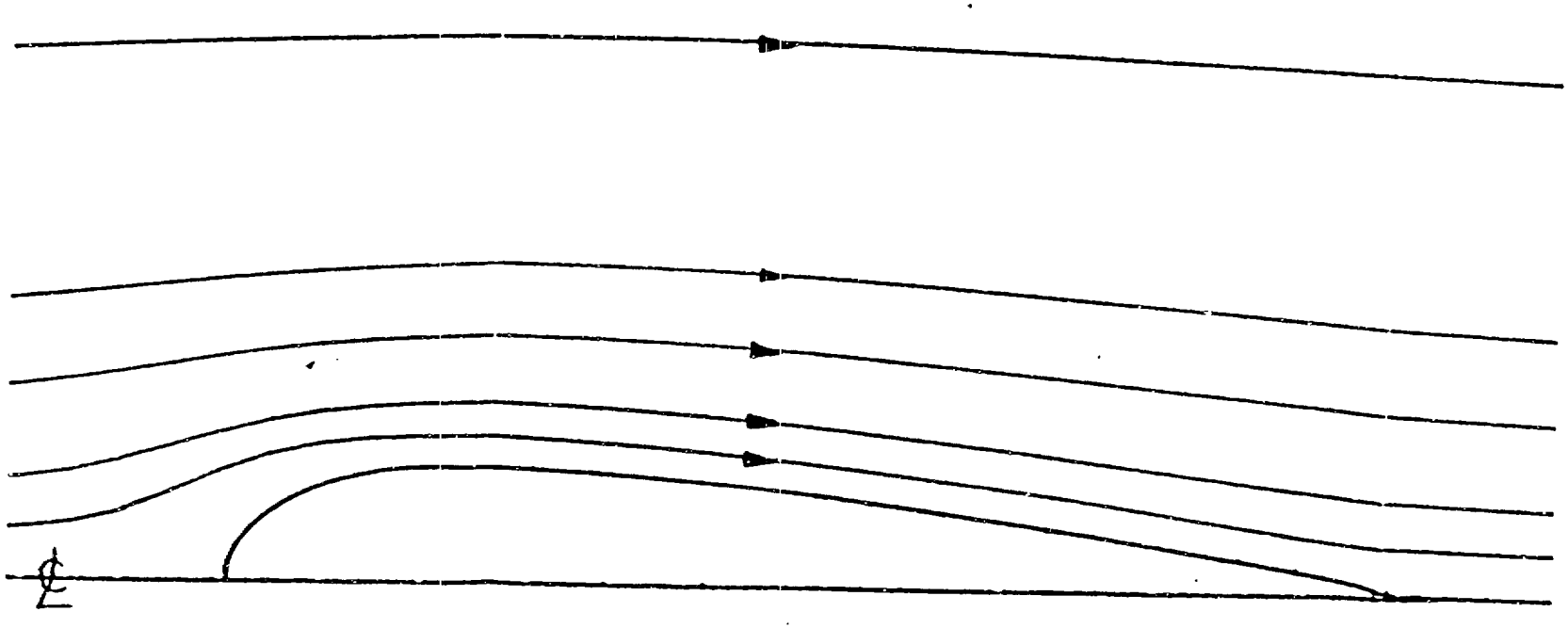

Figure 2.3. Streamlines Produced by Baseline Geometry in an Unbounded Potential Flow (from Devenport and Simpson, 1990a)

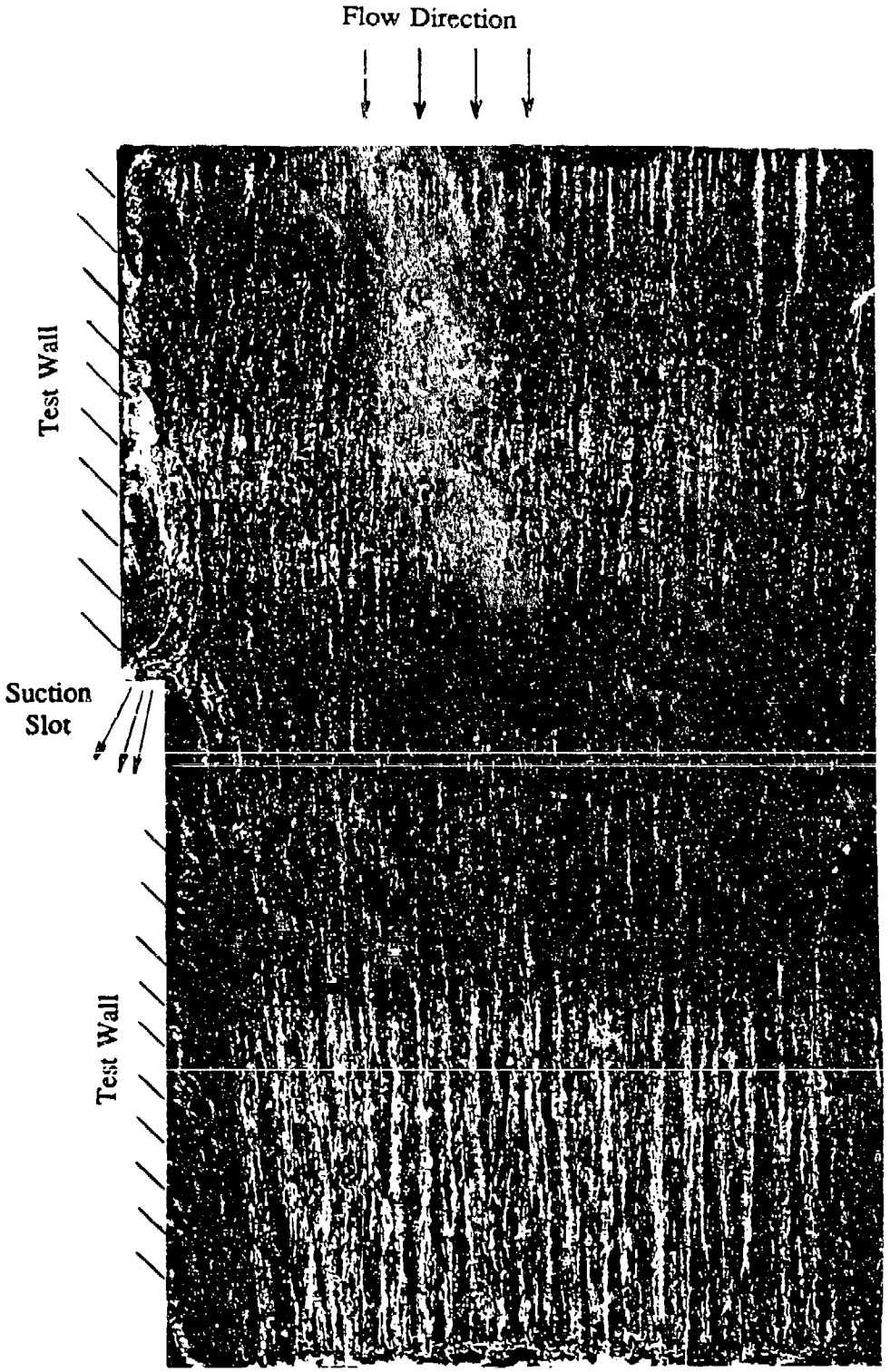

Figure 2.4. Oil-Flow Visualization of Region Around Port Suction Slot, Test Section Side Wall on Left

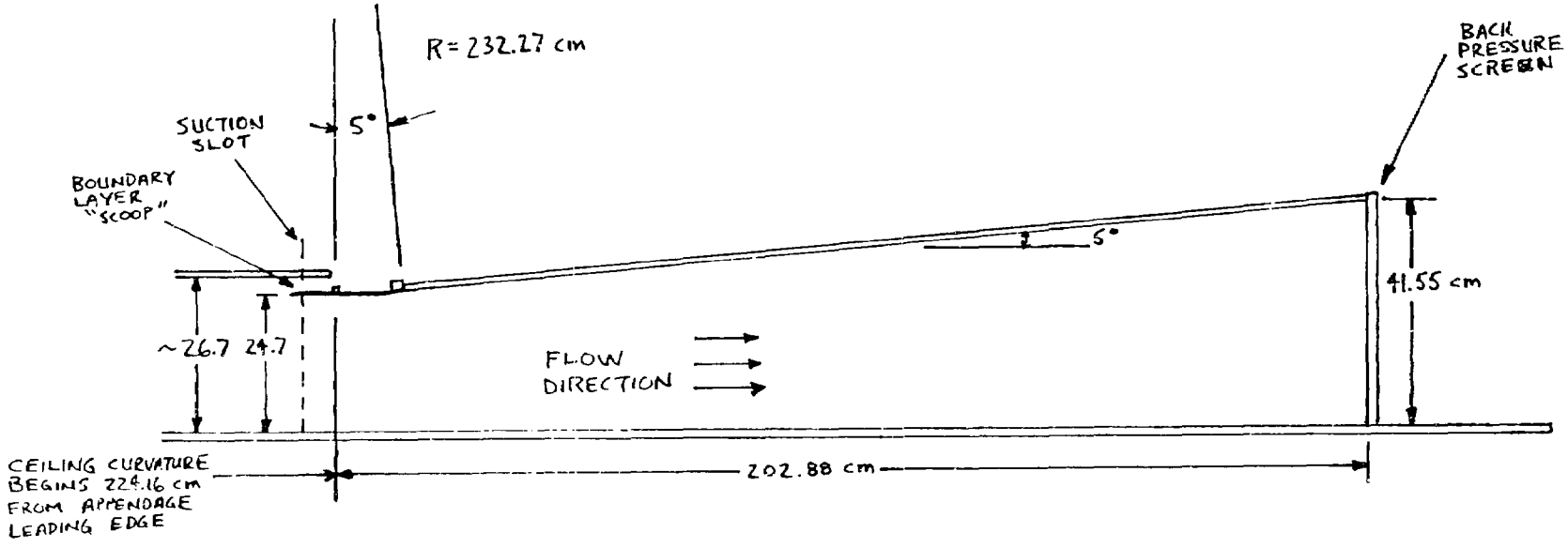

Figure 2.5. Sketch of Diverging Flow Section Used to Produce Adverse Pressure Gradient Region (not to scale, all dimensions in cm)

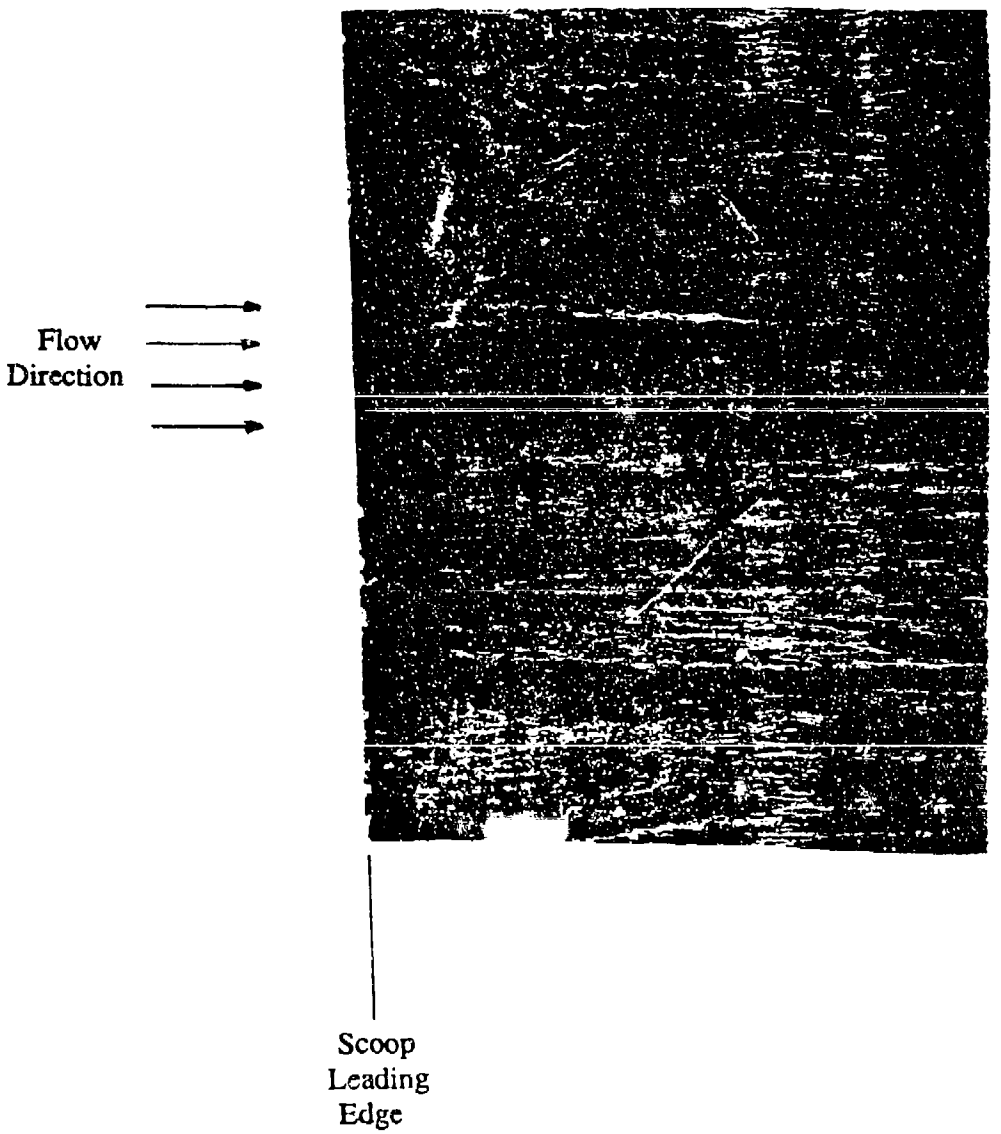

Figure 2.6. Portion of Oil-Flow Visualization From Leading Edge of Separation, Showing Lack of Separation

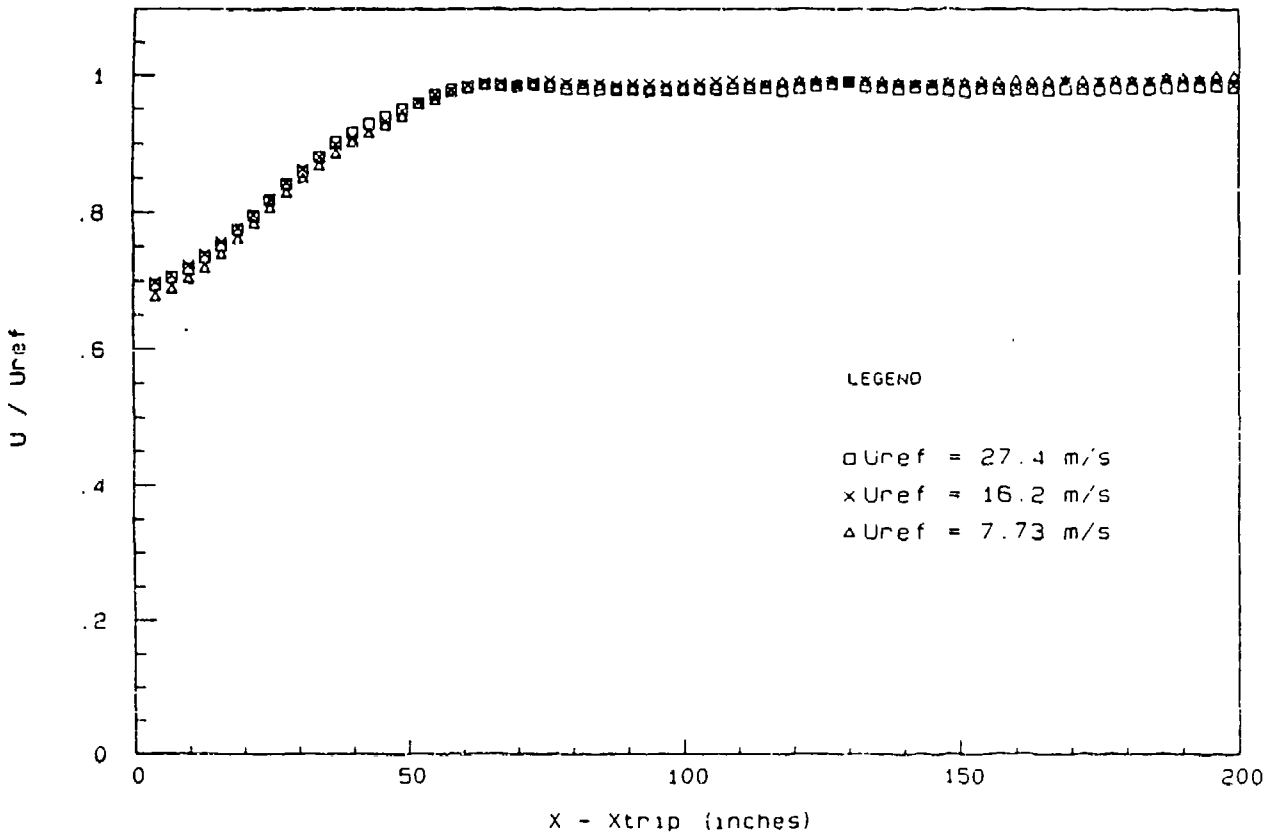

Figure 2.7. Variation of U/U_{ref} in Regions 1 and 2 of Wind Tunnel (from Devenport and Simpson, 1990a)

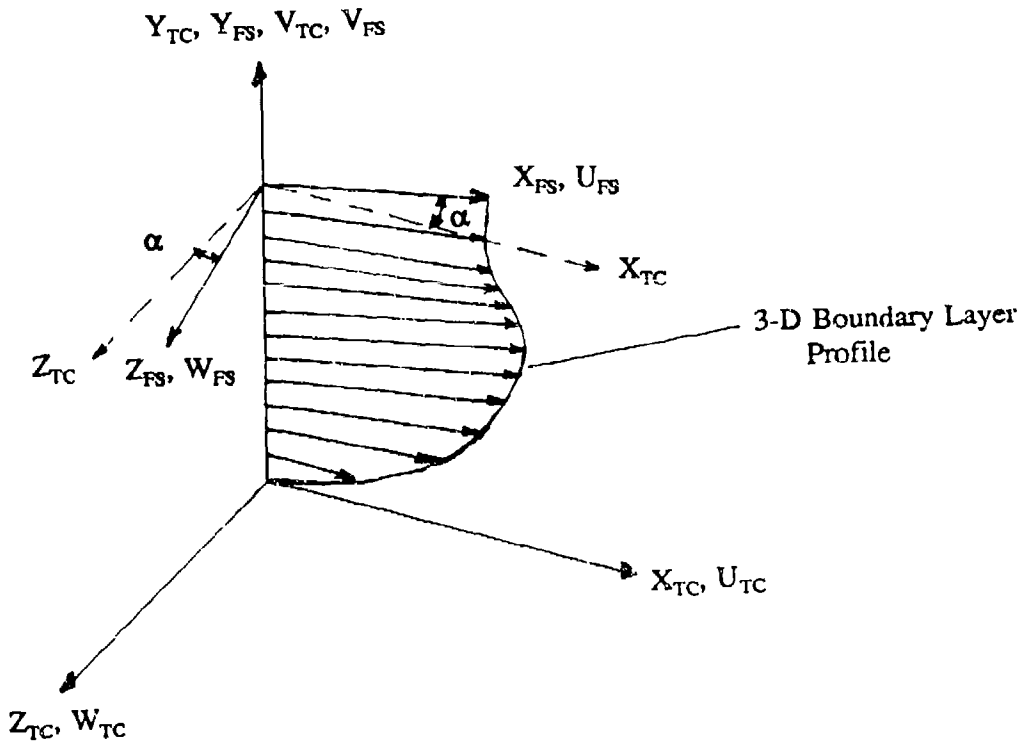

Figure 2.8. Sketch of Tunnel and Freestream Coordinate Systems

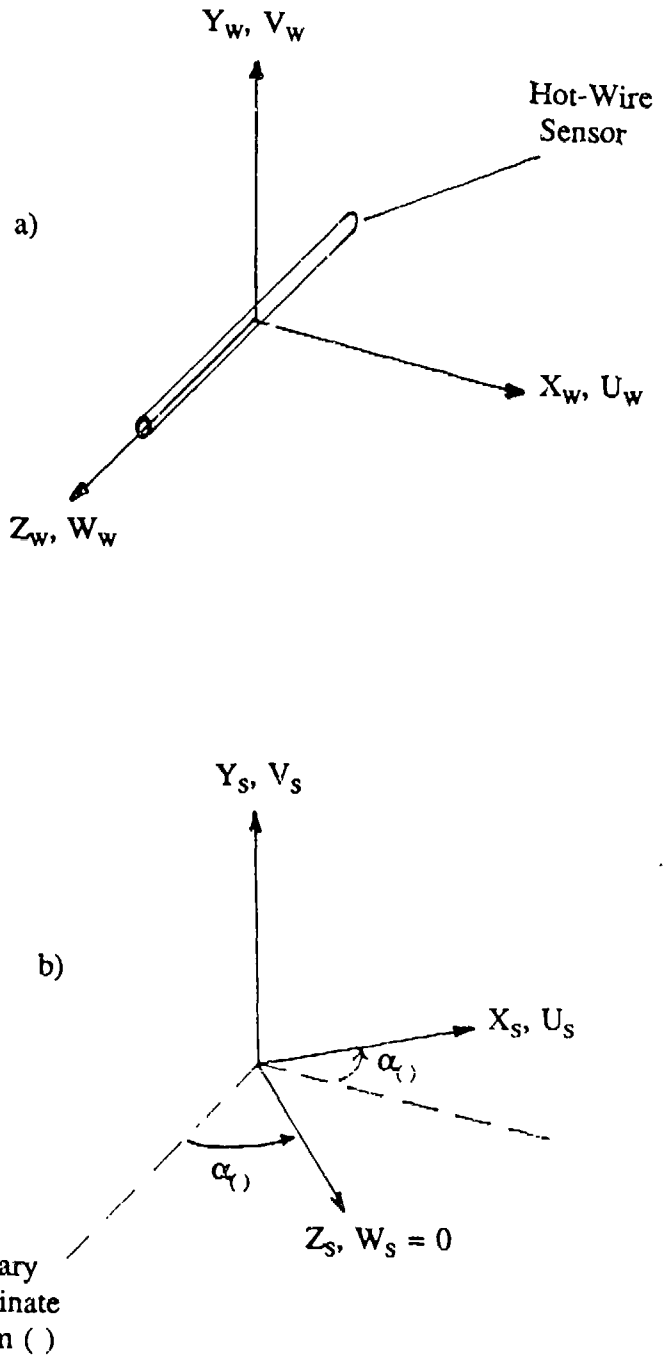

Figure 2.9. Sketches of a) Wire Coordinate System and Velocity Components and b) Local Streamwise Coordinate System and Velocity Components

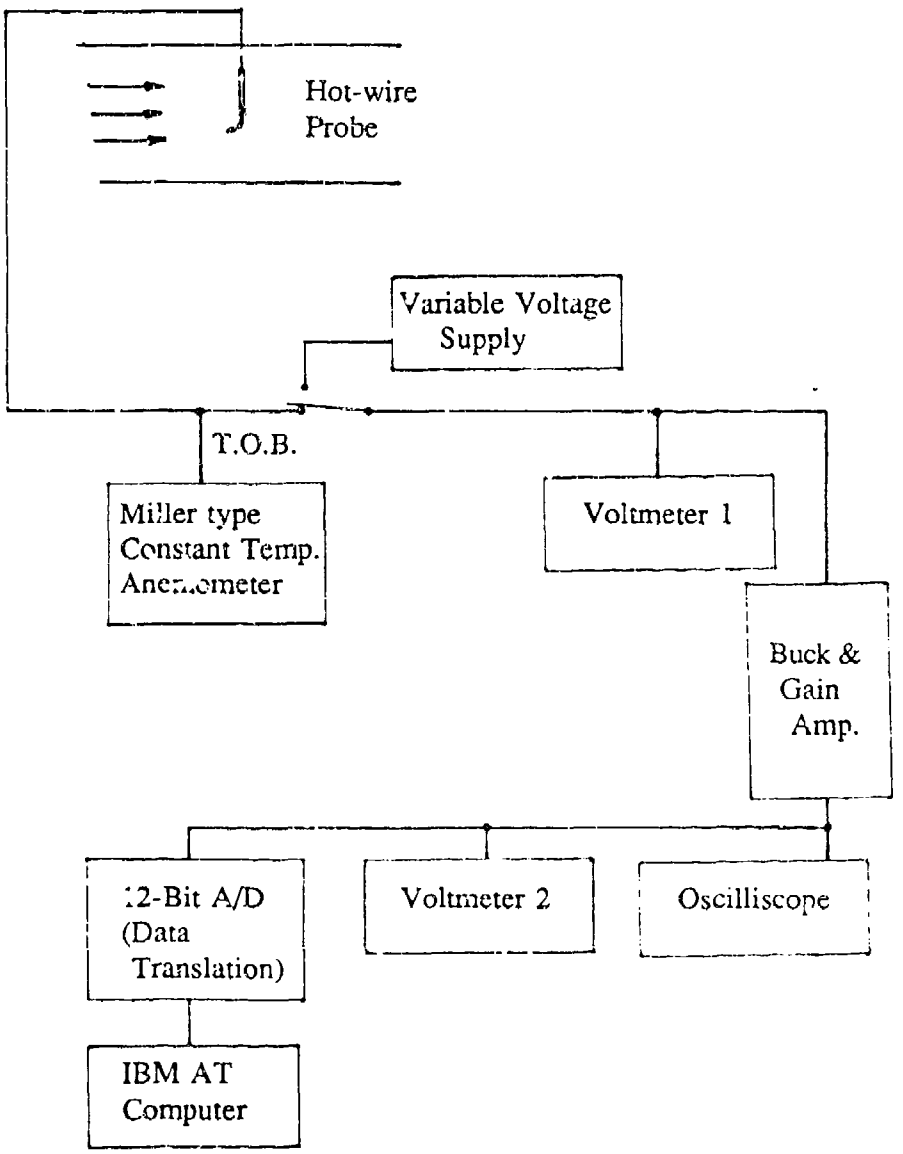

Figure 2.10. Schematic of Experimental Instrumentation

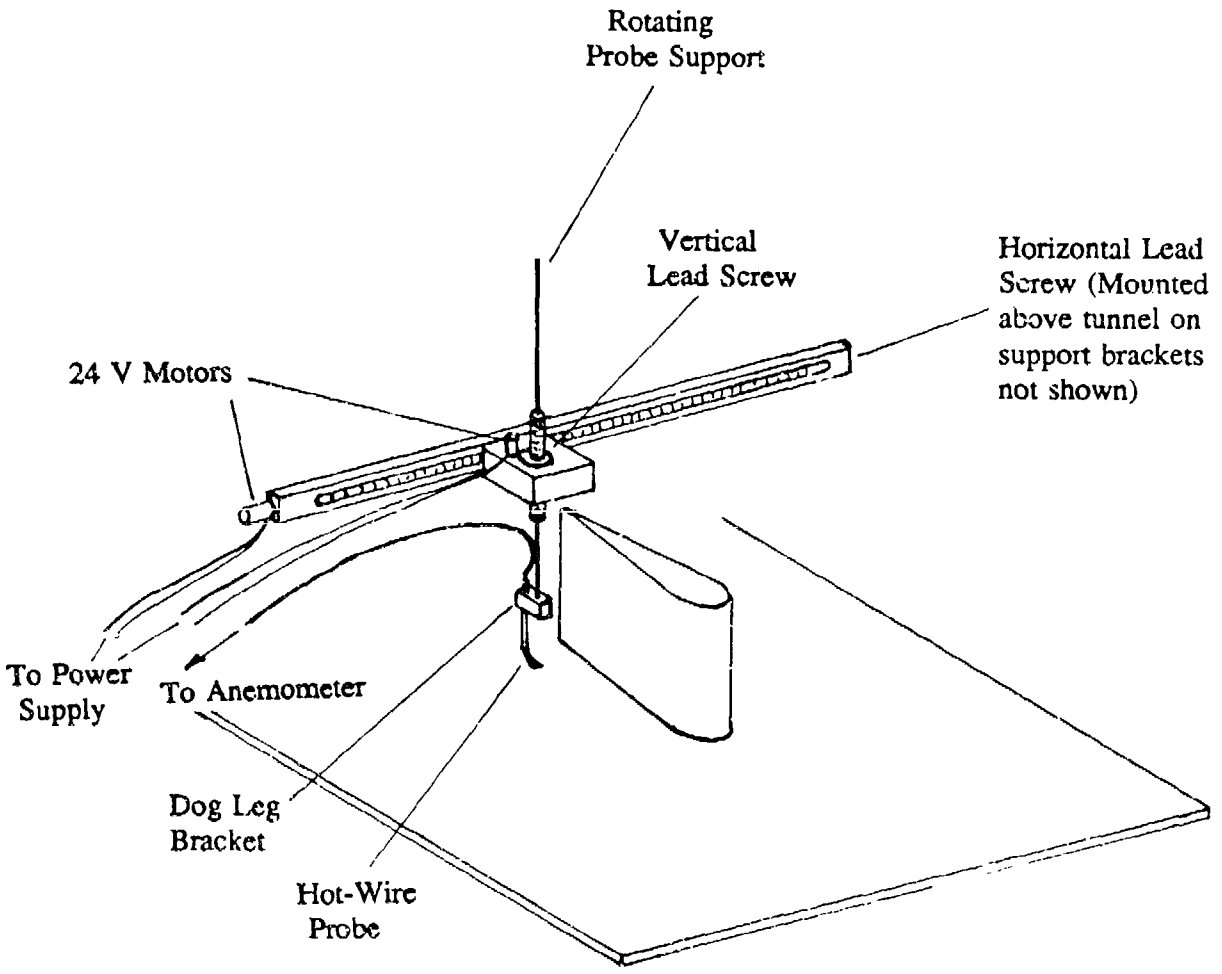

Figure 2.11. Sketch of Hot-Wire Probe Traverse System

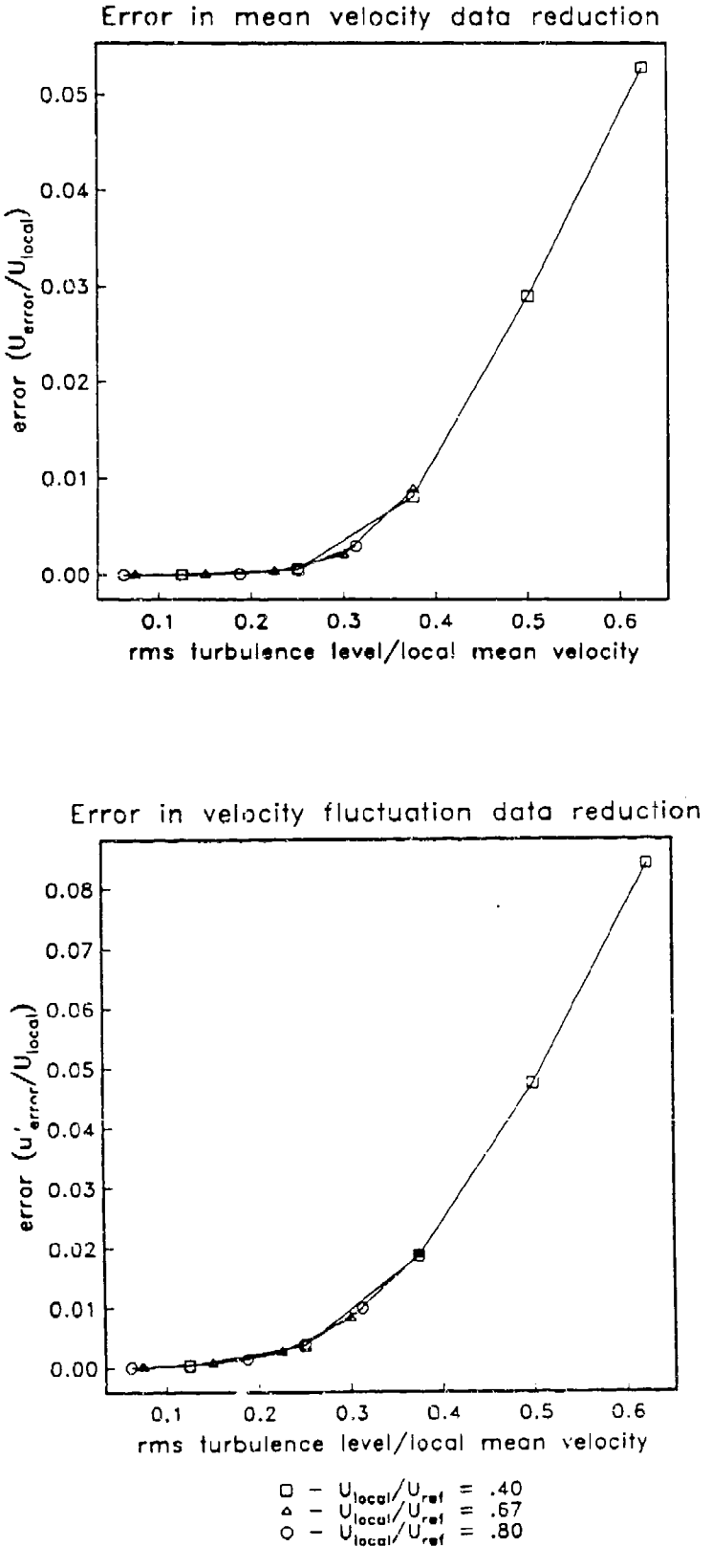

Figure 2.12a. Inherent Data Reduction Errors for U and u', linear scale

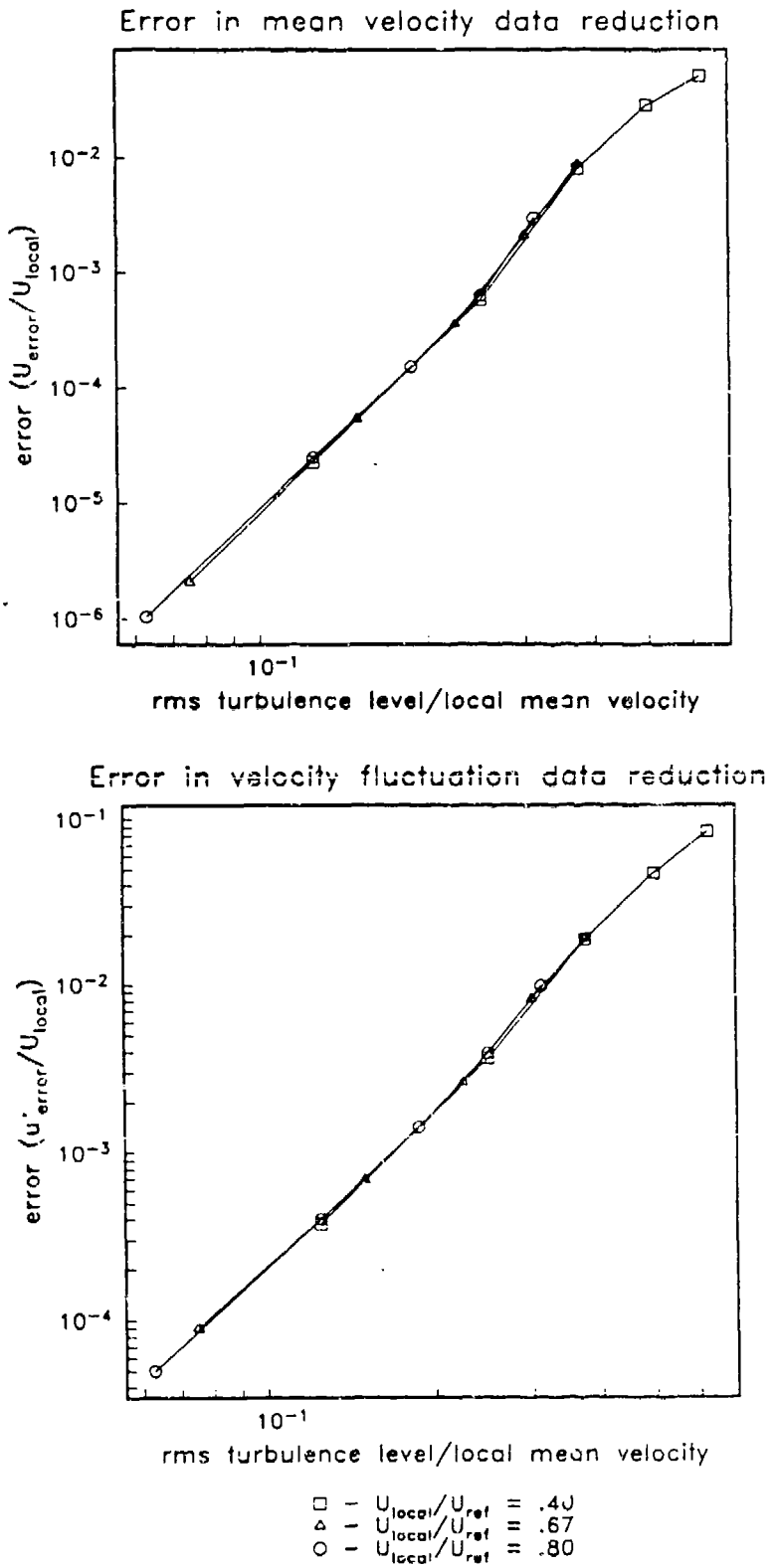

Figure 2.12b. Inherent Data Reduction Errors for U and u', log-log scale

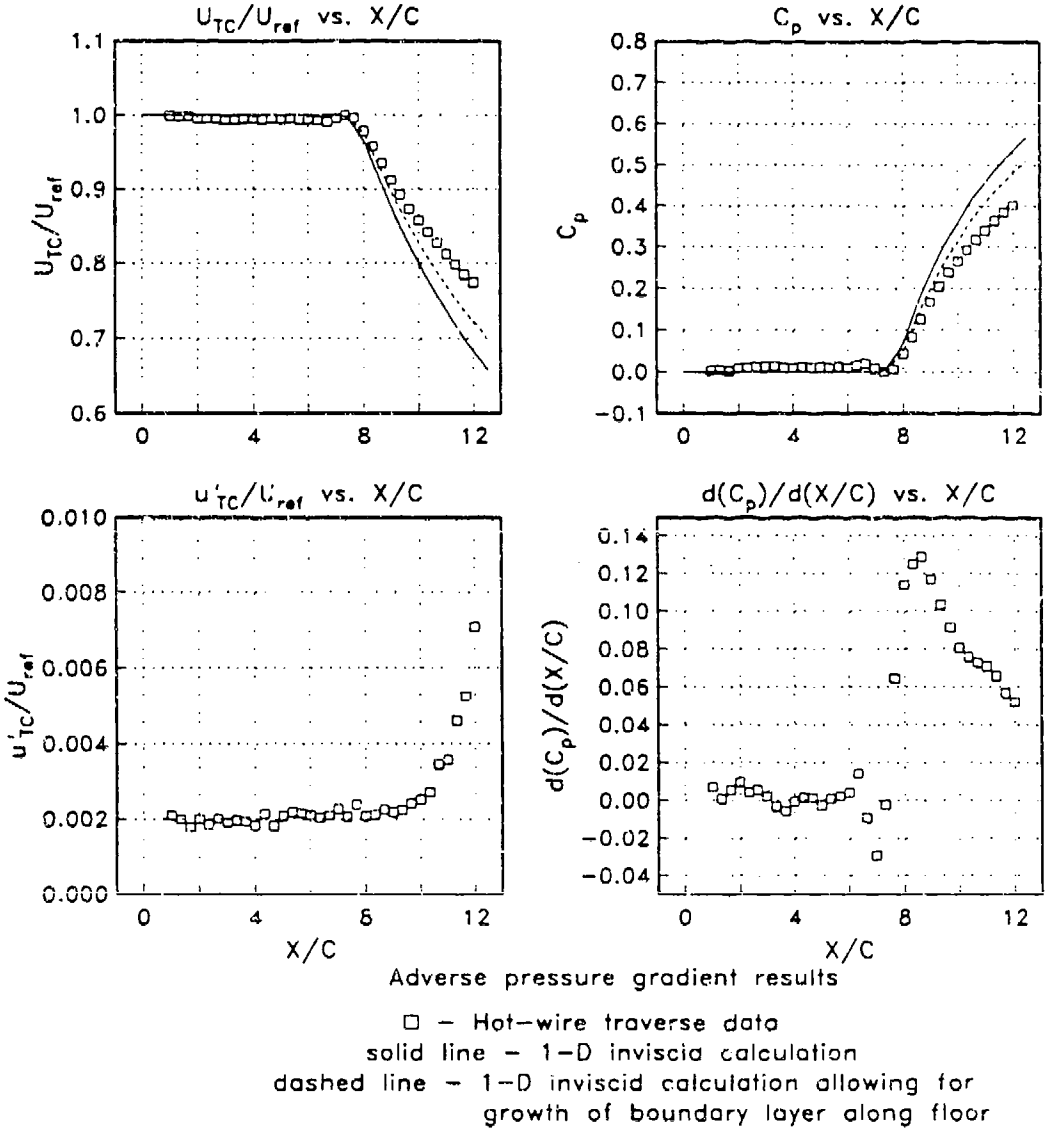

Figure 3.1. Characteristics of the Potential Core Flow in the Adverse Pressure Gradient Section (Region 3)

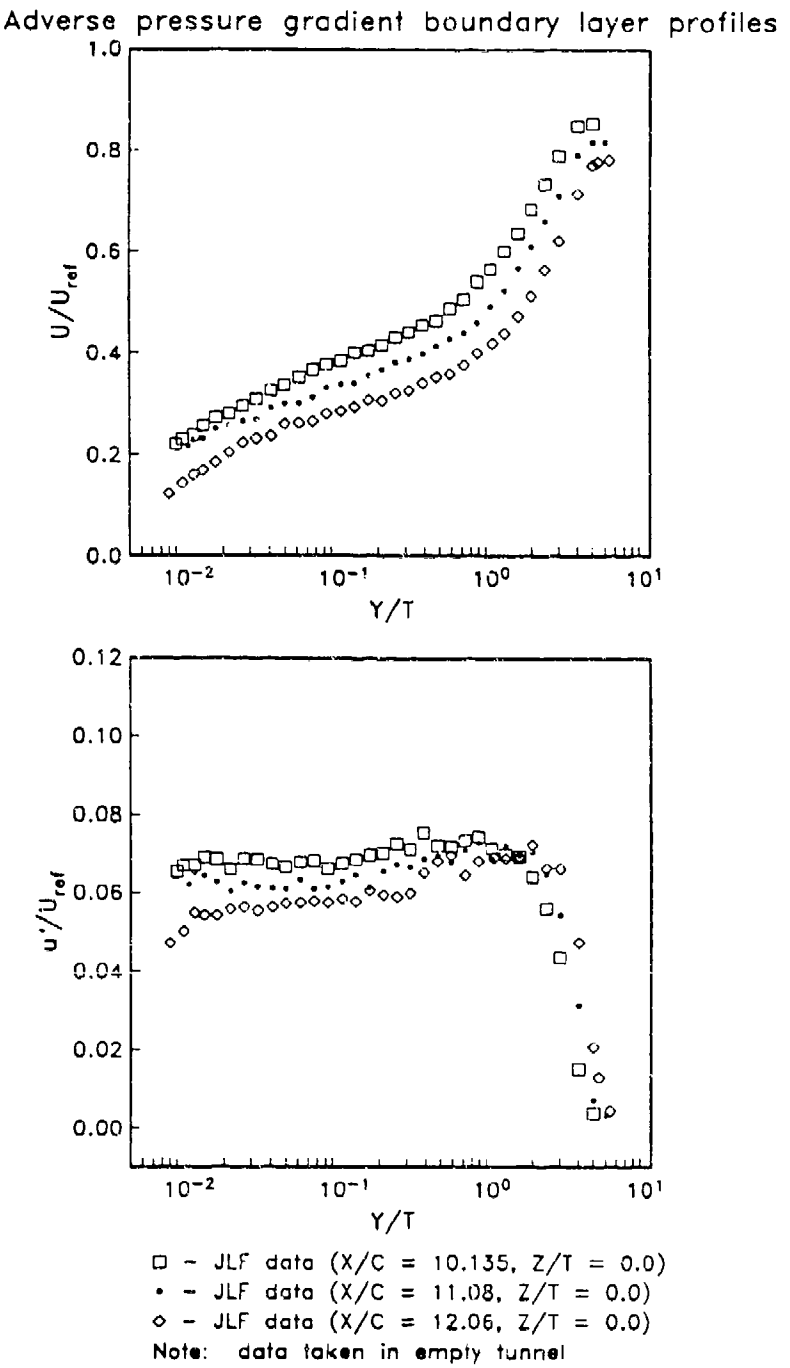

Figure 3.2. Boundary Layer Profiles of U/U_{ref} and u'/U_{ref} in Adverse Pressure Gradient Section, No Appendage in Tunnel

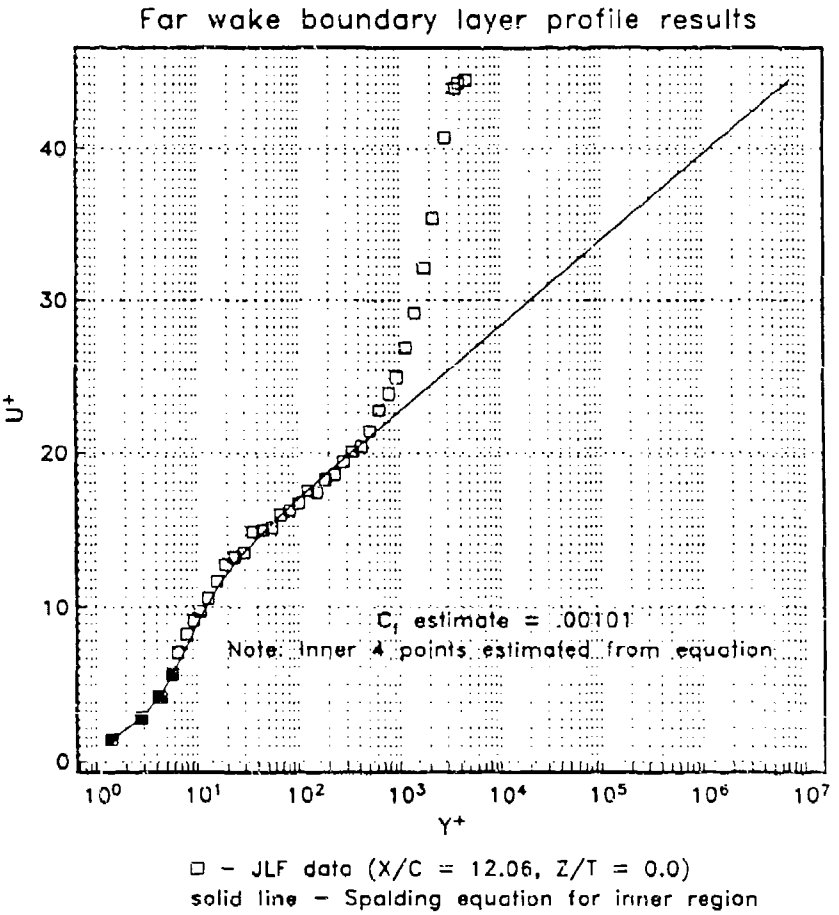

Figure 3.3. Sample of Curve Fit to Adverse Pressure Gradient Section Mean Velocity Data Using Spalding Wall-Law

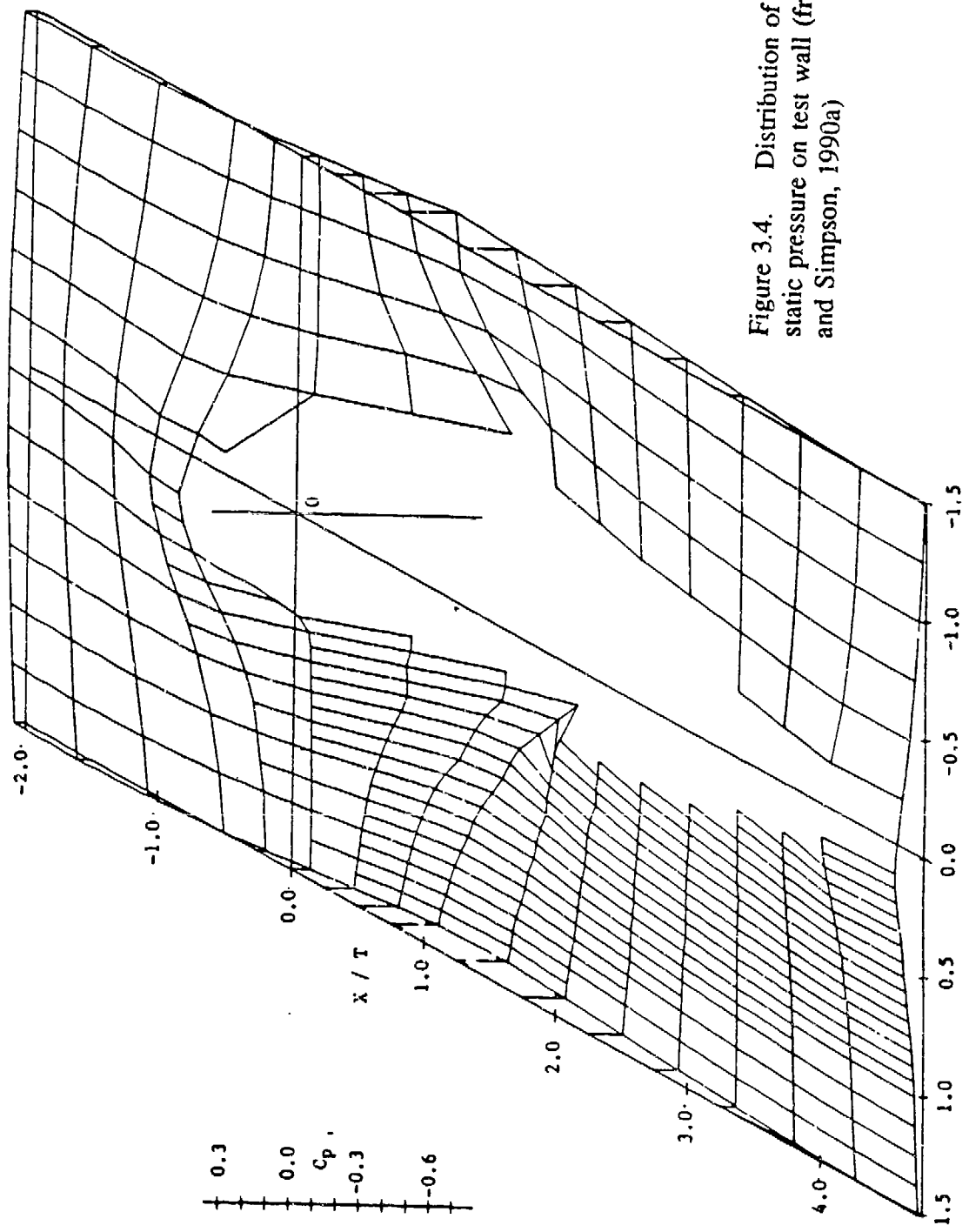

Figure 3.4. Distribution of time-mean static pressure on test wall (from Devenport and Simpson, 1990a)

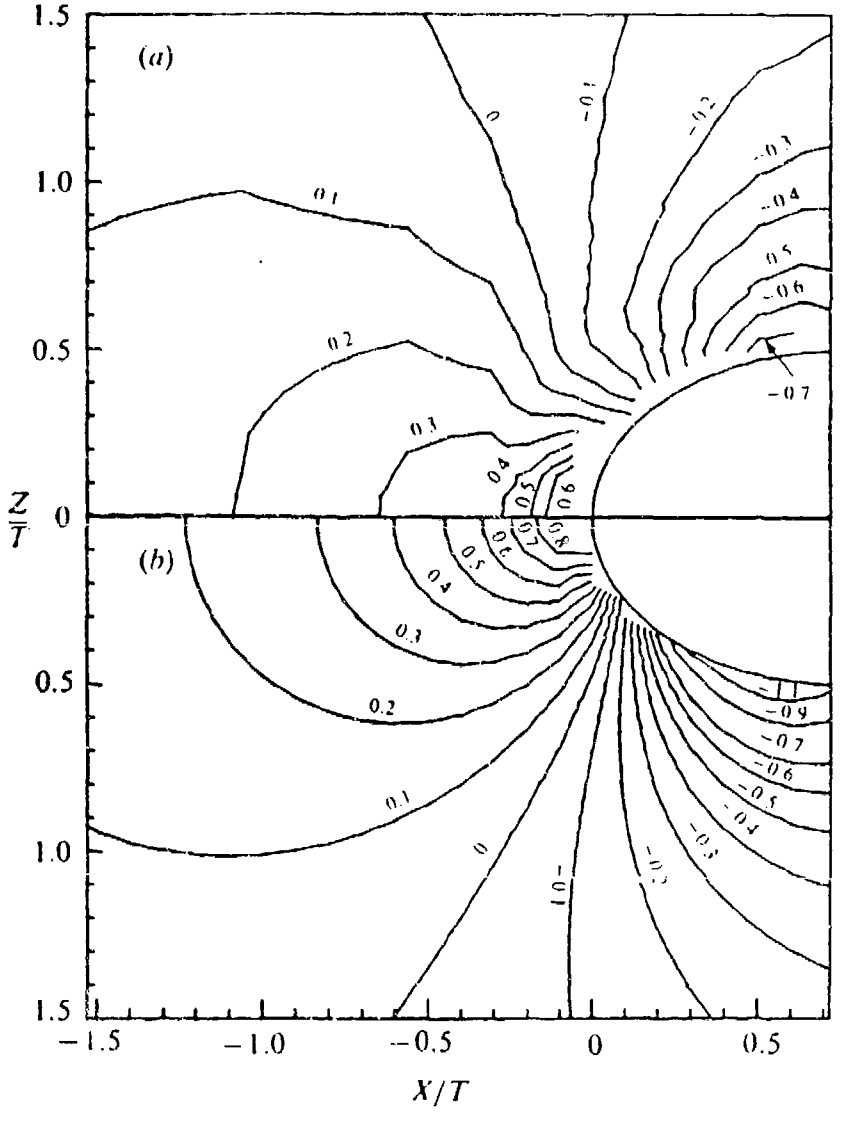

Figure 3.5. Contours of Time-Mean Static Pressure in Appendage Nose Region, a) Measured on Test Wall, and b) Calculated for Freestream (from Devenport and Simpson, 1990b)

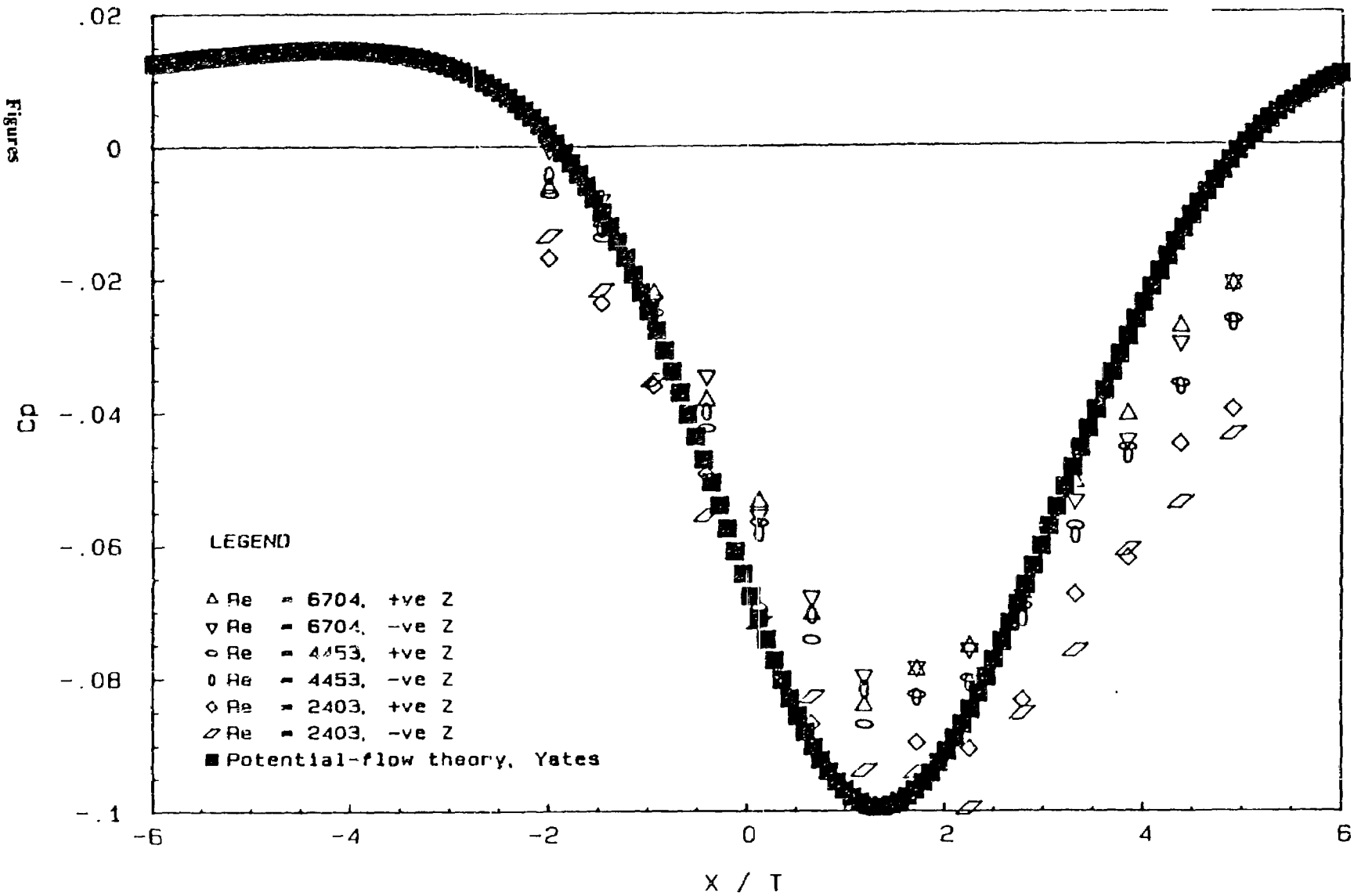

Figure 3.6. Distributions of Time-Mean Static Pressure Along Z/T = ±3.17, Compared to Potential Flow Calculation (from Devenport and Simpson, 1990a)

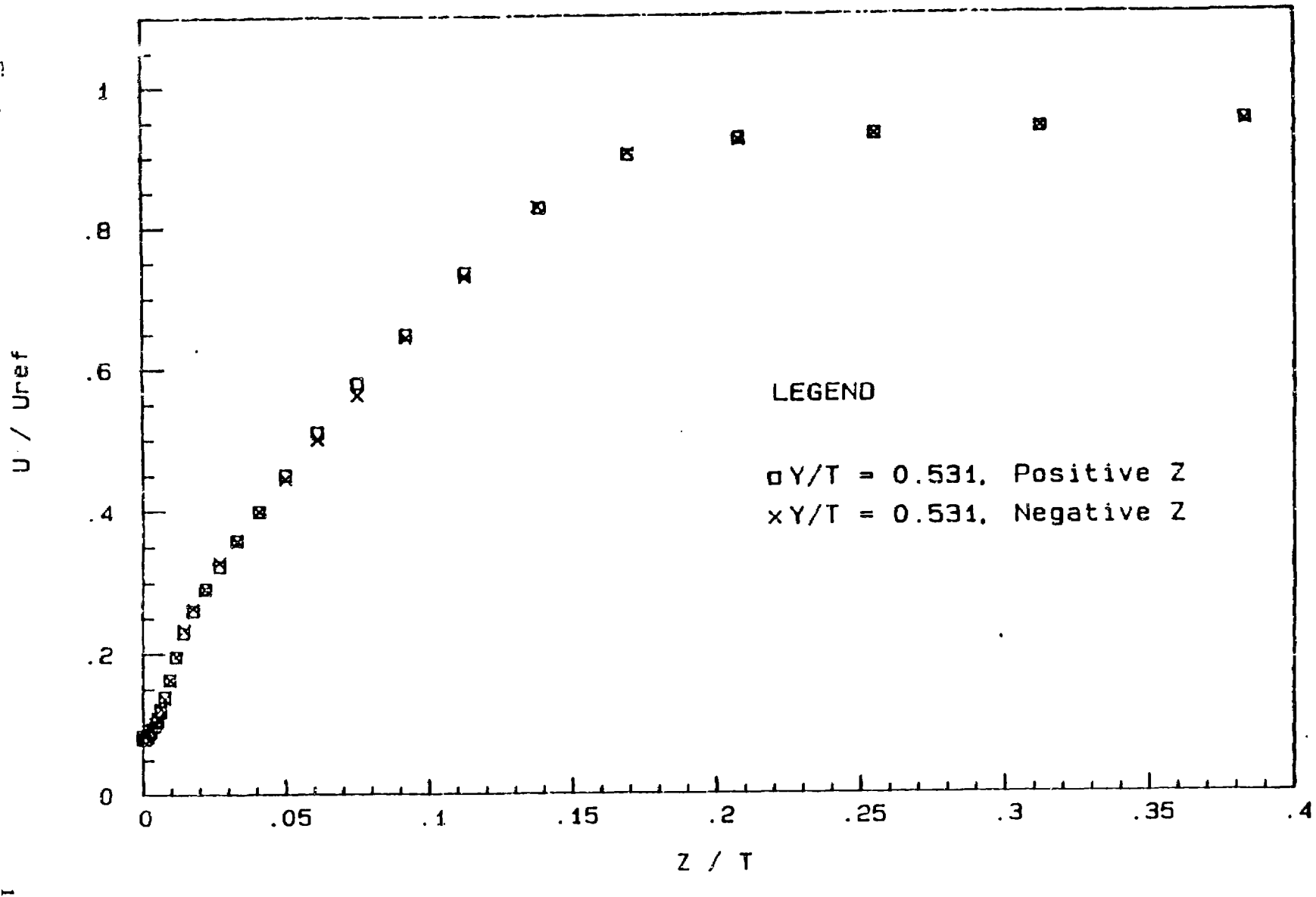

Figure 3.7. Profiles of $(u'/U_{ref})^2$ Measured on Either Side of Wing, 1 mm Downstream of Wing Trailing Edge (from Devenport and Simpson, 1990a)

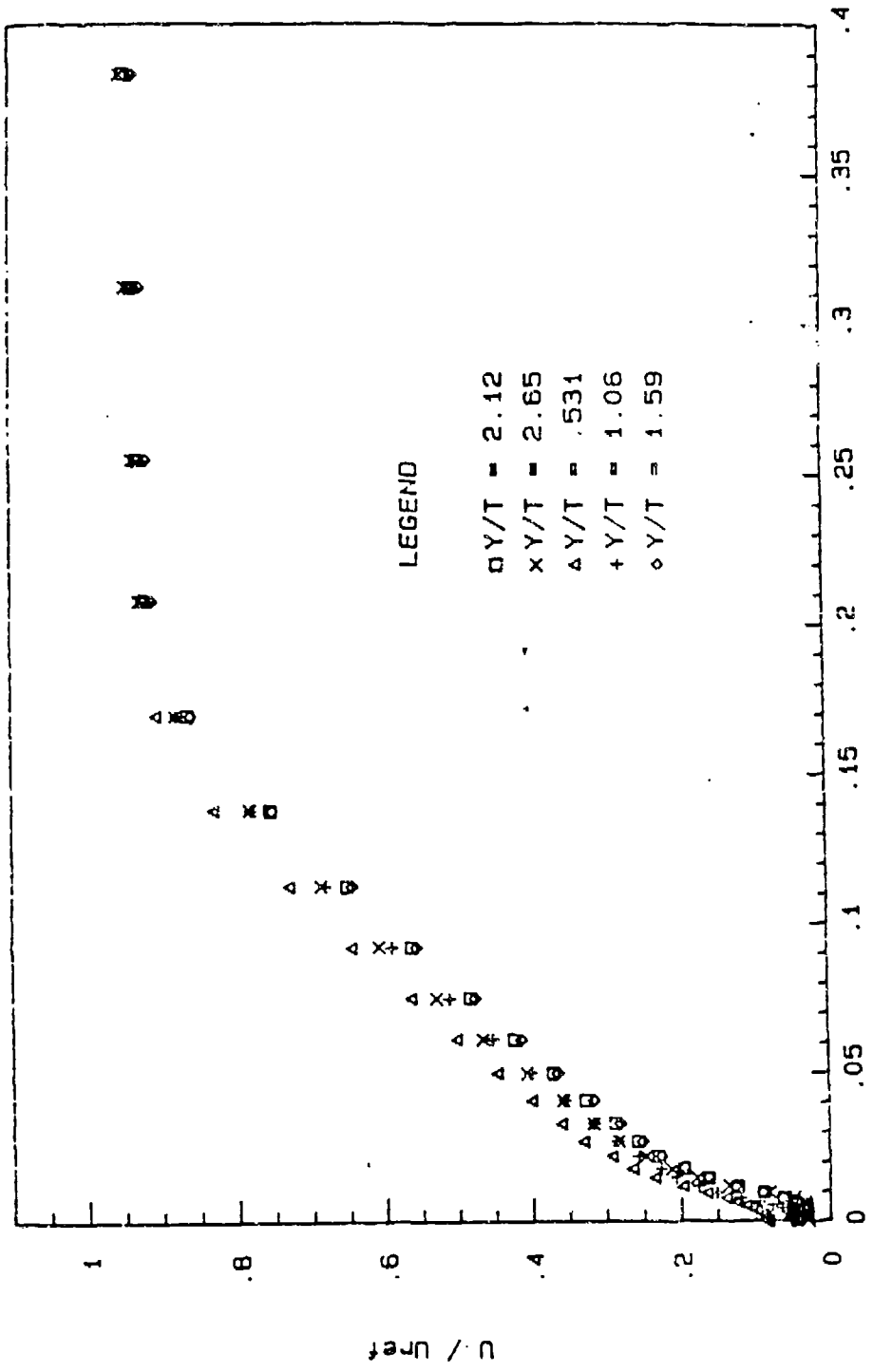

Figure 3.8. Profiles of U/U_{ref}, Measured at Various Y/T Locations 1 mm Downsteam of Wing Trailing Edge (from Devenport and Simpson, 1990a)

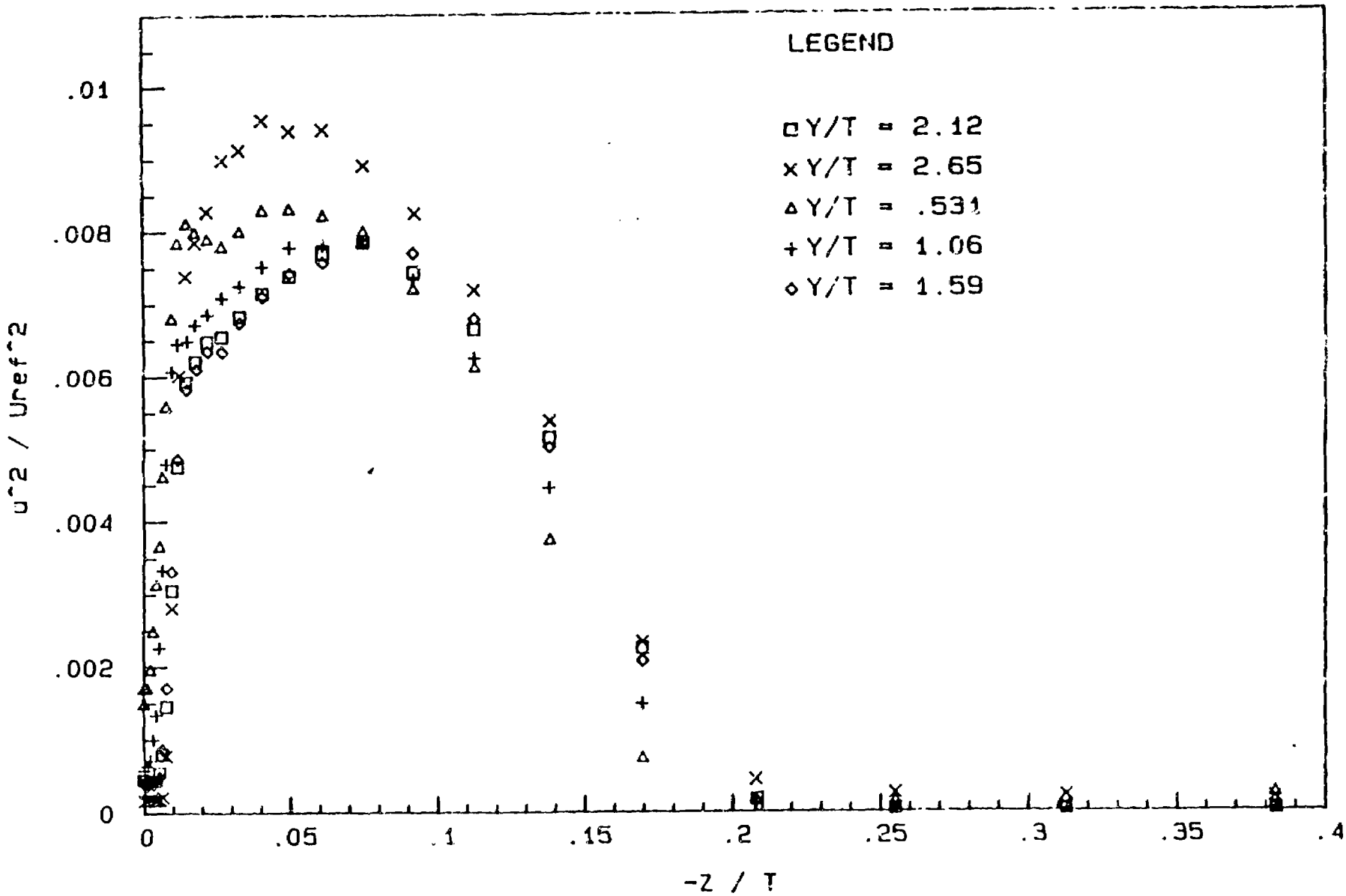

Figure 3.9. Comparison of Profiles of $(u'/U_{ref})^2$, Measured at Various Y/T Locations 1 mm Downstream of Wing Trailing Edge (from Devenport and Simpson, 1990a)

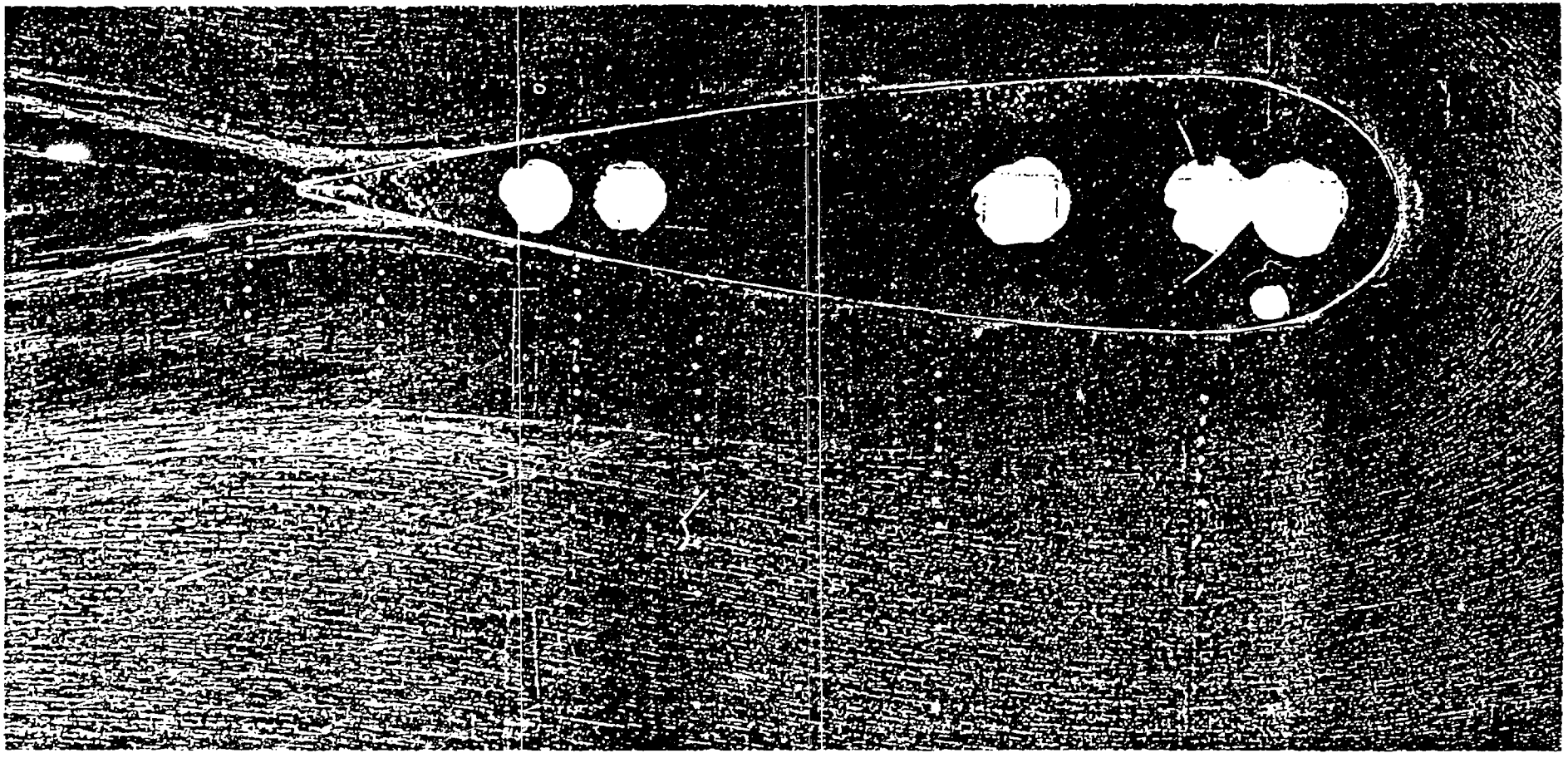

Plane 10 Plane 9 Plane 8 Plane 7 Plane 6 Plane 5

Figure 3.10a. Results of Oil-Flow Visualization, Showing Measurement Locations in Planes 5-10

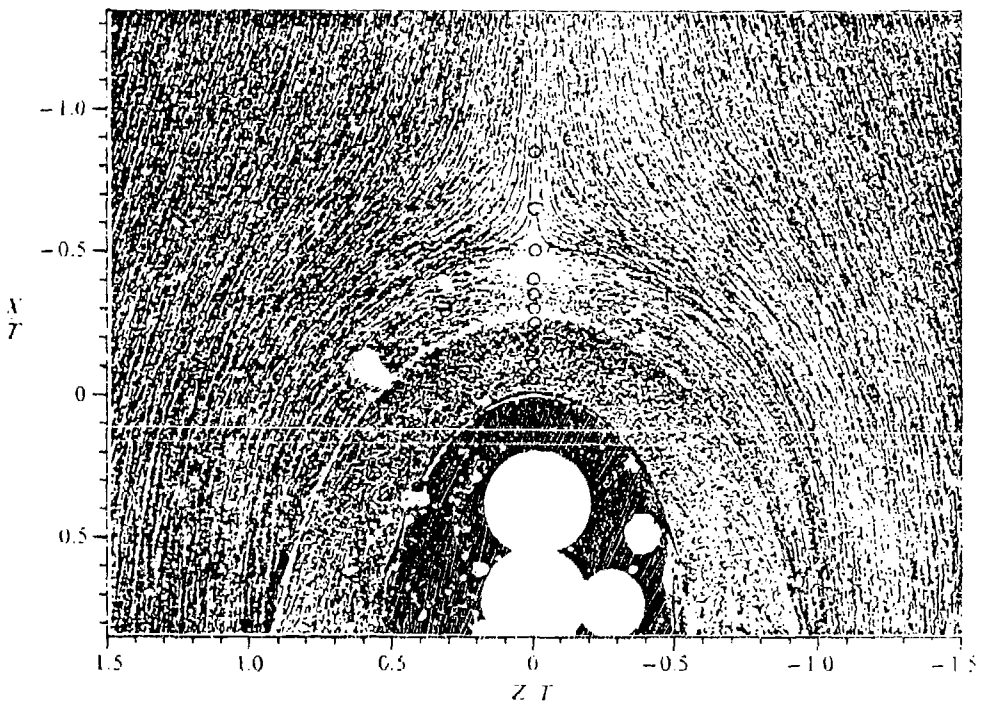

Figure 3.10b. Detail of Oil-Flow Visualization in Nose Region, Showing Primary Separation Point and Line of Low Shear (from Devenport and Simpson, 1990b)

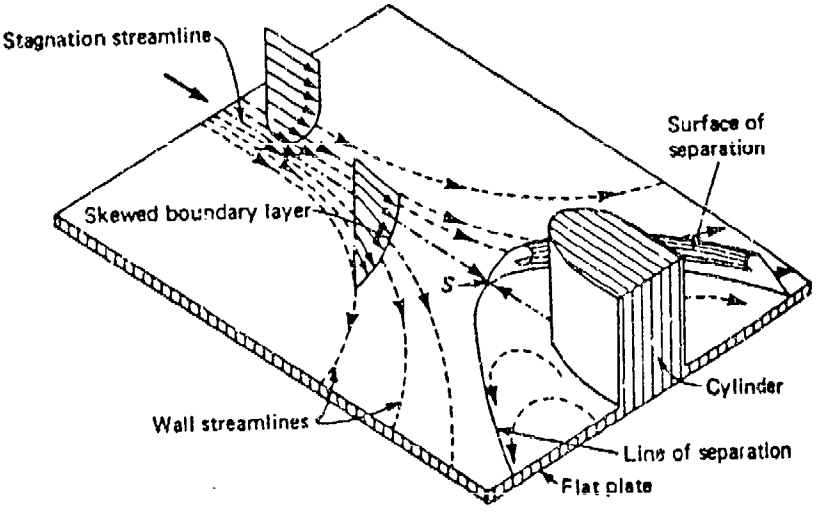

Figure 3.11. Simplified Sketch Showing Skewing of Outer Streamlines and the Primary Separation (from White, 1974)

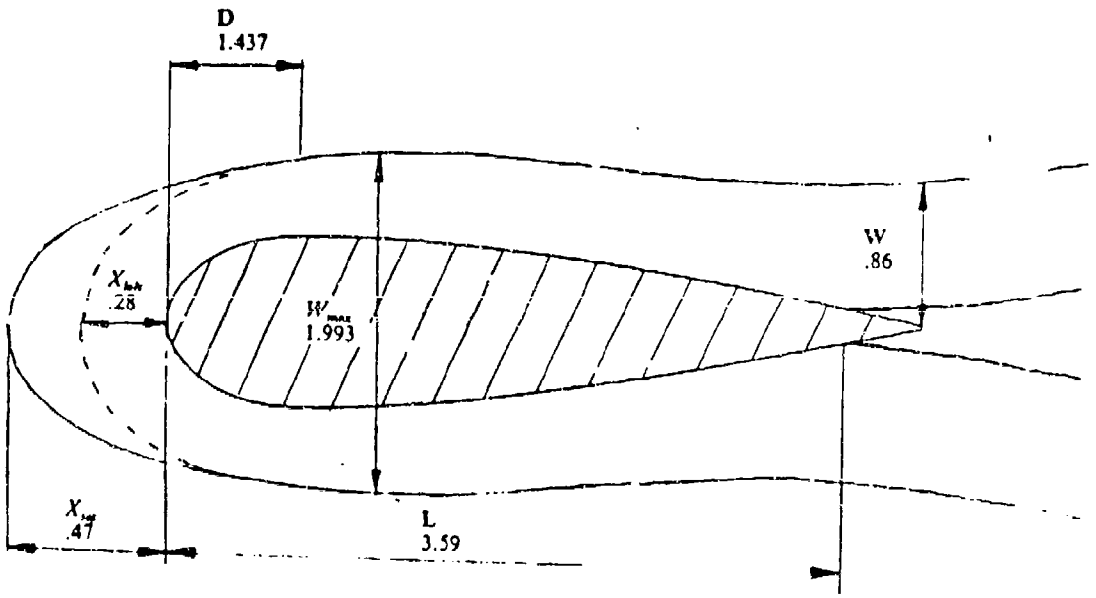

Figure 3.12. Sketch Showing Dimensions of Characteristic Oil-Flow Patterns for Baseline Wing (from Olcmen, 1990)

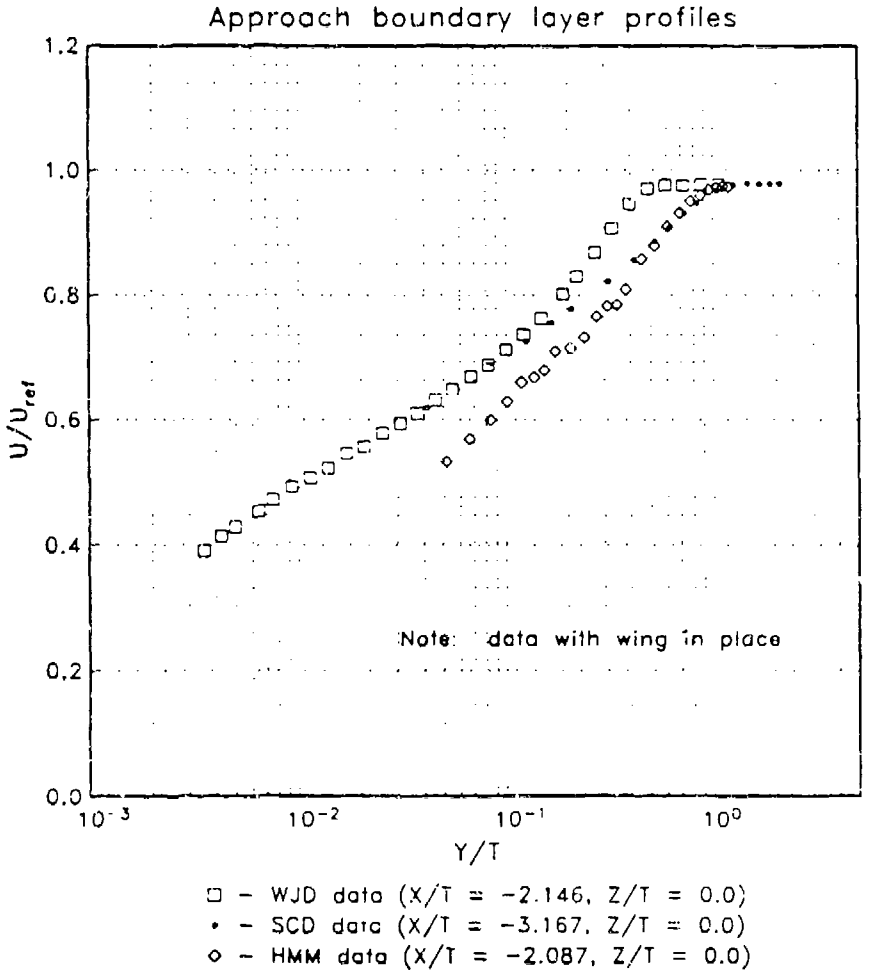

Figure 3.13. Profiles of U/U_{ref} for the Approach Boundary Layers of Devenport and Simpson (1990a), Dickinson (1986a,b), and McMahon *et al.* (1987). (author's approach flow is identical to WJD data)

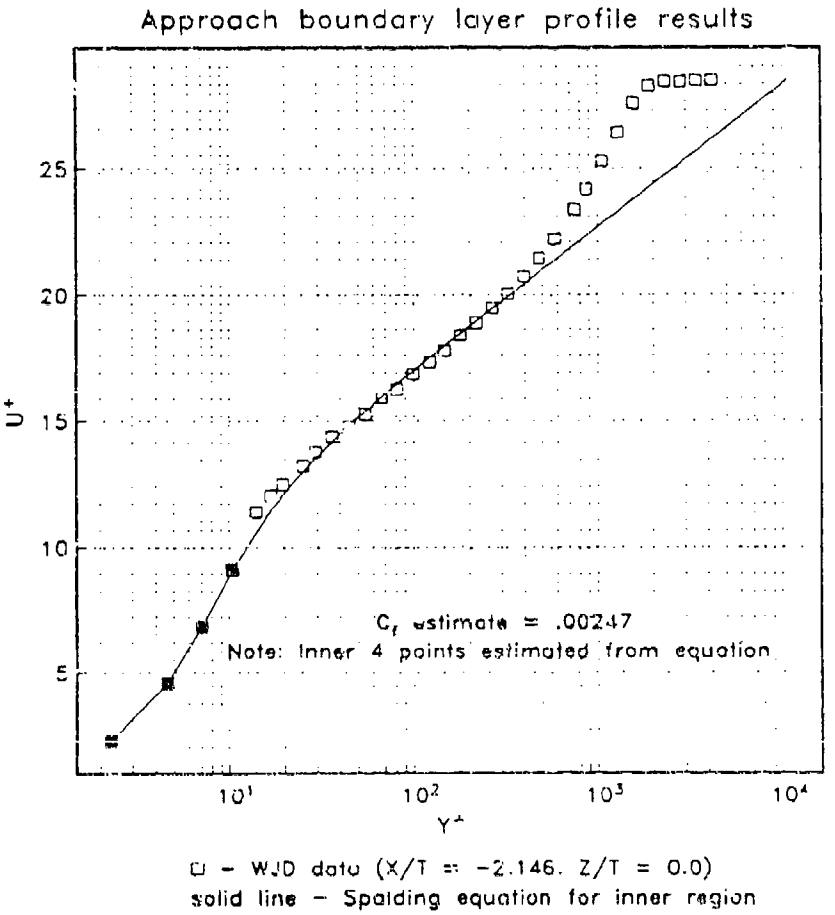

Figure 3.14a. Spalding Wall-Law Curve Fit Applied to the WJD Approach Flow Data

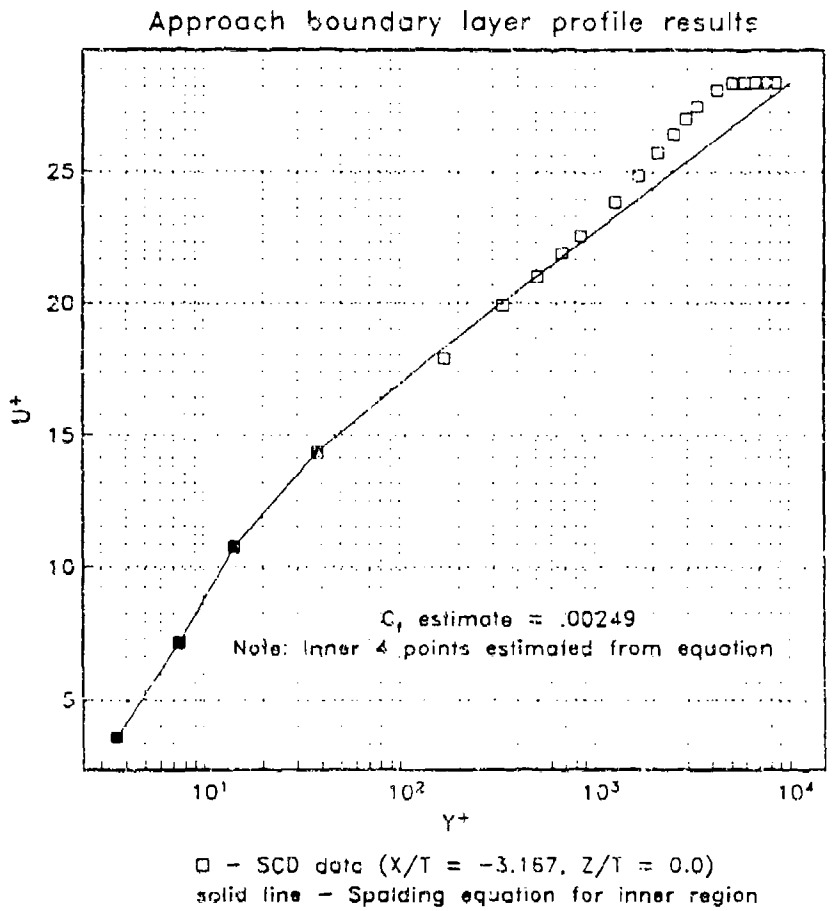

Figure 3.14b. Spalding Wall-Law Curve Fit Applied to the SCD Approach Flow Data

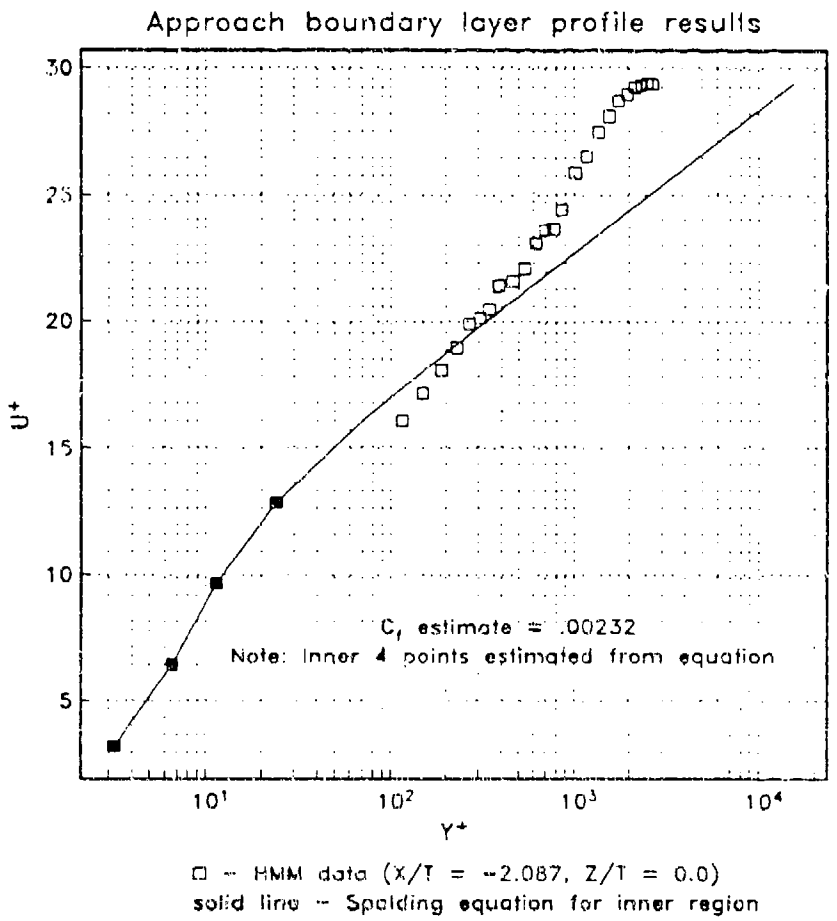

Figure 3.14c. Spalding Wall-Law Curve Fit Applied to the HMM Approach Flow Data

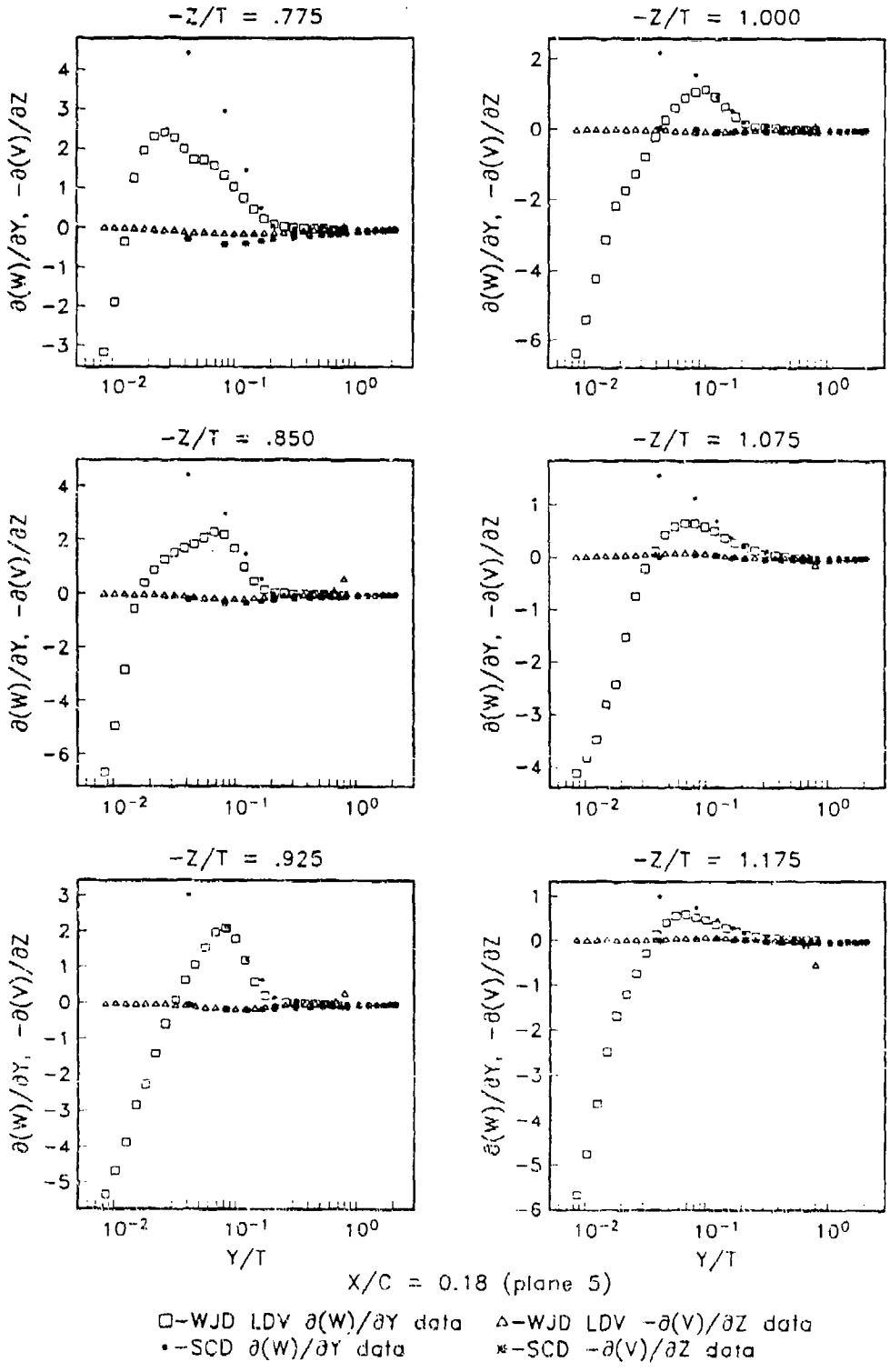

Figure 4.1a. Profiles of $(\partial(W)/\partial Y)\delta/U_{ref}$ and $-(\partial(V)/\partial Z)\delta/U_{ref}$, Plane 5

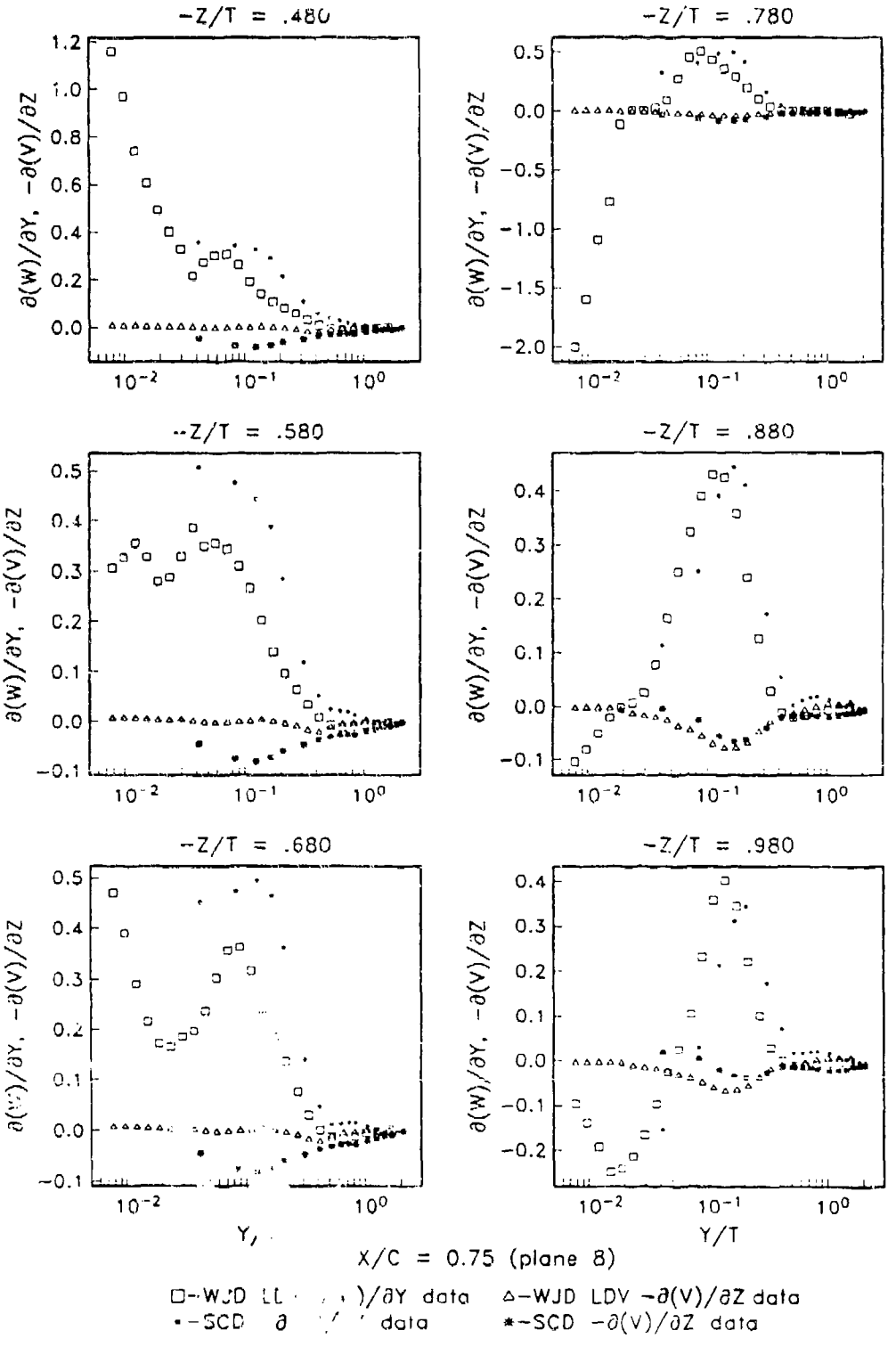

Figure 4.1b. Profiles of $(\partial(W)/\partial Y)\delta/U_{ref}$ and $-(\partial(V)/\partial Z)\delta/U_{ref}$, Plane 8

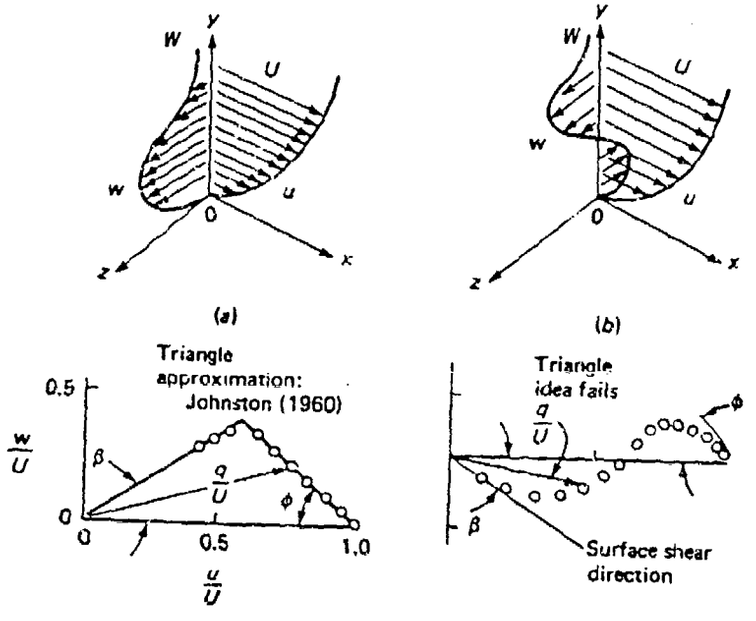

Figure 4.2. Three-Dimensional Boundary Layer Profiles, Showing a) Uni-directional Skewing, and b) Bi-directional Skewing (from White, 1974)

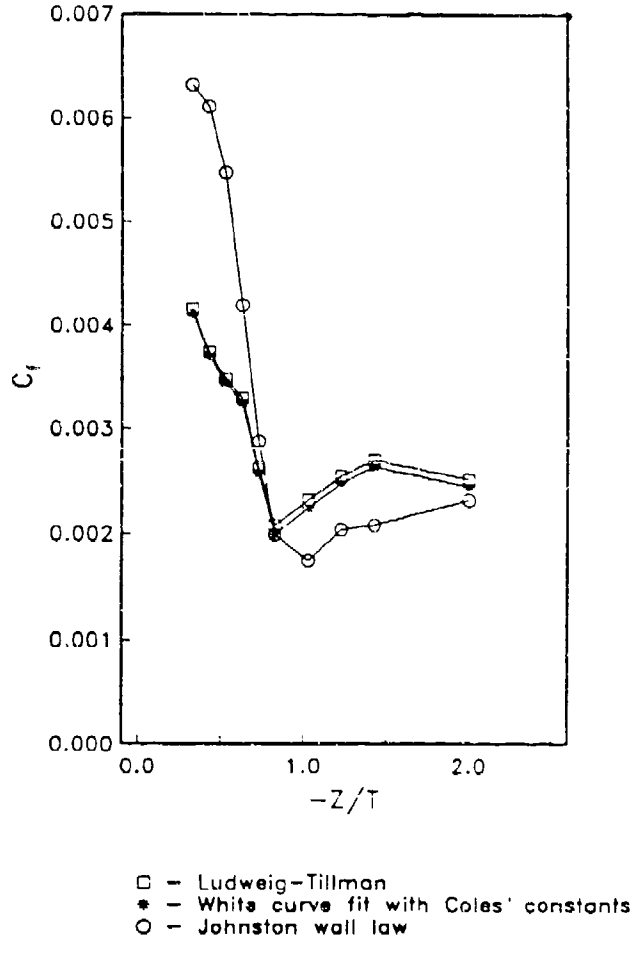

Figure 4.3. Comparison of $(C_f)_{FS}$ Estimating Methods, Plane 9, JLF Data

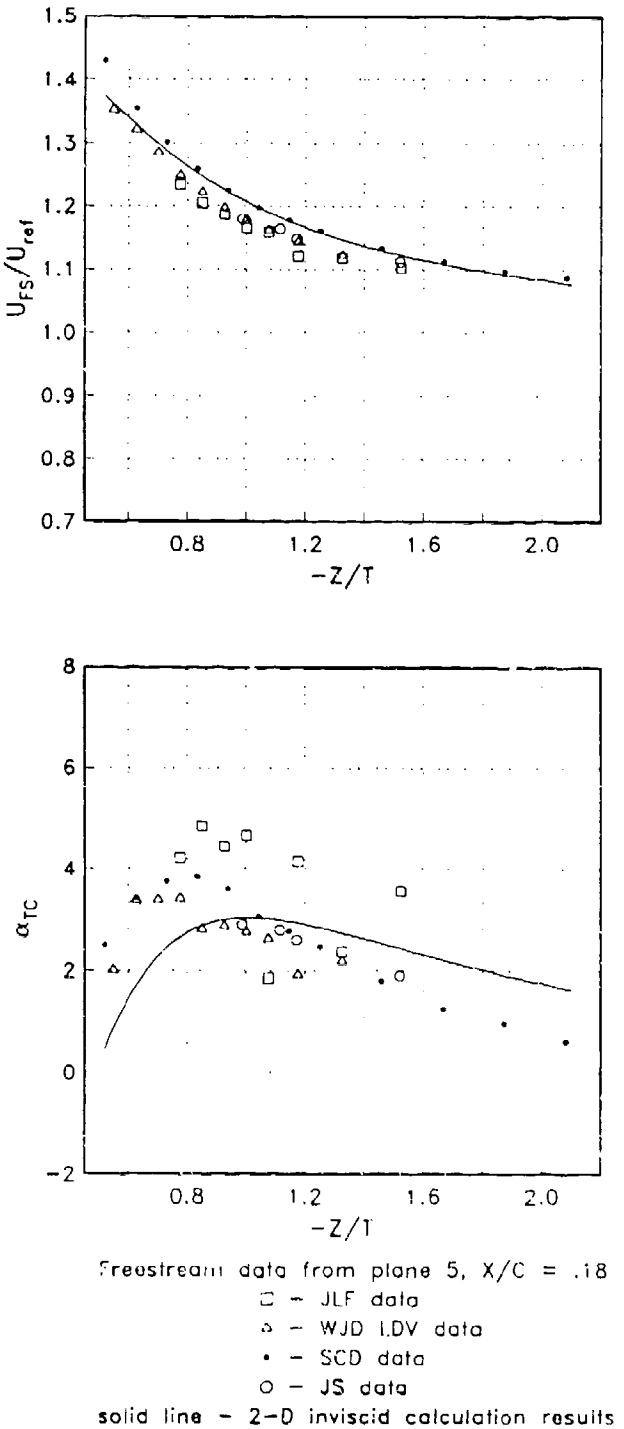

Figure 4.4a. Comparison of Freestream Mean Velocity and Flow Angle Results to 2-D Potential Flow Calculation Results (Plane 5)

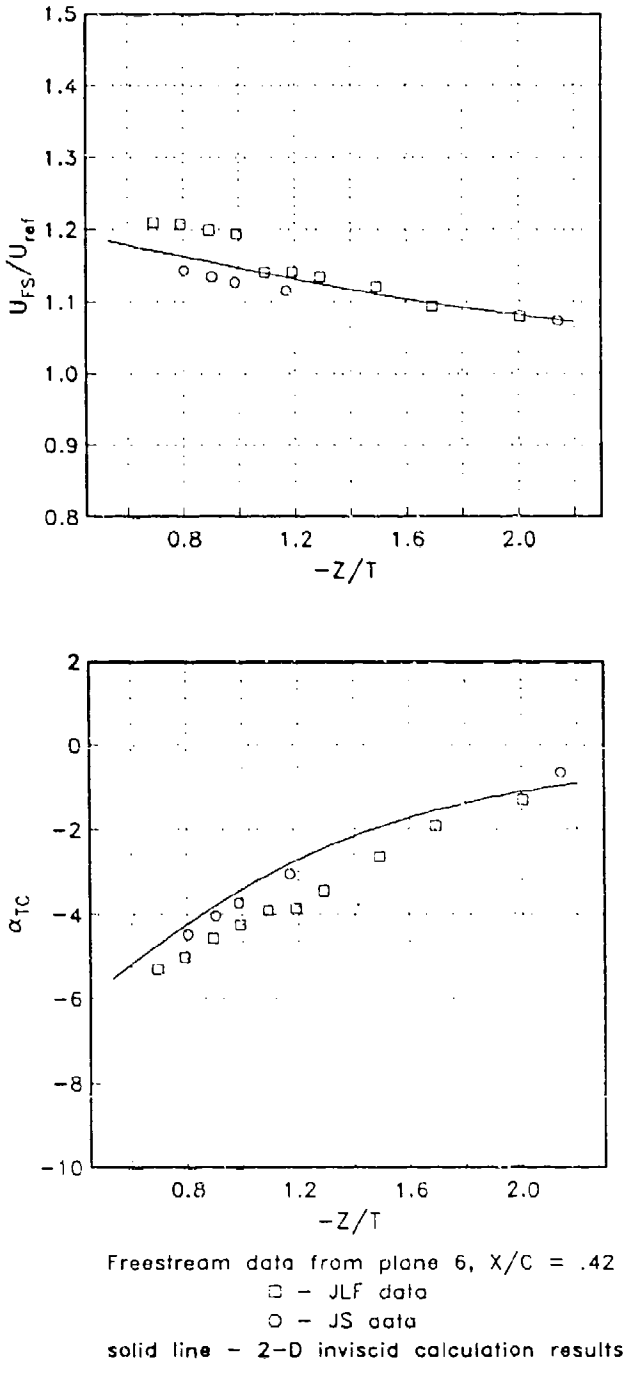

Figure 4.4b. Comparison of Freestream Mean Velocity and Flow Angle Results to 2-D Potential Flow Calculation Results (Plane 6)

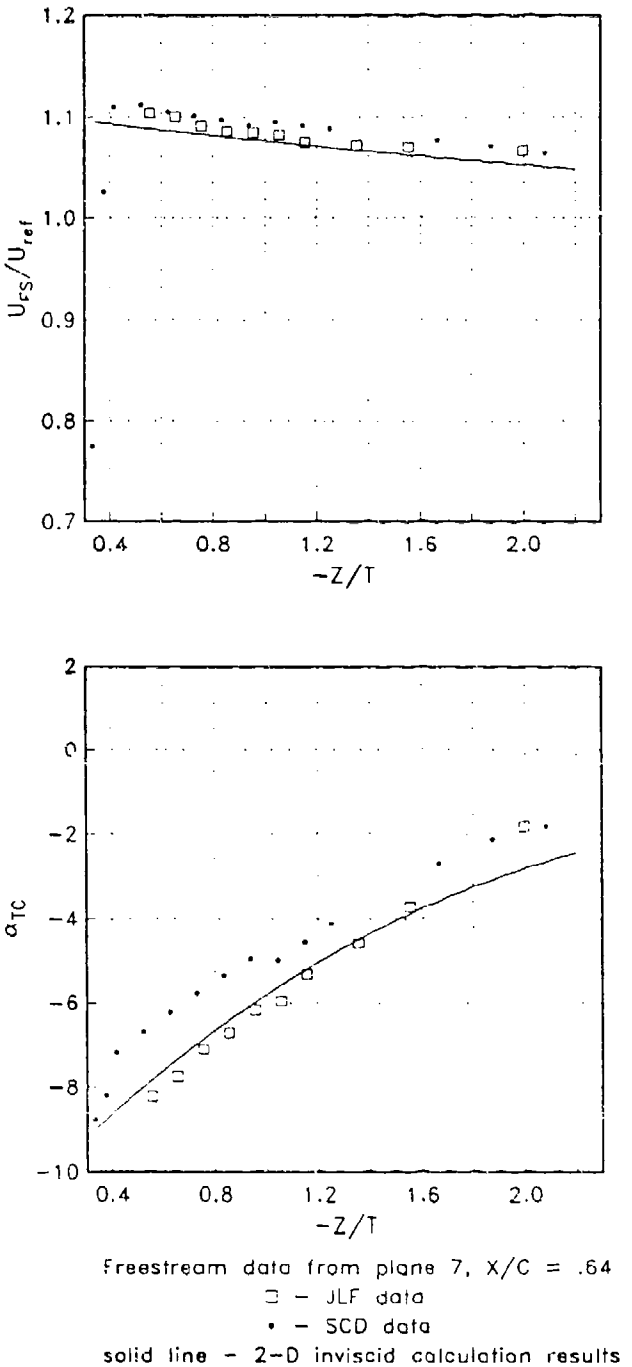

Figure 4.4c. Comparison of Freestream Mean Velocity and Flow Angle Results to 2-D Potential Flow Calculation Results (Plane 7)

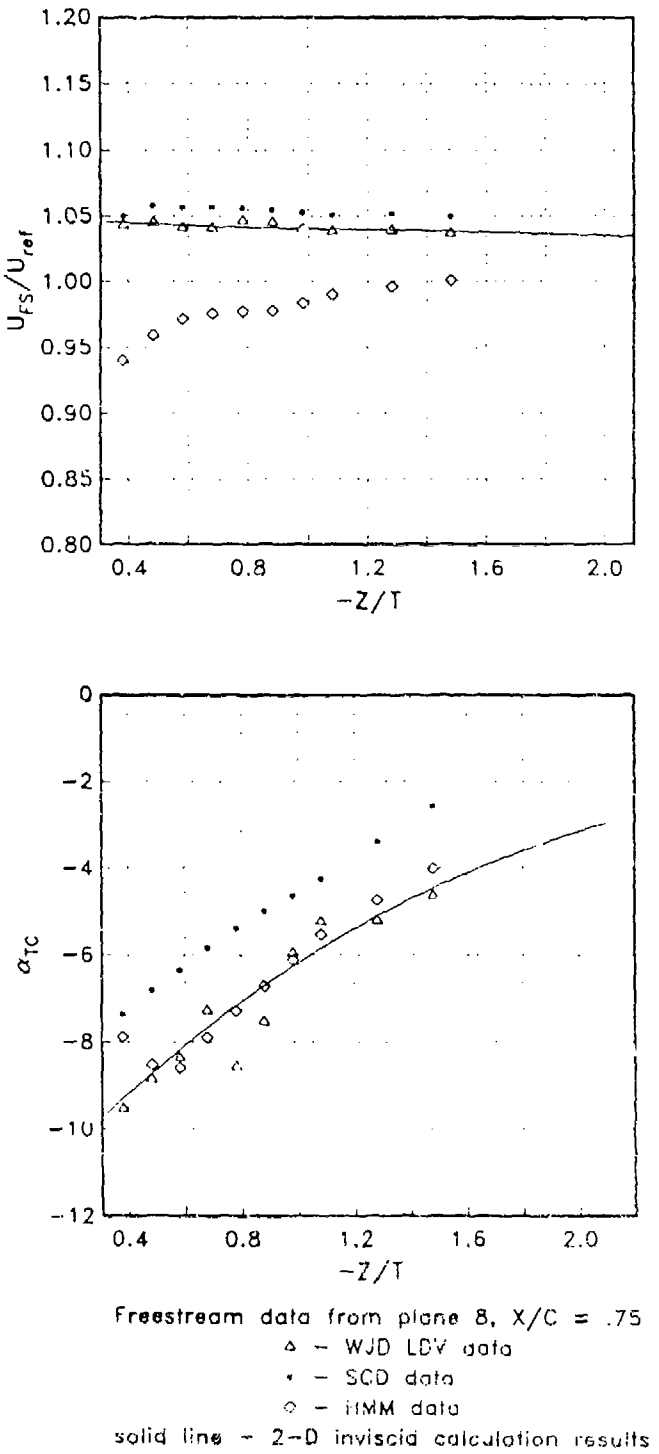

Figure 4.4d. Comparison of Freestream Mean Velocity and Flow Angle Results to 2-D Potential Flow Calculation Results (Plane 8)

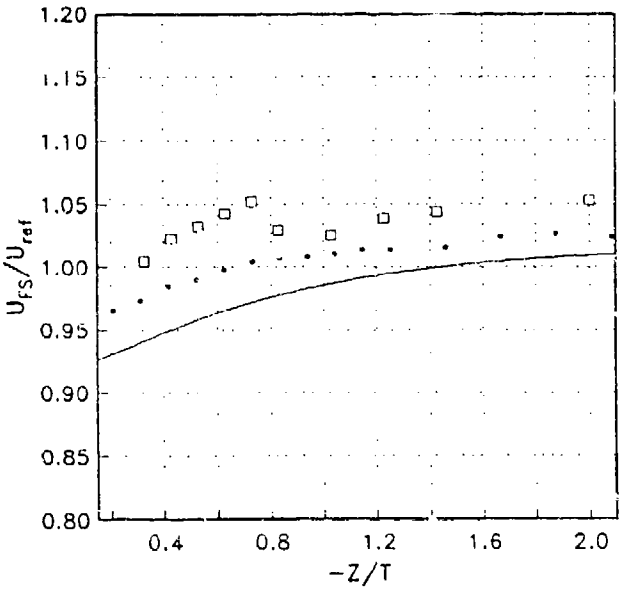

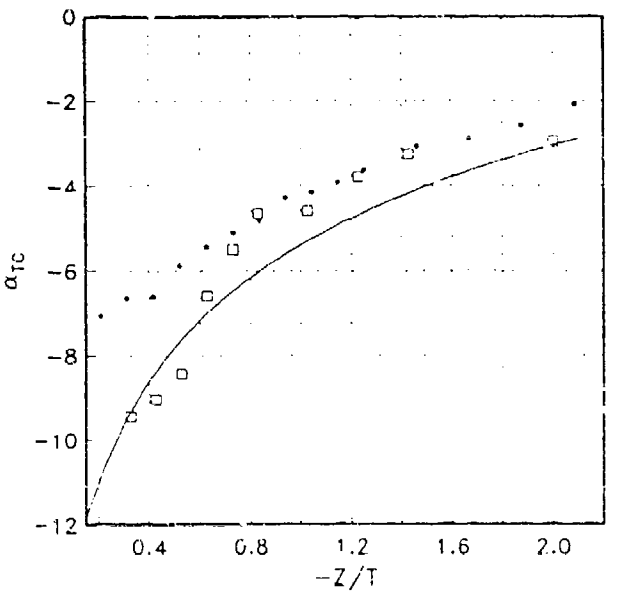

Freestream data from plane 9, X/C = .93
□ – JLF data
• – SCD data
solid line – 2-D inviscid calculation results

Figure 4.4e. Comparison of Freestream Mean Velocity and Flow Angle Results to 2-D Potential Flow Calculation Results (Plane 9)

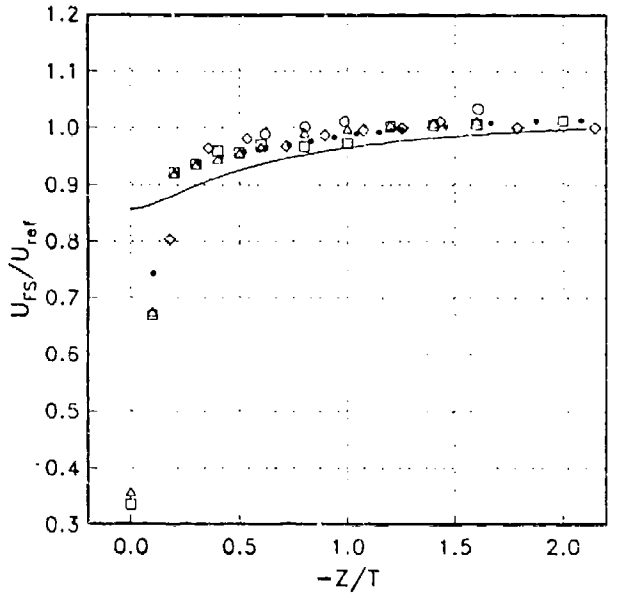

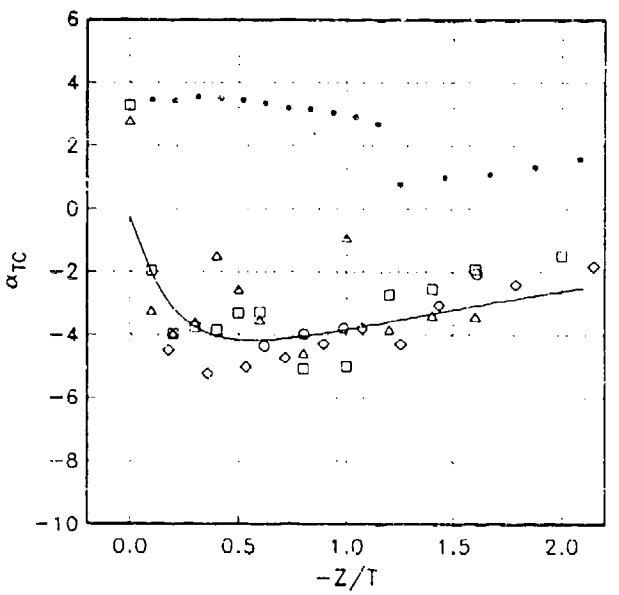

Freestream data from plane 10, X/C = 1.05
□ – JLF data
△ – WJD LDV data
• – SCD data
○ – JS data
◇ – HMM data
solid line – 2–D inviscid calculation results

Figure 4.4f. Comparison of Freestream Mean Velocity and Flow Angle Results to 2-D Potential Flow Calculation Results (Plane 10)

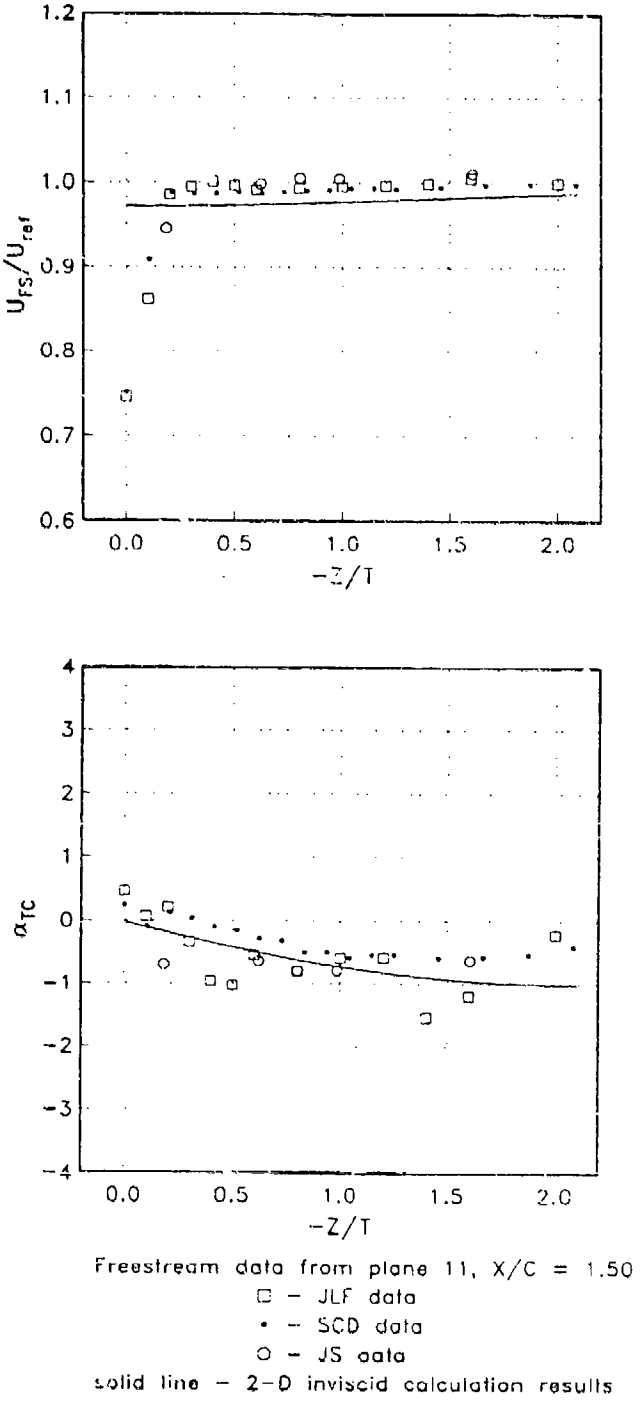

Figure 4.4g. Comparison of Freestream Mean Velocity and Flow Angle Results to 2-D Potential Flow Calculation Results (Plane 11)

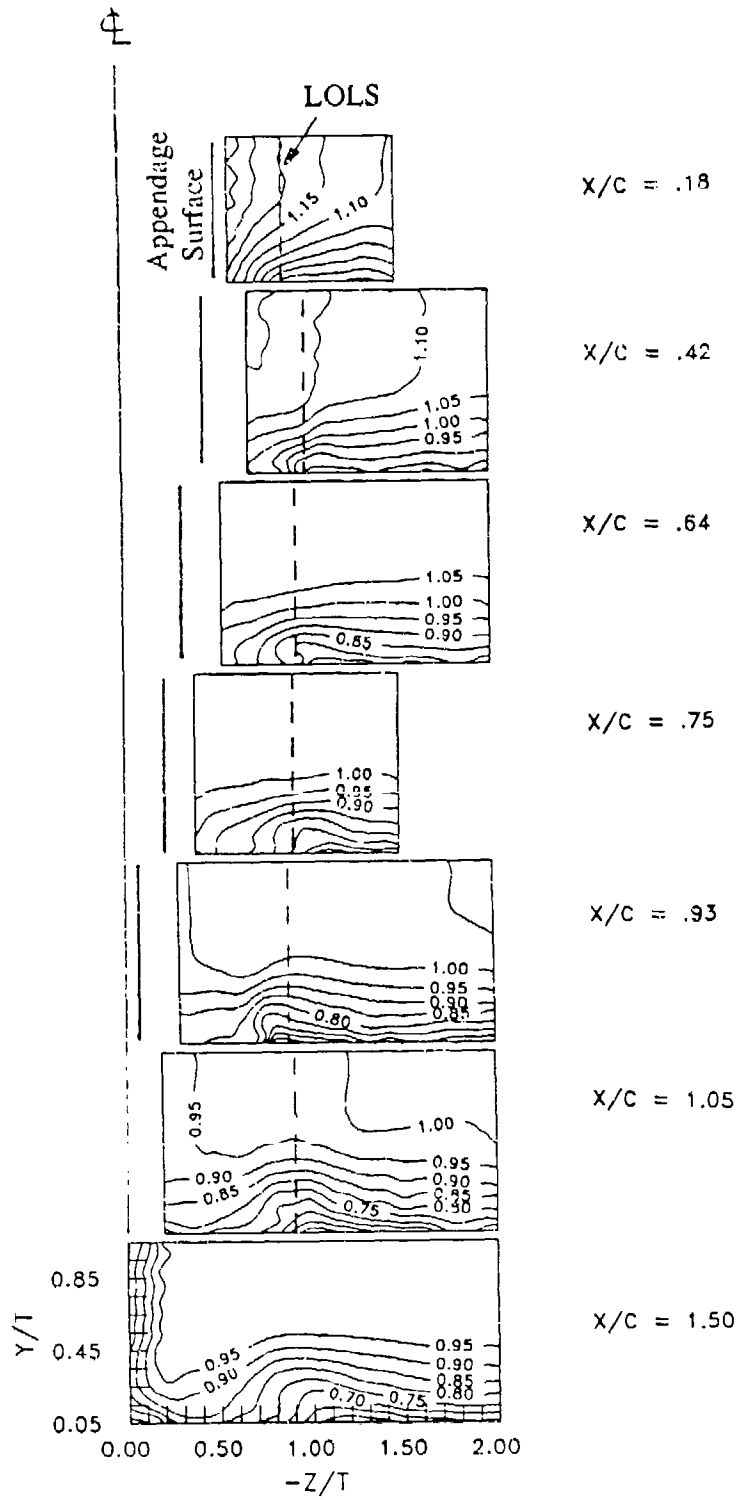

Figure 4.5a. Contours of U_{TC}/U_{ref}, Planes 5-11 (All data from present study except X/C = .18 and .75 from Devenport and Simpson (1990a))

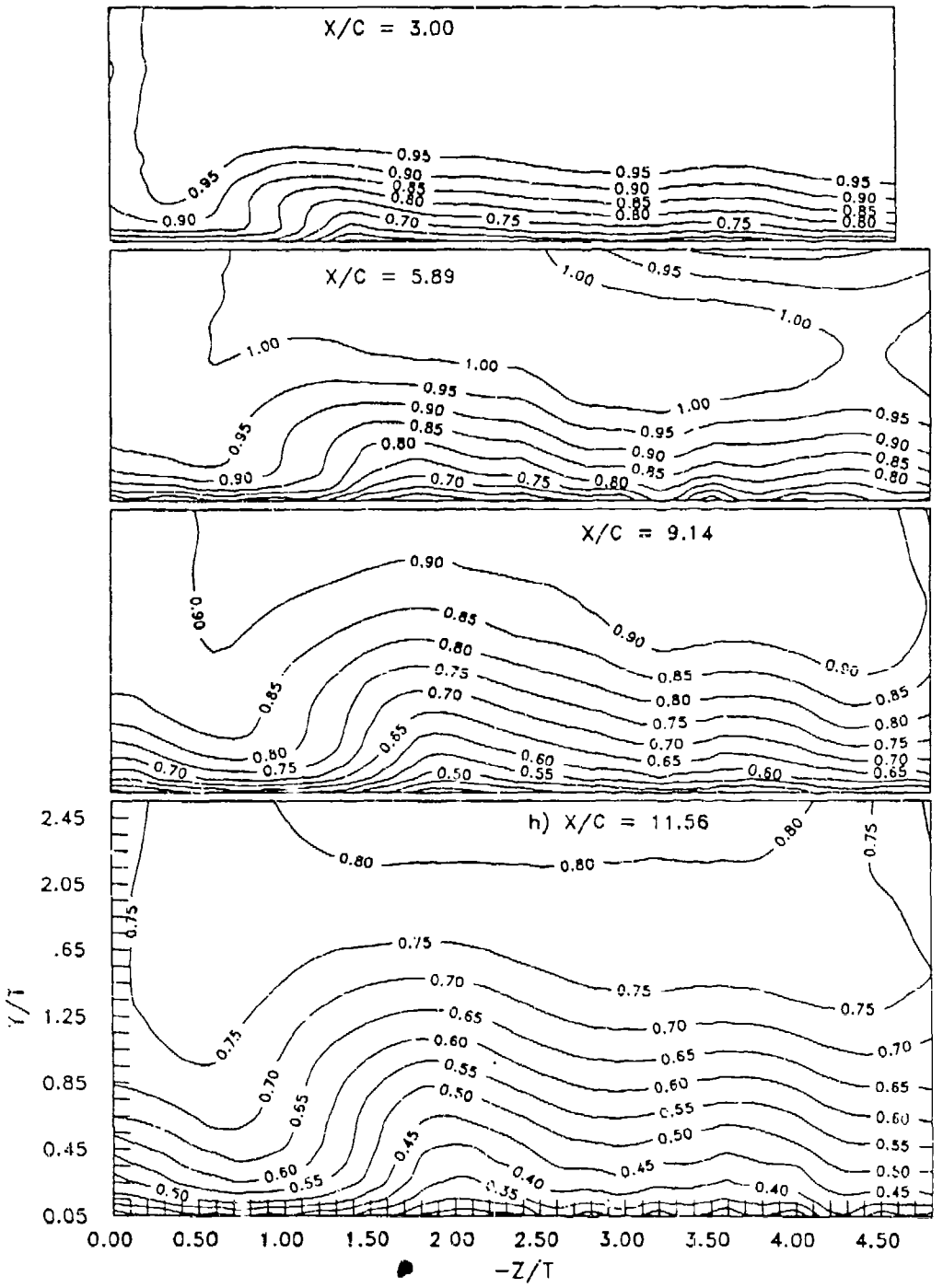

Figure 4.5b. Contours of U_{TC}/U_{ref}, Planes 12-15 (All data from present study except X/C = 3.00 from Devenport *et al.* (1990))

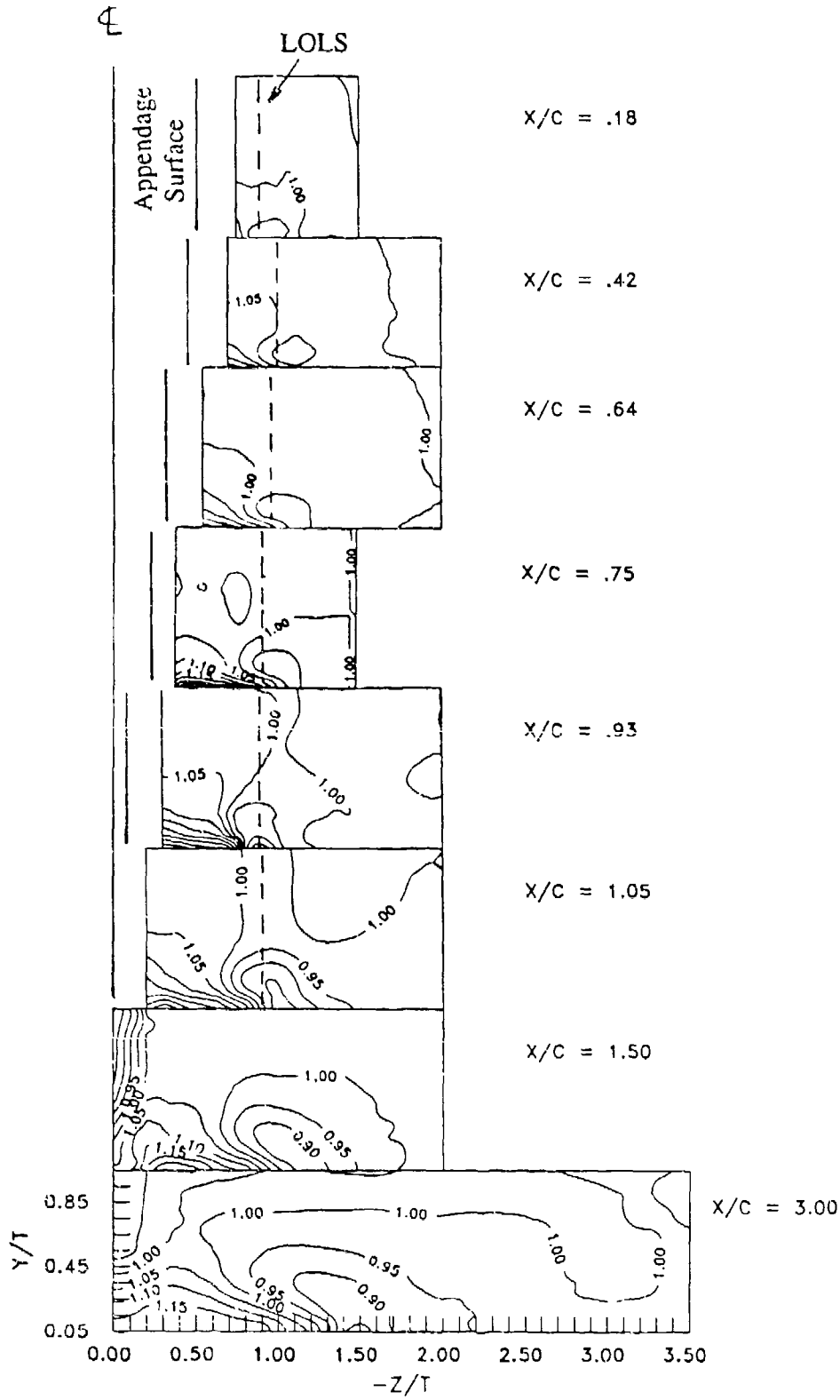

Figure 4.6a. Contours of Distortion Function, f_D, Planes 5-12 (All data from present study except X/C = .18 and .75 from Devenport and Simpson (1990a) and X/C = 3.00 from Devenport *et al.* (1990))

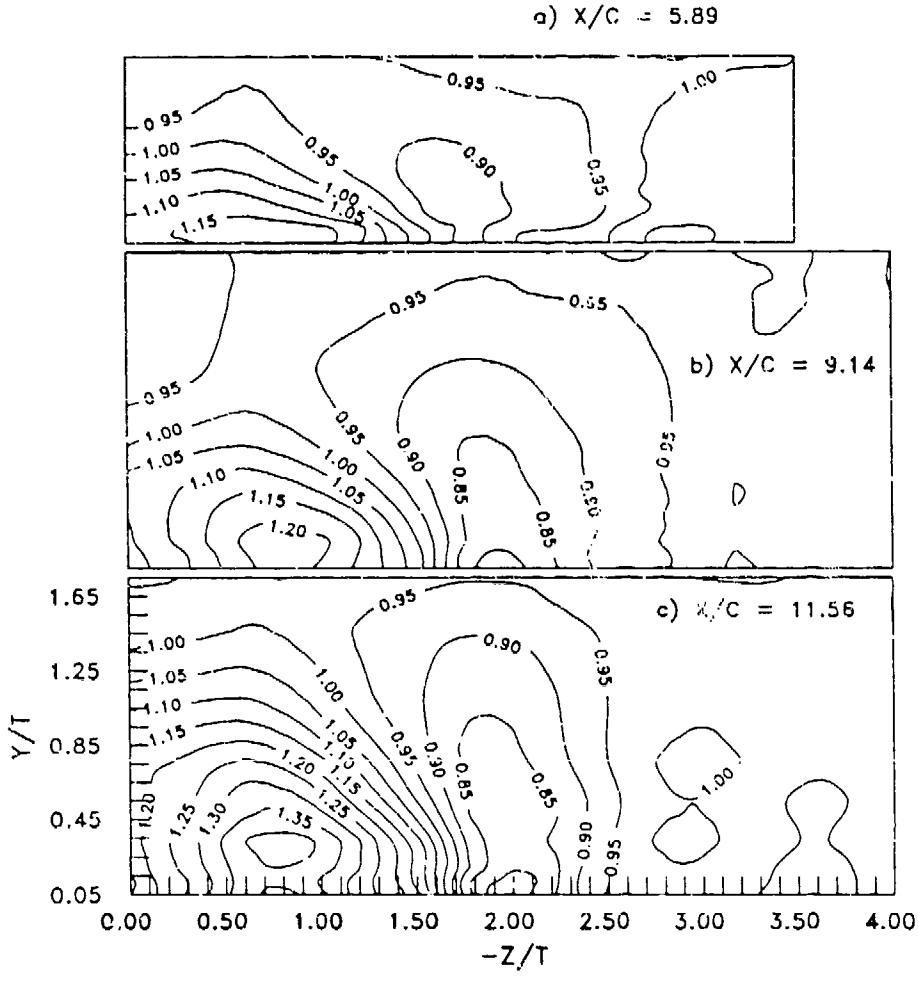

Figure 4.6b. Contours of Distortion Function, f_D, Planes 13-15

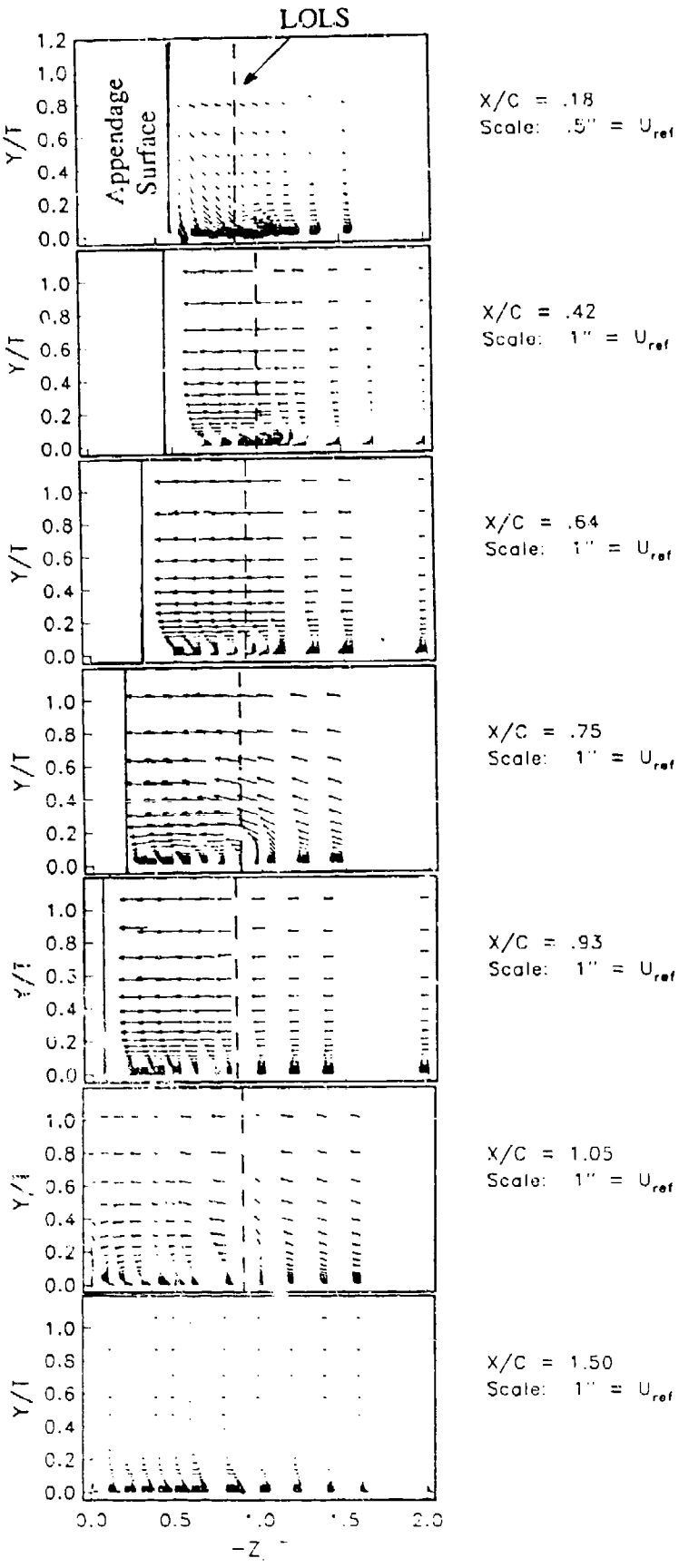

Figure 4.7. Secondary Velocity Vectors, Planes 5-11 (All data from present study except X/C = .18, .75, and 1.05 from Devenport and Simpson (1990a). JLF data presents only W component of secondary velocities)

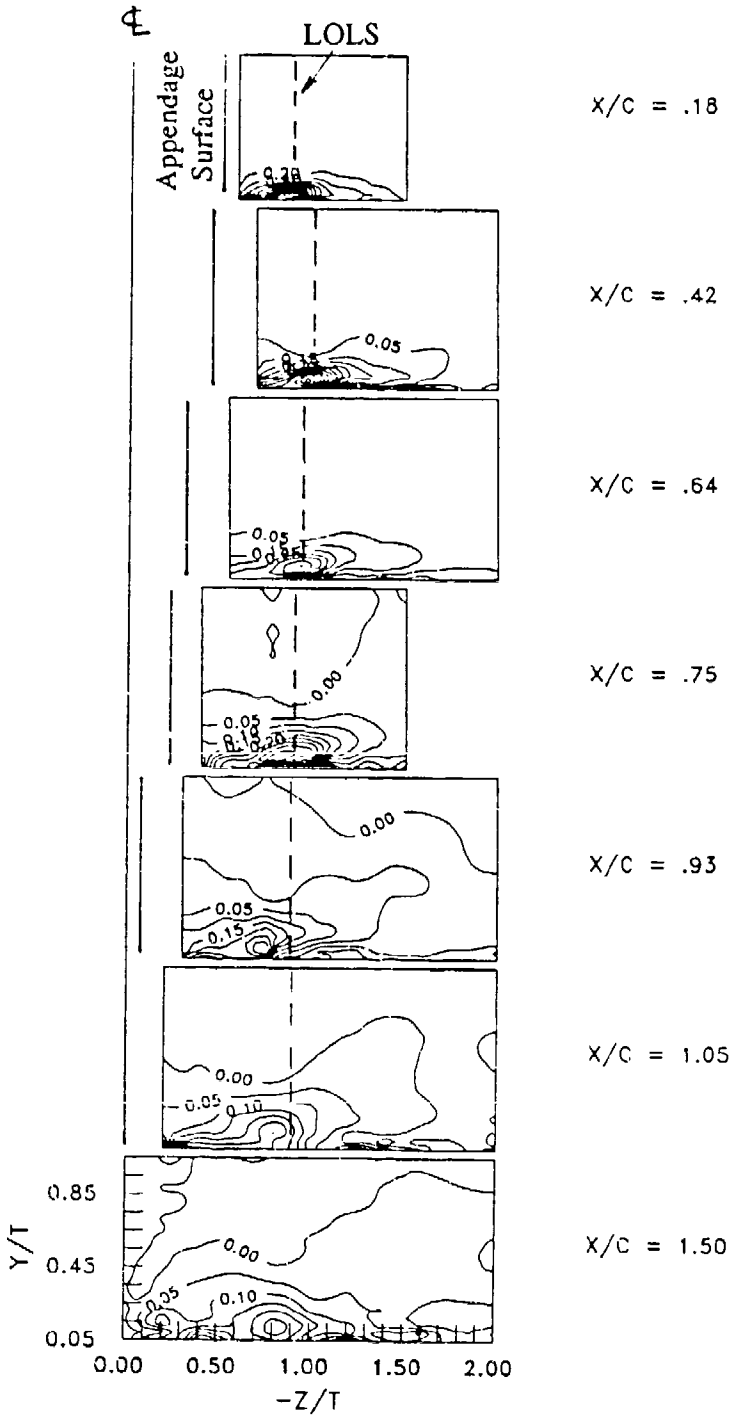

Figure 4.8. Contours of $(\partial(W)/\partial Y)\delta/U_{ref}$, Planes 5-11 (All data from present study except X/C = .18 and .75 from Devenport and Simpson (1990a))

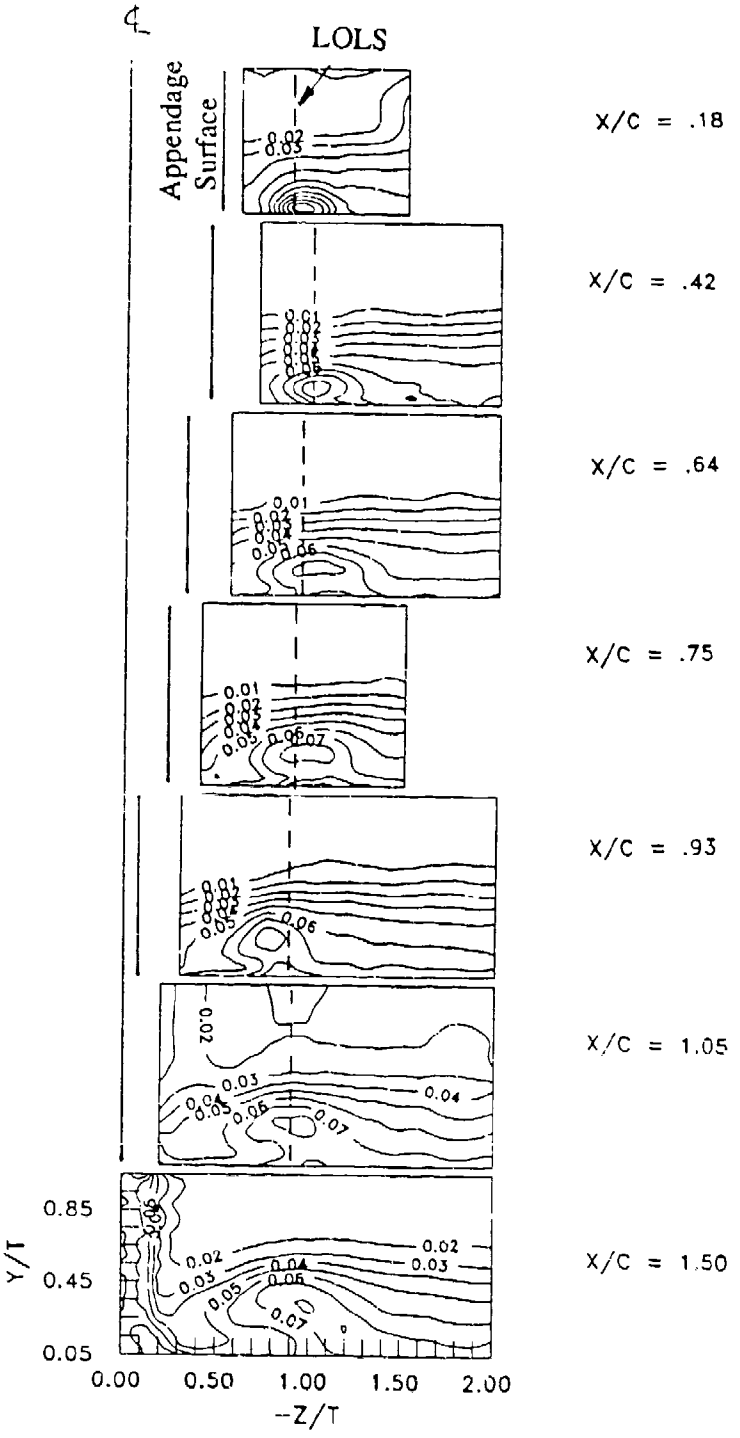

Figure 4.9a. Contours of u'_{TC}/U_{ref}, Planes 5-11 (All data from present study except X/C = .18 and .75 from Devenport and Simpson (1990a))

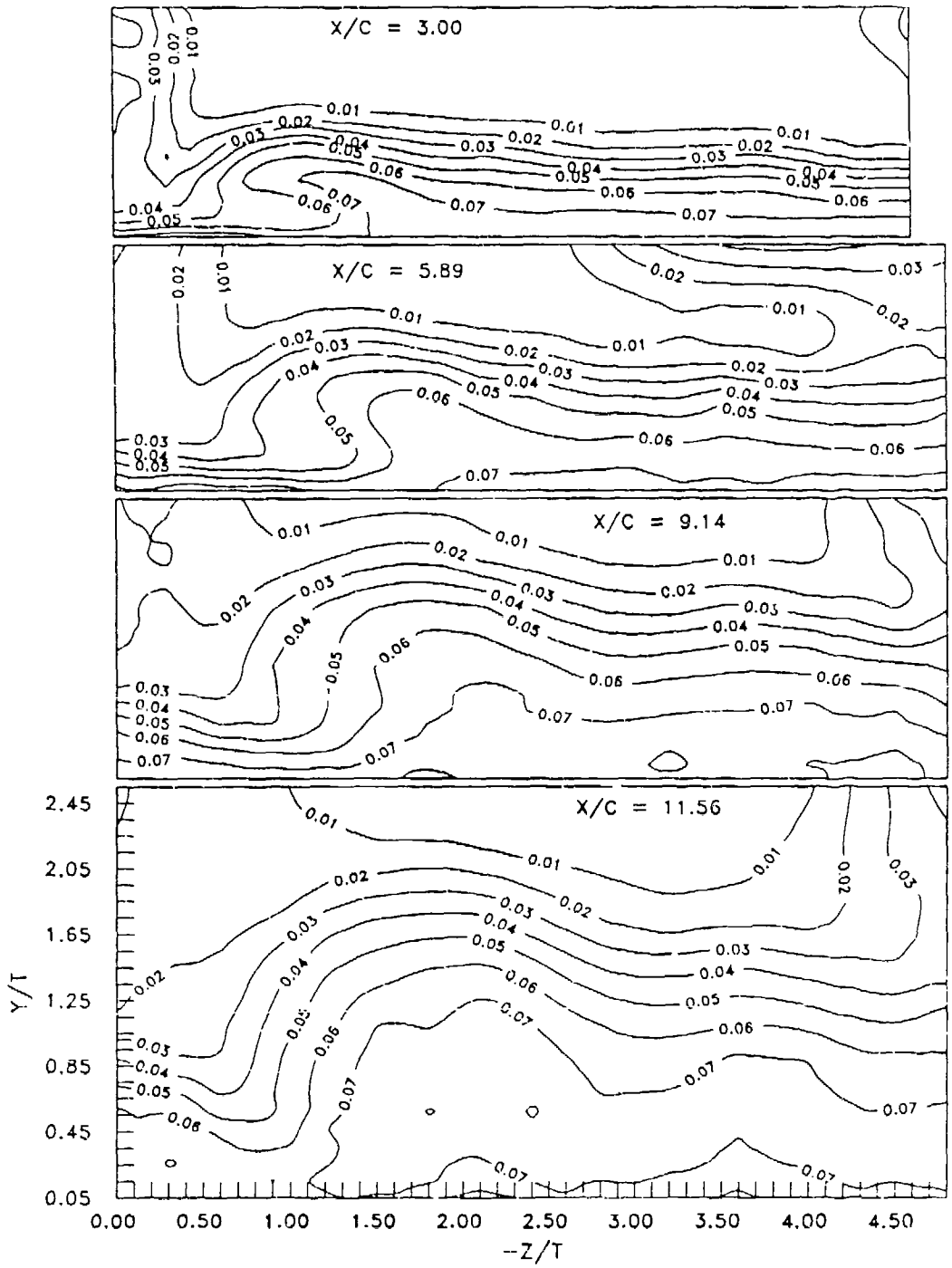

Figure 4.9b. Contours of u'_{TC}/U_{ref}, Planes 12-15 (All data from present study except X/C = 3.00 from Devenport *et al.* (1990))

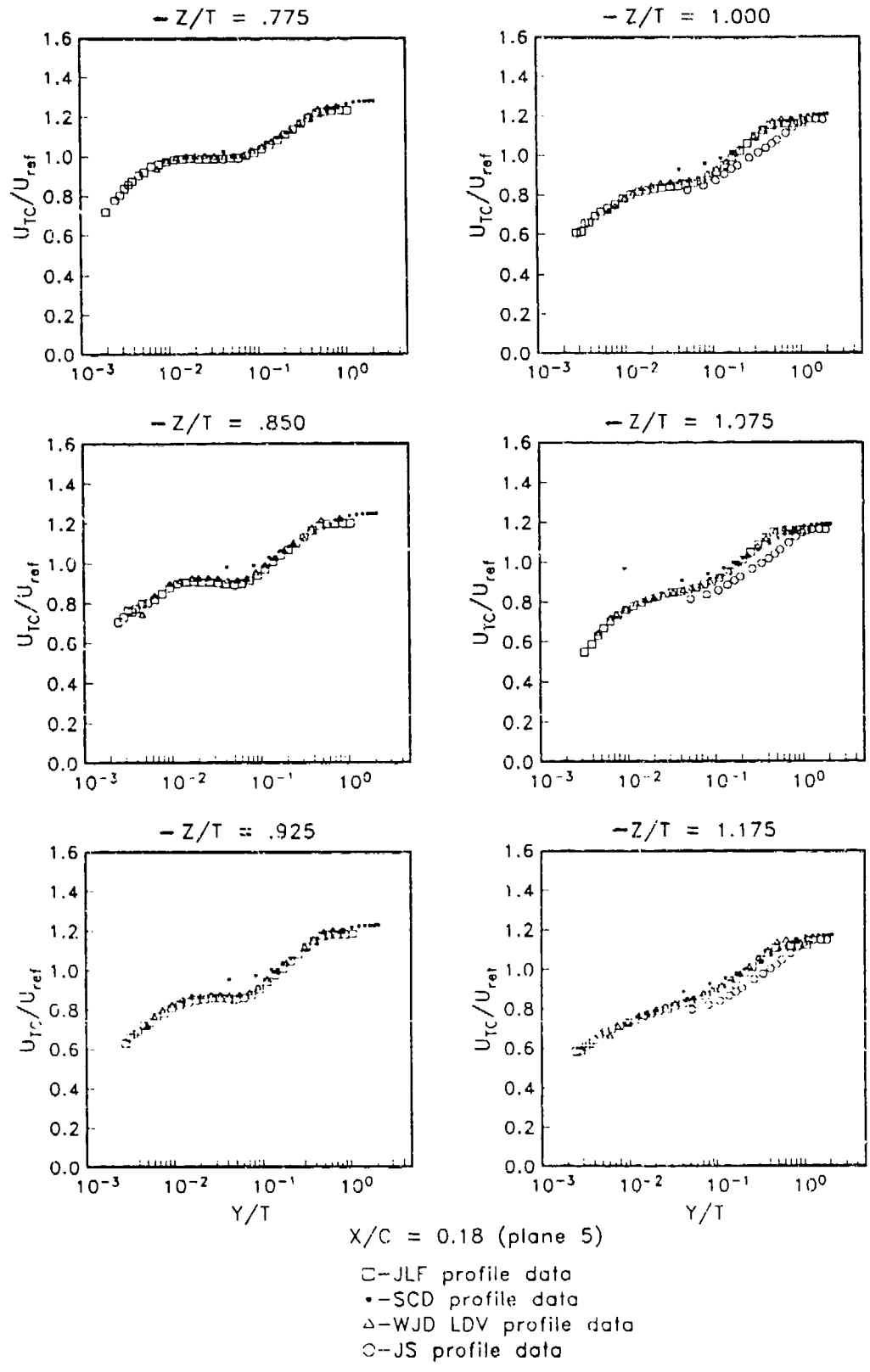

Figure 4.10. Profiles of U_{TC}/U_{ref}, Plane 5

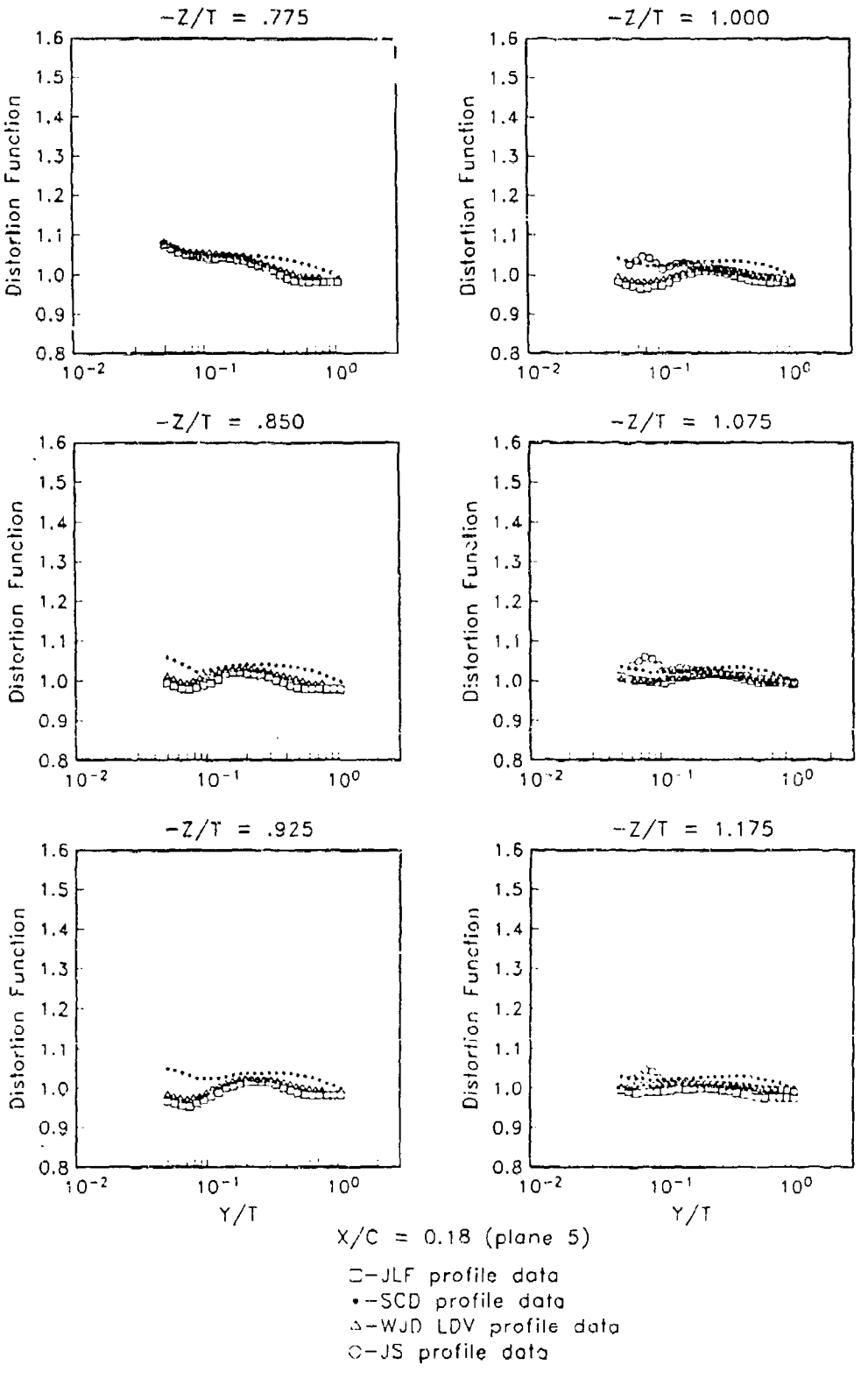

Figure 4.11. Profiles of Distortion Function, f_D, Plane 5

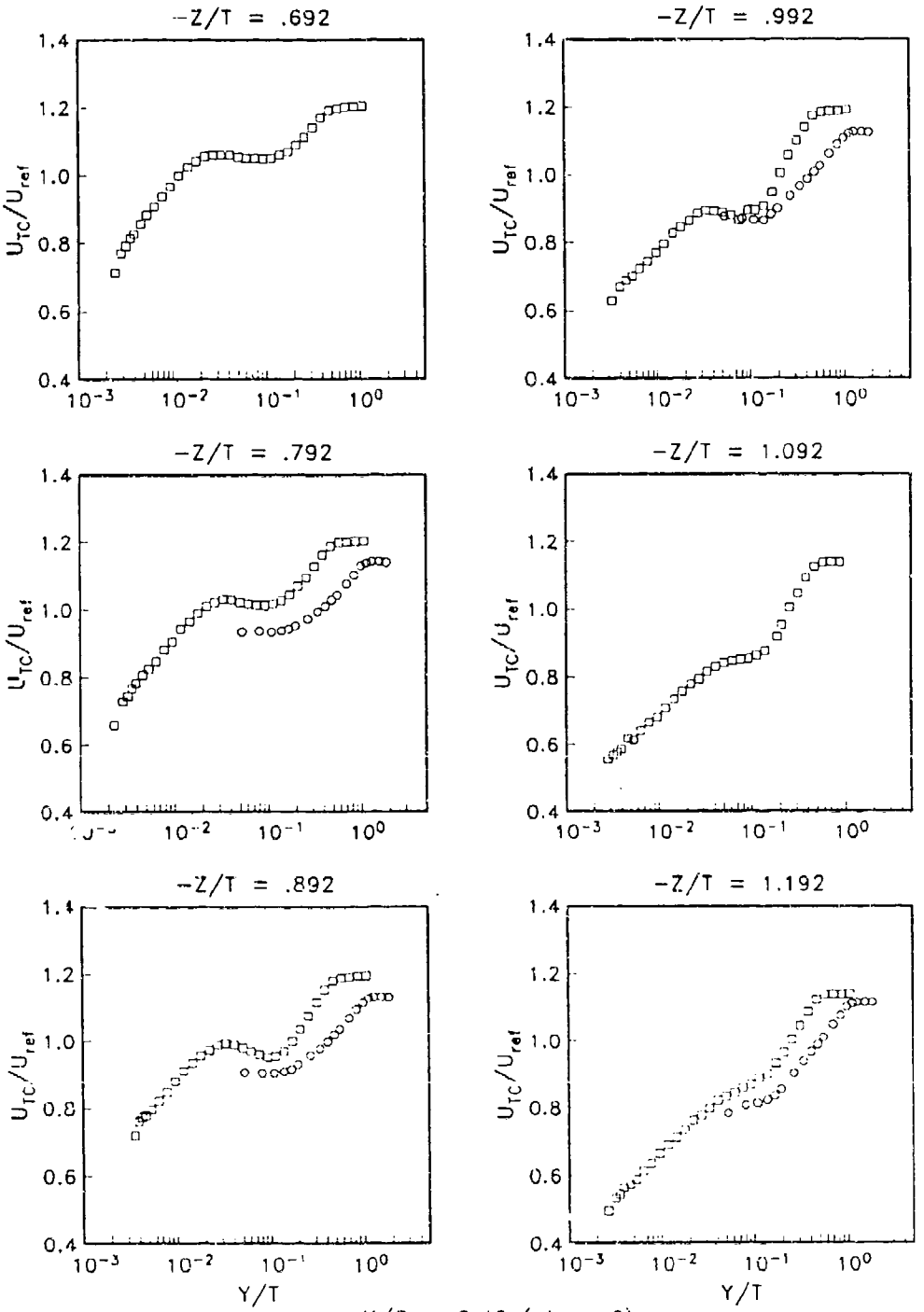

Figure 4.12. Profiles of U_{TC}/U_{ref}, Plane 6

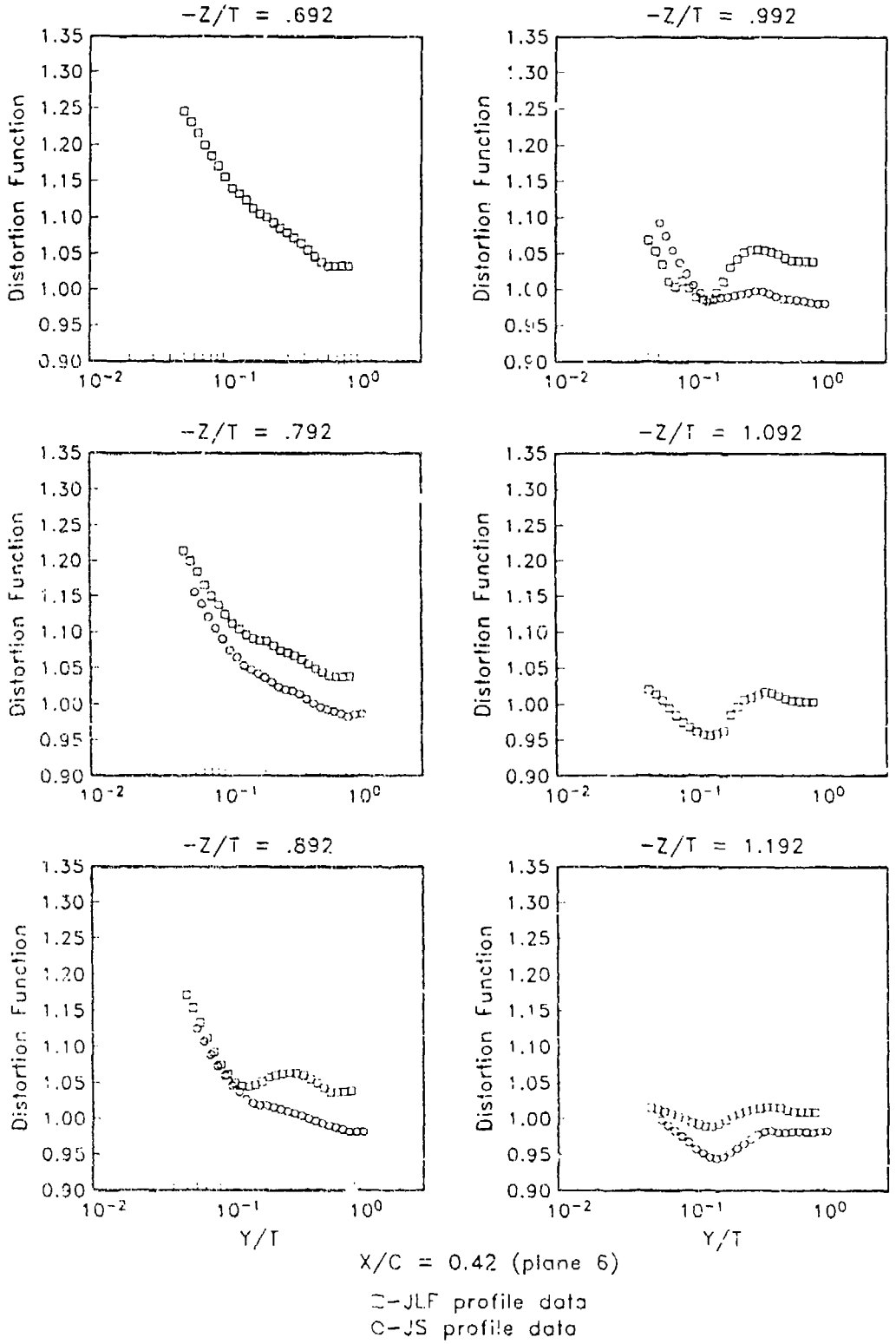

Figure 4.13. Profiles of Distortion Function, f_D, Plane 6

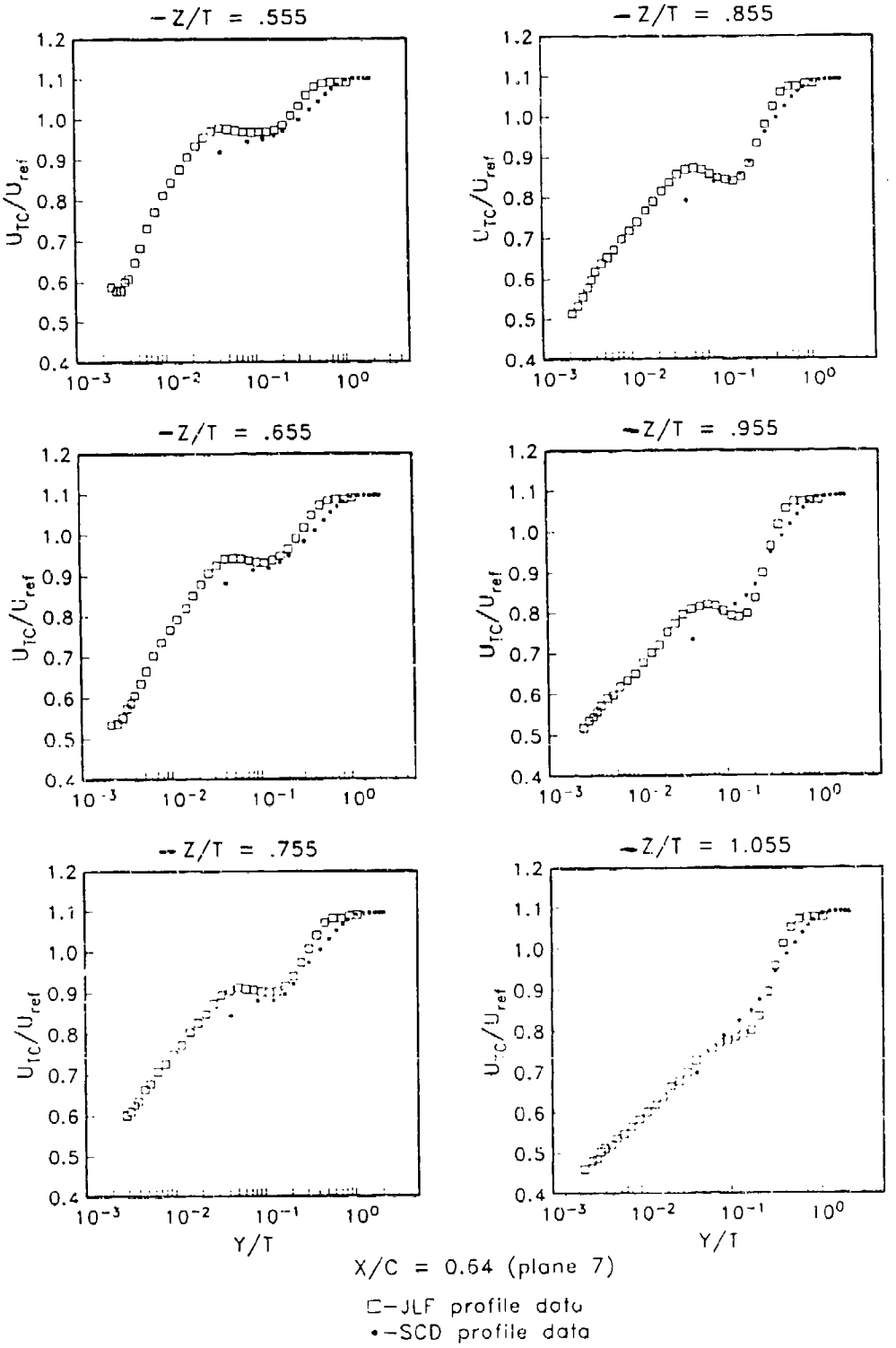

Figure 4.14. Profiles of U_{TC}/U_{ref}, Plane 7

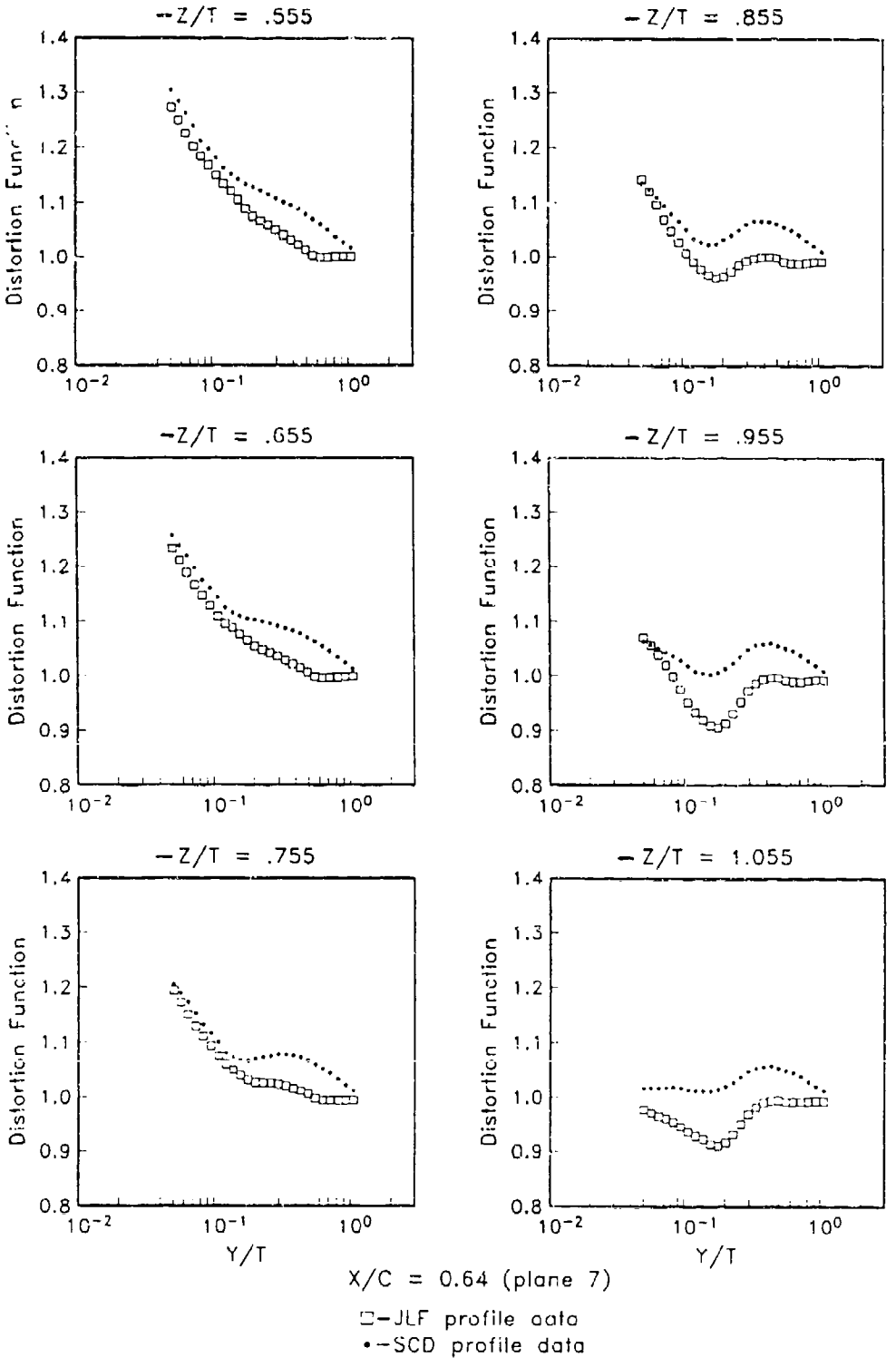

Figure 4.15. Profiles of Distortion Function, f_D, Plane 7

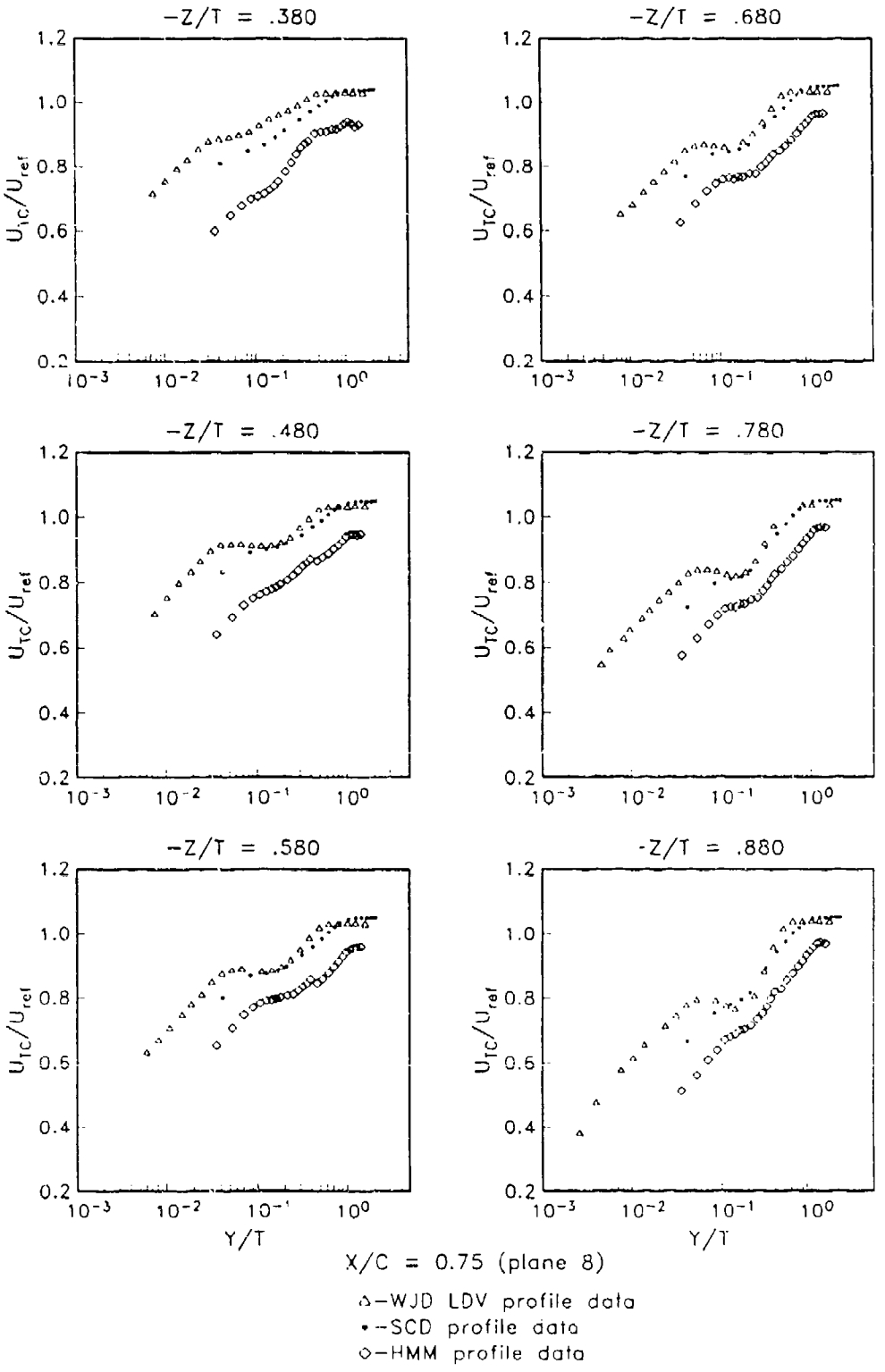

Figure 4.16. Profiles of U_{TC}/U_{ref}, Plane 8

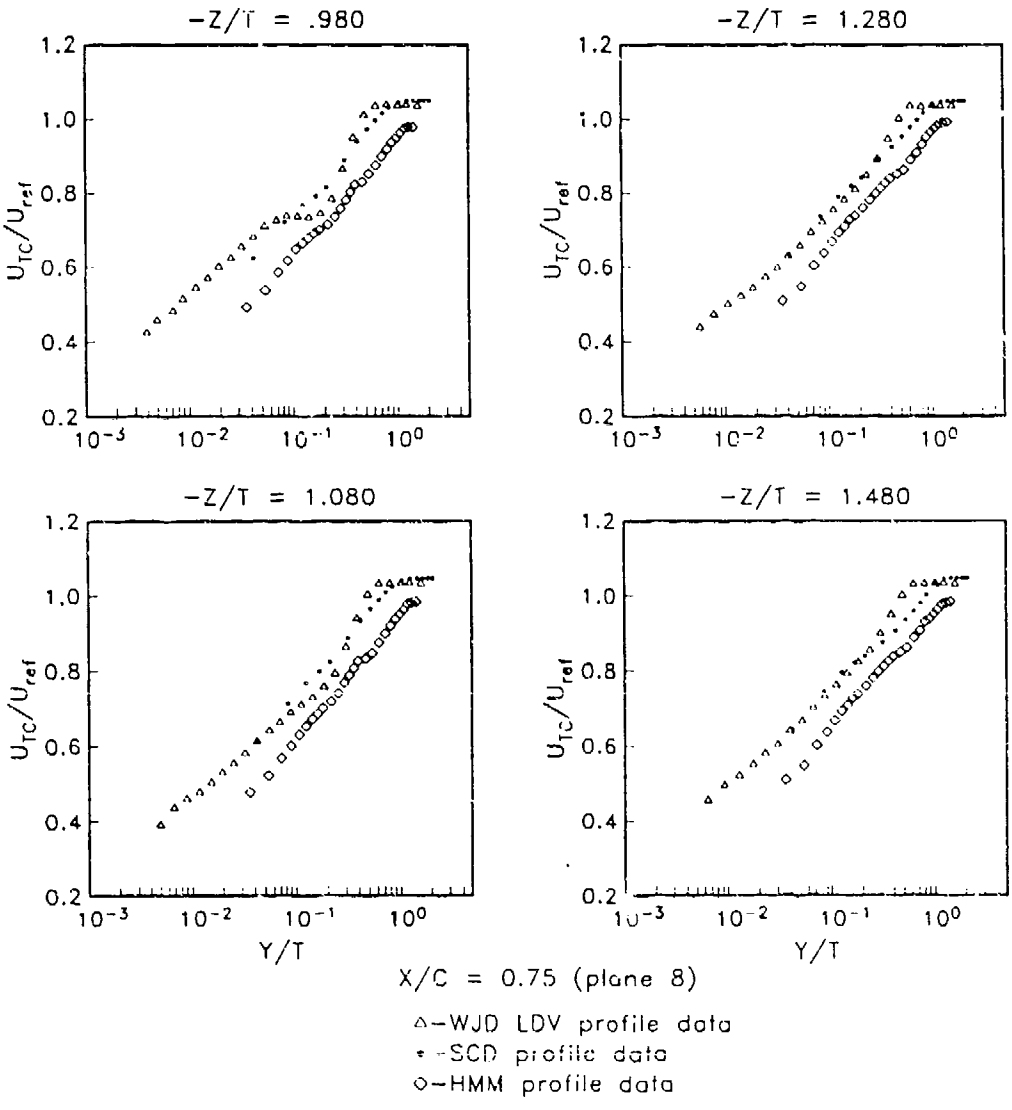

Figure 4.16 (cont.). Profiles of U_{TC}/U_{ref}, Plane 8

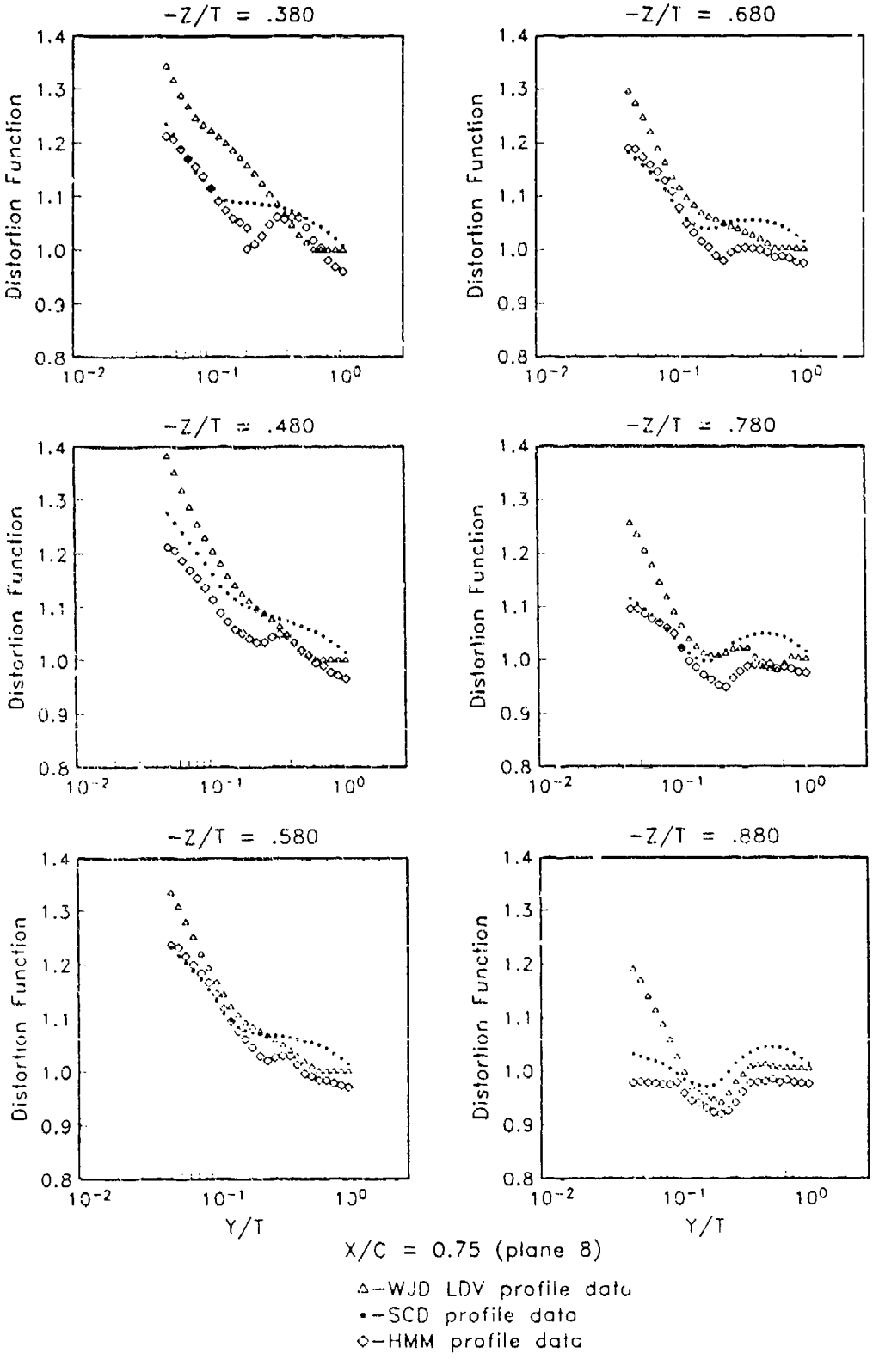

Figure 4.17. Profiles of Distortion Function, f_D, Plane 8

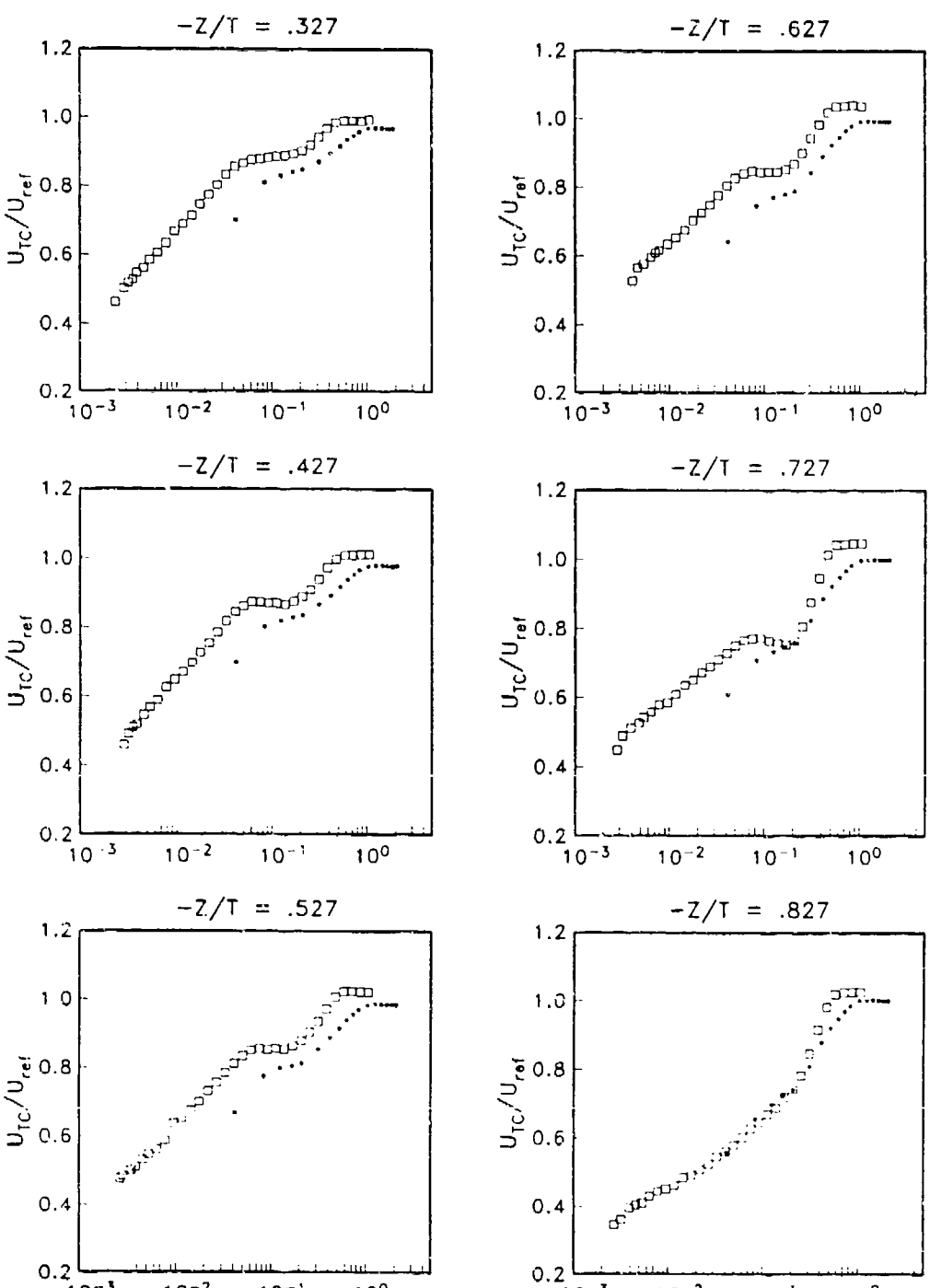

Figure 4.18. Profiles of U_{TC}/U_{ref}, Plane 9

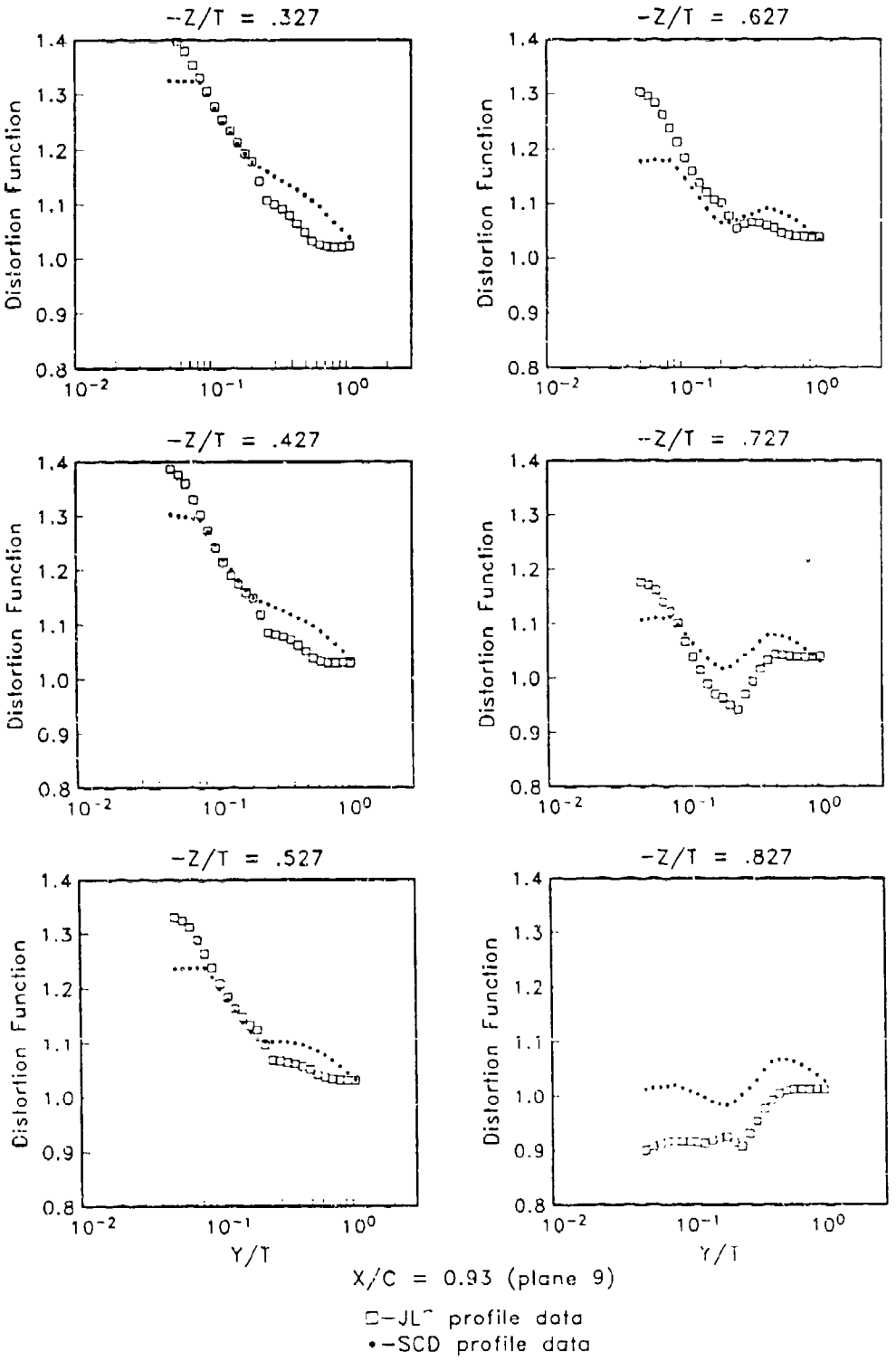

Figure 4.19. Profiles of Distortion Function, f_D, Plane 9

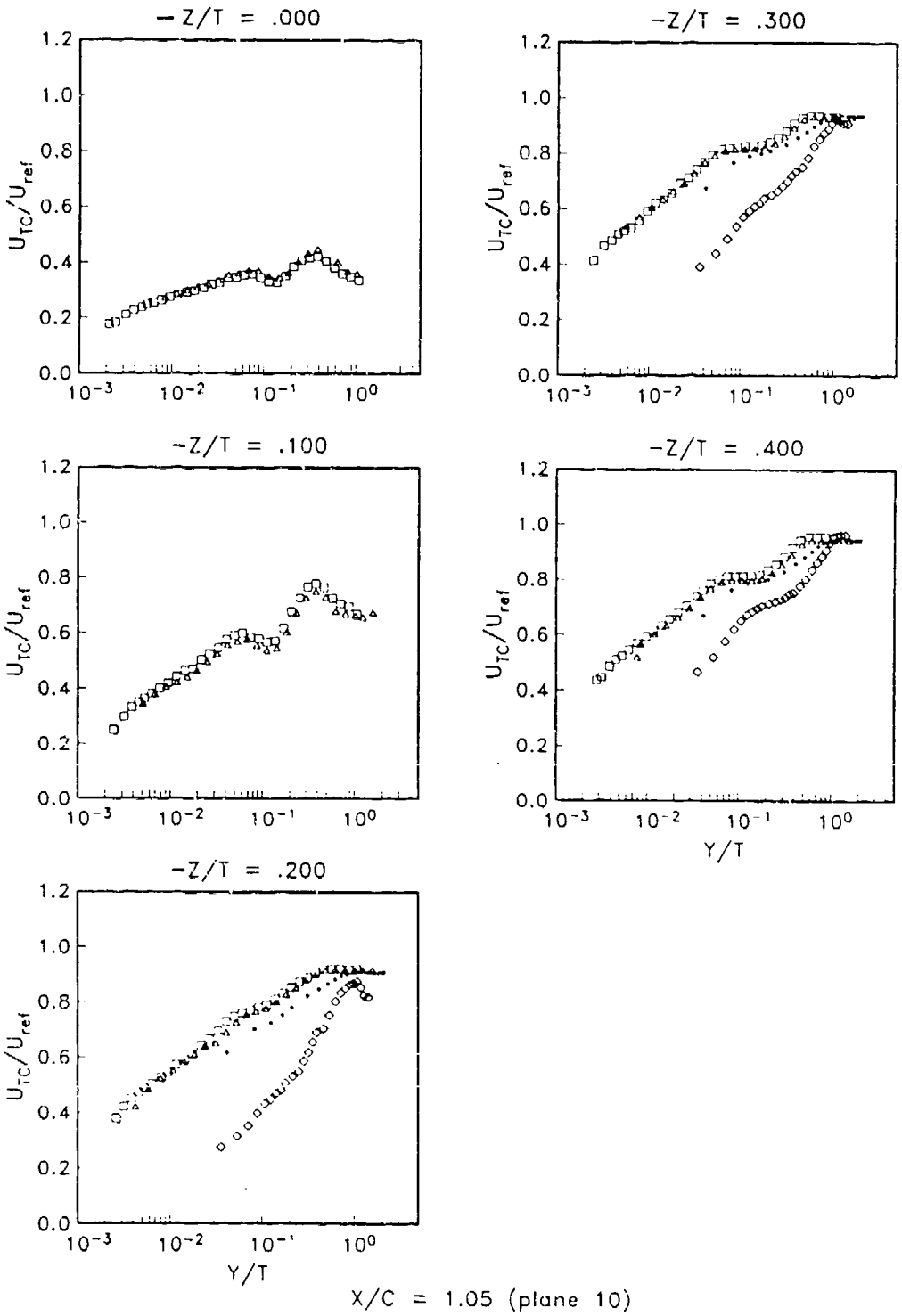

Figure 4.20. Profiles of U_{TC}/U_{ref}, Plane 10

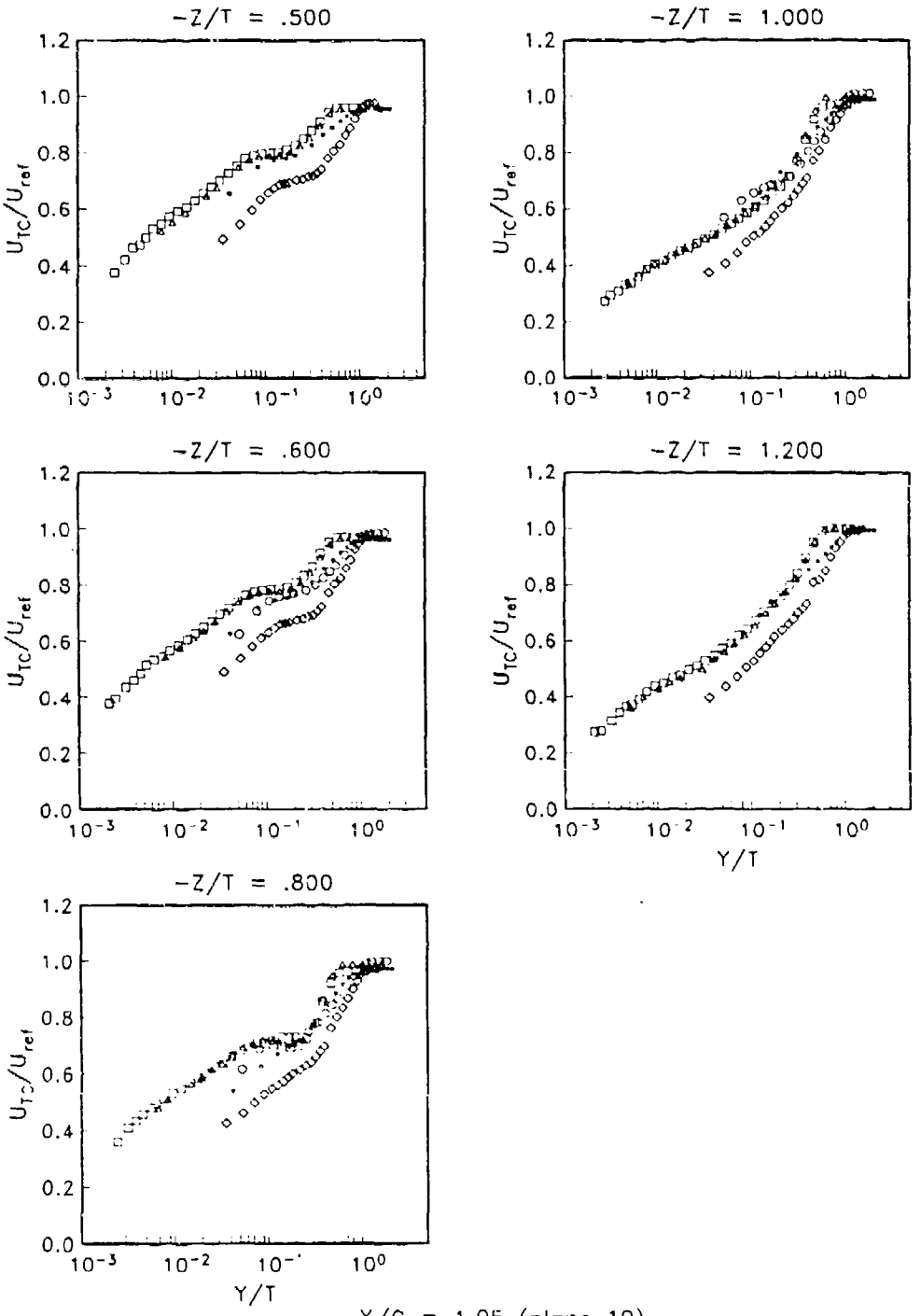

Figure 4.20. (cont.). Profiles of U_{TC}/U_{ref}

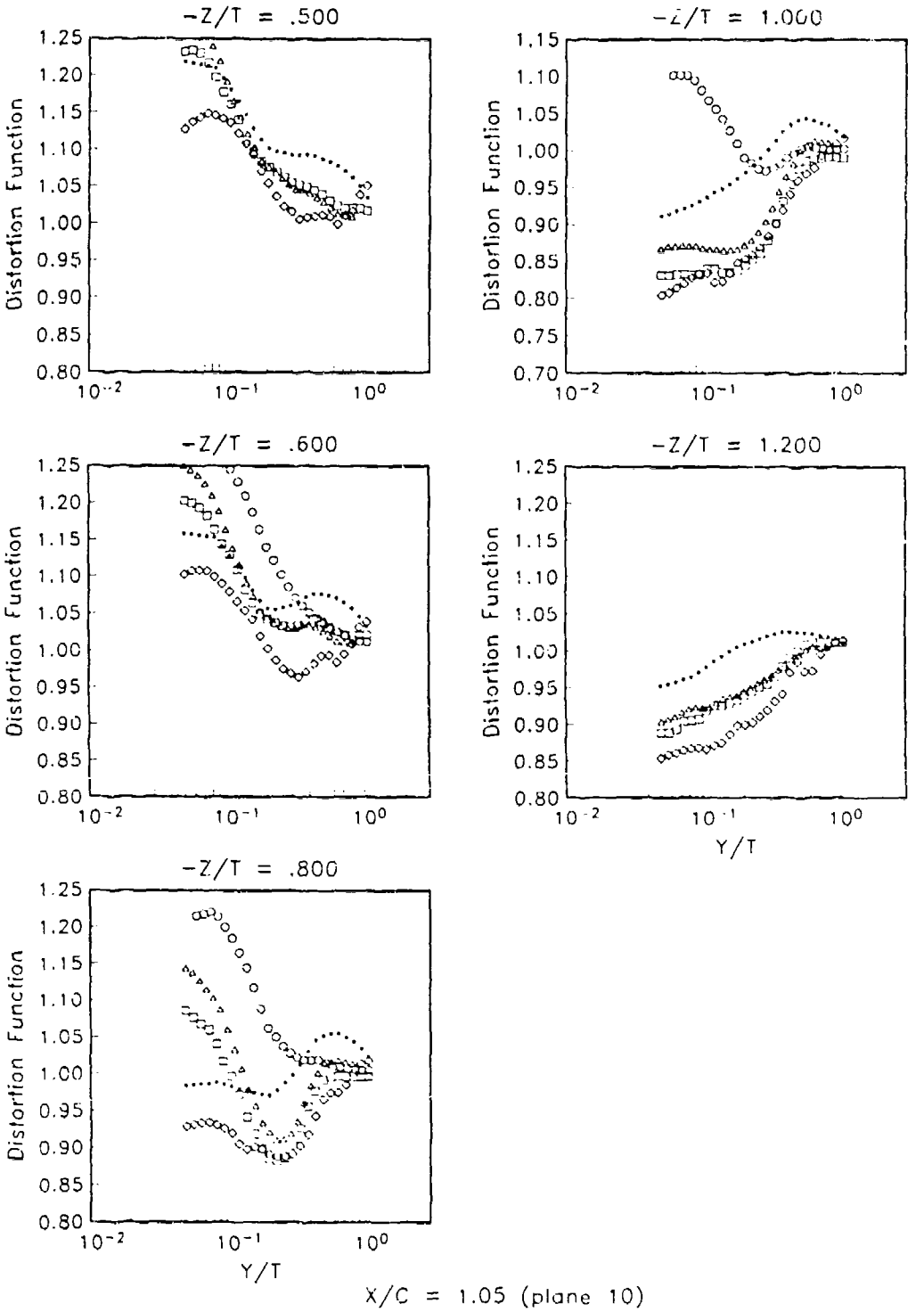

Figure 4.21. Profiles of Distortion Function, f_D, Plane 10

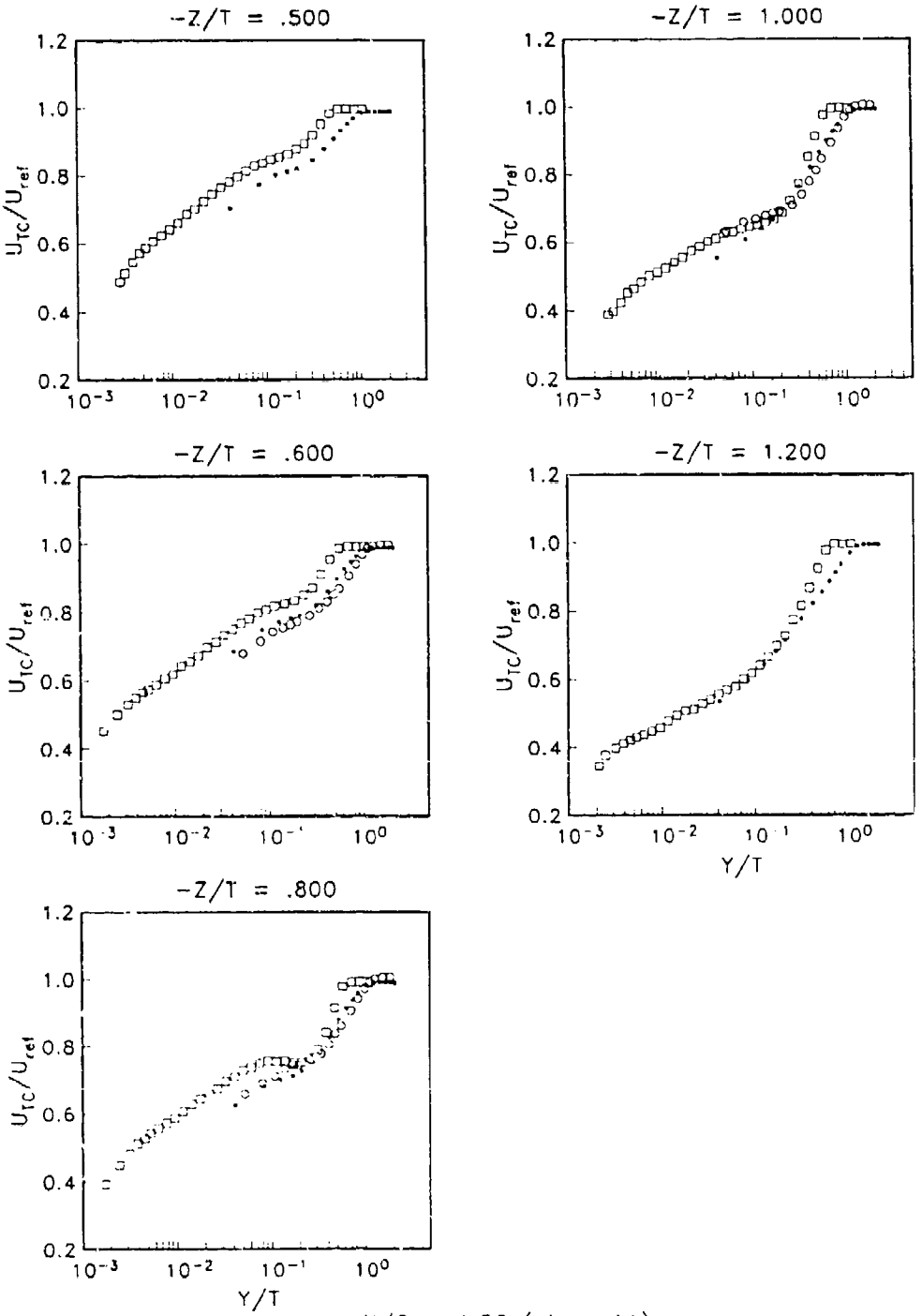

Figure 4.22. Profiles of U_{TC}/U_{ref}, Plane 11

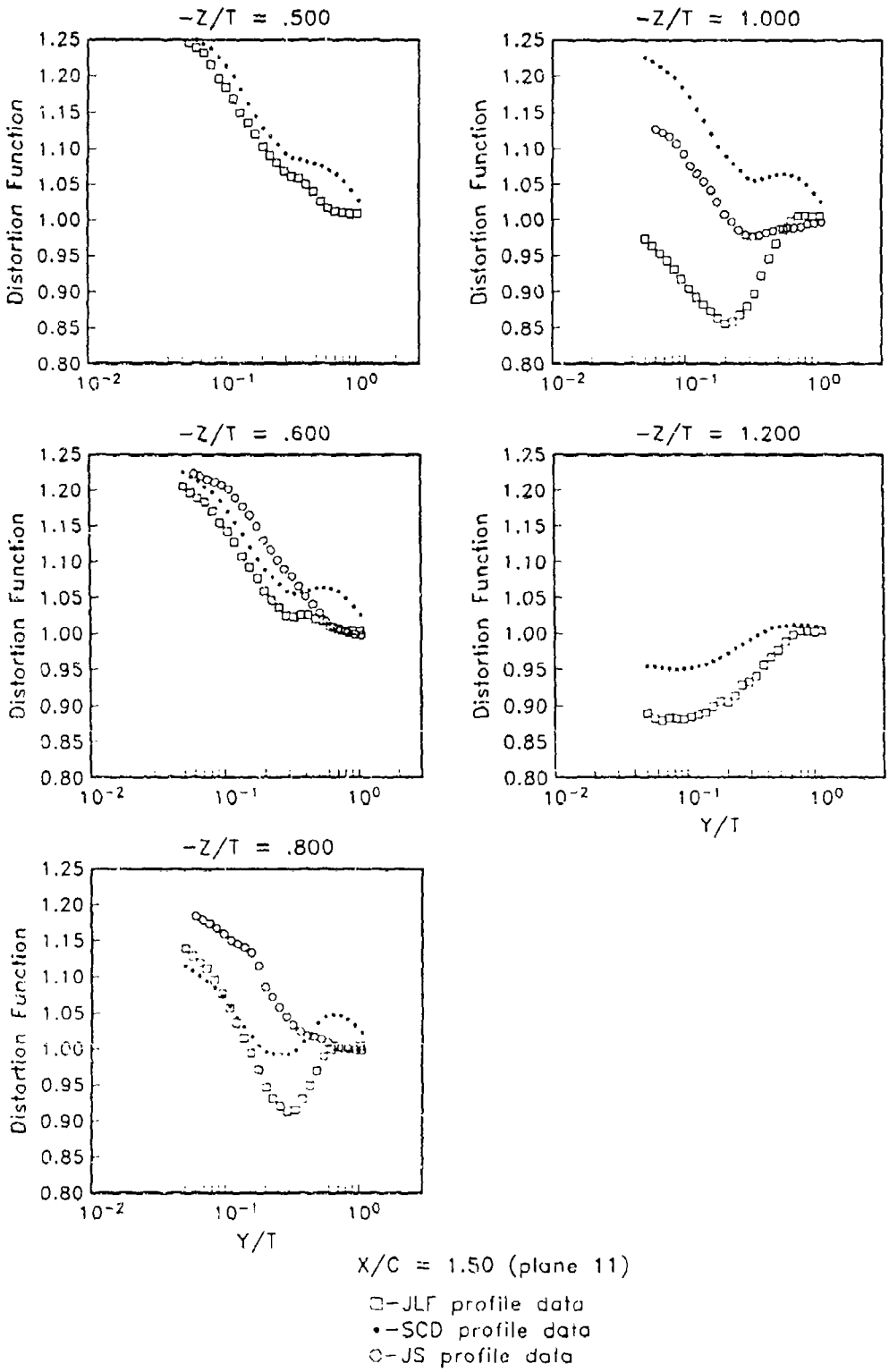

Figure 4.23. Profiles of Distortion Function, f_D, Plane 11

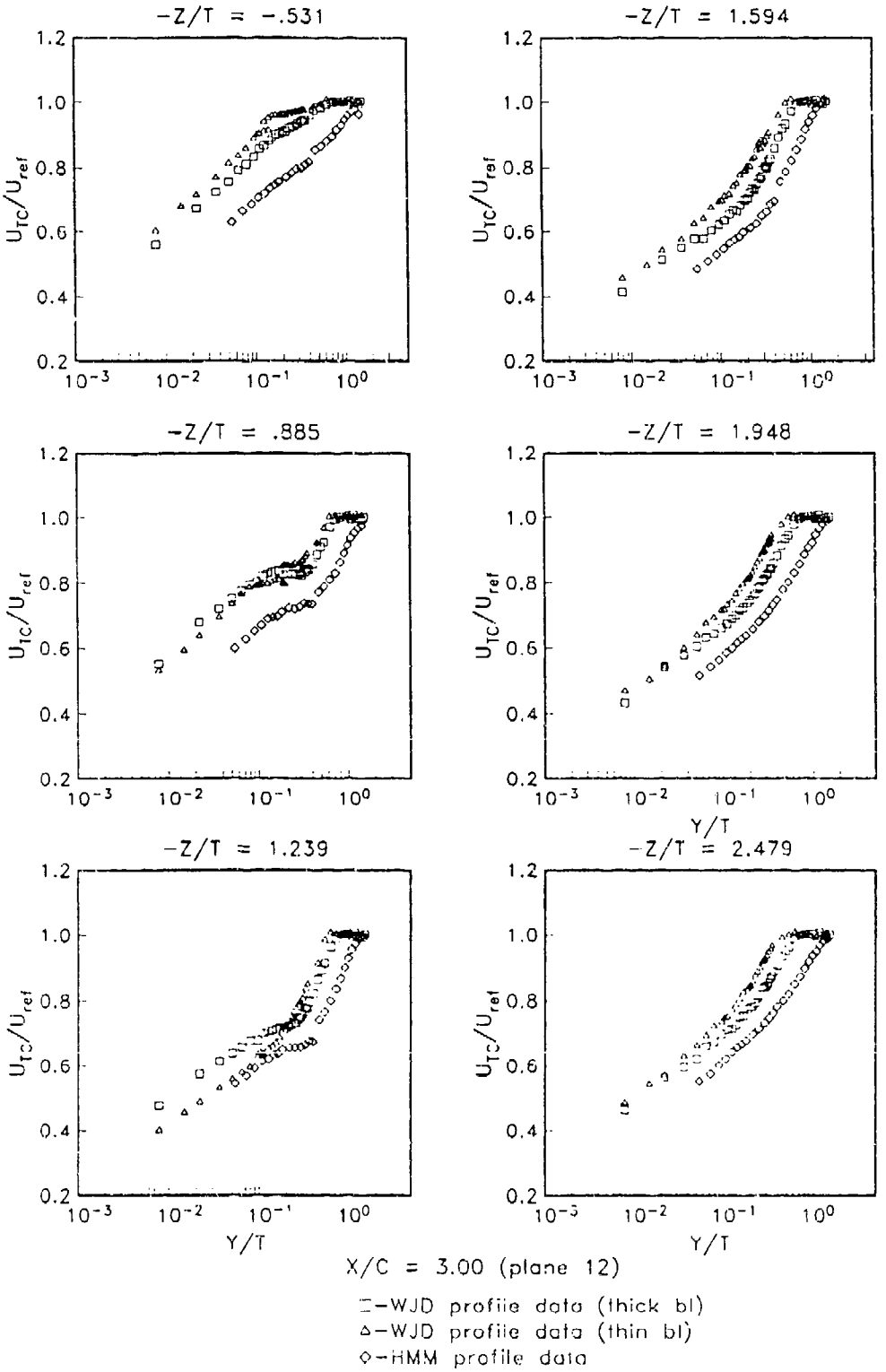

Figure 4.24. Profiles of U_{TC}/U_{ref}, Plane 12

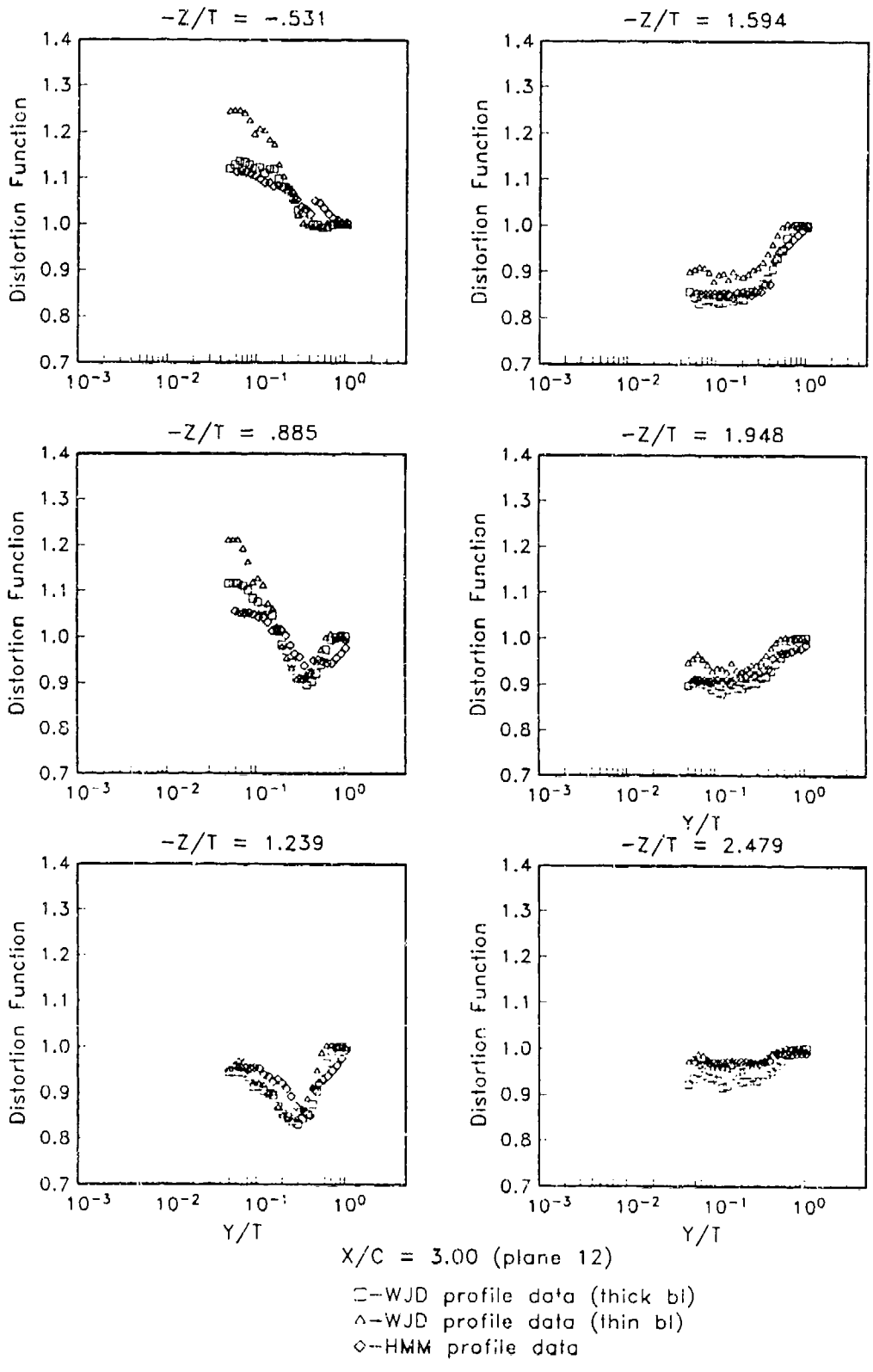

Figure 4.25. Profiles of Distortion Function, f_D, Plane 12

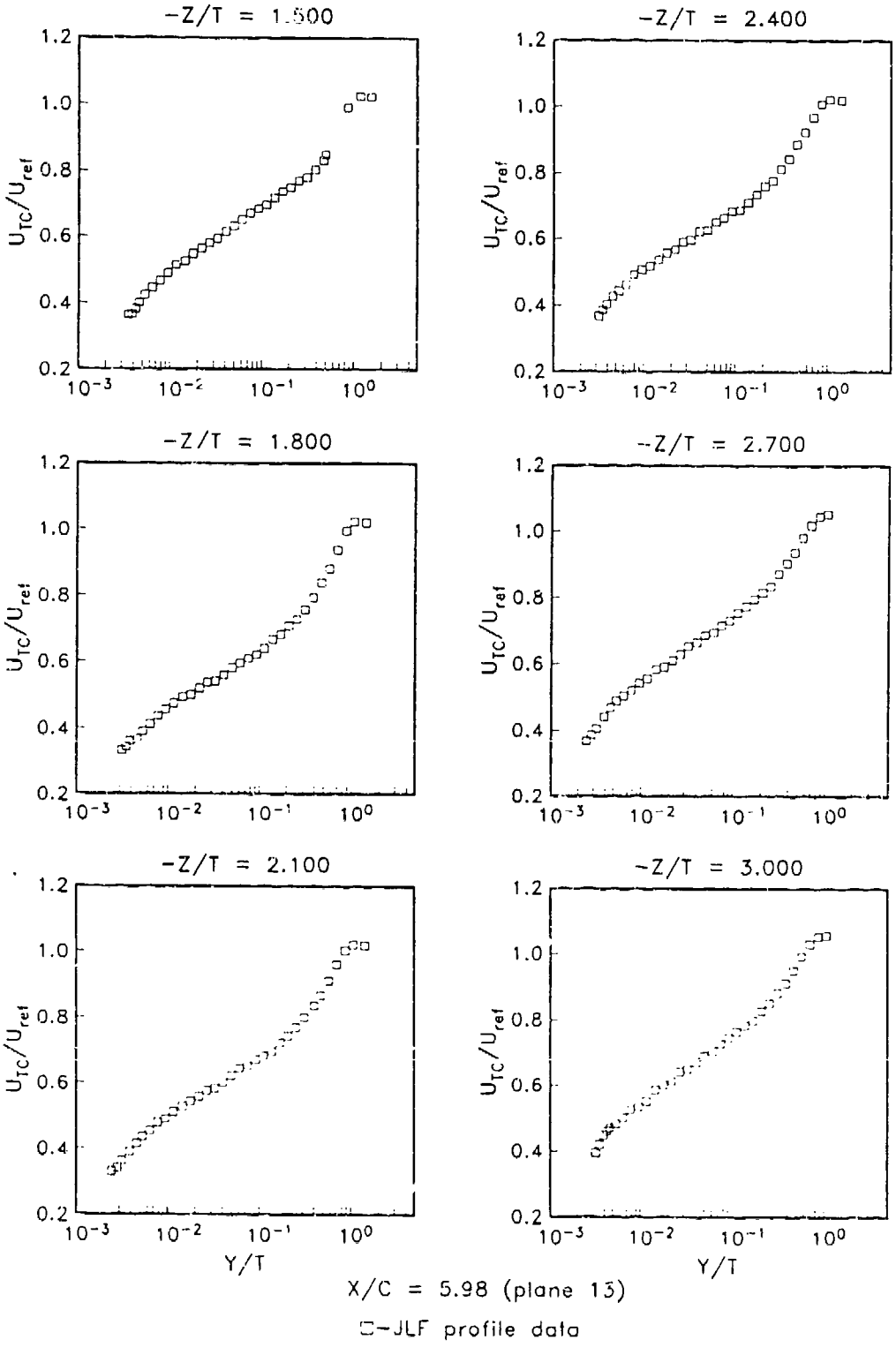

Figure 4.26. Profiles of U_{TC}/U_{ref}, Plane 13

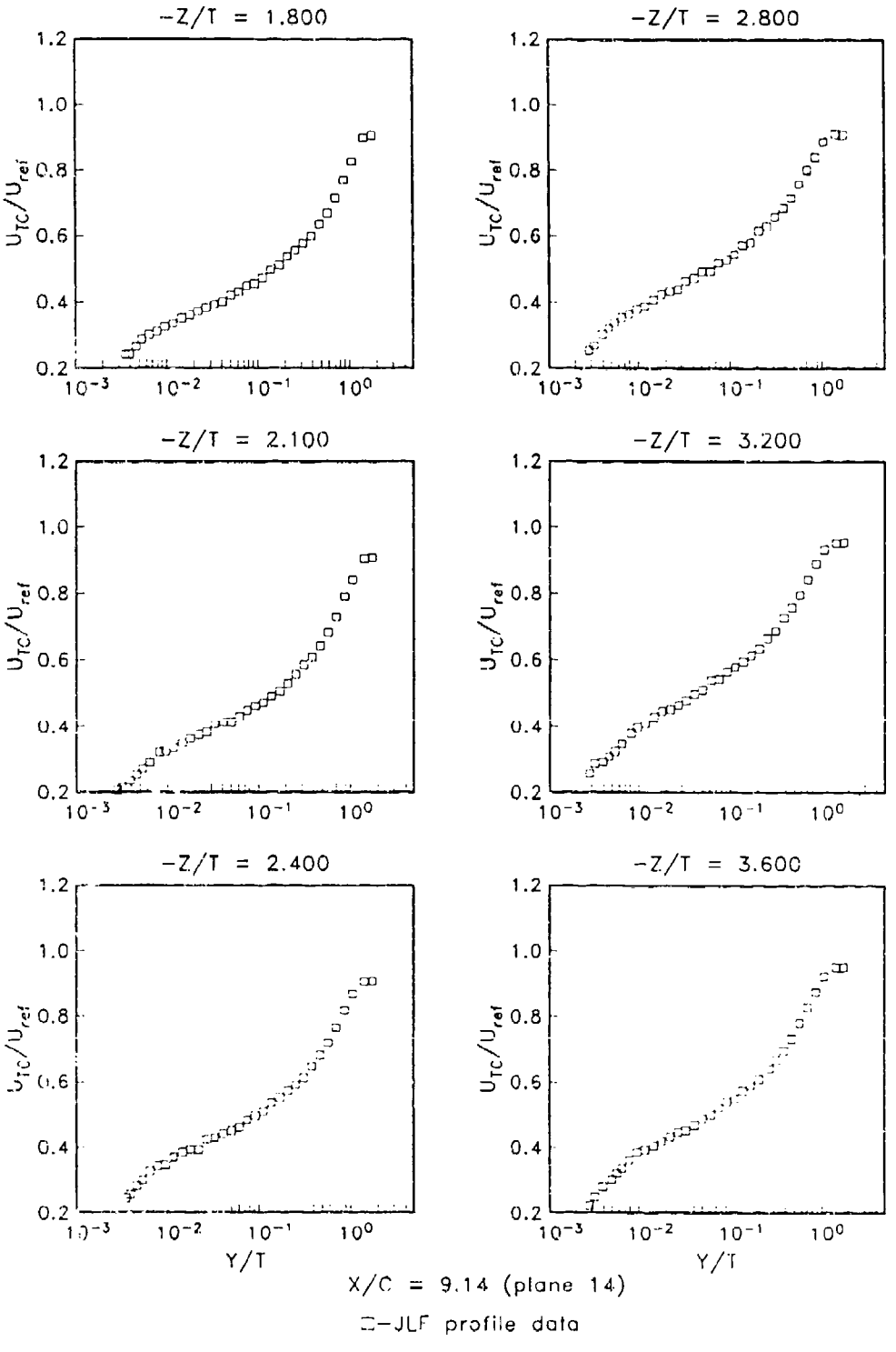

Figure 4.27. Profiles of U_{TC}/U_{ref}, Plane 14

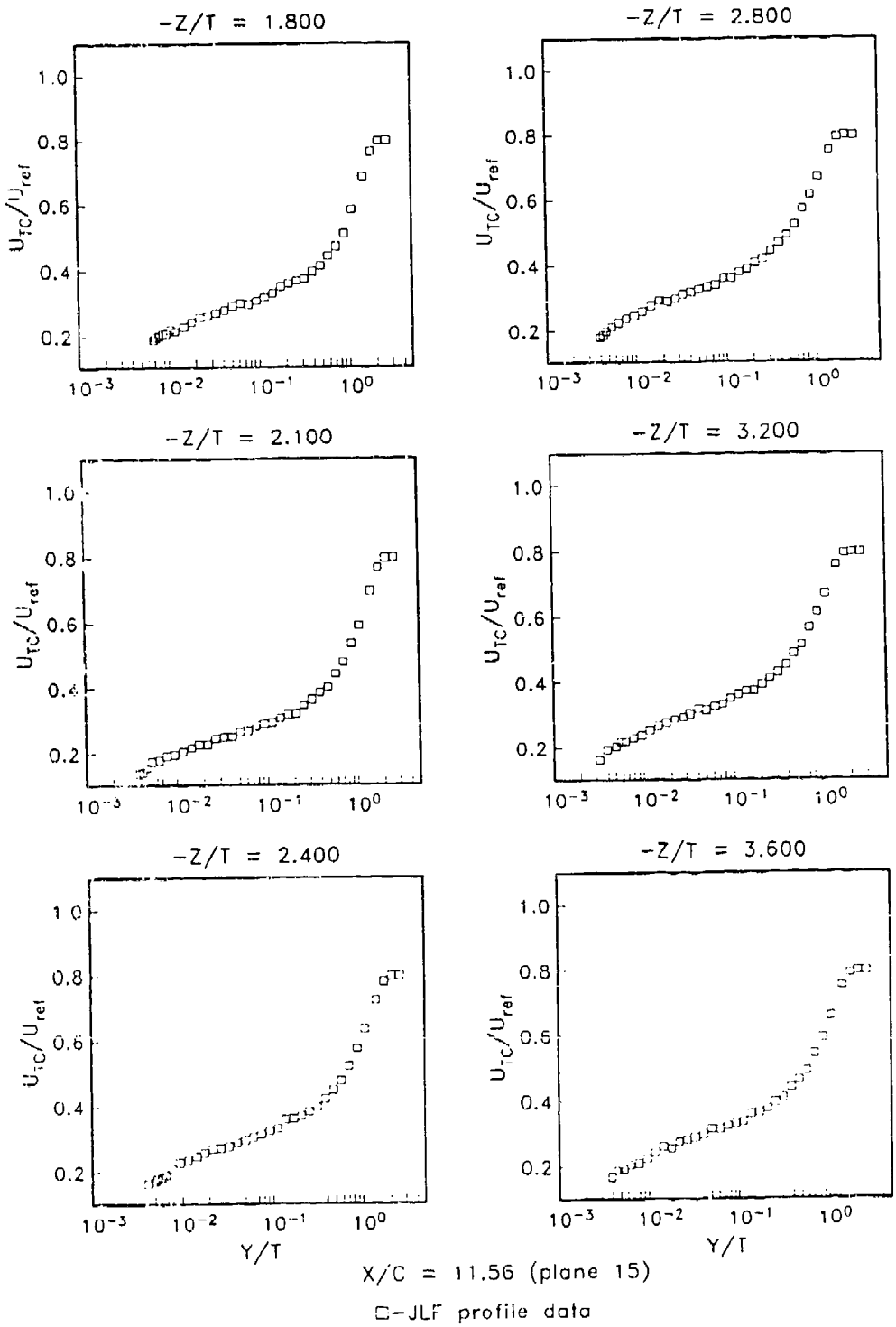

Figure 4.28. Profiles of U_{TC}/U_{ref}, Plane 15

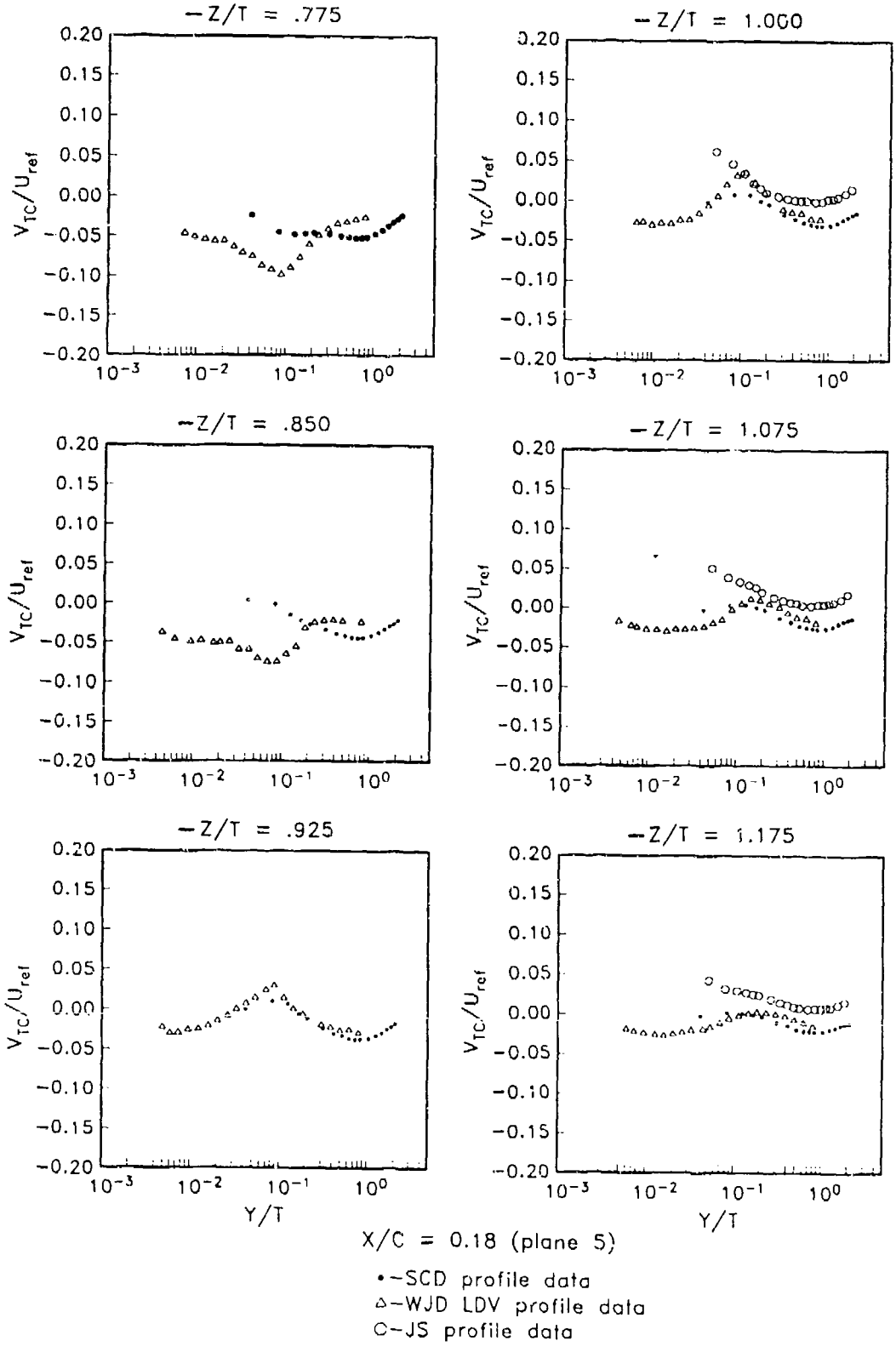

Figure 4.29. Profiles of V_{TC}/U_{ref}, Plane 5

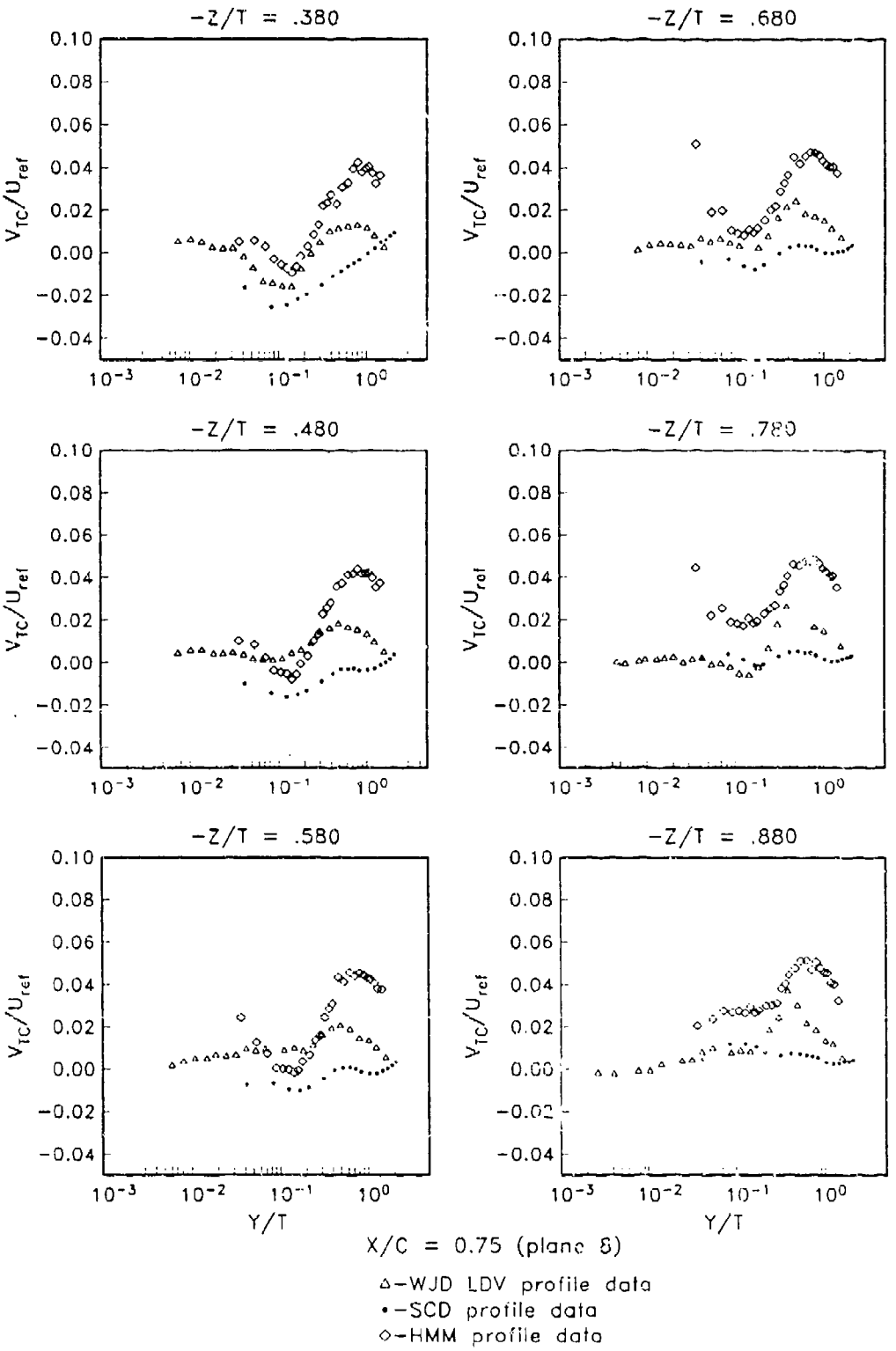

Figure 4.30. Profiles of V_{TC}/U_{ref}, Plane 8

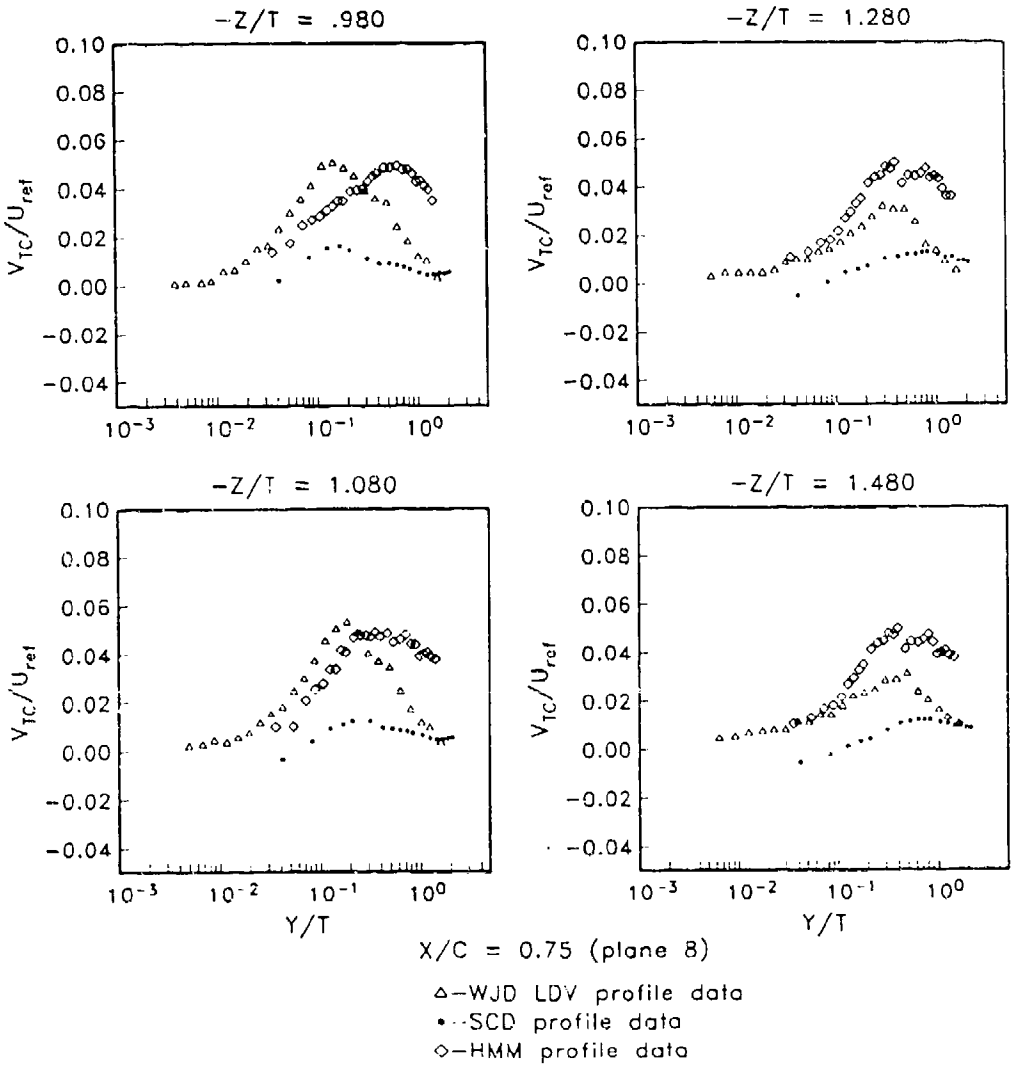

Figure 4.30. (cont.). Profiles of V_{TC}/U_{ref}, Plane 8

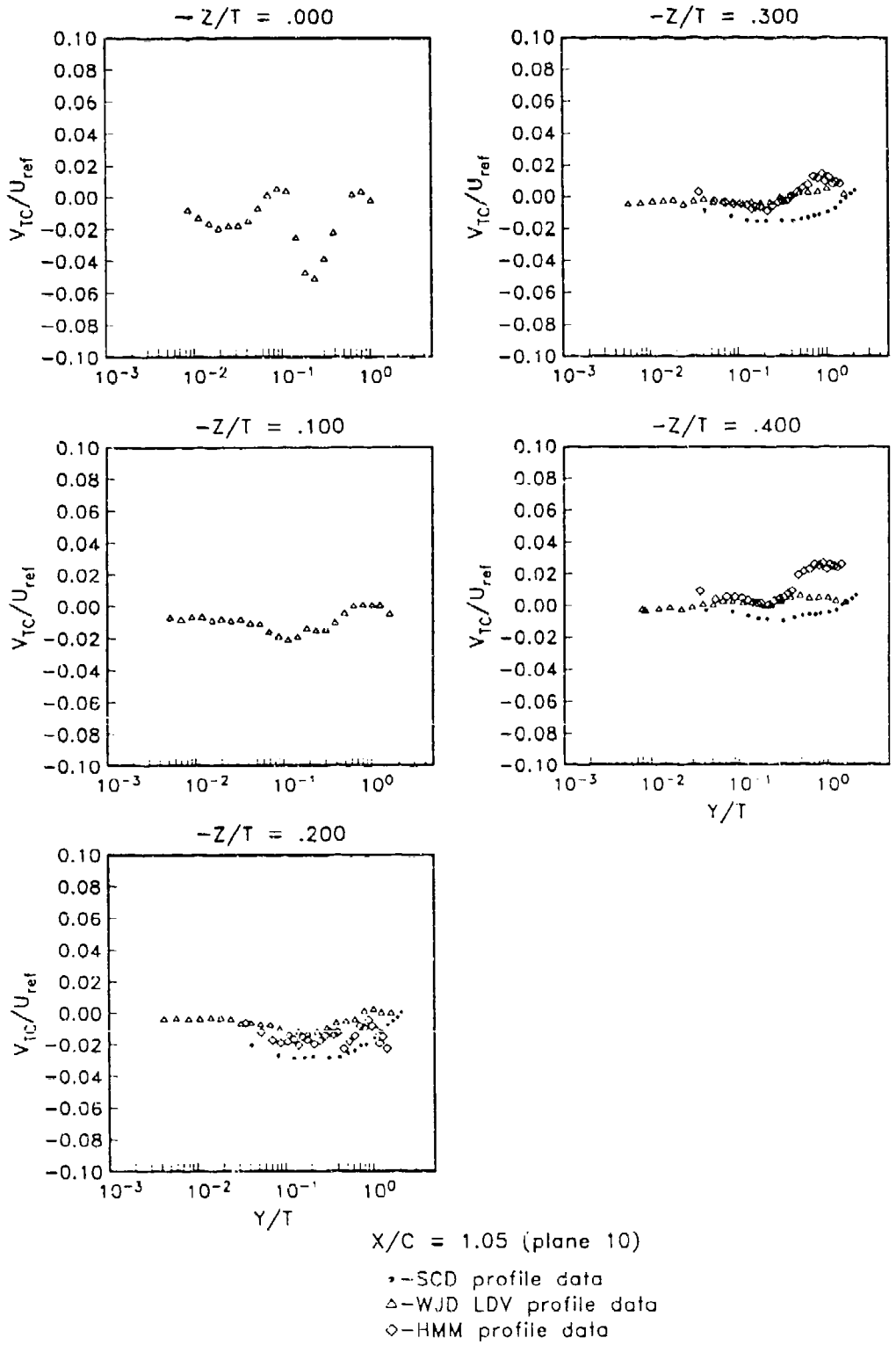

Figure 4.31. Profiles of V_{TC}/U_{ref}, Plane 10

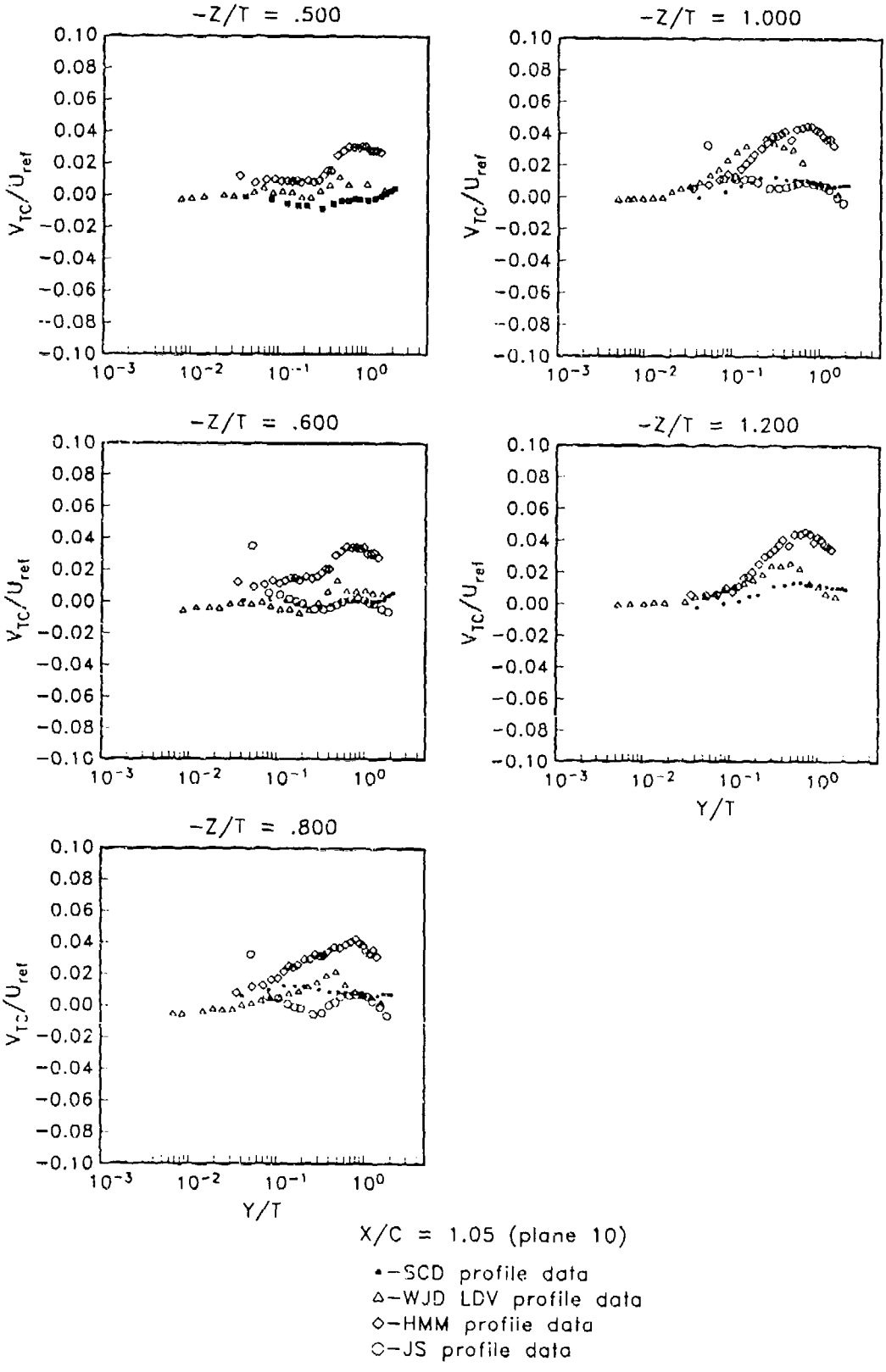

Figure 4.31. (cont.). Profiles of V_{TC}/U_{ref}, Plane 10

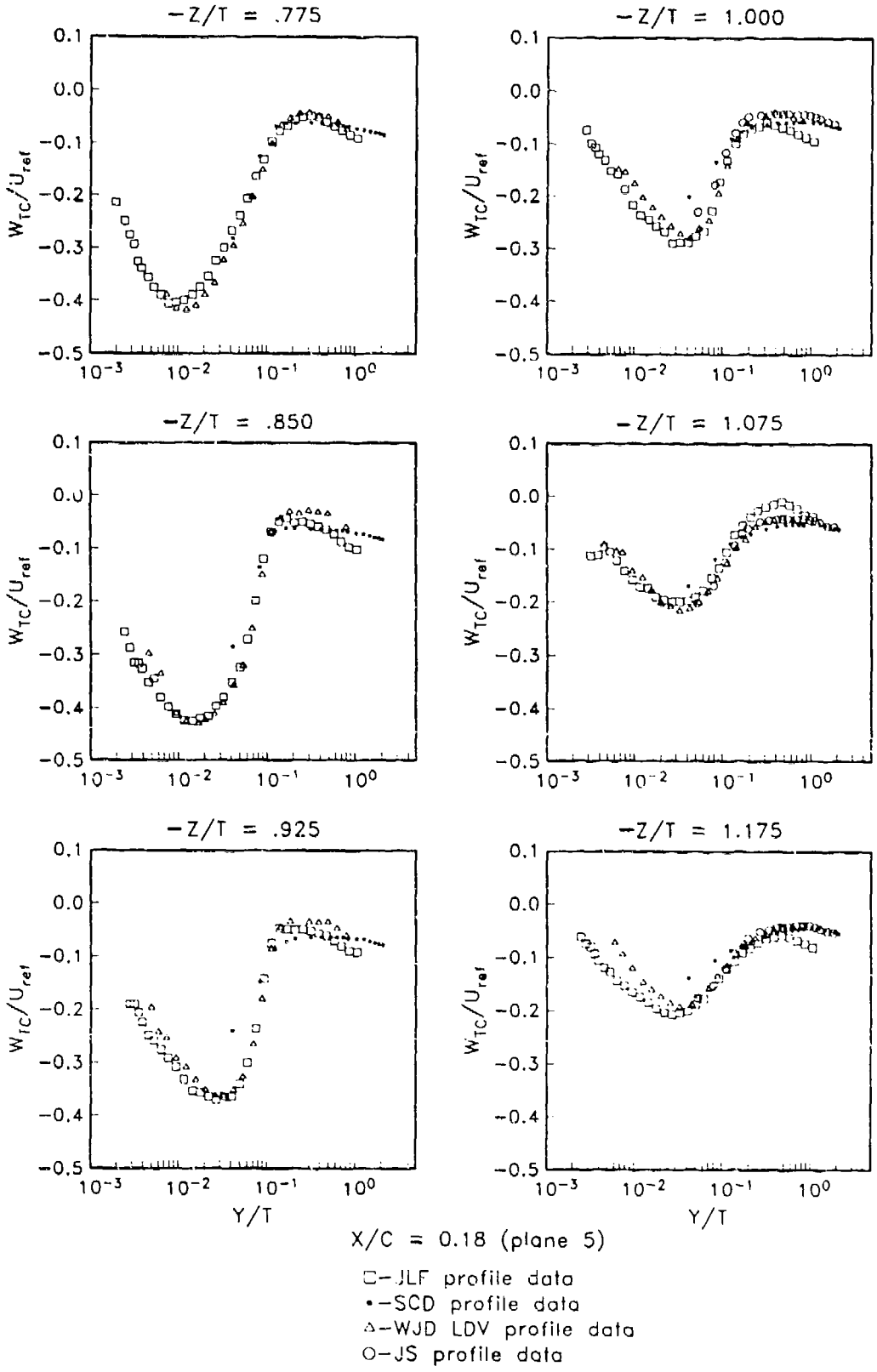

Figure 4.32. Profiles of W_{TC}/U_{ref}, Plane 5

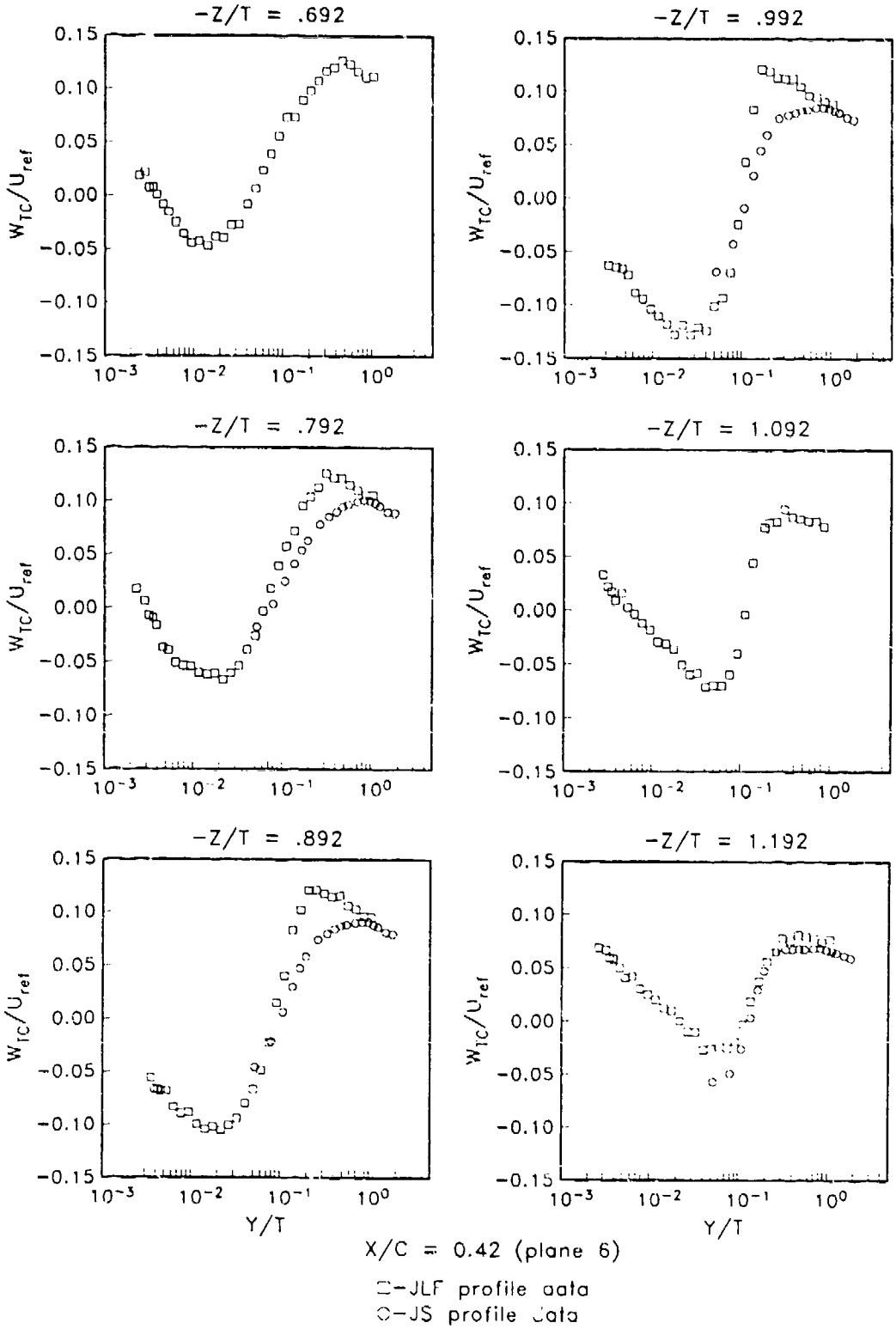

Figure 4.33. Profiles of W_{TC}/U_{ref}, Plane 6

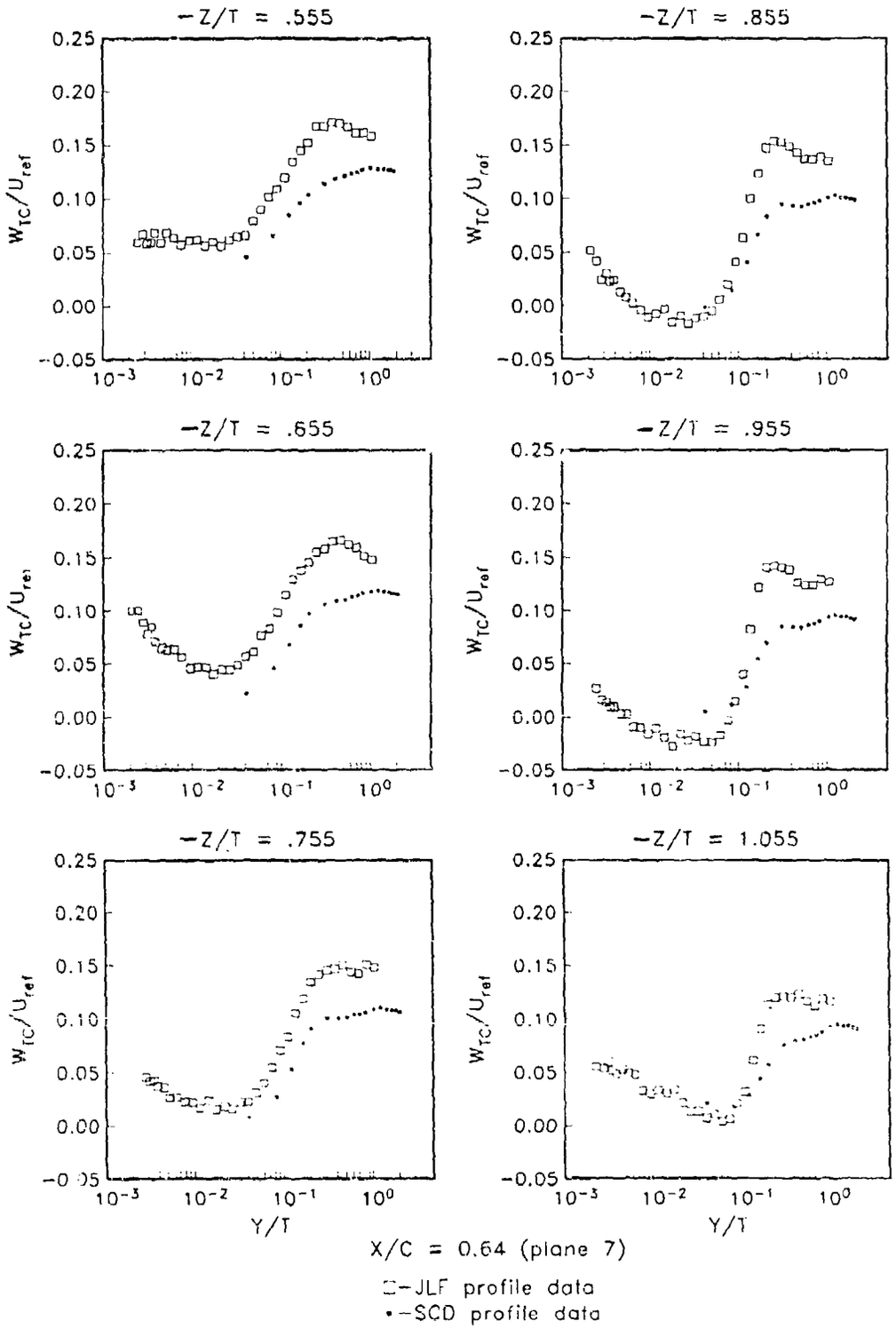

Figure 4.34. Profiles of W_{TC}/U_{ref}, Plane 7

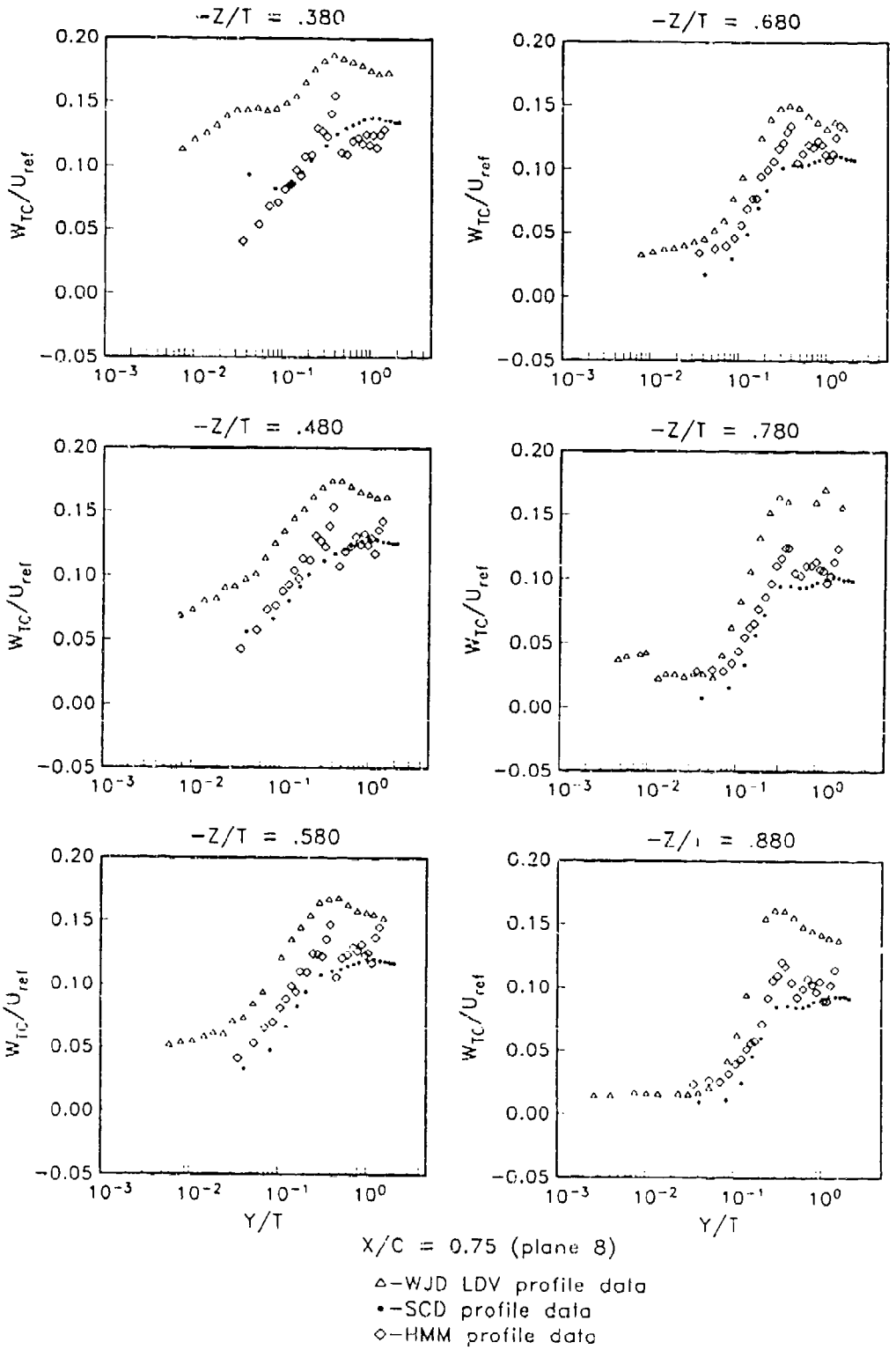

Figure 4.35. Profiles of W_{TC}/U_{ref}, Plane 8

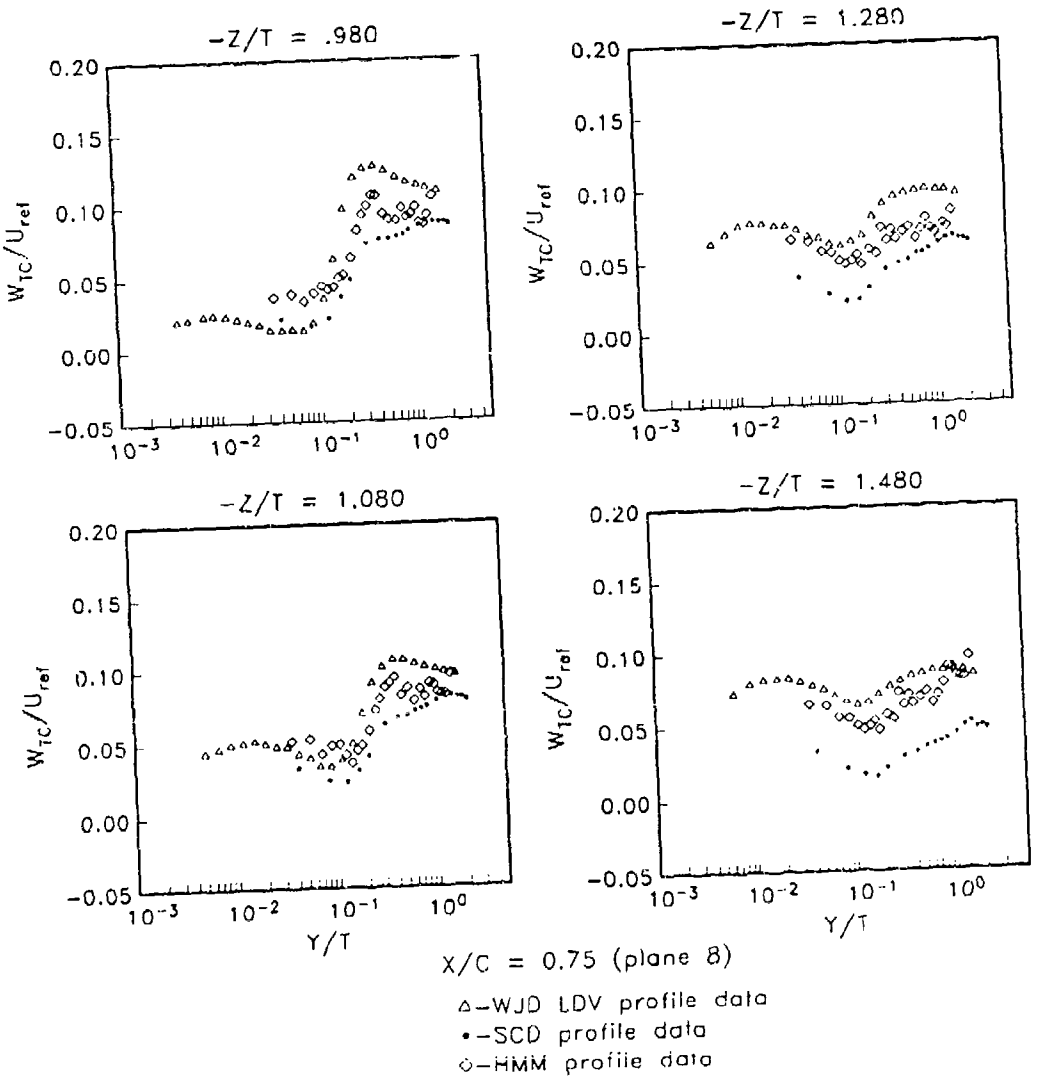

Figure 4.35. (cont.). Profiles of W_{TC}/U_{ref}, Plane 8

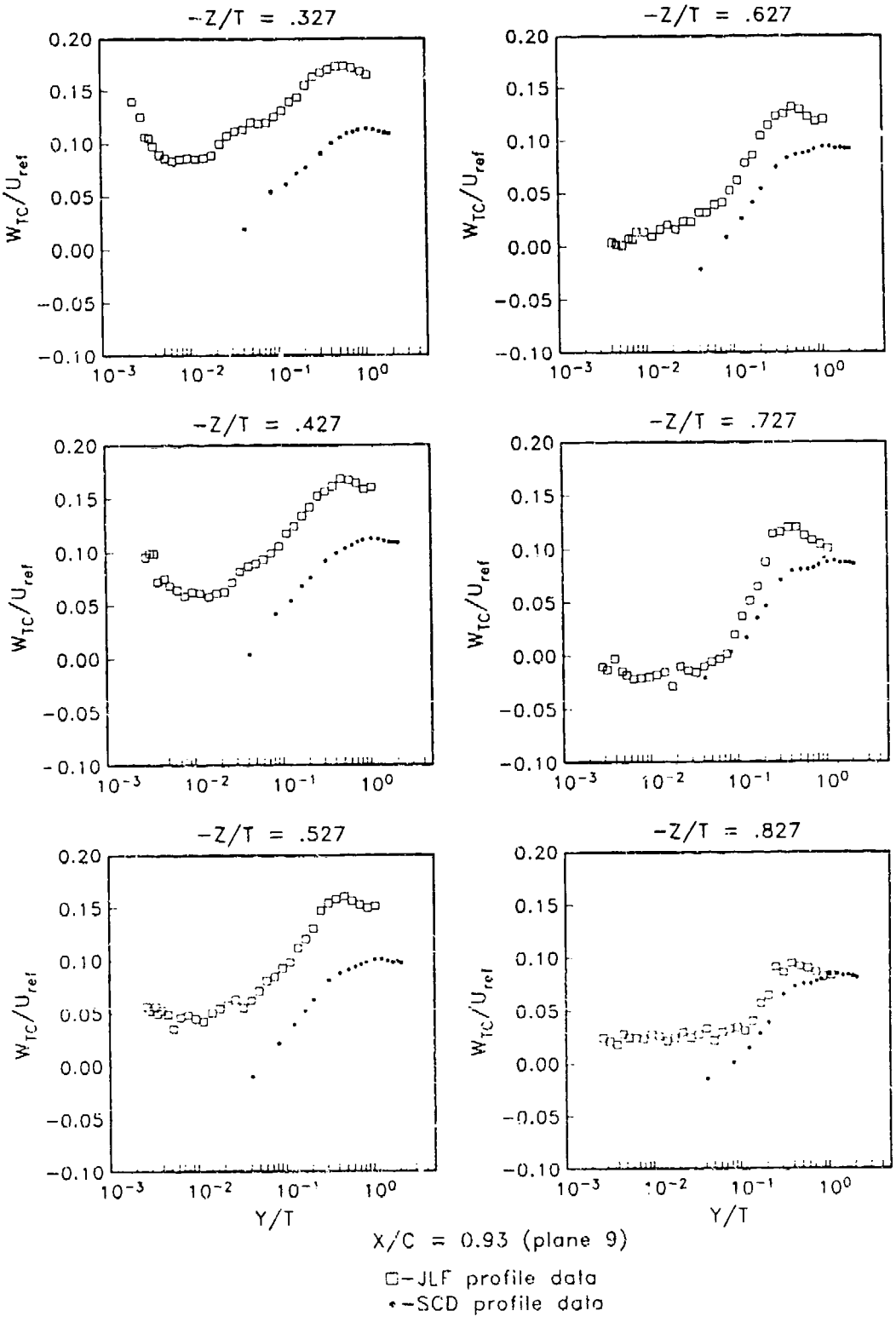

Figure 4.36. Profiles of W_{TC}/U_{ref}, Plane 9

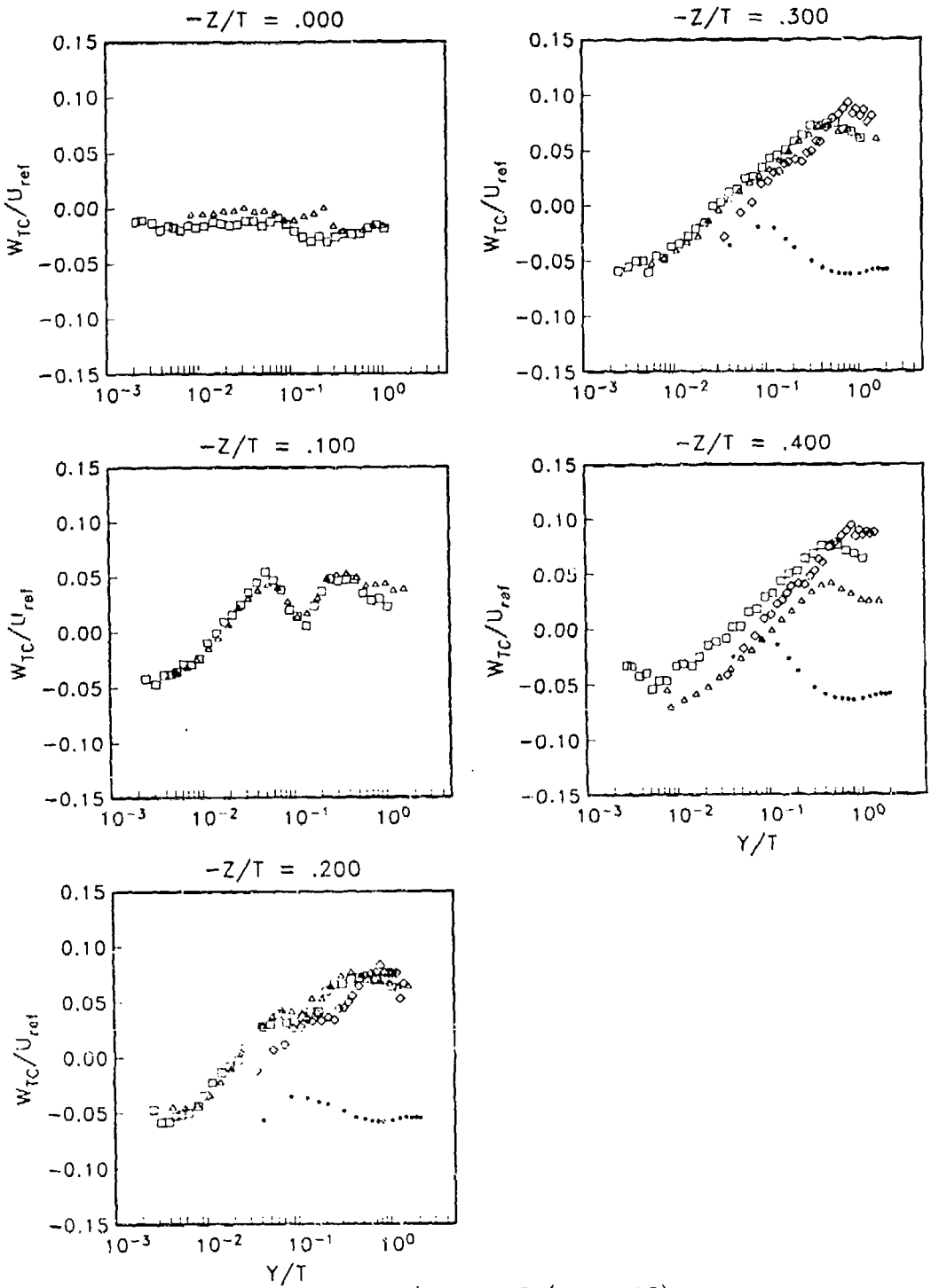

Figure 4.37. Profiles of W_{TC}/U_{ref}, Plane 10

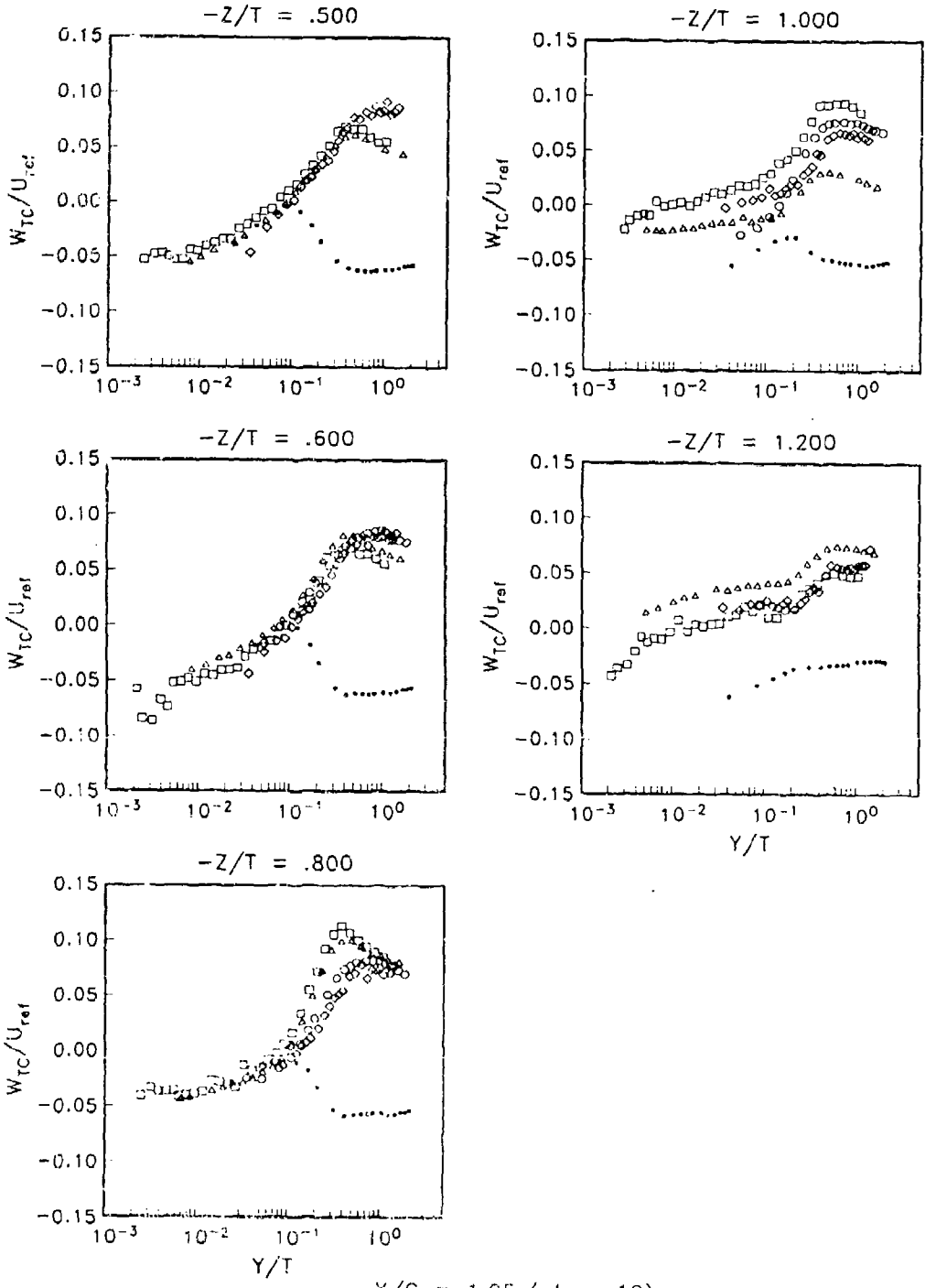

Figure 4.37. (cont.). Profiles of W_{TC}/U_{ref}, Plane 10

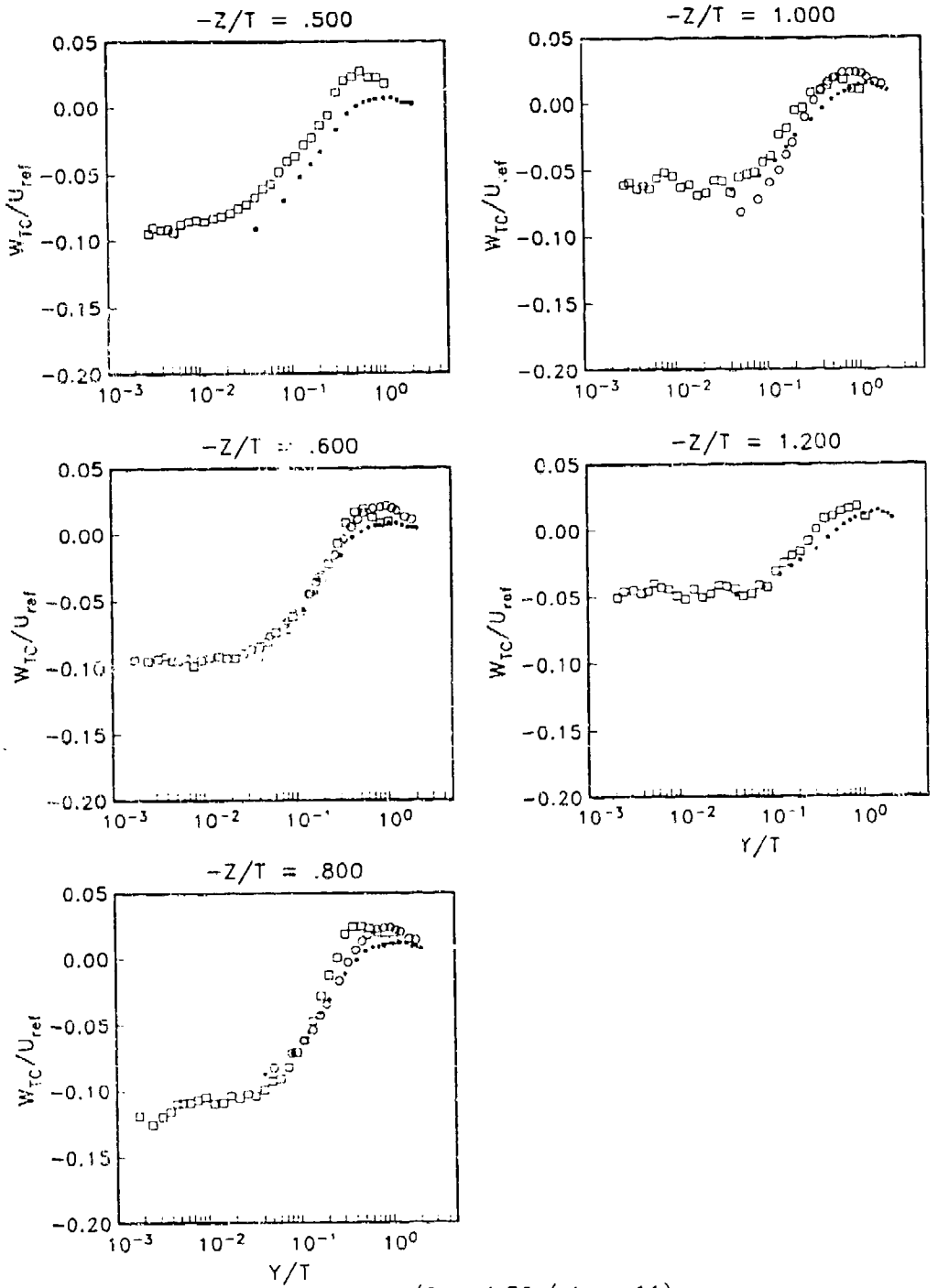

Figure 4.38. Profiles of W_{TC}/U_{ref}, Plane 11

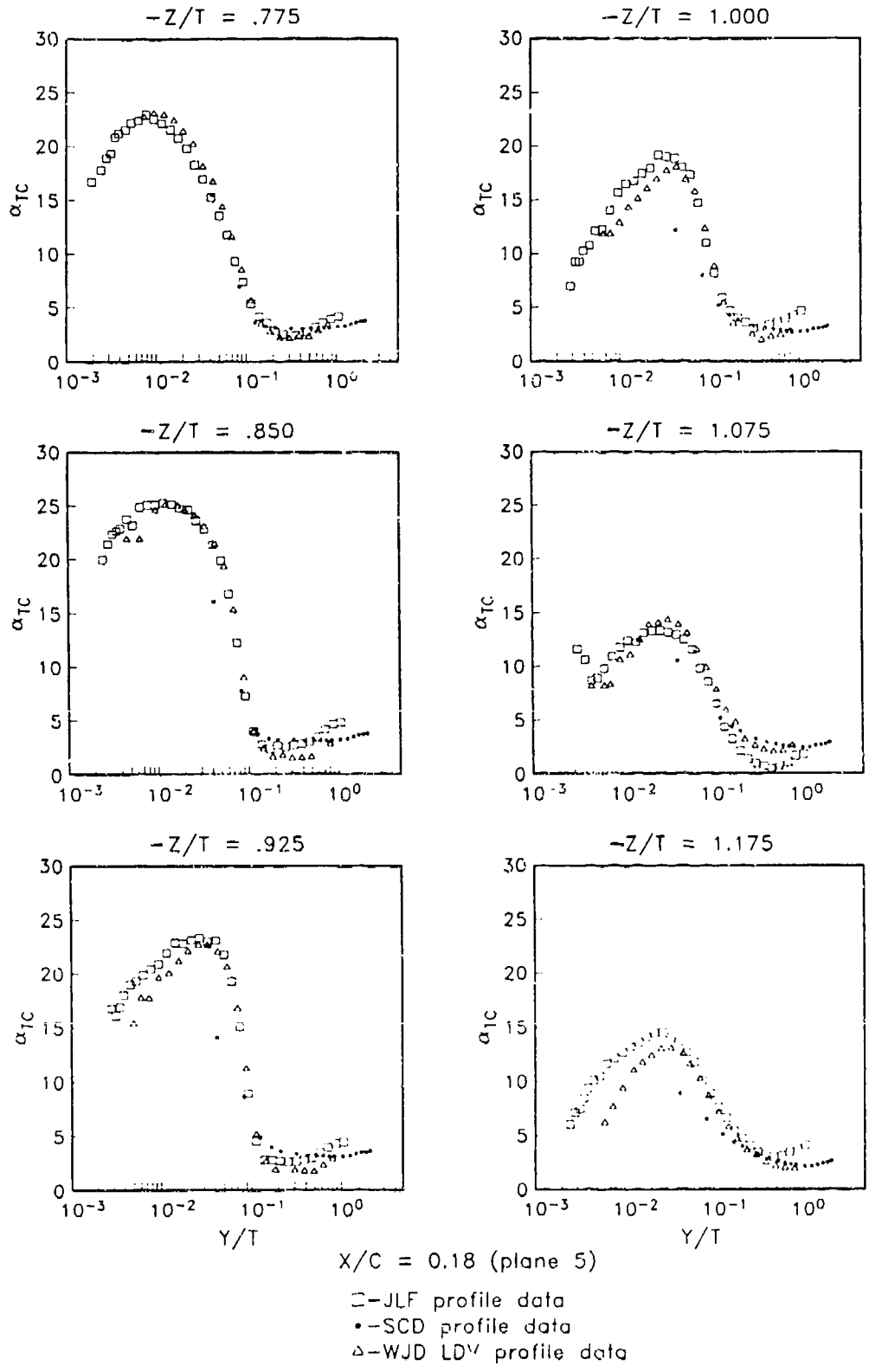

Figure 4.39. Profiles of α_{TC}, Plane 5

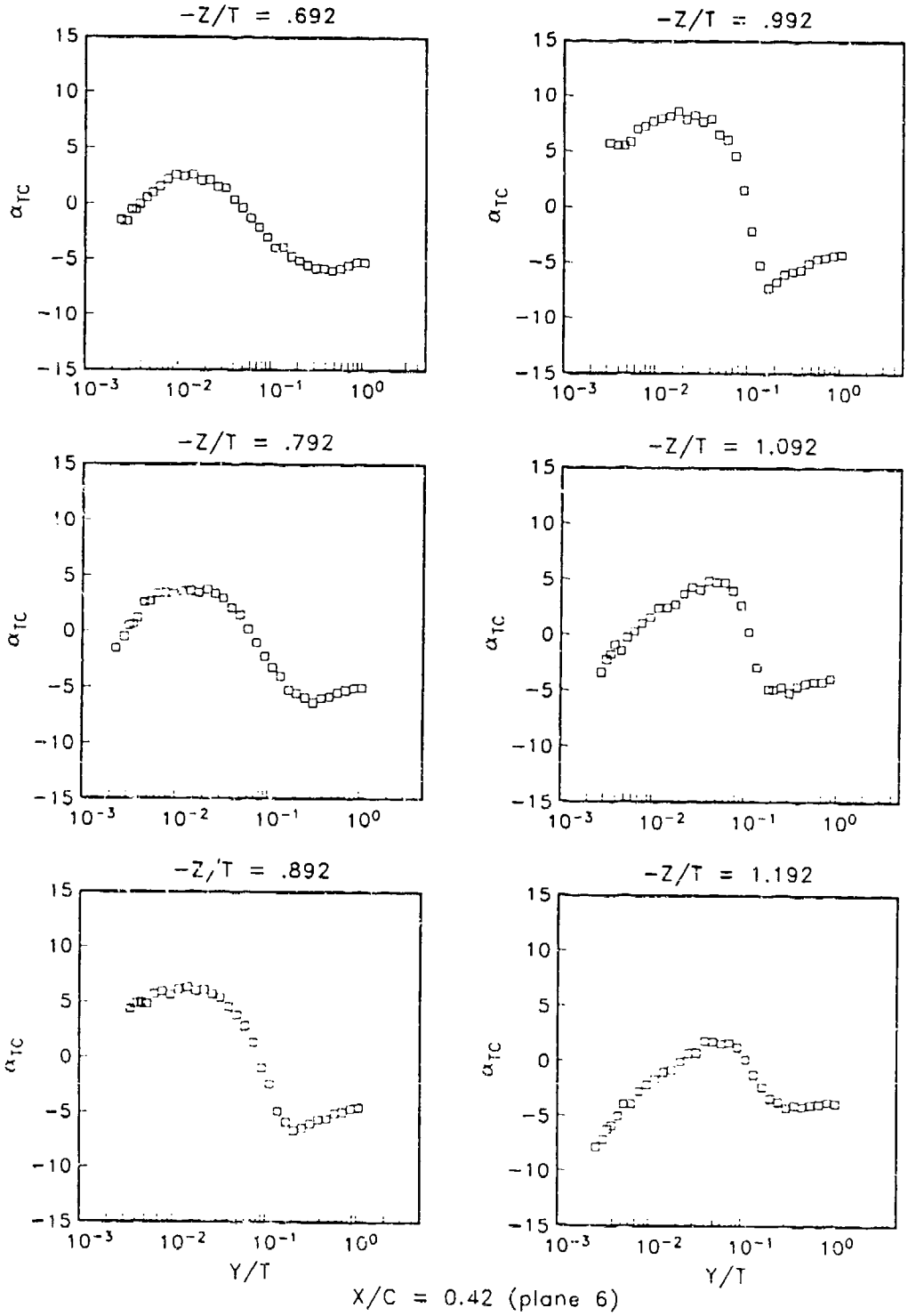

Figure 4.40. Profiles of α_{TC}, Plane 6

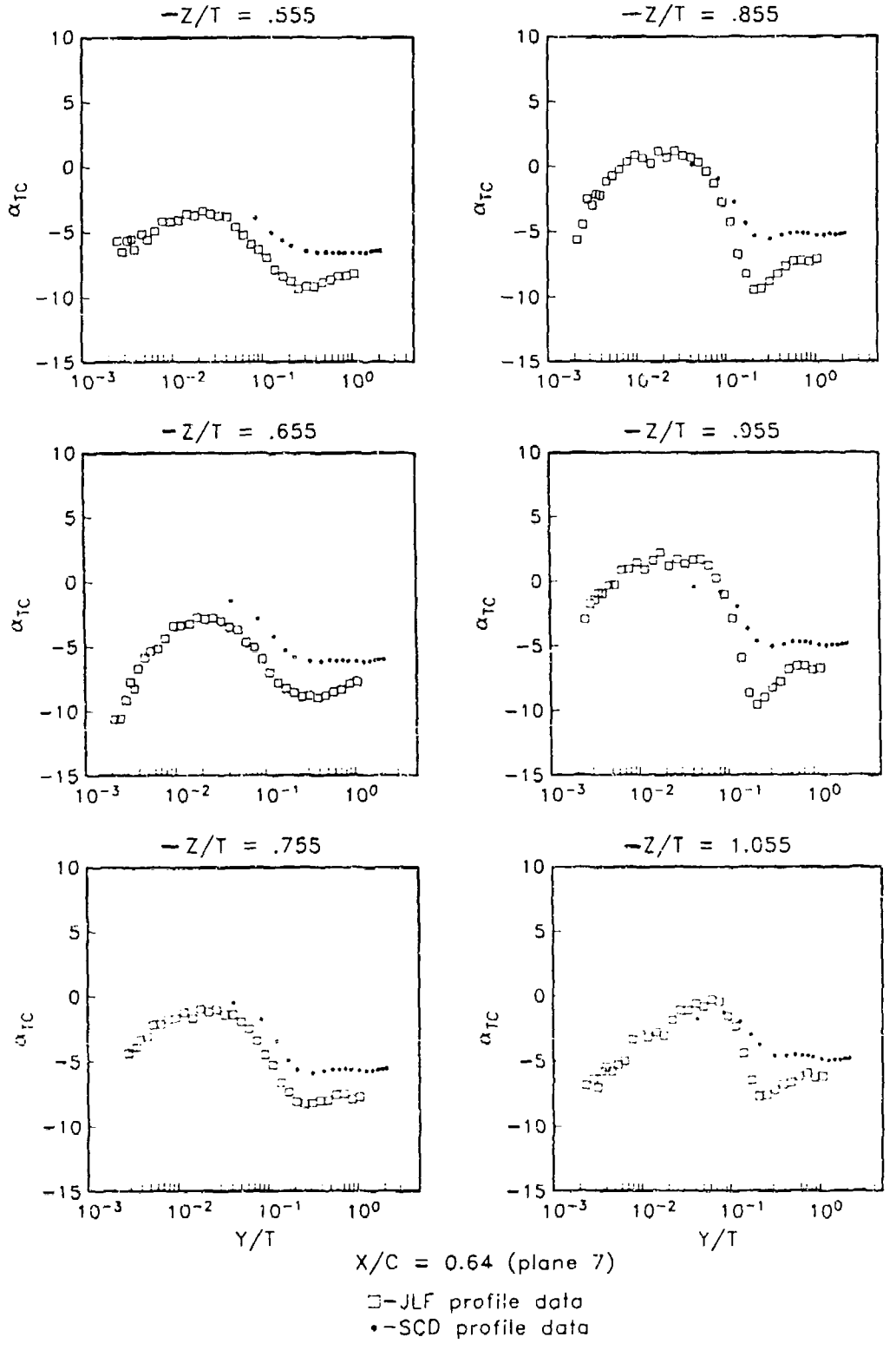

Figure 4.41. Profiles of α_{TC}, Plane 7

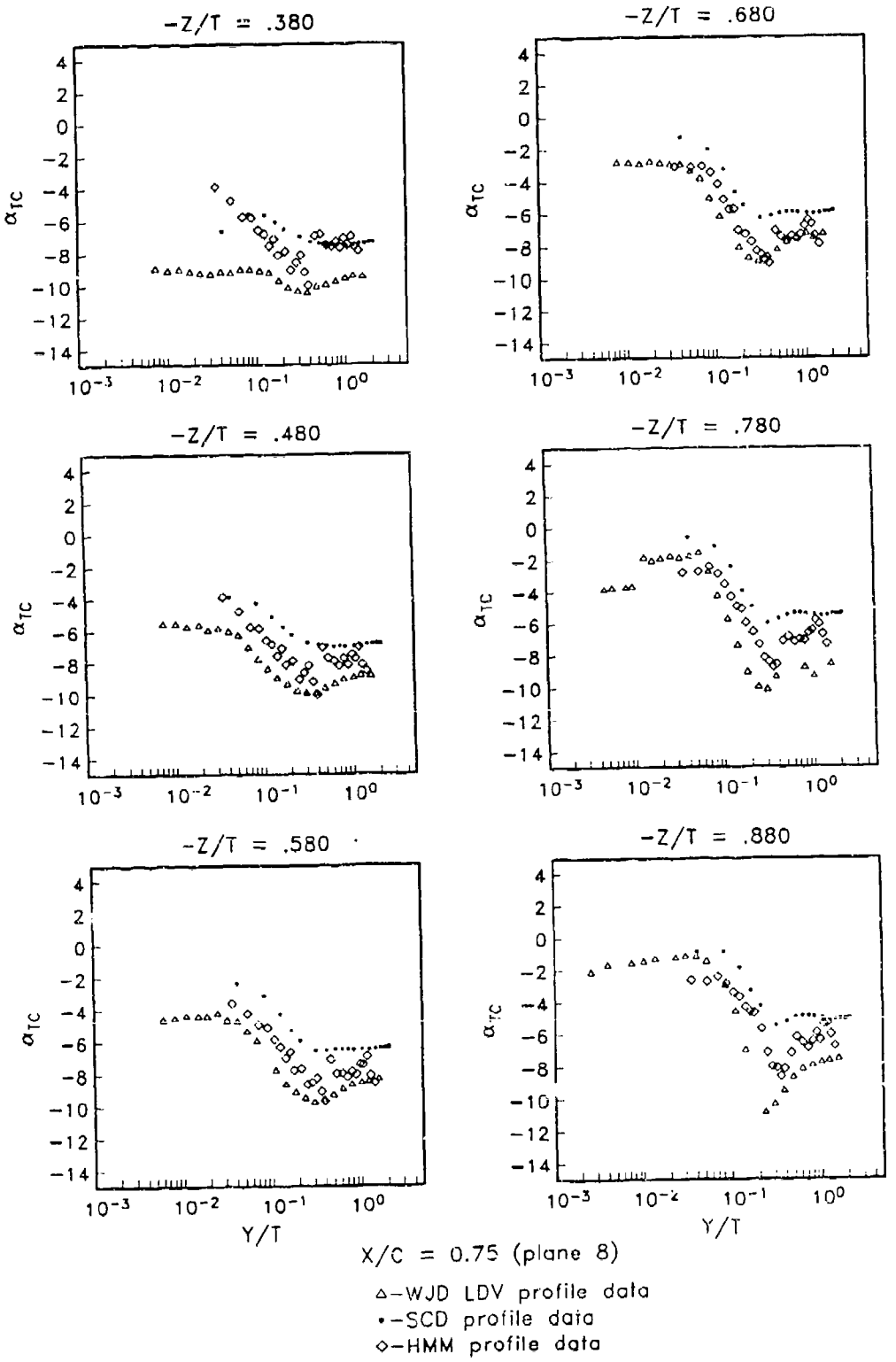

Figure 4.42. Profiles of α_{TC}, Plane 8

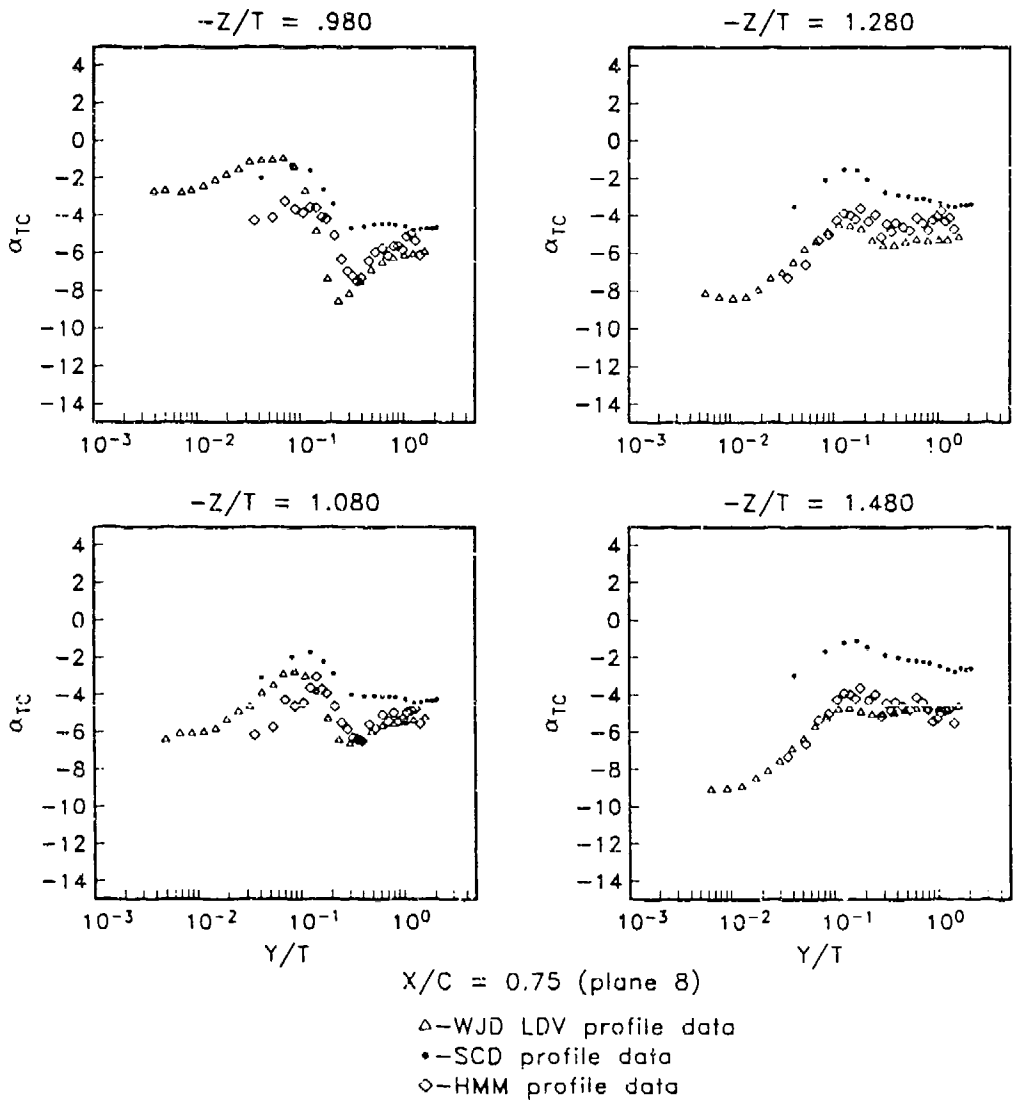

Figure 4.42. (cont.). Profiles of α_{TC}, Plane 8

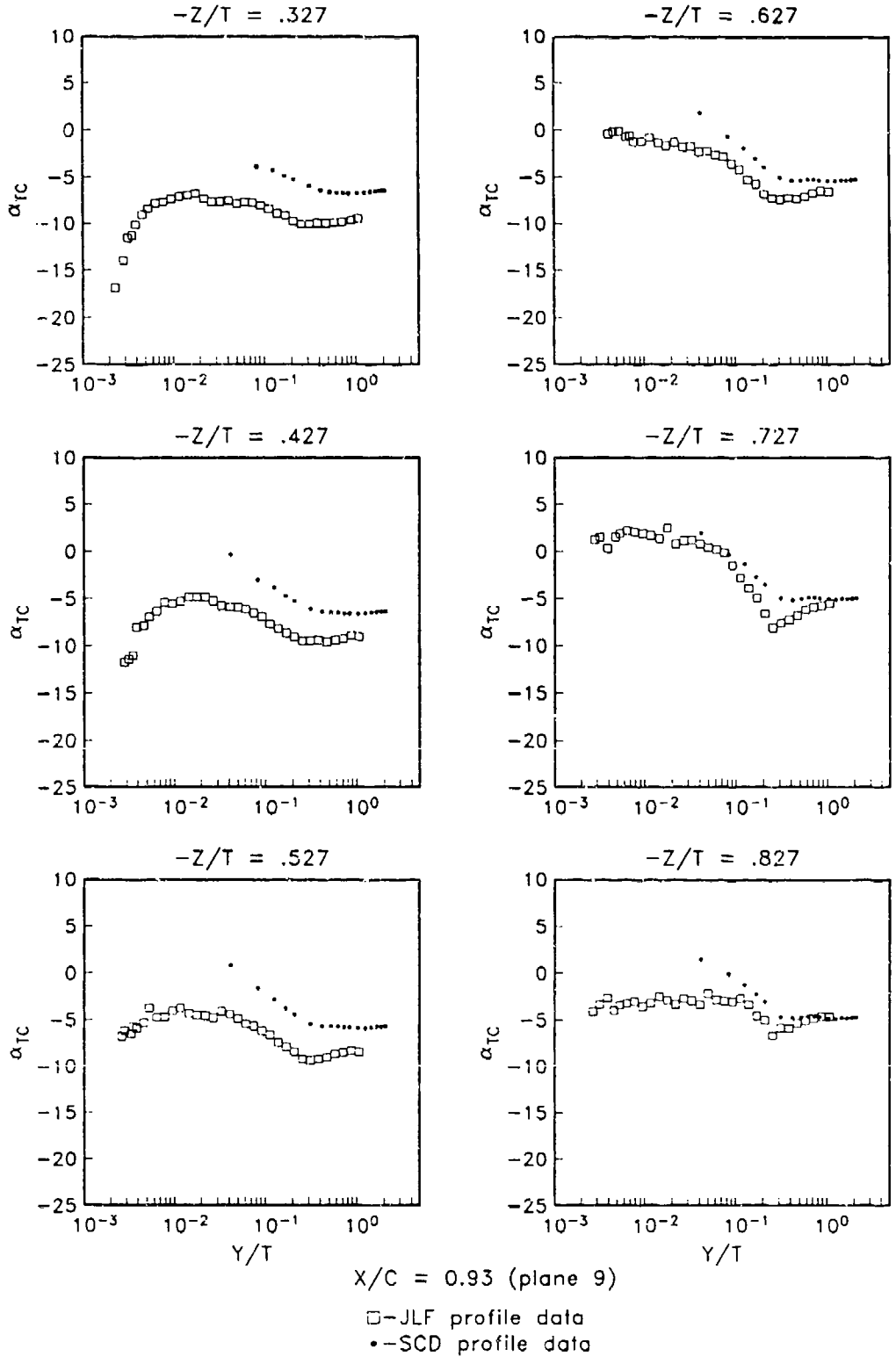

Figure 4.43. Profiles of α_{TC}, Plane 9

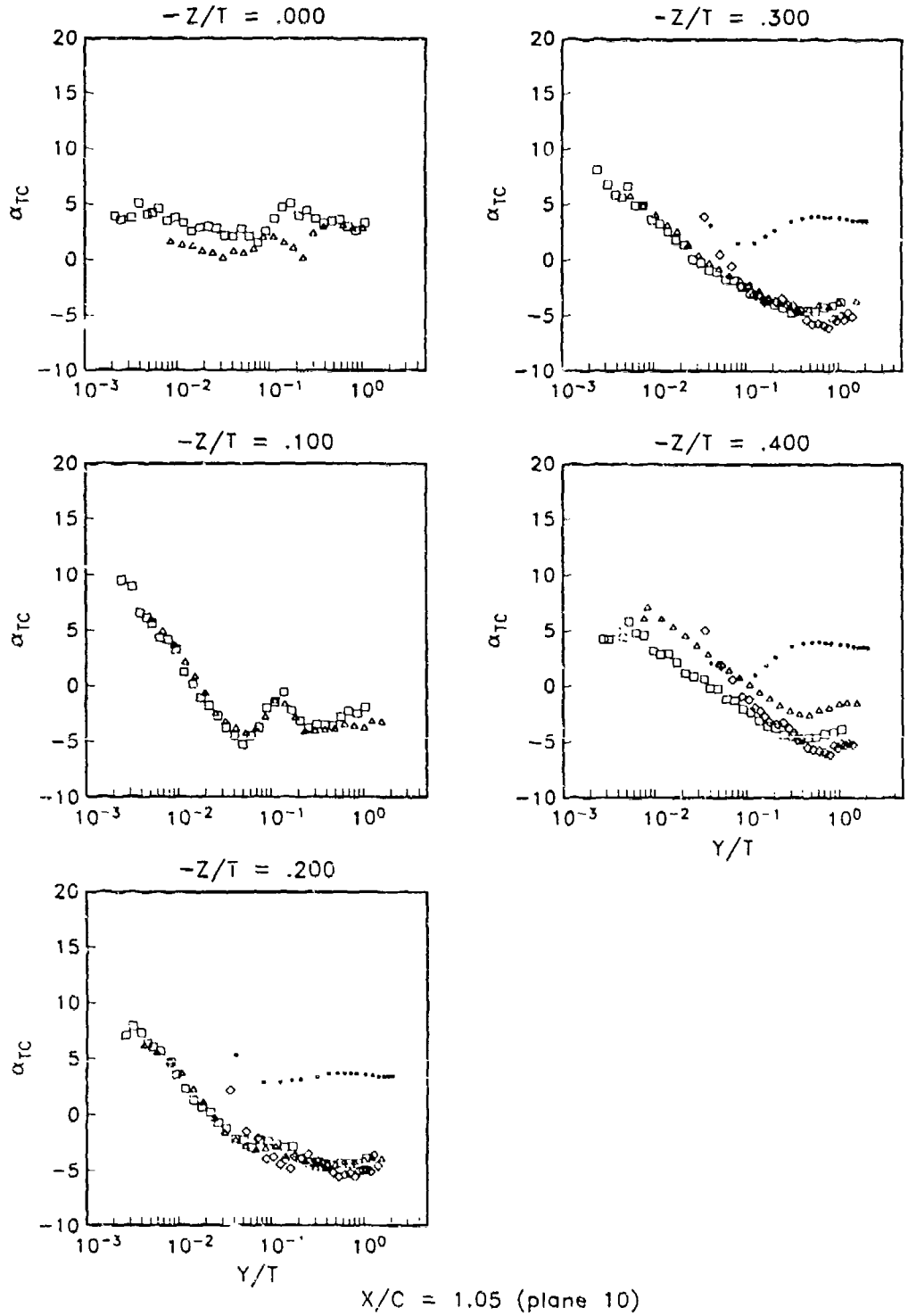

Figure 4.44. Profiles of α_{TC}, Plane 10

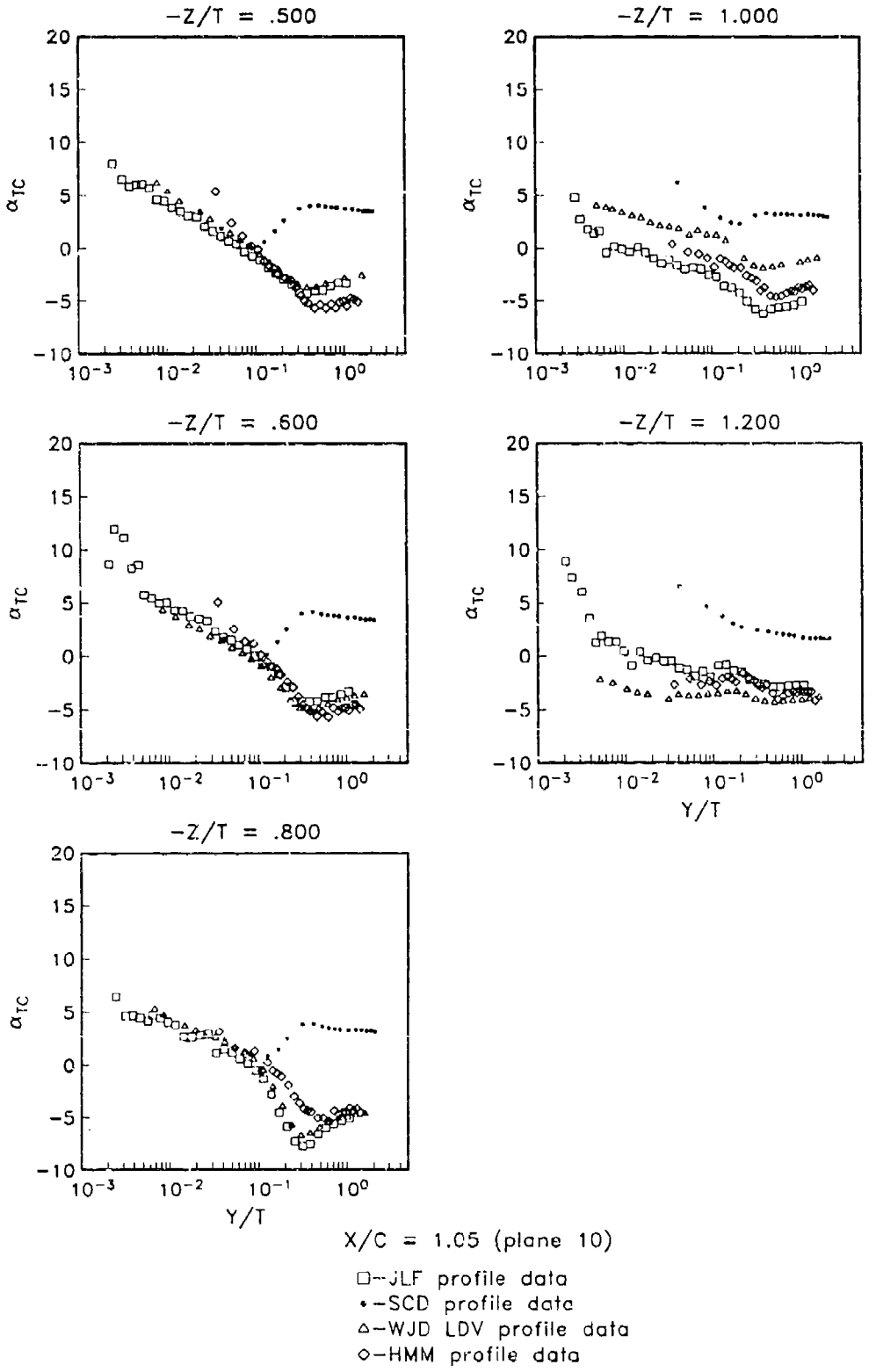

Figure 4.44. (cont.). Profiles of α_{TC}, Plane 10

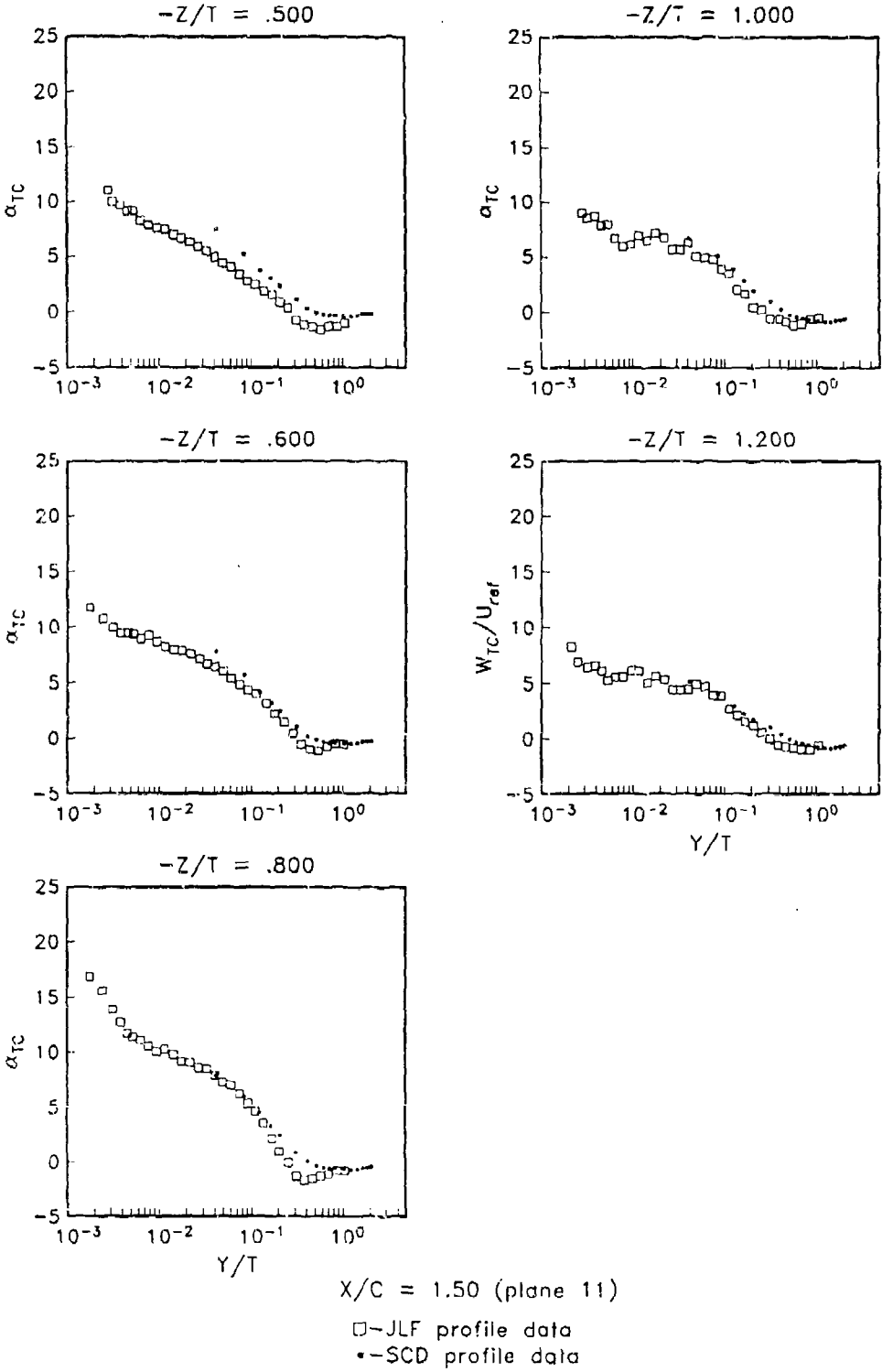

Figure 4.45. Profiles of α_{TC}, Plane 11

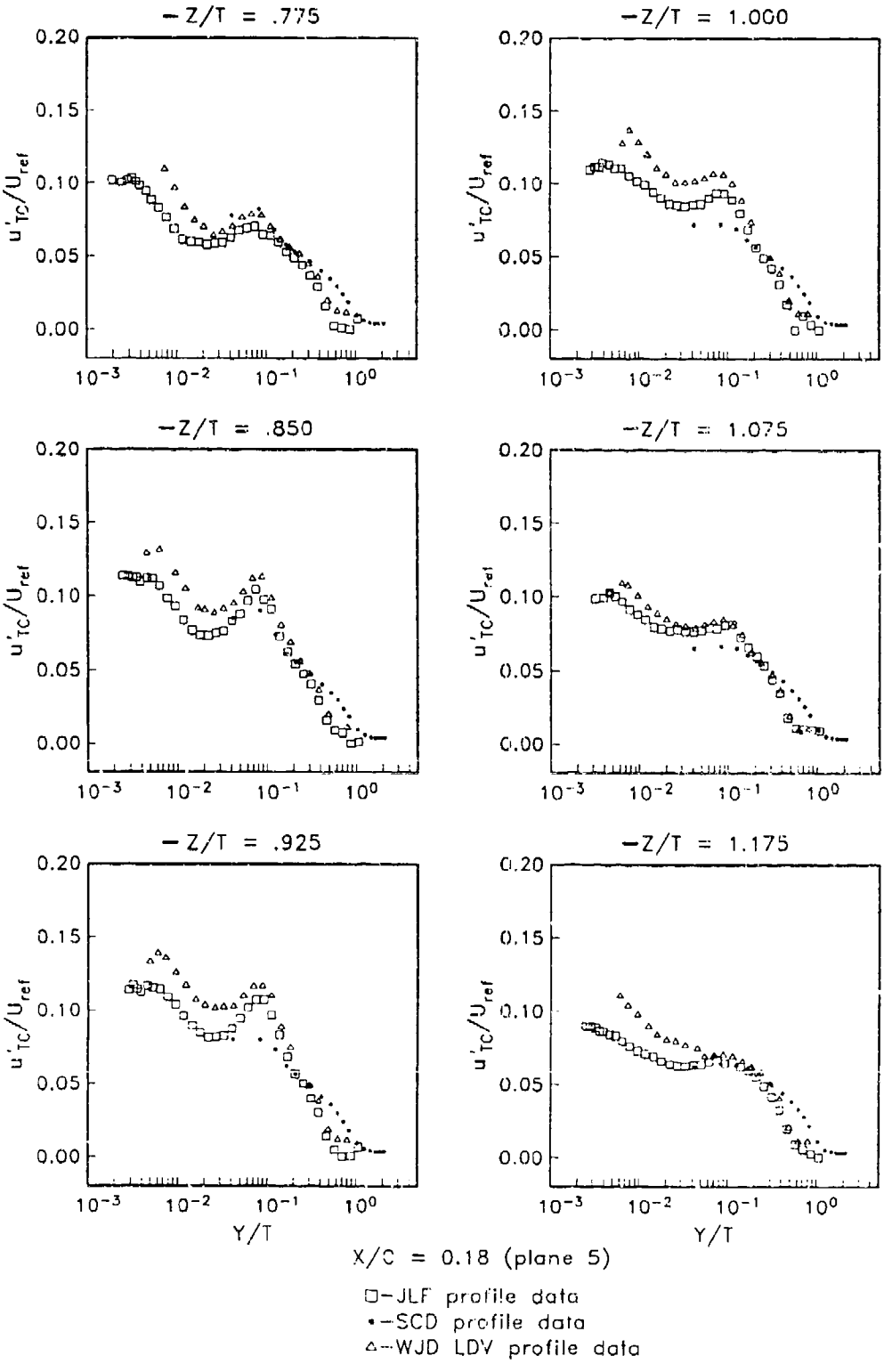

Figure 4.46. Profiles of u'_{TC}/U_{ref}, Plane 5

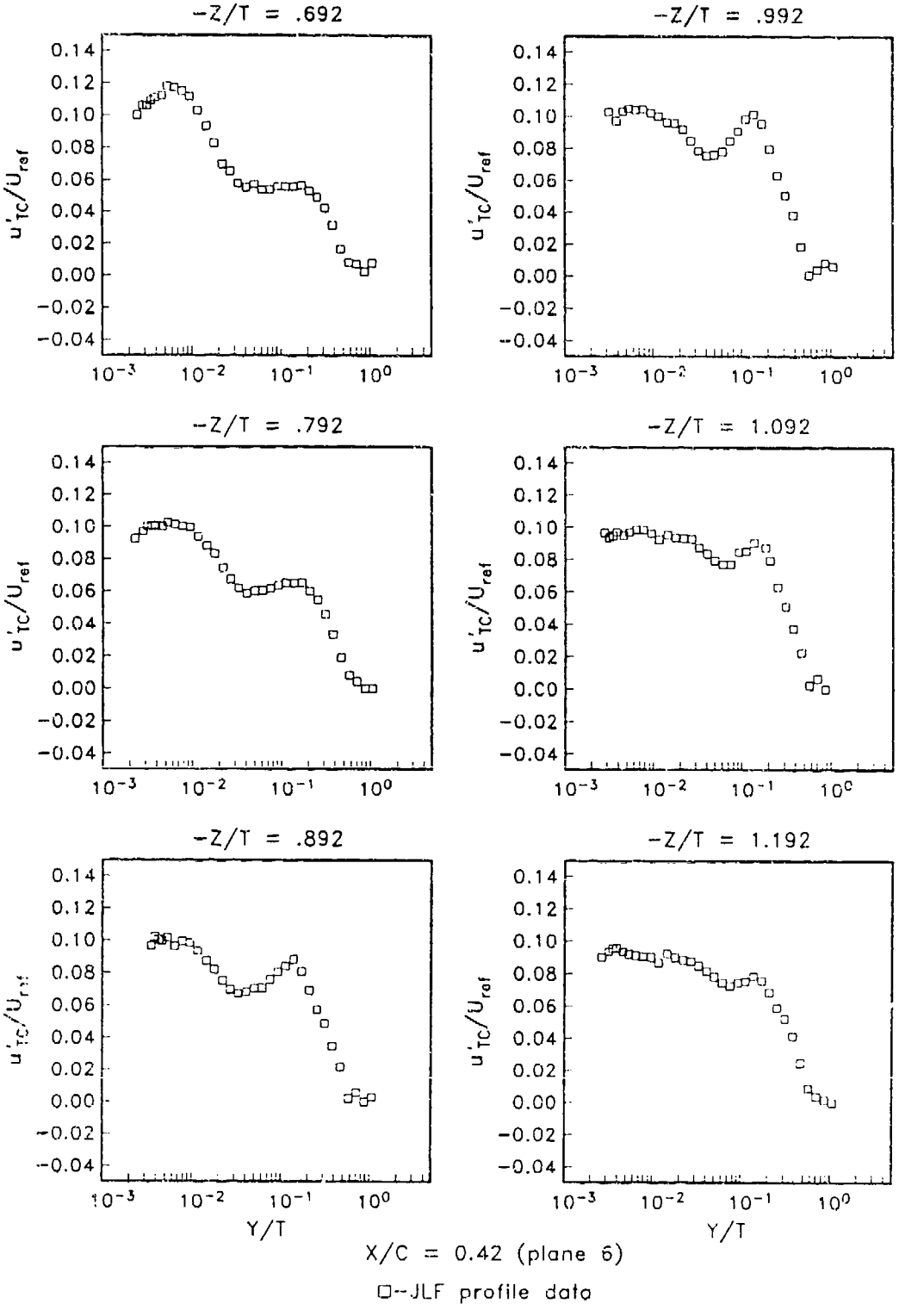

Figure 4.47. Profiles of u'_{TC}/U_{ref}, Plane 6

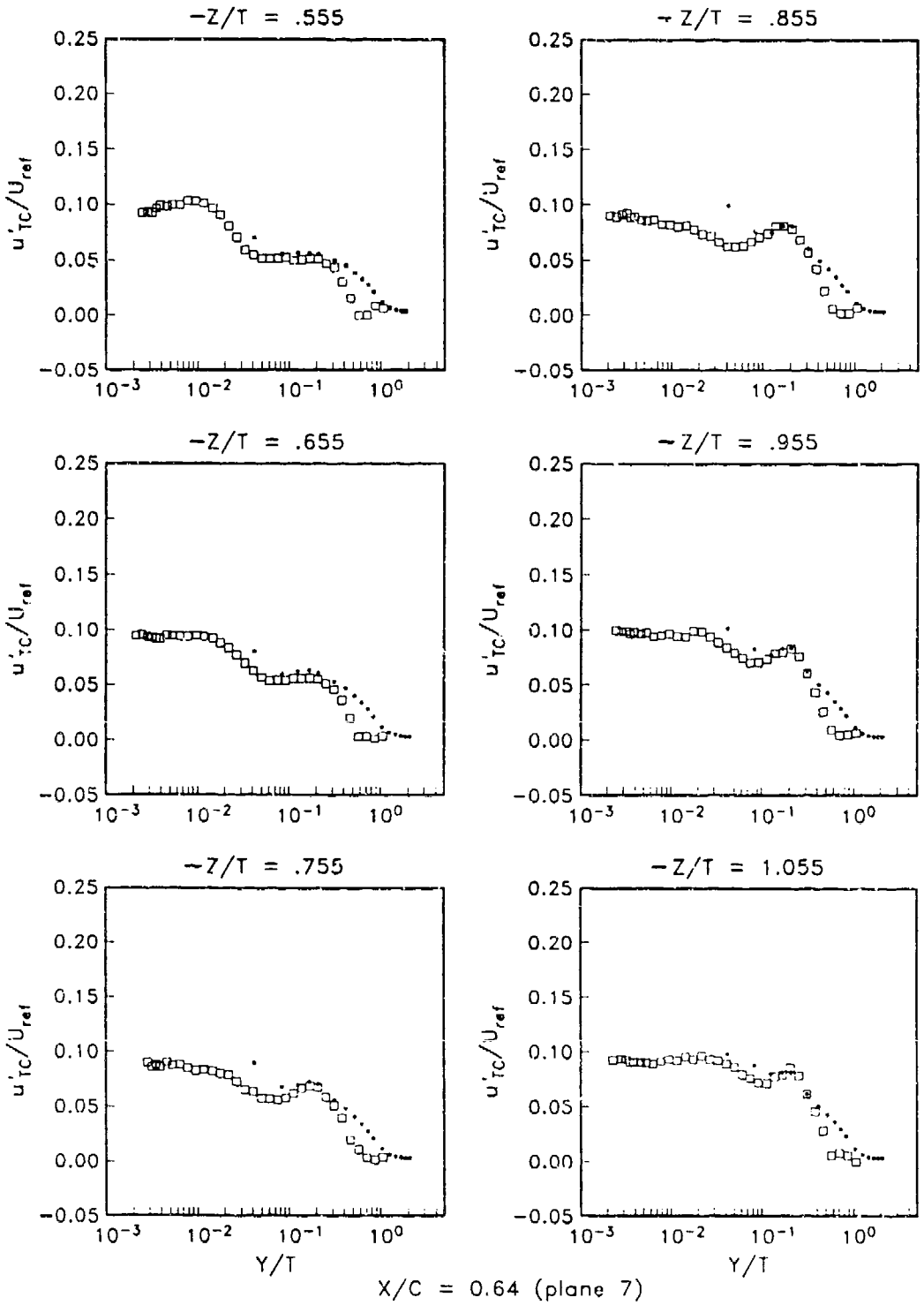

Figure 4.48. Profiles of u'_{TC}/U_{ref}, Plane 7

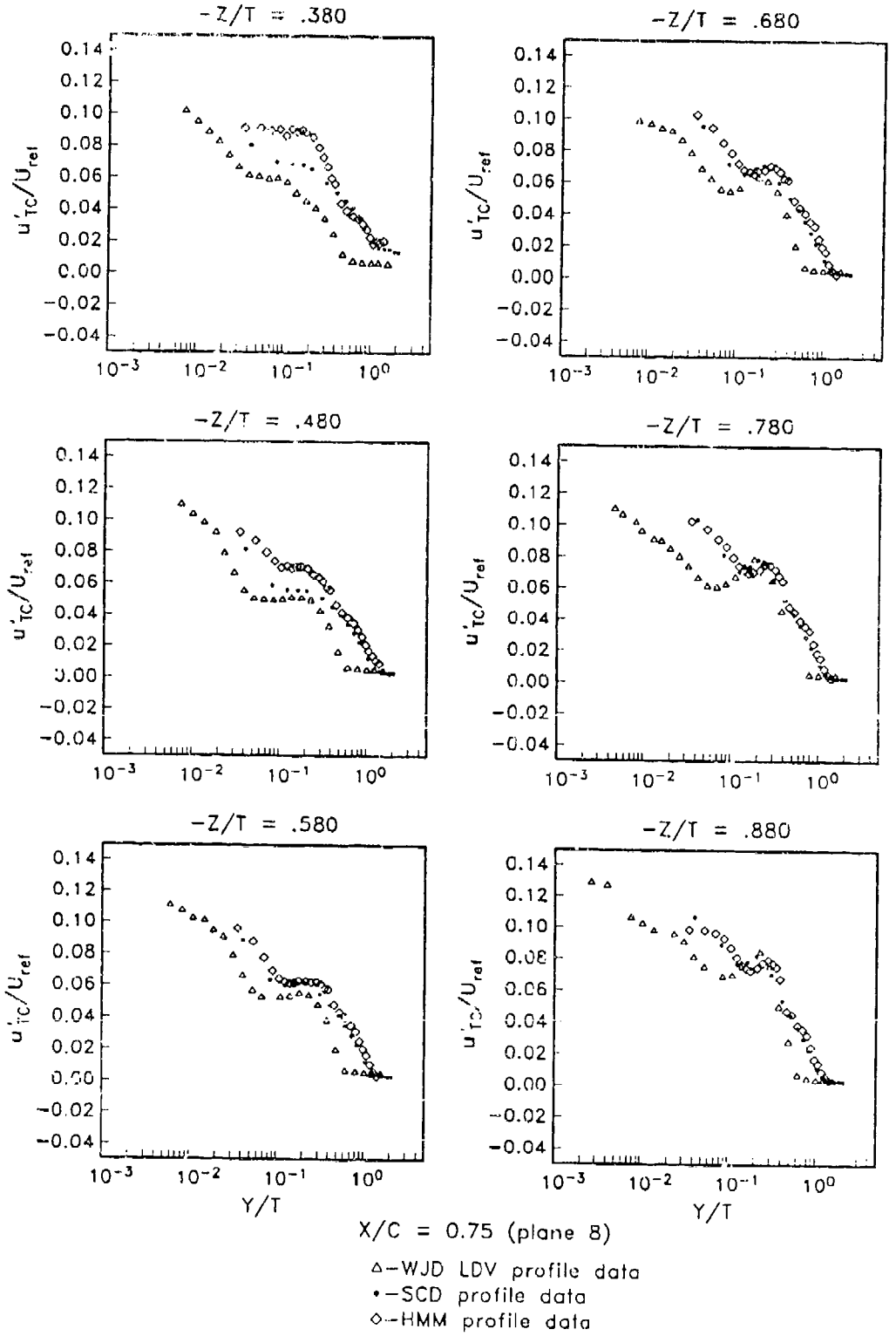

Figure 4.49. Profiles of u'_{TC}/U_{ref}, Plane 8

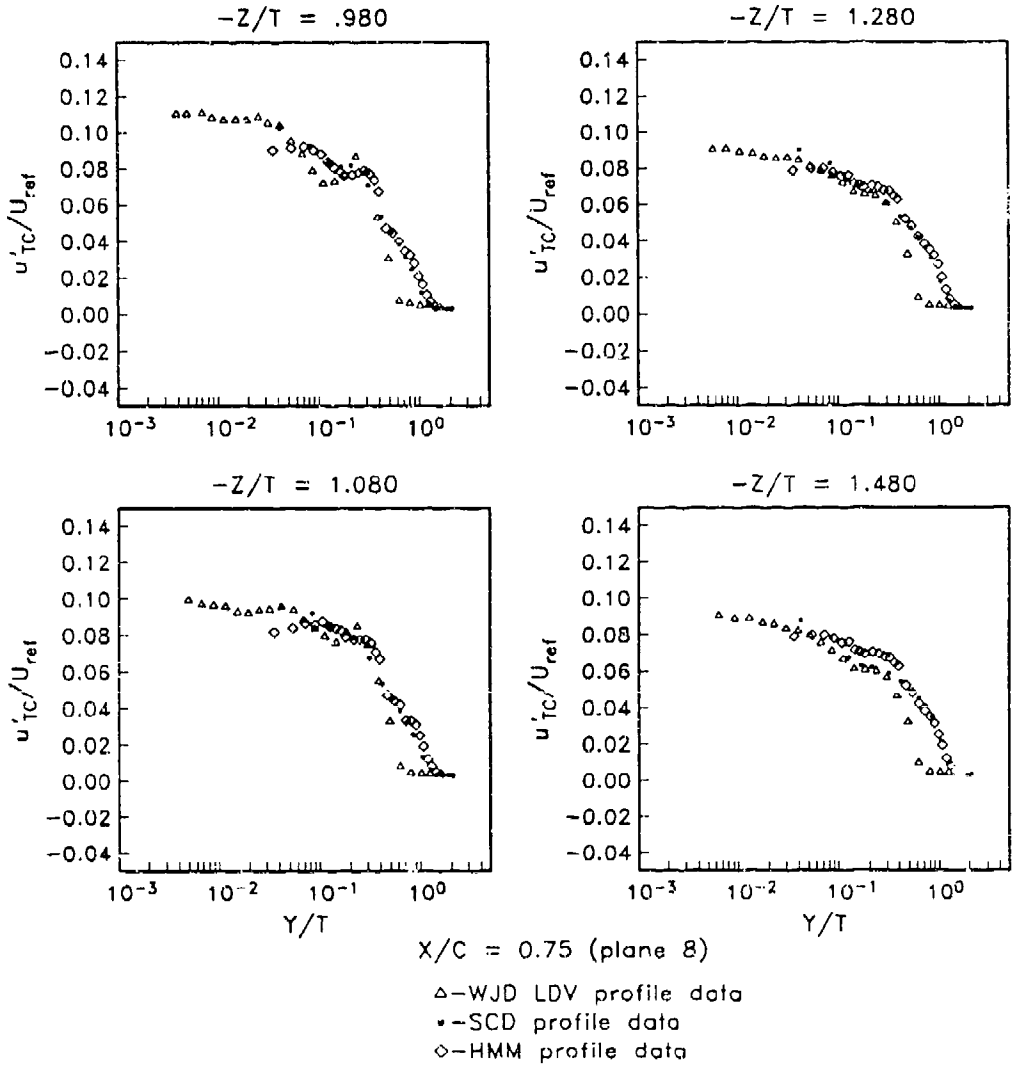

Figure 4.49. (cont.). Profiles of u'_{TC}/U_{ref}, Plane 1.

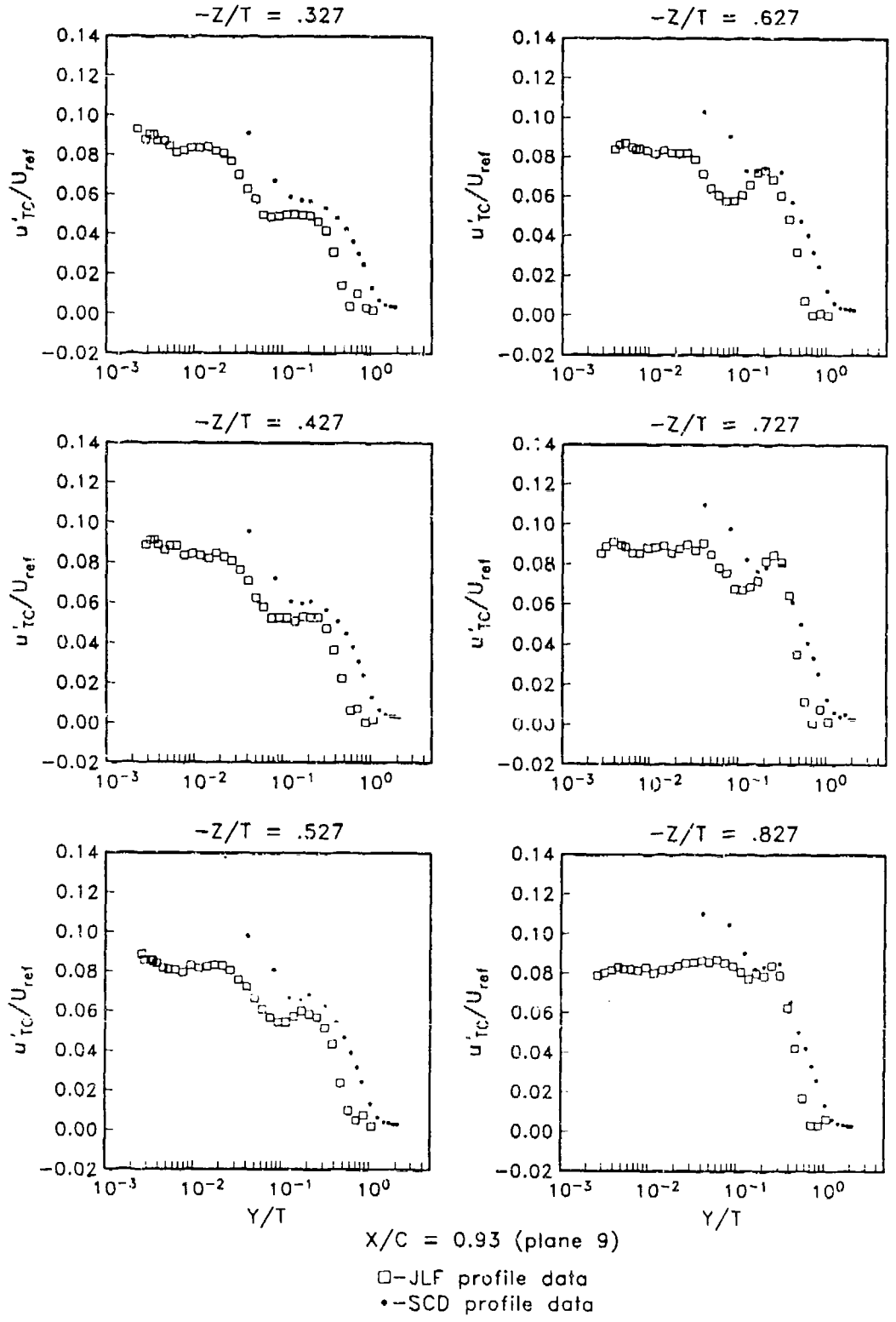

Figure 4.50. Profiles of u'_{TC}/U_{ref}, Plane 9

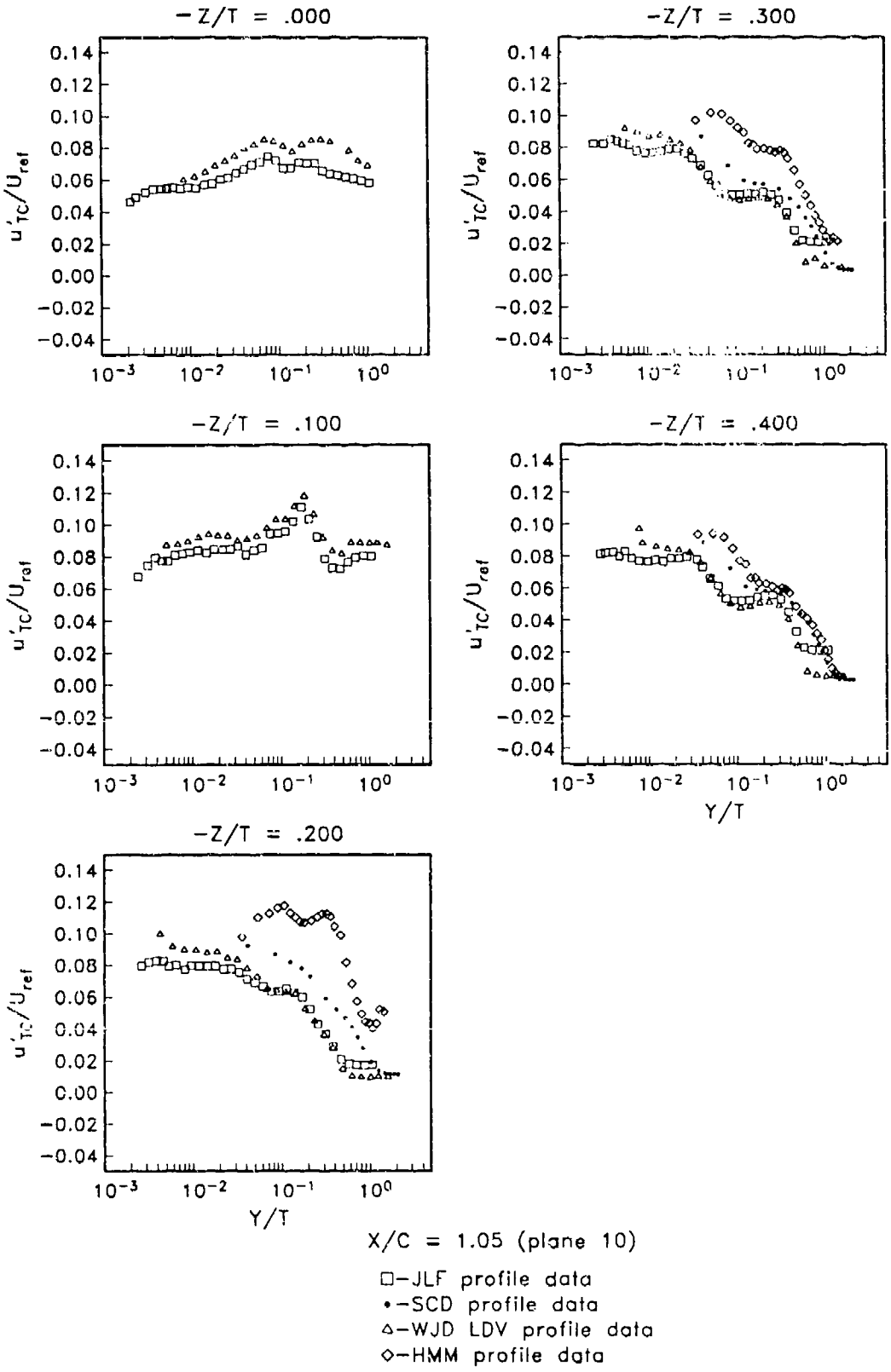

Figure 4.51. Profiles of u'_{TC}/U_{ref}, Plane 10

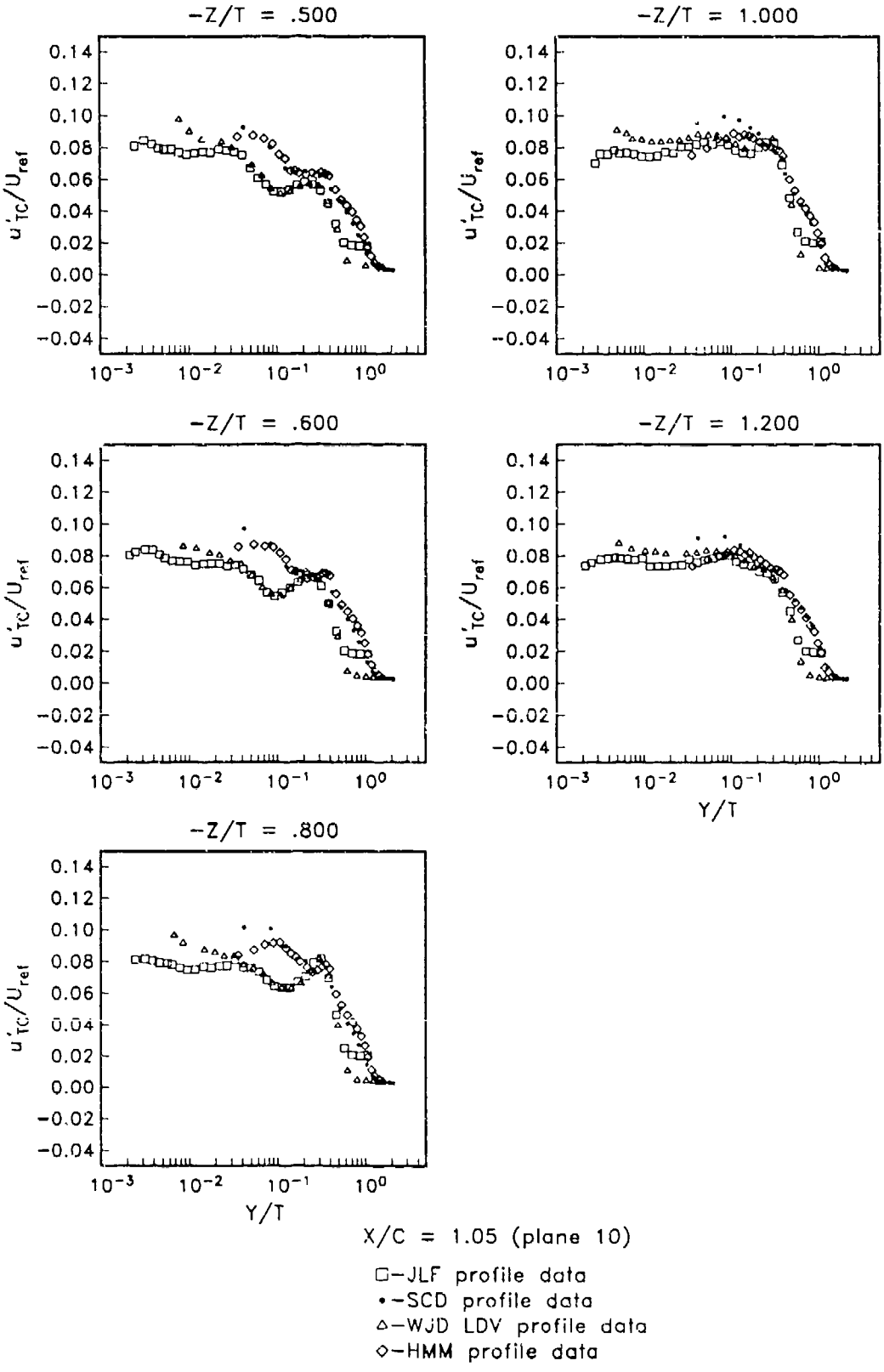

Figure 4.51. (cont.). Profiles of u'_{TC}/U_{ref}, Plane 10

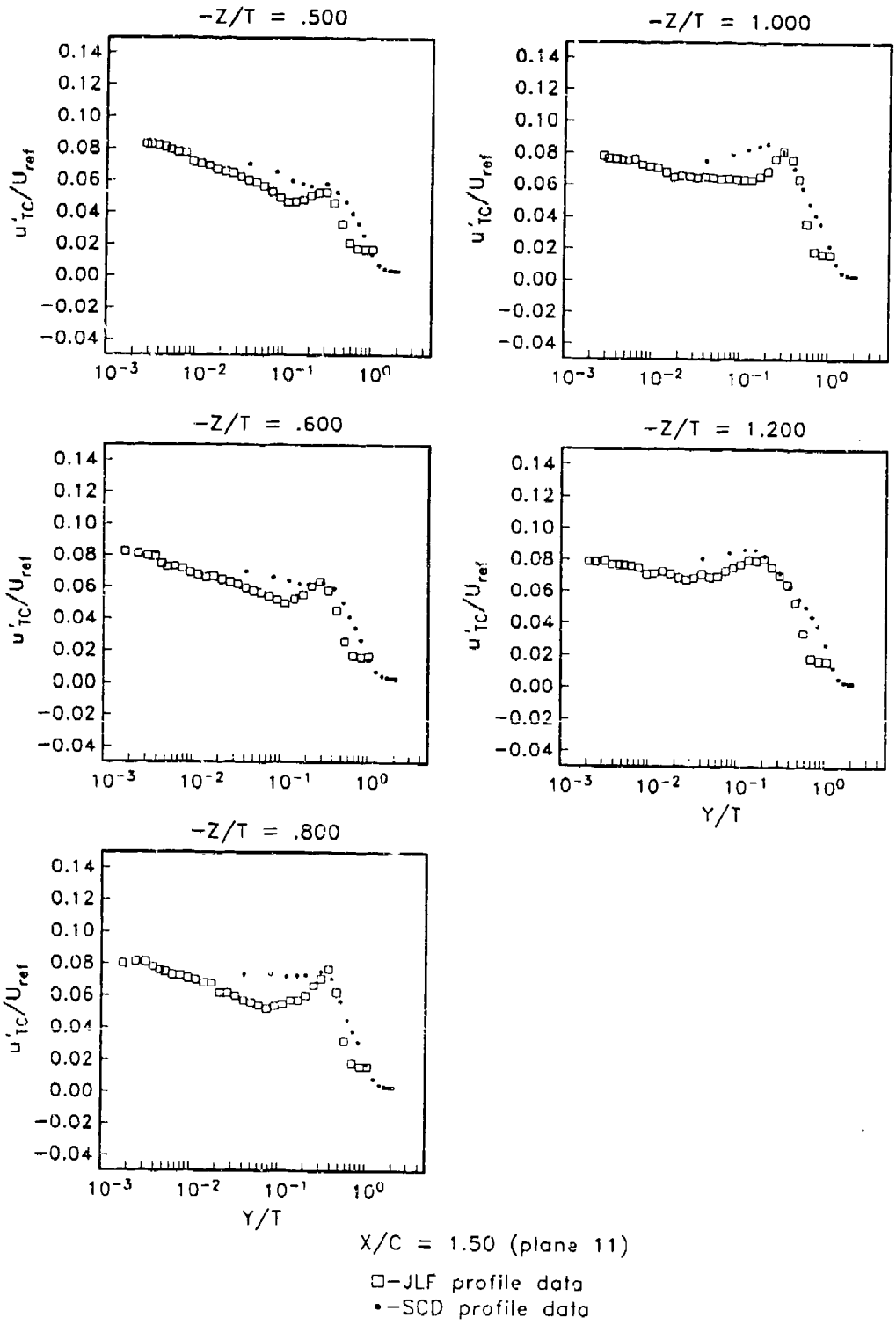

Figure 4.52. Profiles of u'_{TC}/U_{ref}, Plane 11

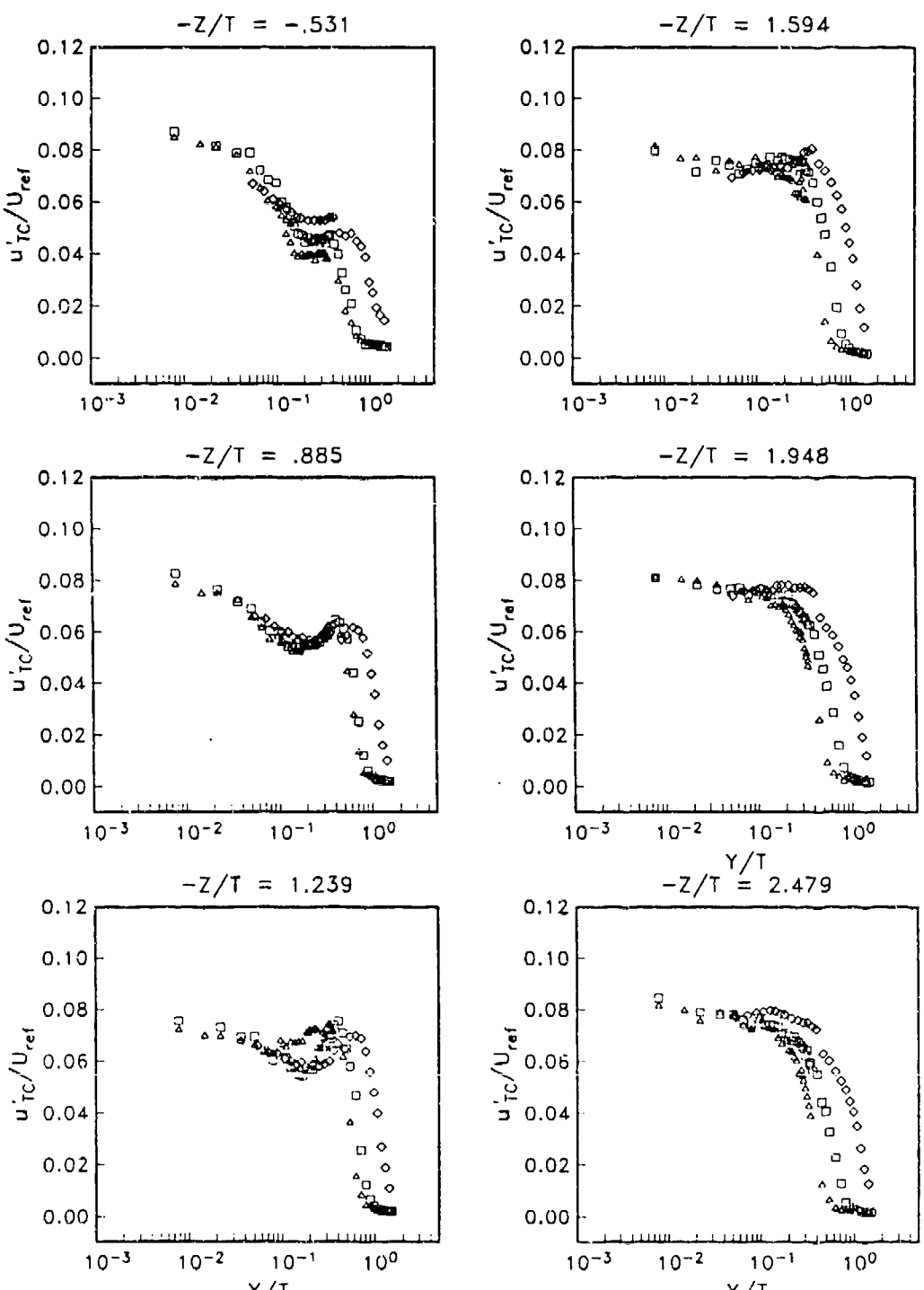

Figure 4.53. Profiles of u'_{TC}/U_{ref}, Plane 12

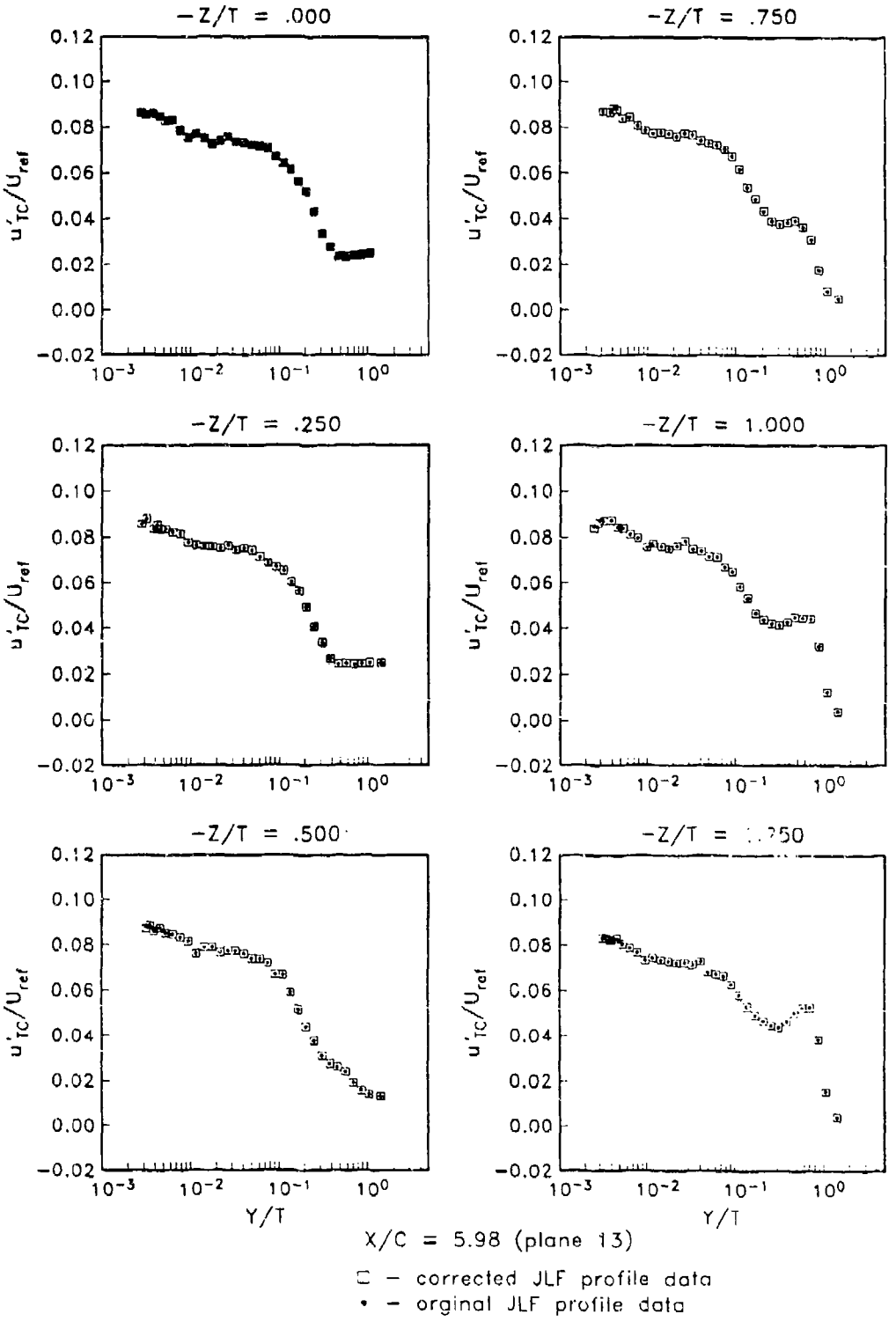

Figure 4.54. Profiles of u'_{TC}/U_{ref}, Plane 13

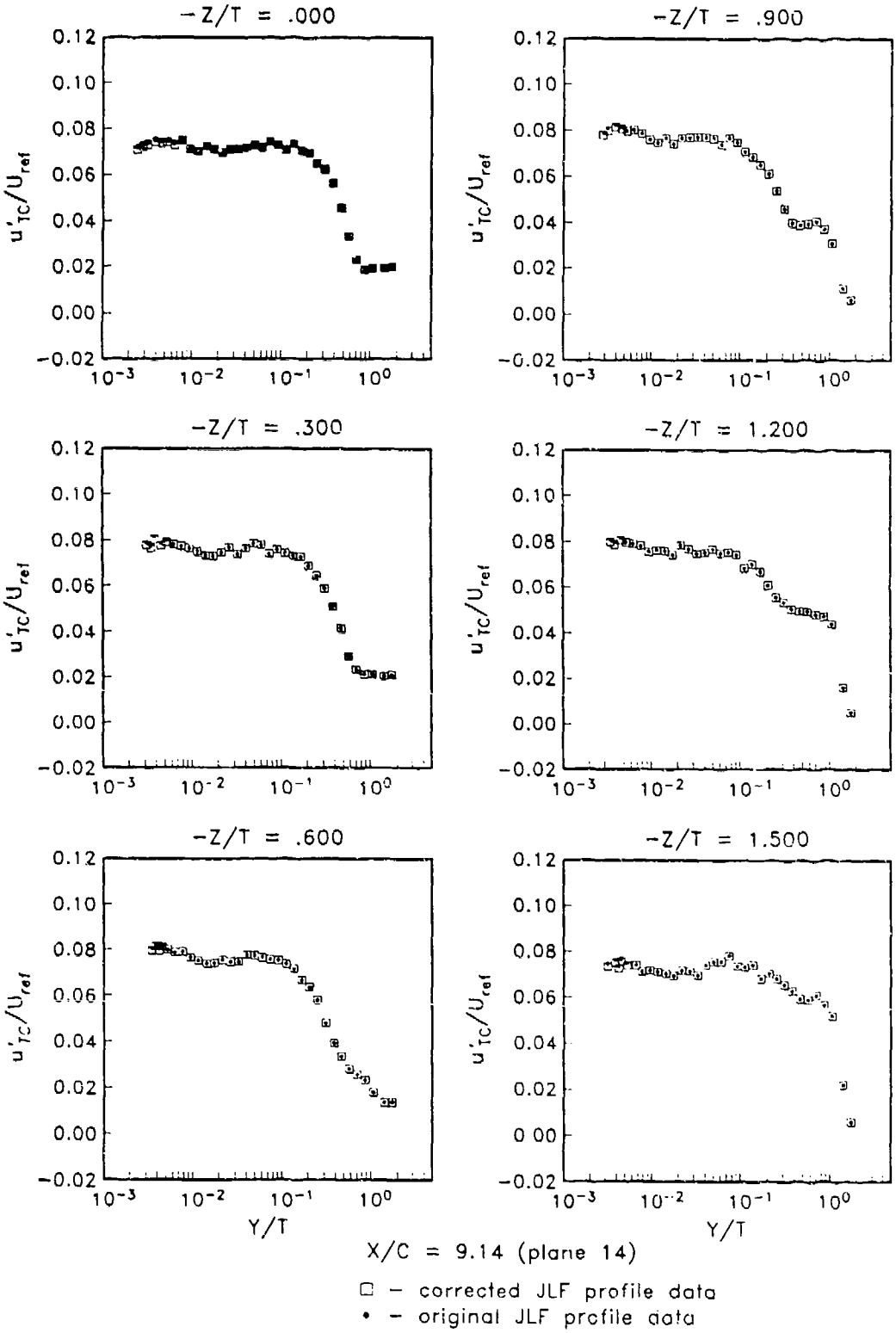

Figure 4.55. Profiles of u'_{TC}/U_{ref}, Plane 14

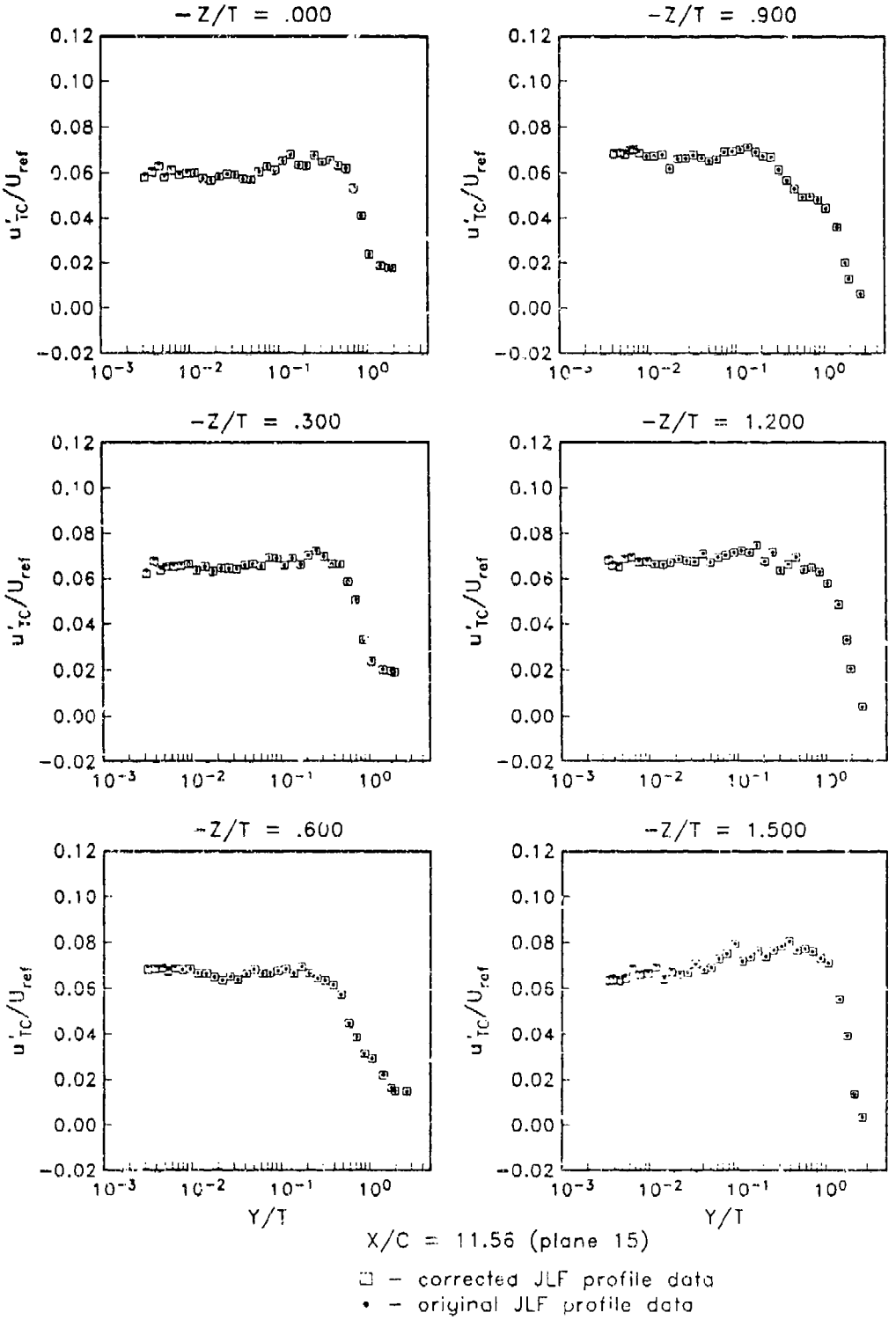

Figure 4.56. Profiles of u'_{TC}/U_{ref}, Plane 15

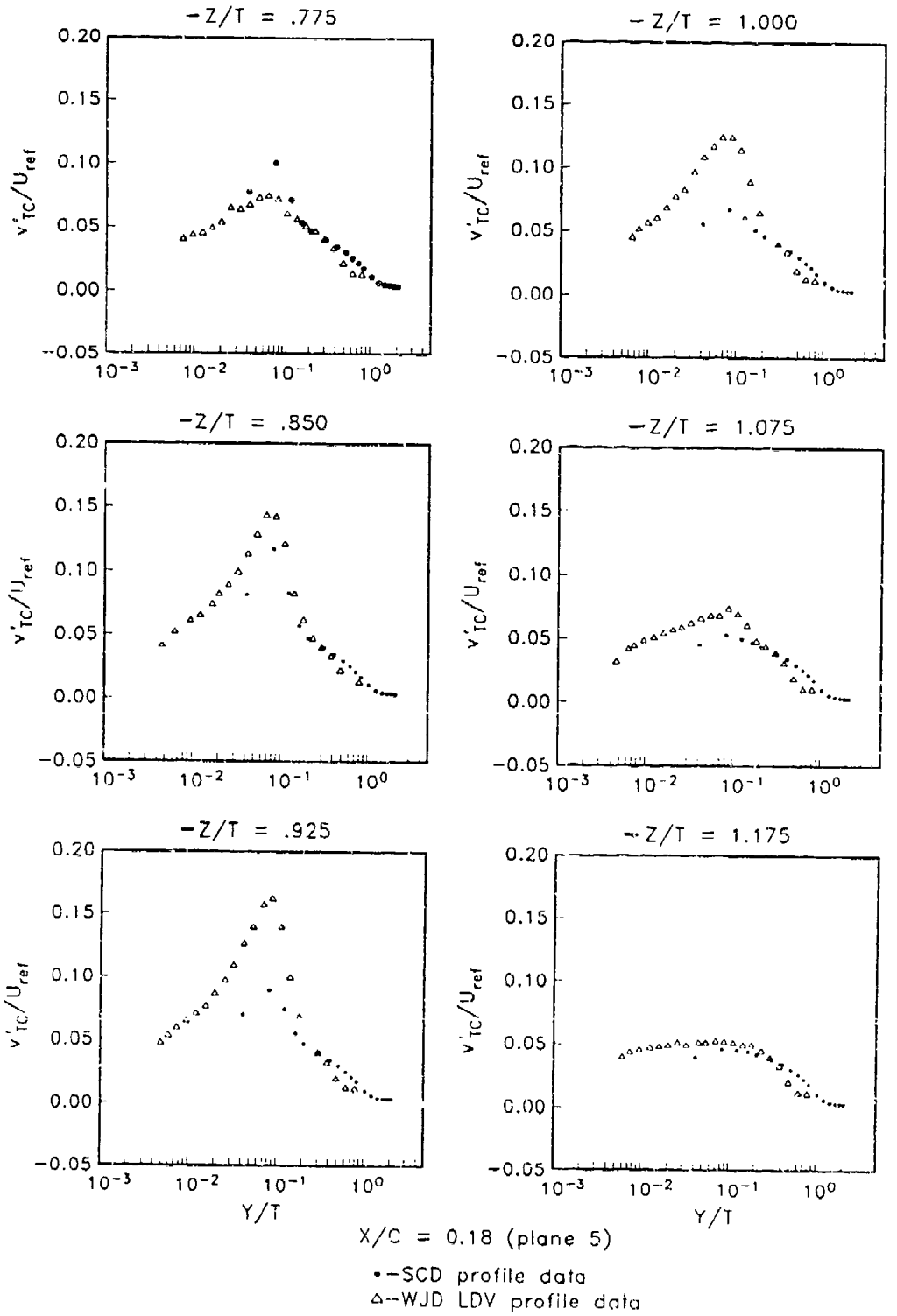

Figure 4.57. Profiles of v'_{TC}/U_{ref}, Plane 5

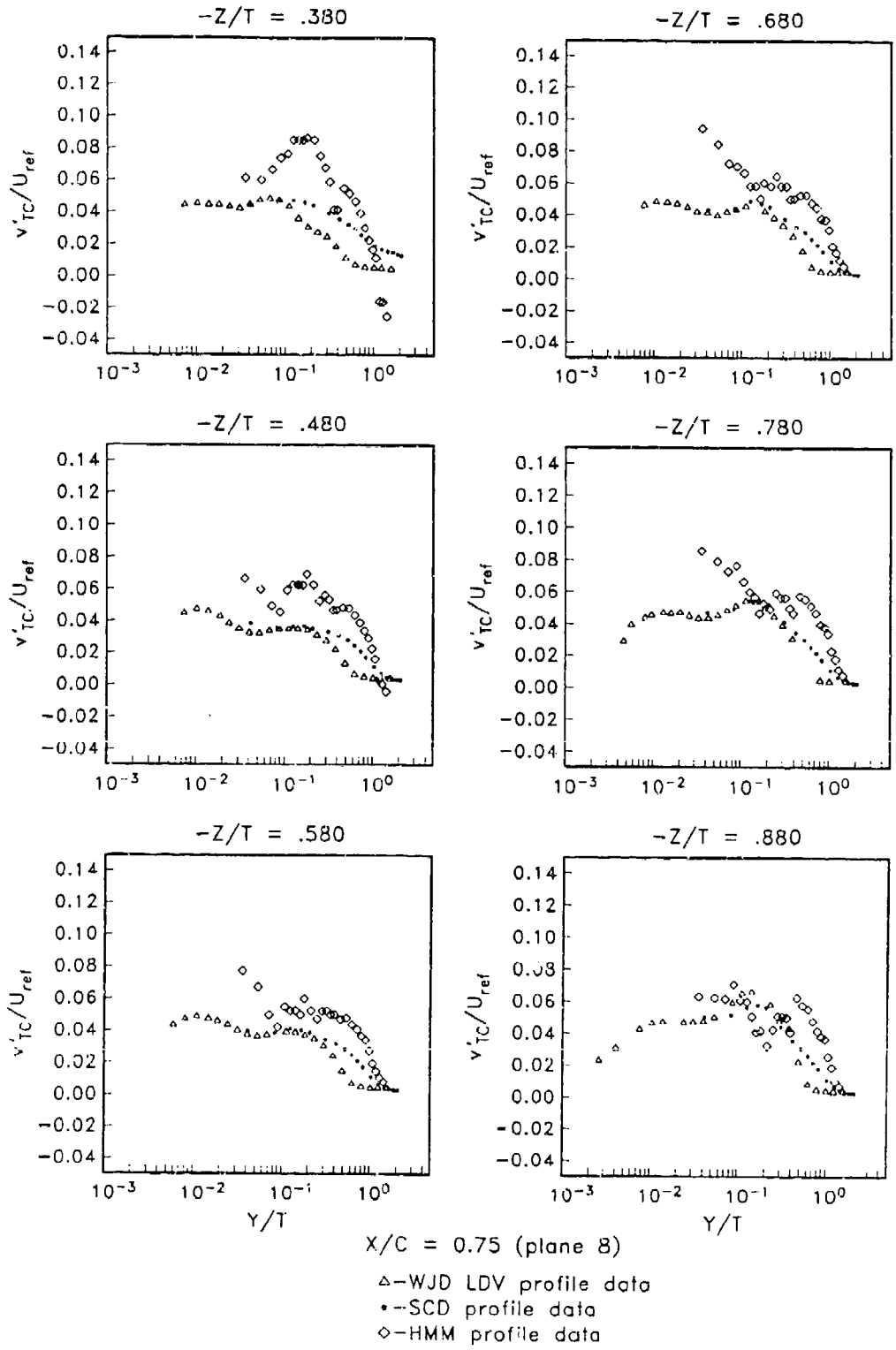

Figure 4.58. Profiles of v'_{TC}/U_{ref}, Plane 8

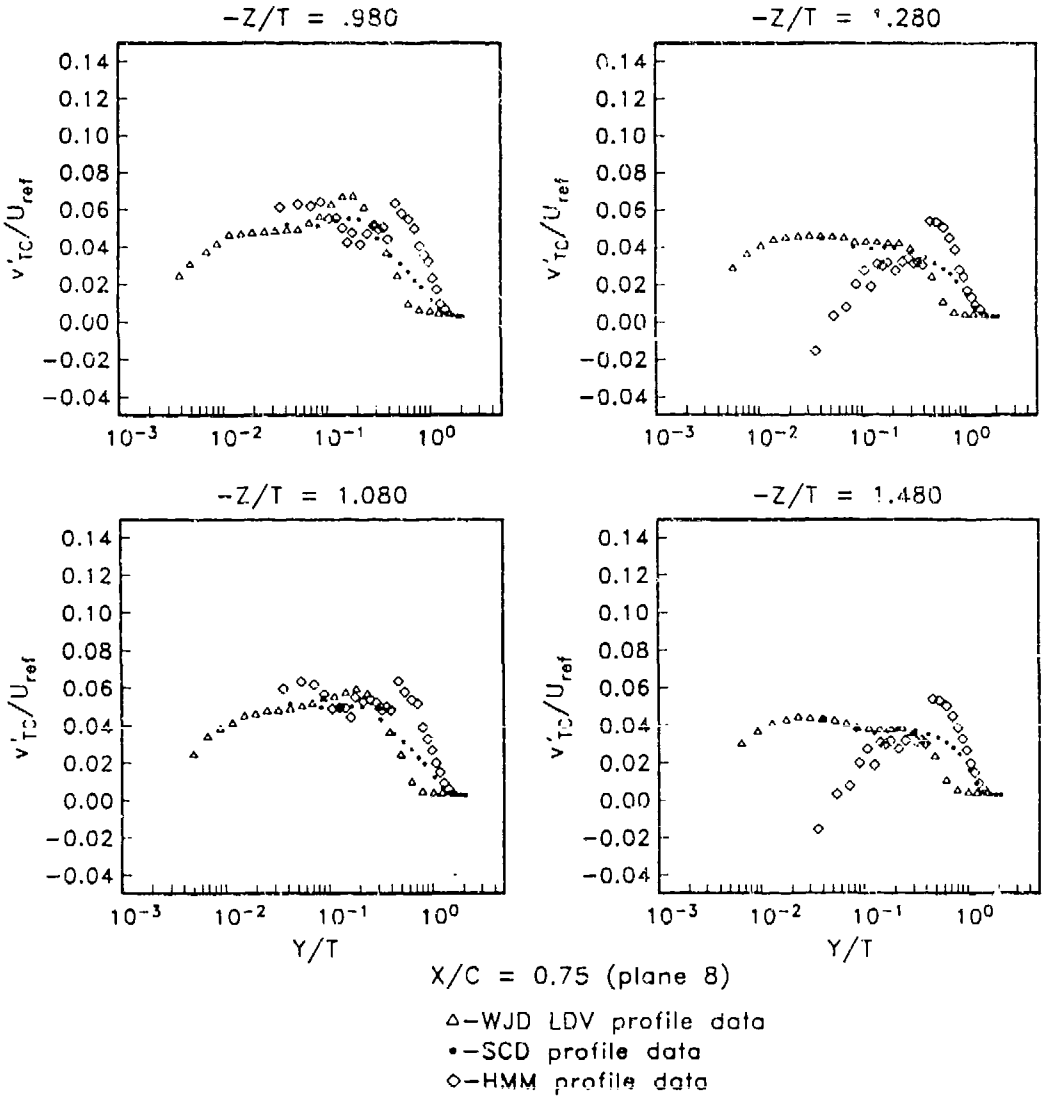

Figure 4.58. (cont.). Profiles of v'_{TC}/U_{ref}, Plane 8

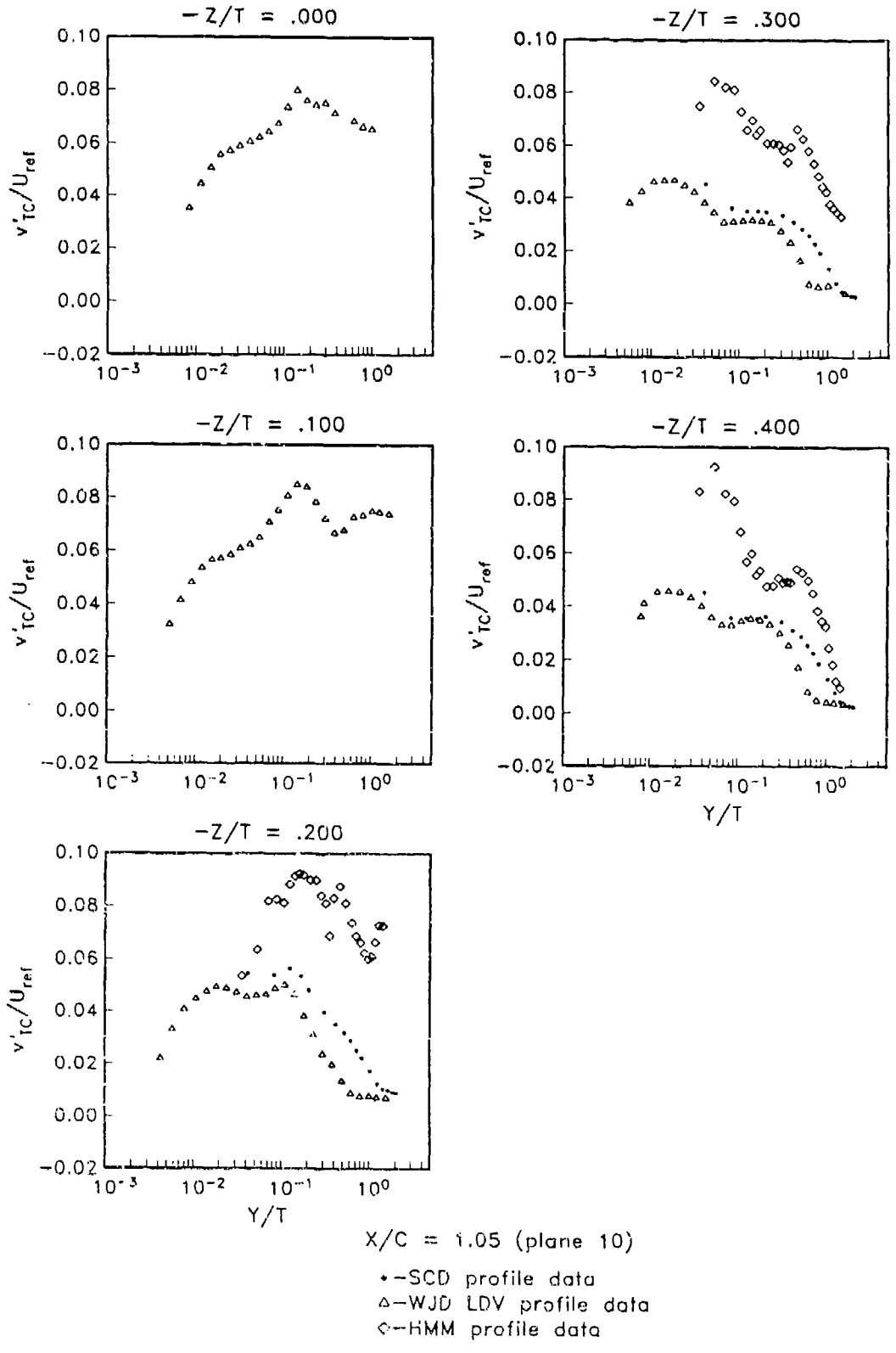

Figure 4.59. Profiles of v'_{TC}/U_{ref}, Plane 10

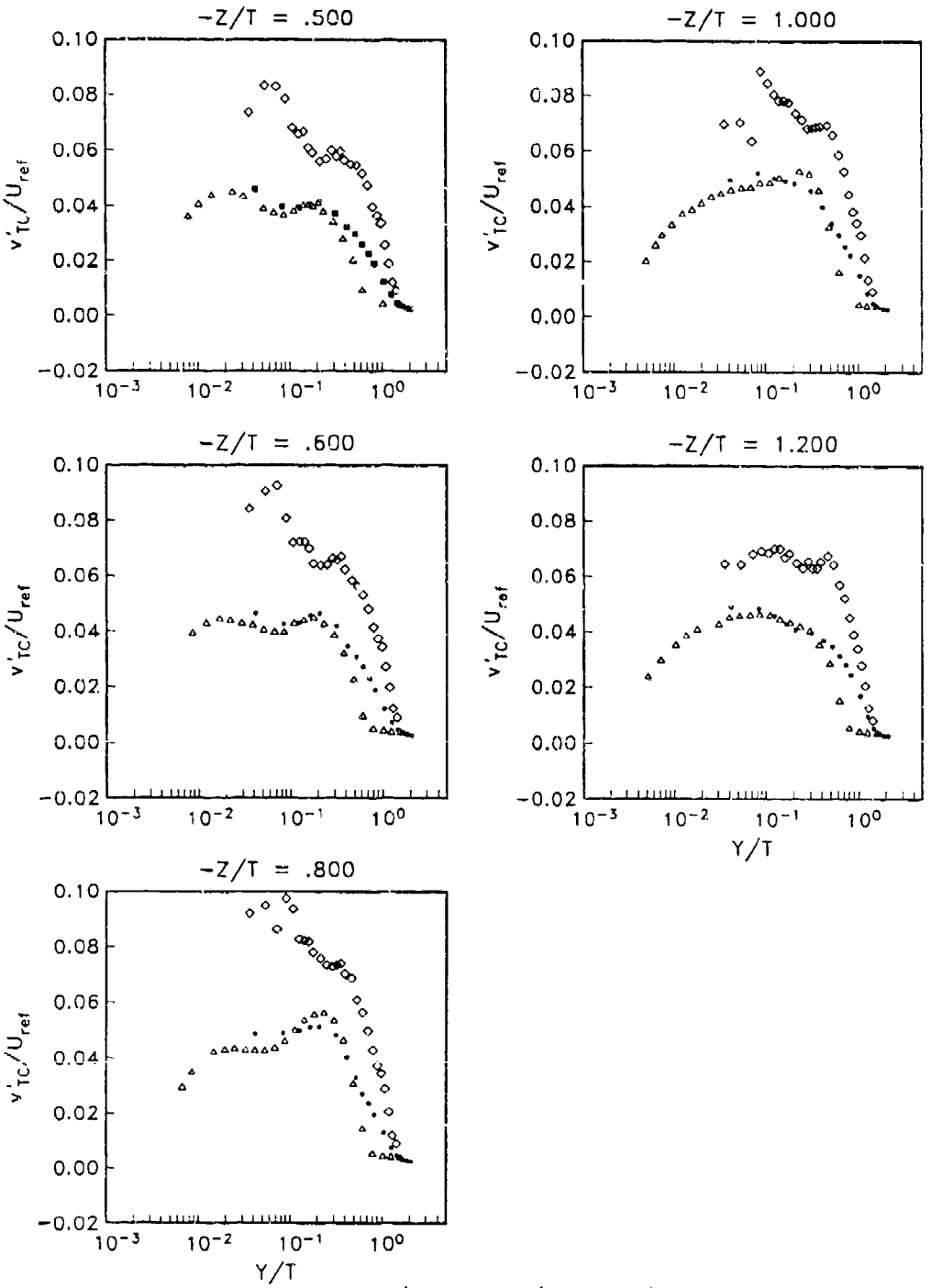

Figure 4.59. (cont.). Profiles of v'_{TC}/U_{ref}, Plane 10

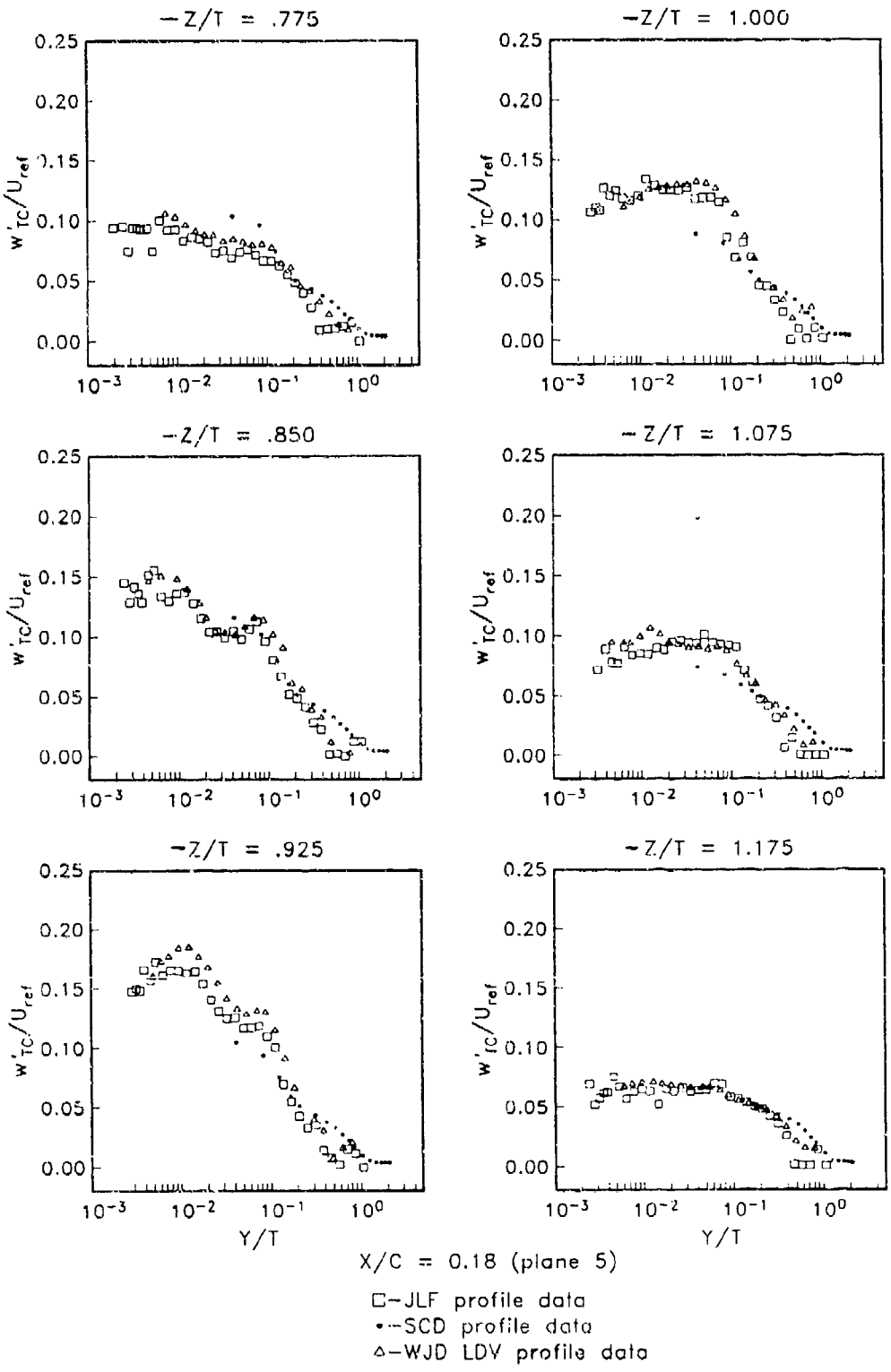

Figure 4.60. Profiles of w'_{TC}/U_{ref}, Plane 5

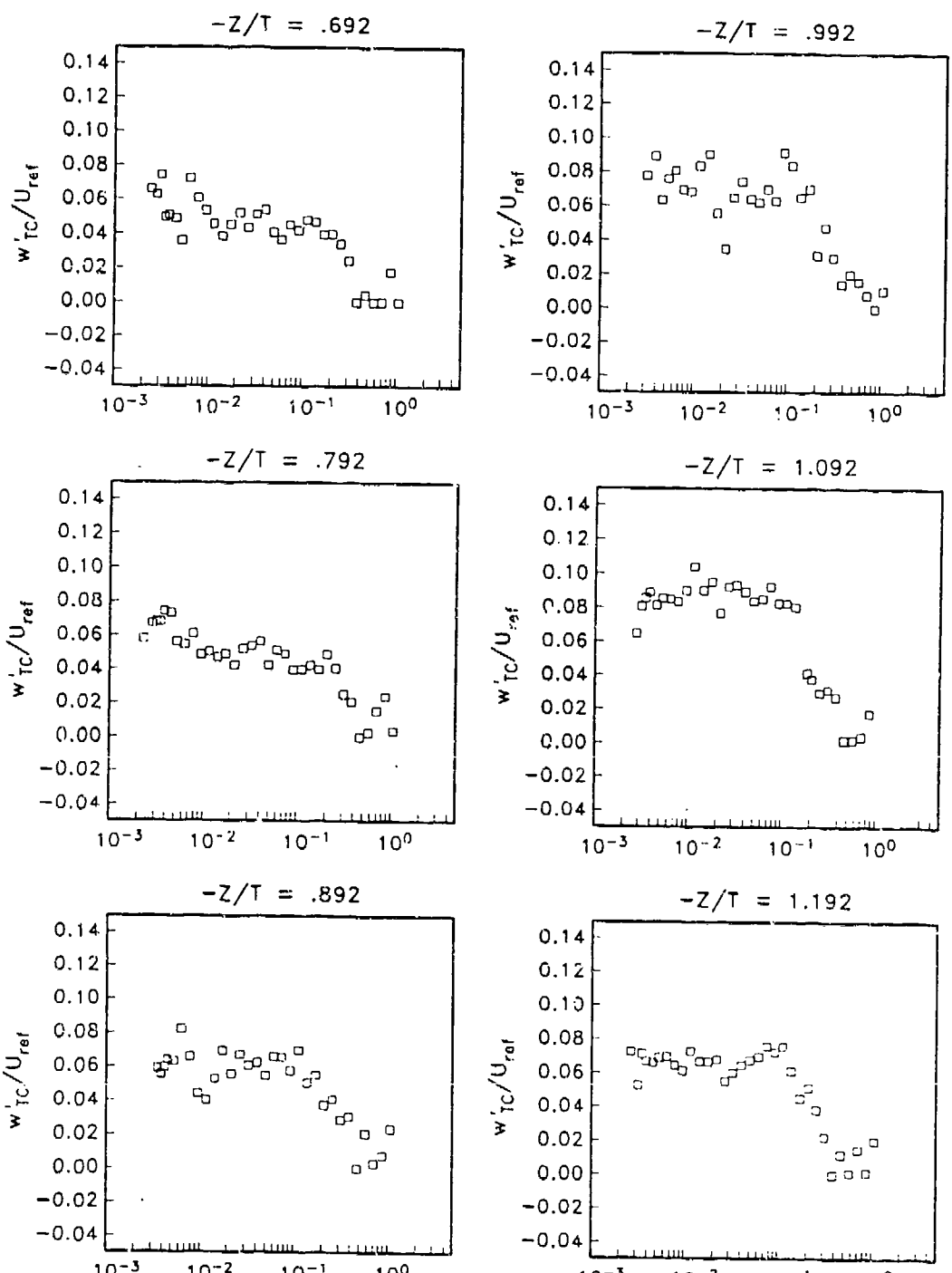

Figure 4.61. Profiles of w'_{TC}/U_{ref}, Plane 6

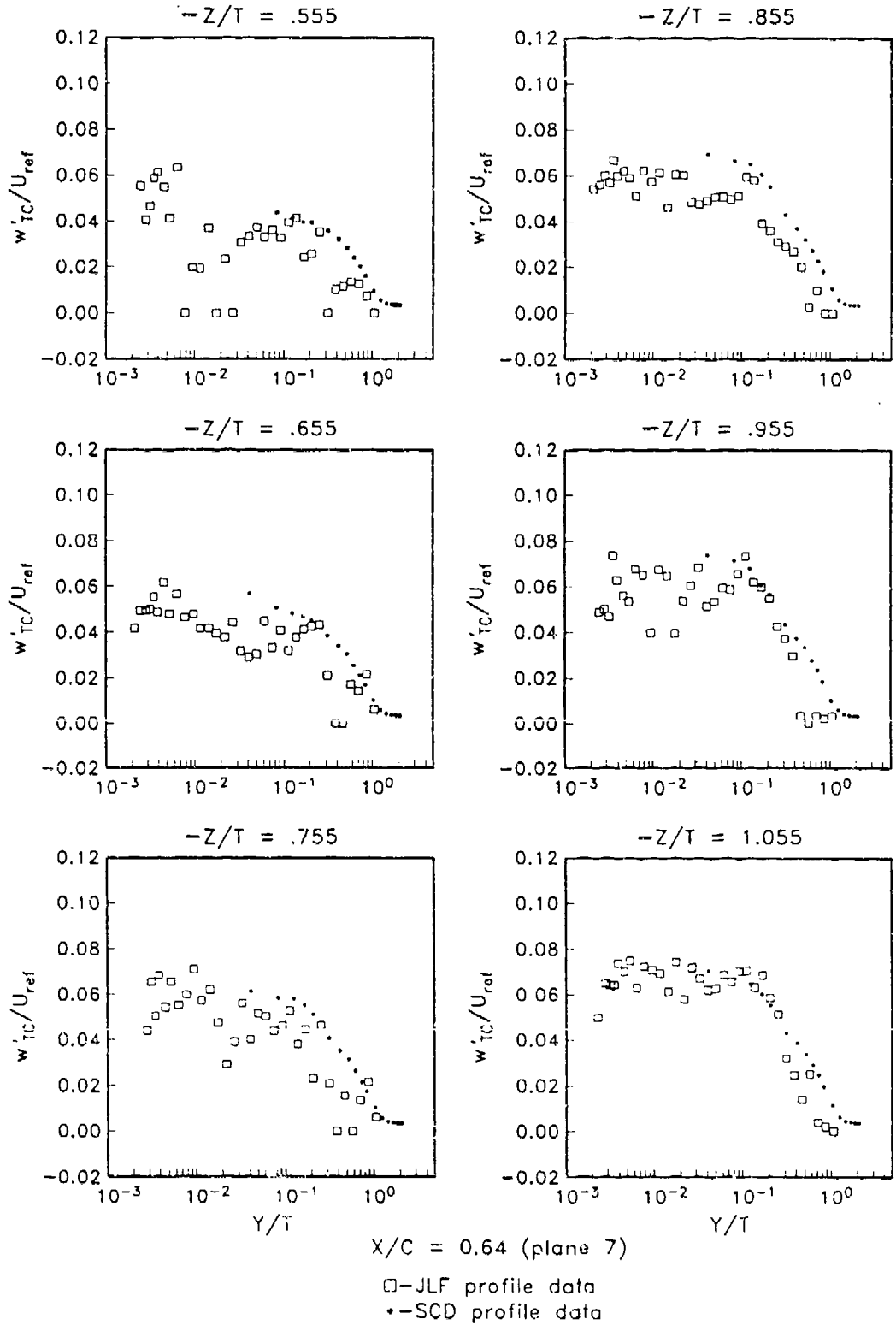

Figure 4.62. Profiles of w'_{TC}/U_{ref}, Plane 7

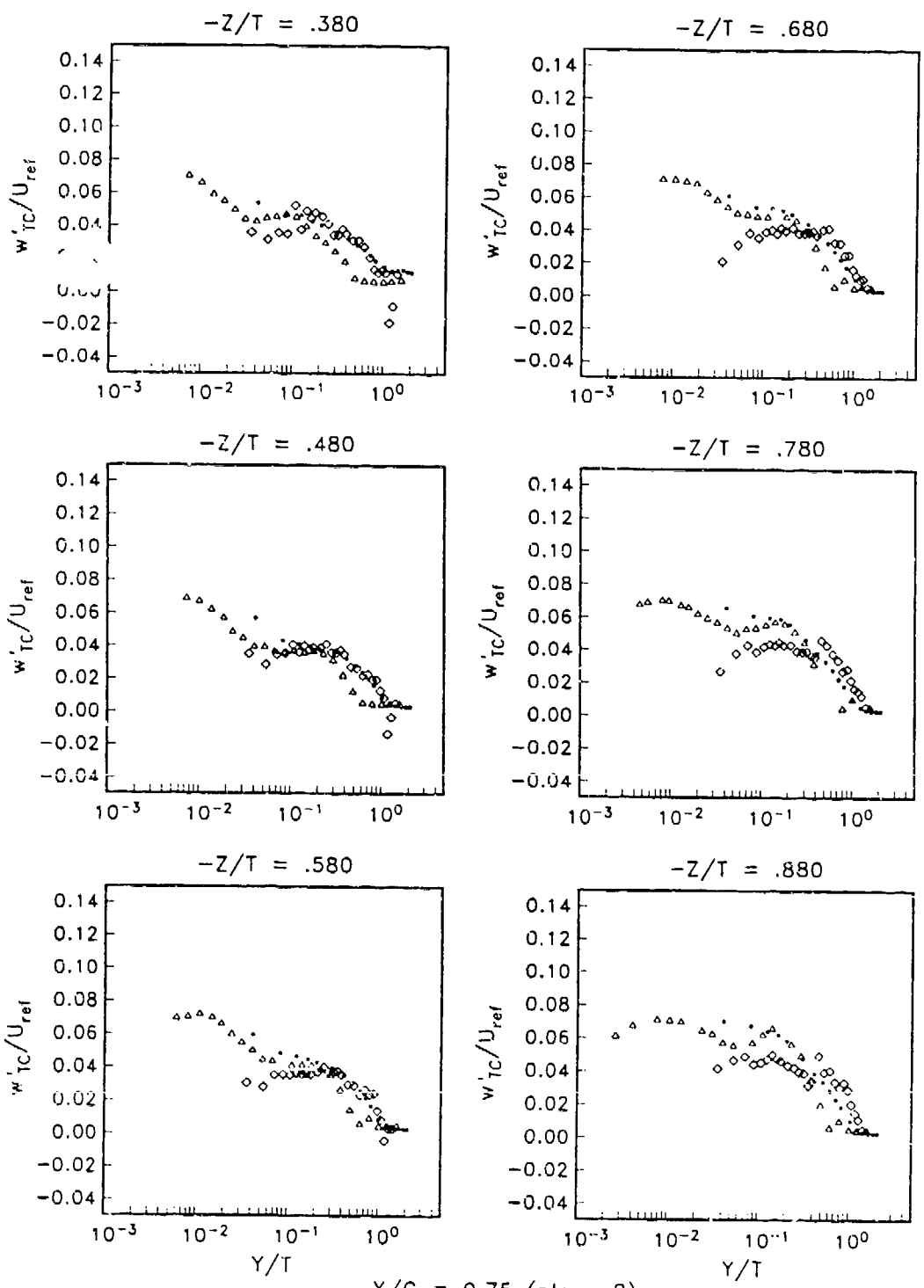

Figure 4.63. Profiles of w'_{TC}/U_{ref}, Plane 8

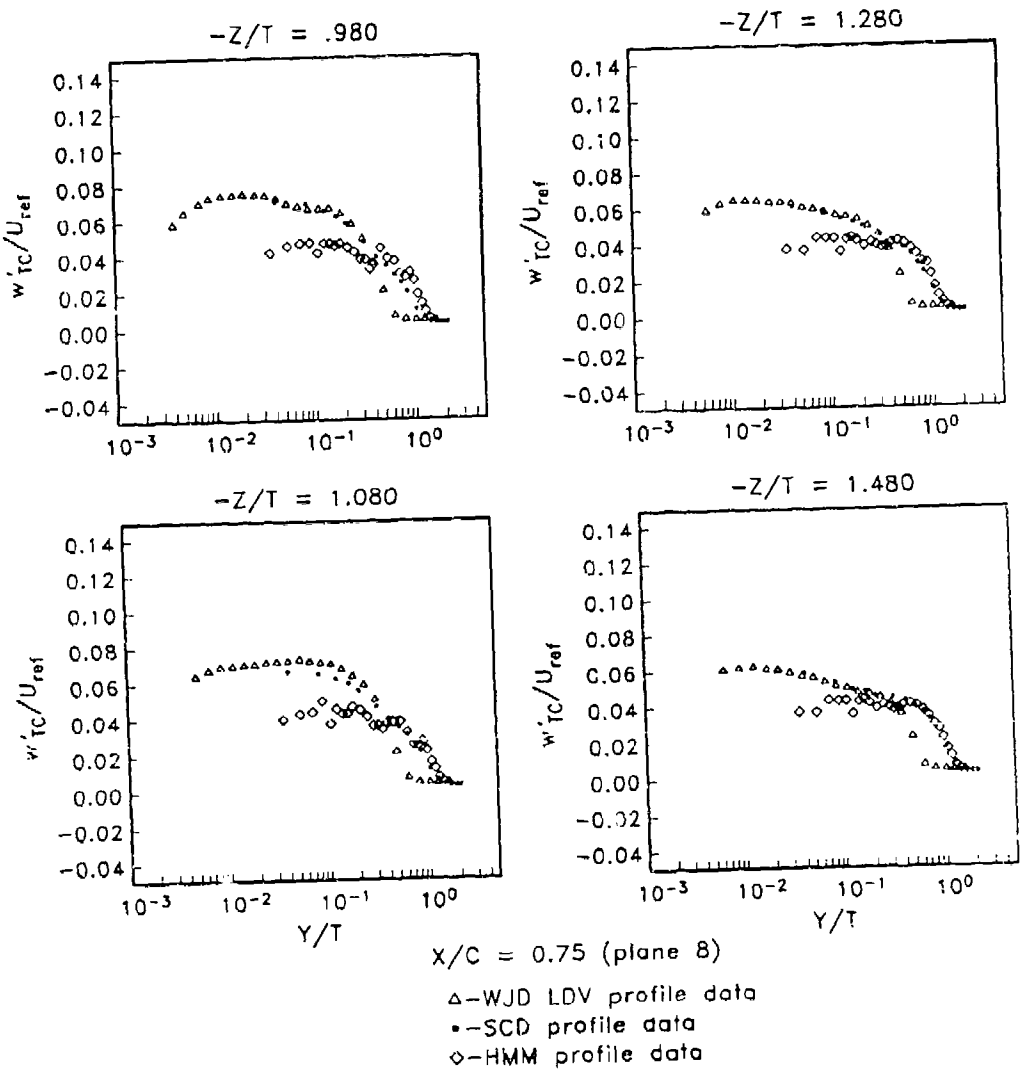

Figure 4.63. (cont.). Profiles of w'_{TC}/U_{ref}, Plane 8

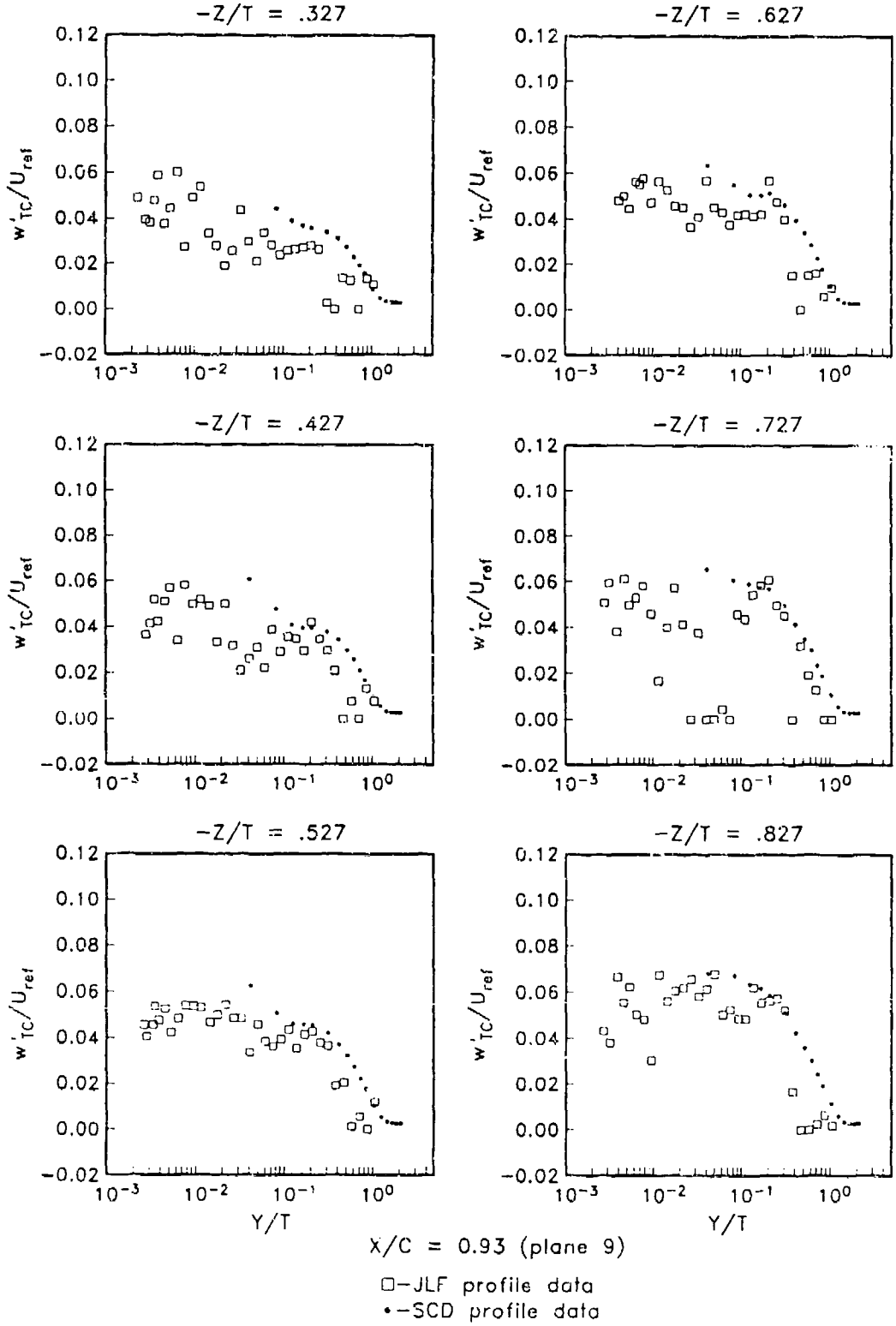

Figure 4.64. Profiles of w'_{TC}/U_{ref}, Plane 9

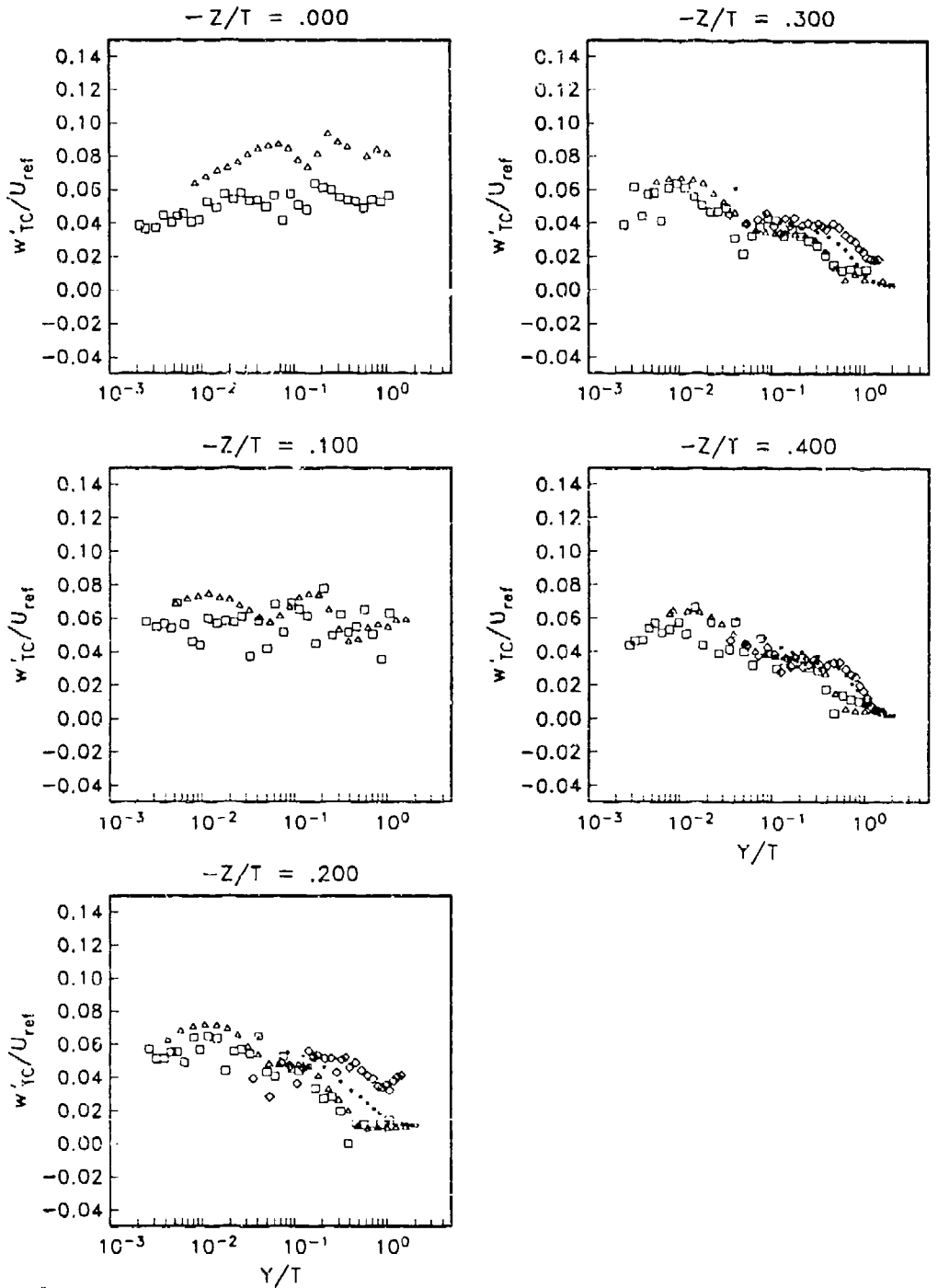

Figure 4.65. Profiles of w'_{TC}/U_{ref}, Plane 10

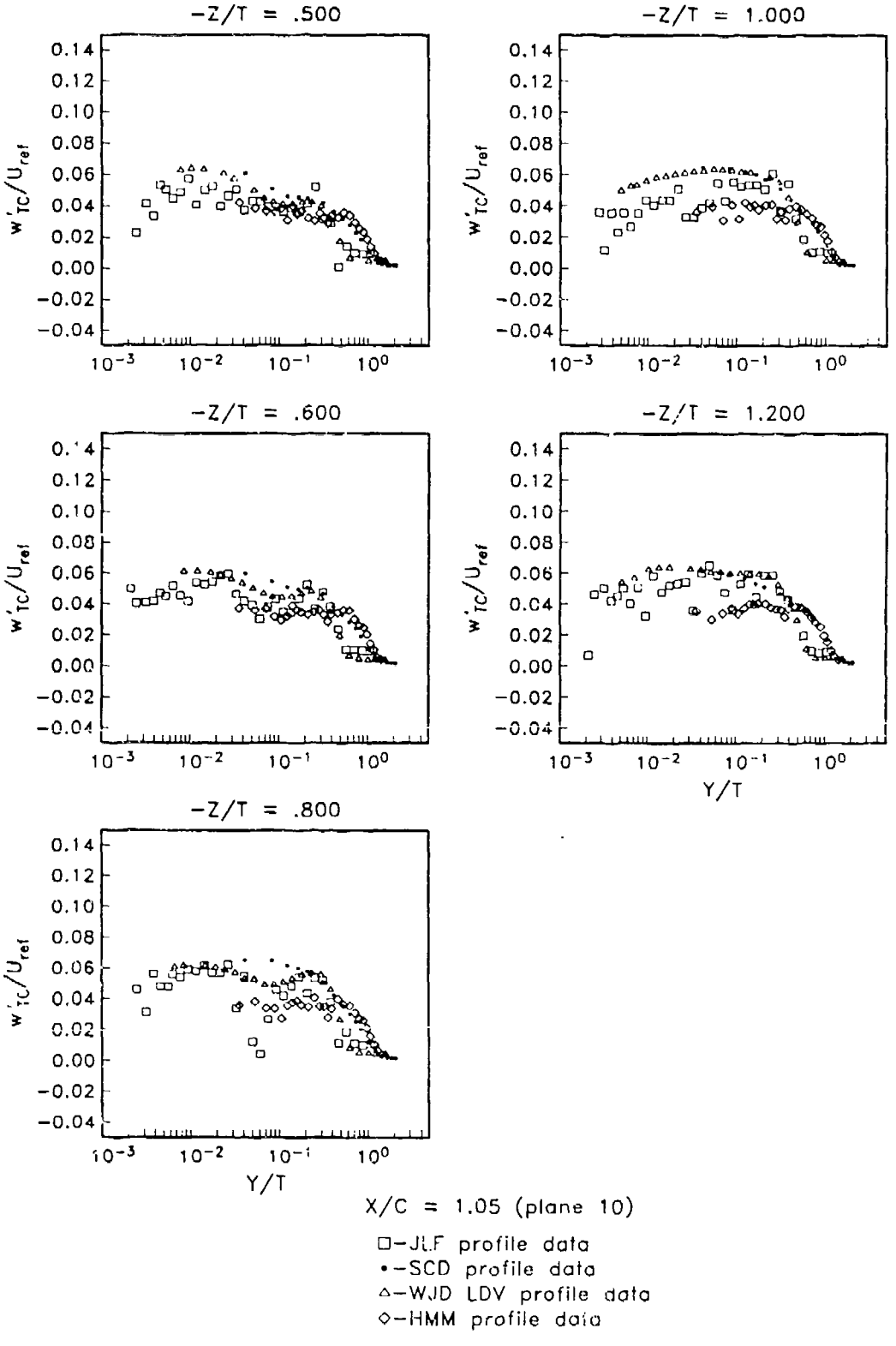

Figure 4.65. (cont.). Profiles of w'_{TC}/U_{ref}, Plane 10

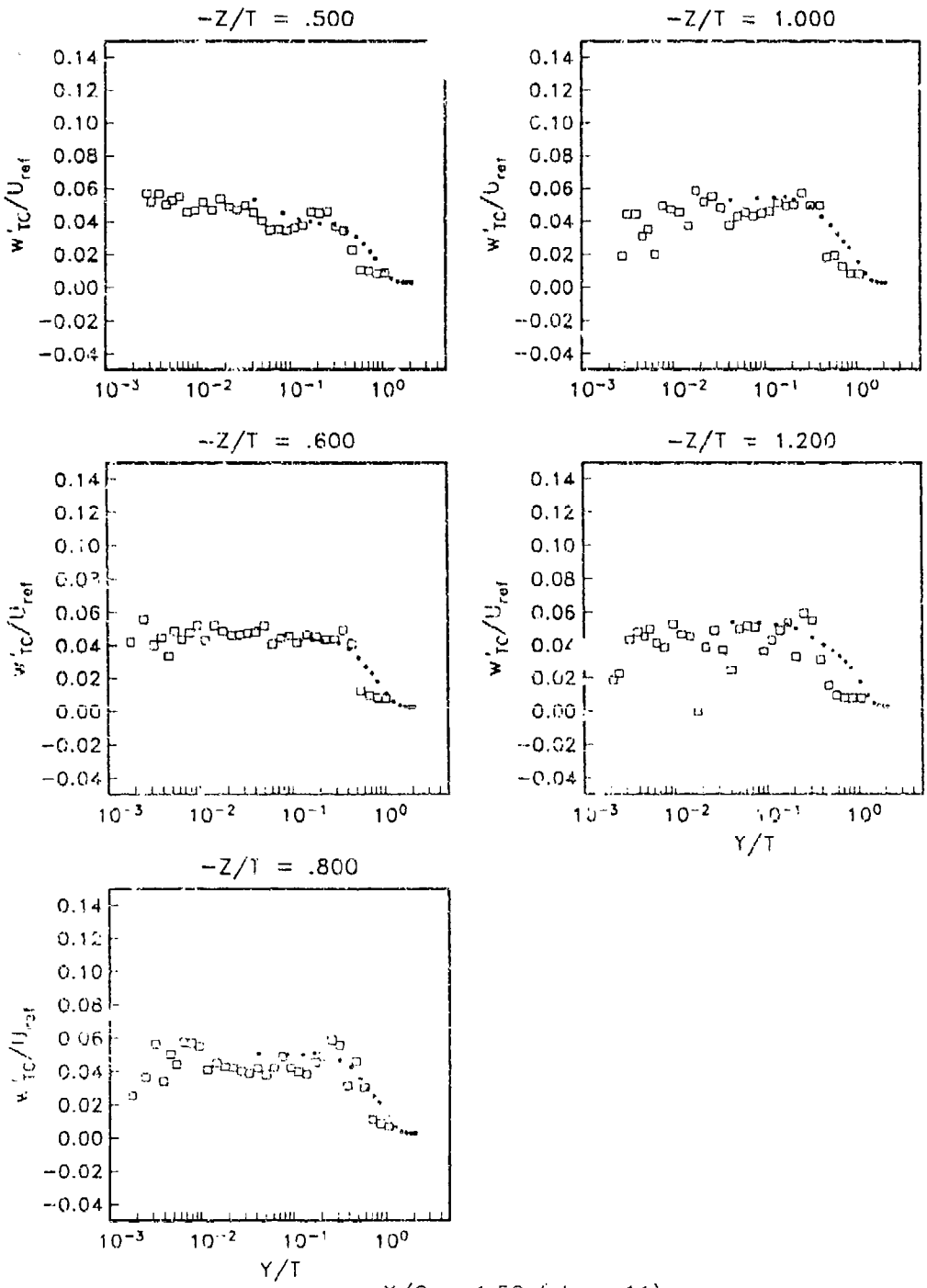

Figure 4.66. Profiles of w'_{TC}/U_{ref}, Plane 11

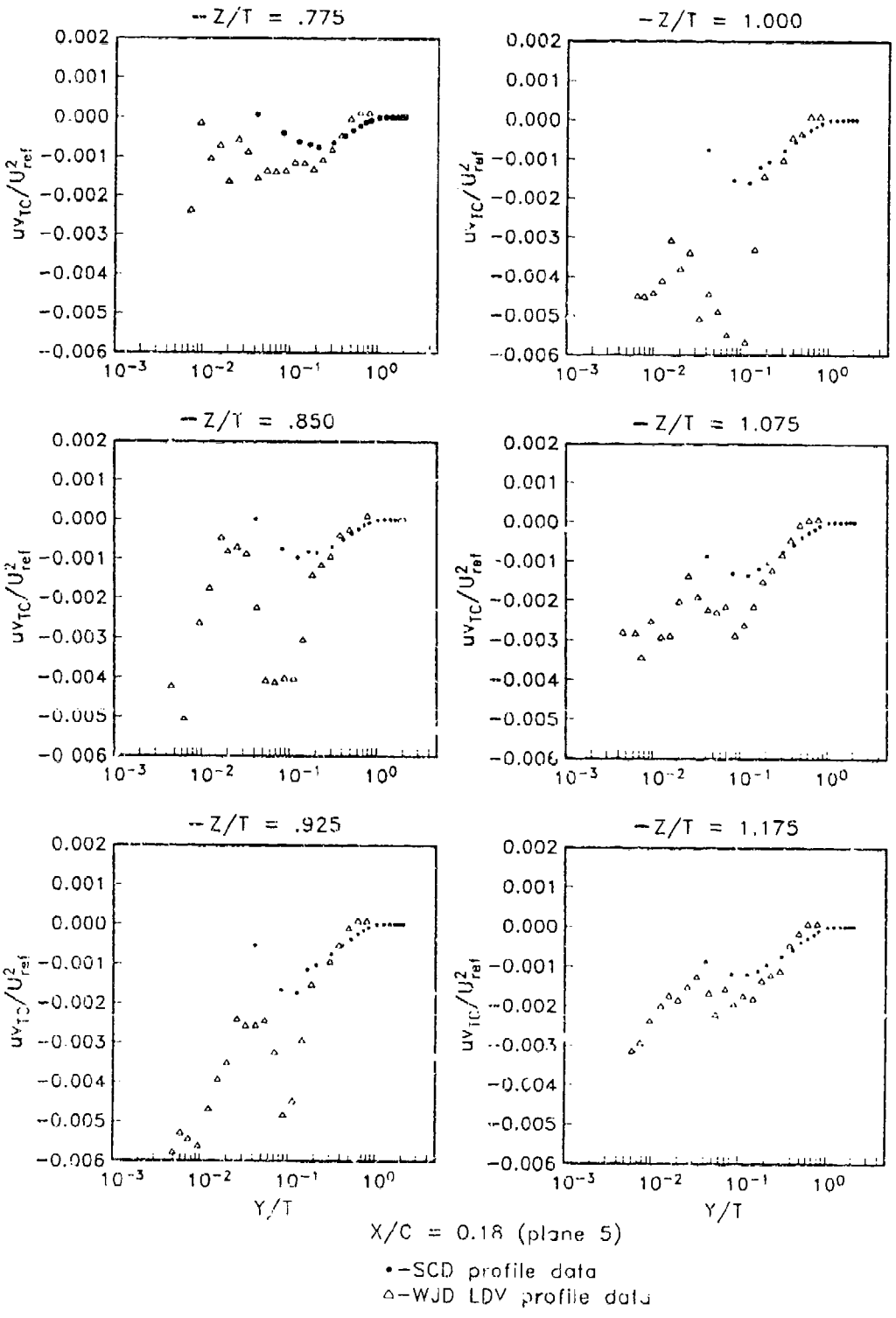

Figure 4.67. Profiles of $\tilde{u}\tilde{v}_{TC}/(U_{ref})^2$, Plane 5

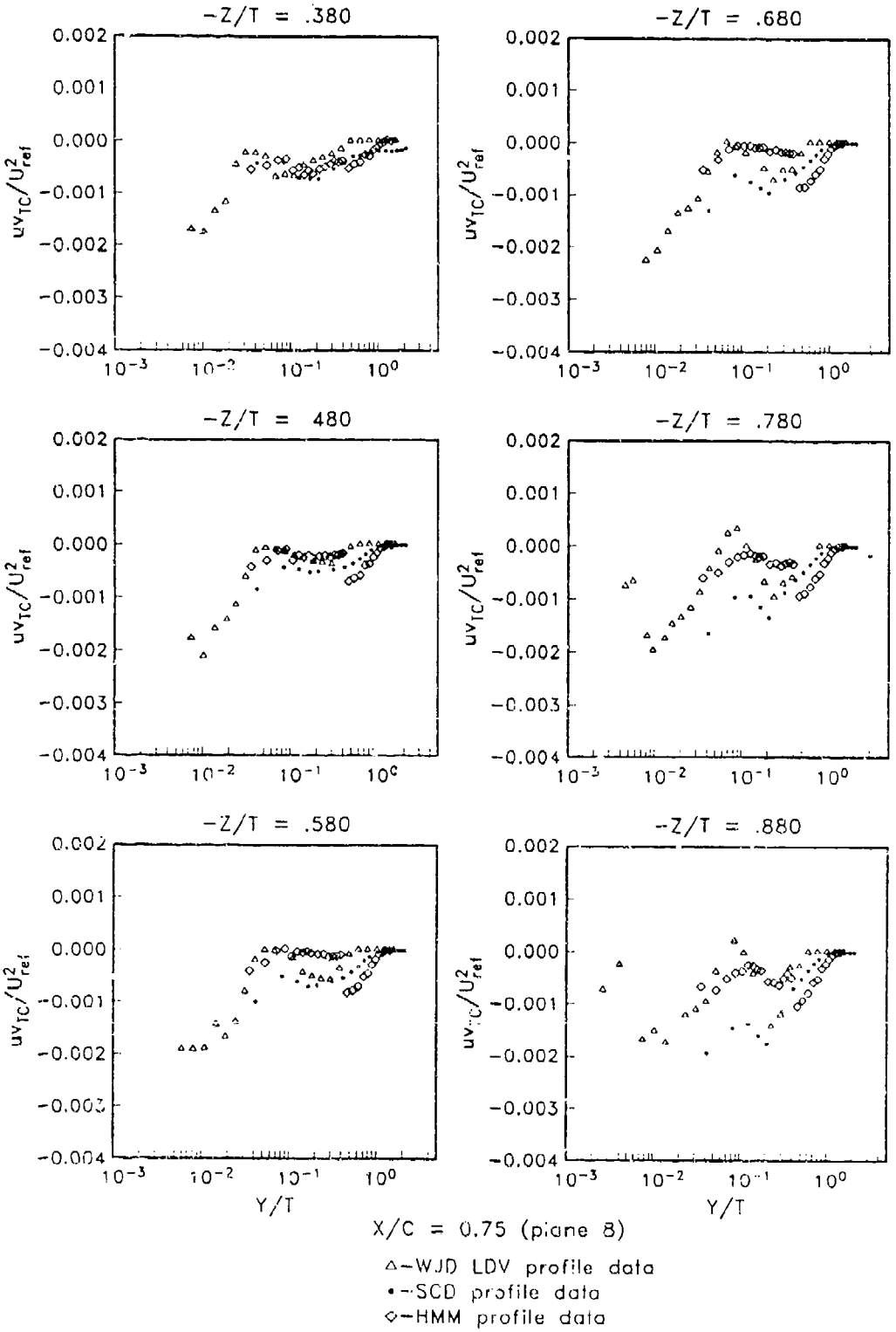

Figure 4.63. Profiles of $\bar{u}\bar{v}_{TC}/(U_{ref})^2$, Plane 8

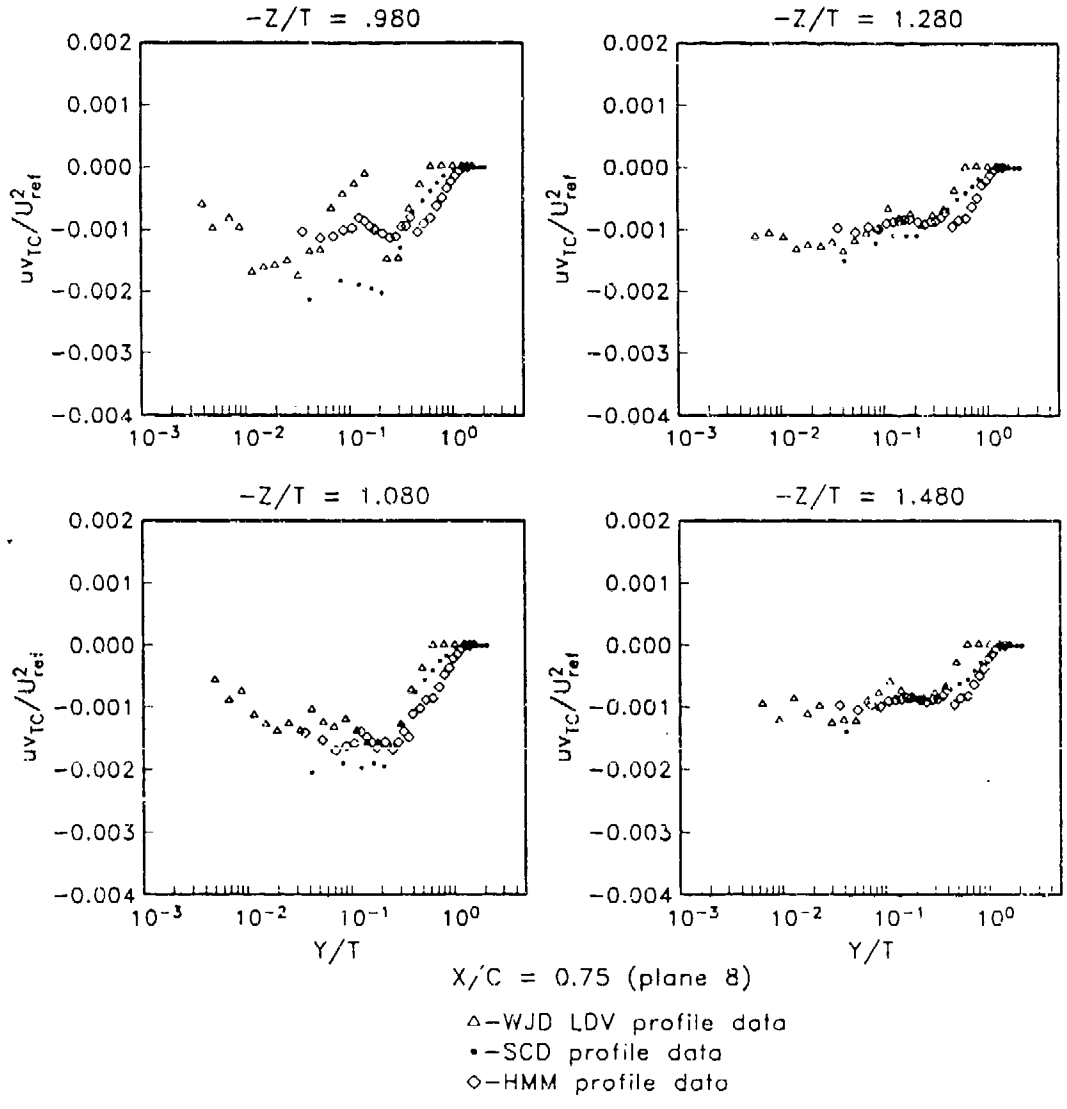

Figure 4.68. (cont.). Profiles of $\bar{u}\bar{v}_{TC}/(U_{ref})^2$, Plane 8

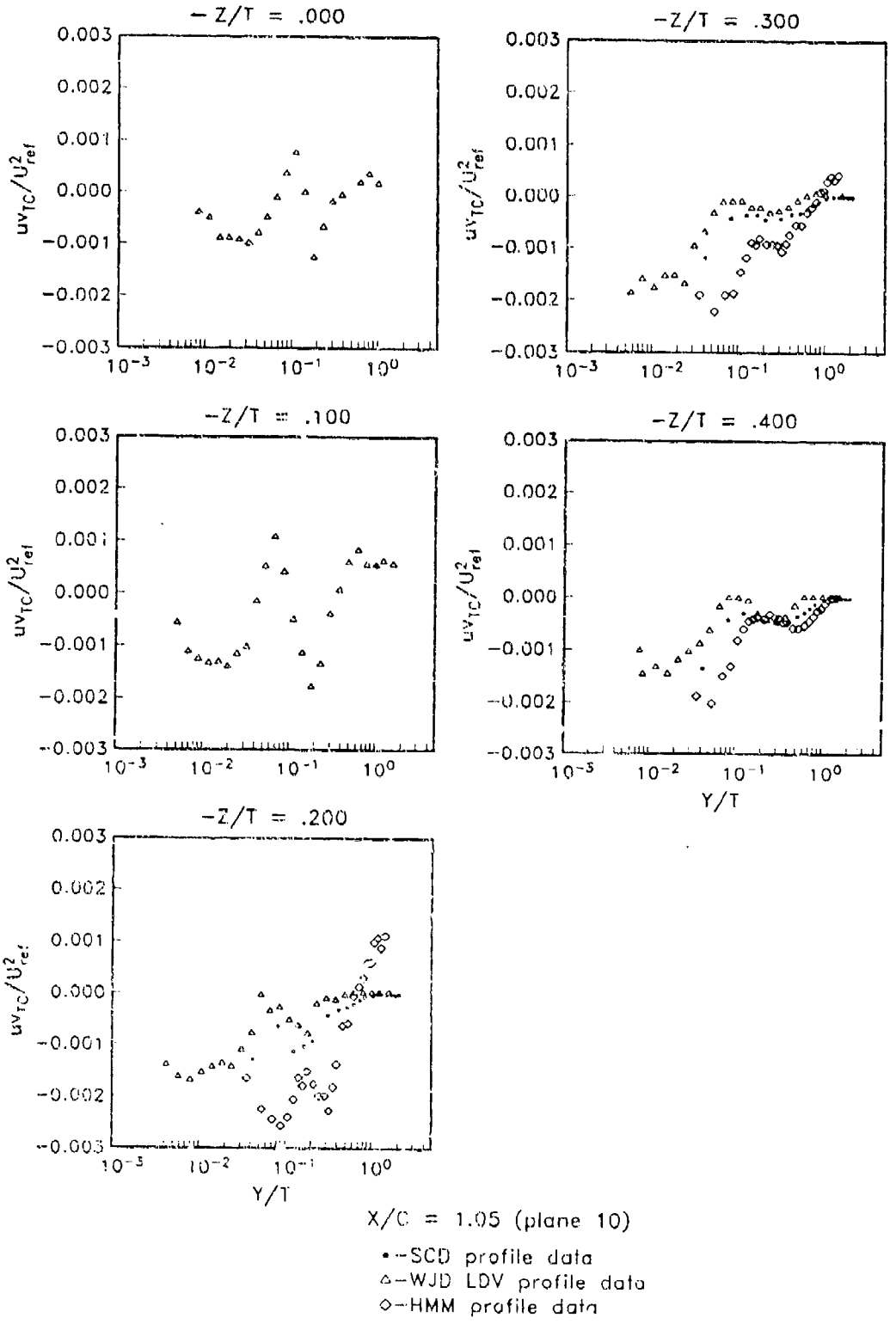

Figure 4.69. Profiles of $\overline{uv}_{TC}/(U_{ref})^2$, Plane 10

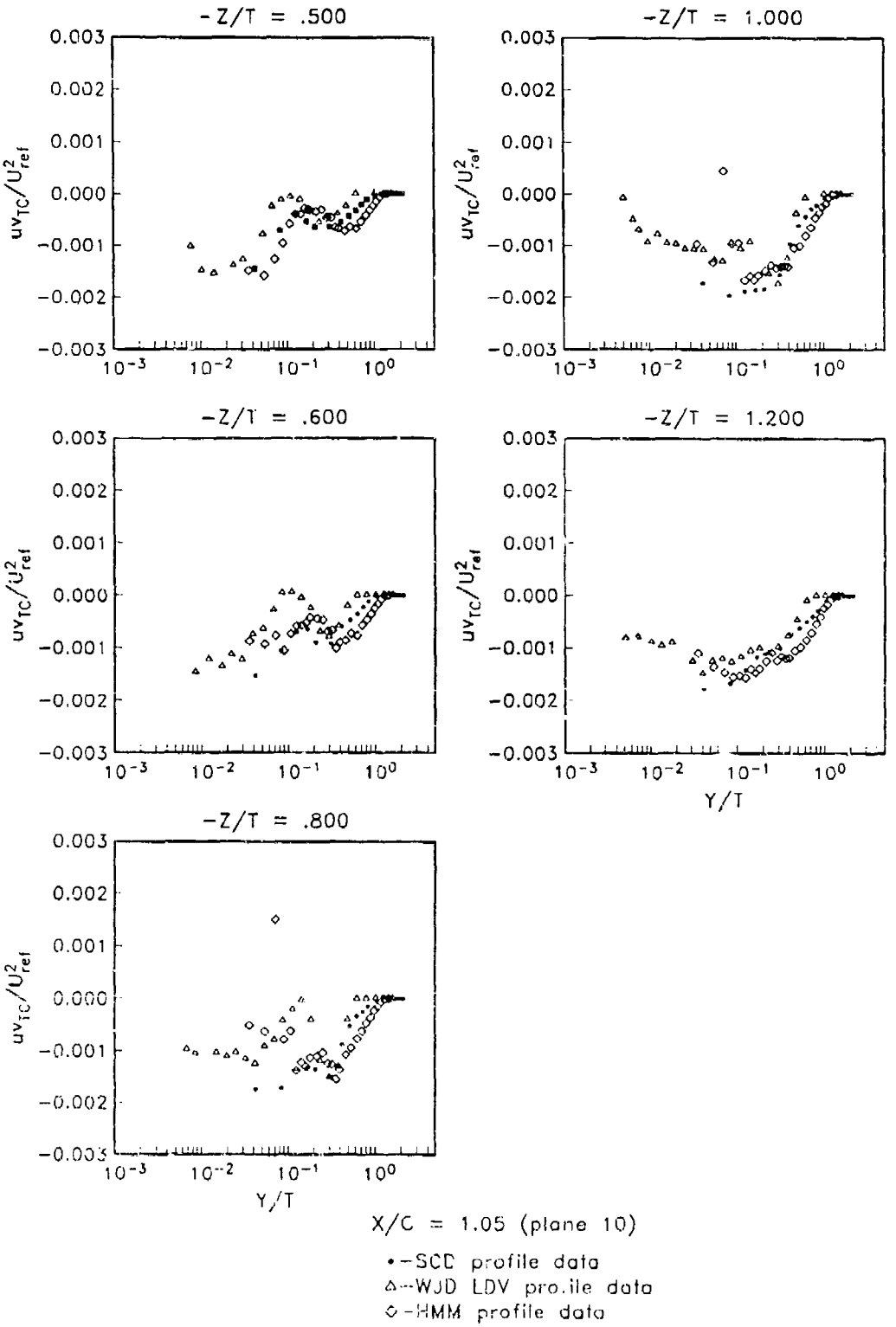

Figure 4.69. (cont.). Profiles of $\overline{uv}_{TC}/(U_{ref})^2$, Plane 10

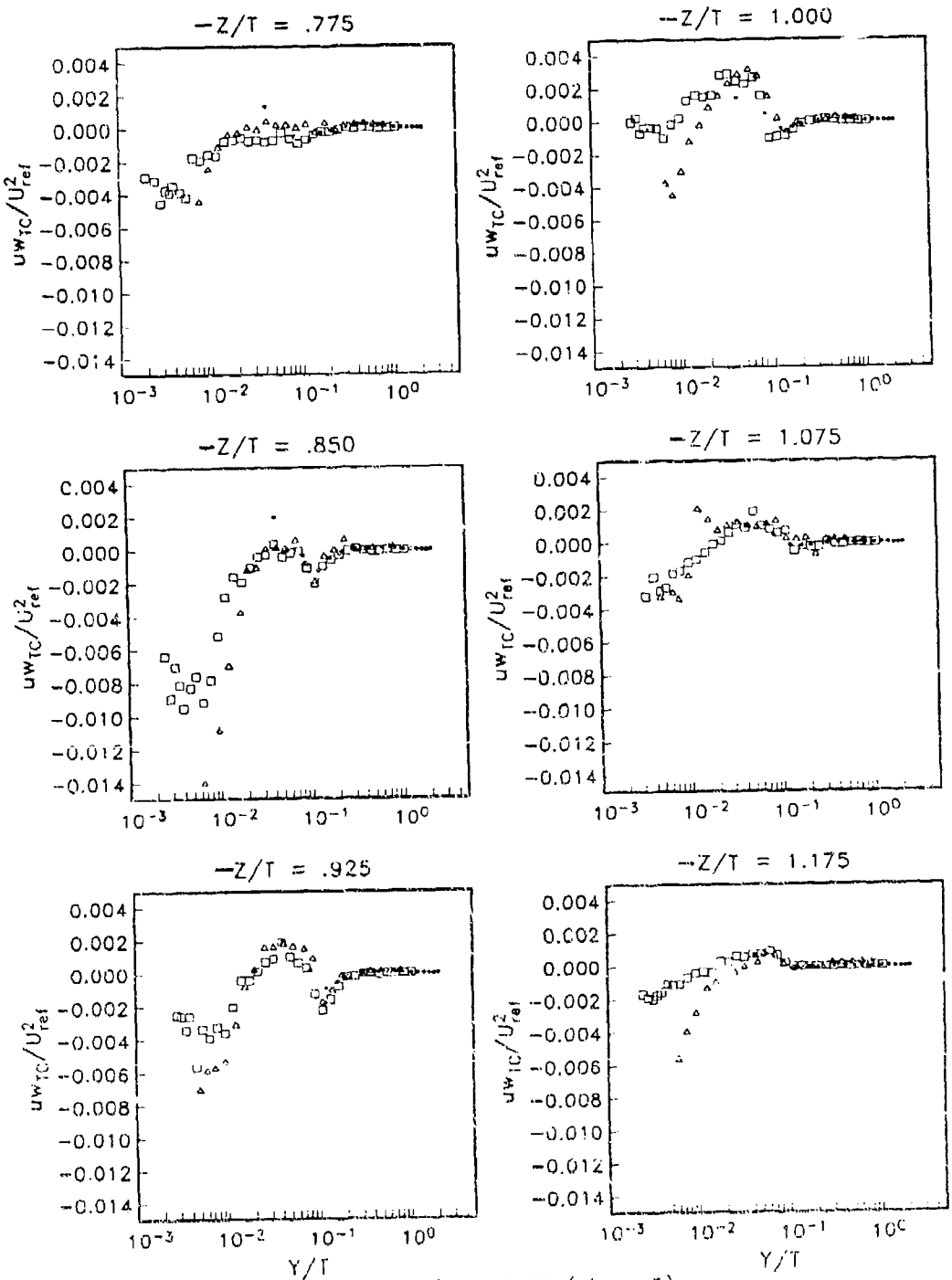

Figure 4.70. Profiles of $\overline{uw}_{TC}/(U_{ref})^2$, Plane 5

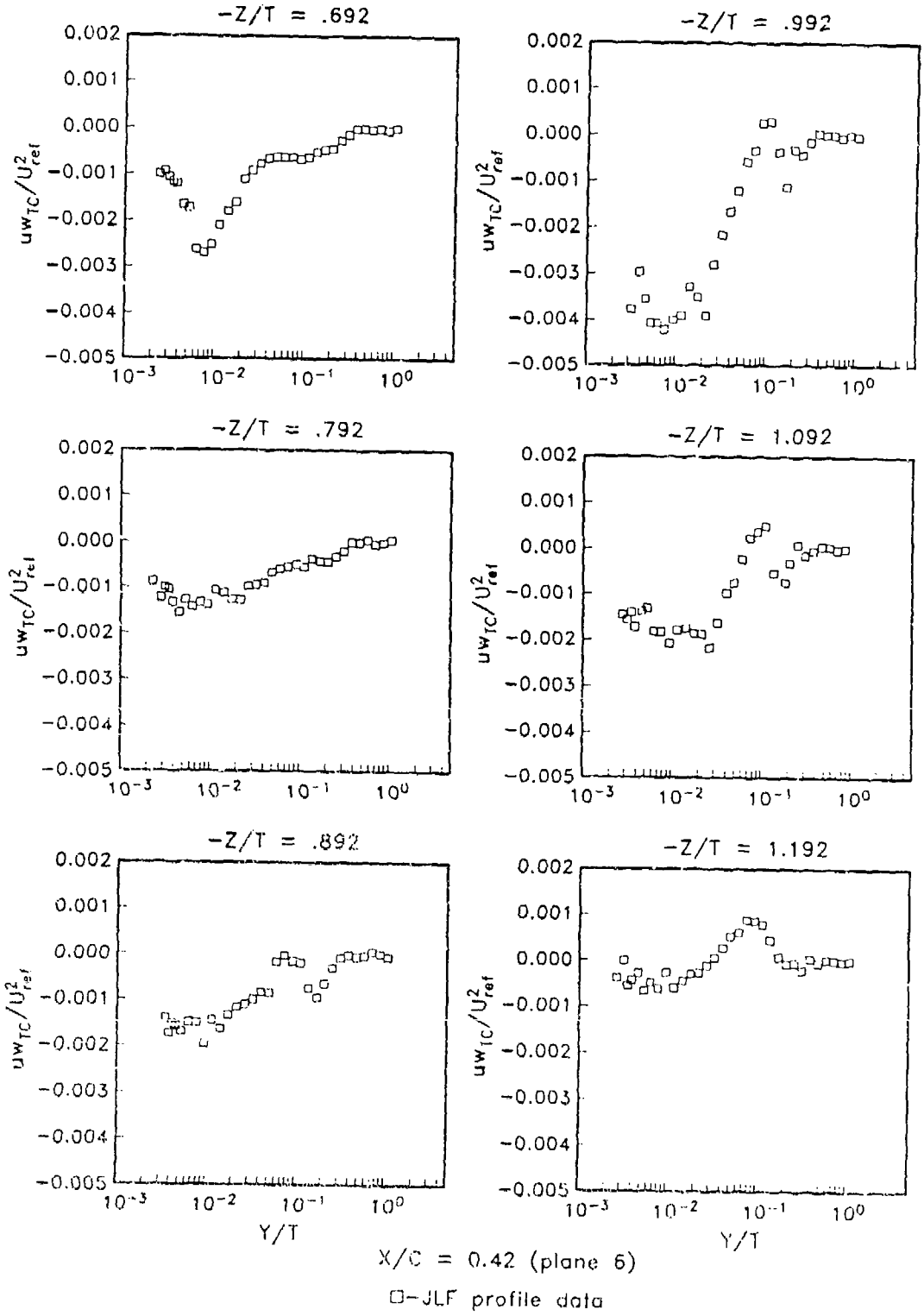

Figure 4.71. Profiles of $\overline{uw}_{TC}/(U_{ref})^2$, Plane 6

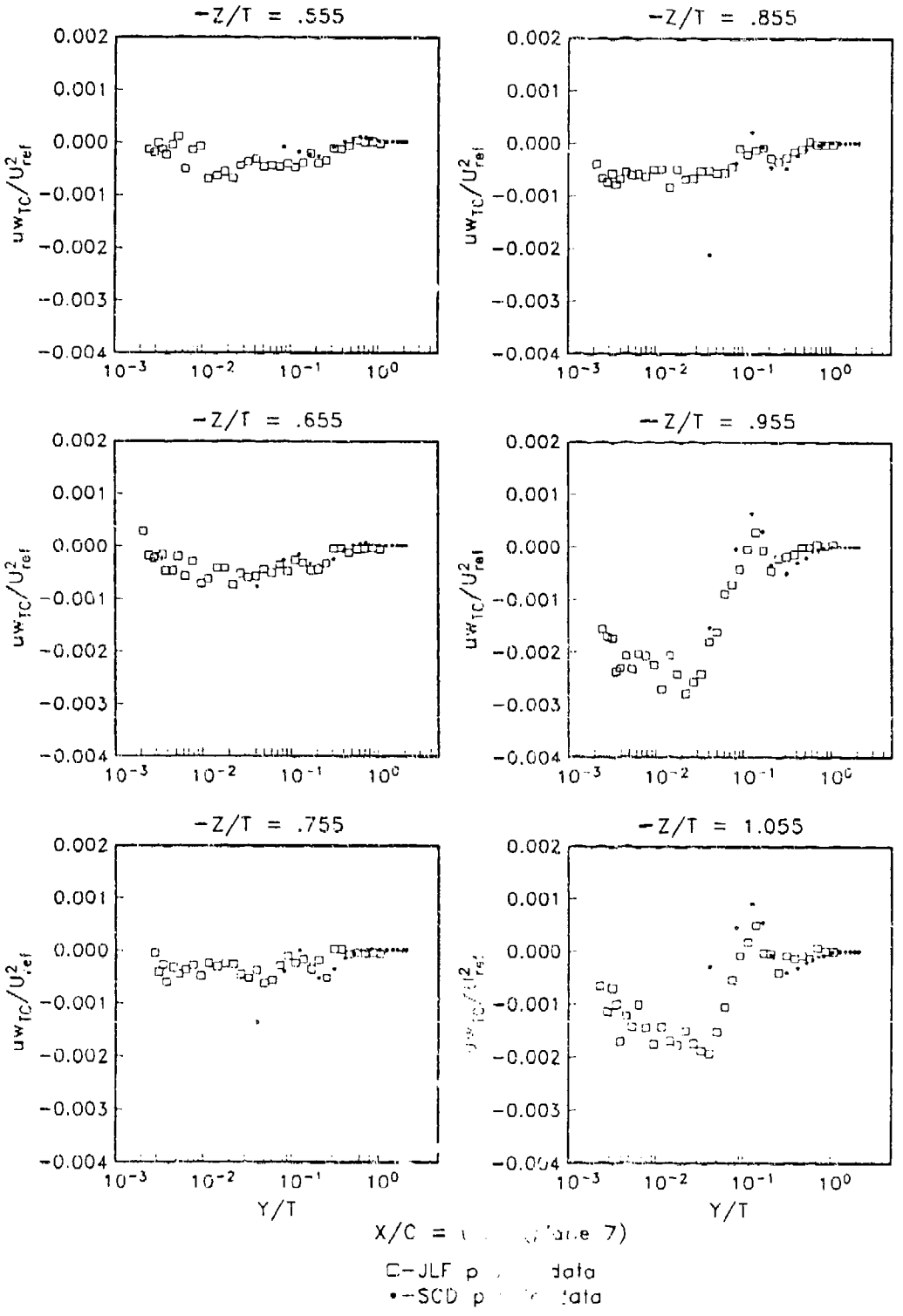

Figure 4.72. Profiles of $\overline{uw}_{TC}/(U_{ref})^2$, Plane 7

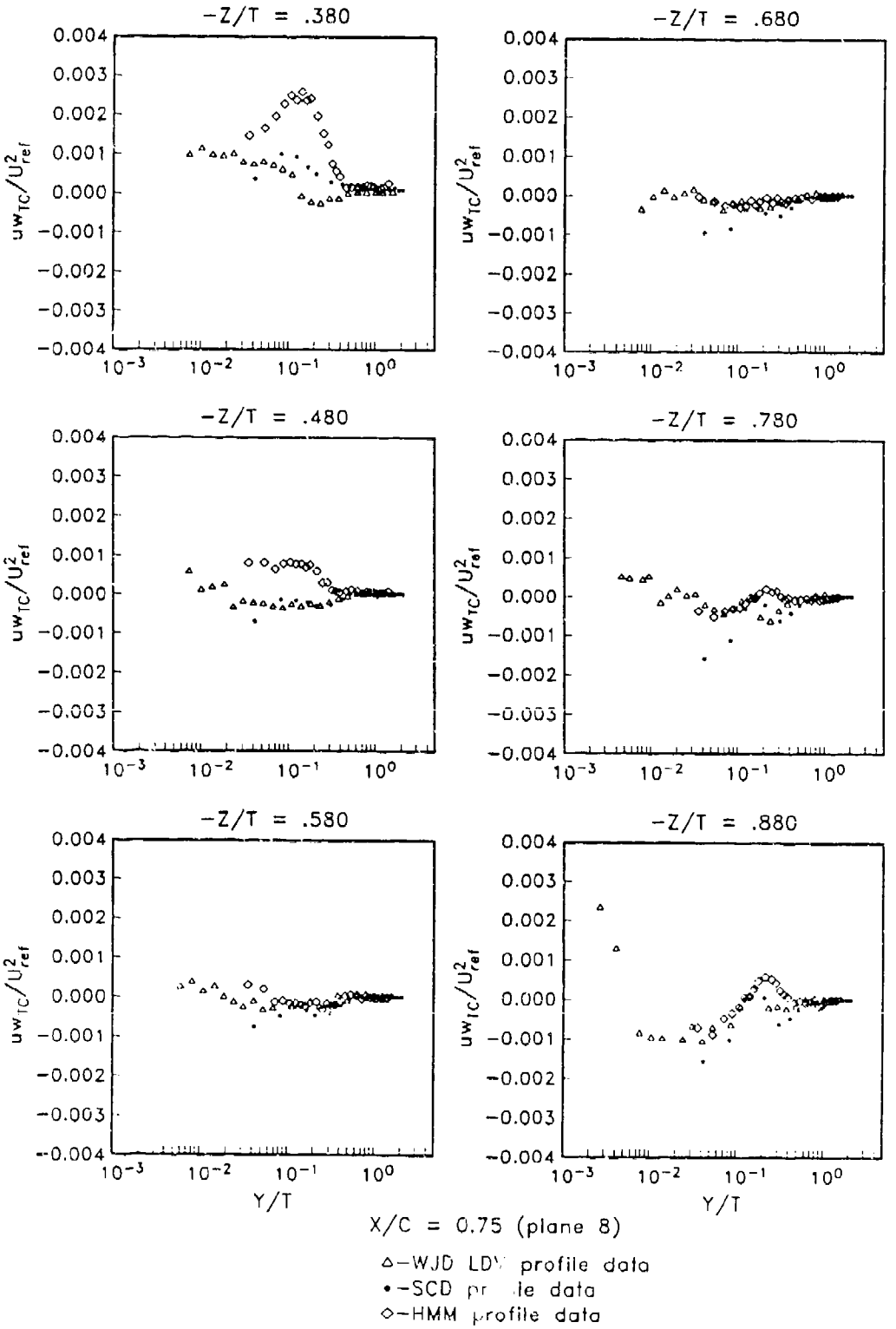

Figure 4.73. Profiles of $\overline{uw}_{TC}/(U_{ref})^2$, Plane 8

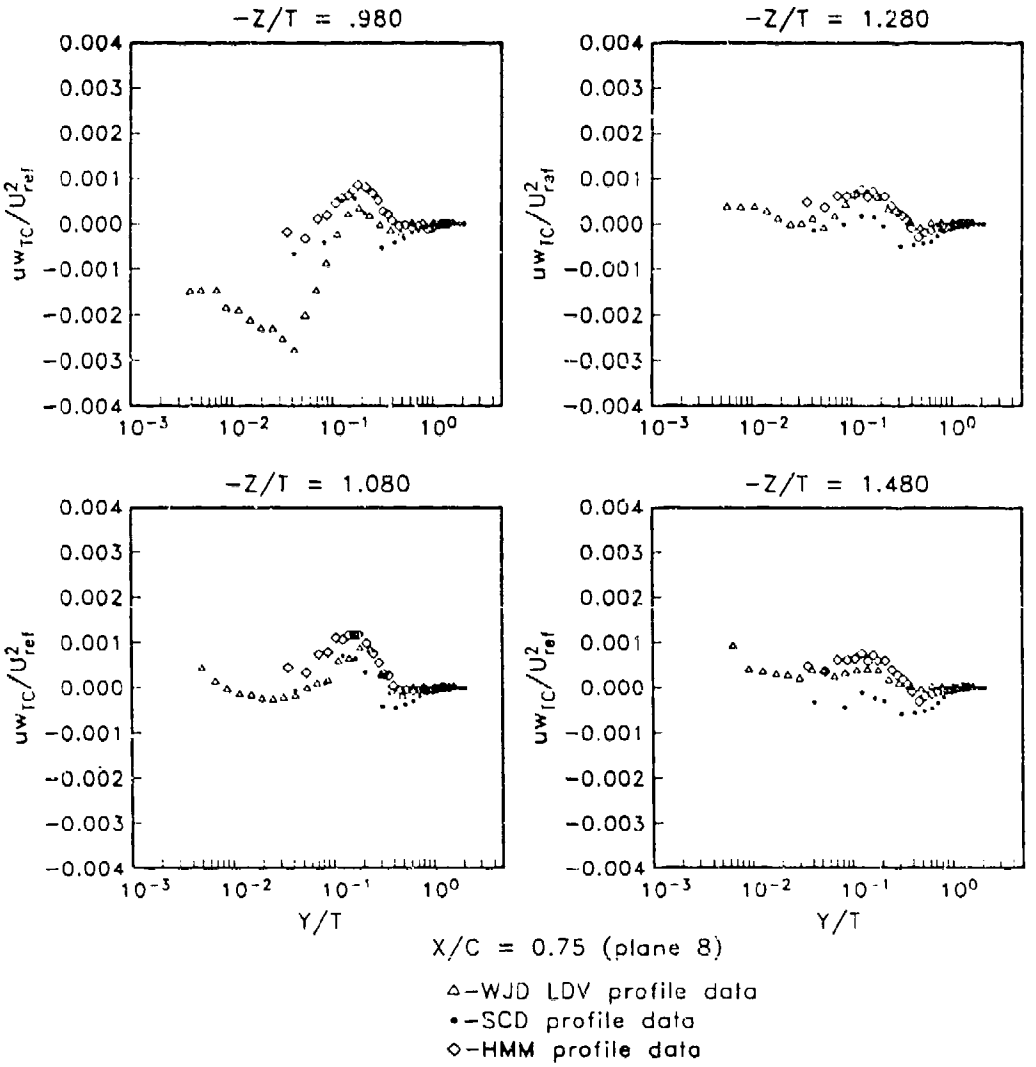

Figure 4 73. (cont.). Profiles of $\overline{uw}_{TC}/(U_{ref})^2$, Plane 8

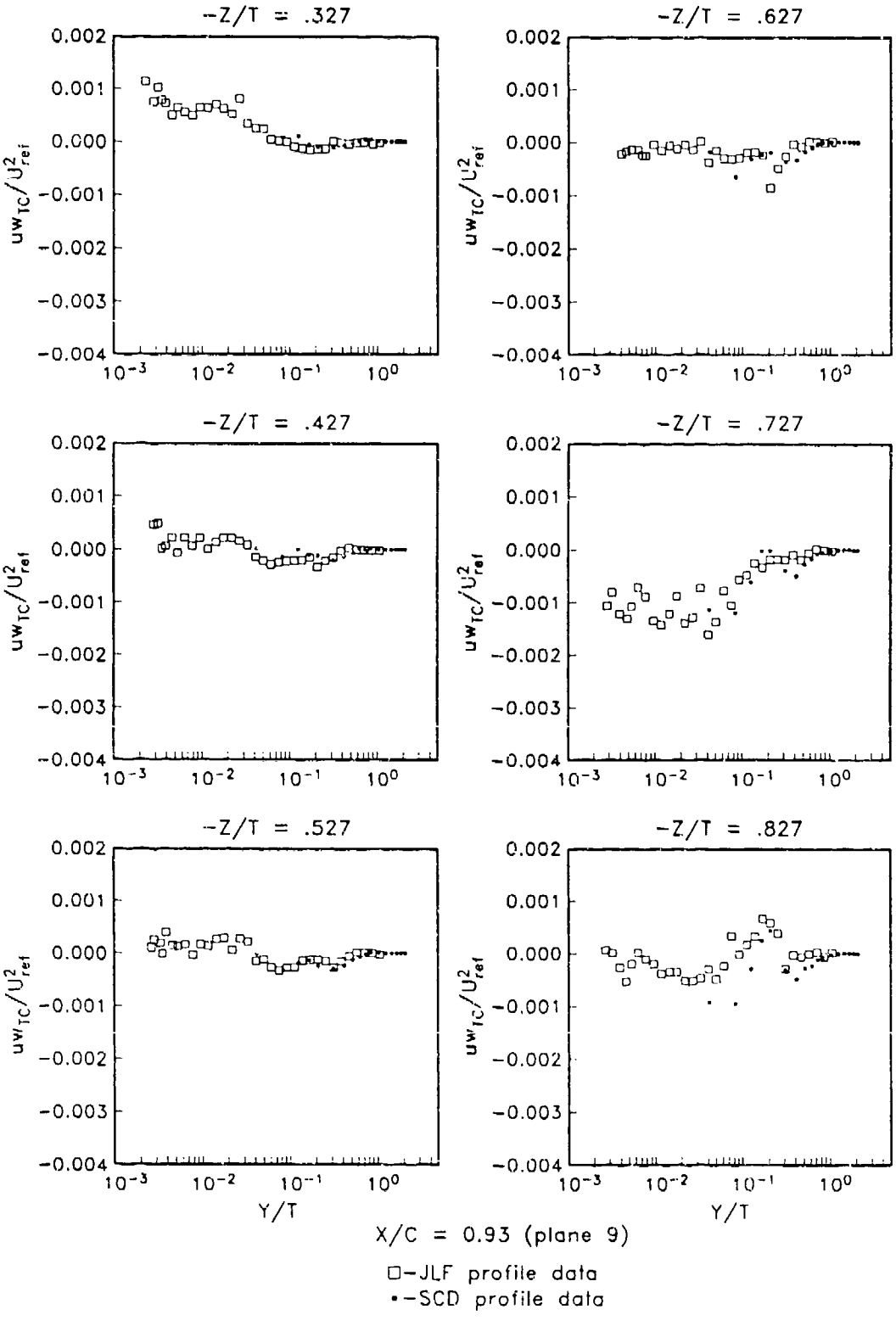

Figure 4.74. Profiles of $\overline{uw}_{TC}/(U_{ref})^2$, Plane 9

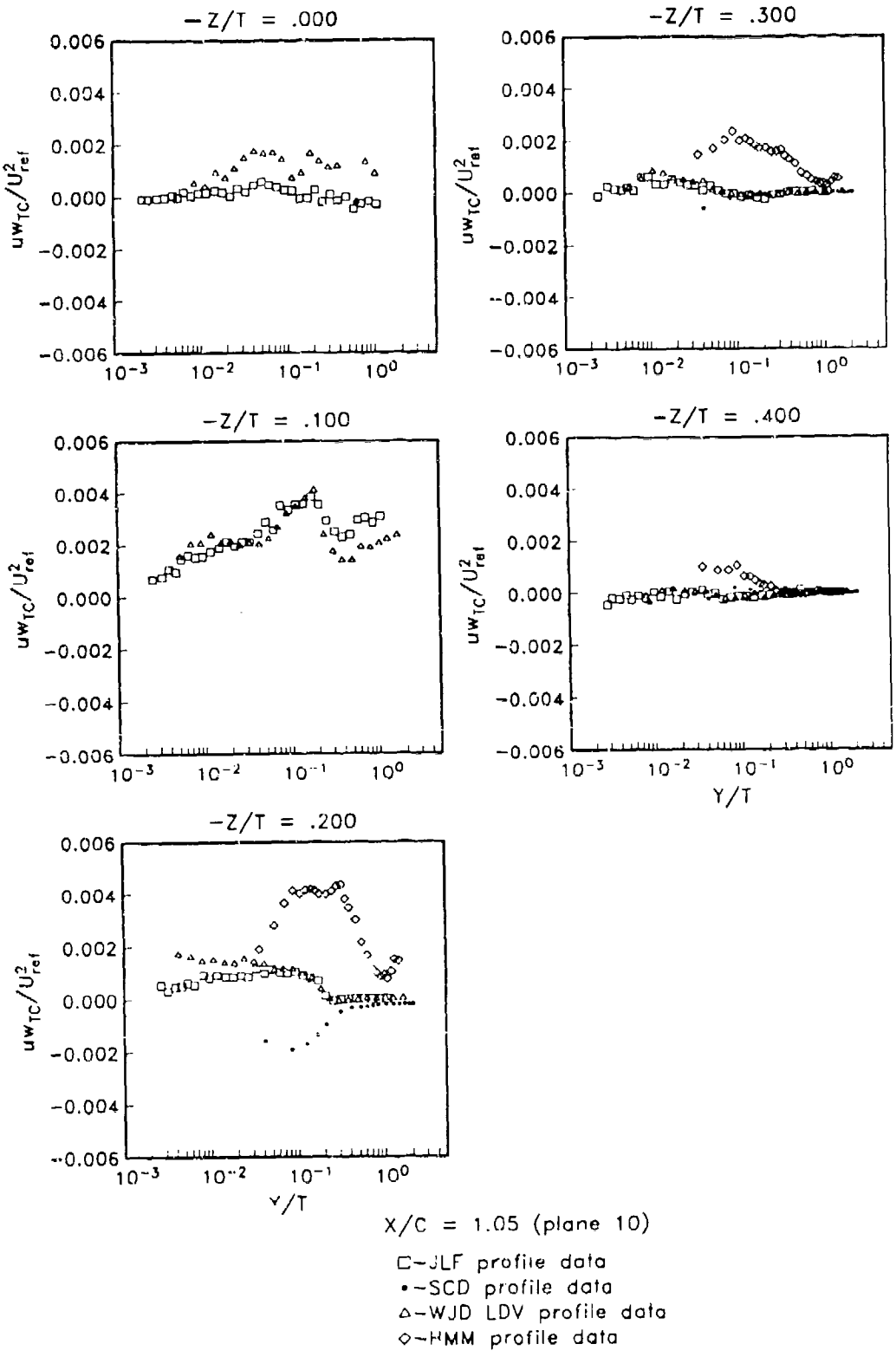

Figure 4.75. Profiles of $\overline{uw}_{TC}/(U_{ref})^2$, Plane 10

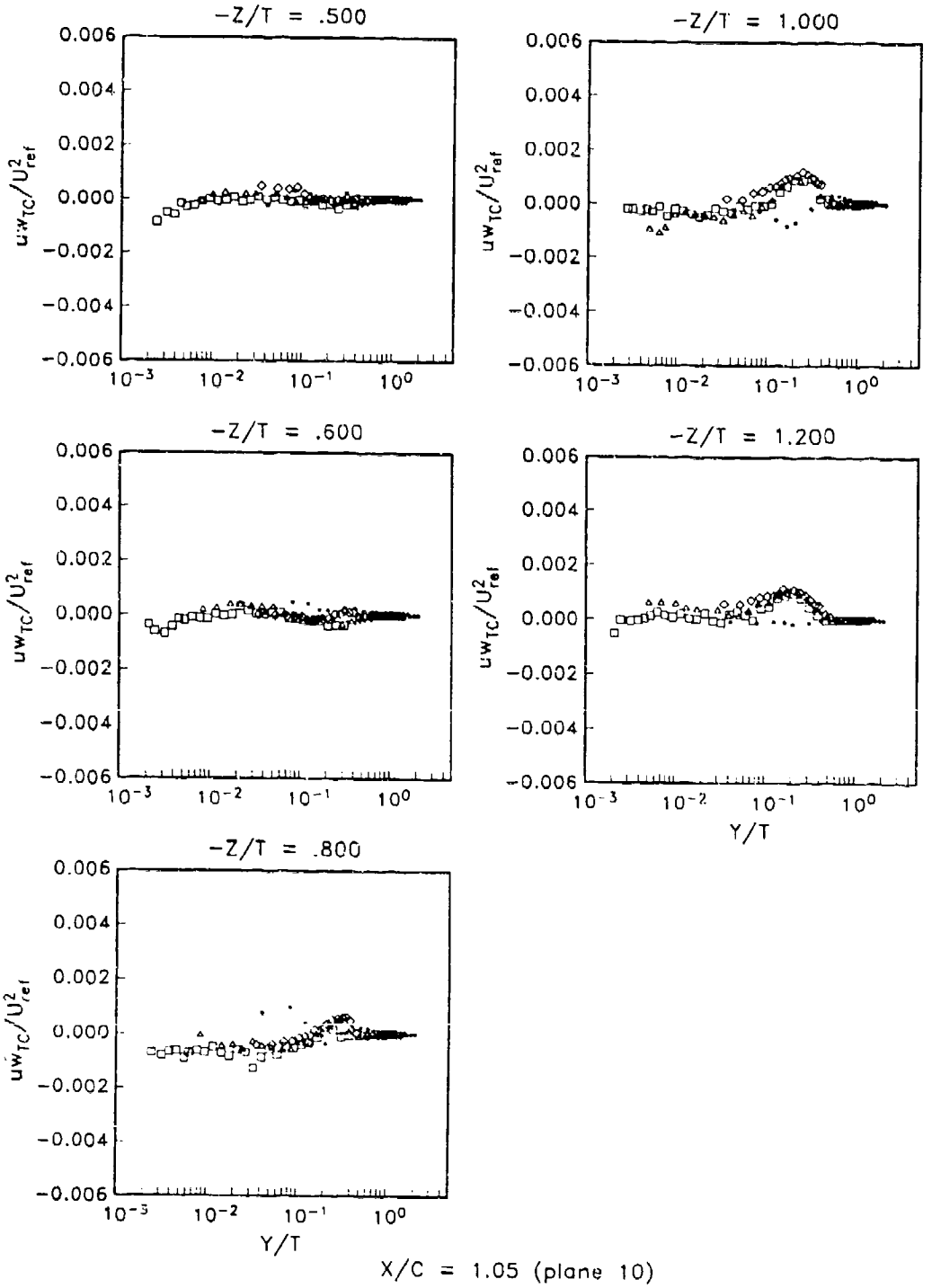

Figure 4.75. (cont.). Profiles of $\overline{uw}_{TC}/(U_{ref})^2$, Plane 10

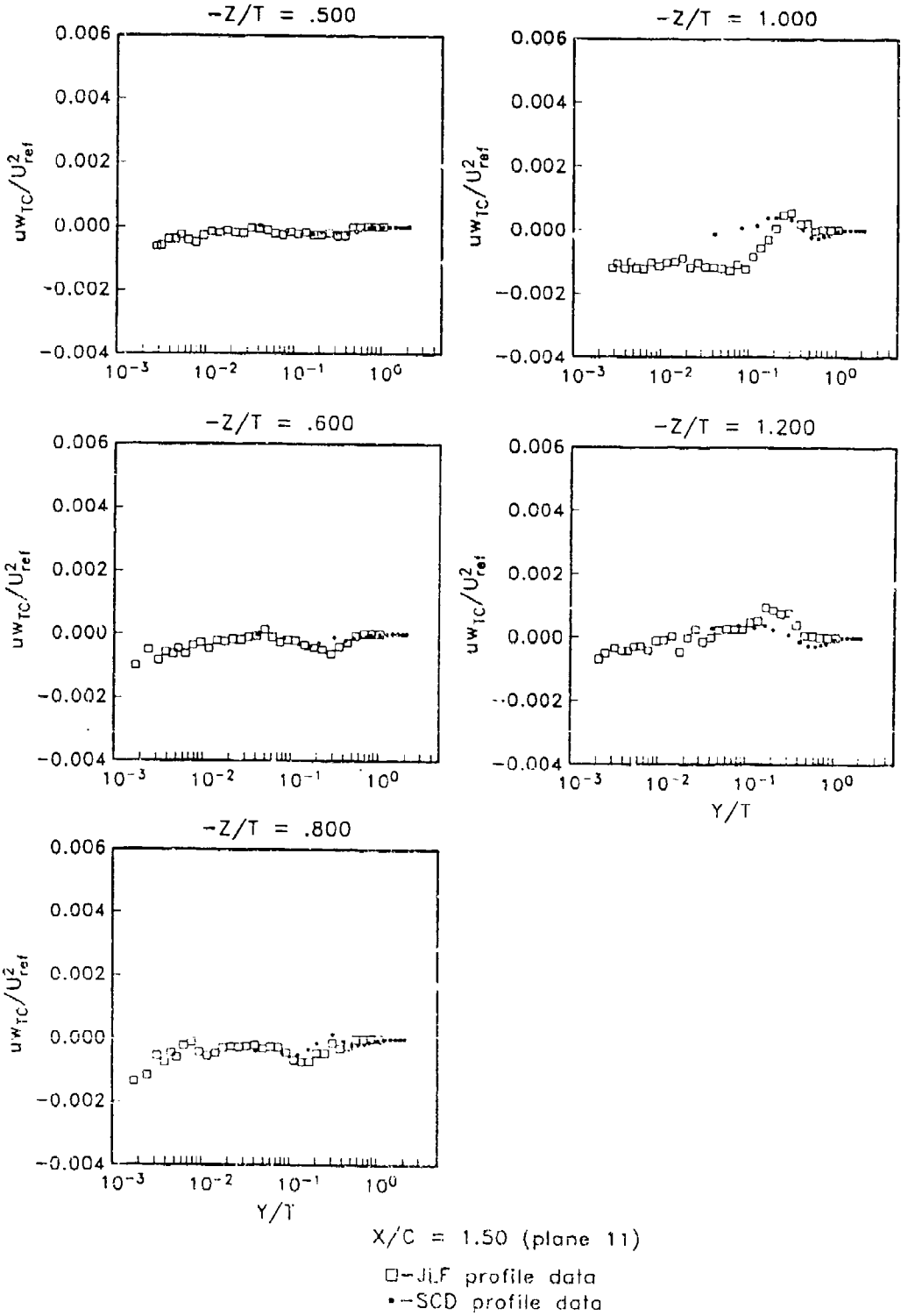

Figure 4.76. Profiles of $\overline{uw}_{TC}/(U_{ref})^2$, Plane 11

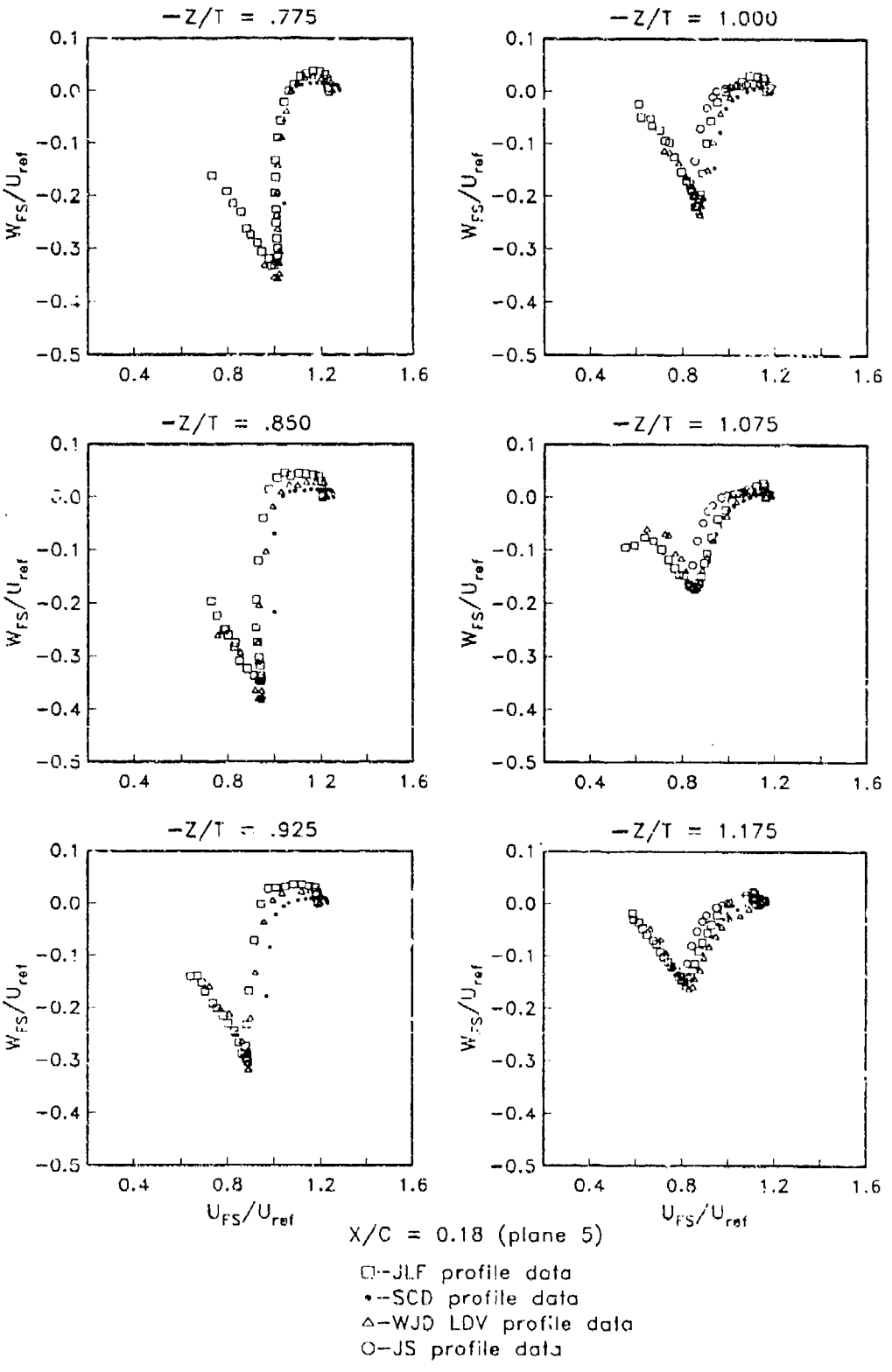

Figure 4.77. Boundary Layer Hodograph Plots, Plane 5

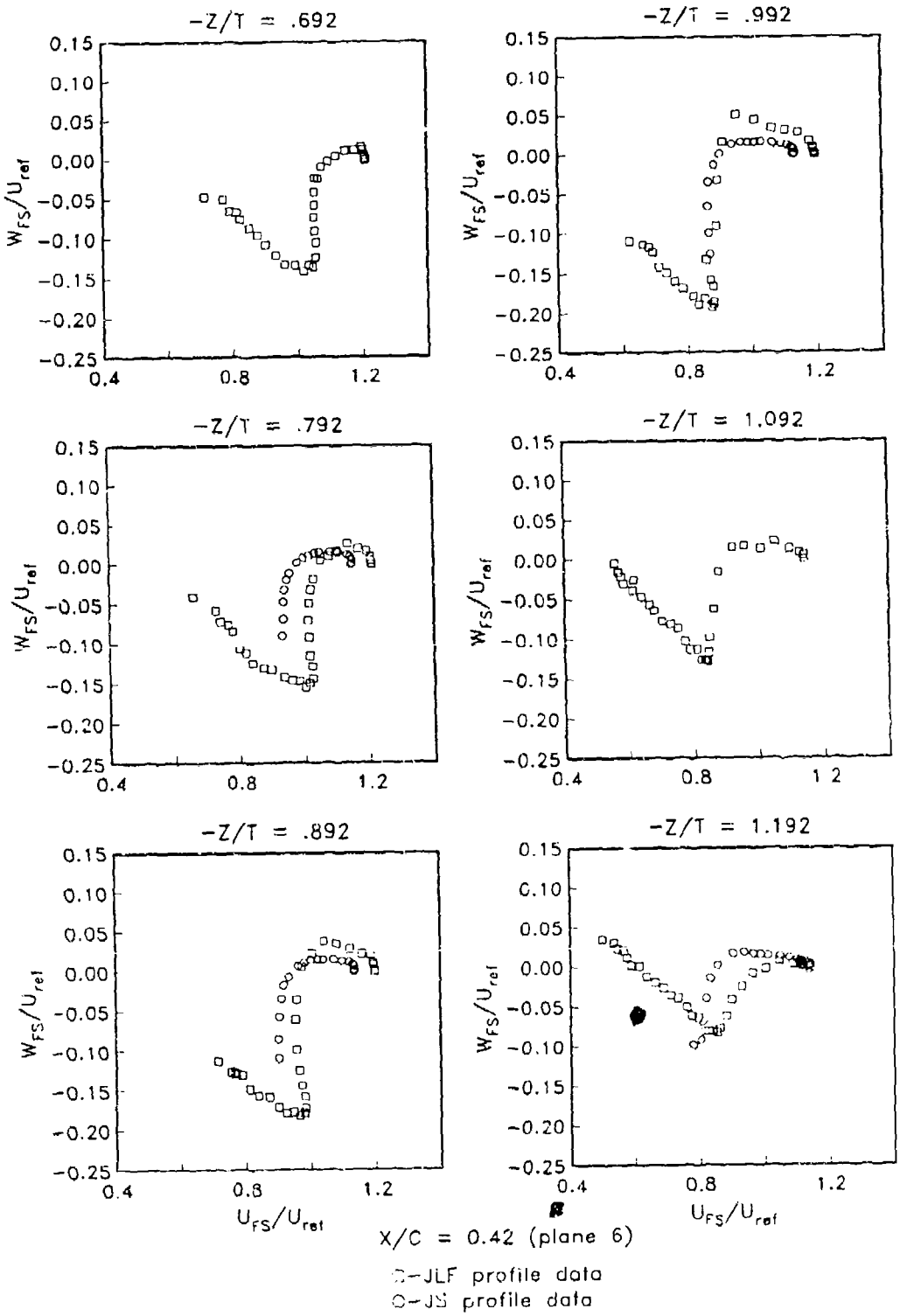

Figure 4.78. Boundary Layer Hodograph Plots, Plane 6

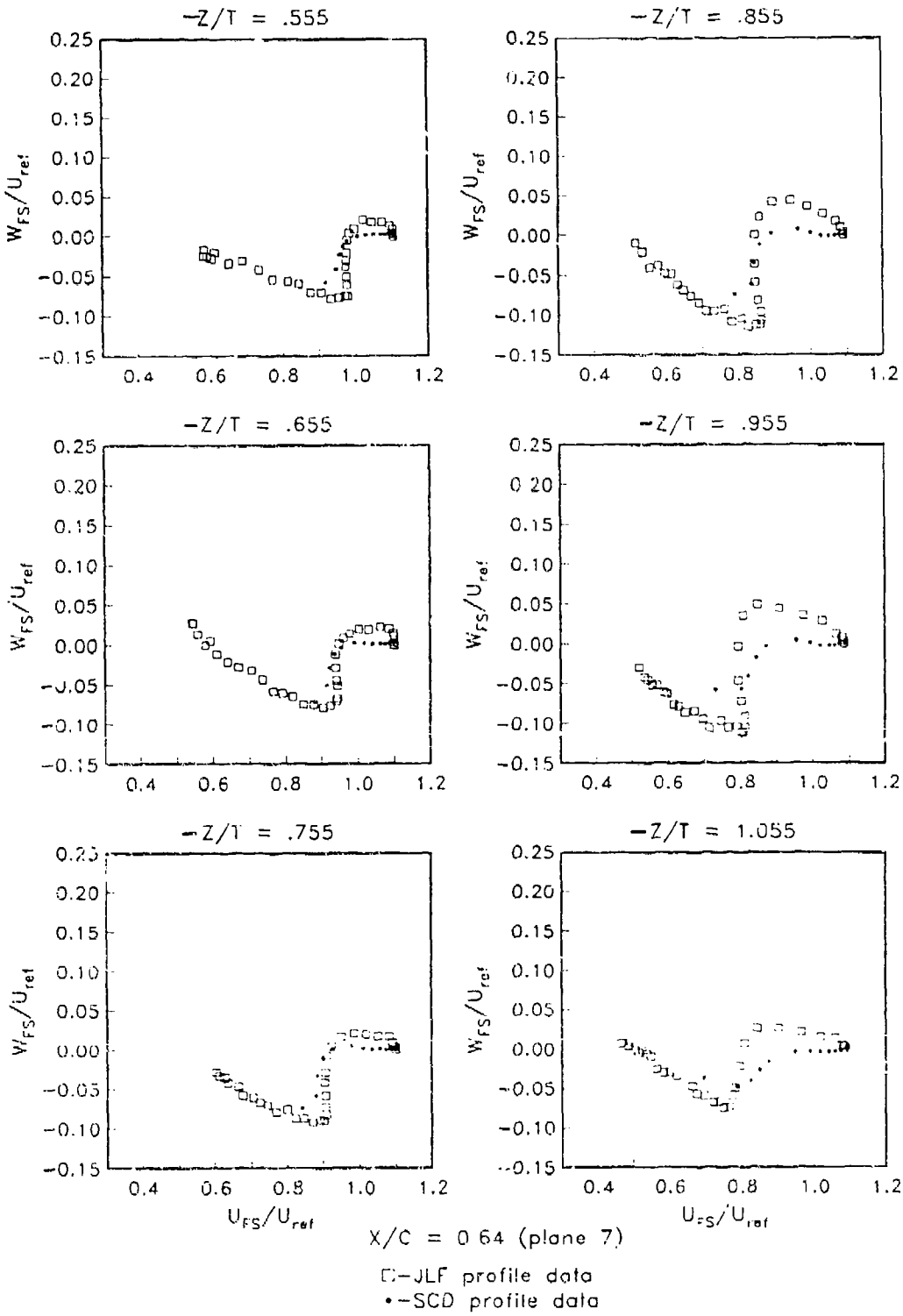

Figure 4.79. Boundary Layer Hodograph Plots, Plane 7

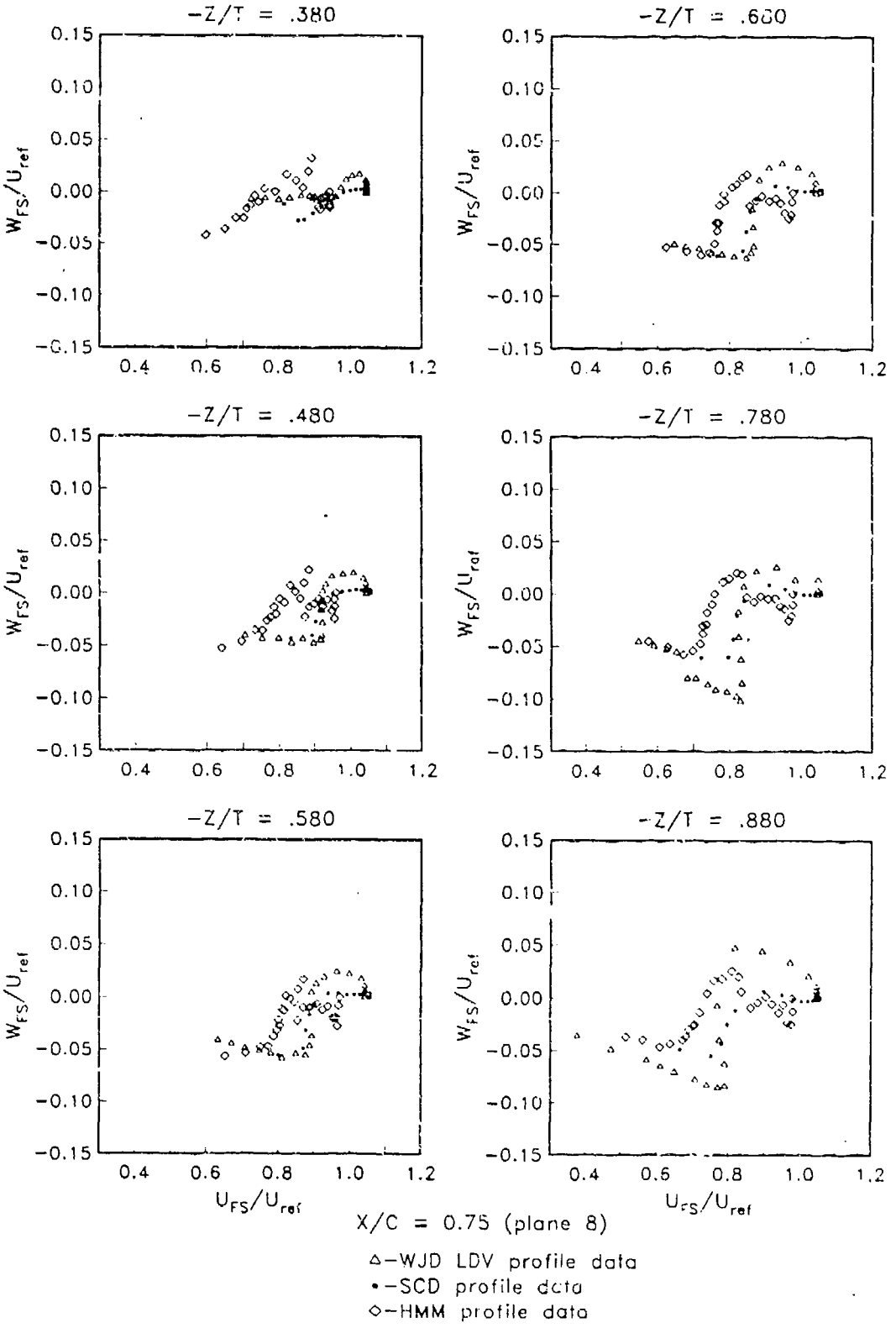

Figure 4.80. Boundary Layer Hodograph Plots, Plane 8

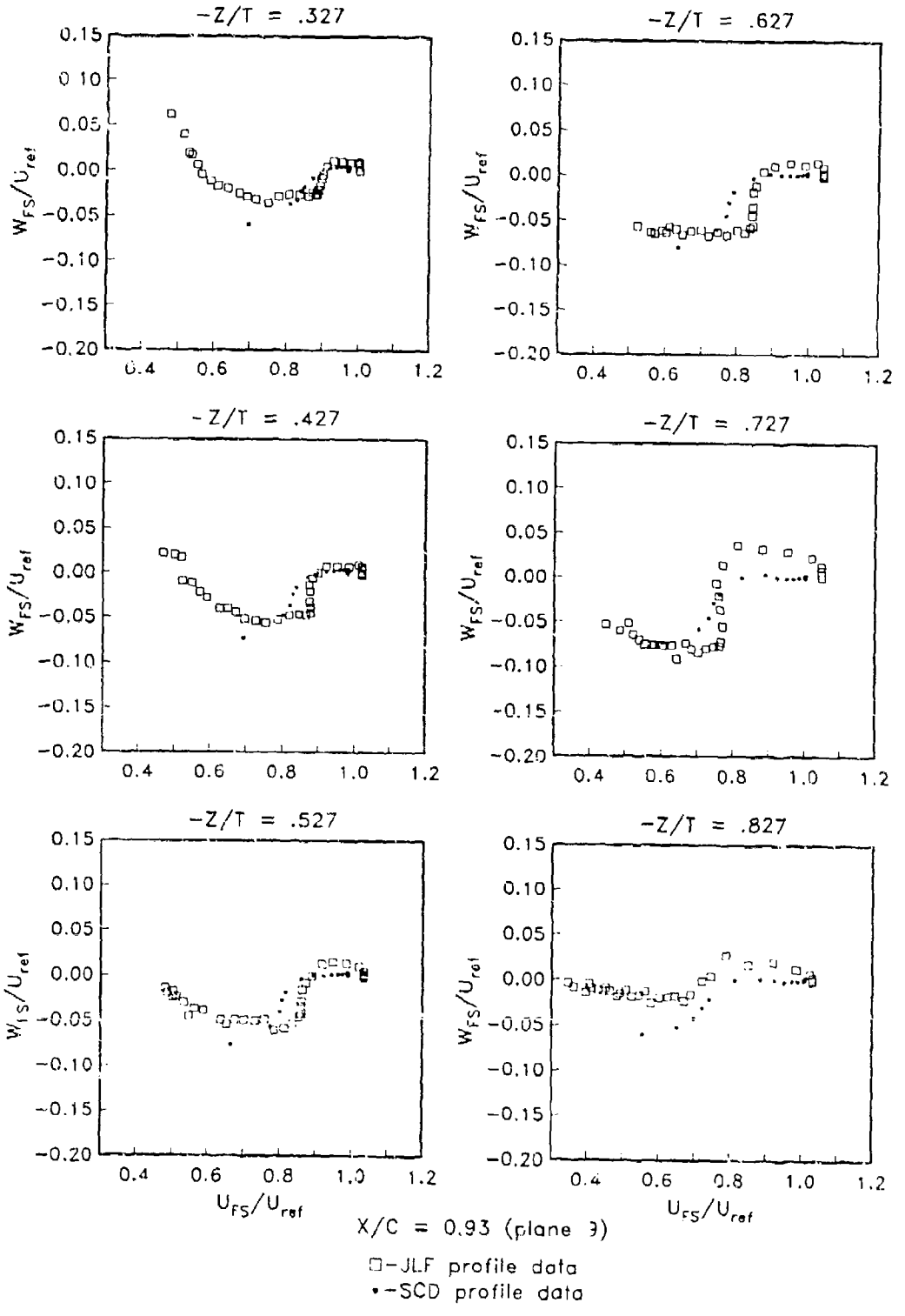

Figure 4.81. Boundary Layer Hodograph Plots, Plane 9

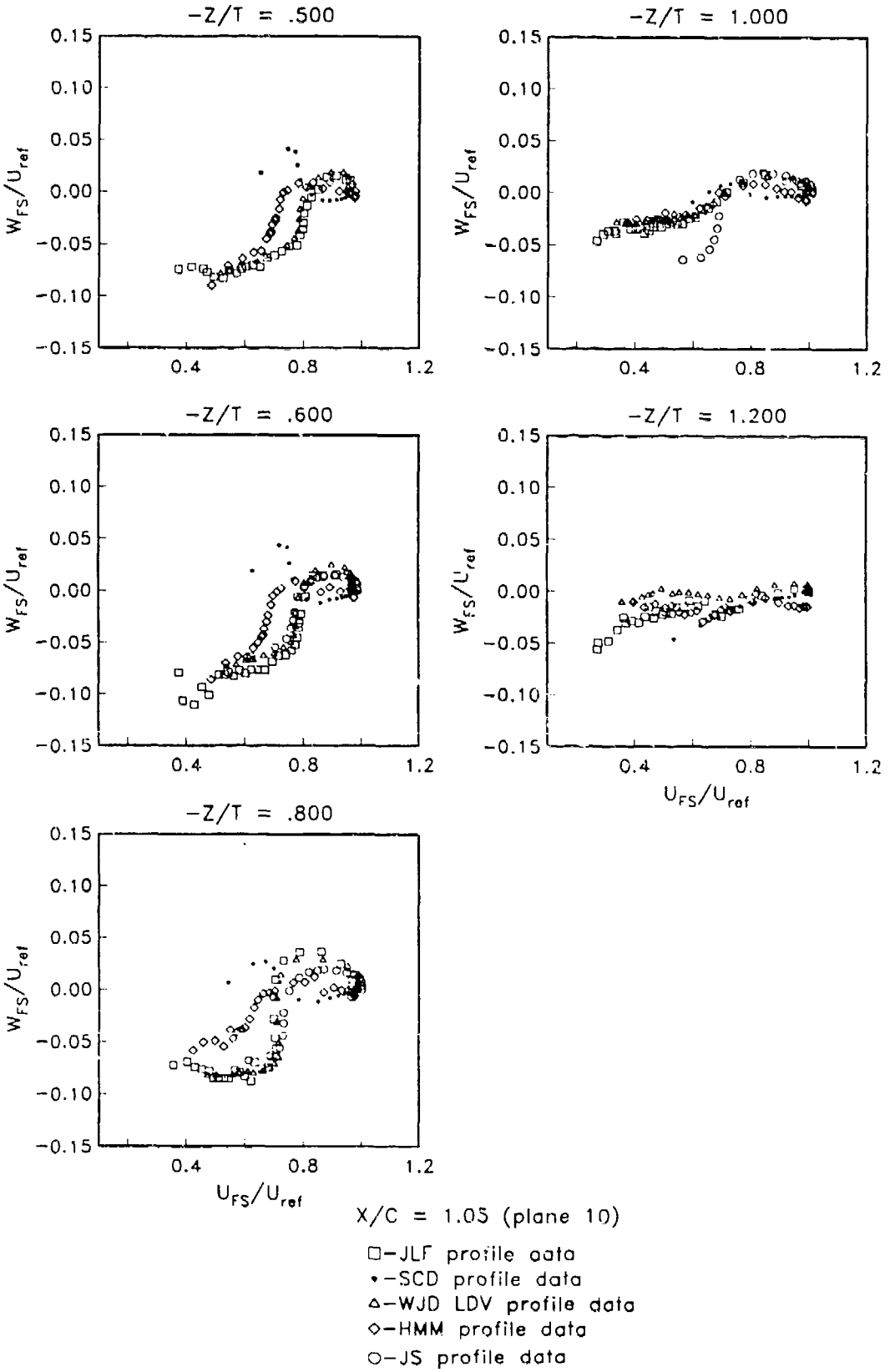

Figure 4.82. Boundary Layer Hodograph Plots, Plane 10

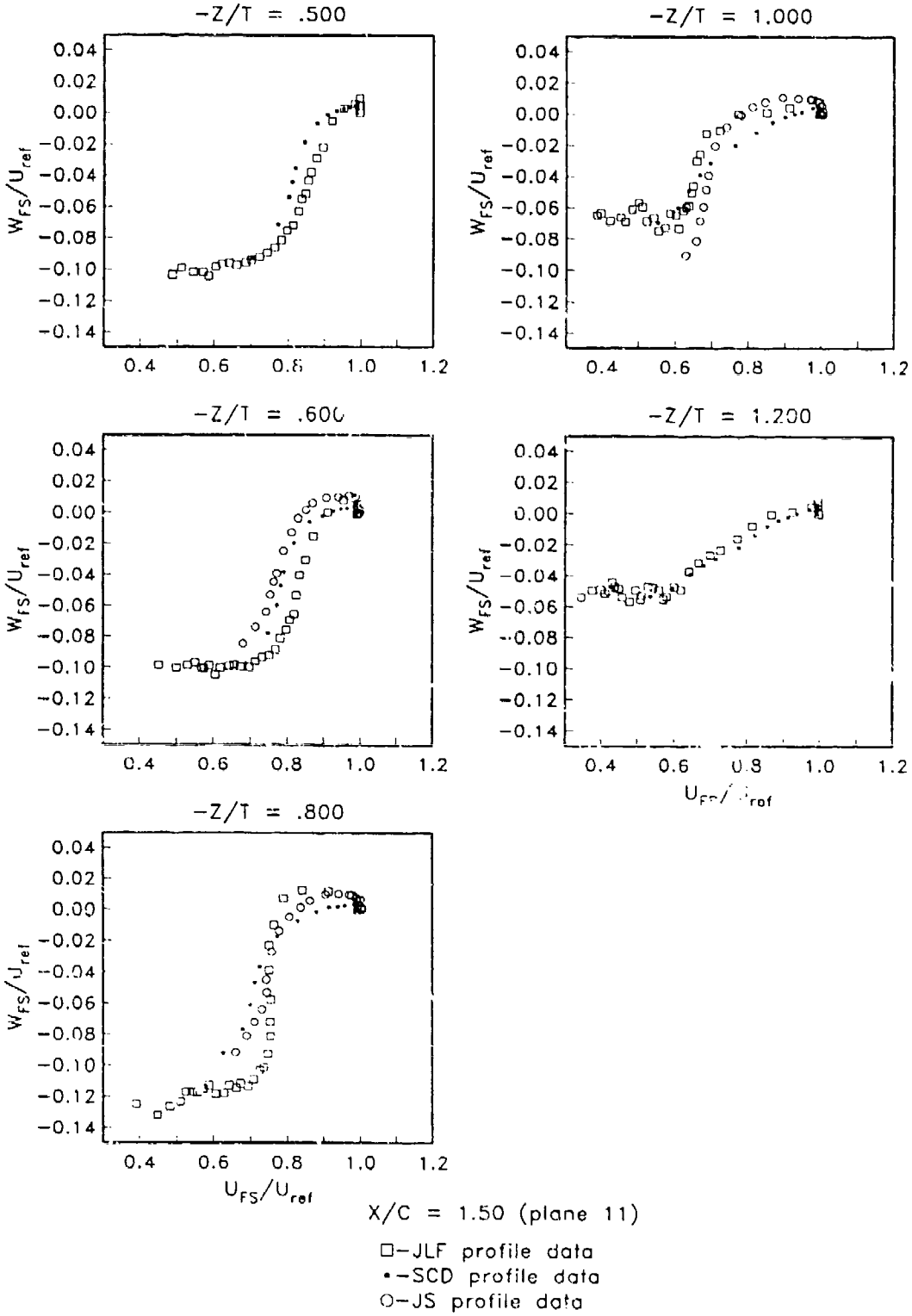

Figure 4.83. Boundary Layer Hodograph Plots, Plane 11

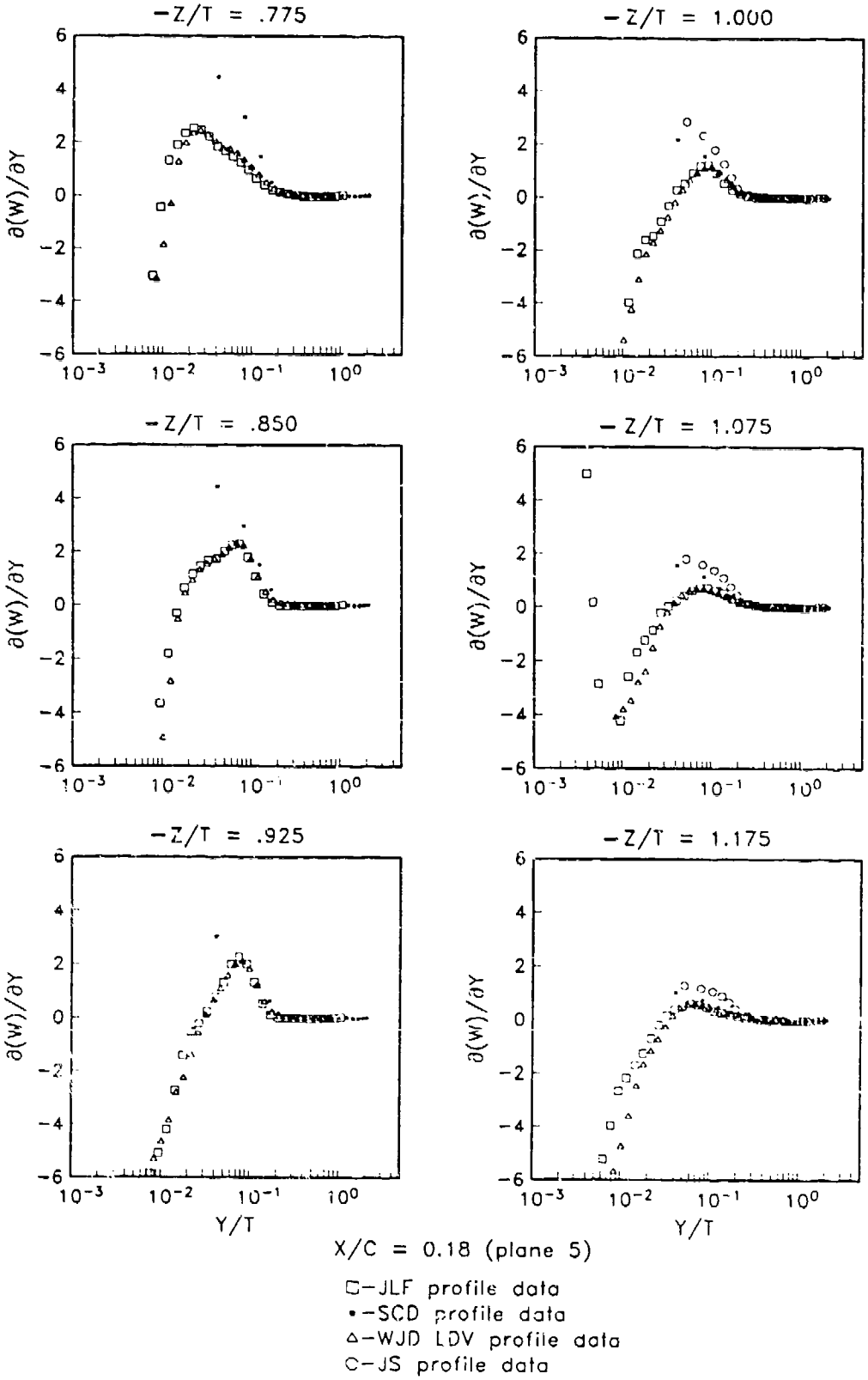

Figure 4.84. Profiles of $(\partial(W)/\partial Y)\delta/U_{ref}$, Plane 5

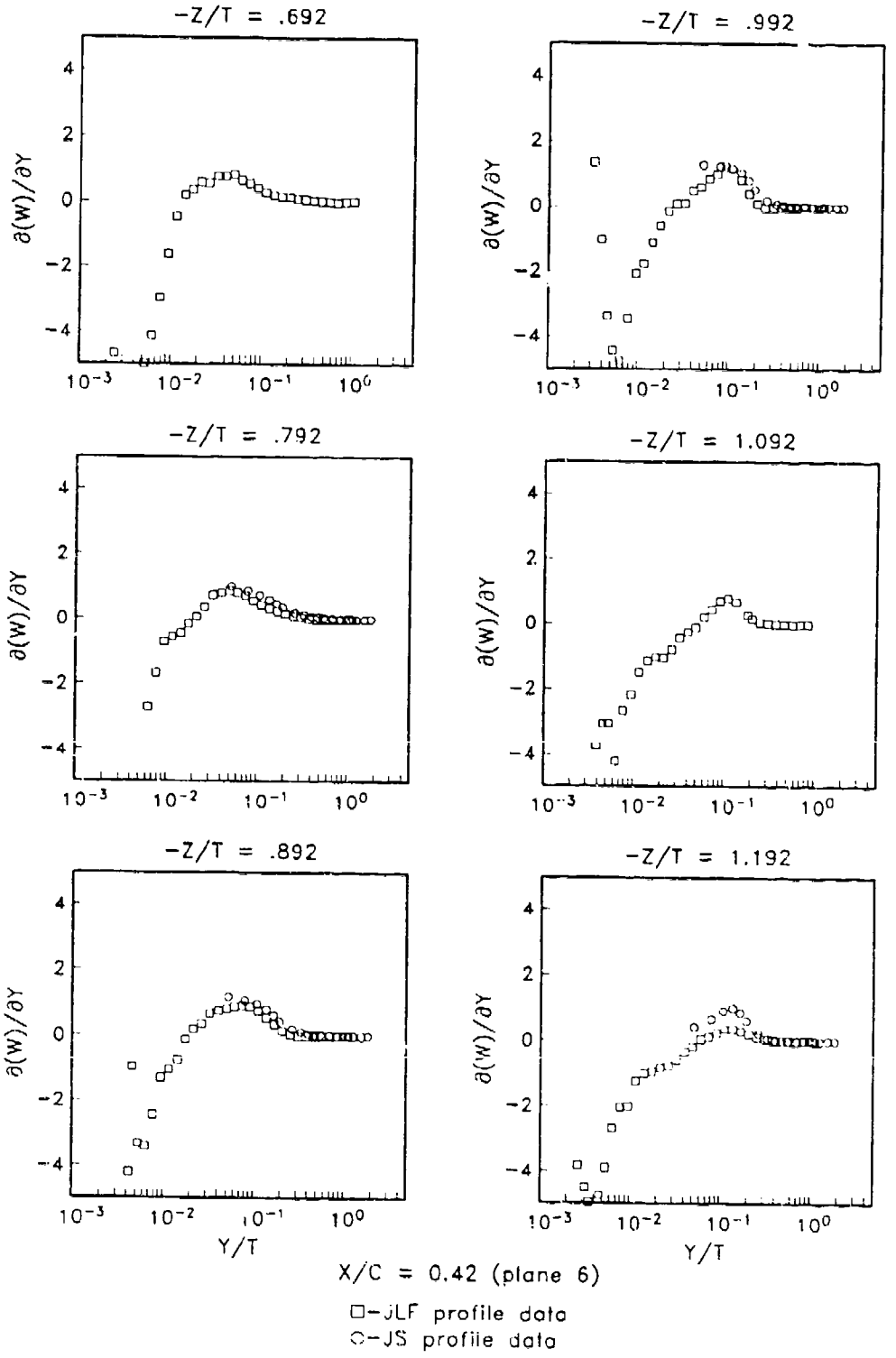

Figure 4.85. Profiles of $(\partial(W)/\partial Y)\delta/U_{ref}$, Plane 6

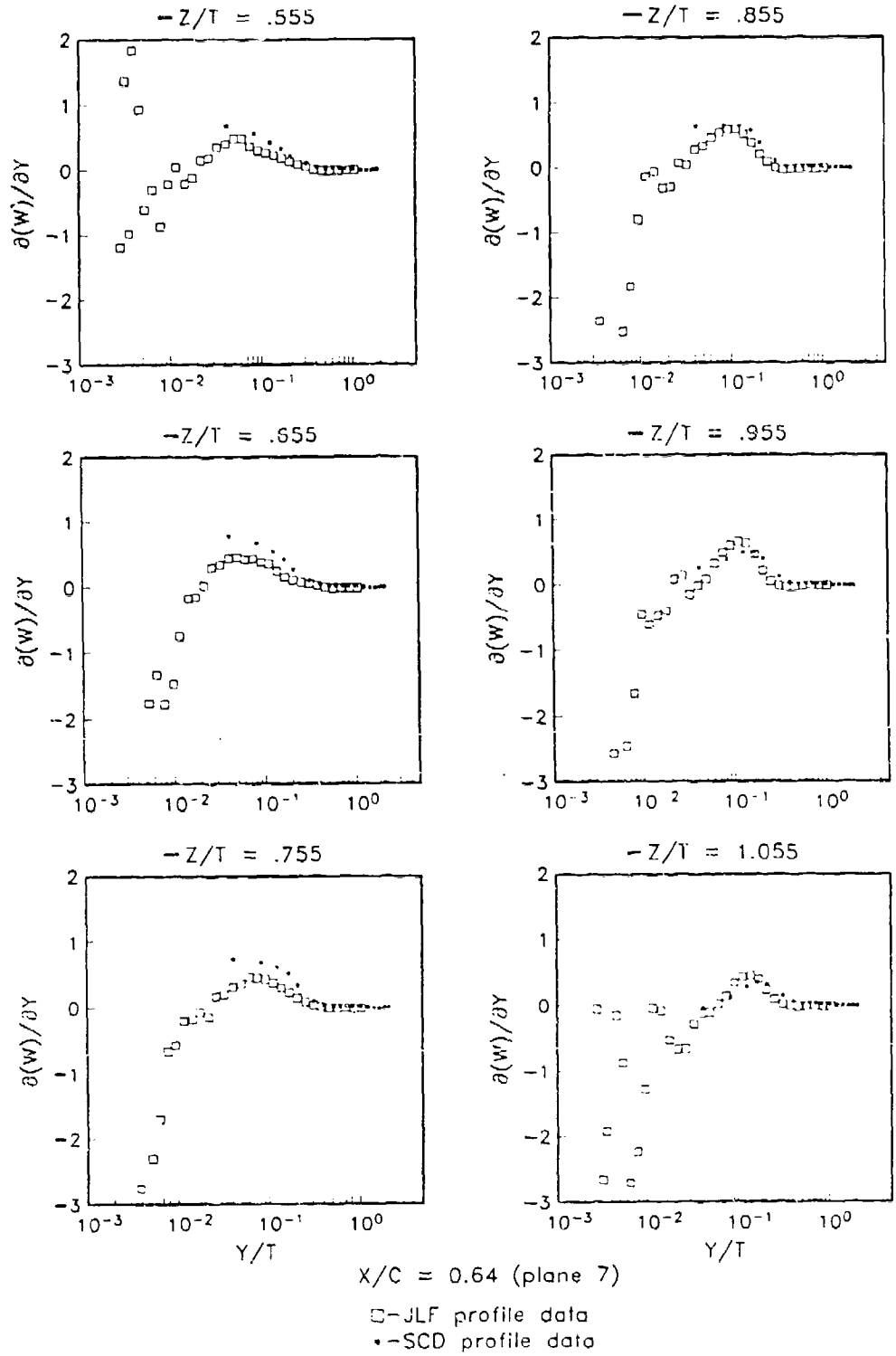

Figure 4.86. Profiles of $(\partial(W)/\partial Y)\delta/U_{ref}$, Plane 7

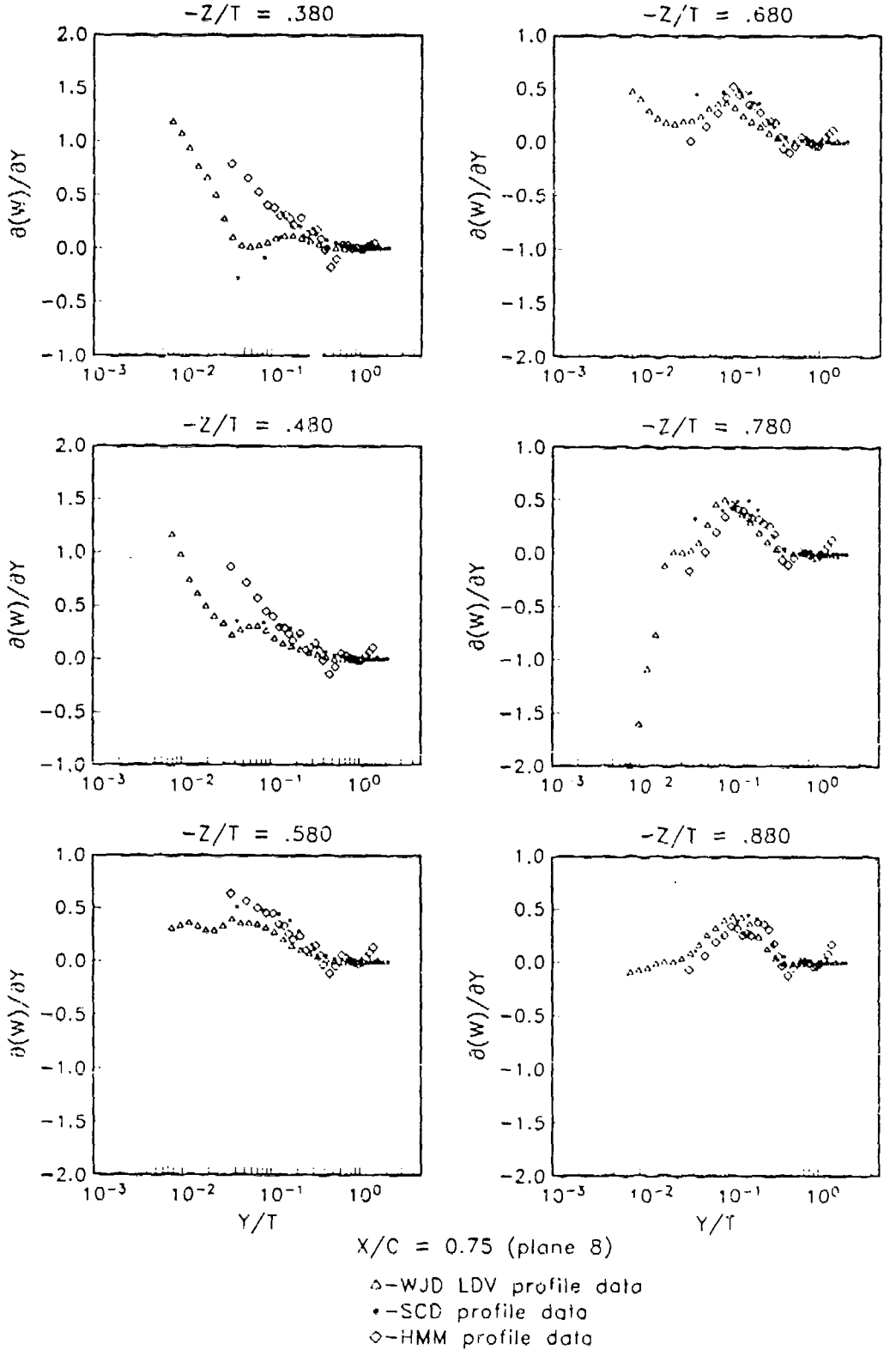

Figure 4.87. Profiles of $(\partial(W)/\partial Y)\delta/U_{ref}$, Plane 8

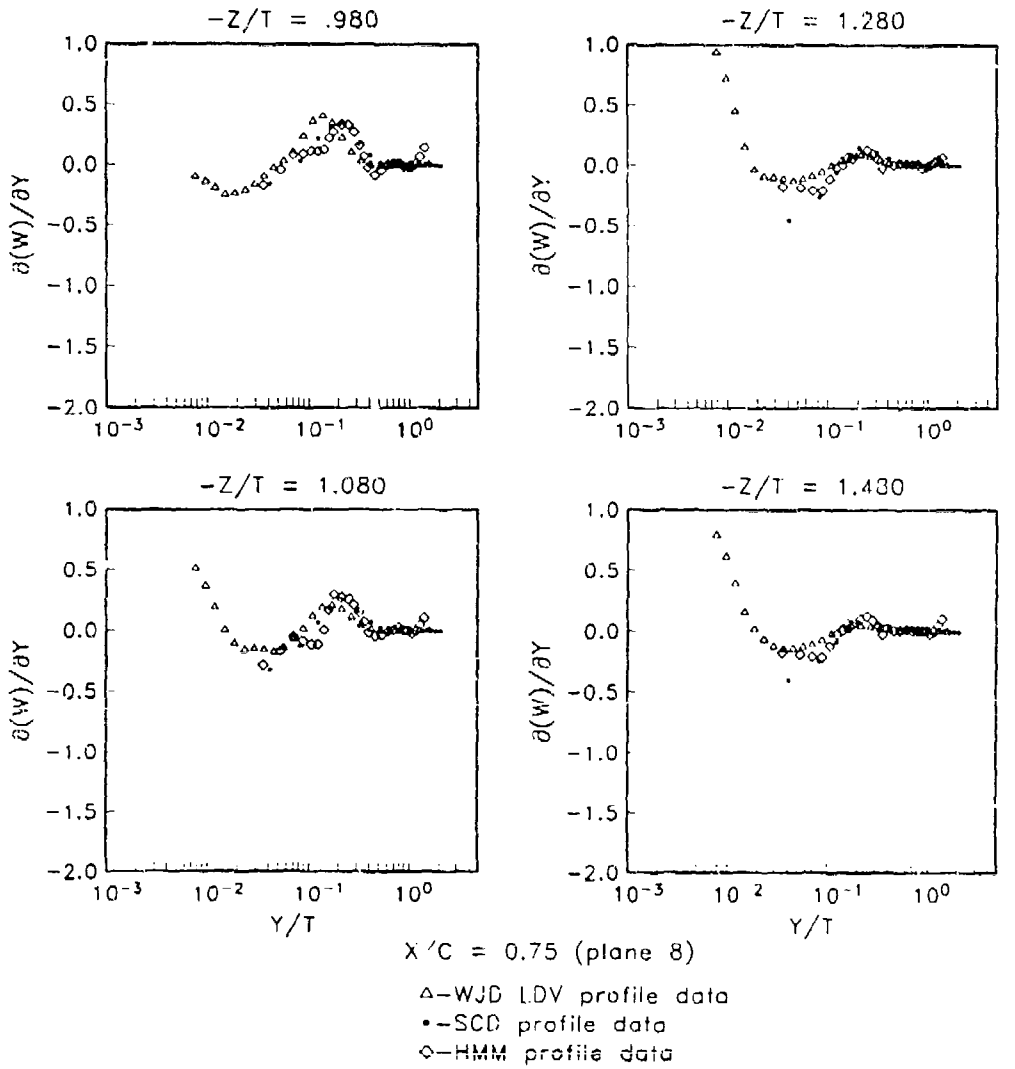

Figure 4.87. (cont.). Profiles of $(\partial(W)/\partial Y)\delta/U_{ref}$, Plane 8

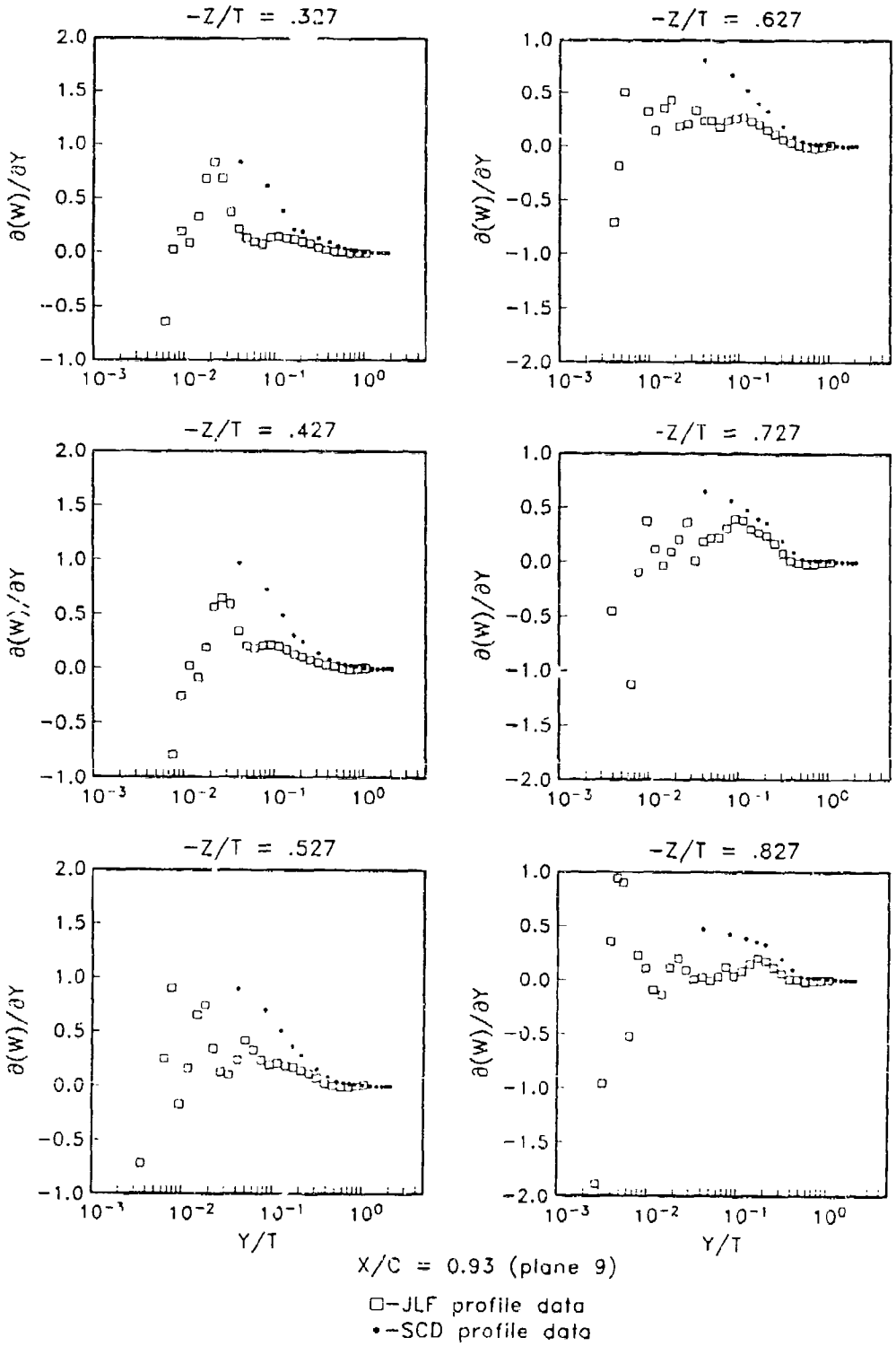

Figure 4.88. Profiles of $(\partial(W)/\partial Y)\delta/U_{ref}$, Plane 9

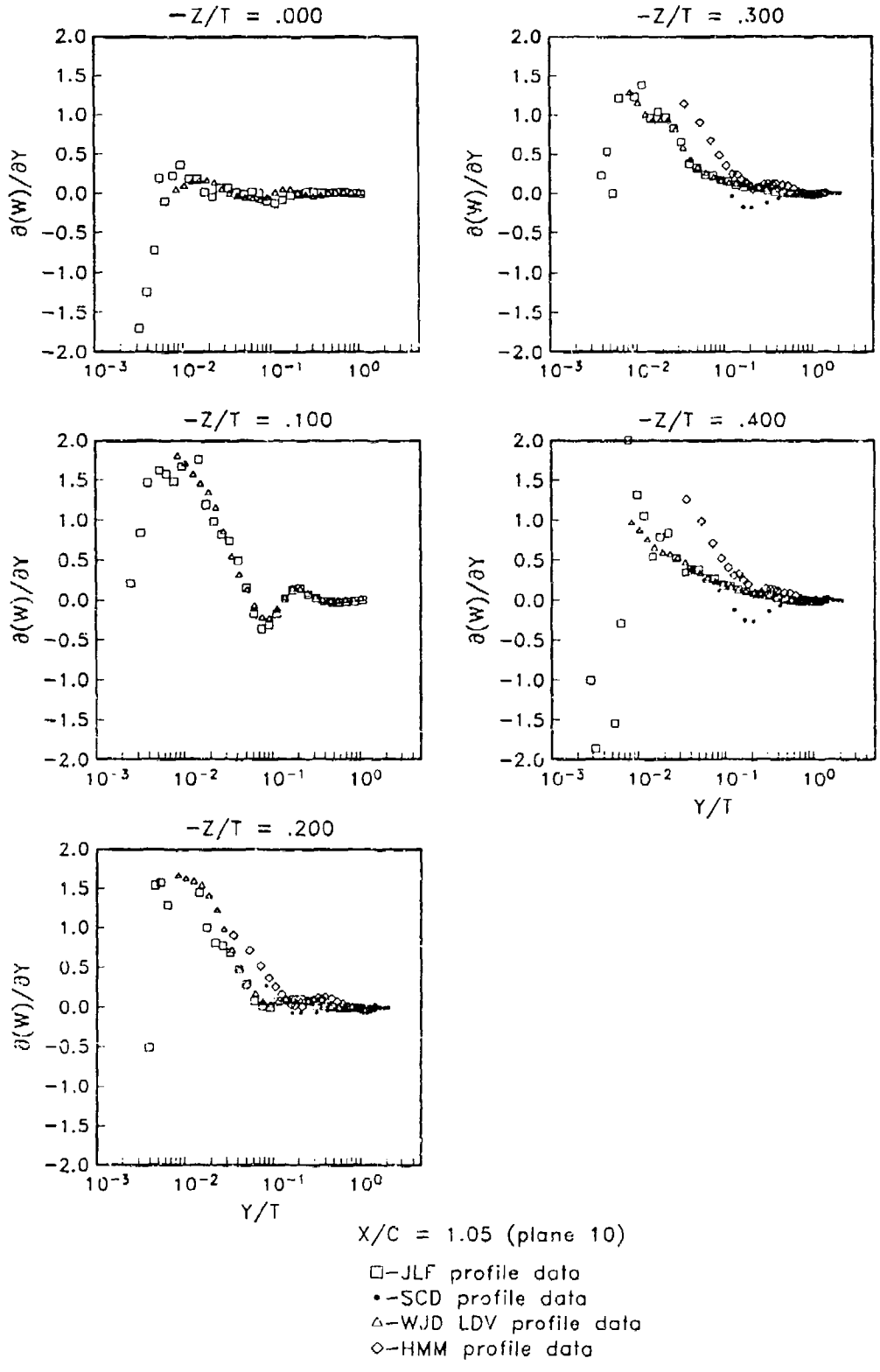

Figure 4.89. Profiles of $(\partial(W)/\partial Y)\delta/U_{ref}$, Plane 10

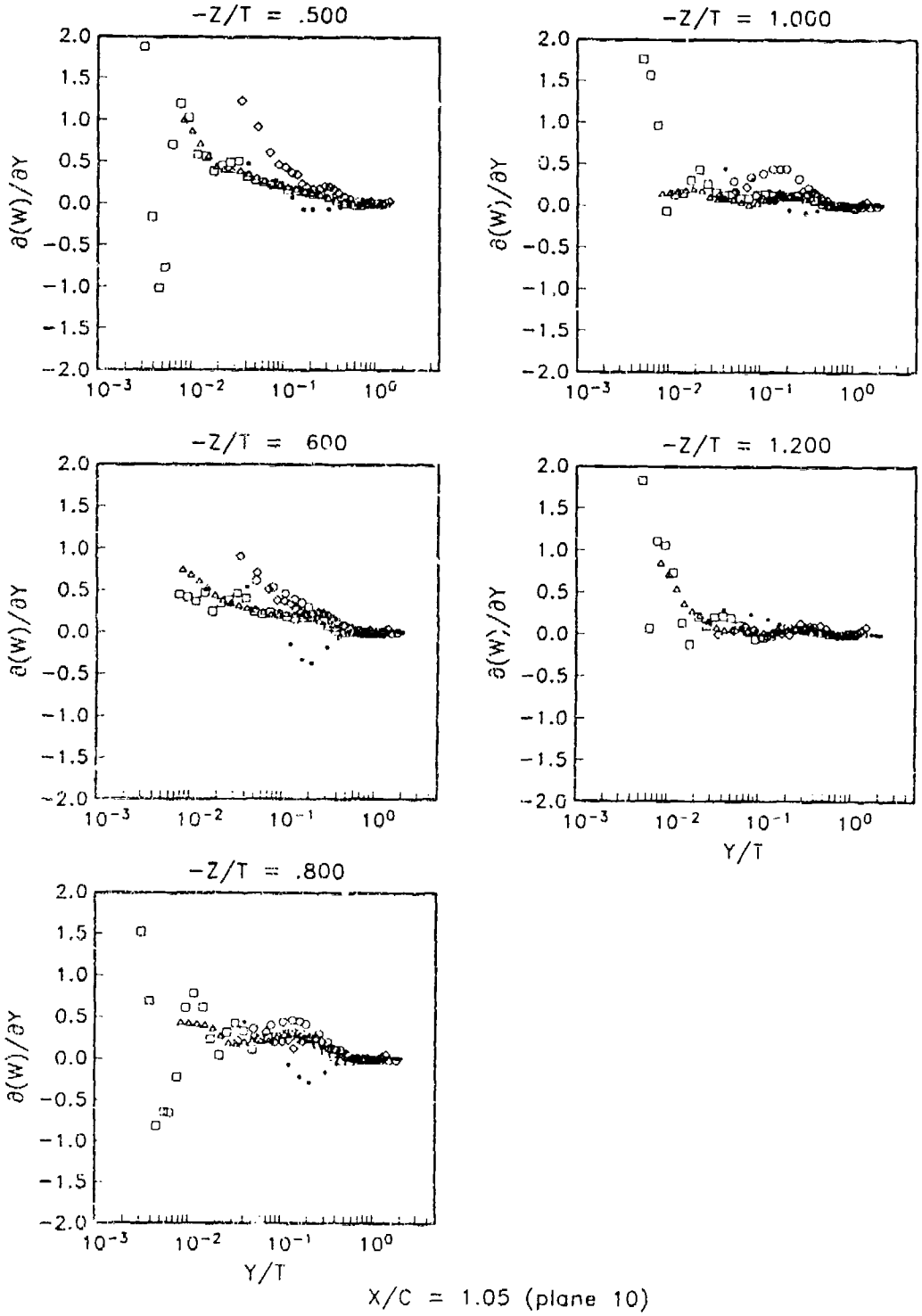

Figure 4.89. (cont.). Profiles of $(\partial(W)/\partial Y)\delta/U_{ref}$, Plane 10

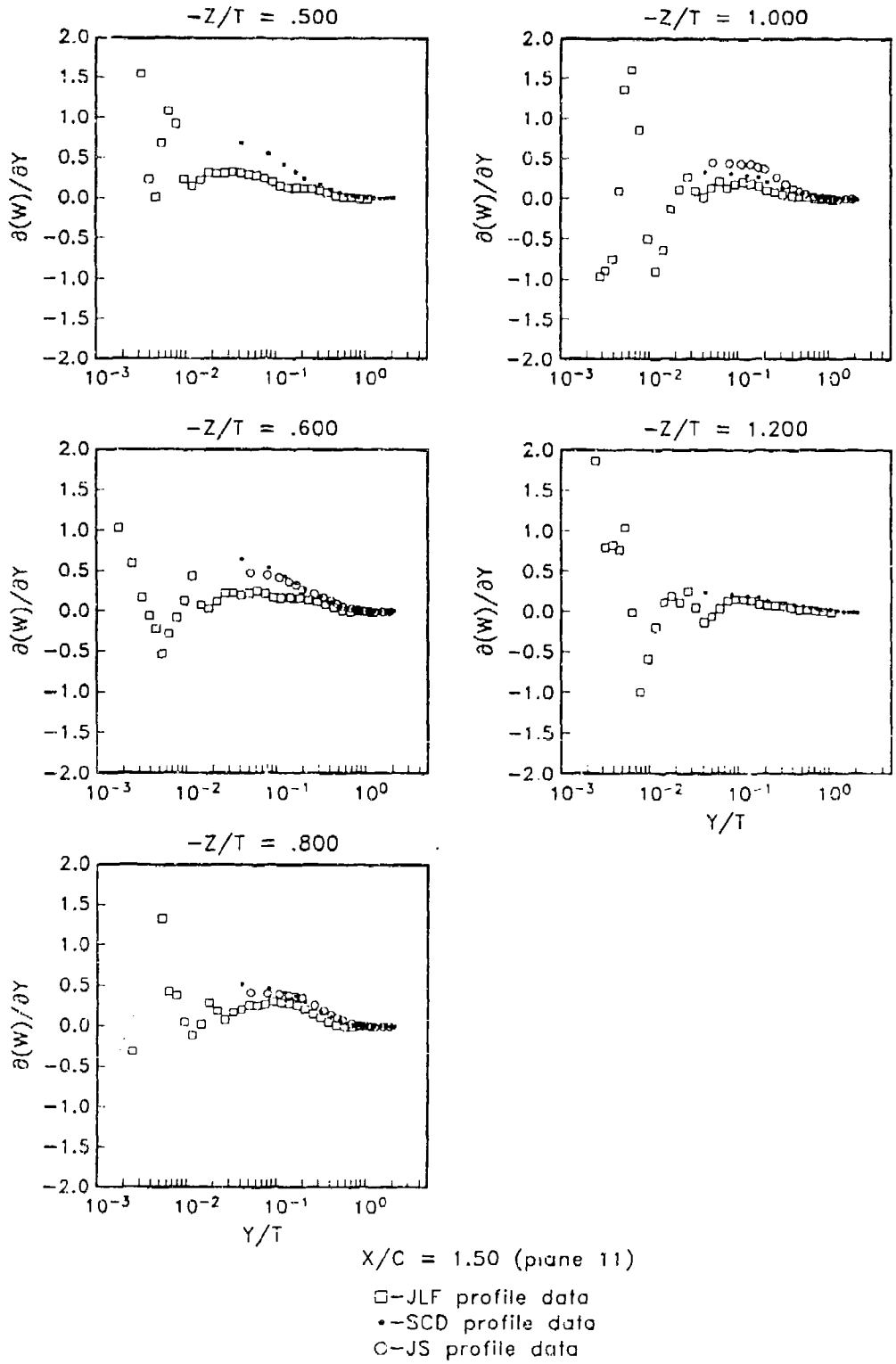

Figure 4.90. Profiles of $(\partial(W)/\partial Y)\delta/U_{ref}$, Plane 11

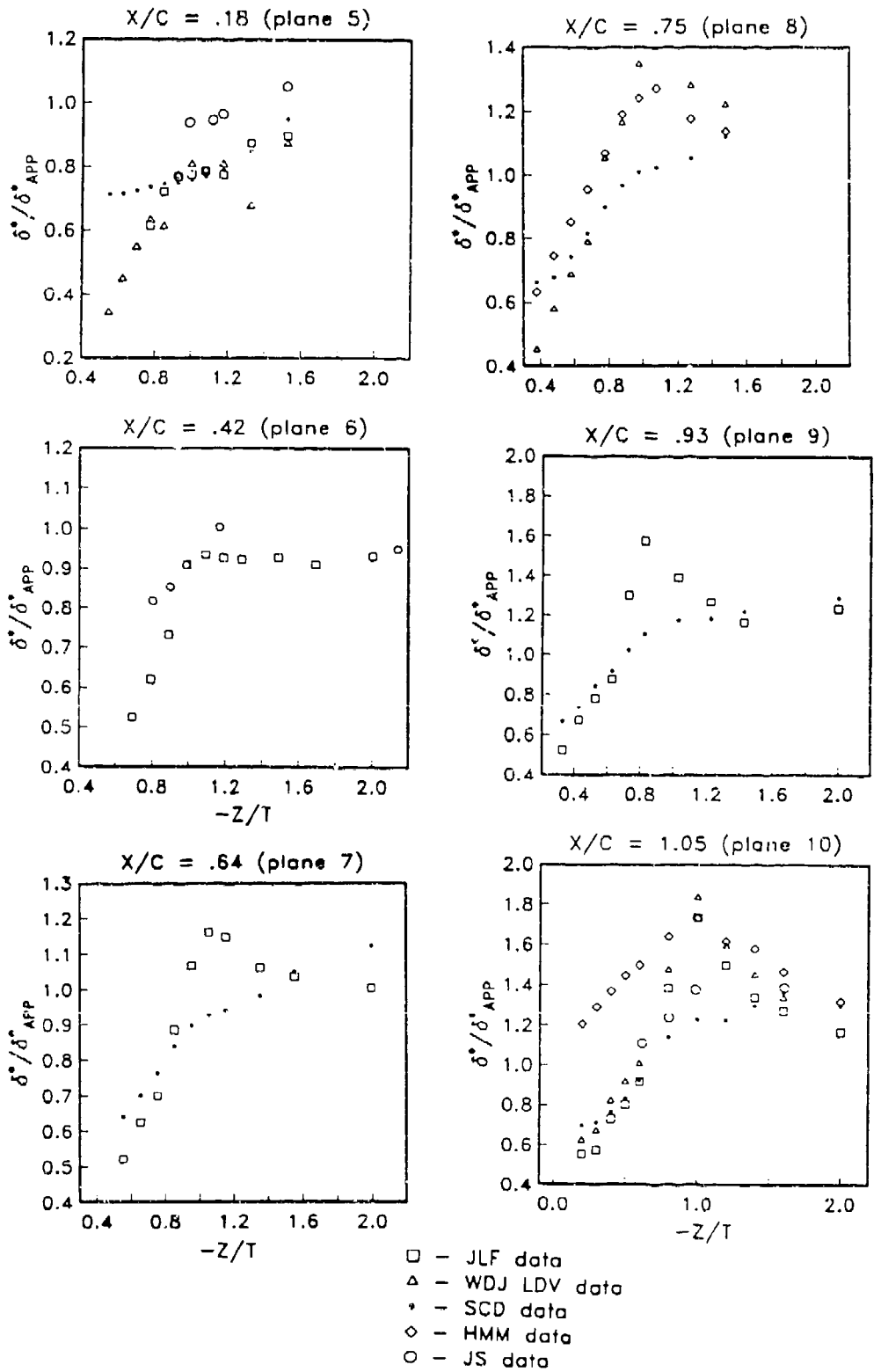

Figure 4.91a. Plots of δ^*/δ^*_{APP} vs. Z/T, Planes 5-10

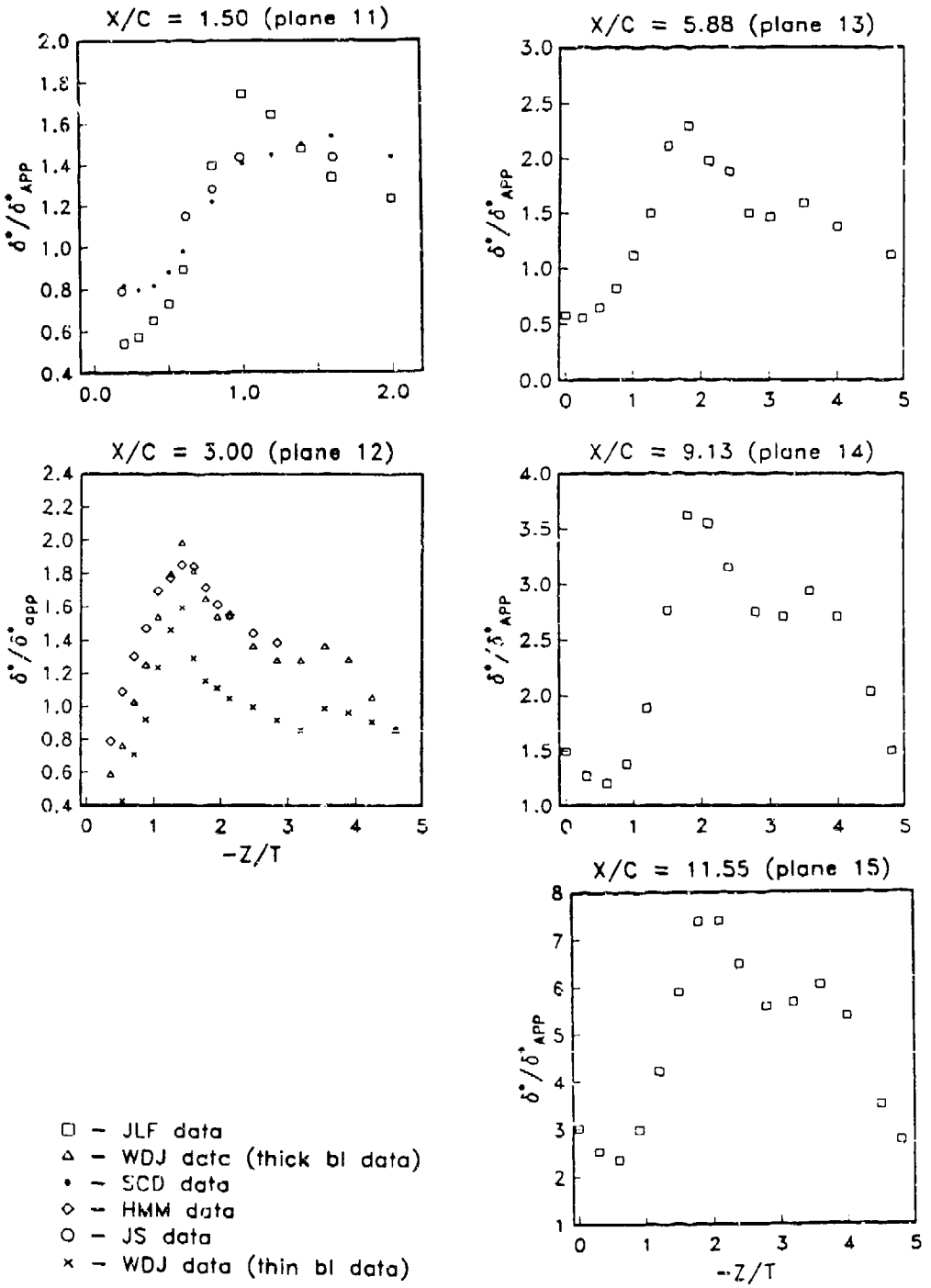

Figure 4.91b. Plots of δ^*/δ^*_{APP} vs. Z/T, Planes 11-15

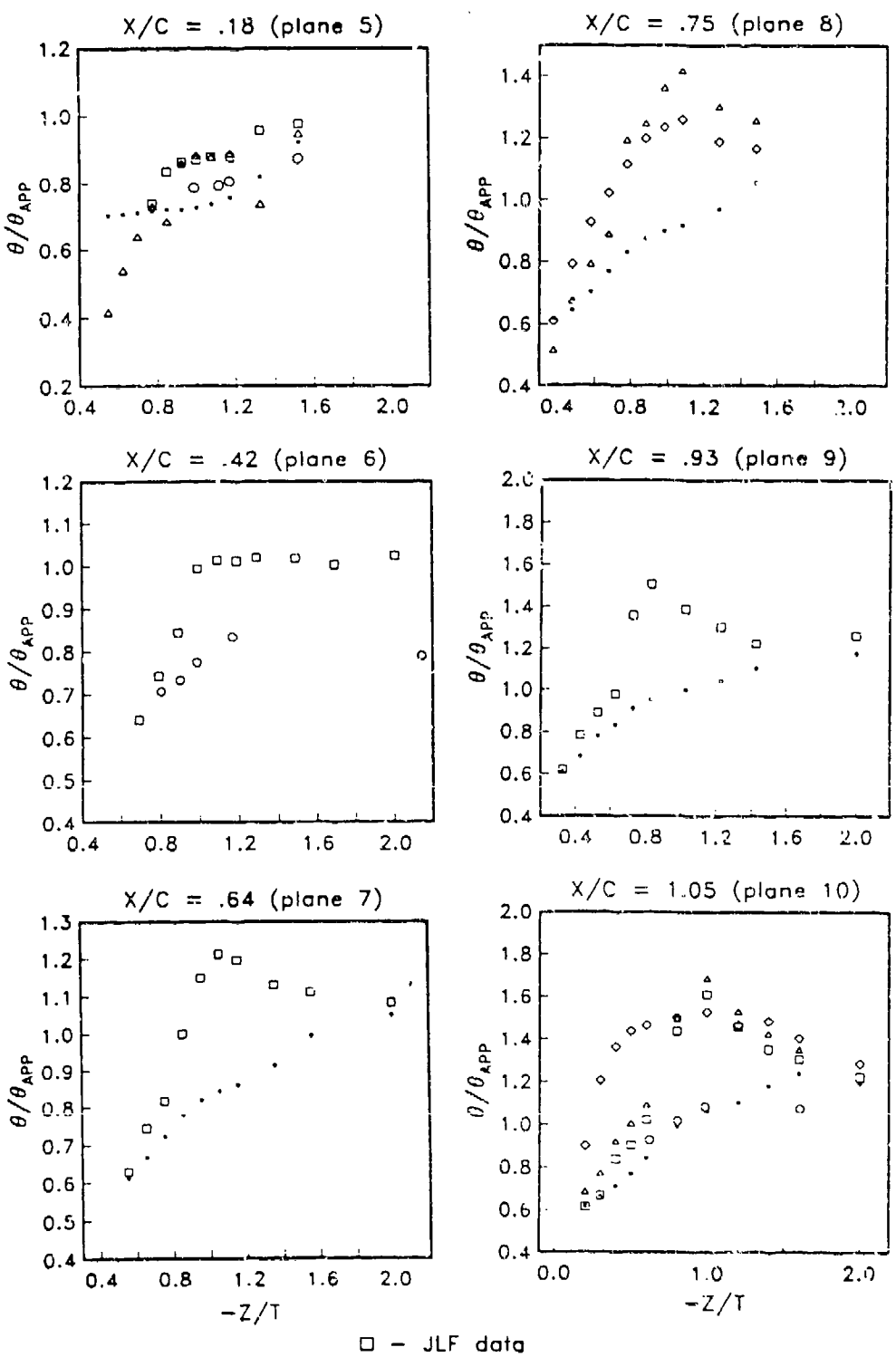

Figure 4.92a. Plots of θ/θ_{APP} vs. Z/T, Planes 5-10

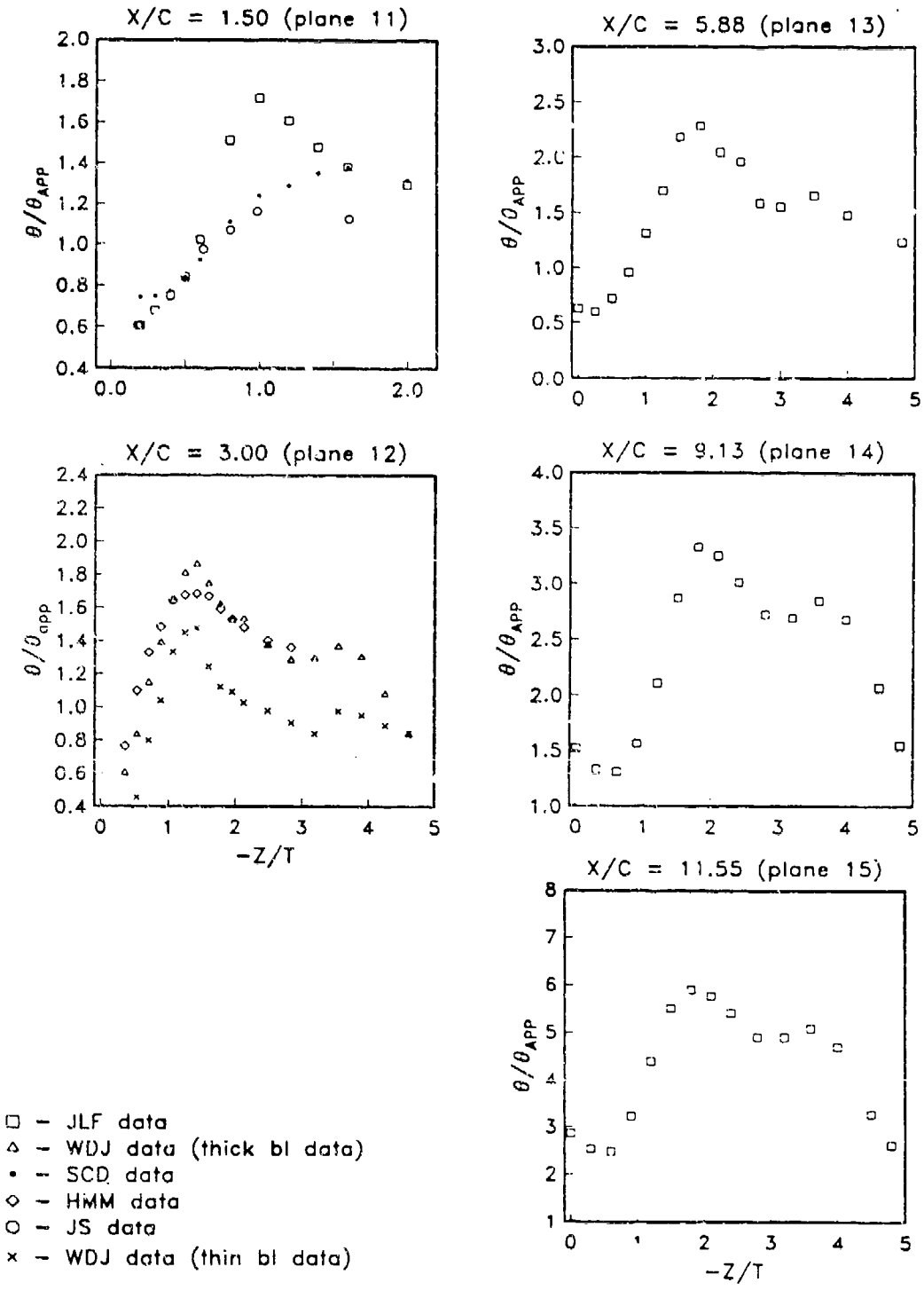

Figure 4.92b. Plots of θ/θ_{APP} vs. Z/T, Planes 11-15

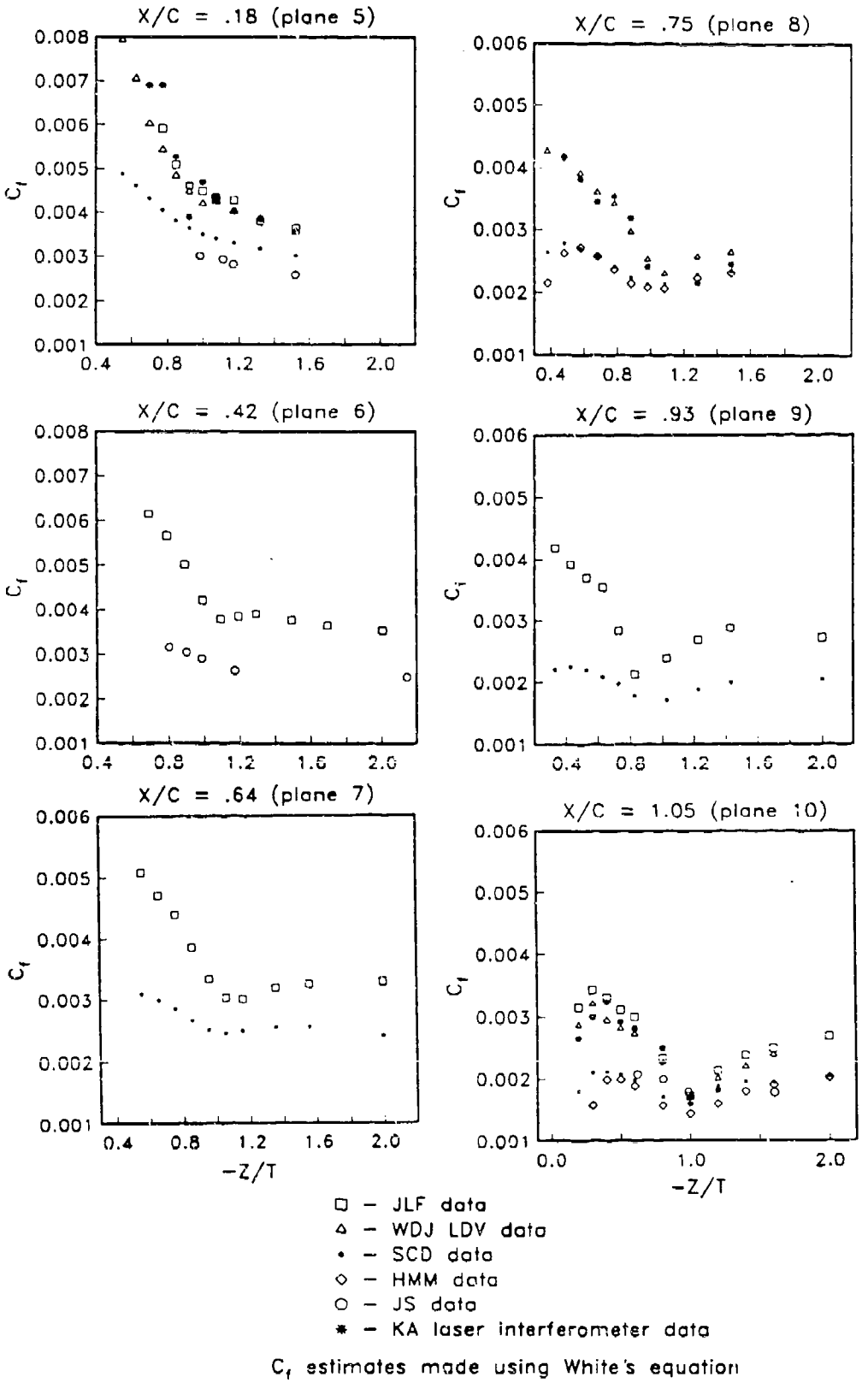

Figure 4.93a. Plots of C_f vs. Z/T, Planes 5-10

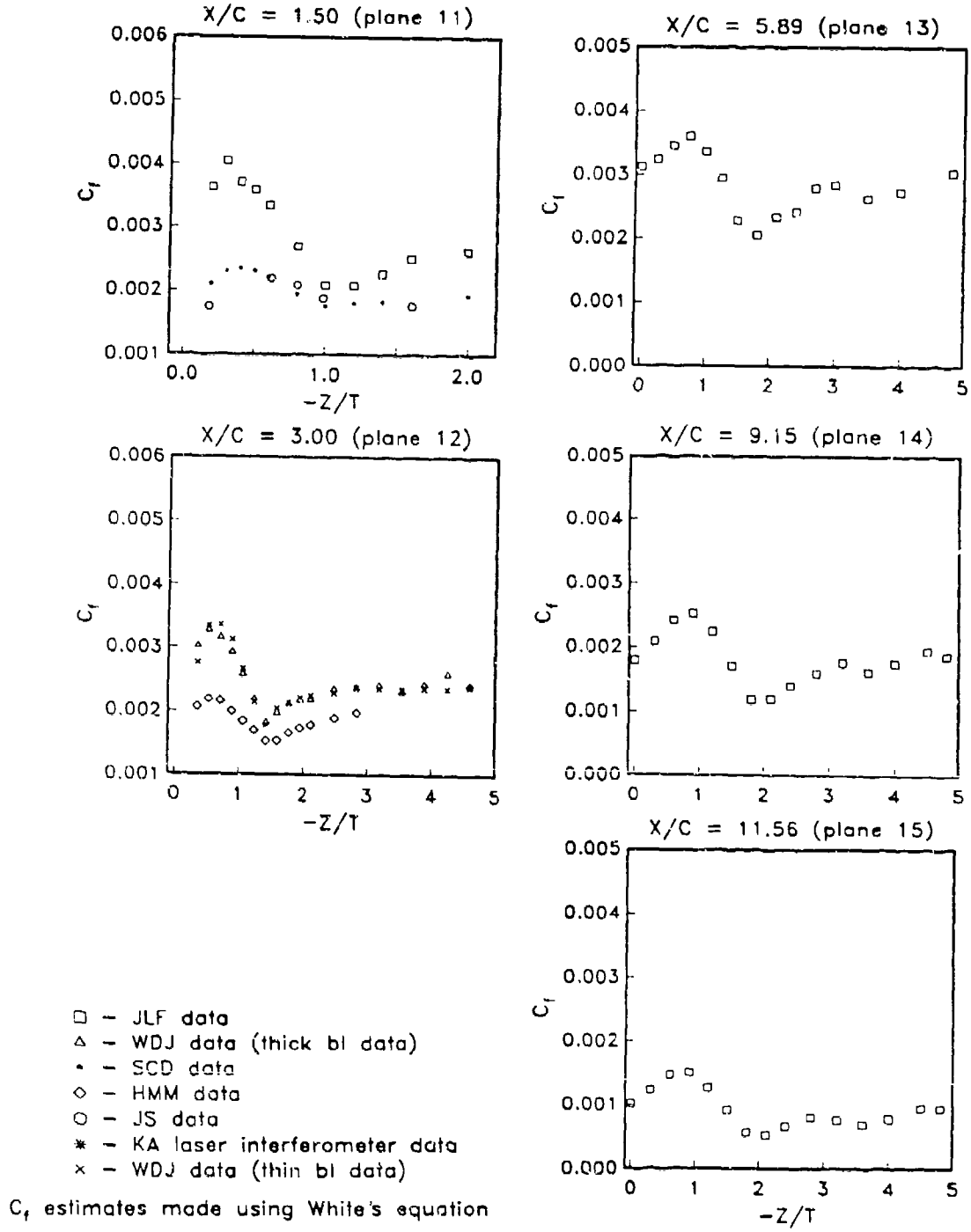

Figure 4.93b. Plots of C_f vs. Z/T, Planes 11-15

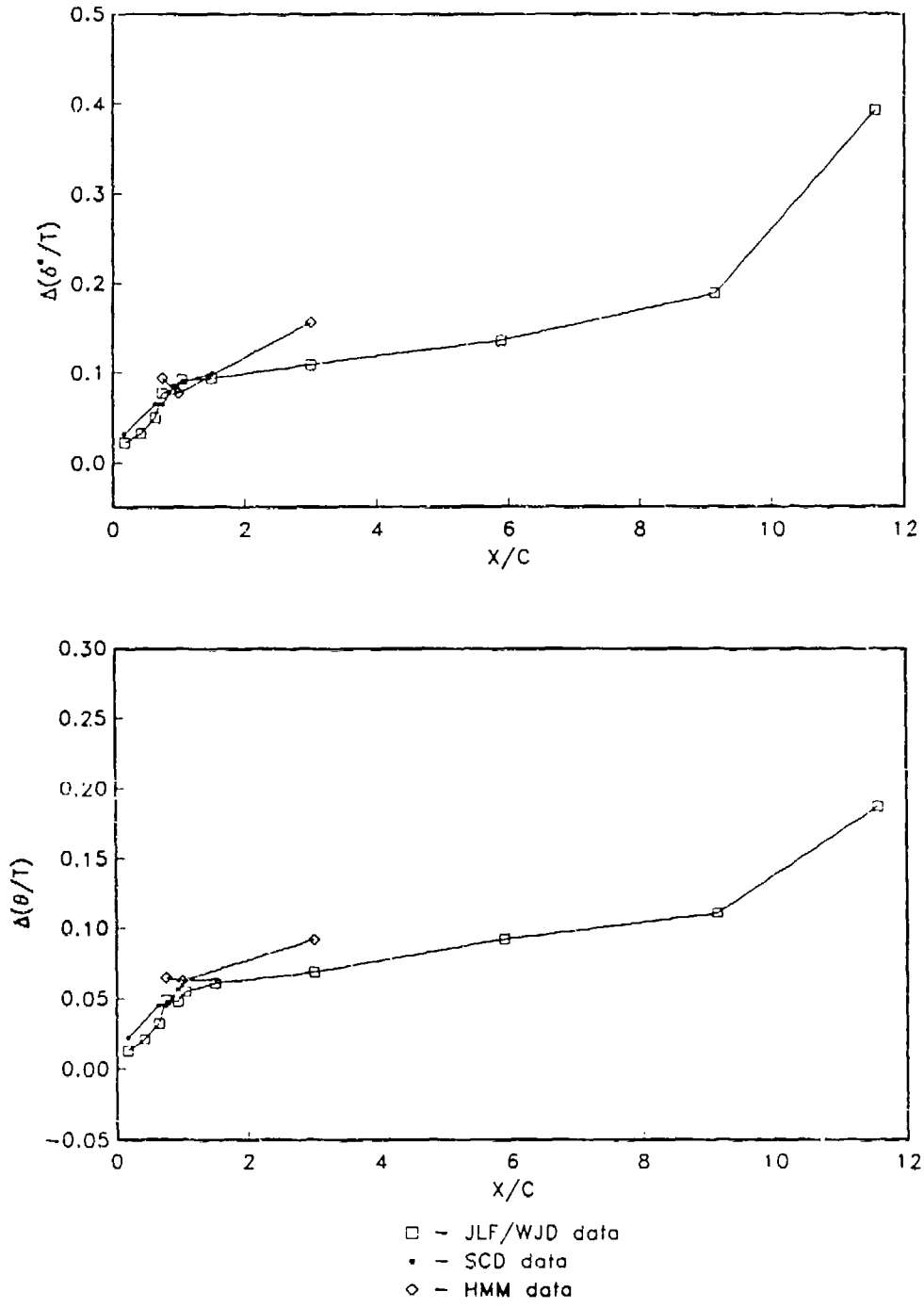

Figure 4.94. Plots of $\Delta(\delta^*/T)$ and $\Delta(\theta/T)$ vs. X/C

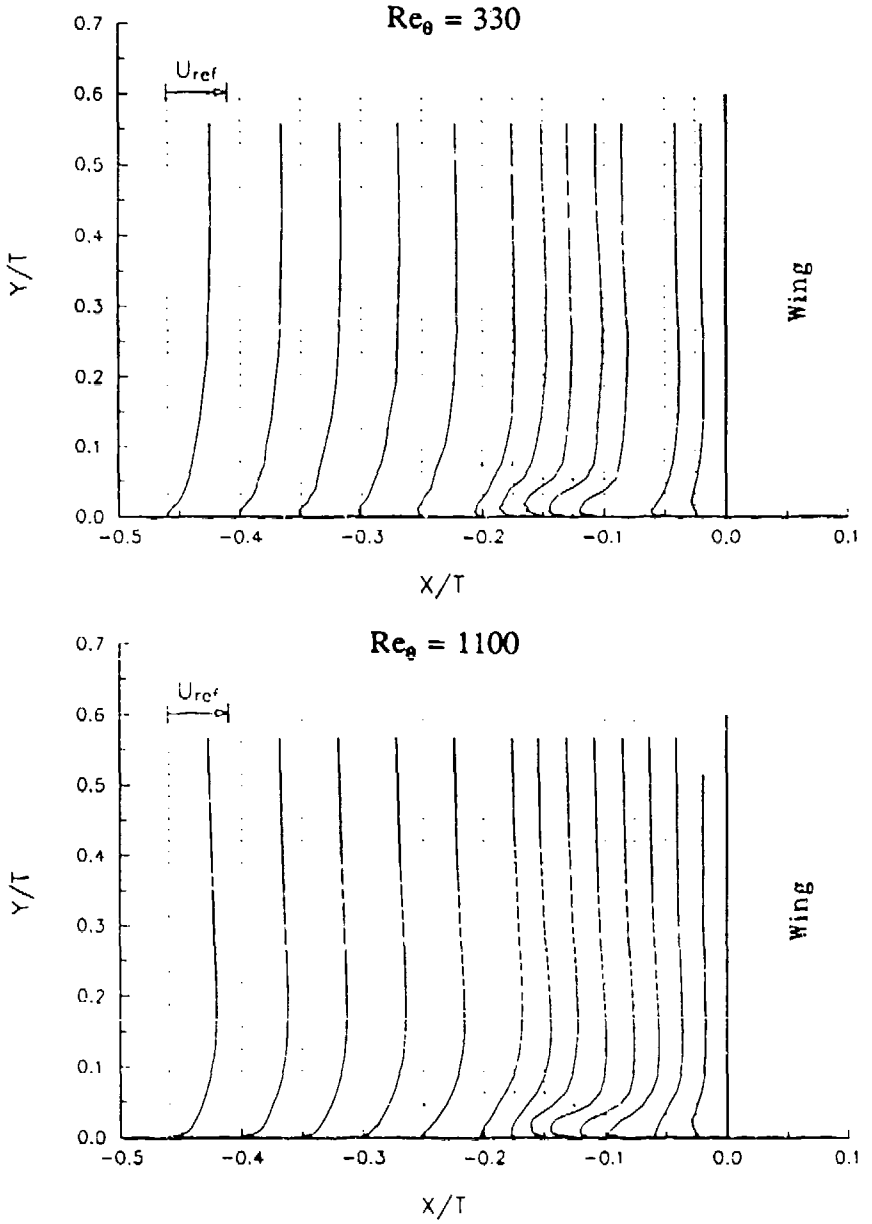

Figure 5.1. Profile Plots of U_{TC}/U_{ref} for Re_θ = 330 and 1100 Along the Centerline Ahead of the Baseline Wing (from Kim, 1991)

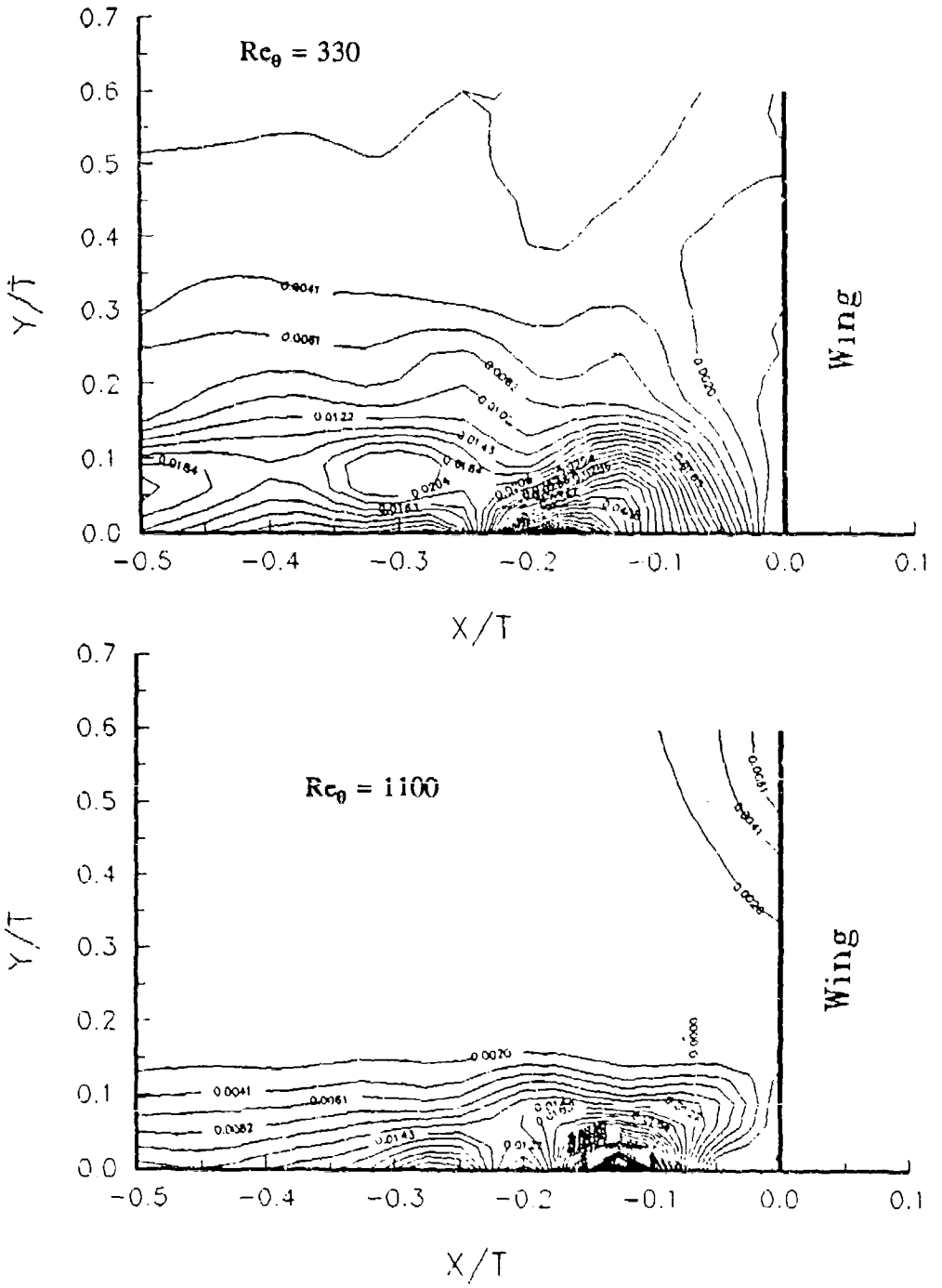

Figure 5.2. Contours of Streamwise Velocity Fluctuations for Re_θ = 330 and 1100 Along the Centerline Ahead of the Baseline Wing (from Kim, 1991)

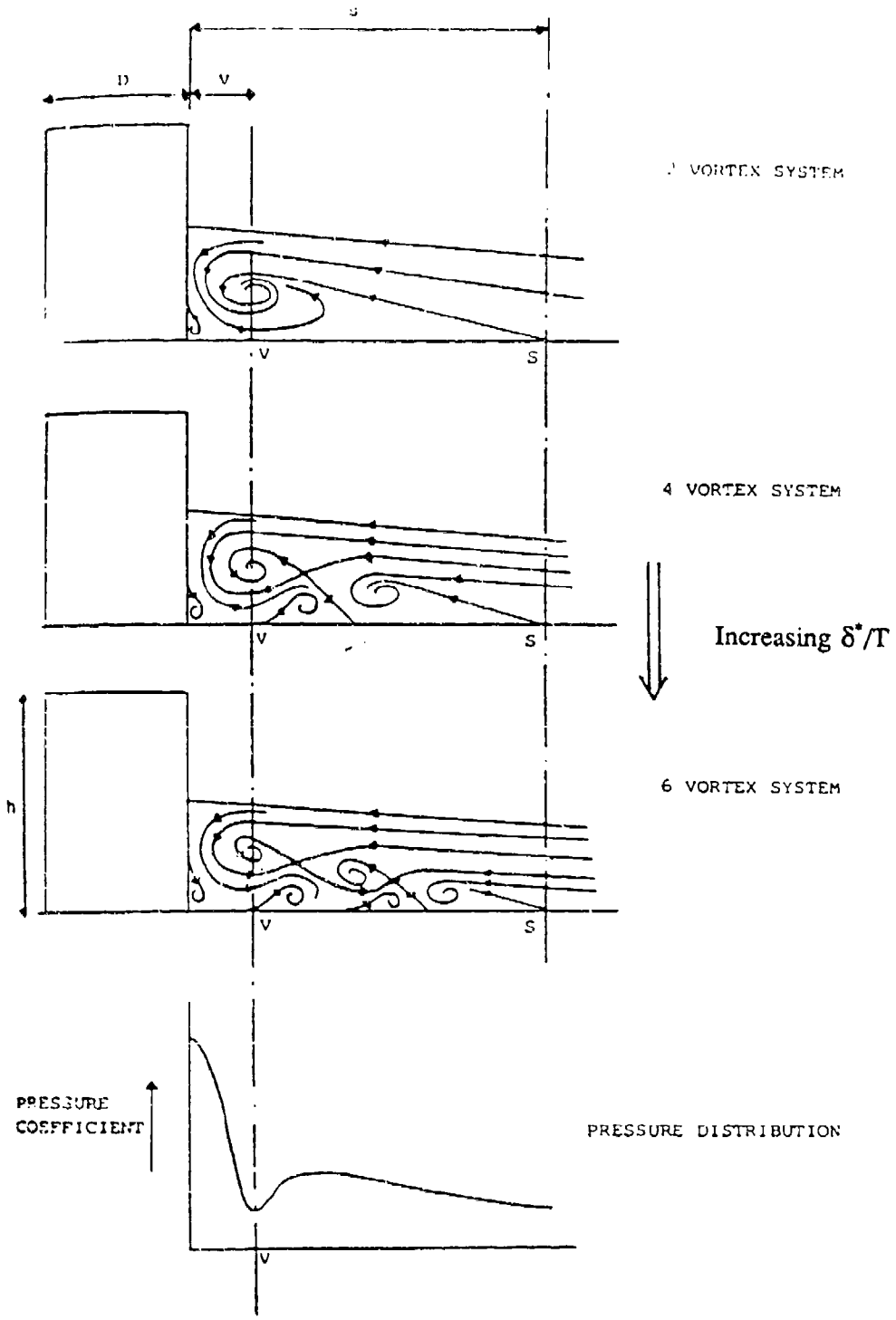

Figure 5.3. Vortex Structures Which May Exist Ahead of Cylinder/Floor Junctions (from Baker, 1985)

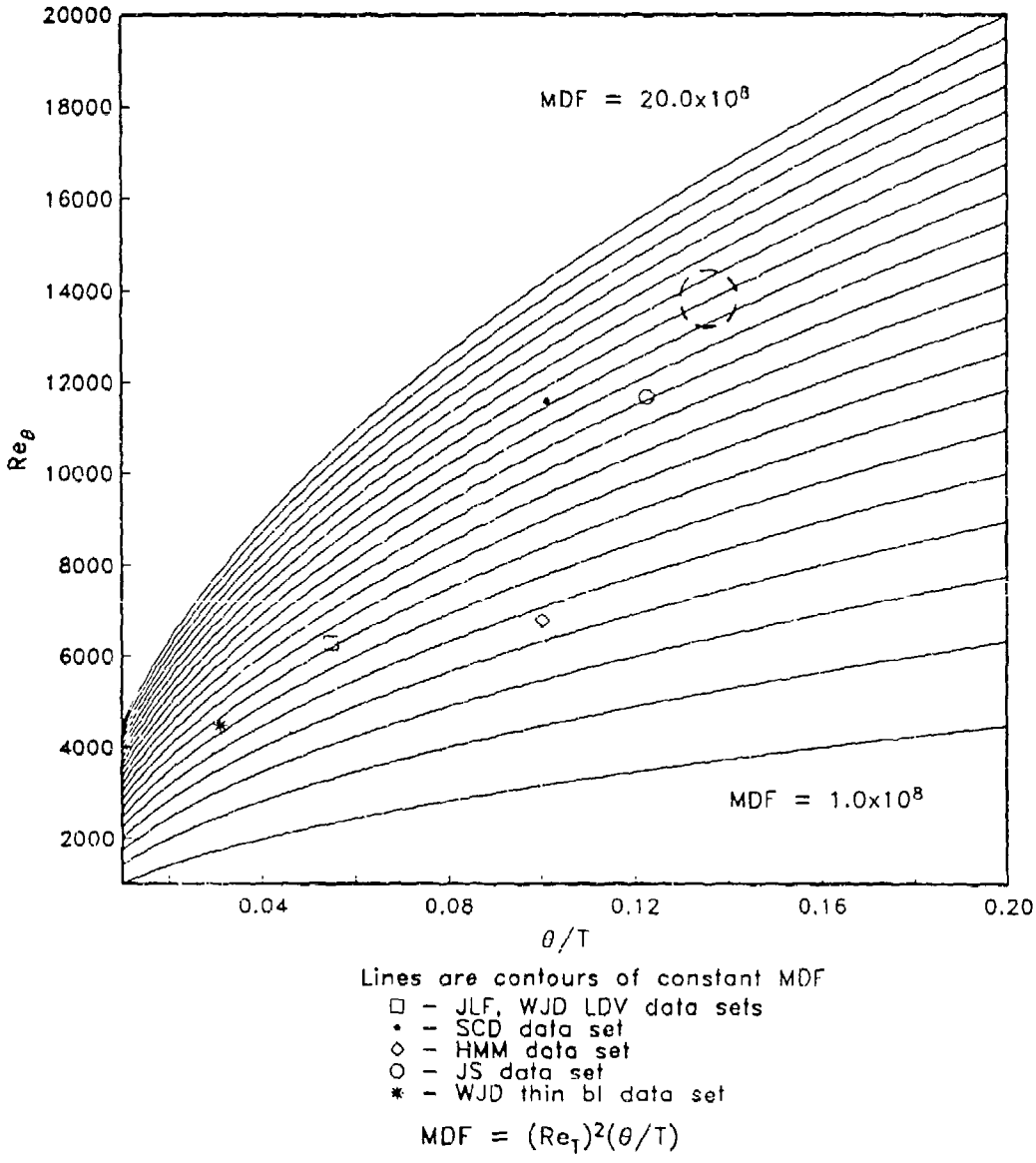

Figure 5.4. Parametric Space of Data Sets, Displaying Lines of Constant MDF (Region enclosed by dashed line indicates area where Shin's data set may actually lie)

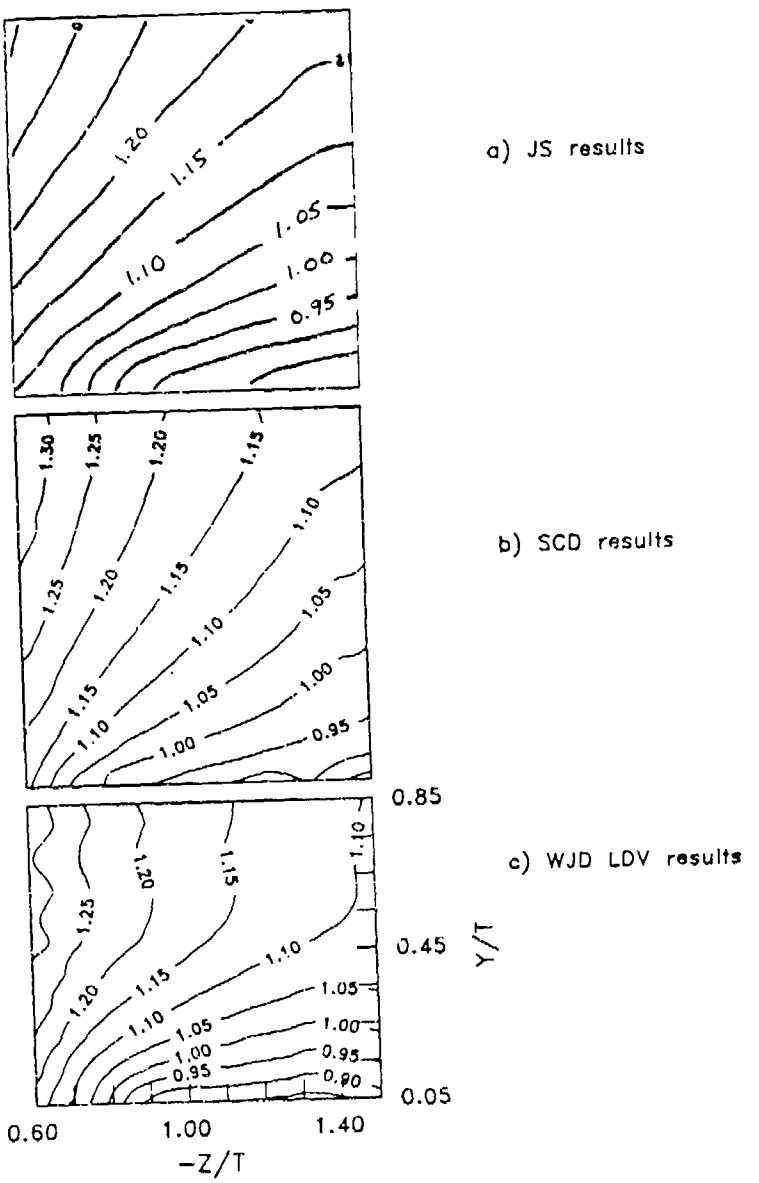

Figure 5.5. Comparison of Contours of U_{TC}/U_{ref}, Plane 5

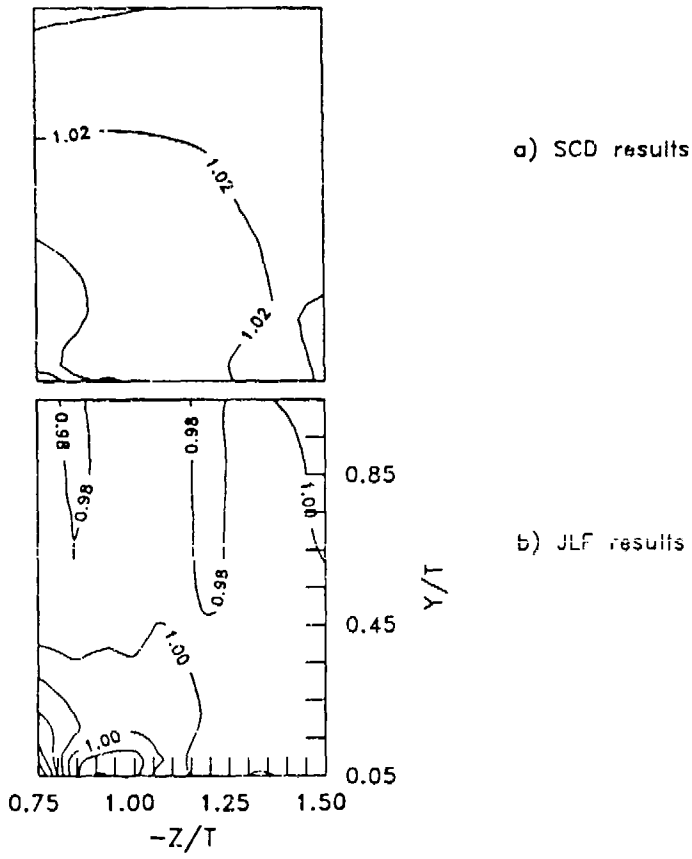

Figure 5.6. Comparison of Contours of Distortion Function, f_D, Plane 5

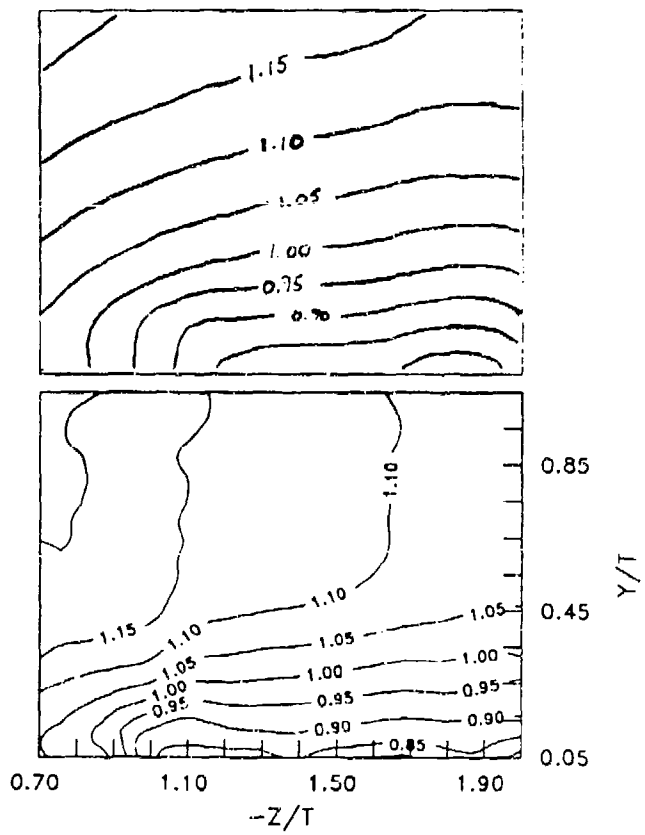

Figure 5.7. Comparison of Contours of U_{TO}/U_{ref}, Plane 6

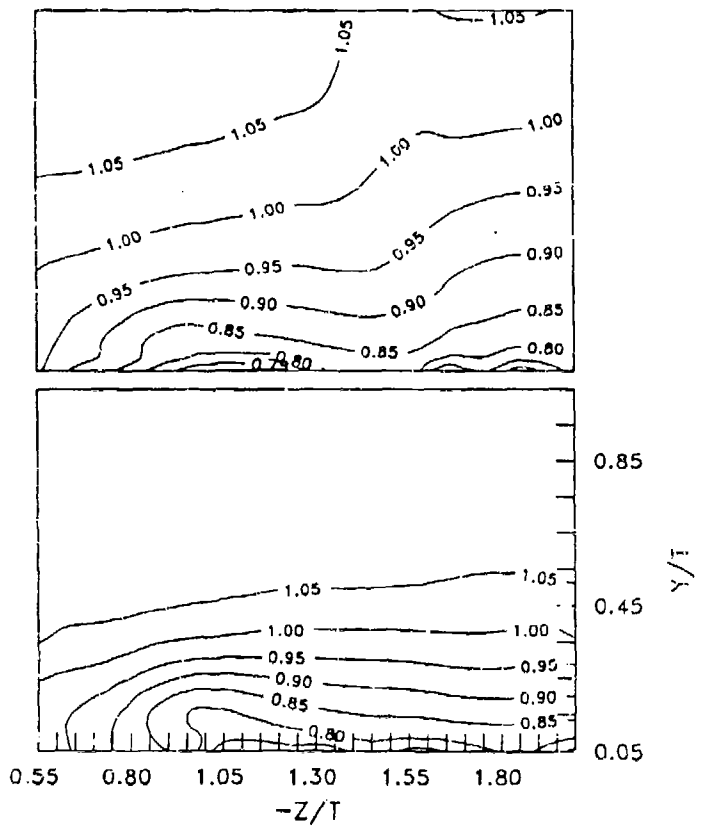

Figure 5.8. Comparison of Contours of U_{TC}/U_{ref}, Plane 7

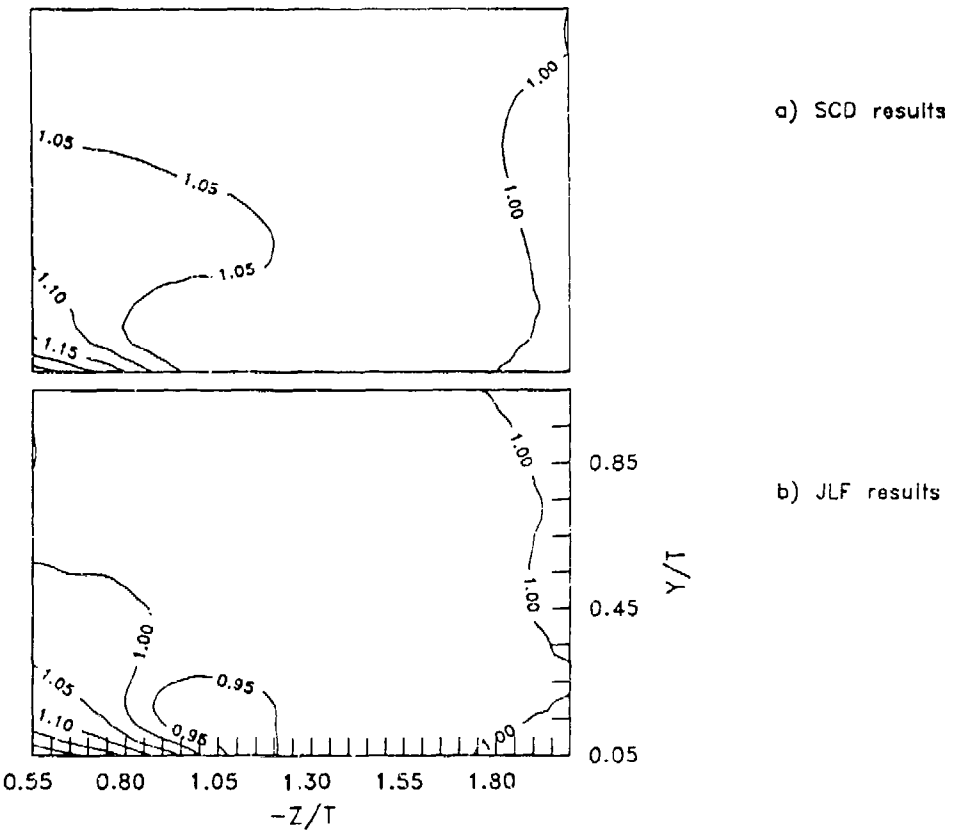

Figure 5.9. Comparison of Contours of Distortion Function, f_D, Plane 7

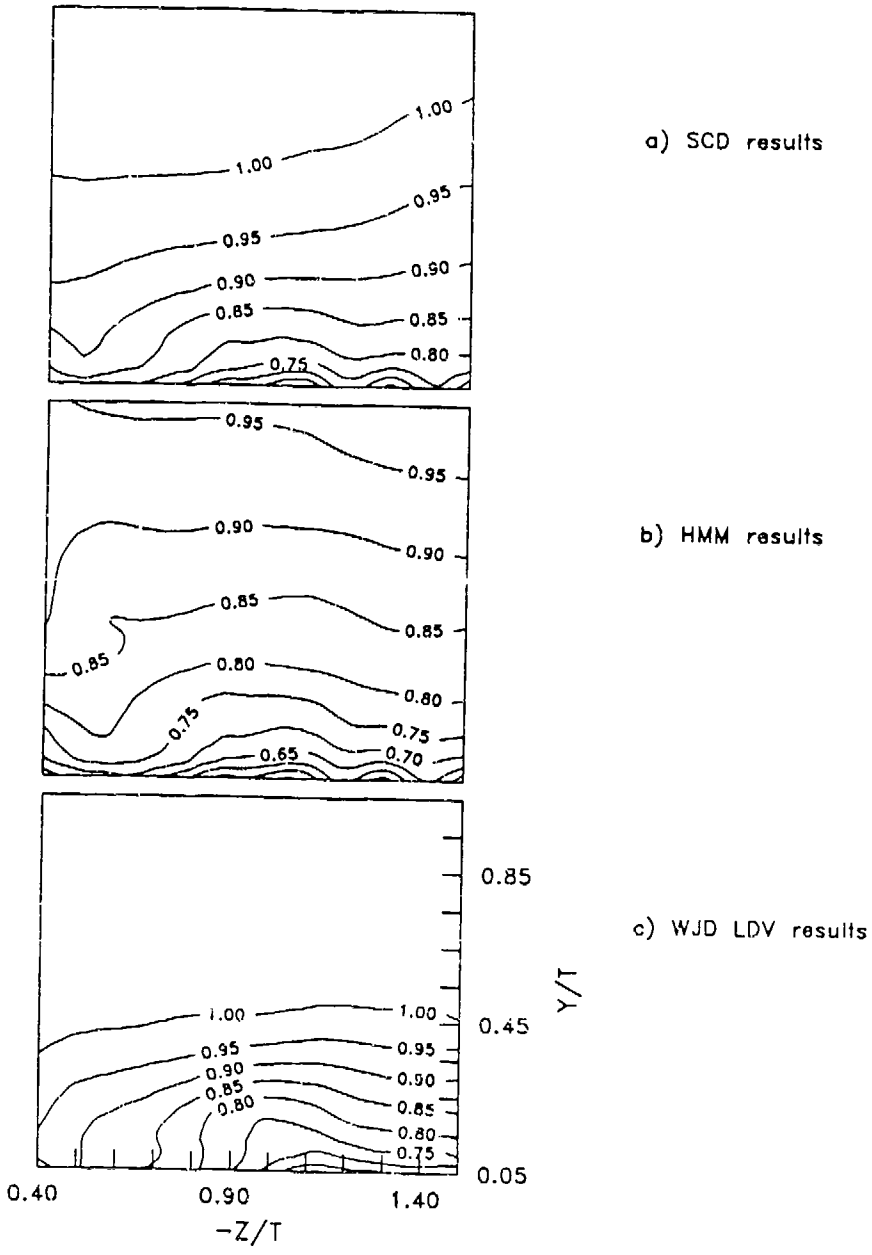

Figure 5.10. Comparison of Contours of U_{TC}/U_{ref}, Plane 8

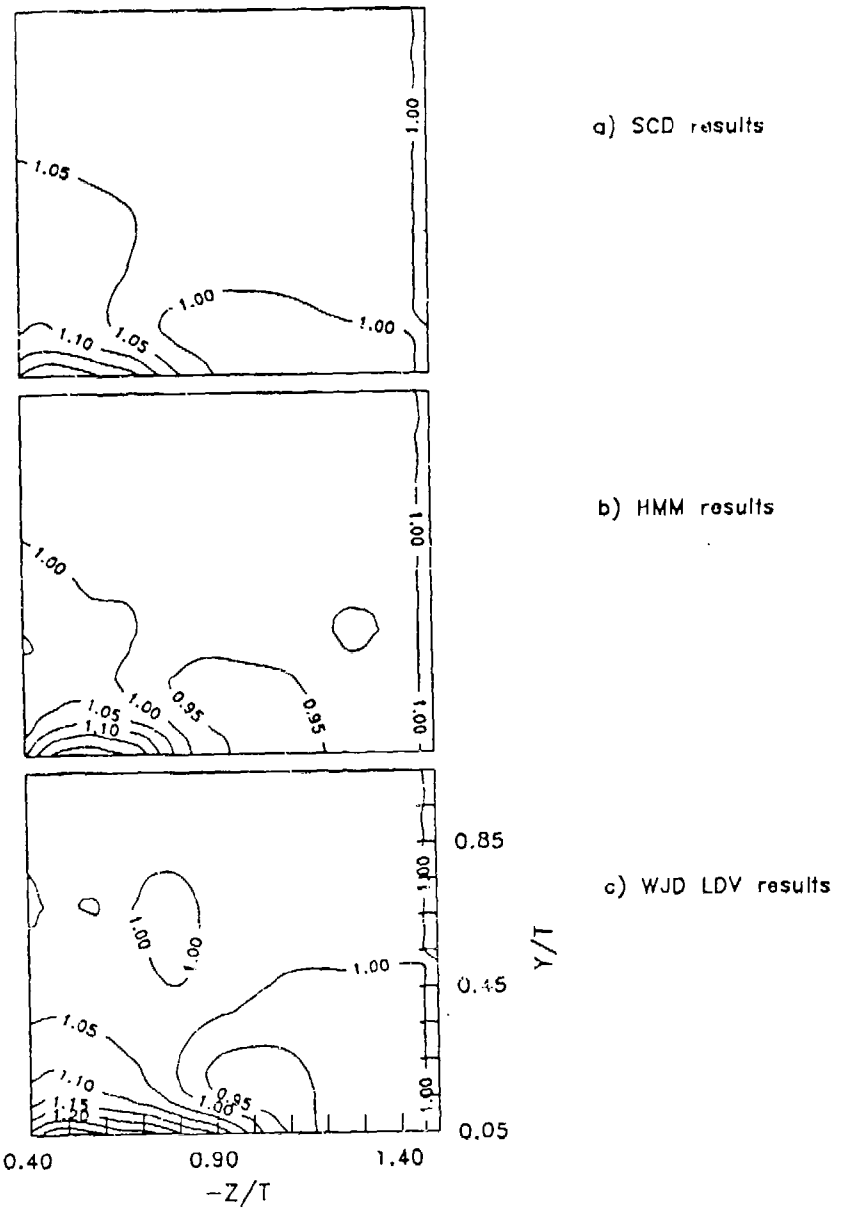

Figure 5.11. Comparison of Contours of Distortion Function, f_D, Plane 8

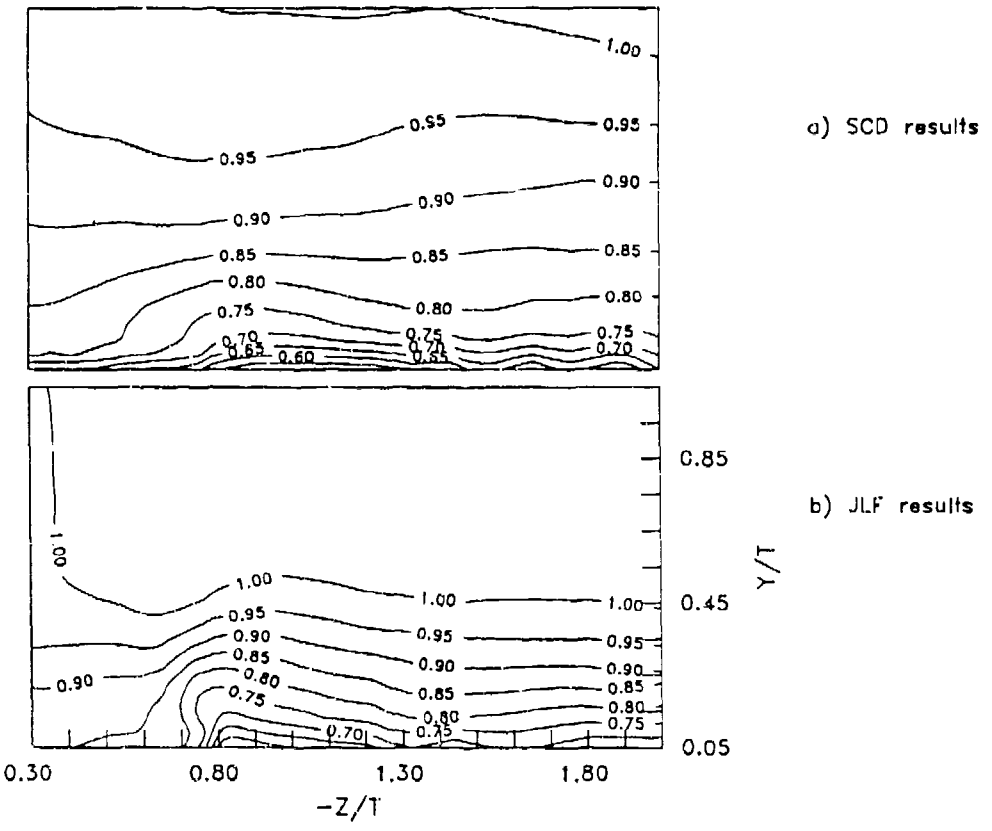

Figure 5.12. Comparison of Contours of U_{TC}/U_{ref}, Plane 9

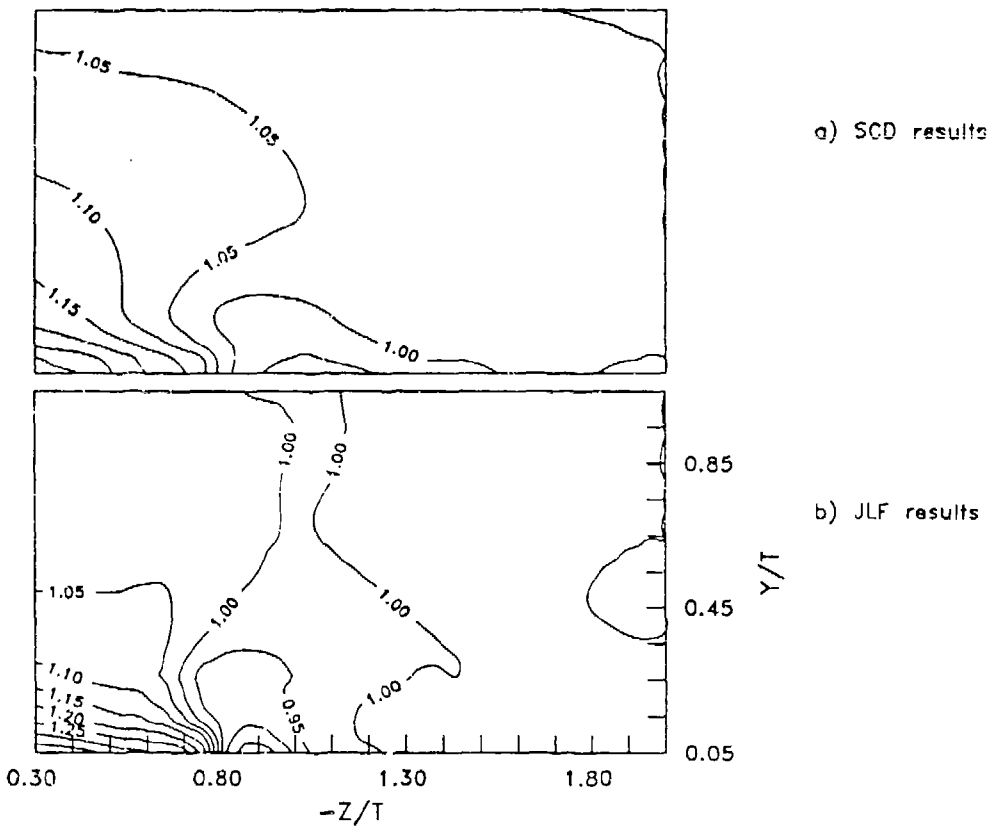

Figure 5.13. Comparison of Contours of Distortion Function, f_D, Plane 9

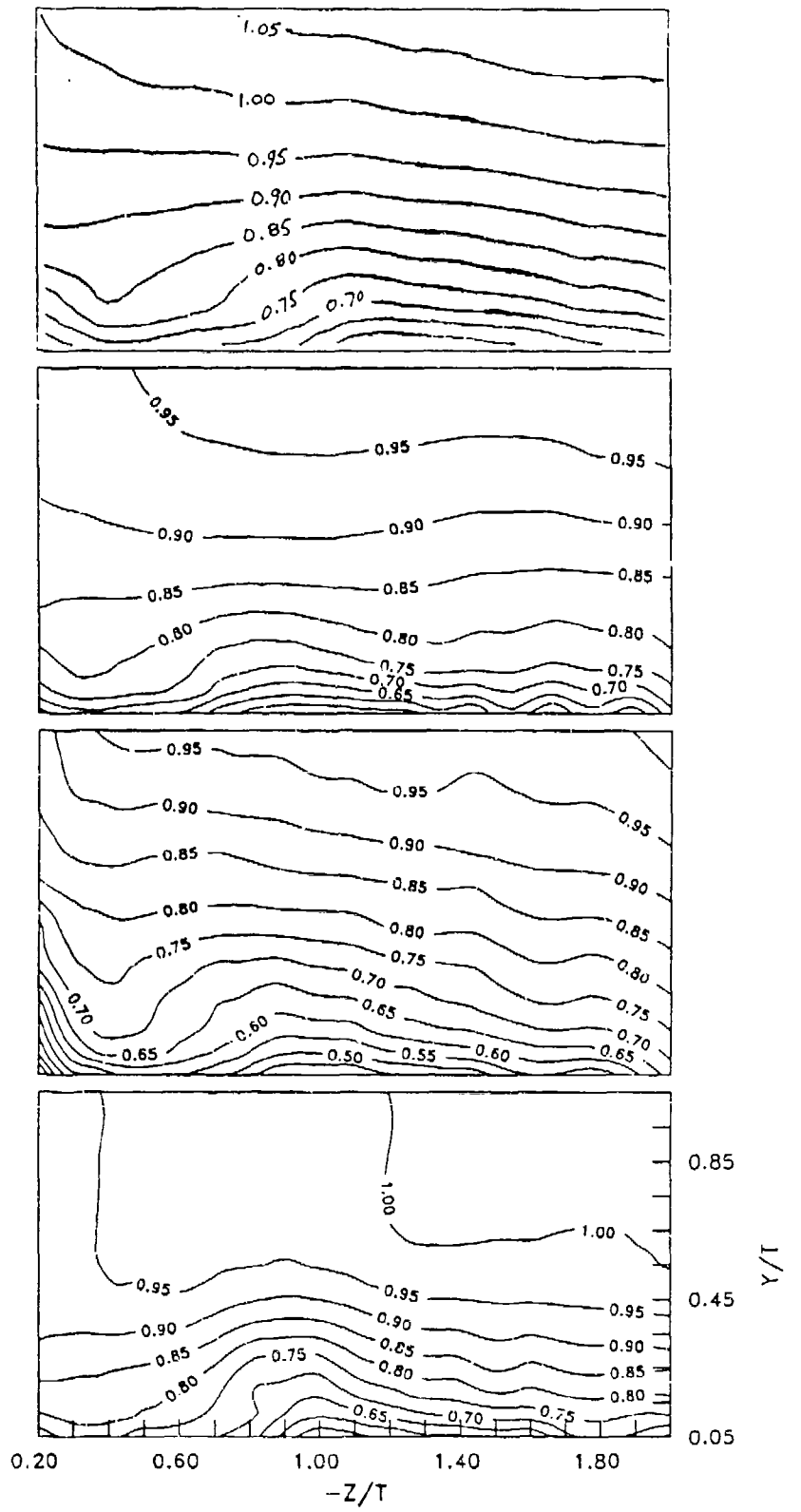

Figure 5.14. Comparison of Contours of U_{TC}/U_{ref}, Plane 10

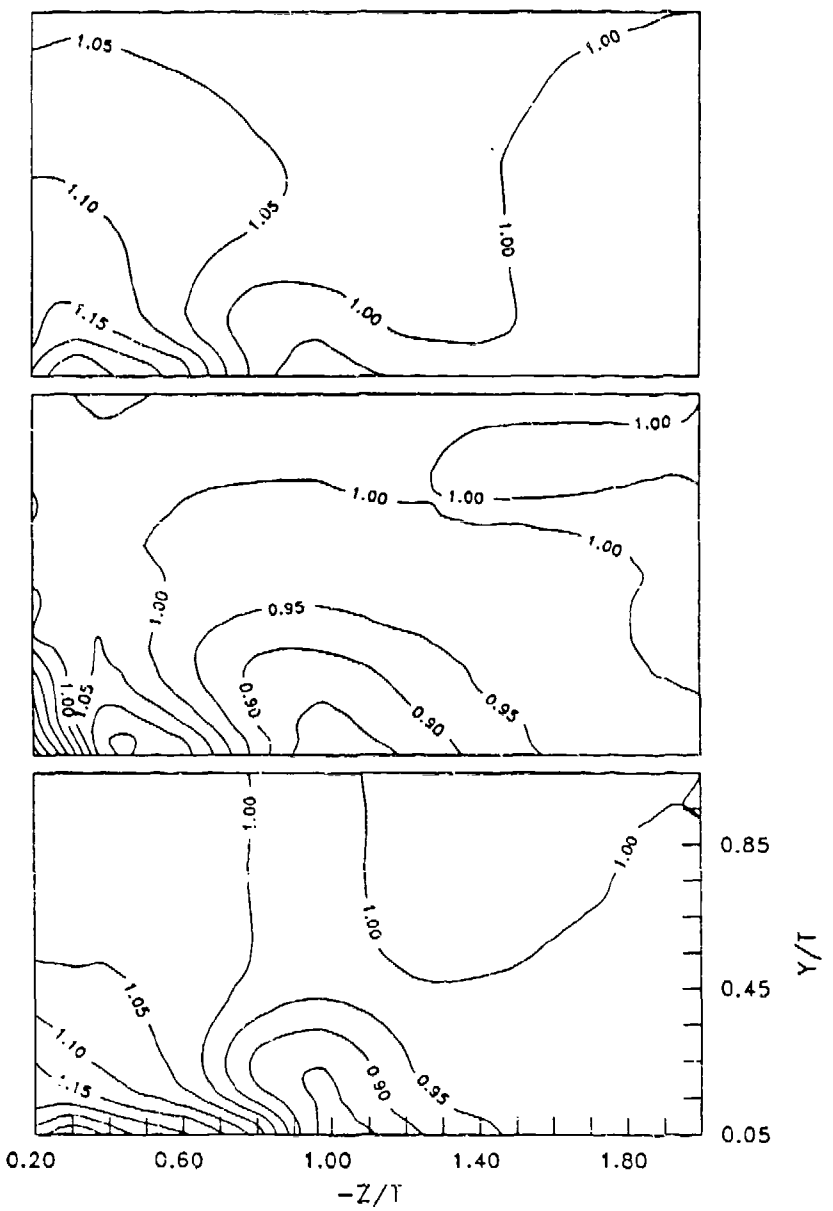

Figure 5.15. Comparison of Contours of Distortion Function, f_D, Plane 10

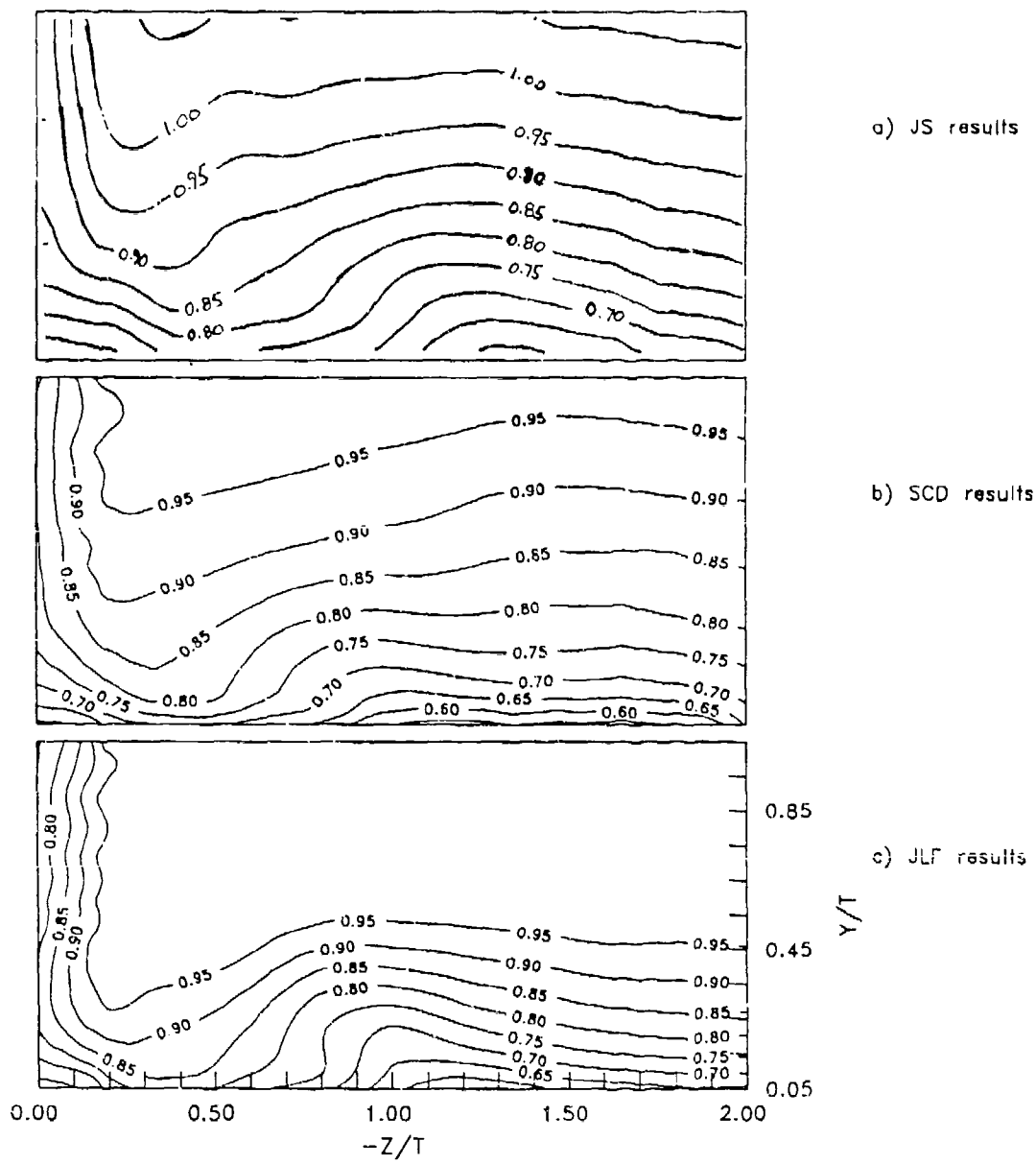

Figure 5.16. Comparison of Contours of U_{TC}/U_{ref}, Plane 11

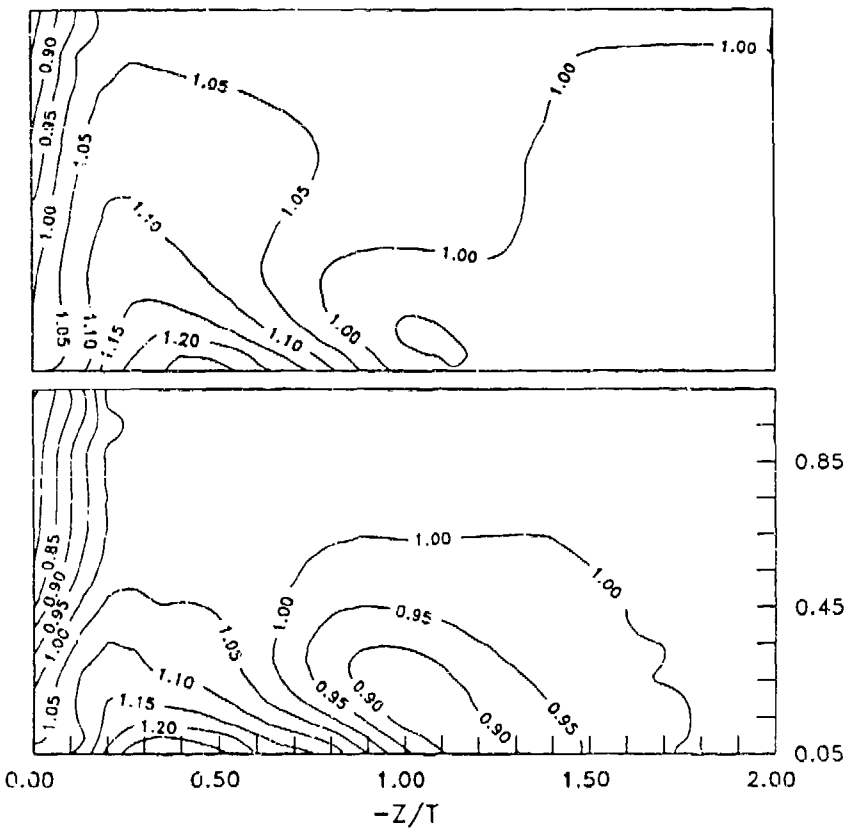

Figure 5.17. Comparison of Contours of Distortion Function, f_D, Plane 11

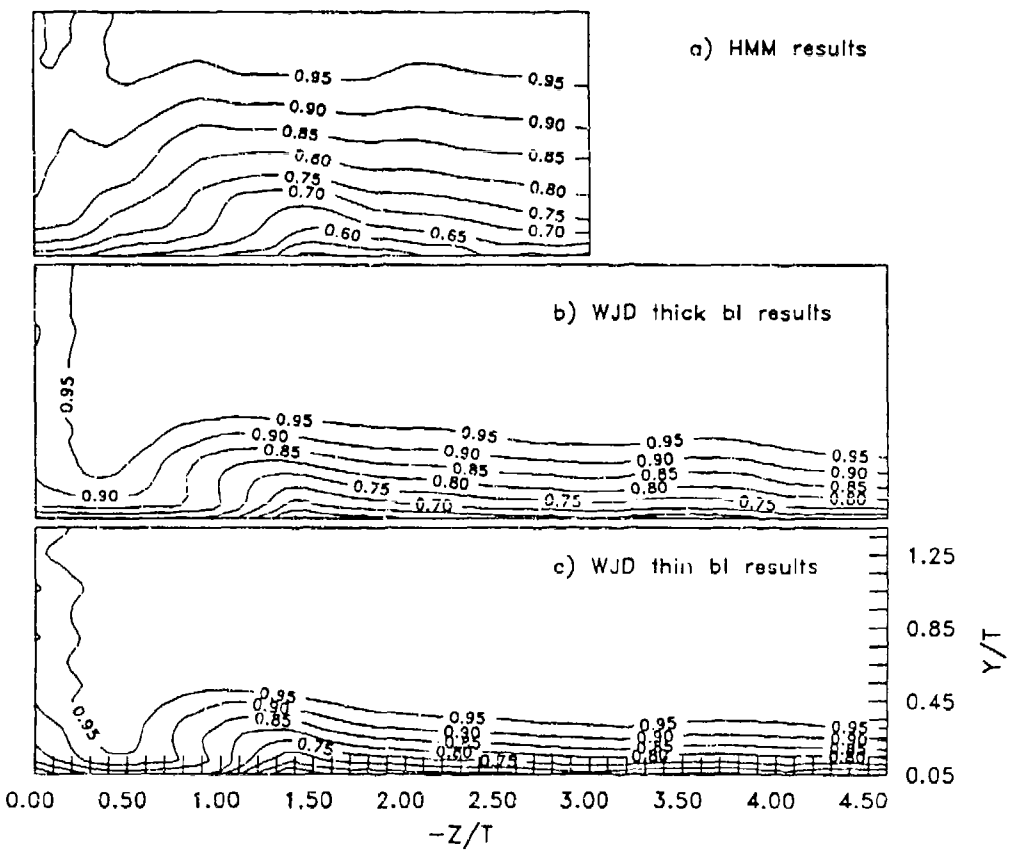

Figure 5.18. Comparison of Contours of U_{TC}/U_{ref}, Plane 12

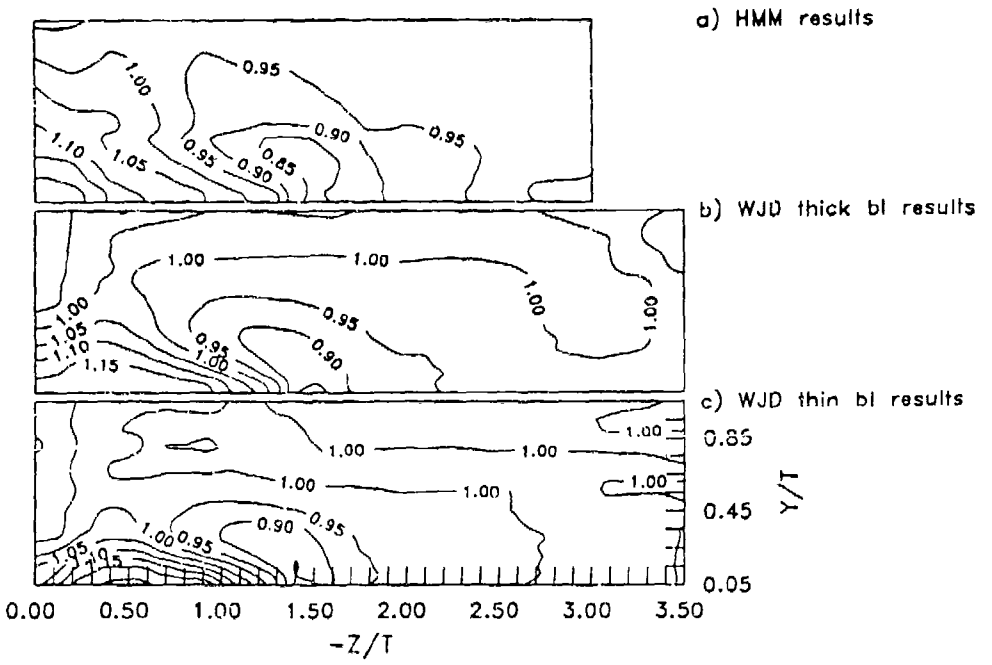

Figure 5.19. Comparison of Contours of Distortion Function, f_D, Plane 12

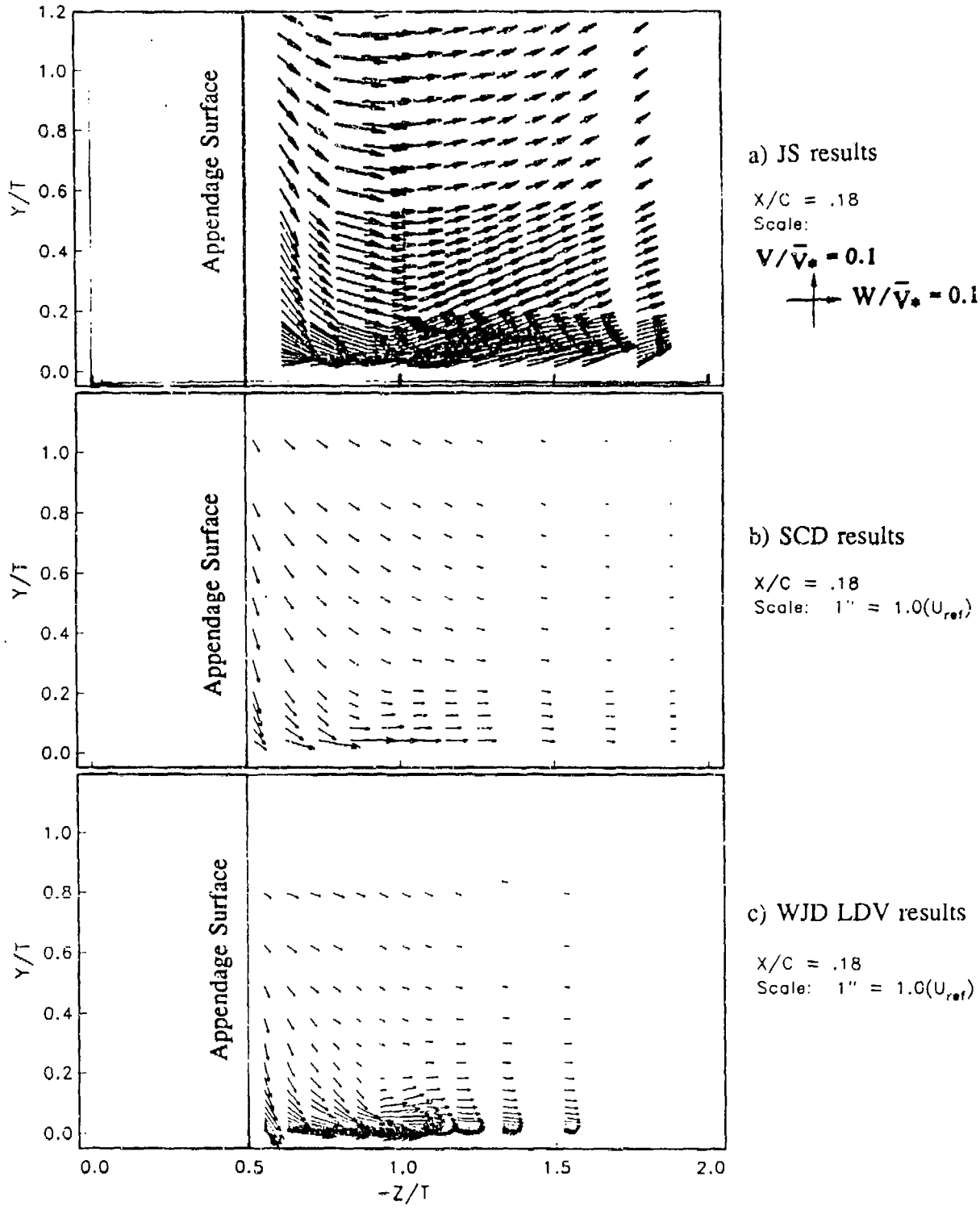

Figure 5.20. Comparison of Secondary Velocity Vectors, Plane 5

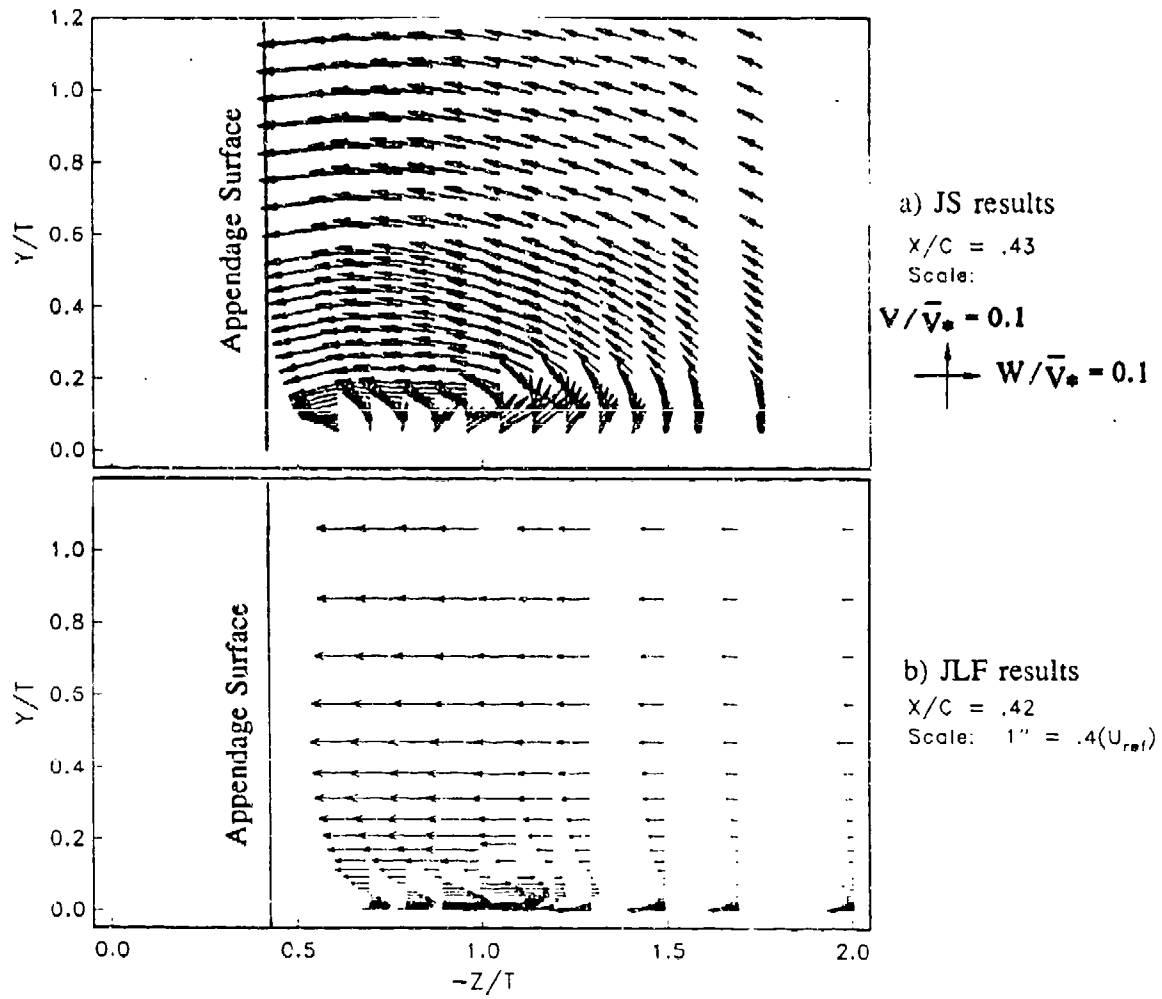

Figure 5.21. Comparison of Secondary Velocity Vectors, Plane 6 (JLF data presents only W component of vectors)

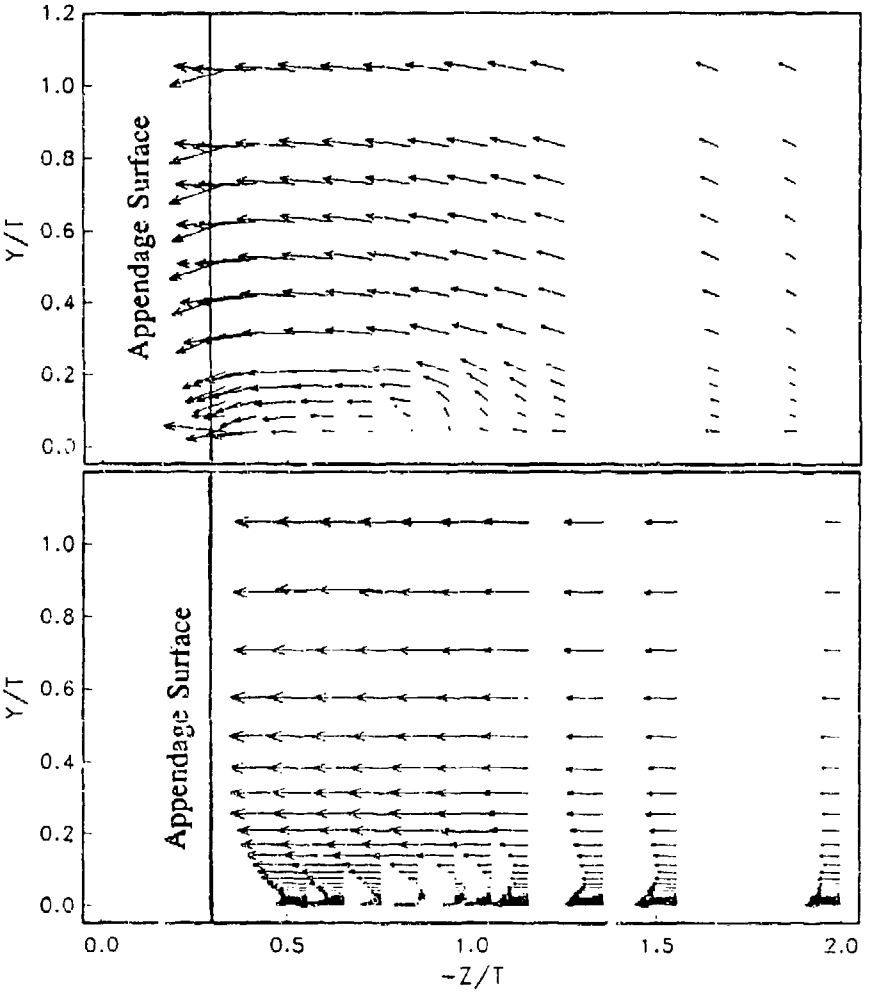

Figure 5.22. Comparison of Secondary Velocity Vectors, Plane 7 (JLF data presents only W component of vectors)

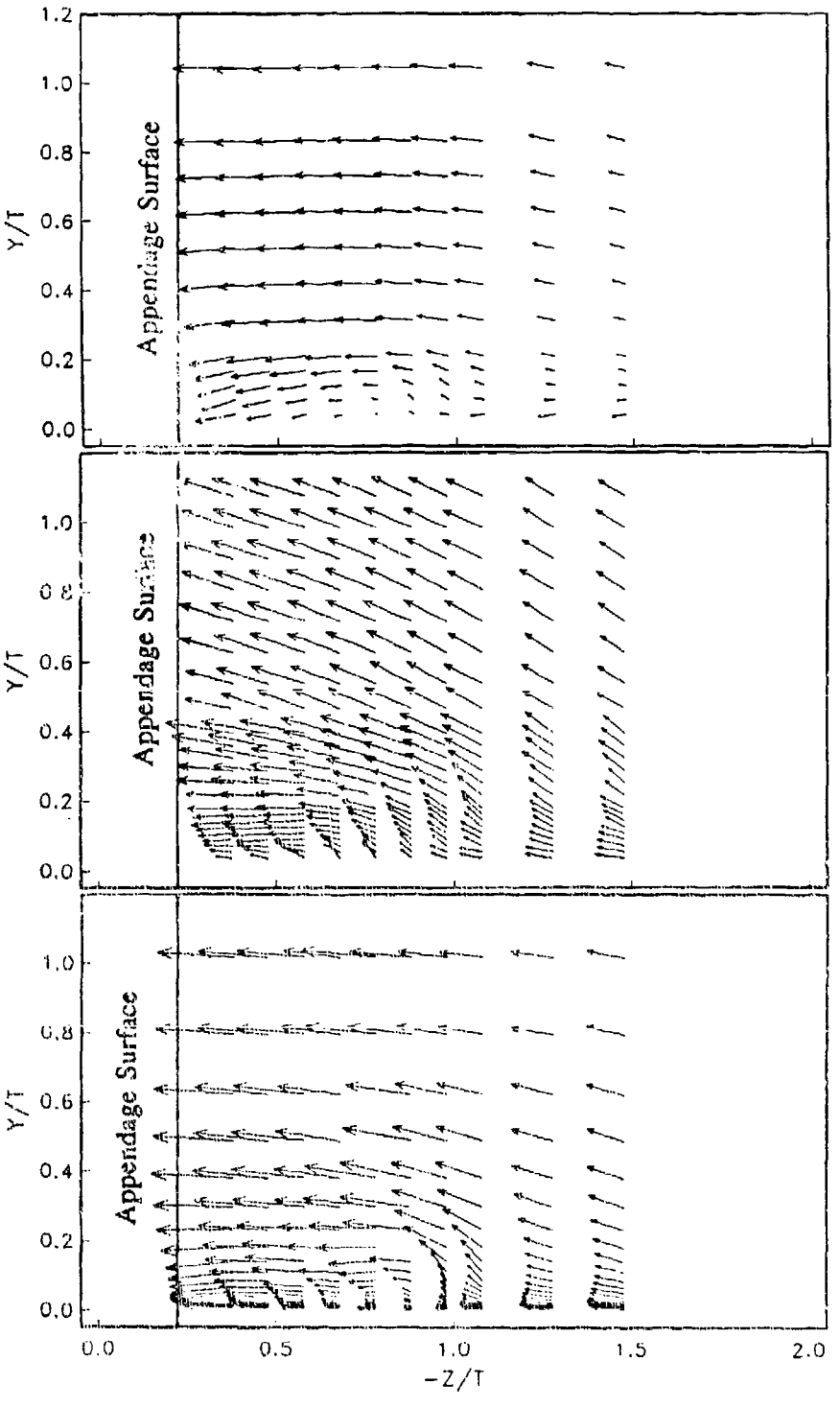

Figure 5.23. Comparison of Secondary Velocity Vectors, Plane 8

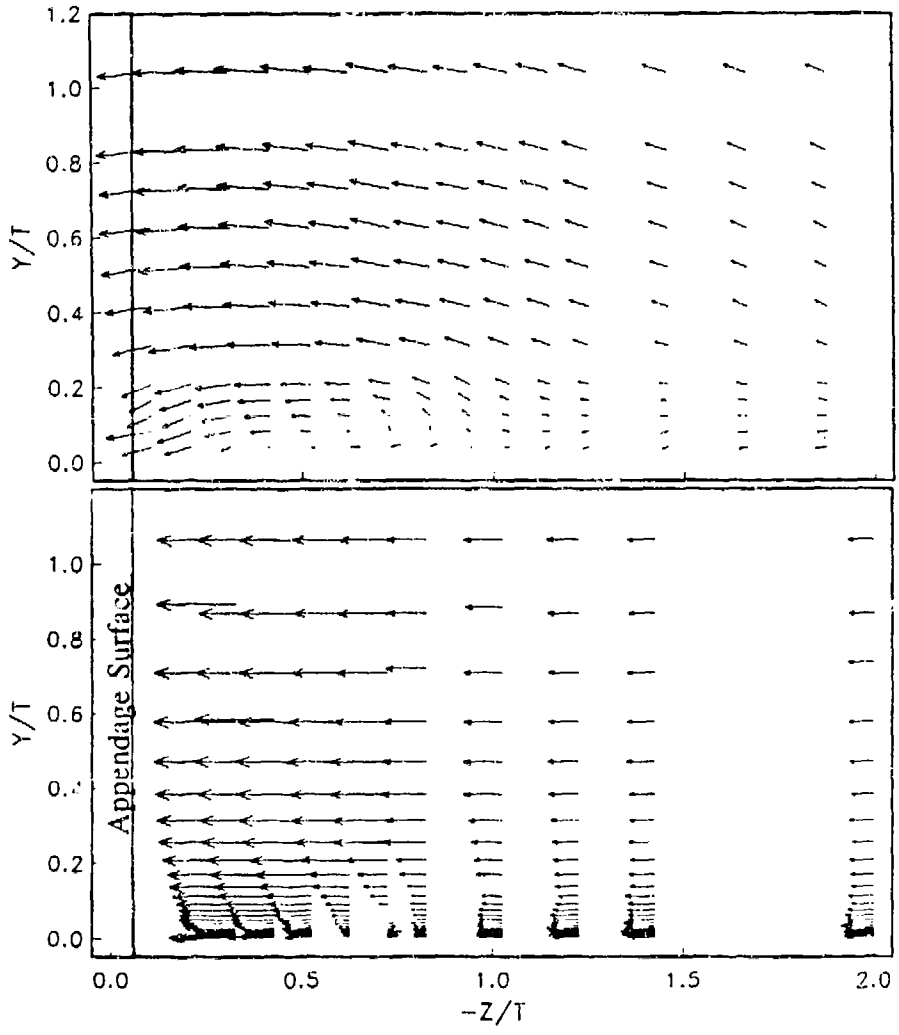

Figure 5.24. Comparison of Secondary Velocity Vectors, Plane 9 (JLF data presents only W component of vectors)

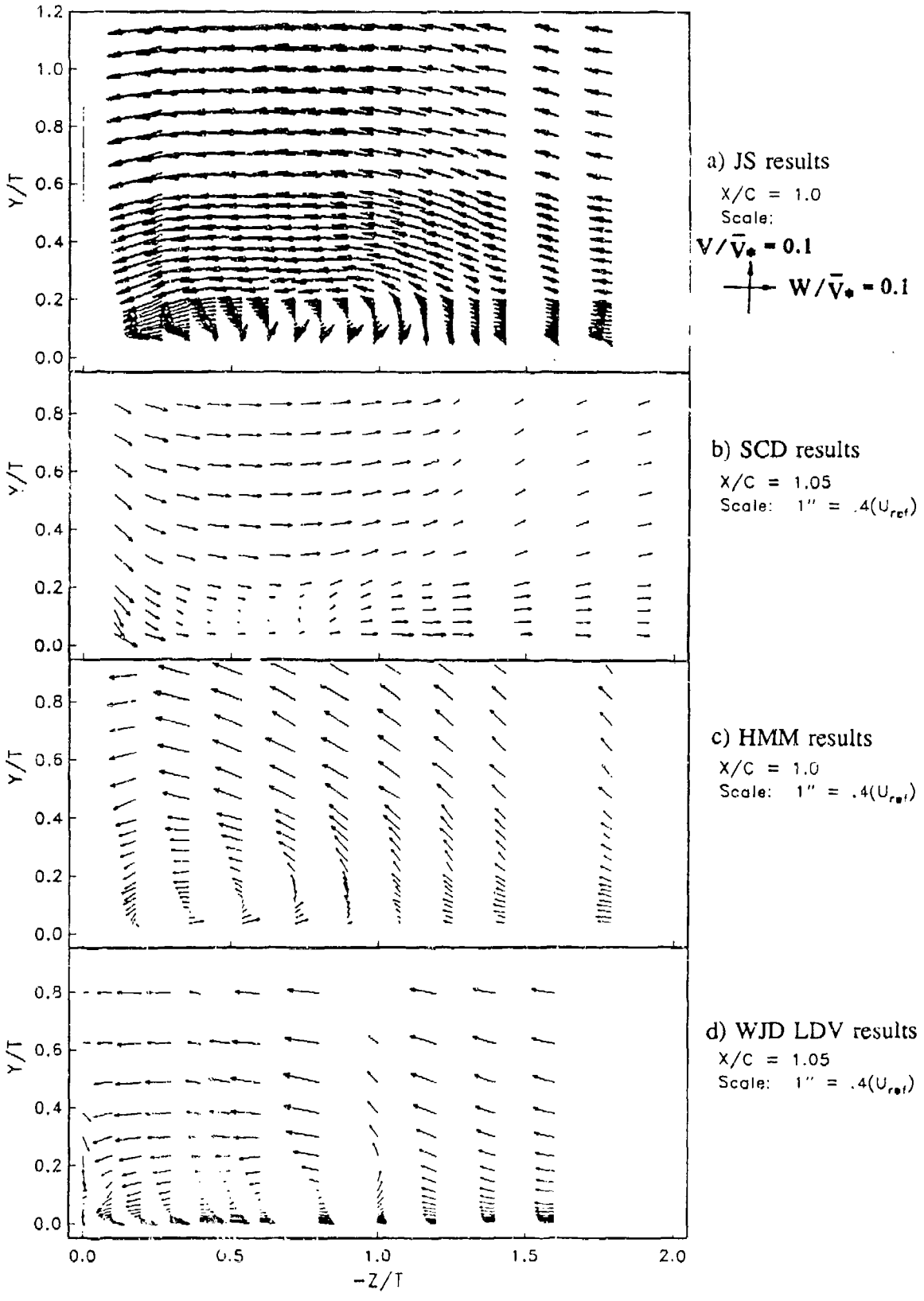

Figure 5.25. Comparison of Secondary Velocity Vectors, Plane 10

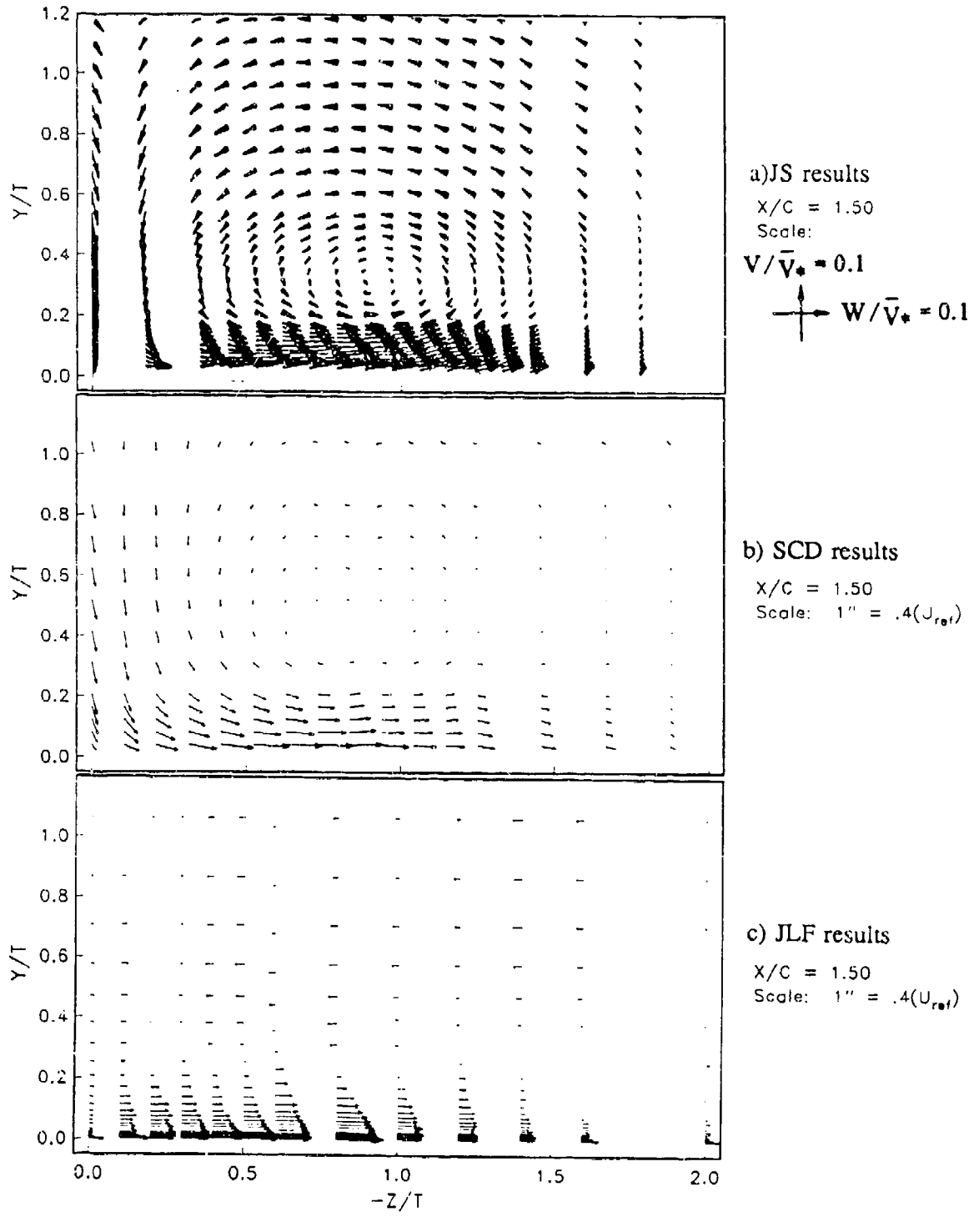

Figure 5.26. Comparison of Secondary Velocity Vectors, Plane 11 (JLF data presents only W component of vectors)

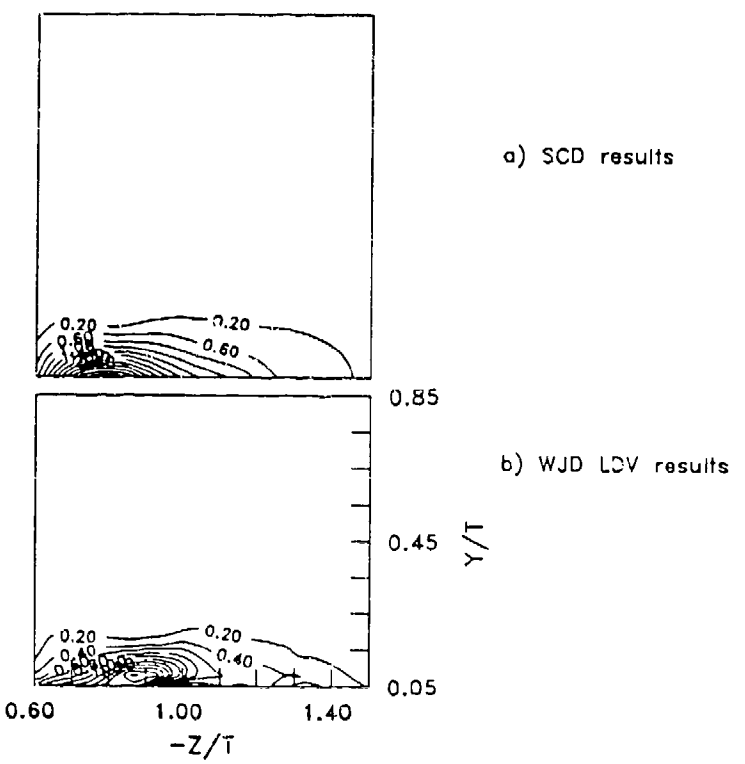

Figure 5.27. Comparison of Contours of $(\partial(W)/\partial Y)\delta/U_{ref}$, Plane 5

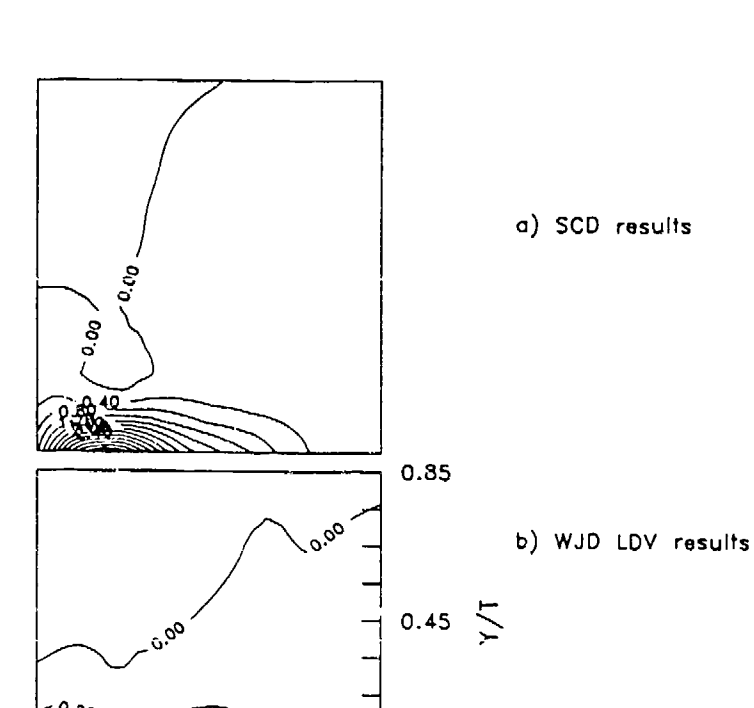

Figure 5.28. Comparison of Contours of h, Plane 5

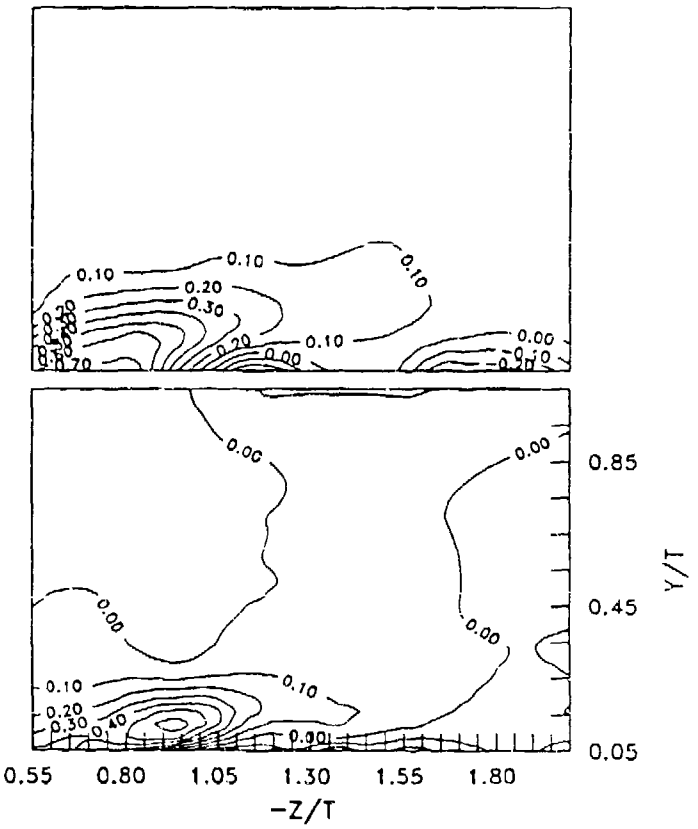

Figure 5.29. Comparison of Contours of $(\partial(W)/\partial Y)\delta/U_{ref}$, Plane 7

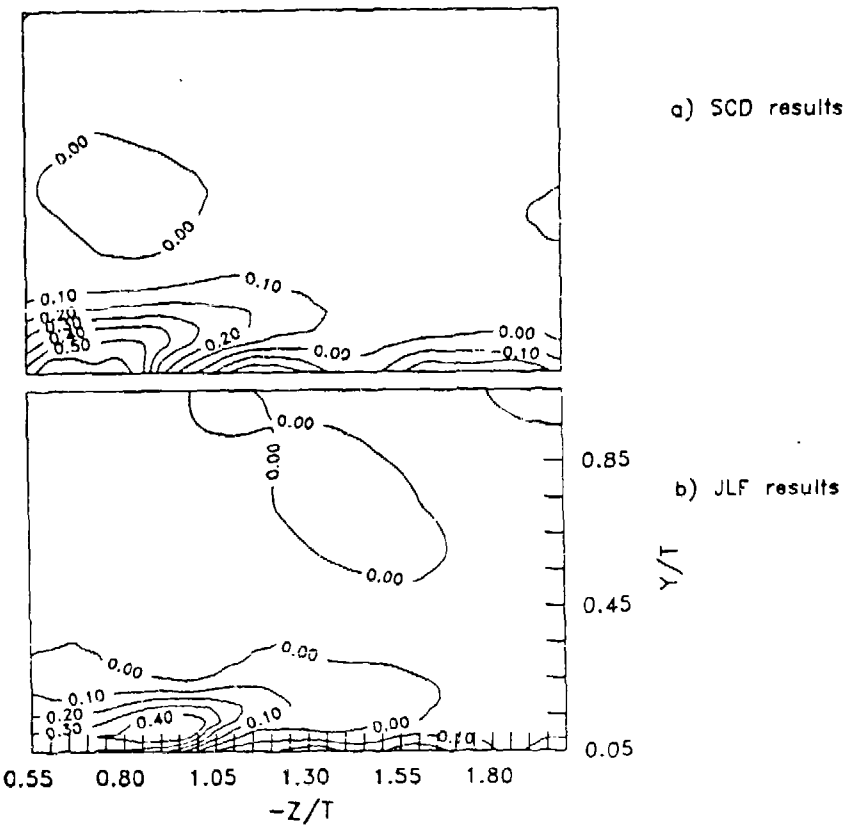

Figure 5.30. Comparison of Contours of h, Plane 7

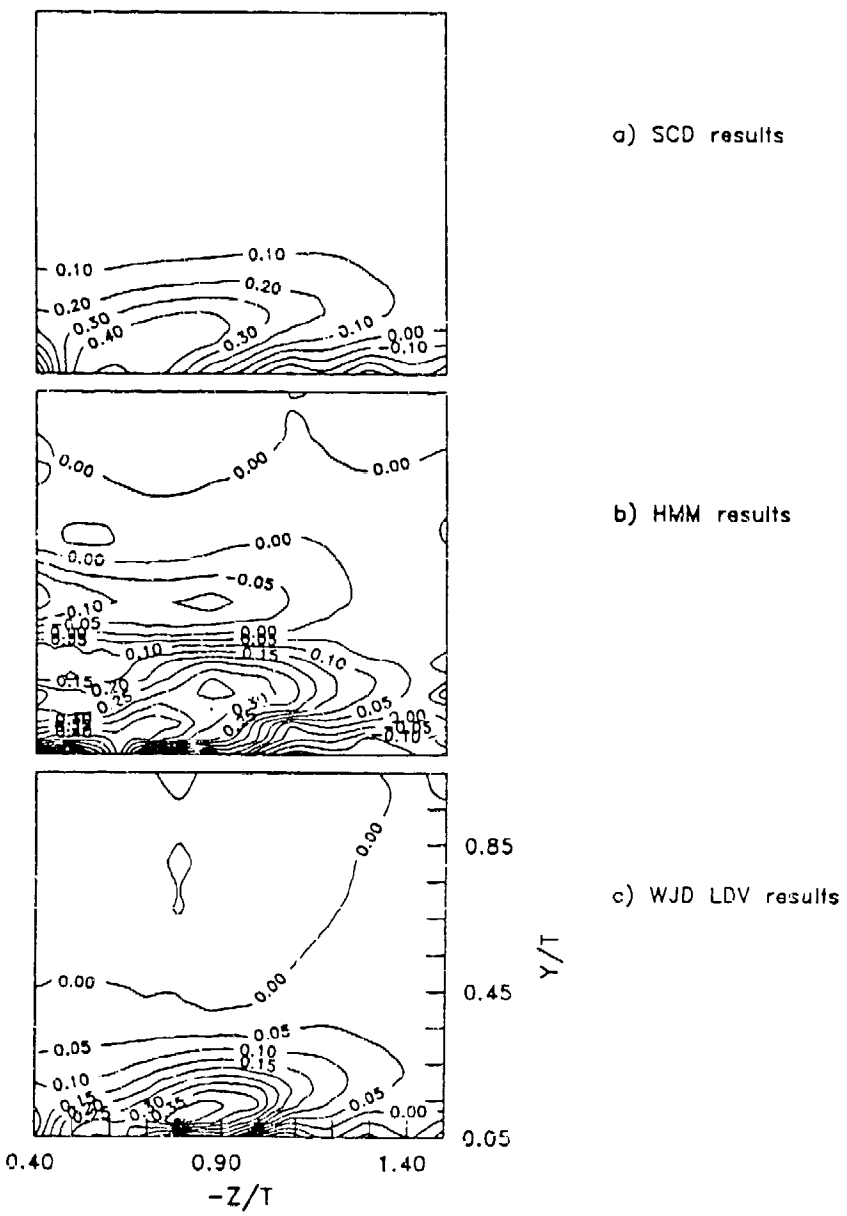

Figure 5.31. Comparison of Contours of $(\partial(W)/\partial Y)\delta/U_{ref}$, Plane 8

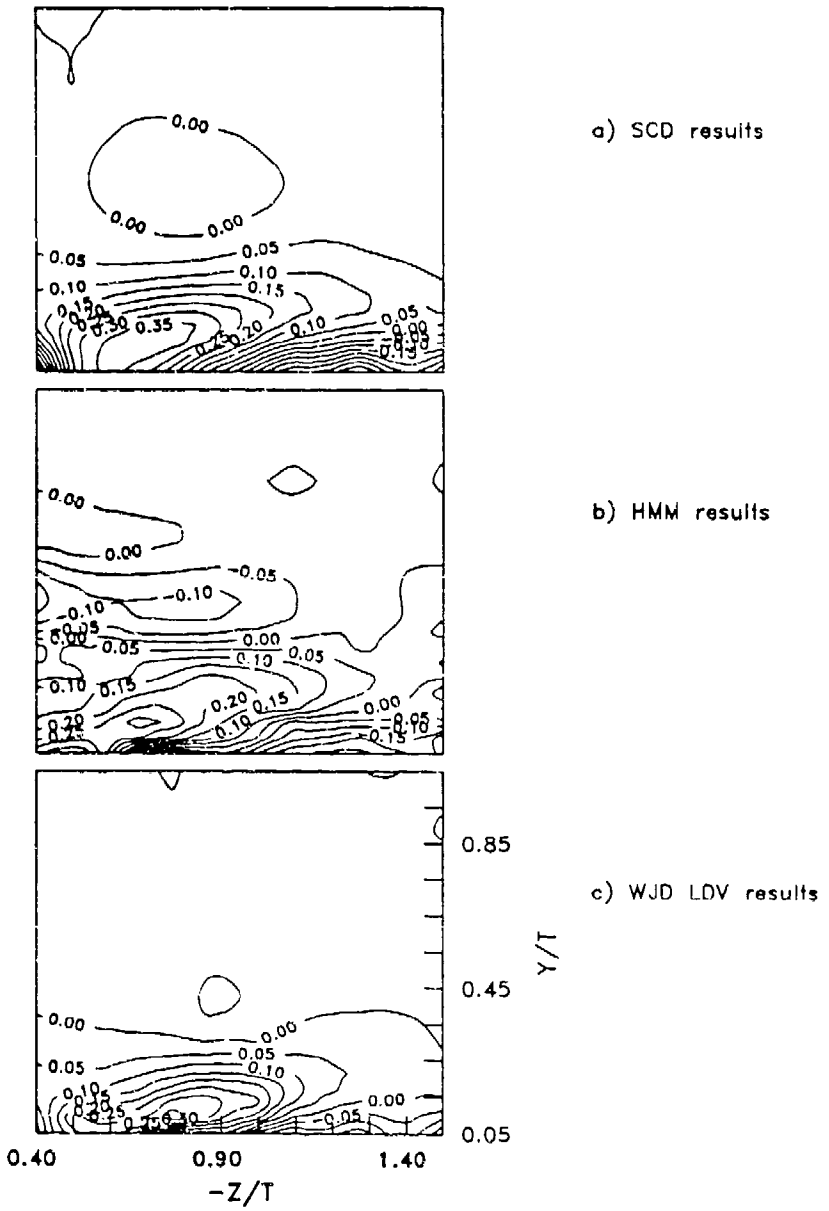

Figure 5.32. Comparison of Contours of h, Plane 8

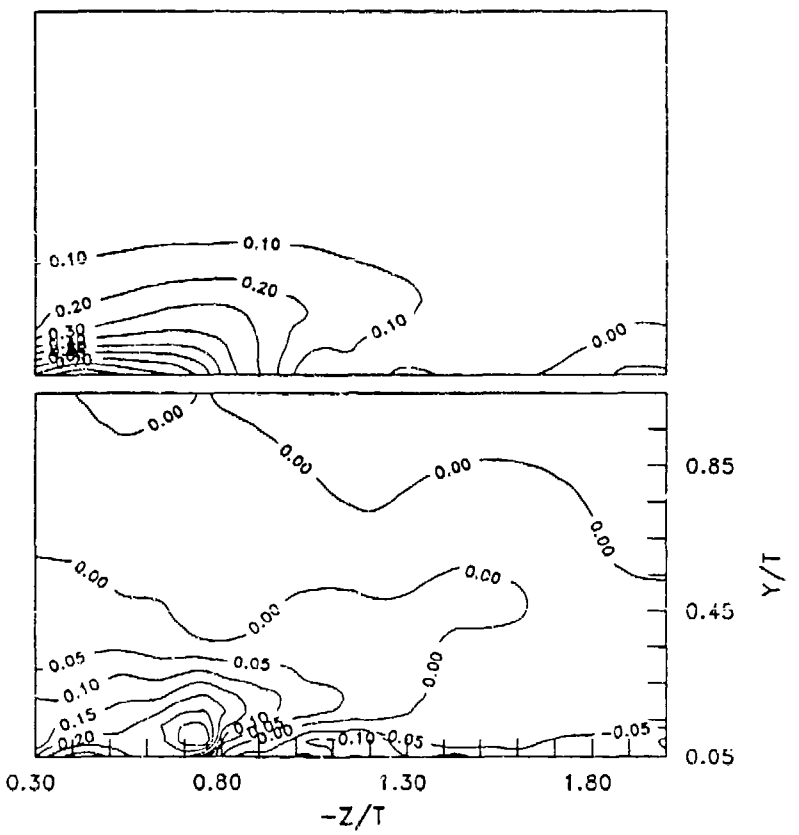

Figure 5.33. Comparison of Contours of $(\partial(W)/\partial Y)\delta/U_{ref}$, Plane 9

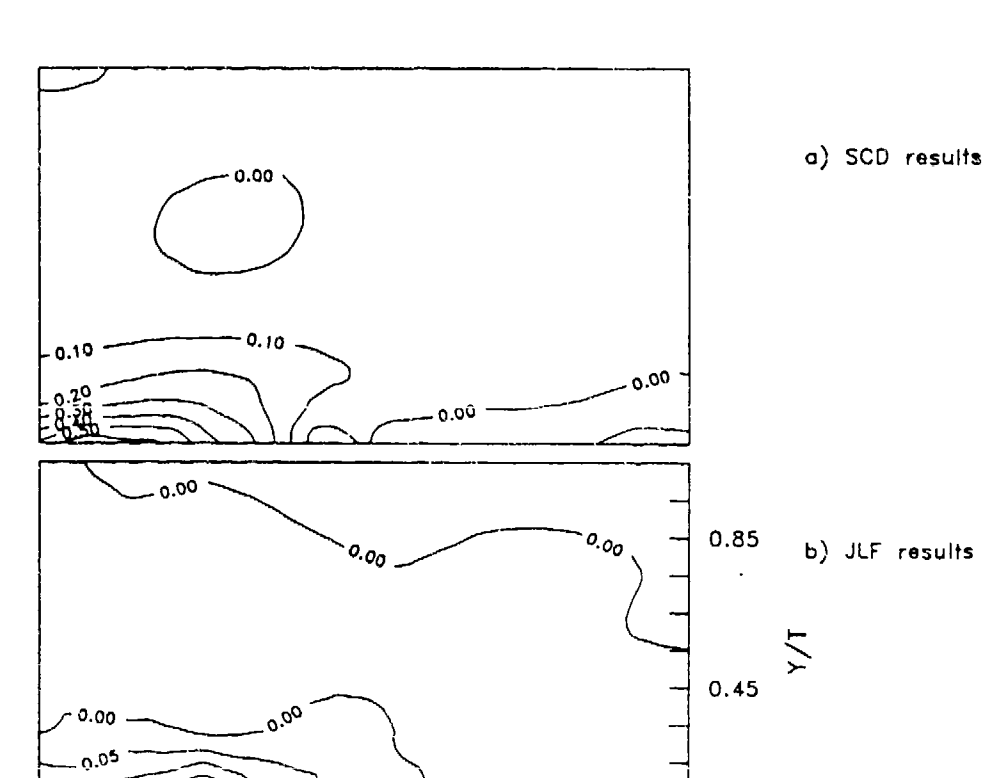

Figure 5.34. Comparison of Contours of h, Plane 9

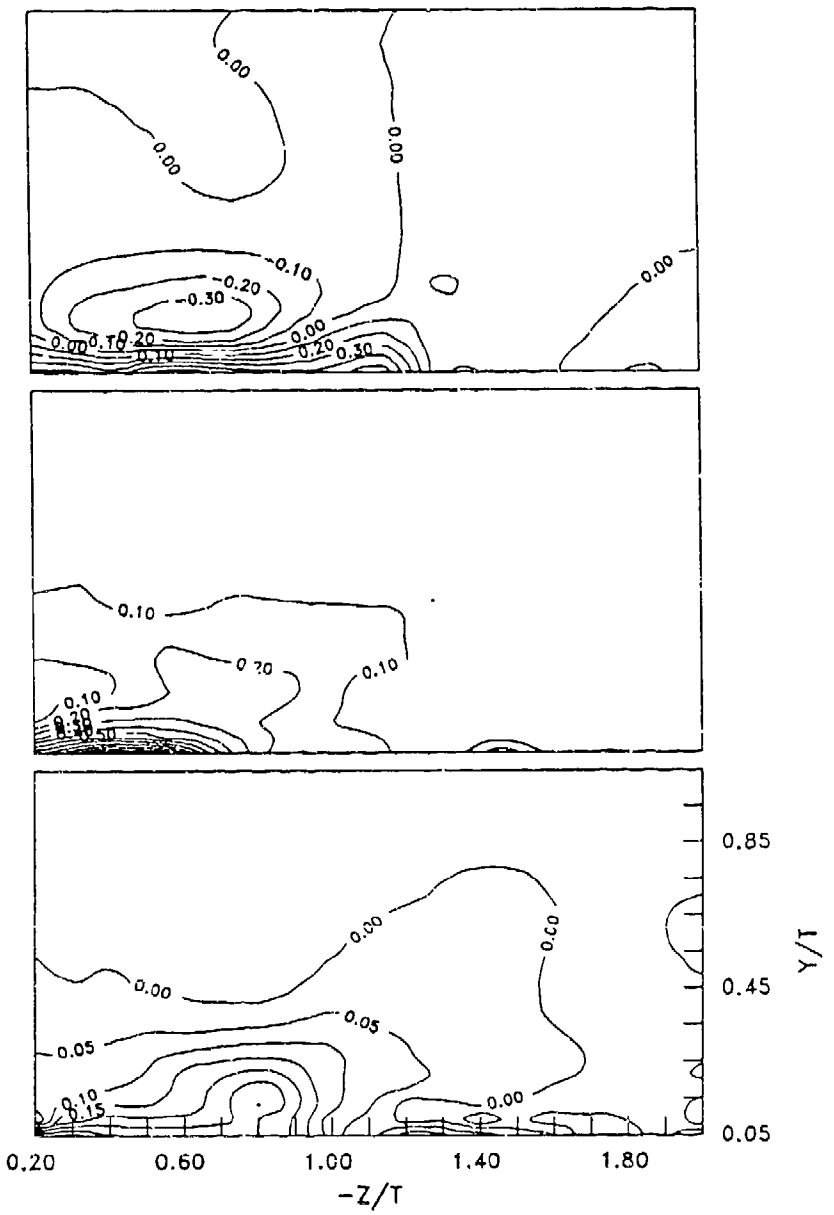

Figure 5.35. Comparison of Contours of $(\partial(W)/\partial Y)\delta/U_{ref}$, Plane 10

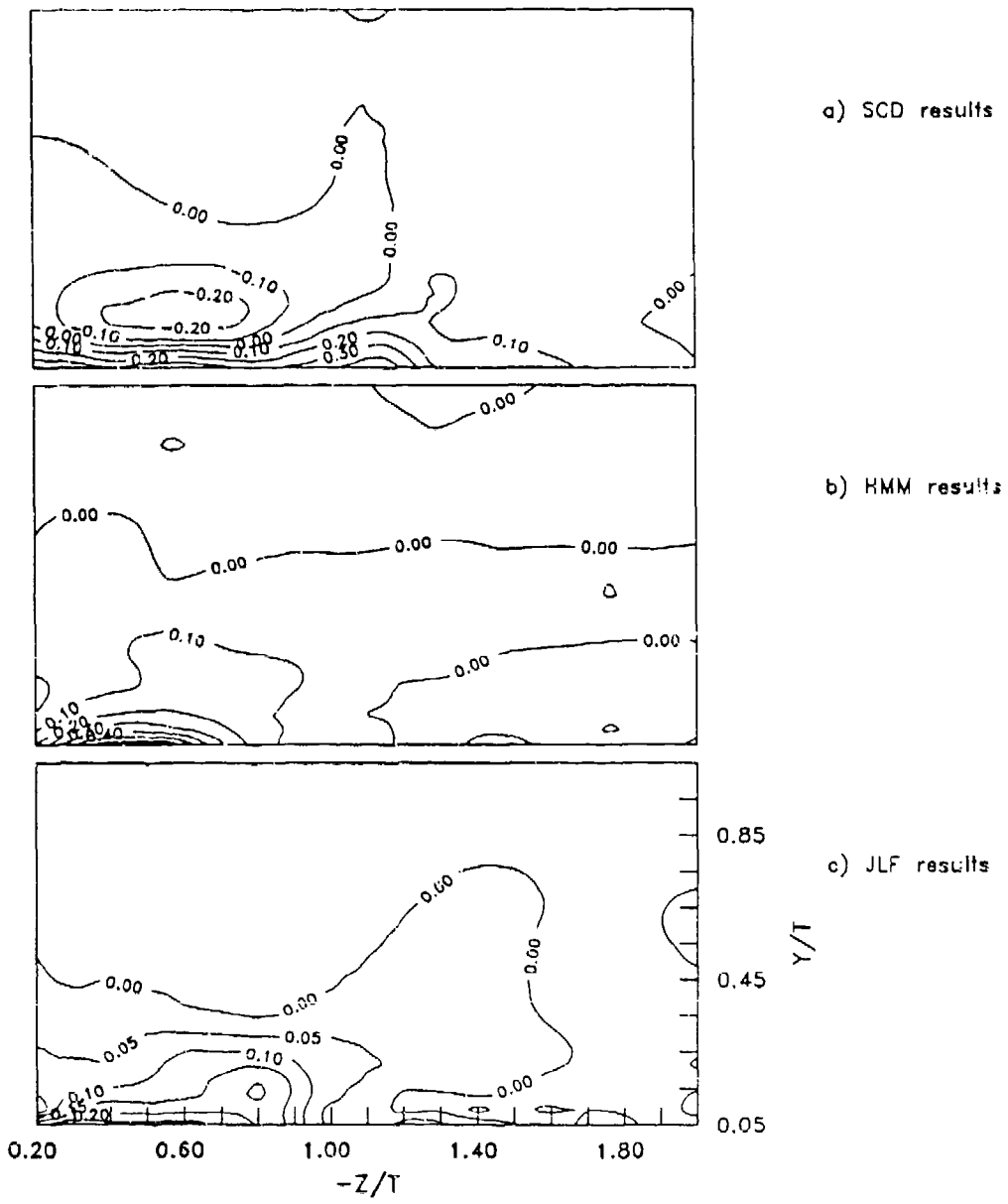

Figure 5.36. Comparison of Contours of h, Plane 10

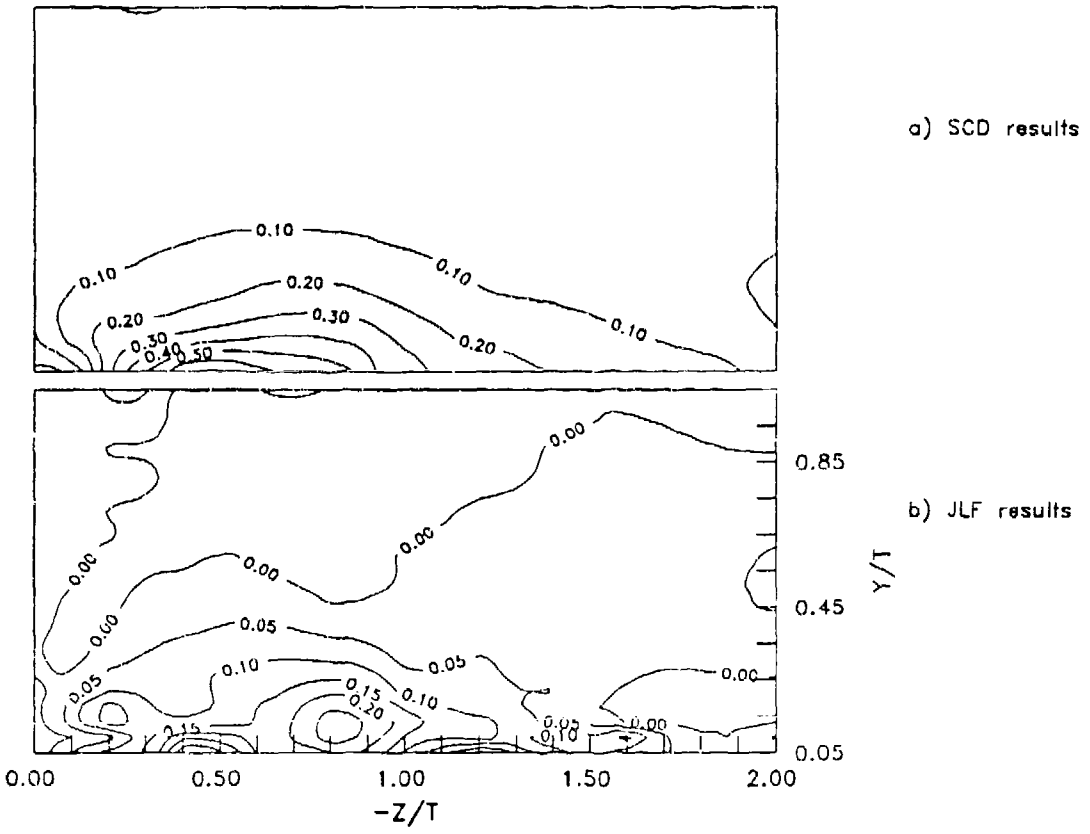

Figure 5.37. Comparison of Contours of $(\partial(W)/\partial Y)\delta/U_{ref}$, Plane 11

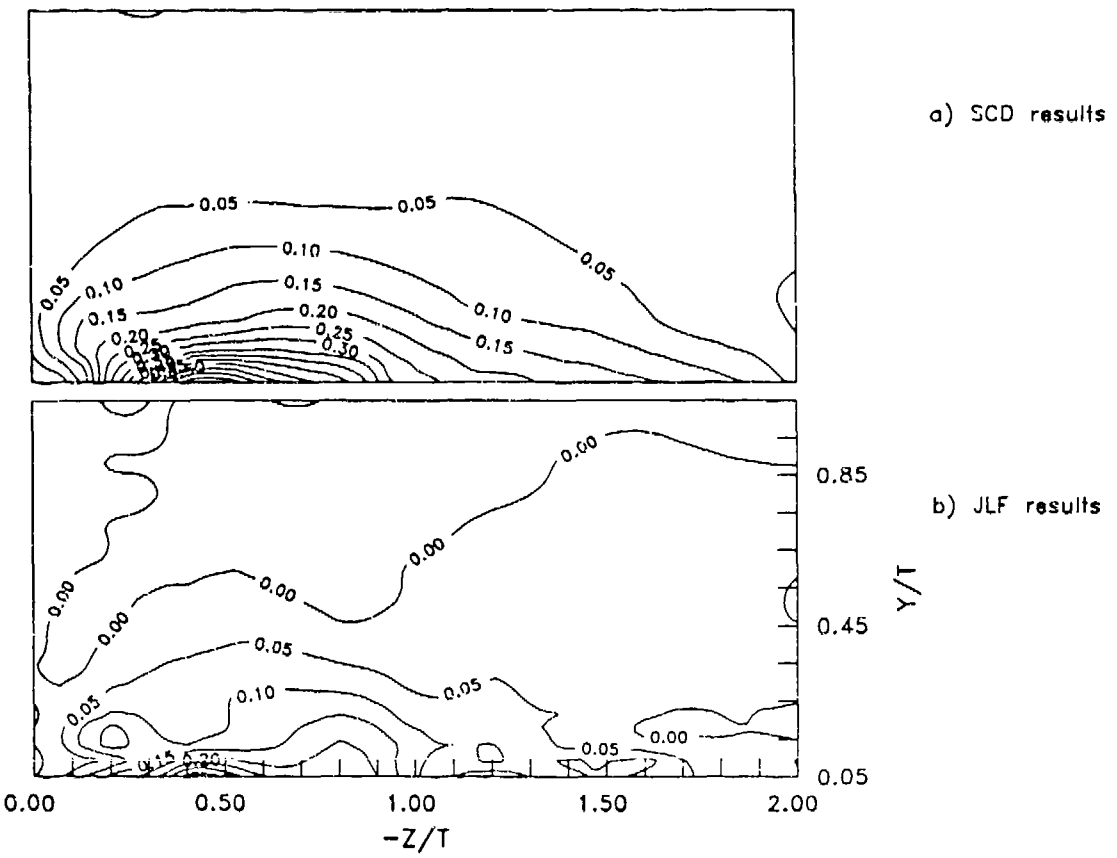

Figure 5.38. Comparison of Contours of h, Plane 11

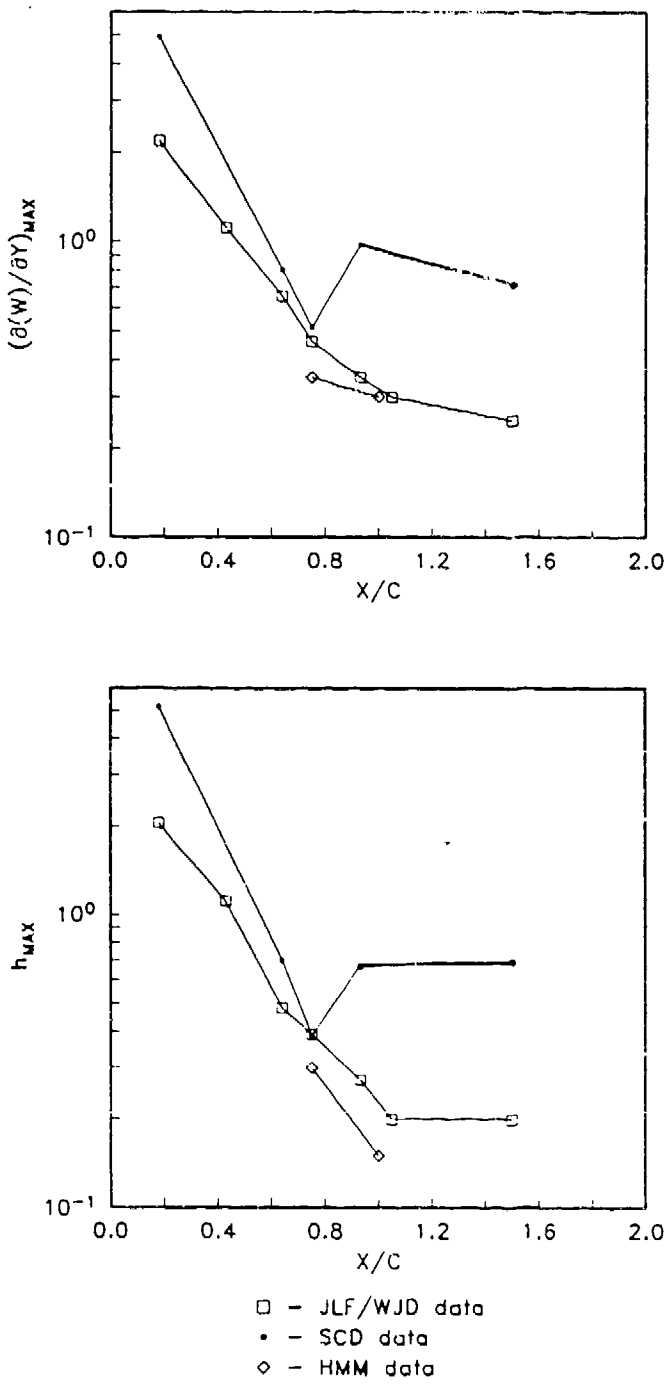

Figure 5.39. Variation of Core Values of $(\partial(W)/\partial Y)\delta/U_{ref}$ and h vs. X/C

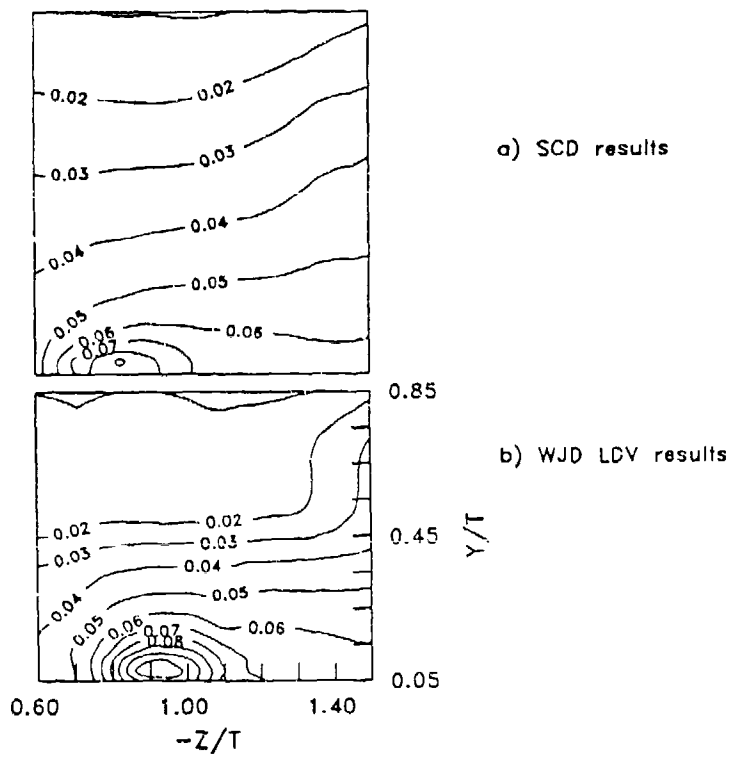

Figure 5.40. Comparison of Contours of u'_{TC}/U_{ref}, Plane 5

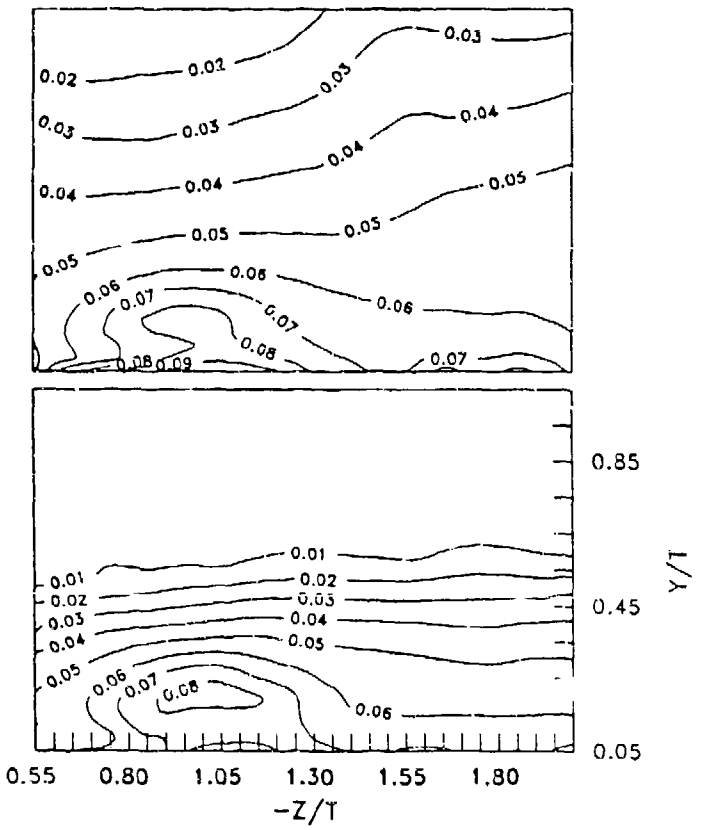

Figure 5.41. Comparison of Contours of u'_{TC}/U_{ref}, Plane 7

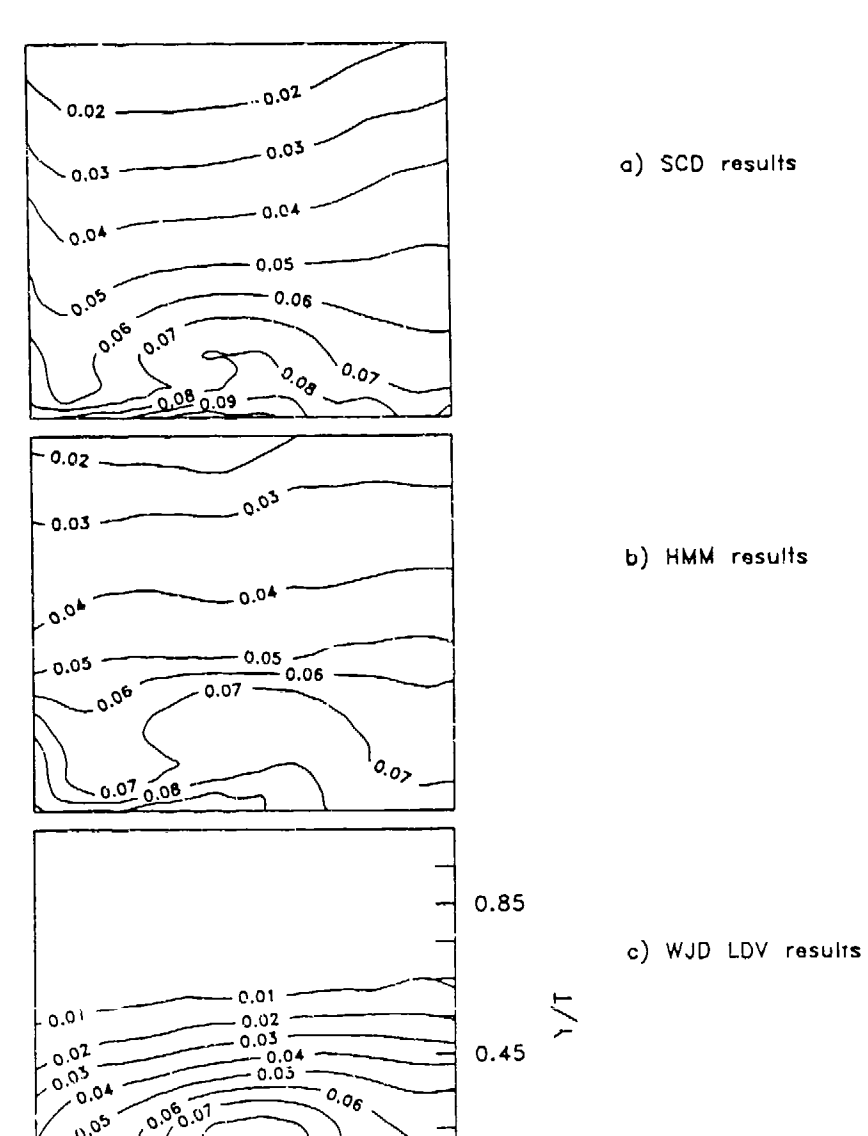

Figure 5.42. Comparison of Contours of u'_{TC}/U_{ref}, Plane 8

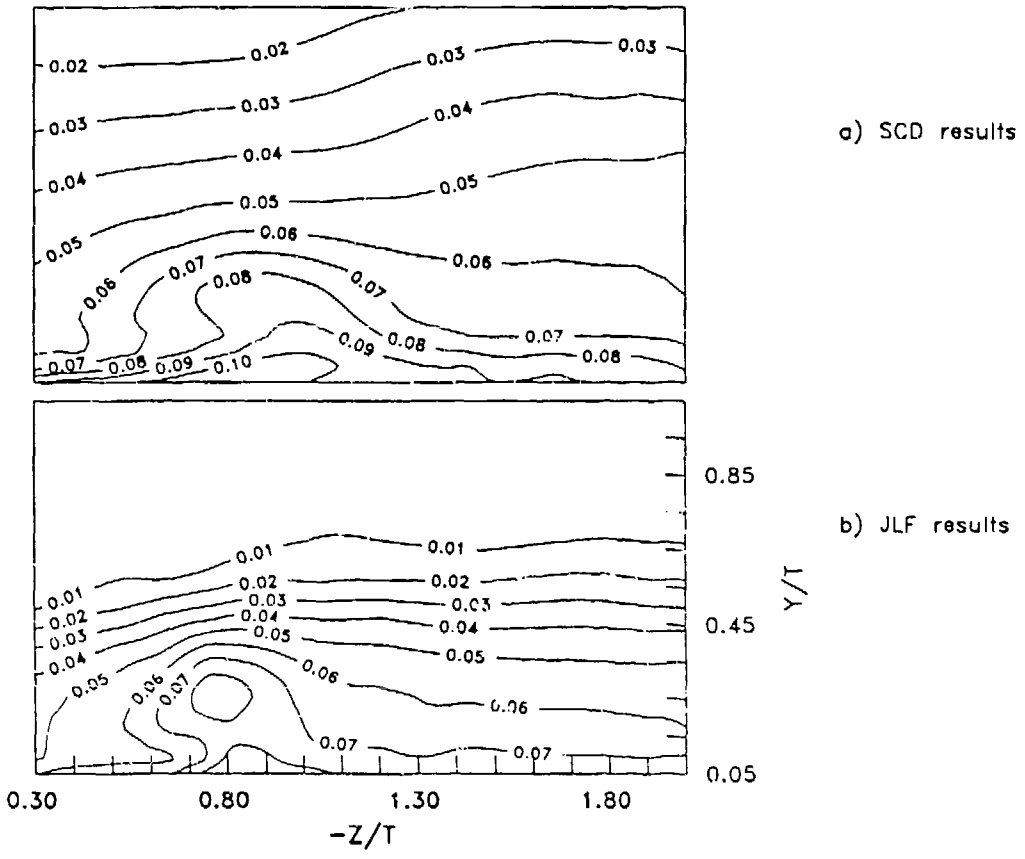

Figure 5.43. Comparison of Contours of u'_{TC}/U_{ref}, Plane 9

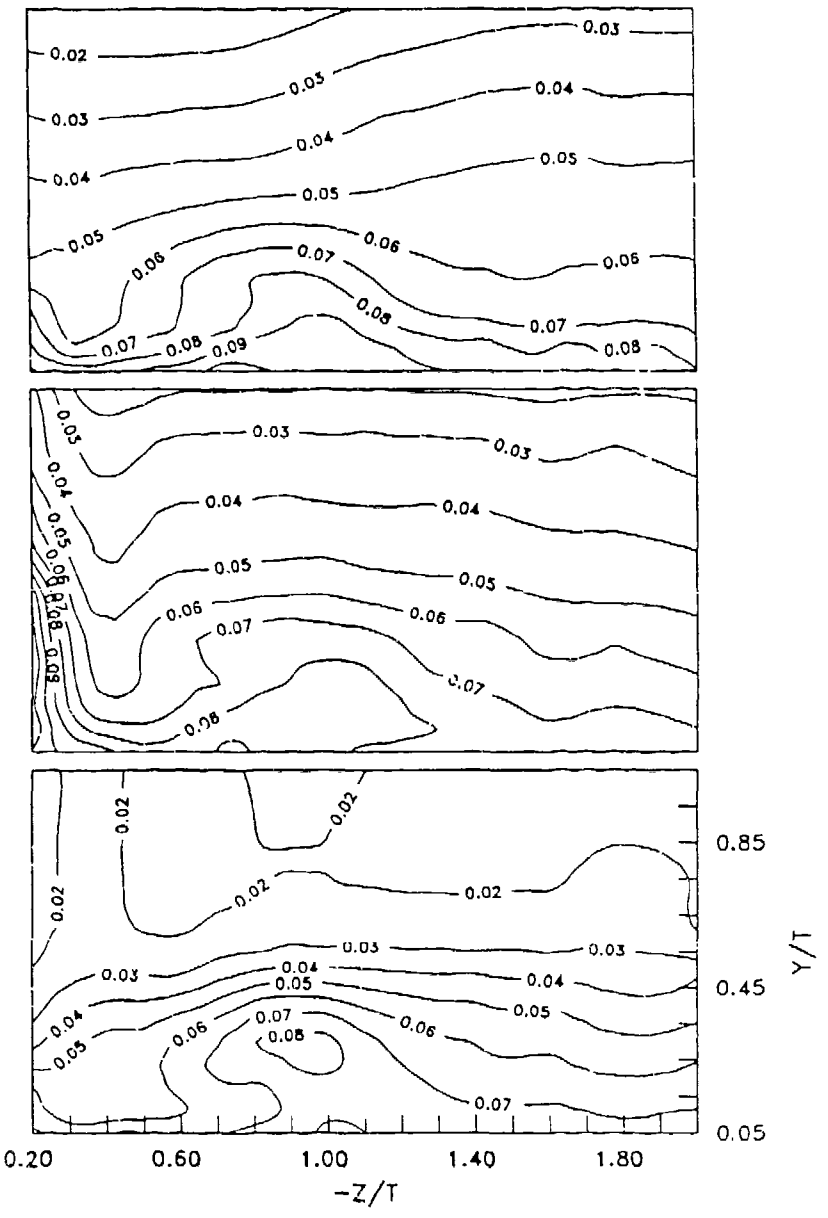

Figure 5.44. Comparison of Contours of u'_{TC}/U_{ref}, Plane 10

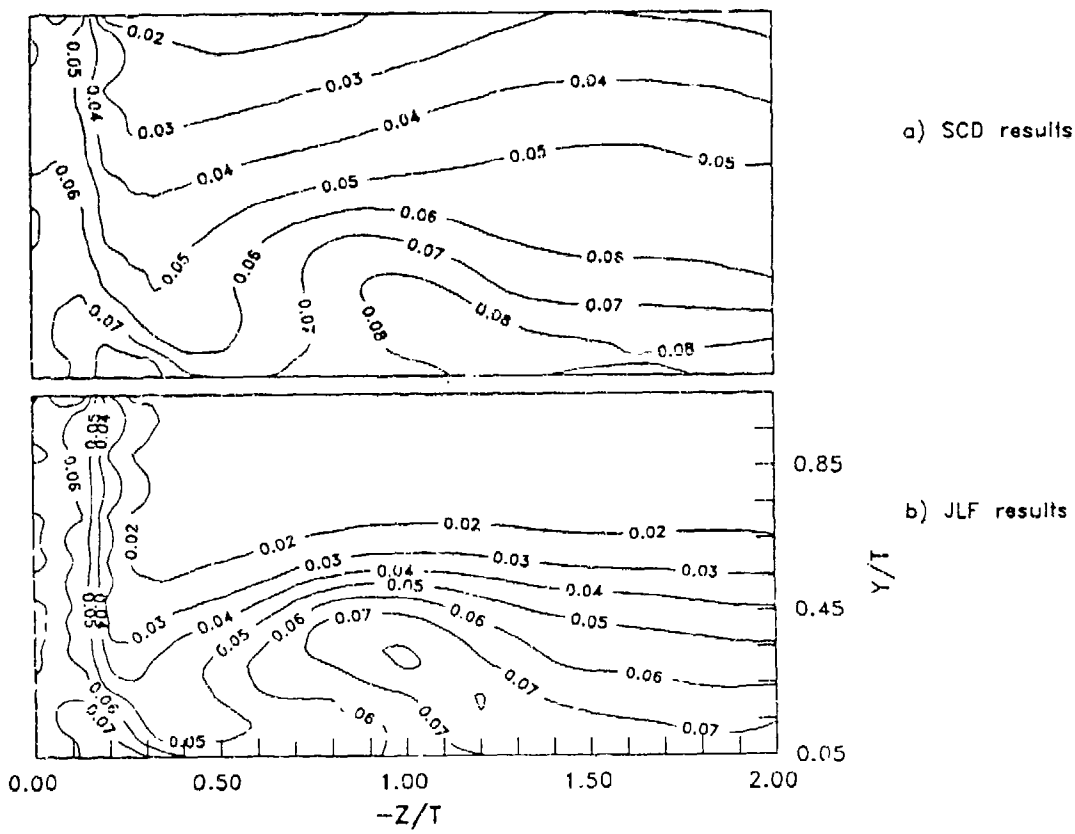

Figure 5.45. Comparison of Contours of u'_{TC}/U_{ref}, Plane 11

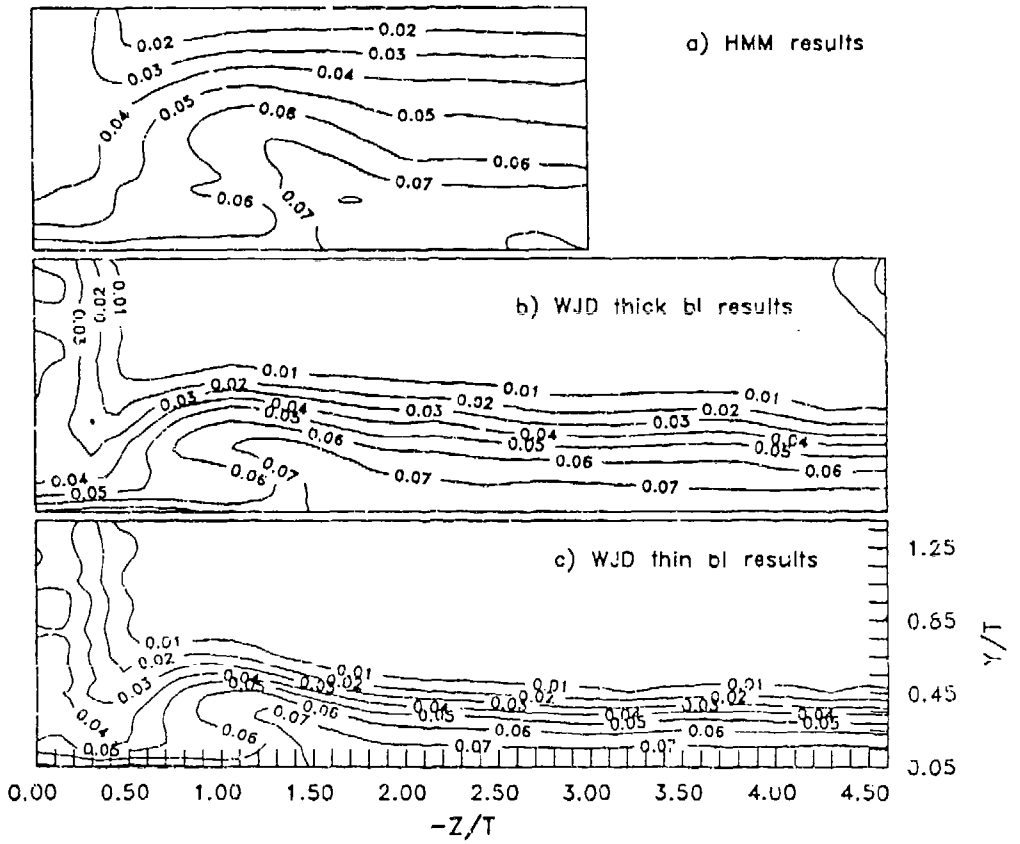

Figure 5.46. Comparison of Contours of u'_{TC}/U_{ref}, Plane 12

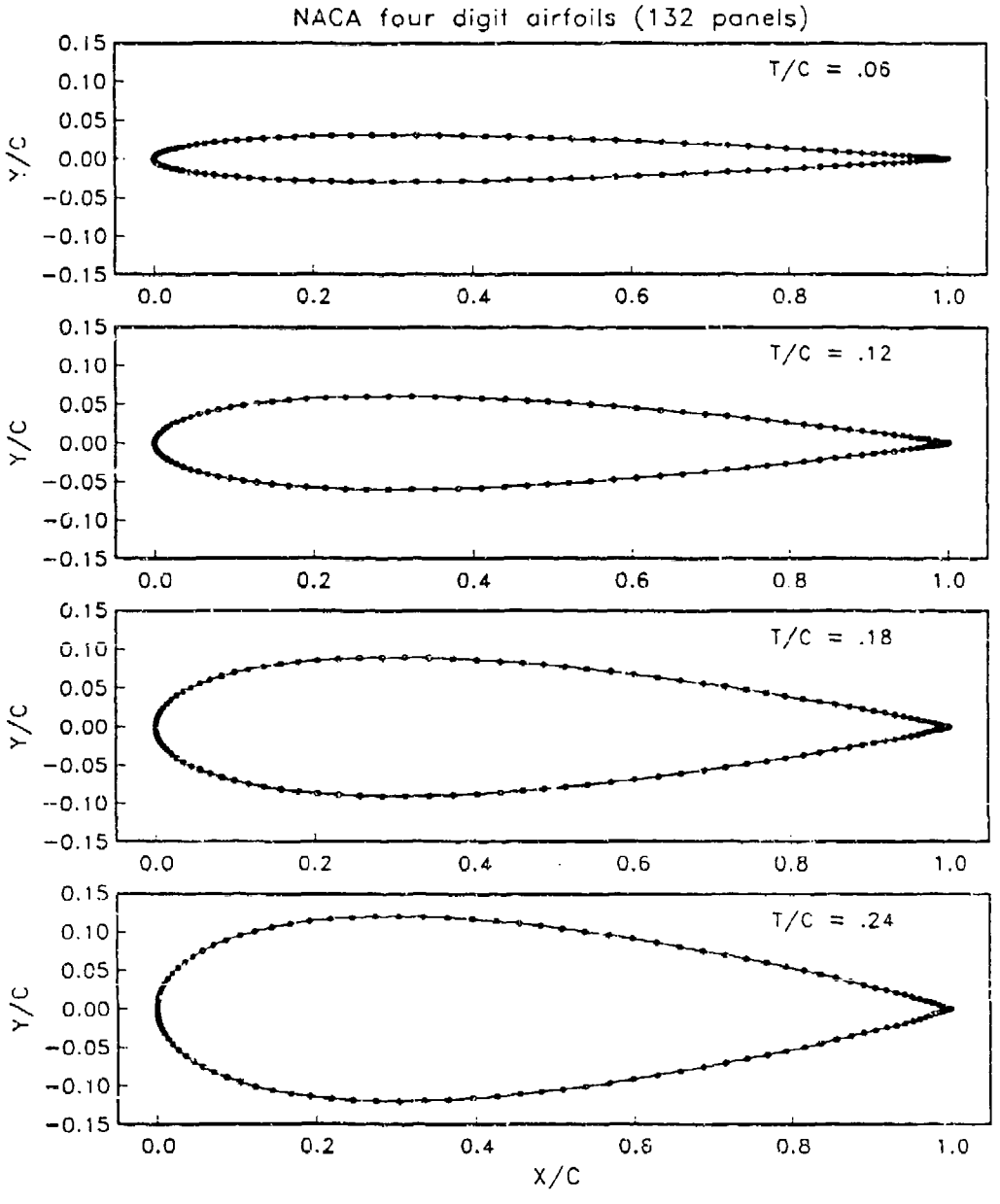

Figure 6.1a. Paneling Schemes for NACA Airfoils, 132 Panels

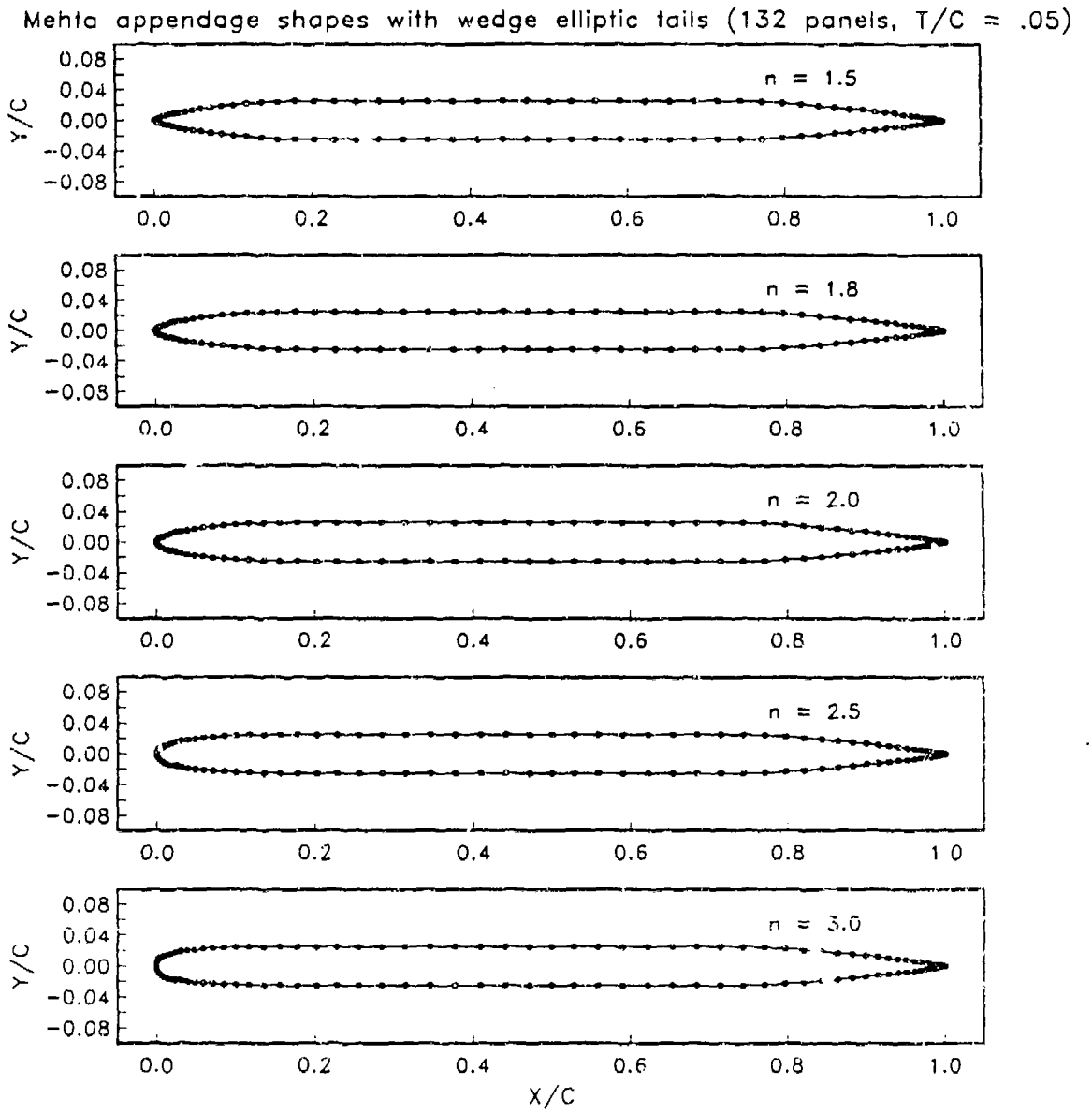

Figure 6.1b. Mehta Paneling Schemes, 132 Panels, T/C = .05

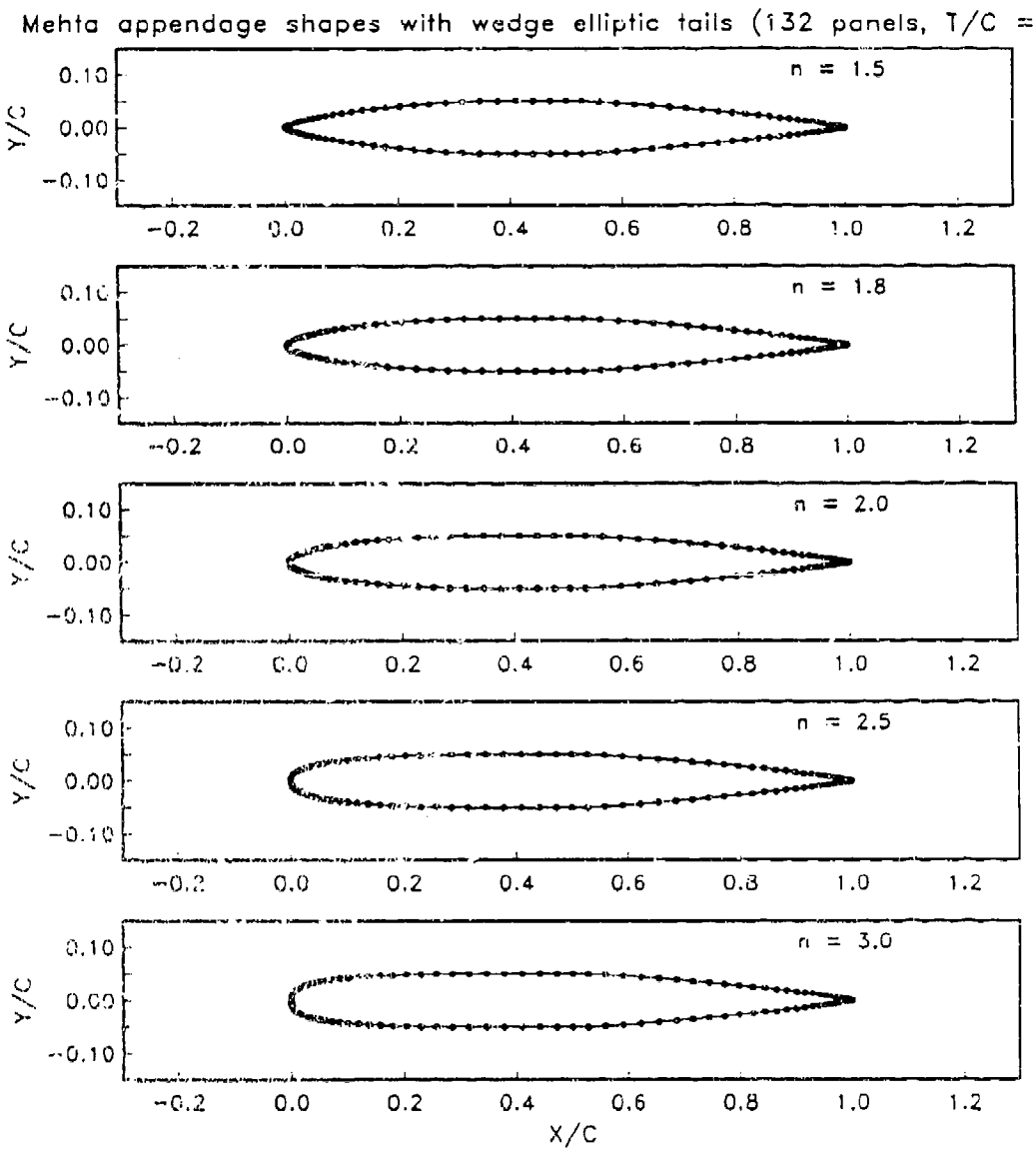

Figure 6.1c. Mehta Paneling Schemes, 132 Panels, T/C = .10

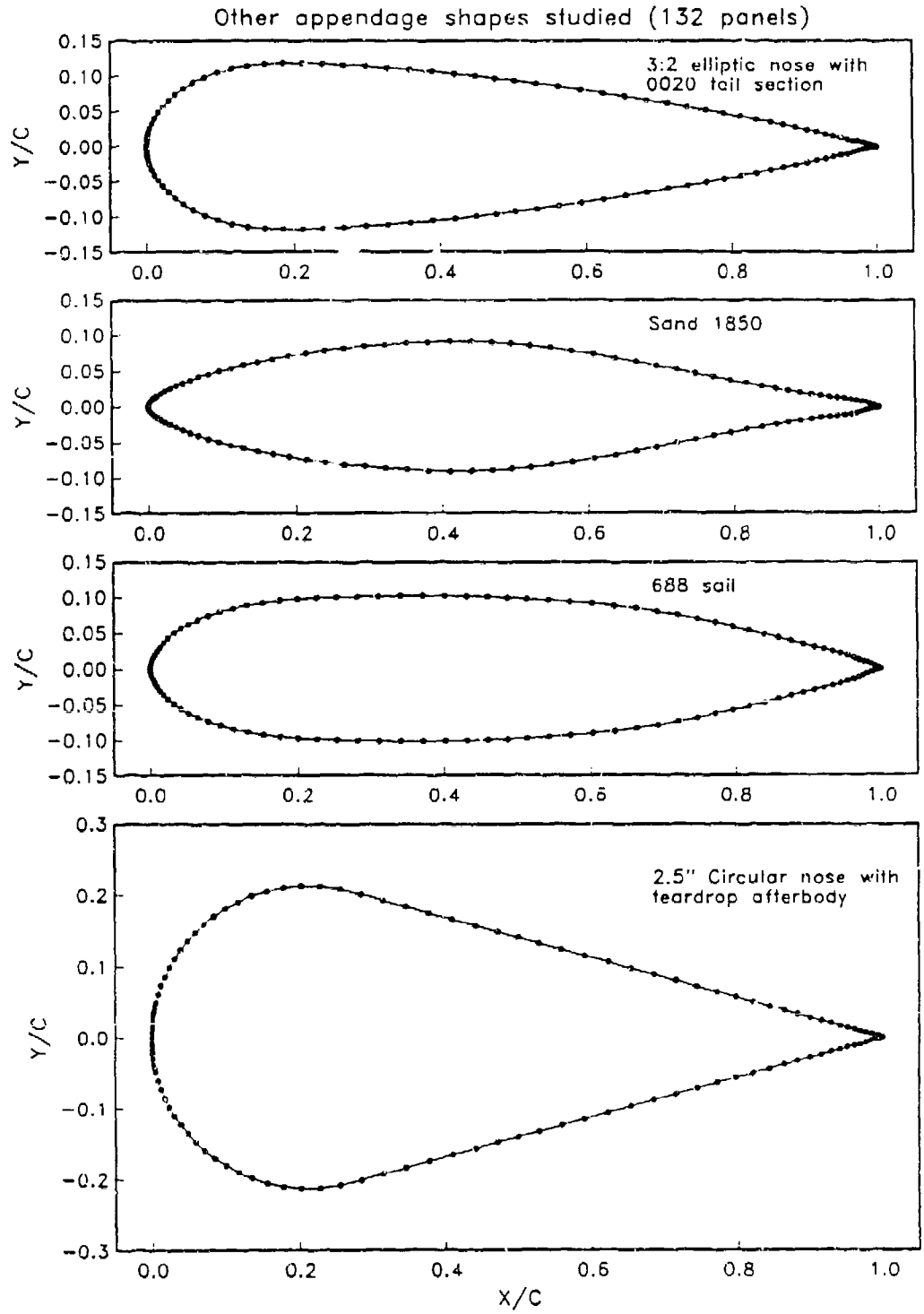

Figure 6.1d. Paneling Results for Miscellaneous Geometries, 132 Panels

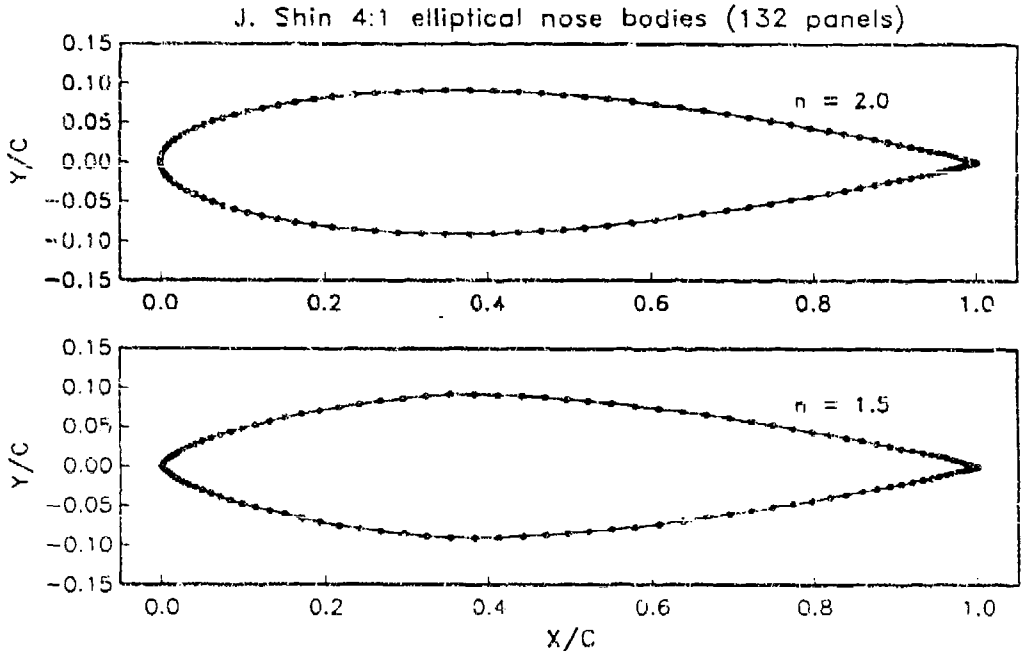

Figure 6.1e. Shin Paneling Schemes, 132 Panels

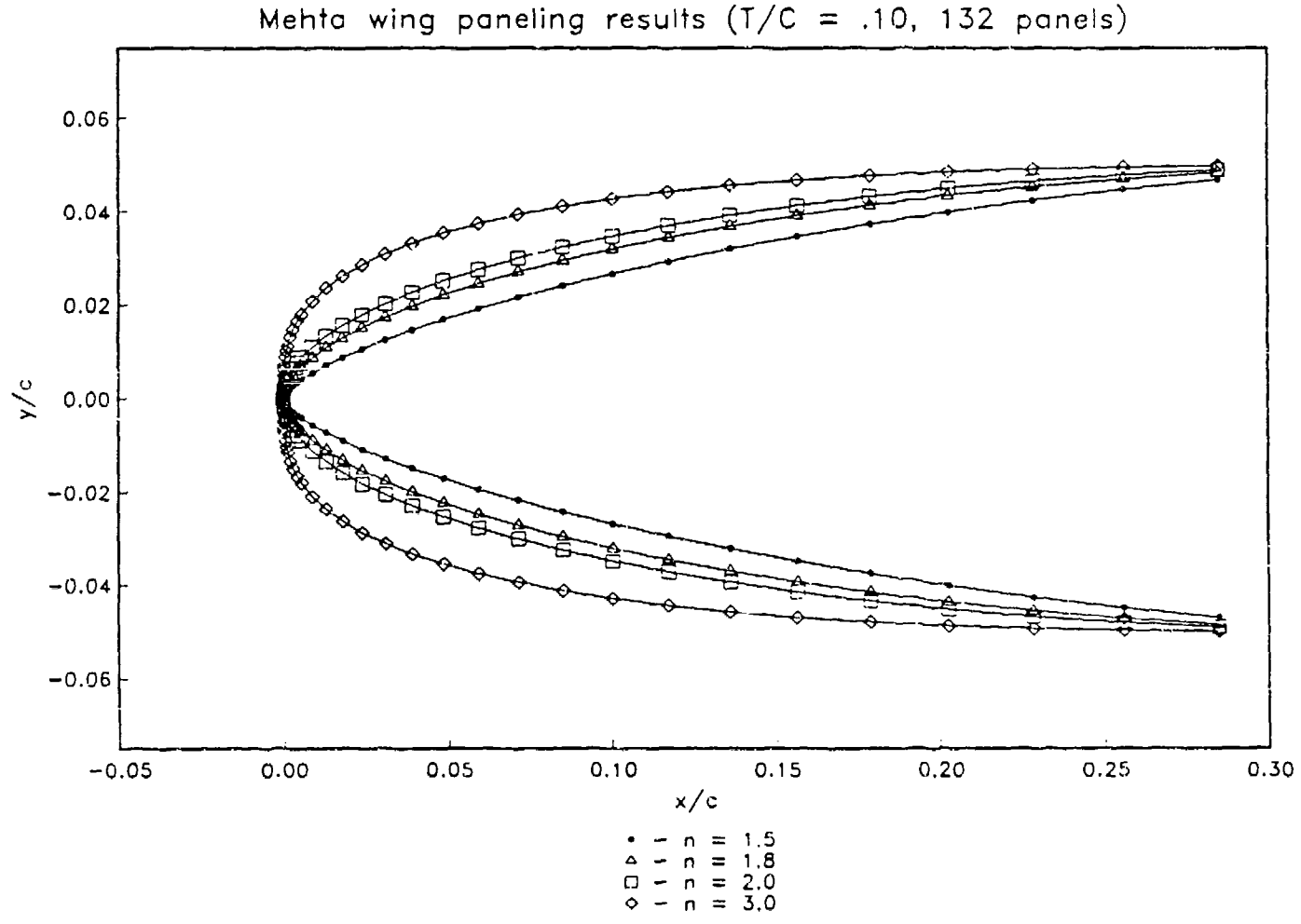

Figure 6.2. Affects of the Exponent n on Mehta's Appendage Nose Geometries

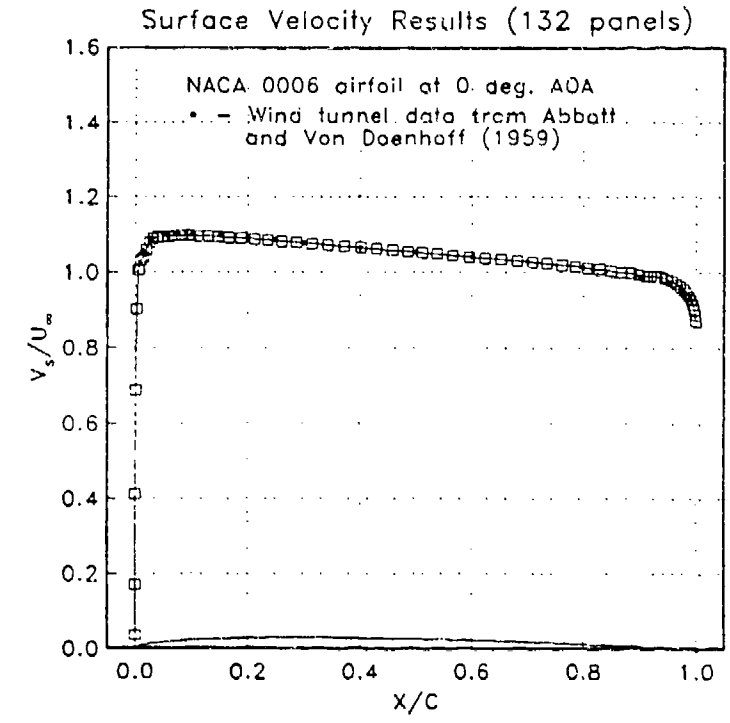

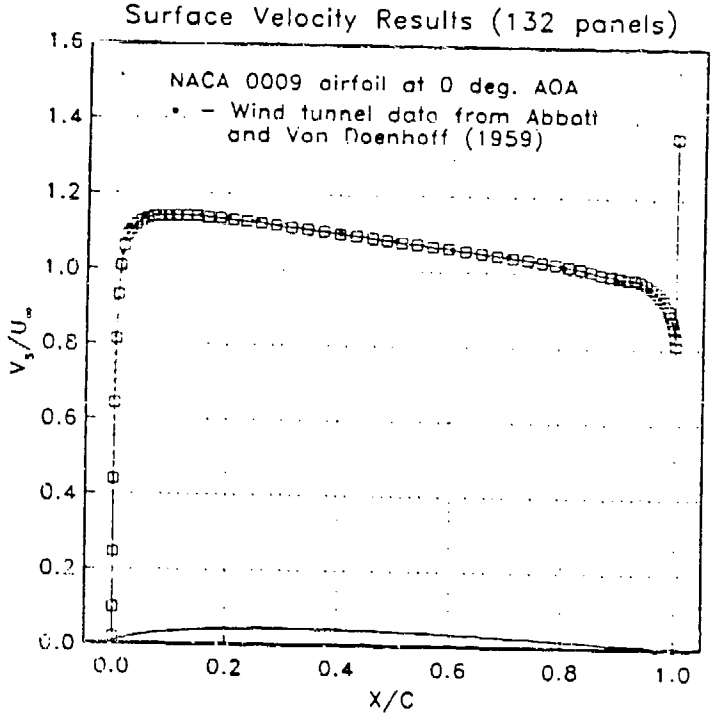

Figure 6.3a,b. NACA Appendage Velocity Distribution Results, 0° AoA

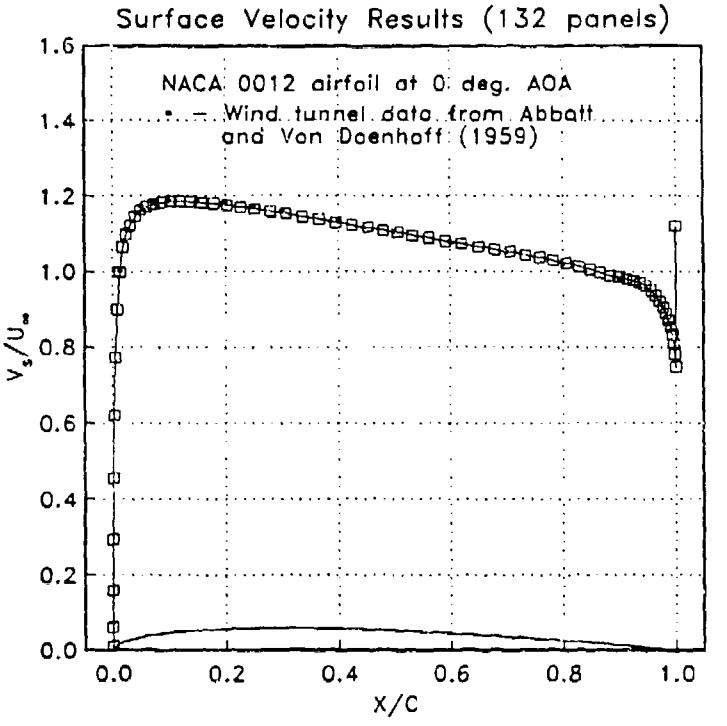

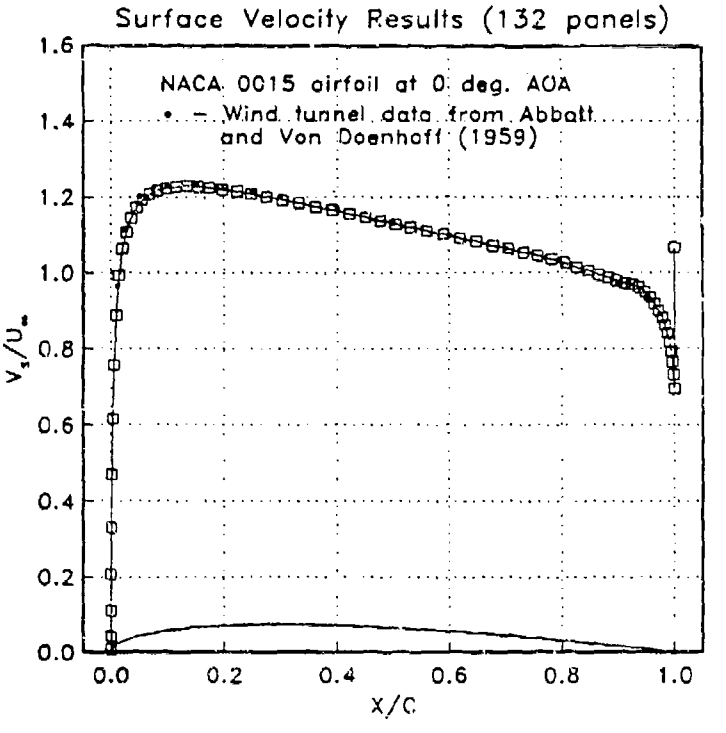

Figure 6.3c,d. NACA Appendage Velocity Distribution Results, 0° AoA

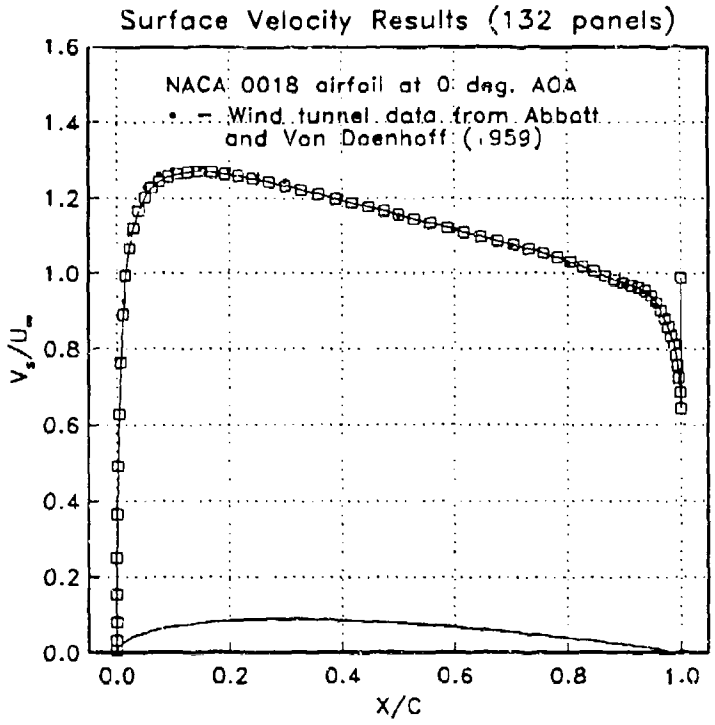

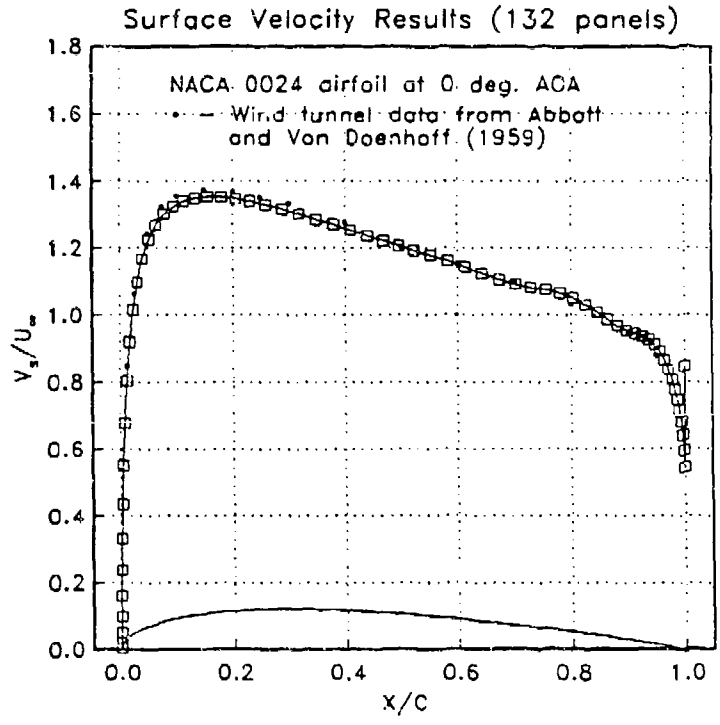

Figure 6.3e,f. NACA Appendage Velocity Distribution Results, 0° AoA

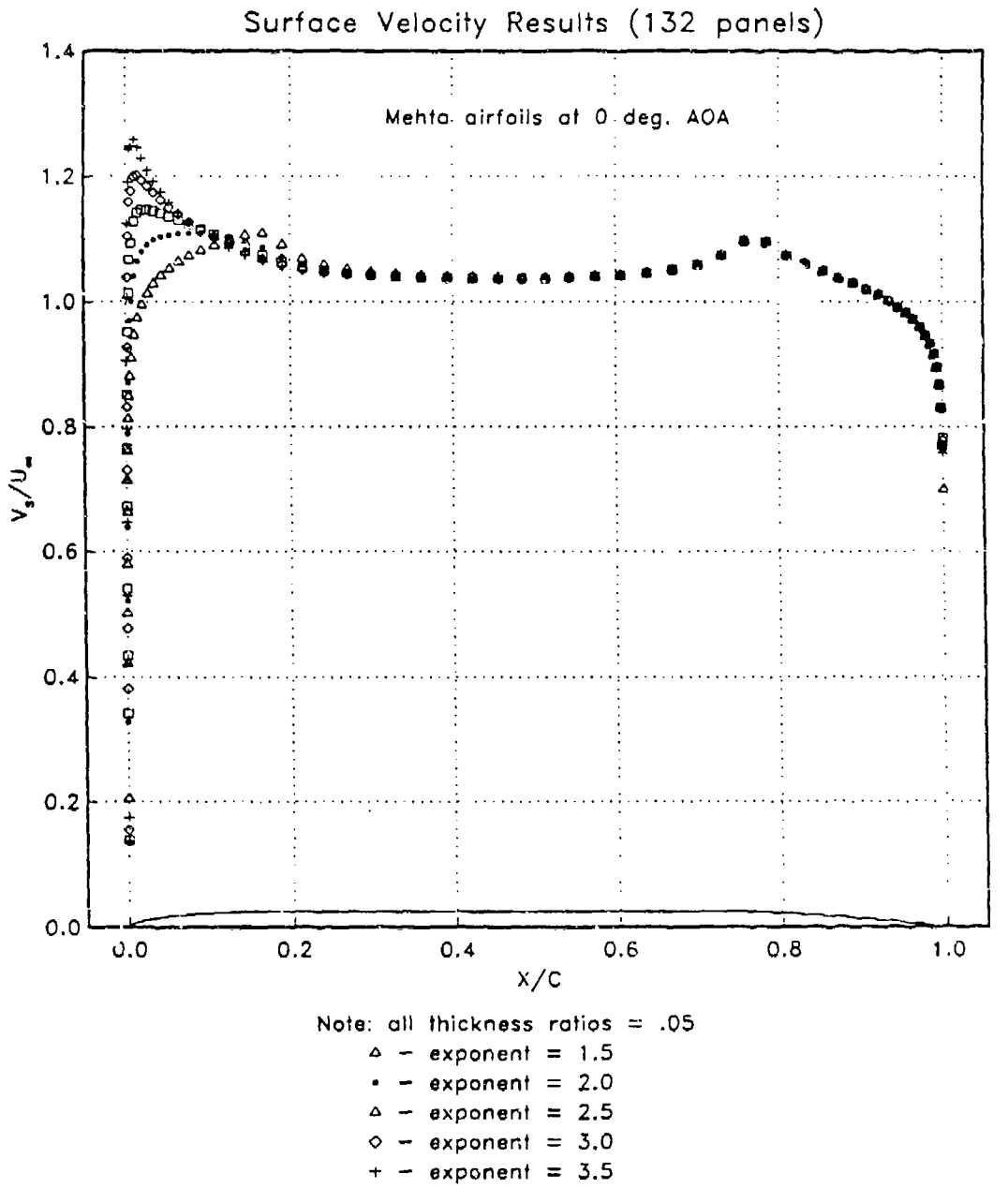

Figure 6.4a. Mehta Appendage Velocity Distribution Results, 0° AoA, T/C = .05

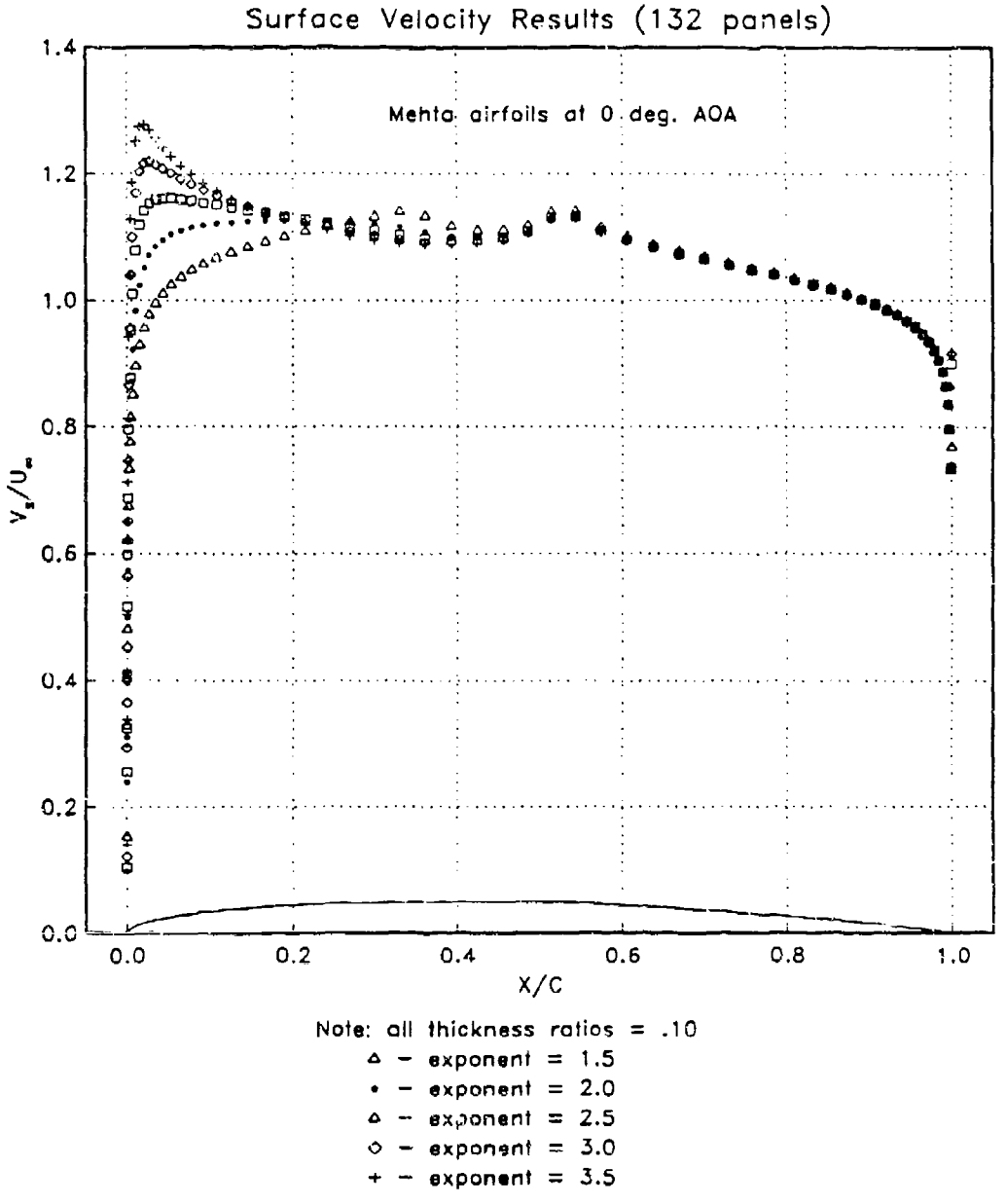

Figure 6.4b. Mehta Appendage Velocity Distribution Results, 0° AoA, T/C = .10

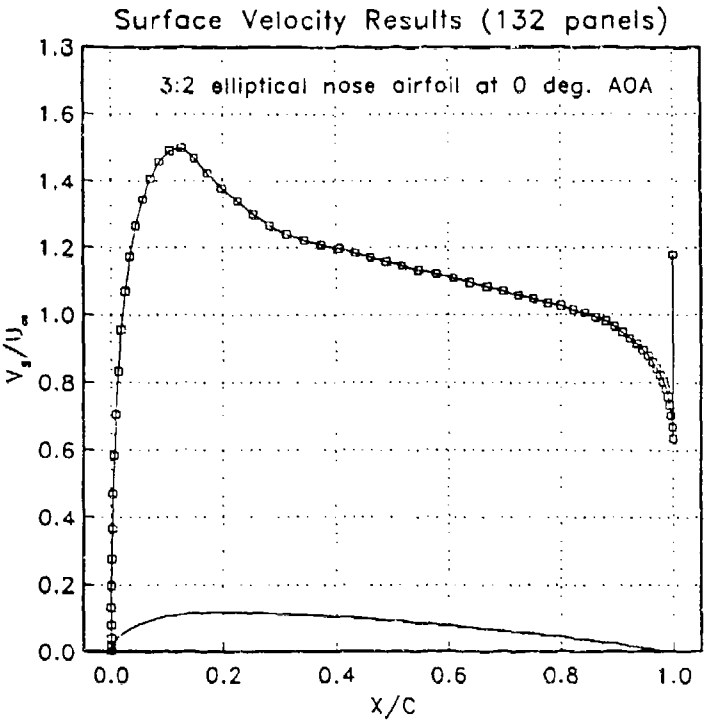

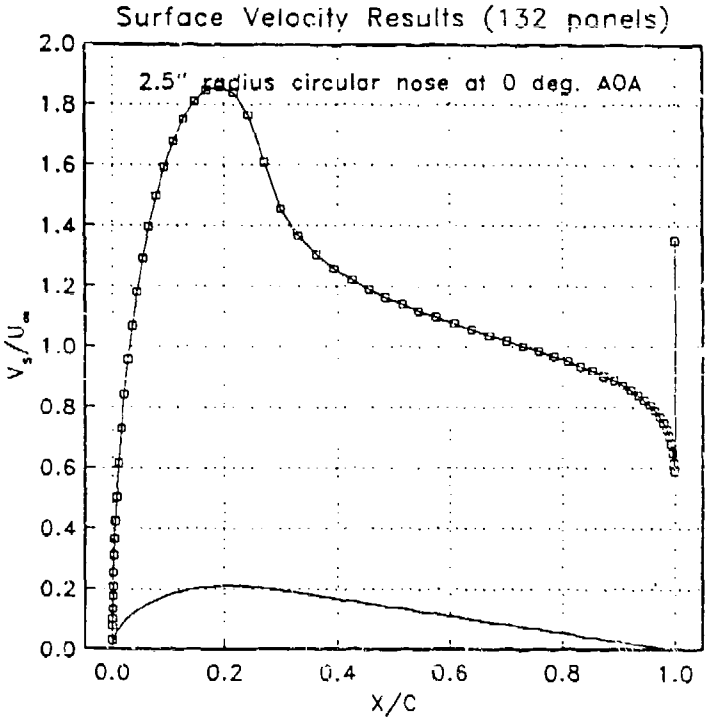

Figure 6.5a,b. Baseline and Teardrop Appendage Velocity Results, 0° AoA

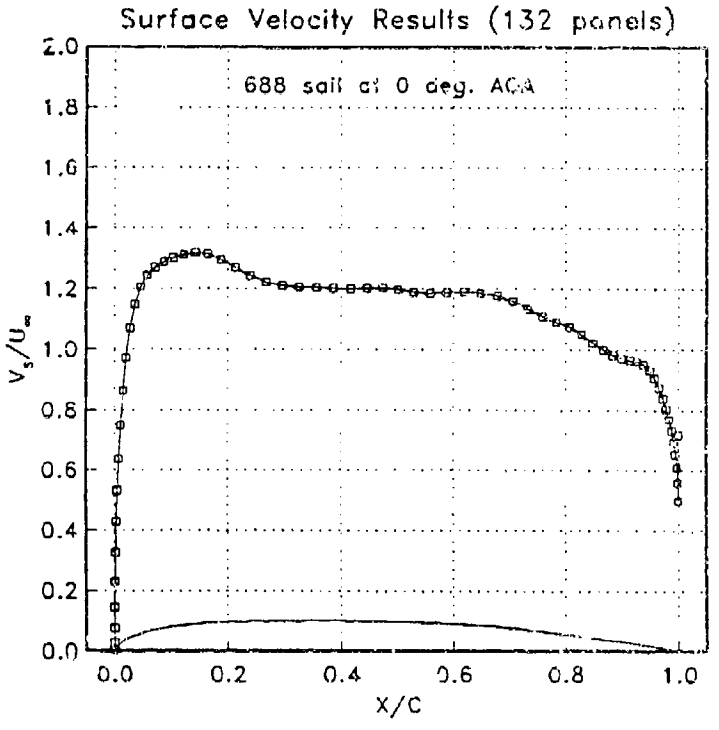

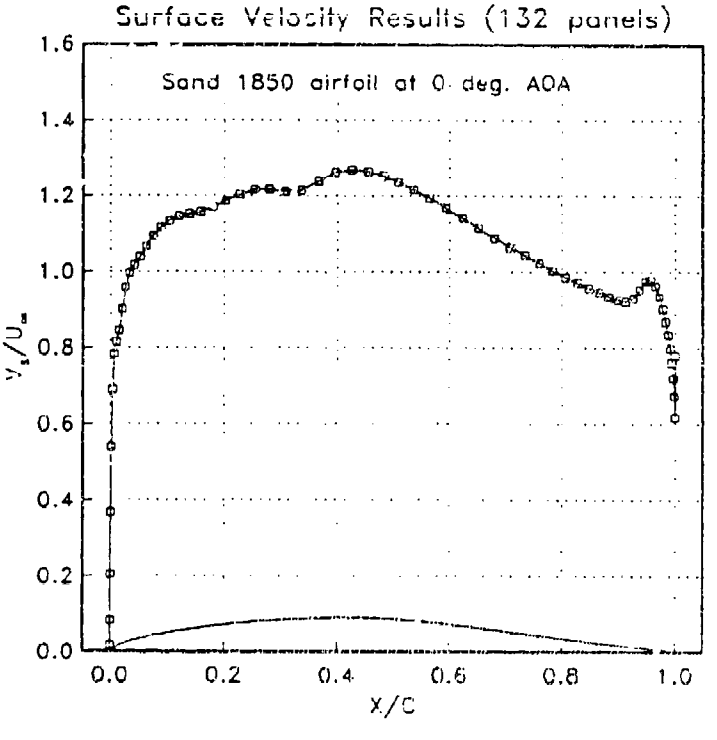

Figure 6.5c,d. 688 Sail and Sand 1850 Appendage Velocity Results, 0° AoA

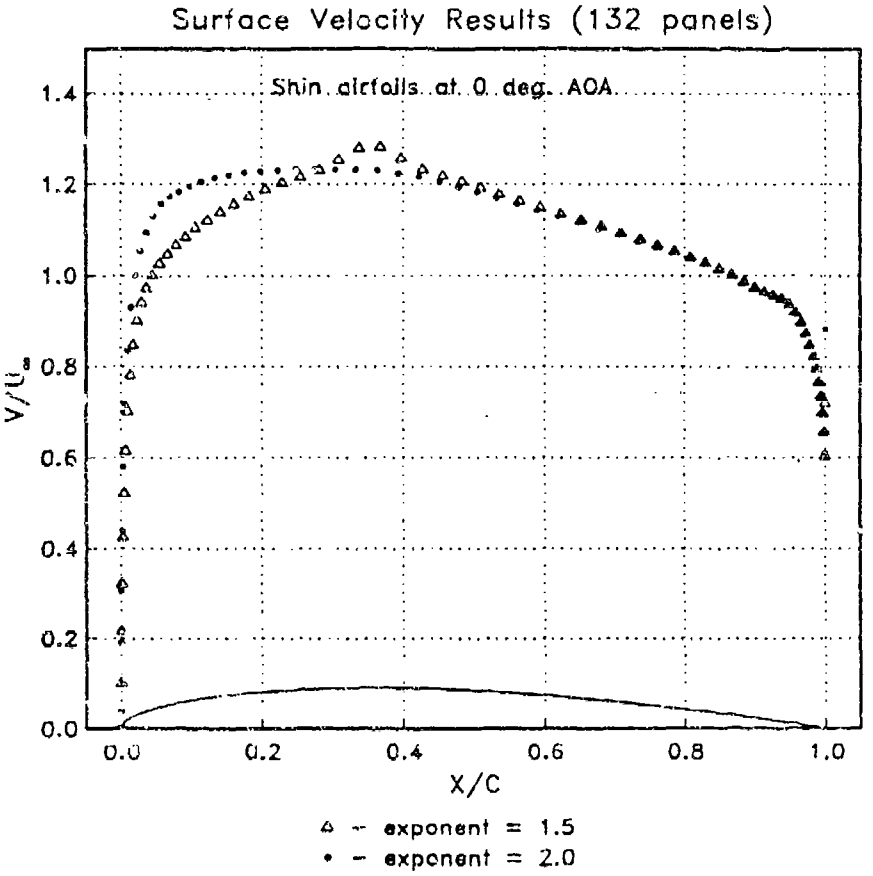

Figure 6.5e. Shin Appendage Velocity Results, 0° AoA

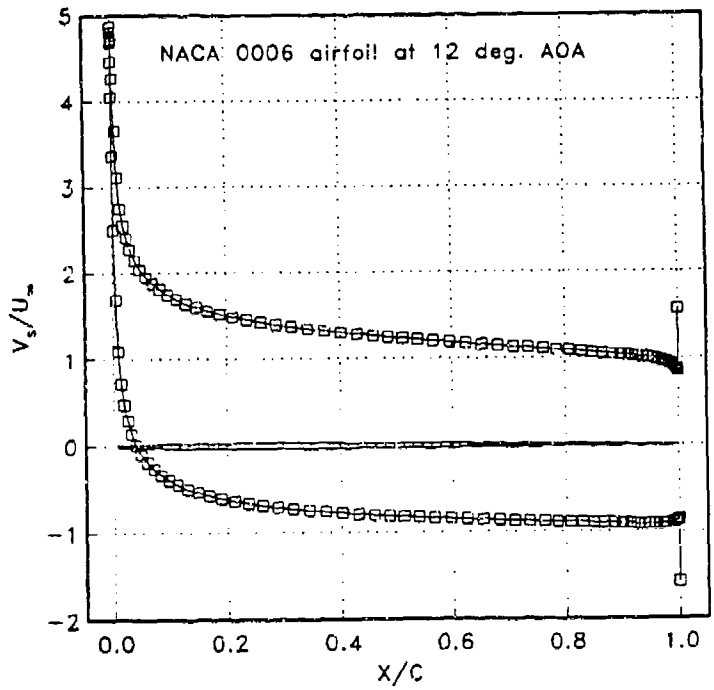

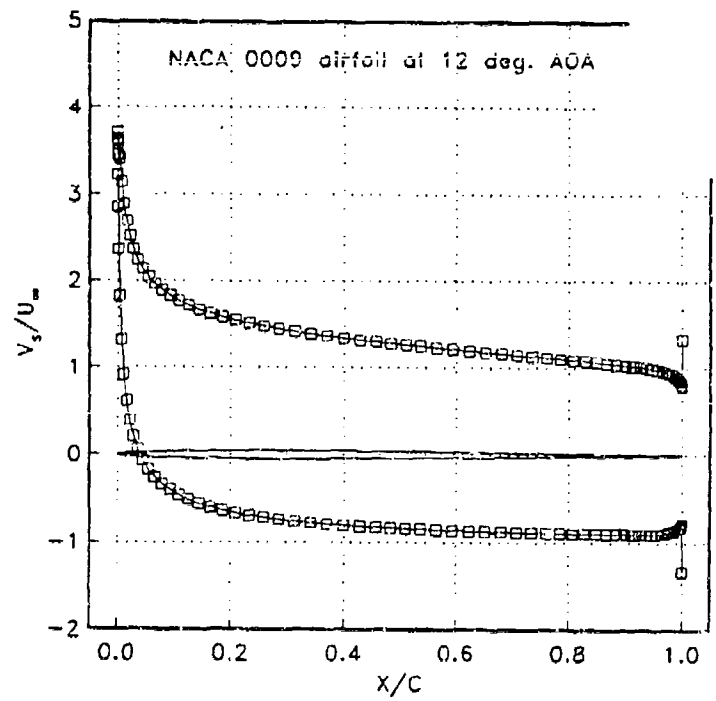

Figure 6.6a,b. NACA Appendage Velocity Results, 12° AoA

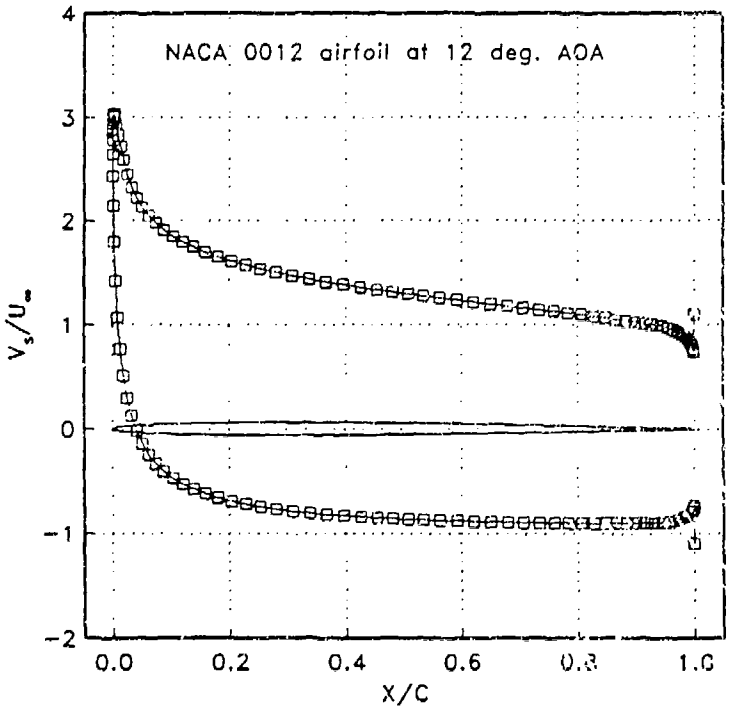

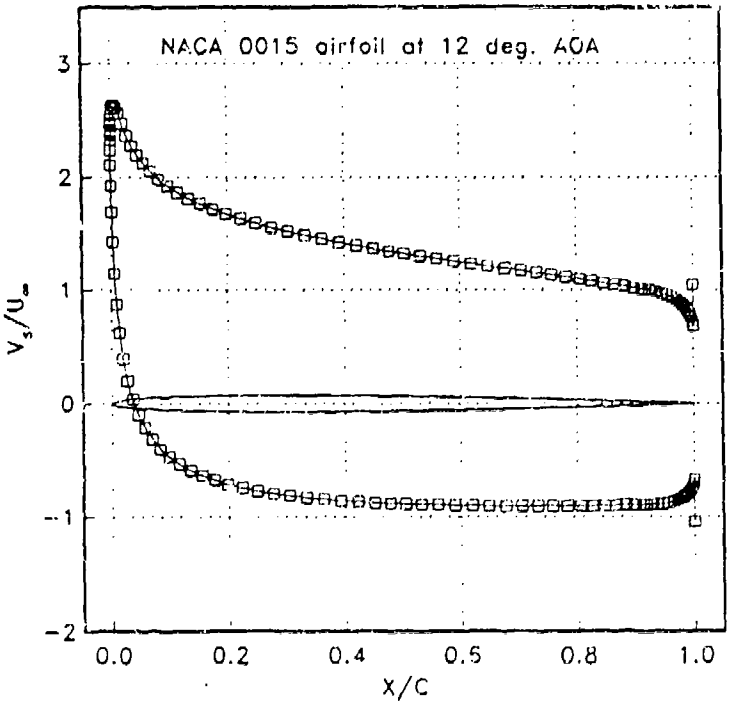

Figure 6.6c,d. NACA Appendage Velocity Results, 12° AoA

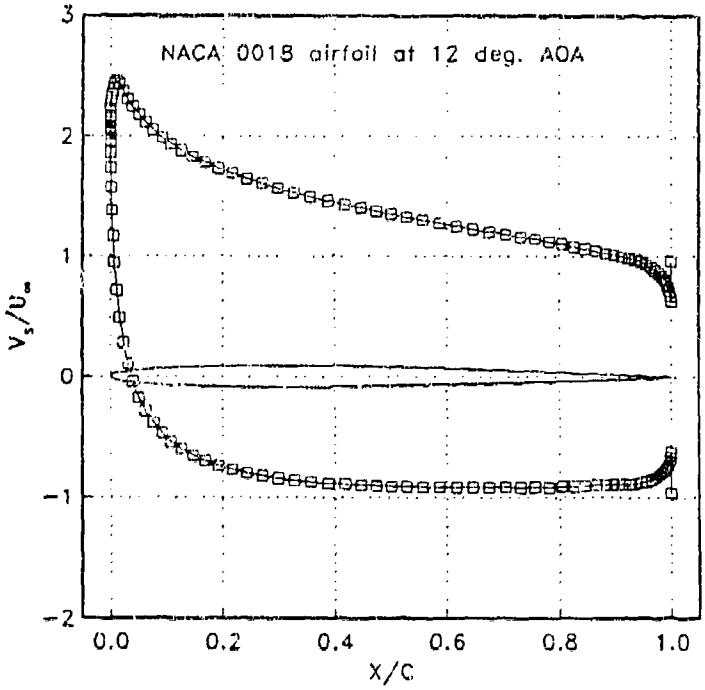

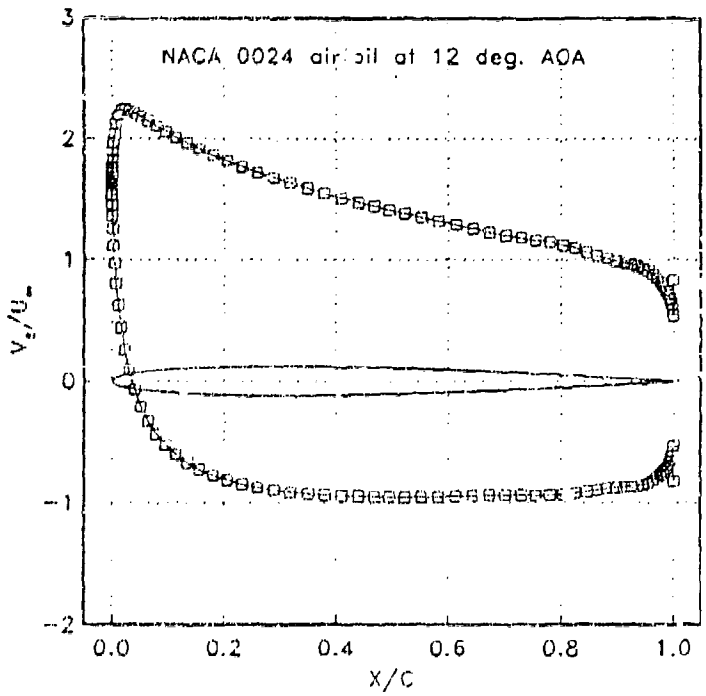

Figure 6.6c,f. NACA Appendage Velocity Results, 12° AoA

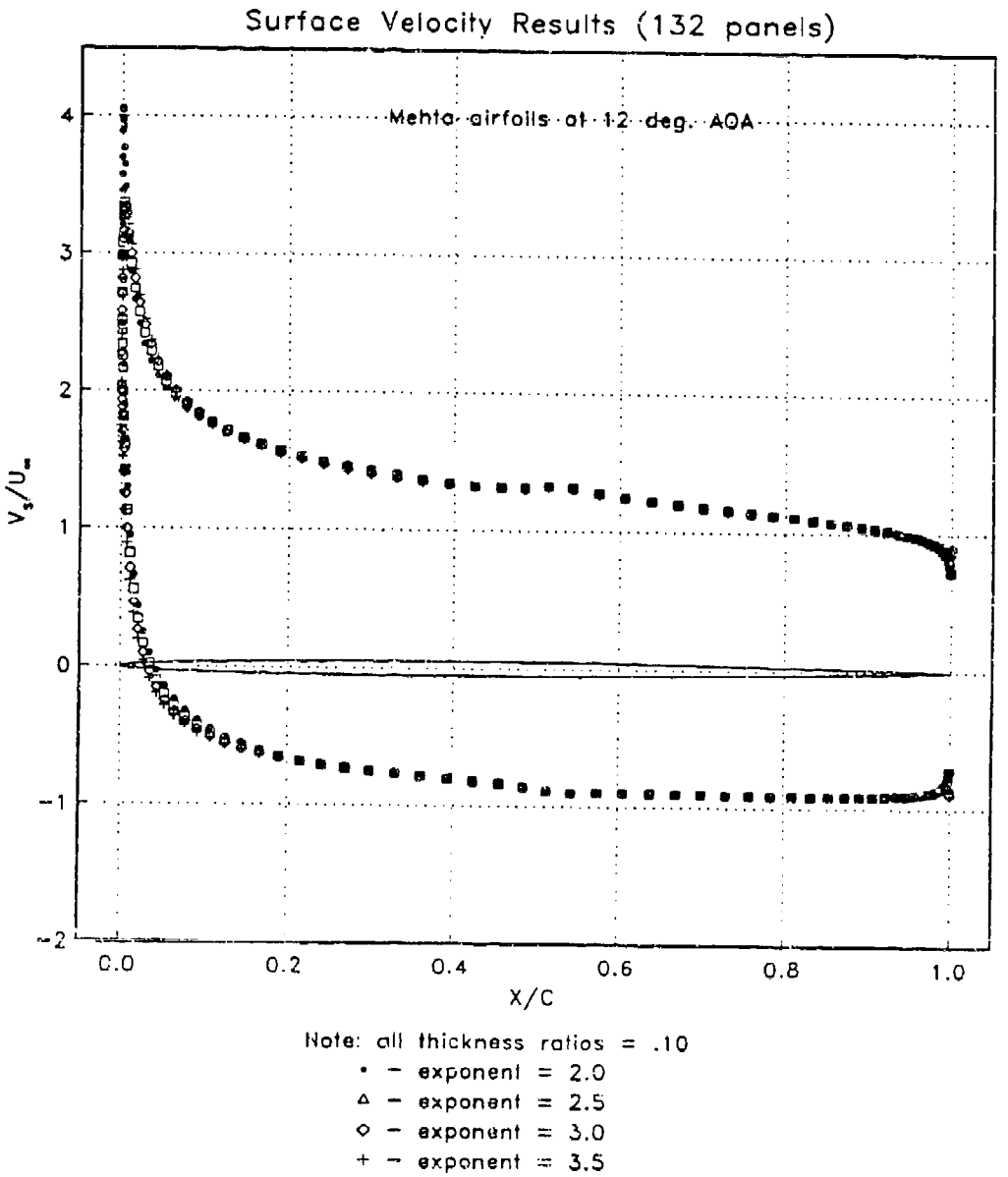

Figure 6.6g. Mehta Appendage Velocity Results, 12° AoA

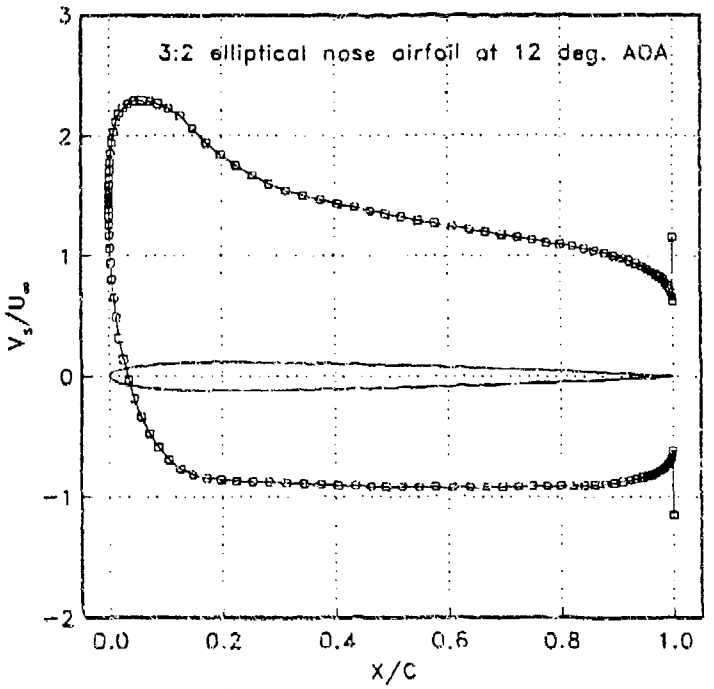

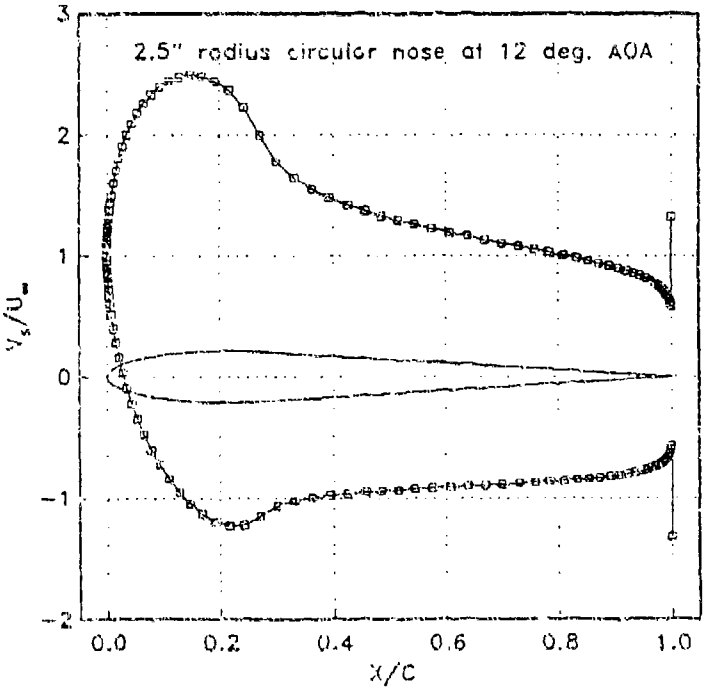

Figure 6.6h,i Baseline and Teardrop Appendage Velocity Distributions, 12° AoA

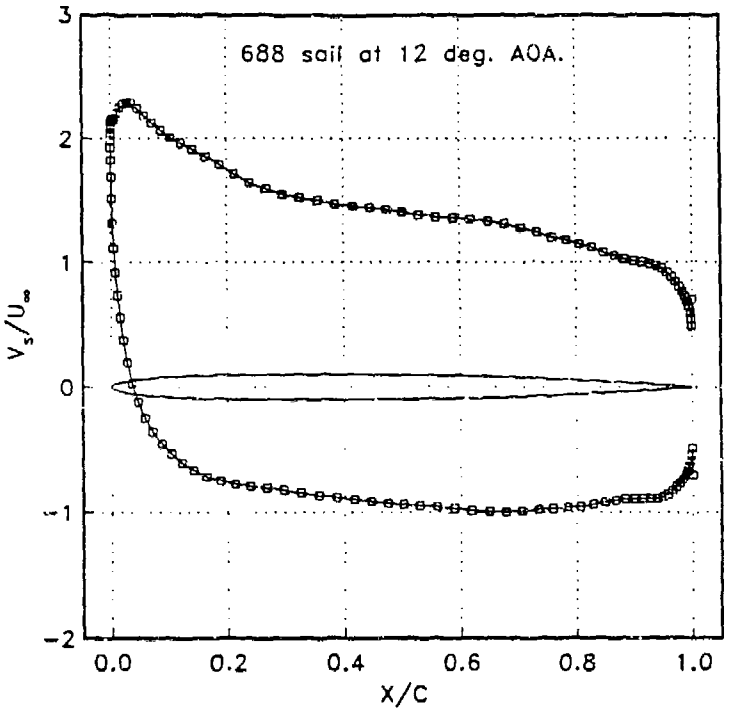

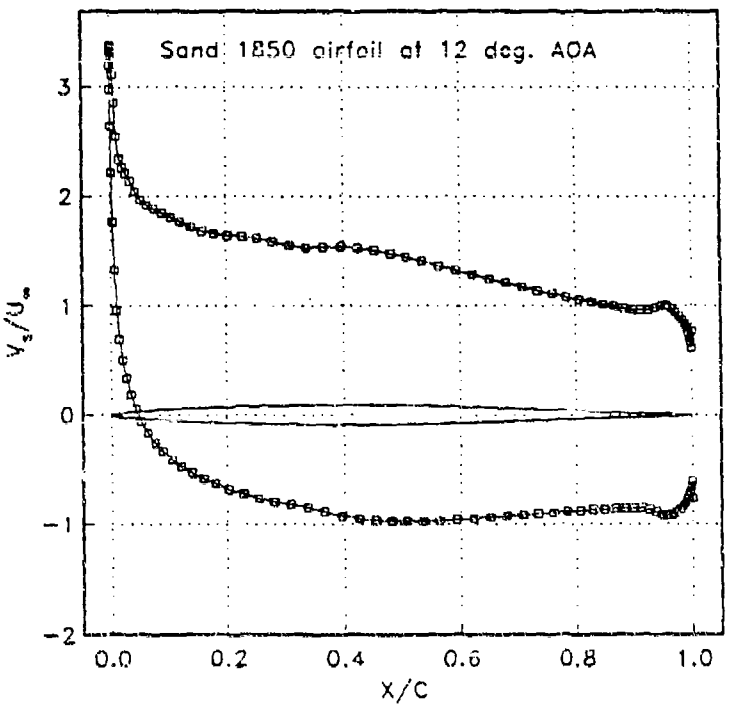

Figure 6.6j,k 688 Sail and Sand 1850 Appendage Velocity Distributions, 12° AoA

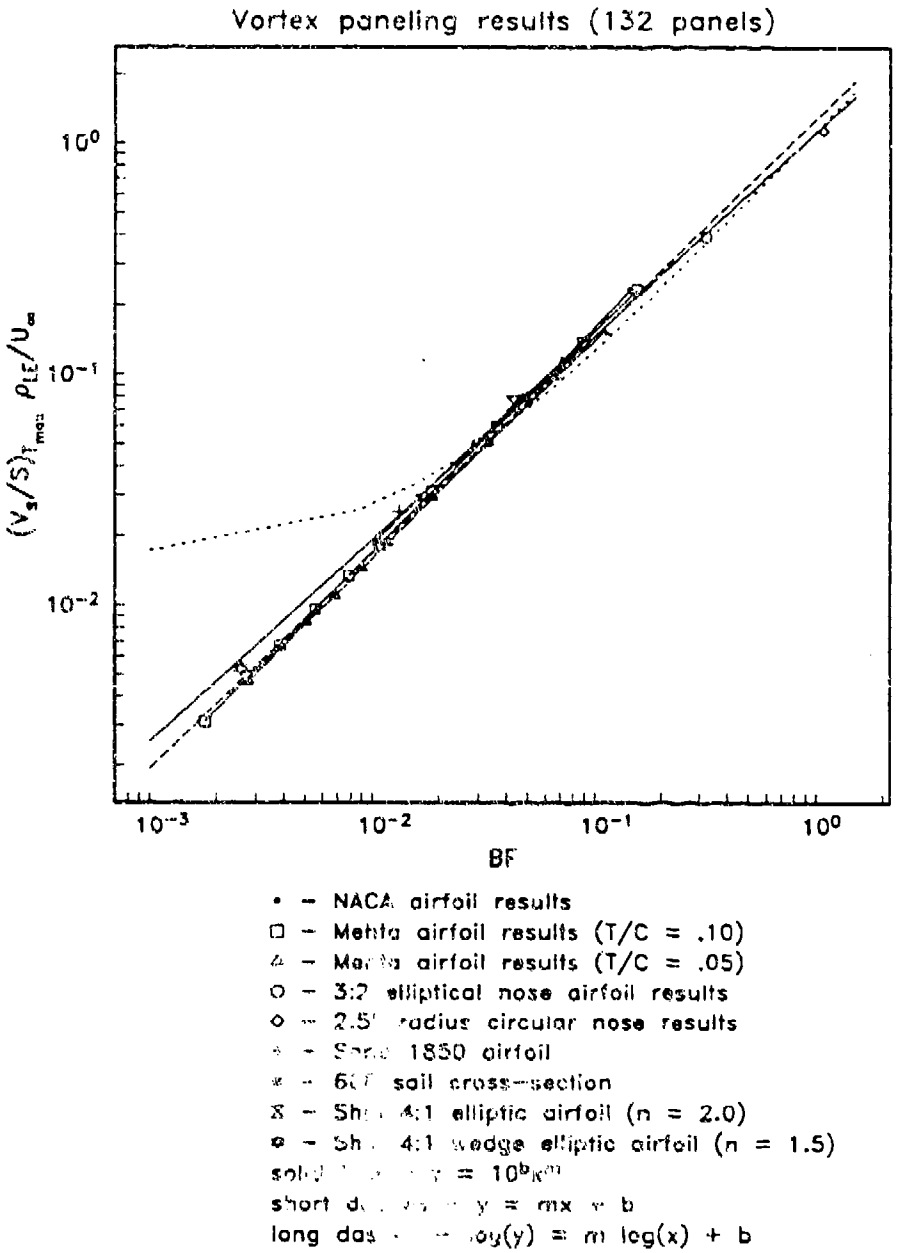

Figure 6.7a. Average Vortex Stretching [illegible] vs. Bluntness Factor, 0° AoA, Log-Log Scale

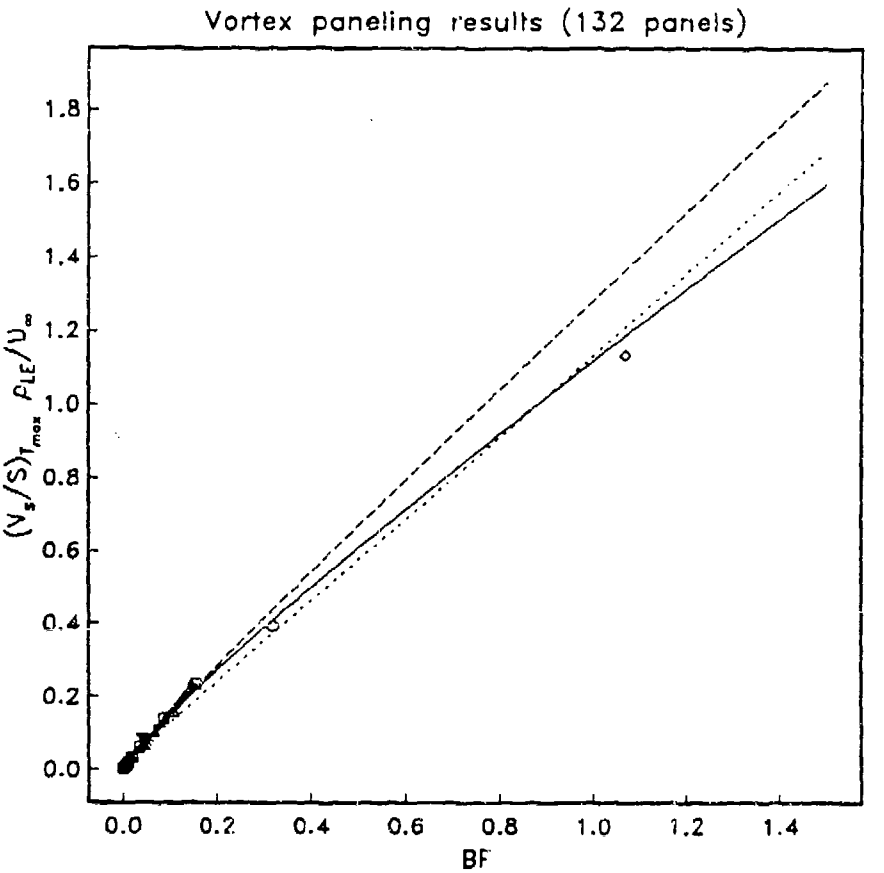

Figure 6.7b. Average Vortex Stretching Rate vs. Bluntess Factor, 0° AoA, Linear Scale

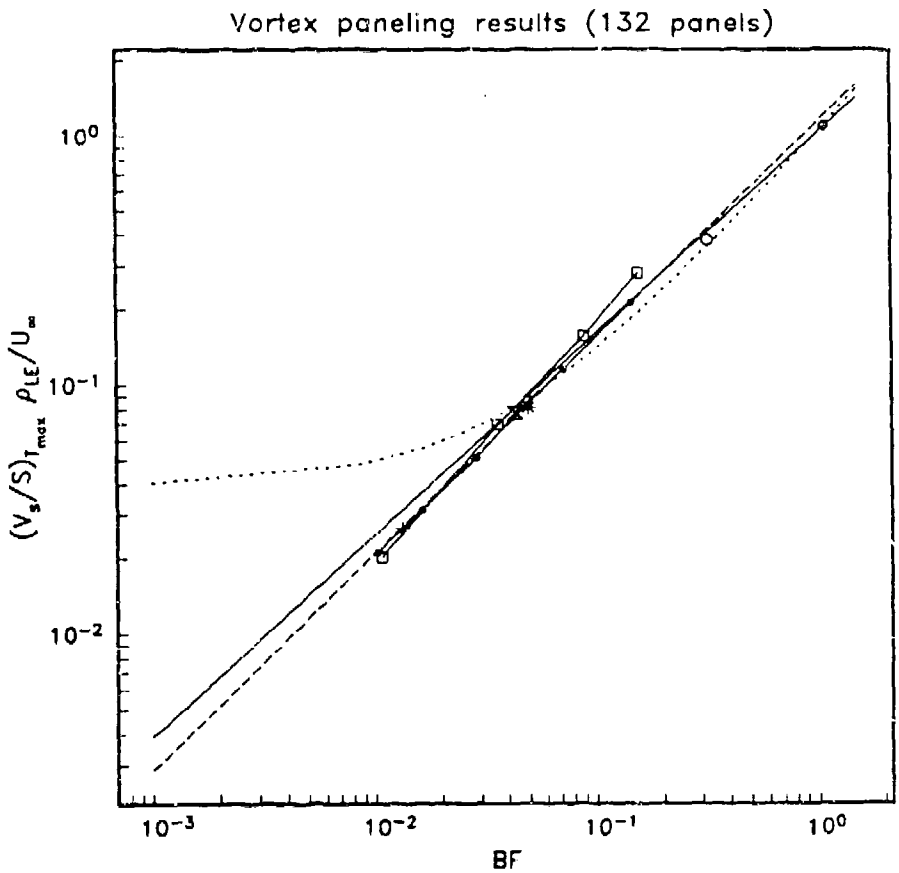

Figure 6.7c. Average Vortex Stretching Rate vs. Bluntness Factor, 12° AoA, Log-Log Scale

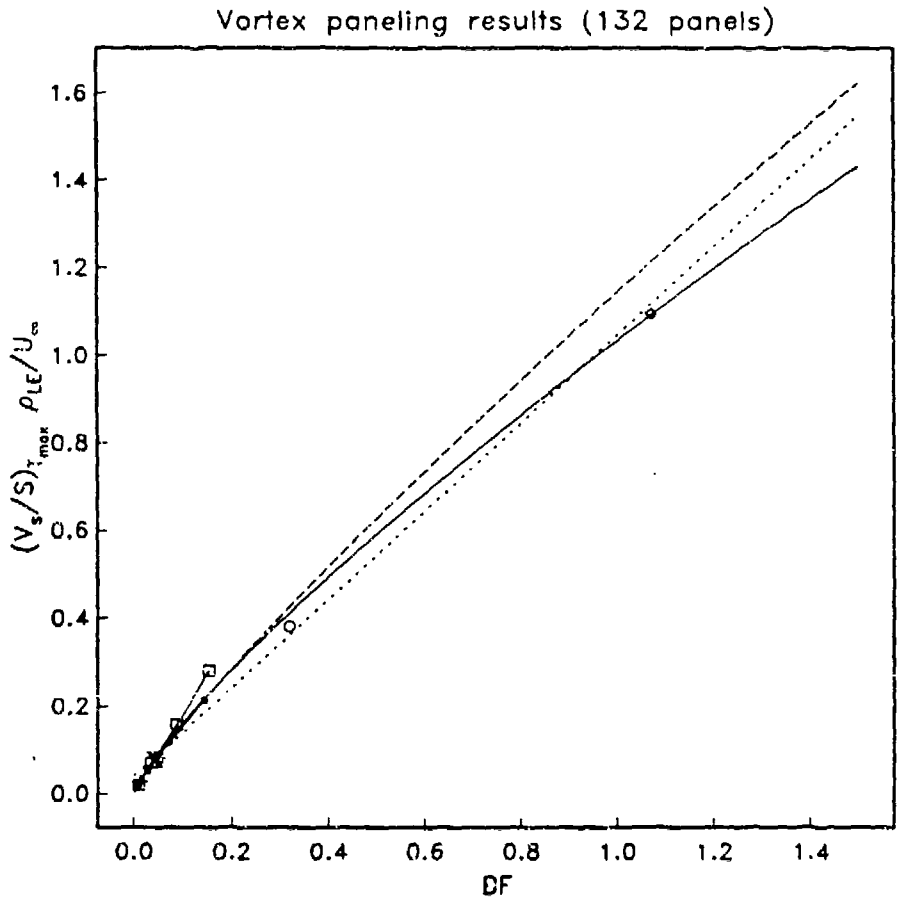

Figure 6.7d. Average Vortex Stretching Rate vs. Bluntess Factor, 12° AoA, Linear Scale

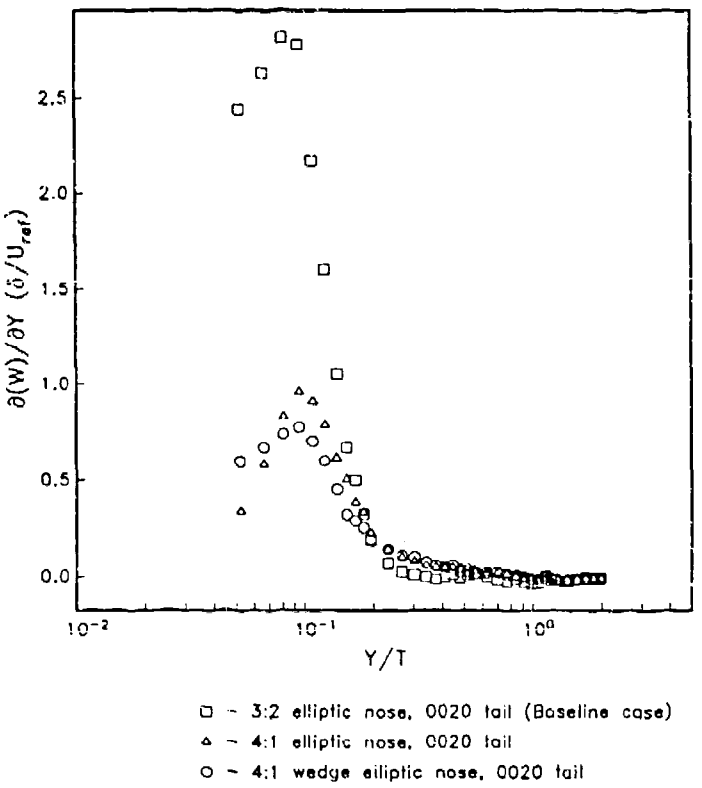

Figure 6.8. $(\partial(W)/\partial Y)\delta/U_{ref}$ vs. Y/T Results from Shin's Data

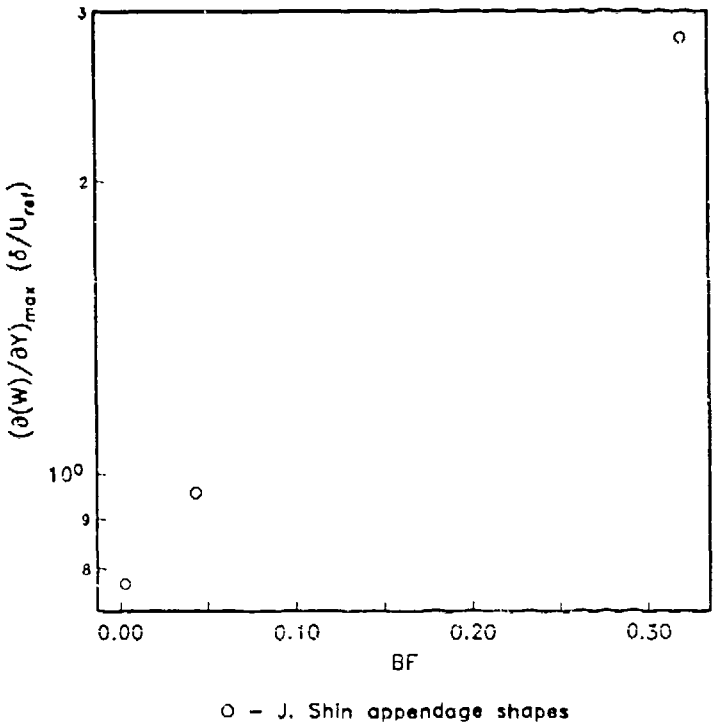

Figure 6.9. $(\partial(W)/\partial Y)_{MAX}\delta/U_{ref}$ vs. Bluntness Factor for Shin's Appendages

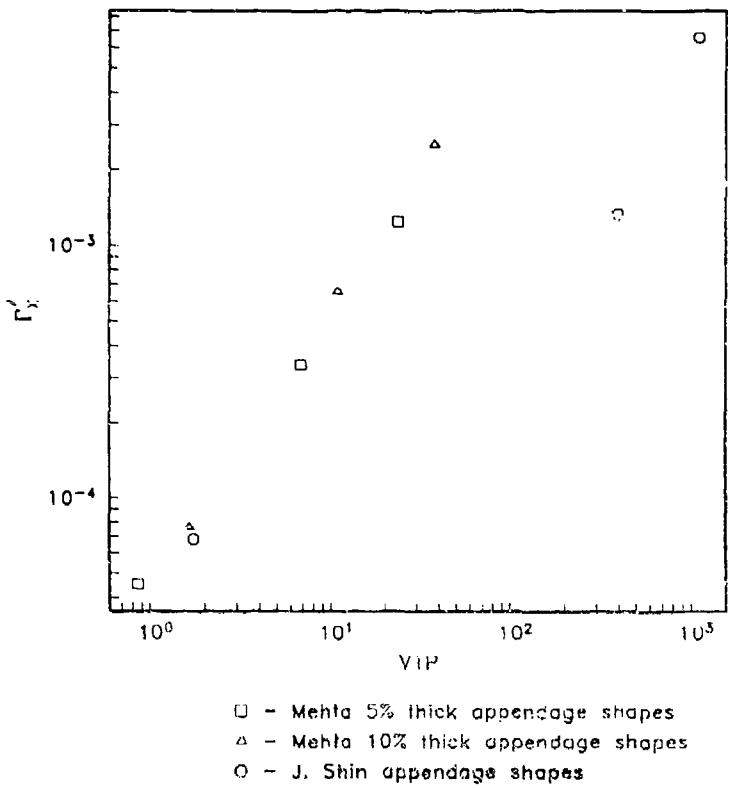

Figure 6.10. Γ'_x vs. Vortex Transport Parameter for Mehta's and Shin's Appendages

Appendix A. Hot-Wire Data Reduction

As previously mentioned in section 2.5, the calculation of U_S, u'_S, w'_S, $-\overline{uw}_S$, and α_S is taken from Devenport and Simpson (1990a). Note that in the following equations, an overbar designates a time averaged quantity. Using equations 3.2, 3.3, and 3.4, f(E') can be expanded in a Taylor series about E (mean voltage):

$$U'_{eff} = f(E') = f(\bar{E}) + (E'-\bar{E})f(\bar{E}) + (E'-\bar{E})^2\frac{f''(\bar{E})}{2!} + \ldots \qquad (A.1)$$

Dropping terms higher than second order and taking the time average of this equation yields:

$$\bar{U}_{eff} = f(\bar{E}) + \overline{E'^2}\frac{f''(\bar{E})}{2} \qquad (A.2)$$

Calculation of u'_{eff} follows along similiar lines:

$$u_{eff} = U'_{eff} - \bar{U}_{eff} = E'f'(\bar{E}) + (E'^2 - \overline{E'^2})\frac{f''(\bar{E})}{2} \qquad (A.3)$$

Squaring equation A.3 and taking the time mean average, the result is:

$$\overline{u'^2}_{eff} = \overline{E'^2}(f(\bar{E}))^2 + \frac{1}{4}(f''(\bar{E}))^2(\overline{E'^4} - \overline{E'^2}^2) + f'(\bar{E})f''(\bar{E})(\overline{E'^3}) \qquad \text{(A.4)}$$

Note that these equations are in terms of mean voltages only. The mean fluctuating voltages can be expressed in terms of mean powers of voltages. The equations needed are:

$$\begin{aligned} \overline{E'^2} &= \overline{E^2} - \bar{E}^2 \\ \overline{E'^3} &= \overline{E^3} - 3\overline{E^2}\bar{E} + 2\bar{E}^3 \\ \overline{E'^4} &= \overline{E^4} - 4\overline{E'^3}\bar{E} - 6\overline{E'^2}\bar{E}^2 - \bar{E}^4 \end{aligned} \qquad \text{(A.5)}$$

Utilizing these equations enables the reduction of U_{rms} and u'_{eff} by looping through the array of voltages only once.

Appendix B. Wing-Body Junction Approach Flow Data

This appendix contains listings of the approach flow boundary layer data for the data sets of Devenport and Simpson (1990a), Dickinson (1986a,b) and McMahon *et al.*, (1987). The approach flow for Devenport and Simpson's case is the same as for the author's hot-wire data.

The author's data data is available on magnetic disk, and includes all measurements taken in planes 5-11, 13-15 in both tunnel and freestream coordinates. The text file "FILELIST.DOC" contains information regarding the organization of the data files and their contents. This file is shown in this appendix as well. The other data sets, in similiar format, are available on request. This data is archived using **PKZIP** v. 1.02.

Devenport and Simpson thick approach boundary layer data
(Fleming's approach boundary layer is the same)
X/T = -2.146, Z/T = 0.0
wing thickness = 7.17 cm
nominal reference velocity = 26.38 m/s
temperature = 23 C Pressure = 940 mb
number of points = 30

Y/T	U/Uref
.0035411	.39103
.0042493	.41412
.0049575	.42840
.0063739	.45372
.0074363	.47239
.0092068	.49328
.011331	.50678
.013810	.52328
.016997	.54596
.020538	.55712
.025142	.57837
.030807	.59453
.037181	.61043
.045326	.63060
.055241	.64853
.067635	.66889
.082153	.68786
.10021	.71183
.12181	.735
.14837	.762
.18945	.802[illegible]
.21990	.83043
.26806	.86820
.32613	.90733
.39766	.94622
.48336	.96978
.58853	.97587
.71671	.97498
.87252	.97695
1.0623	.97722

Dickinson approach boundary layer data
X/T = -3.1667, Z/T = 0.0
wing thickness = 6.1 cm
nominal reference velocity = 30.75 m/s
number of points = 17

Y/T	U/Uref
.041667	.6186
.08333	.6879
.12500	.7253
.1667	.7556
.20833	.7782
.3125	.8221
.41667	.8570
.5208	.8864
.6250	.9097
.729167	.9310
.8333	.9465
1.04167	.9677
1.2500	.9765
1.4583	.9780
1.6667	.9775
1.875	.9778
2.0833	.9781

McMahon, et al. approach boundary layer data
X/T = -2.087, Z/T = 0.0
wing thickness = 7.1 cm
nominal reference velocity = 15.24 m/s
number of points = 24

Y/T	U/Uref
0.051355	0.533333
0.066386	0.568957
0.083922	0.599491
0.101458	0.629008
0.118994	0.659542
0.136530	0.667684
0.152813	0.678880
0.172855	0.709415
0.205421	0.715522
0.237988	0.731807
0.274313	0.765394
0.309385	0.782697
0.344457	0.784733
0.380781	0.809160
0.450925	0.858015
0.519816	0.879389
0.606243	0.909924
0.695176	0.931298
0.779098	0.950636
0.868030	0.959796
0.956963	0.968957
1.042138	0.972010
1.112282	0.974046
1.180000	0.973000

J. Fleming's data files are organized in the following manner:

YpXX??.dat - XX indicates the YZ plane number (05-15)
- ?? - "tc" indicates tunnel coordinate system used to present data
- "fc" indicates freestream coordinate system used to present data

data file contents:

file descriptive header
X/T location of YZ plane
average reference velocity (m/s)
number of profiles measured in YZ plane
no. of pts for 1st profile temp(C) pressure(mb) uref(m/s) fs flow angle
.
.
.
. (one line for each profile)
.
.
no. of pts for last profile temp(C) pressure(mb) uref(m/s) fs flow angle
Y/T Z/T U/Uref u'/Uref W/Uref w'/Uref uw/Uref^2 flow angle
.
.
.
. etc....

Note: The far wake planes contain only U/Uref and u'/Uref data

Appendix C. Vortex Panel Code Data

This appendix contains listings of data discussed in Chapter 5. This data is also available on disk. The listings containing the data from the Mehta appendage shapes are "padded" for the Γ_X and $\Gamma_X/(d(V_S)/dS)_o$ data, since Γ_X data was available only for n = 1.5, 2.0, and 3.0. The padding was done so that the data could be read into a plotting program correctly.

3:2 elliptic nose w/ 0020 tail (baseline wing)

BF	d(V/Uref)/d(S/C)o	ave. vort. str.	VTP	rhole/C
.319564	21.2476	.392097	1110.91	.0725128
at 12 degrees aoa				
.319564	13.9120	.381382	-7 96157	.0725128

688 sail section

BF	d(V/Uref)/d(S/C)o	ave. vort. str.	VTP	rhole/C
.0494182	40.4319	.0787788	388.372	.0258028
at 12 degrees aoa.				
.0494182	12.6335	.0813323	-18.2782	.0258028

Mehta appendages (5% thick, 0 angle of attack)

n	BF	d(V/Uref)/d(S/C)o	ave. vort. str.	VTP	Gamma	G/(dV/dS)o	rhole/C
1.5	.00279715	1683.47	.00465945	.856895	.076	4.5145e-5	.000932762
1.7	.00508421	695.745	.0084677	2.78959	.0001	1.0e-8	.00168978
1.8	.00683234	500.126	.0110025	4.03173	.0001	1.0e-8	.00226667
1.9	.00904611	380.278	.0144661	5.39849	.0001	1.0e-8	.00299552
2.0	.0117591	302.285	.0186674	6.86739	.102	3.3743e-4	.0038866
2.2	.0187575	211.107	.0293085	10.01652	.0001	1.0e-8	.00617673
2.5	.0332238	145.409	.0505872	15.0588	.0001	1.0e-8	.0108828
3.0	.0668013	99.564	.0973200	23.7873	.124	1.2454e-3	.0217128
3.5	.109117	79.5194	.152306	32.4570	.0001	1.0e-8	.0352400

Mehta appendages (10% thick, 0 deg. angle of attack)

n	BF	d(V/Uref)/d(S/C)o	ave. vort. str.	VTP	Gamma	G/dV/dS	rhole/C
1.5	.00177800	997.312	.00311492	1.65820	.076	7.6205e-5	.00122342
1.7	.00386479	378.020	.00669791	4.68615	.0001	1.0e-8	.00266154
1.8	.00557815	265.324	.00962287	6.59602	.0001	1.0e-8	.00383466
1.9	.00784436	198.335	.0134593	8.69654	.0001	1.0e-8	.00538276
2.0	.0107324	155.745	.0182997	10.9562	.102	6.55e-4	.00735104
2.2	.0185901	107.118	.0312528	15.8482	.0001	1.0e-8	.012687
2.5	.0360552	72.9092	.0592239	23.8528	.0001	1.0e-8	.0244796
3.0	.0885042	49.4740	.137765	38.1035	.124	2.5064e-3	.0541469
3.5	.155162	39.3555	.232173	52.6940	.0001	1.0e-8	.0942971

Mehta appendages (10% thick, 12 deg. angle of attack)

n	BF	d(V/Uref)/d(S/C)o	ave. vort. str.	VTP	Gamma	G/dV/dS	rhole/C
2.0	.0107324	14.0409	.0203631	100)	.102	1.0e-8	.00735104
2.5	.0360552	13.2468	.0697550	1000	.0001	1.0e-8	.0244796
3.0	.0885042	17.1085	.157409	1000	.124	1.0e-8	.0541469
3.5	.155162	16.1884	.281178	1000	.0001	1.0e-8	.0942971

Sand 1850 section

BF	d(V/Uref)/d(S/C)o	ave. vort. str.	VTP	rhole/C
.0132594	116.567	.0254399	134.168	.00904039
at 12 degrees AOA				
.0132594	10.8357	.0265676	5.47818	.00904039

NACA appendages (0 deg. angle of attack)

ID	BF	d(V/Uref)/d(S/C)o	ave. vort. str.	VTP	rhole/C
0006	.0102643	254.638	.0187964	86.5650	.00525416
0009	.0161689	142.179	.0292247	140.193	.00859113
0012	.0286892	87.8263	.0502008	220.685	.0142638
0015	.0452494	59.1695	.0761781	328.404	.0210323
0018	.0713588	42.7751	.115218	464.314	.0309974
0024	.144320	25.8816	.231'0	840.104	.0547926

NACA appendages (12 deg angle of attack)

ID	BF	d(V/Uref)/d(S/C)o	ave. vort. str.	VTP	rhole/C
0006	.0102643	11.9686	.0213268	-8.28003	.00525416
0009	.0161689	13.6685	.0314099	5.10029	.00859113
0012	.0286892	15.5696	.0510680	-8.52875	.0142638
0015	.0452494	13.1528	.0803768	-7.86633	.0210323
0018	.0713588	14.4878	.115761	-2.13589	.0309974
0024	.144320	12.8868	.213215	-11.3552	.0547926

J. Shin 4:1 elliptic appendage (n = 2.0)

BF	d(V/Uref)/d(S/C)o	ave. vort. str.	VTP	rhole/C
.0429412	53.8657	.0749548	397.908	.023866
at 12 degrees aoa				
.0429412	12.2378	.0777543	-9.91513	.023866

J. Shin 4:1 wedge elliptic appendage (n = 1.5)

BF	d(V/Uref)/d(S/C)o	ave. vort. str.	VTP	rhole/C
.00258427	885.798	.00531556	1.74629	.00149406

Circular nose appendage (teardrop)

BF	d(V/Uref)/d(S/C)o	ave. vort. str.	VTP	rhole/C
1.07089	9.18305	1.13362	73.6825	.210591
at 12 degrees aoa				
1.07089	8.66207	1.09447	-27.5522	.210591